frontiers | Research Topics

Mechanisms and ecology of suspended-particle capture in marine systems

Edited by
Jeff Shimeta, Marco Ghisalberti, Nicole Rita Posth and Stuart Humphries

Published in
Frontiers in Marine Science

ISSN 1664-8714
ISBN 978-2-8325-5980-2
DOI 10.3389/978-2-8325-5980-2

About Frontiers

Frontiers is more than just an open access publisher of scholarly articles: it is a pioneering approach to the world of academia, radically improving the way scholarly research is managed. The grand vision of Frontiers is a world where all people have an equal opportunity to seek, share and generate knowledge. Frontiers provides immediate and permanent online open access to all its publications, but this alone is not enough to realize our grand goals.

Frontiers journal series

The Frontiers journal series is a multi-tier and interdisciplinary set of open-access, online journals, promising a paradigm shift from the current review, selection and dissemination processes in academic publishing. All Frontiers journals are driven by researchers for researchers; therefore, they constitute a service to the scholarly community. At the same time, the *Frontiers journal series* operates on a revolutionary invention, the tiered publishing system, initially addressing specific communities of scholars, and gradually climbing up to broader public understanding, thus serving the interests of the lay society, too.

Dedication to quality

Each Frontiers article is a landmark of the highest quality, thanks to genuinely collaborative interactions between authors and review editors, who include some of the world's best academicians. Research must be certified by peers before entering a stream of knowledge that may eventually reach the public - and shape society; therefore, Frontiers only applies the most rigorous and unbiased reviews. Frontiers revolutionizes research publishing by freely delivering the most outstanding research, evaluated with no bias from both the academic and social point of view. By applying the most advanced information technologies, Frontiers is catapulting scholarly publishing into a new generation.

What are Frontiers Research Topics?

Frontiers Research Topics are very popular trademarks of the *Frontiers journals series*: they are collections of at least ten articles, all centered on a particular subject. With their unique mix of varied contributions from Original Research to Review Articles, Frontiers Research Topics unify the most influential researchers, the latest key findings and historical advances in a hot research area.

Find out more on how to host your own Frontiers Research Topic or contribute to one as an author by contacting the Frontiers editorial office: frontiersin.org/about/contact

Mechanisms and ecology of suspended-particle capture in marine systems

Topic editors

Jeff Shimeta — RMIT University, Australia

Marco Ghisalberti — University of Western Australia, Australia

Nicole Rita Posth — University of Copenhagen, Denmark

Stuart Humphries — University of Lincoln, United Kingdom

Citation

Shimeta, J., Ghisalberti, M., Posth, N. R., Humphries, S., eds. (2025). *Mechanisms and ecology of suspended-particle capture in marine systems*. Lausanne: Frontiers Media SA. doi: 10.3389/978-2-8325-5980-2

Table of contents

frontiers | Frontiers in Marine Science

TYPE Editorial
PUBLISHED 19 November 2024
DOI 10.3389/fmars.2024.1521561

OPEN ACCESS

EDITED AND REVIEWED BY
Stelios Katsanevakis,
University of the Aegean, Greece

*CORRESPONDENCE
Jeff Shimeta
jeff.shimeta@rmit.edu.au

RECEIVED 02 November 2024
ACCEPTED 08 November 2024
PUBLISHED 19 November 2024

CITATION
Shimeta J, Ghisalberti M, Posth NR and Humphries S (2024) Editorial: Mechanisms and ecology of suspended-particle capture in marine systems.
Front. Mar. Sci. 11:1521561.
doi: 10.3389/fmars.2024.1521561

Editorial: Mechanisms and ecology of suspended-particle capture in marine systems

Jeff Shimeta[1]*, Marco Ghisalberti[2], Nicole Rita Posth[3] and Stuart Humphries[4]

[1]School of Science, RMIT University, Melbourne, VIC, Australia, [2]School of Engineering, University of Western Australia, Perth, WA, Australia, [3]Department of Geosciences and Natural Resource Management, University of Copenhagen, Frederiksberg, Denmark, [4]Lincoln Institute for Advanced Studies, University of Lincoln, Lincoln, United Kingdom

KEYWORDS

particle capture, marine systems, microplastics, nanoplastics, particle aggregation, filter feeding, suspension feeding, larval settlement

Editorial on the Research Topic
Mechanisms and ecology of suspended-particle capture in marine systems

The movements of water and suspended particles (inert or alive) are among the most fundamental dynamical aspects of oceans, underlying numerous biological, physical, chemical, and geological processes. The mechanisms by which particles make contact with and adhere to surfaces are major determinants of animal feeding, trophic interactions, larval and propagule settlement, seagrass pollination, viral infection, microbe-mineral interaction, fates of microplastics, particle aggregation, sediment deposition, and more. Research in all these areas is united by the need to understand fundamental aspects of hydrodynamics and particle dynamics that drive contact of particles with surfaces or with each other, and factors that constrain the net capture of particles. Suspended particle capture is a rich, interdisciplinary field of study, drawing on fluid and particle dynamics, filtration theory, cell and animal behaviour, surface chemistry, and modelling and experimentation with marine organisms.

The papers in this Research Topic review and present advances on the diverse topics of particle capture by suspension feeding in marine animals from invertebrates to fishes and whales; hydromechanics of and around feeding structures; the roles of predator and prey behaviours in feeding interactions; and hydromechanics of sediment deposition in marine vegetation canopies.

Comprehensive reviews by Sanderson and Werth and Potvin critically evaluate recent progress in understanding particle-capture mechanisms in suspension-feeding fishes and baleen whales, respectively, focusing on improved understanding of morphology-flow interactions and key emerging directions for future research. Sanderson presents the first literature synthesis on the particle separation mechanisms of marine, estuarine, and freshwater suspension-feeding fishes. The review addresses eight particle separation mechanisms in fishes, identifies key unresolved questions, enables comparisons with invertebrate suspension-feeding processes and offers perspectives on future research priorities. Werth and Potvin focus on baleen filter feeding and explain how recent

advances have expanded our understanding of this process. Such advances challenge the view of baleen as a static sieve and recognize: (i) the mechanism of cross-flow filtration, (ii) the flow-dependence of the filter porosity, and (iii) the biomechanical complexity and variation of the baleen metafilter.

The reviews of vertebrate feeding are extended by the experimental study of Hamann et al., which elucidates mechanisms of cross-flow and dead-end filtration in the gill arch system of diverse ram-feeding fish species. The results reveal how the morphologies of gill rakers and denticles constrain fluid flow and ultimately particle retention, explaining important aspects of feeding ecology and suggesting biomimetic applications to filtration engineering in non-biological systems.

Three papers continue on the theme of fish feeding with experimental studies of zooplankton capture by both swimming and anchored fishes. In all three, flow is shown to be a significant determinant of capture success. Genin et al. show that for coral-reef fishes, capture efficiency declines with increasing flow speed due to reduced manoeuvrability, as the fish orient more narrowly head-on into the flow, and that high prey density and low flow lead to higher capture rates. Ella and Genin further show that site-attached coral reef fishes adjust their strike dynamics based on the flow speed and prey path, suggesting that they assess the prey's drifting speed and path to effectively intercept them. Responses from strongly anchored garden eels (*Gorgasia sillneri*) are compared to Genin et al.'s results by Khrizman et al. Garden eels show a qualitatively similar response but with lower efficiency, presumably due to a fixed location and limited manoeuvrability.

Two experimental papers address particle capture by cylindrical collectors: Beaudry and Cameron on the capture of oil droplets by polychaete feeding structures, and Sewak et al. on the role of mechanical flexibility of morphological structures in hydromechanics and particle capture. Beaudry and Cameron present evidence that oil droplets behave essentially as solid particles in terms of capture, with direct interception and sieving driving most droplet capture. Neither species of polychaete appears to show much selectivity based on oil type, suggesting mechanical processes dominate. Sewak et al. demonstrate that the flexibility of particle collectors can impact their ability to capture suspended particles when large-scale vortex-induced oscillations of the collector are generated. Many aquatic biological collectors have significant flexibility; their capture efficiency may indeed be underpredicted by modelling approaches that assume a rigid collector.

Finally, Deitrick et al. also experiment with biological morphology that influences flow and particle separation, in this case for vegetation canopies such as mangrove pneumatophores that generate turbulence which influences sediment deposition. With a combination of modelling and flume experiments, they found that the turbulence reduces local sediment deposition, which can increase the distance that sediment travels into a mangrove forest.

These papers are united by applying fundamental aspects of fluid dynamics, particle dynamics, and fluid-morphology interactions to make advances in predictive understanding of particle capture processes. They furthermore illustrate the cross-discipline inspiration potential of these principles across a wide range of ecological systems, as well as potential bioinspired applications in engineered systems.

Author contributions

JS: Writing – review & editing, Writing – original draft, Conceptualization. MG: Writing – review & editing, Writing – original draft, Conceptualization. NP: Writing – review & editing, Conceptualization. SH: Writing – review & editing, Writing – original draft, Conceptualization.

Conflict of interest

The authors declare that the research was conducted in the absence of any commercial or financial relationships that could be construed as a potential conflict of interest.

The author(s) declared that they were an editorial board member of Frontiers, at the time of submission. This had no impact on the peer review process and the final decision.

Publisher's note

frontiers | Frontiers in Marine Science

TYPE Original Research
PUBLISHED 10 October 2023
DOI 10.3389/fmars.2023.1266241

OPEN ACCESS

EDITED BY
Jeff Shimeta,
RMIT University, Australia

REVIEWED BY
Pallav Ranjan,
University of Illinois at Urbana-Champaign, United States
Masaya Yoshikai,
University of Waikato, New Zealand
Tracy Mandel,
University of New Hampshire, United States

*CORRESPONDENCE
Autumn R. Deitrick
autumnd@alum.mit.edu

RECEIVED 24 July 2023
ACCEPTED 22 September 2023
PUBLISHED 10 October 2023

CITATION
Deitrick AR, Hovendon EH, Ralston DK and Nepf H (2023) The influence of vegetation-generated turbulence on deposition in emergent canopies. *Front. Mar. Sci.* 10:1266241. doi: 10.3389/fmars.2023.1266241

The influence of vegetation-generated turbulence on deposition in emergent canopies

Autumn R. Deitrick[1,2*], Erin H. Hovendon[1], David K. Ralston[3] and Heidi Nepf[1]

[1]Department of Civil and Environmental Engineering, Massachusetts Institute of Technology, Cambridge, MA, United States, [2]MIT-WHOI Joint Program in Oceanography/Applied Ocean Science and Engineering, Cambridge and Woods Hole, MA, United States, [3]Department of Applied Ocean Physics and Engineering, Woods Hole Oceanographic Institution, Woods Hole, MA, United States

Laboratory experiments measured sediment deposition and turbulent kinetic energy (TKE) in bare and vegetated channels. The model vegetation represented a mangrove pneumatophore canopy. Three solid volume fractions were considered (ϕ = 0.01, 0.02, and 0.04). For the same channel-averaged velocity, the vegetated region had elevated near-bed TKE compared to the bare region. Net deposition in both regions was measured by adding a sediment slurry of 11-micron solid glass spheres to the flume and collecting the deposited sediment from the flume baseboards after a 4-hr experiment. The elevated near-bed TKE in the vegetated region resulted in lower deposition compared to the bare region. A model for deposition probability written in terms of near-bed TKE (TKE model) more accurately predicted the measured deposition than a model based on bed shear stress (τ_b model). Application of the model to field conditions suggested that, by inhibiting deposition, vegetation-generated TKE facilitates the delivery of sediment farther into the mangrove forest than would be achieved without vegetation-generated TKE.

KEYWORDS

mangroves, pneumatophores, sediment, deposition, turbulence

1 Introduction

As one of the most productive ecosystems on earth, mangroves provide a variety of ecosystem services with environmental and economic benefits (Nellemann et al., 2009; Barbier et al., 2011; de Groot et al., 2012). Mangroves can protect coastal communities from storm surge events by dissipating energy from waves and currents with their above-ground biomass (e.g., branches, leaves, and aerial roots) (Mazda et al., 1997; Mazda et al., 2006; Vo-Luong and Massel, 2008; Horstman et al., 2014). Energy dissipation by mangrove forests also creates shelter for many aquatic species and supports fisheries, which provide jobs and food for millions of people (Barbier et al., 2011; Hutchison et al., 2014).

On a global scale, mangroves provide an important mechanism for mitigating climate change by trapping and sequestering carbon-rich sediment in their soils (Mcleod et al.,

2011; Twilley et al., 2017; Kauffman et al., 2020) at a rate of 200 g C m^{-2} $year^{-1}$ (Temmink et al., 2022). Despite occupying only 0.5% of the global coastal area, mangroves store 10-15% of total coastal carbon (Alongi, 2014) and have a carbon density of 900 Mg C ha^{-1} (Temmink et al., 2022). The mangrove carbon budget is comprised of carbon-rich sediment from autochthonous (i.e., produced *in situ* by the mangrove) and allochthonous (i.e., produced outside the forest) sources (Woodroffe et al., 2016). Allochthonous sediment enters the forest via tidal inundation or storm surge events, and it is the ability of mangroves to trap this sediment that makes them such a significant carbon sink (Jennerjahn and Ittekkot, 2002; Adame and Lovelock, 2011; Woodroffe et al., 2016).

Above-ground biomass, including mangrove pneumatophores (i.e., vertical aerial root structures, Figure 1), creates conditions that facilitate deposition by enhancing drag and slowing currents near the bed (Furukawa and Wolanski, 1996; Horstman et al., 2017; Mullarney et al., 2017b). However, mangrove pneumatophores also generate root-scale turbulence that enhances turbulent kinetic energy (TKE), which can promote sediment resuspension and lead to erosion (Mullarney et al., 2017a; Norris et al., 2017; Norris et al., 2019; Norris et al., 2021). Because of the competing effects of velocity reduction and turbulence enhancement, the relationship between vegetation density and sediment stability is not straightforward (Fagherazzi et al., 2017; Mullarney et al., 2017a; Xu et al., 2022a). Understanding how pneumatophore roots impact the balance of the competing processes of deposition and erosion is critical for improving the assessment of sediment retention and carbon storage in mangrove forests.

The rate of net deposition $\left(\frac{dm}{dt}\right)$ can be described in terms of a deposition probability,

$$\frac{dm}{dt} = pw_sC \tag{1}$$

in which m is the net mass deposited per bed area over time t , p is the probability that particles reaching the bed will remain deposited, w_s is the settling velocity, and C is the near-bed suspended sediment concentration in a vertically mixed system. In Equation 1, the probability p captures the influence of resuspension on mass accumulation. In the absence of resuspension, there is pure deposition ($p = 1$). When resuspension is present, $p < 1$. Engelund and Fredsøe (1976) developed a model to predict the probability (p') that a particle on the bed is put in motion by the bed shear stress, and Zong and Nepf (2010) used this to describe the probability that a particle remains at the bed, $p = 1 - p'$.

$$p = 1 - \left[1 + \left(\frac{\beta\ \pi}{6(\theta-\theta_c)}\right)^4\right]^{-\frac{1}{4}}. \tag{2}$$

β is a bed friction coefficient, which we set to $\beta = 1$. θ is the dimensionless shear stress (Shields parameter),

$$\theta = \frac{\tau_b}{(\rho_s-\rho)gd_s} \tag{3}$$

in which τ_b is the bed shear stress, ρ_s is the sediment density, ρ is the water density, g is the gravitational acceleration, and d_s is the particle diameter. The Shields parameter is a ratio of destabilizing (time-mean stress) and stabilizing (grain weight) forces acting on a single grain. The critical Shields parameter (θ_c) is defined by the critical bed shear stress ($\tau_{b,c}$) needed to initiate sediment motion. When $\theta < \theta_c$, $p = 1$, indicating pure deposition. When, $\theta \leq \theta_c$ $p < 1$, indicating the presence of resuspension.

In vegetated systems, vegetation-generated turbulence enhances resuspension by two means: (1) mixing momentum toward the bed, which enhances τ_b (Liu et al., 2008; Conde-Frias et al., 2023) and (2) directly interacting with the bed and mobilizing sediment with enhanced instantaneous shear and normal stress (e.g., Xu et al., 2022b). Many previous studies have described the importance of instantaneous forces (both lift and stress) associated with turbulence in mobilizing sediment grains (e.g., Bagnold, 1941; Nino and Garcia, 1996; Zanke, 2003; Smart and Habersack, 2007; Diplas et al., 2008). Sediment transport models written in terms of bed shear stress (Equation 2) have yielded inaccurate predictions for vegetated systems, because they do not account for vegetation-generated turbulence (Yang et al., 2016; Tinoco and Coco, 2018; Yang and Nepf, 2018; Liu et al., 2022). Yang et al. (2016) and Tinoco and Coco (2018) found that near-bed TKE ($k_{t(\mathrm{nb})}$) is a better predictor of sediment motion in vegetated systems. Therefore, we hypothesized that Equation 2 might better predict deposition in vegetated systems if it were recast in terms of ($k_{t(\mathrm{nb})}$),

$$p = 1 - \left[1 + \left(\frac{\pi}{6(\theta_{k_t}-\theta_{k_{t,c}})}\right)^4\right]^{-\frac{1}{4}}. \tag{4}$$

In bare channels, near-bed TKE is generated by the bed shear, such that bed shear stress and TKE are linearly related ($\tau_b = \rho\omega k_{t(\mathrm{nb})}$, with $\omega = 0.2$, Soulsby, 1981). This relation suggests a method for redefining the critical Shields parameter (Equation 3) in terms of TKE,

$$\theta_{k_t} = \frac{\rho\omega k_{t(\mathrm{nb})}}{(\rho_s-\rho)gd_s} \tag{5}$$

with $\theta_{k_{t,c}}$ defined by the critical near-bed TKE ($k_{t,c}$) needed to initiate sediment resuspension (Zhao and Nepf, 2021; Liu et al., 2022). Rewriting the Shields parameter in terms of TKE respects the original physical meaning, but expands the understanding of the destabilizing forces to include the effects of turbulence (e.g., Tinoco and Coco, 2018). Because the critical level of turbulence is the same

FIGURE 1
Black mangrove (*Avicennia germinans*) pneumatophores with mean diameter 1.0 ± 0.2 cm.

in vegetated and bare channels (Yang et al., 2016), the critical turbulence level can be inferred from bare bed conditions. Specifically, $k_{t,c} = \tau_{b,c}/\rho\omega$, such that $\theta_{k_{t,c}} = \theta_c$.

Liu et al. (2022) used Equation 4 to predict deposition within a model canopy of *Phragmites australis*, which has a morphology consisting of a central stem surrounded by multiple leaves. Good agreement was achieved in Case 4 (Figure 8 in Liu et al., 2022), but agreement was not as good for other cases (Figure 5 in Liu et al., 2022). The robustness of the deposition model was not discussed in a systematic way across flow conditions. Further, no bare bed conditions were examined. In contrast, the present study systematically considered paired vegetated and bare bed conditions across the same range of velocity, and also extended to higher values of solid volume fraction. This facilitated a more detailed description of the parameter range over which the model may be successfully applied. Advancing existing deposition models will help to improve the modeling of sediment transport in mangrove systems and facilitate the assessment of sediment and carbon retention.

2 Materials and methods

Experiments were conducted in a recirculating Plexiglas flume with a 283 cm x 20 cm x 39 cm working section (dashed black outline in Figure 2). Plexiglas inserts (gray in Figure 2) were used to constrict the test section width to 20 cm. The water depth measured at the downstream end of the test section was $H = 10$ cm, which is within depth ranges typically observed in mangrove forests (Furukawa and Wolanski, 1996; Norris et al., 2021). A sharp-crested weir ($h = 5$ cm) located at the downstream end of the flume was used to fix the water depth.

Rigid vegetation, like pneumatophores, has been modeled using cylindrical dowels in several laboratory studies (Zong and Nepf, 2010; Yang et al., 2016; Tinoco and Coco, 2018; Liu et al., 2021). In this study, 0.8-cm diameter (d) PVC dowels were used to represent pneumatophores. The dowels were screwed into a PVC board that was inverted and inserted downward into the channel until the dowels just touched the bed. This allowed the dowels to be easily removed at the end of the experiment without disturbing the deposited sediment (Figure 2). In the field, pneumatophore canopies are spatially heterogeneous, and the pneumatophores vary in diameter (0.5 to 2 cm), height (1 to 30 cm), and solid volume fraction ($\phi = \frac{\pi}{4} nd^2 = 0.005$ to 0.04, in which n is roots per bed area) (Tomlinson, 2016; Yando et al., 2016; Norris et al., 2017; Norris et al., 2021). Three solid volume fractions were considered in this study: $\phi = 0.01$, 0.02, and 0.04. The positions of the dowels within the dowel array boards were determined using a random array generator code (MATLAB).

To characterize the flow field, a Nortek Vectrino recorded instantaneous velocity components in the streamwise ($u(t)$), lateral ($v(t)$), and vertical ($w(t)$) directions in both the bare and vegetated test sections. Four channel-averaged velocities (U_o) were considered (Table 1). These velocities spanned a typical range of flow conditions observed within mangrove forests (Furukawa and Wolanski, 1996; Norris et al., 2021). Velocity was measured at multiple locations across the flume at $z = 0.5$ cm (near-bed) elevation for each channel-averaged velocity. Due to the short length of the flume, the flow was not fully developed in the bare test section, so that both wall- and bed-boundary layers were small compared to the flume width and depth. However, due to the channel constriction (Figure 2), the velocity changed 10 to 20% across the bare test-section width. This variation was captured by a five-point lateral profile in the bare section. Within the dowel array, the velocity varied at the scale of the dowel, but the laterally-averaged conditions were fully developed after just a few cylinder rows. To capture the spatial heterogeneity in the dowel array, the lateral profile included 15 positions. At each position, the velocity was measured at 200 Hz for 60 s. Tests with longer records confirmed that 60 s was sufficient to capture the mean and turbulent velocity statistics.

To estimate depth-averaged velocity, a profile was constructed from measurements at 0.5-cm increments from $z = 0.5$ to 4.5 cm at a lateral position that was closest to the laterally averaged near-bed velocity. The vertical profile in the bare test section was used to calculate U_o. Each velocity record was decomposed into time-averaged ($\bar{u}, \bar{v}, \bar{w}$) and fluctuating ($u'(t), v'(t), w'(t)$) components and processed using the Goring and Nikora (2002) method to remove

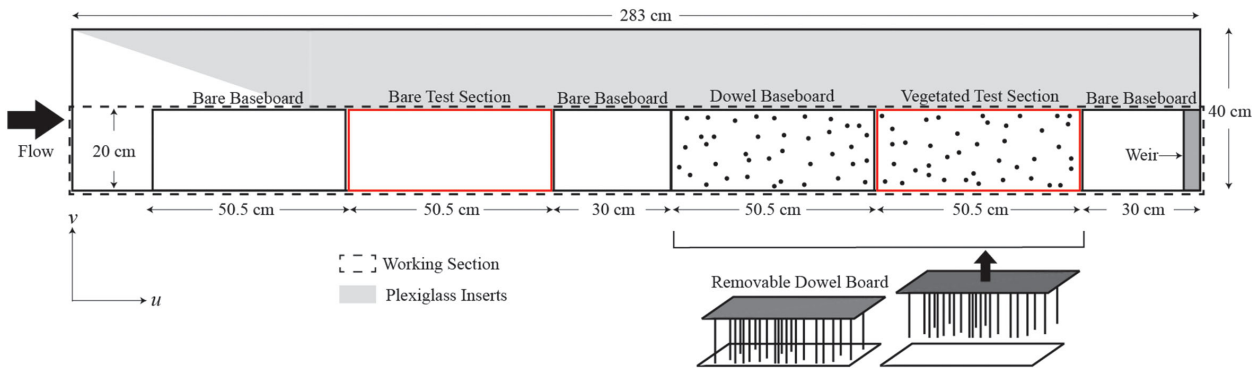

FIGURE 2
Top view of channel. Plexiglass inserts (gray shading) constricted the test section to 20-cm width. Deposition was measured on the baseboards shown with a red outline.

TABLE 1 Measured velocity and turbulent kinetic energy.

			ϕ = 0.01	ϕ = 0.02	ϕ = 0.04
Case	U_o (cm/s)	$k_{t,b(\mathrm{nb})}$ (cm^2/s^2)	$k_{t,v(\mathrm{nb})}$ (cm^2/s^2)	$k_{t,v(\mathrm{nb})}$ (cm^2/s^2)	$k_{t,v(\mathrm{nb})}$ (cm^2/s^2)
1	4.39 ± 0.11	0.80 ± 0.19*	0.73 ± 0.10*	1.84 ± 0.19*	1.91 ± 0.19*
2	8.78 ± 0.18	1.6 ± 0.3*	2.8 ± 0.3*	4.4 ± 0.4	4.1 ± 0.3
3	17.3 ± 0.3	3.5 ± 0.4	7.7 ± 0.5	10.3 ± 0.9	15.1 ± 1.0
4	21.7 ± 0.3	4.6 ± 0.3	11.6 ± 0.9	16.8 ± 1.6	19.6 ± 1.4

Uncertainty is based on standard error among the multiple measurement positions. Asterisks indicate conditions for which the near-bed TKE is less than the critical TKE for resuspension ($k_{t(\mathrm{nb})} < k_{t,c}$ = 2.6 cm^{2}s^{-2}).

spikes. The acceleration and velocity variance threshold parameters for this method were set to $\lambda = 1$ and $k = 1.5$, respectively. Turbulent kinetic energy per fluid mass is $k_t = \frac{1}{2}(\overline{u'^2} + \overline{v'^2} + \overline{w'^2})$. Near-bed laterally averaged TKE was calculated for the bare ($k_{t,b(\mathrm{nb})}$) and vegetated ($k_{t,v(\mathrm{nb})}$) test sections using measurements at z = 0.5 cm (Table 1). Velocity measurements were made separately from the deposition experiments to avoid disturbances to the water column that could impact deposition.

The experiments used solid glass spheres with diameter d_s = 11 µm and density ρ_s = 2500 kg/m^3, which were selected based on grain size measured at field sites in a black mangrove forest (O(10µm)[1]). Deposition experiments began by weighing 16.3 g of glass spheres, adding them to a 1 L container with water and surfactant (Windex® Original Glass Cleaner was added to help the sediment slurry mix with the water), and shaking the container vigorously. This mass of glass spheres was chosen to achieve an initial concentration of $C \approx 20$ mg/L throughout the flume, which is within the range of suspended sediment concentrations observed in mangrove forests (Furukawa et al., 1997; Horstman et al., 2017). The non-cohesive sediment mixture was poured across the width of the tail tank, and the recirculating pump mixed the sediment and water into a uniform concentration. Each deposition experiment ran for 4 hrs. The methodology for these deposition experiments was adapted from Zong and Nepf (2010) and Liu et al. (2022).

An optical backscatter sensor (OBS, Seapoint Sensors, Inc.) was used to measure the evolution of C over the duration of the experiment (Supplementary Section 1). The OBS (20 Hz sampling rate) was located at the upstream end of the first bare baseboard and positioned at mid-depth. Preliminary studies confirmed that throughout an experiment C was the same at the upstream and downstream end of the flume, so only one OBS was needed to measure C. This reflected the fact that the time-scale over which deposition occurred (hours) was much longer than the time-scale of mixing (minutes), with complete mixing occurring each time water passed through the pumps. Therefore, the concentration remained uniform in the test section, even as it declined due to deposition. The OBS output voltage was calibrated using prepared concentrations ranging from 0 to 44 mg/L (Supplementary Section 2).

After 4 hrs, the flume was left to slowly drain for 1 hr. Using the methodology discussed in Zhang et al. (2020), we found that the flume draining period had a negligible impact on the deposition pattern, and negligible additional deposition occurred during this time, consistent with the low C at the end of the experiment. The baseboards were left to dry in the flume for 1 day. Once the baseboards were dry, the dowels were carefully lifted off the baseboards, and the bare and vegetated test section baseboards (red outline in Figure 2) were carefully removed from the flume with gloves. An acetate template was placed over each board and secured with clips. This template divided the board into three 15 cm x 15 cm windows.

Three glass fiber filters (0.7-µm pore size, 47-mm diameter) were weighed in advance, lightly wet with water, and then used to wipe the sediment off the baseboard within each window (9 filters total). Tests with additional filters indicated that using three filters was sufficient. Adding a fourth filter increased the mass by only 6%. The filters were dried in a 60°C oven for 4 hrs, which was sufficient for the filters to reach a constant weight. After drying, the filters were reweighed, and the average net deposition per bed area for the bare (m_{bare}) and vegetated (m_{veg}) test sections was calculated. The uncertainty in mass deposition predominantly came from the variation among the three windows of each test section.

The deposition probability was estimated by rearranging and integrating Equation 1 over the experiment duration, T,

$$p = \frac{m}{w_s \int_0^T C dt}. \tag{6}$$

Using Equation 6, the deposition probability in the bare (p_{bare}) and vegetated (p_{veg}) test sections were estimated using the mass deposited in each section, $m_{\mathrm{bare}}$and m_{veg}, respectively. Based on Equation 1, $C(t)$should follow an exponential decay with rate constant $-pw_s$. So, it was reasonable to smooth the concentration record by fitting the form $C = C_o e^{-bt}$with initial concentration C_o and constant b. Because the flume was a closed system, the temporal change in C was due only to deposition. The fitted concentration record was used in Equation 6 (Supplementary Section 3).

The bed shear stress in the vegetated region ($\tau_{b,v}$) was estimated using Equation 7, developed by Conde-Frias et al. (2023), that

1 Deitrick, A. R., Ralston, D. K., Baustian, M. M., Esposito, C. R., Beltrán-Burgos, M., Courtois, A. J., et al. (2023) Cohesive sediment erosion within mangrove pneumatophores, Submitted.

describes the enhancement of bed shear stress by turbulence generated from rigid, emergent vegetation,

$$\tau_{b,v} = \rho\left(\max\left(K\sqrt{\frac{k_{t,v(\mathrm{nb})}}{Re_d}},\ \sqrt{C_f}U_o\right)\right)^2 \quad (7)$$

in which $K = 9.5 \pm 0.4$ is a scale constant. $Re_d = \frac{U_o d}{\nu(1-\phi)}$ is the stem Reynolds number, in which ν is the kinematic viscosity of water. $C_f = 0.002$ is the bed friction coefficient (Supplementary Section 4). In the bare test section, $\tau_b = \rho C_f U_o^2$ was used to estimate bed shear stress. Conde-Frias et al. (2023) validated Equation 7 against data and simulations with $\phi = 0.016$ to 0.25 and Re_p up to 1300 (Table 2 in Conde-Frias et al. (2023)), which spans similar conditions examined in this study. Uncertainty was propagated for all calculations using the constant odds combination method described in Kline and McClintock (1953).

The critical Shields parameter was used to estimate the critical bed shear stress and critical turbulence threshold for resuspension (Zhao and Nepf, 2021). From Julien (2010),

$$\theta_c = 0.25 d_\star^{-0.6} \tan(\phi_R) = 0.32 \quad (8)$$

in which ϕ_R is the angle of repose. For the d_s used in this study, ϕ_R is 30°. $d_\star$ is the dimensionless particle diameter,

$$d_\star = \left(\frac{(\rho_s-\rho)g}{\rho\nu^2}\right)^{\frac{1}{3}} d_s\ . \quad (9)$$

Equation 8 applies for $d_\star = 0.3$ to 1.9. Using the parameters from this study, the critical bed shear stress and critical near-bed TKE were

$$\tau_{b,c} = \theta_c(\rho_s - \rho)g d_s = 0.52\,\frac{\mathrm{g}}{\mathrm{cm{\cdot}s^2}}, \quad (10)$$

$$k_{t,c} = \frac{\tau_{b,c}}{\rho\omega} = 2.6\,\frac{\mathrm{cm}^2}{\mathrm{s}^2}\ . \quad (11)$$

In the bare test section, $k_{t,b(\mathrm{nb})} < k_{t,c}$ (and $\tau_b < \tau_{b,c}$) for the lower velocity Cases 1 and 2 (Table 1). Therefore, the bare test section was considered to be purely depositional ($p = 1$)for these cases, from which Equation 6 can be used to estimate the settling velocity, $\overline{w_s} =$ 0.0038 ±0.0003 cm/s. This was consistent with Zong and Nepf (2010), who found $w_s = 0.004 \pm 0.002$ cm/s for solid glass spheres from the same manufacturer and of the same d and ρ_s as used in this study. The estimated settling velocity was in reasonable agreement with Stokes' Law (Stokes, 1851), $w_s = \frac{g\left(\frac{\rho_s}{\rho}-1\right)d_s^2}{18\nu} = 0.010$ cm/s, given that the manufacturer's specifications included a range of diameters (10% finer: $d_s = 3$ µm; 90% finer: 15 µm). Using Stokes' Law, $\overline{w_s} =$ 0.0038 cm/s suggested a mean diameter of $d_s = 7$ µm. The value of $\overline{w_s}$ estimated from Case 1 and 2 bare test section data was subsequently used in Equation 6 to solve for the deposition probability p in all other cases.

3 Results

For the same channel-averaged velocity, the vegetated test section had elevated TKE compared to the bare test section (Figure 3A). As TKE increased, resuspension increased, which was reflected in lower net deposition in the vegetated test section relative to the bare test section at the same channel-averaged velocity (Figure 3B). At the lowest velocity, all three vegetation densities produced $m_{\mathrm{veg}}/m_{\mathrm{bare}} = 1$ (Figure 3B). This was also observed for $\phi = 0.01$ at the second velocity setting. For each of these cases, the near-bed turbulence was, within uncertainty, less than or equal to $k_{t,c} = 2.6\mathrm{cm}^2/\mathrm{s}^2$ (marked with asterisks in Table 1), confirming the predicted value of $k_{t,c}$ (Equation 11).

For both vegetated and bare test conditions, when $k_{t(\mathrm{nb})} \leq k_{t,c} = 2.6\ \mathrm{cm}^2/\mathrm{s}^2$, the deposition probability (p) (Equation 6) was 1 within uncertainty, and when $k_{t(\mathrm{nb})} > k_{t,c} = 2.6\ \mathrm{cm}^2/\mathrm{s}^2$, p decreased with increasing $k_{t(\mathrm{nb})}$ (Figure 4A). Furthermore, test cases with bare beds (open circles) and arrays of different solid volume fractions (triangles) collapsed to the same trend when plotted versus $k_{t(\mathrm{nb})}$, consistent with the TKE adaptation of the Engelund and Fredsøe

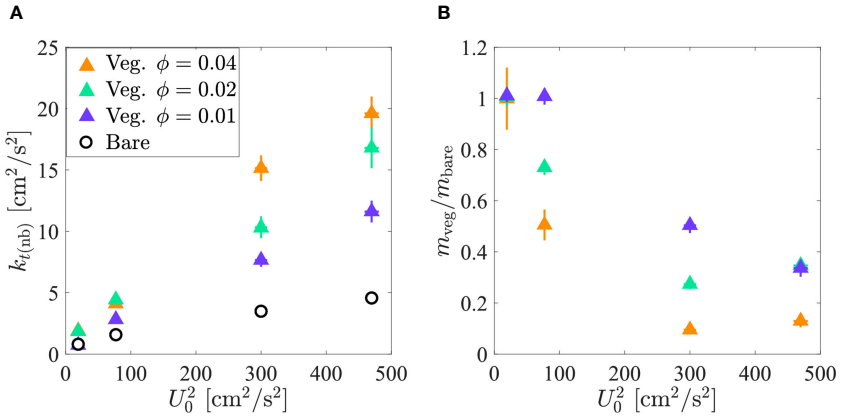

FIGURE 3
(A) Near-bed TKE in the bare (open black circles) and vegetated (triangles: $\phi = 0.01$ (purple), $\phi = 0.02$ (green), $\phi = 0.04$ (orange)) test sections versus channel-averaged velocity squared. **(B)** Net deposition in the vegetated test section (m_{veg}) normalized by net deposition in the bare test section (m_{bare}) versus channel-averaged velocity squared. At the lowest velocity, the three vegetated test section cases overlap. Standard error is shown by horizontal and vertical bars. In some instances, the error bars are contained within the size of the symbol. m_{veg} and m_{bare} data can be found in Supplementary Section 3.

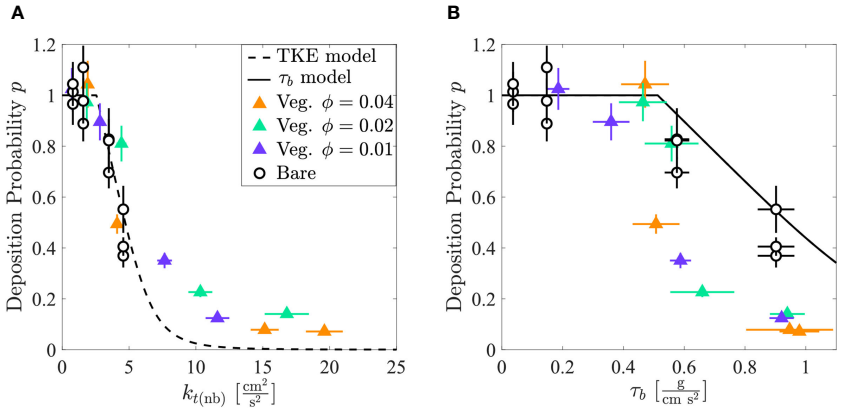

FIGURE 4
(A) Deposition probability in the bare (open black circles) and vegetated (triangles: ϕ = 0.01 (purple), ϕ = 0.02 (green), and ϕ = 0.04 (orange)) test sections versus TKE. The TKE model is the dashed black line. **(B)** Deposition probability versus τ_b . The τ_b model is the solid black line. Standard error is shown by horizontal and vertical bars. In some instances, the error bars are contained within the size of the symbol. p data can be found in Supplementary Section 3.

(1976) model (Equation 4, dashed black line in Figure 4A). In contrast, although p generally decreased with increasing τ_b, the trends were different between bare bed and vegetated conditions (Figure 4B). In the bare test section, the τ_b model (Equation 2, solid black line in Figure 4B) predicted a p value consistent with measurements (open circles). However, in the vegetated test section, the τ_b model (Equation 2 with $\tau_{b,v}$ predicted by Equation 7) overpredicted p by as much as 6-fold, because it failed to fully account for the impact of the vegetation-generated turbulence. The TKE model did best for low $k_{t(\mathrm{nb})}$ but underpredicted p for high $k_{t(\mathrm{nb})}$ (Figure 4A).

4 Discussion

4.1 Deposition probability within submerged vegetation

Zhang et al. (2020) measured deposition in a submerged canopy, and this data was used to estimate deposition probability, which provided a test of Equation 4 within a submerged canopy. Zhang et al. (2020) reported six cases, each with a unique velocity and stem density combination, but all with canopy height h = 7.0 cm and water depth H = 36 cm for Cases 1 to 5 (for Case 6 H = 26 cm). Zhang et al. (2020) used solid glass spheres similar in size to those used in our experiments (d_s = 7 µm, ρ_s = 2500 kg/m^3), for which the critical TKE is $k_{t,c}$ = 2.14 cm^2/s^2 (Equation 11). The methodology for extracting the deposition probability, p, from the reported concentration and net deposition measurements is presented in Supplementary Section 5. The calculated deposition probability, p, exhibited good agreement with the TKE model (Equation 4, dashed black line in Figure 5). Additionally, the deposition probability in the bare (open circles) and vegetated (triangles) regions collapsed to the same trend when plotted versus $k_{t(\mathrm{nb})}$.

Combining the data from Zhang et al. (2020) with the present study (Figure 4), Equation 4 has been shown to apply for bare bed, submerged, and emergent conditions. It is interesting to note that these scenarios have different turbulent length-scales. In an emergent canopy, turbulence is generated by individual roots and has a length-scale comparable to the root diameter (e.g., Tanino and Nepf, 2008). In contrast, for a submerged canopy, turbulence is generated both at the scale of individual roots and at the scale of the canopy shear layer, and both scales exist within the canopy (e.g., Poggi et al., 2004; Ghisalberti and Nepf, 2006). In the bare channel, turbulence length-scales are set by the channel depth (e.g., Nezu and Rodi, 1986). The validation of Equation 4 for all three flow scenarios, suggests that deposition probability is primarily determined by turbulence magnitude, with little dependence on turbulence scale. Possible explanations for this are discussed below.

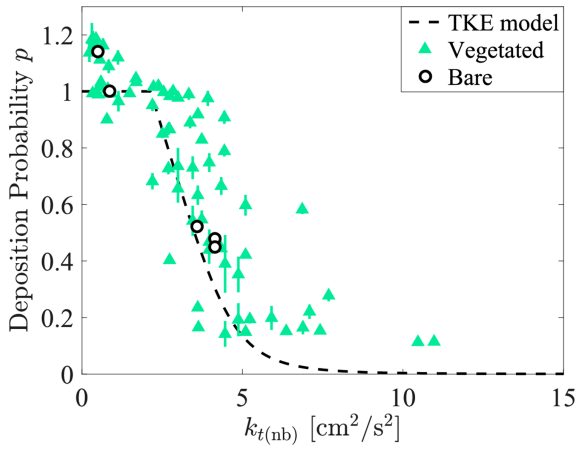

FIGURE 5
Deposition probability, p, in the bare (open black circles) and vegetated (green triangles) regions versus TKE using data from Zhang et al. (2020). The TKE model (dashed black line) was also plotted. Standard error is shown by vertical bars. In some instances, the error bars are contained within the size of the symbol.

Measurements reported in Poggi et al. (2004) show that within the lower part of a submerged canopy the turbulence length-scale is typically the cylinder diameter, and this has also been observed by T. Zhao (2023, unpublished data). Thus, between submerged and emergent canopies, the turbulence length-scales are similar near the bed, which is likely more relevant to deposition. However, this does not explain the consistency between bare bed and vegetated conditions. The lack of dependence on turbulence scale may be explained through two ideas. First, previous studies have made a similar observation for bed-load transport. Specifically, bedload transport within an emergent dowel array was observed to be dependent on the magnitude of turbulent kinetic energy (TKE), with no dependence on turbulence length-scale (Zhao and Nepf, 2021). This was explained using the impulse model for sediment entrainment, by showing that the total impulse was a function of turbulence intensity, but not eddy size. Second, very close to the bed, and specifically closer than the stem diameter, the turbulence becomes constrained in size by the proximity to the bed. For grains in this very near-bed region, the scale of the turbulence at its source (stem or shear layer) may be unimportant, so that again only turbulence magnitude is important in determining deposition probability. Further studies are needed to determine which description is correct.

4.2 Limits of deposition model

The model for deposition probability based on TKE collapsed bare and vegetated conditions better than the model based on bed shear stress. However, for both emergent and submerged vegetation, the TKE model underpredicted deposition for the highest turbulence intensities, specifically for $k_{t(\mathrm{nb})} > 5$ cm^2/s^2 (Figures 4, 5). A similar underprediction of measured deposition was observed in Figure 8 of Liu et al. (2022), but for $k_{t(\mathrm{nb})} > 15$ cm^2/s^2. The higher turbulence threshold might be a function of sediment size, as Liu et al. (2022) considered a larger particle (22 μm), compared to the present study (11 μm). The underprediction at high TKE may be related to the spatial heterogeneity of vegetated flows. The presence of vegetation creates preferential flow patterns that channel higher velocity through more open regions and create some lower velocity regions such as in the lee of stems. The zones of lower velocity and lower TKE may allow for greater deposition than predicted from Equation 4 using the spatially-averaged TKE. In the cases considered here, the deviations of the TKE model occur for $k_{t(\mathrm{nb})}$ greater than 5 cm^2/s^2 and p less than 0.2 to 0.3. None of the bare section cases considered here had $k_{t(\mathrm{nb})}$ high enough or p low enough to evaluate the applicability of the TKE model in that range. Additional measurements in this part of the parameter space could improve the TKE-based deposition probability for both vegetated and unvegetated flow conditions.

4.3 Exploration of field conditions

Vegetation generates drag that reduces the mean flow, which limits the horizontal transport of sediment and promotes deposition. The tendency toward enhanced deposition within vegetated regions may be modified by root-generated turbulence, which can reduce deposition probability and extend the distance sediment travels from a source region before it deposits. To explore the role of root-generated turbulence in sediment retention within a mangrove forest, field conditions were used to evaluate the trends in velocity and deposition probability across a range of typical root density, and these were used to evaluate the time and spatial scales of deposition within the forest. Consider the inundation of a mangrove forest from an ocean edge or channel edge. The velocity entering the mangrove platform depends on the water surface slope, S, set up by an advancing tide. Assuming the pneumatophores are emergent, conservation of momentum predicts the velocity entering the root layer (e.g., Xu et al., 2022a),

$$U = \sqrt{\frac{gHS}{C_f + 0.5 C_d n d H}} \tag{12}$$

in which C_d is the root drag coefficient, C_f is the bed friction coefficient, and n is the root density. To apply the TKE model to describe the deposition probability p, the TKE within the pneumatophore layer was estimated as the sum of bed-generated and root-generated turbulence (Yang et al., 2016),

$$k_{t,\nu(\mathrm{nb})} = \underbrace{\frac{\tau_b}{\rho\omega}}_{k_{t(\mathrm{bed})}} + \underbrace{\delta_{k_t}\left(\frac{C_{d,\mathrm{form}}\, n d^2}{2(1-\phi)}\right)^{\frac{2}{3}} U^2}_{k_{t(\mathrm{root})}} \tag{13}$$

in which δ_{k_t} is a scale constant, and $C_{d,\mathrm{form}}$ is the form drag coefficient for the cylindrical root. Zhao and Nepf (2021) found $\delta_{k_t} = 0.52 \pm 0.07$ based on data over a four-fold variation in stem diameter (0.64 to 2.5 cm). For $Re_d \geq 200$, Etminan et al. (2018) found $C_{d,\mathrm{form}} = 0.9 C_d$. Based on Etminan et al. (2017), $C_d = 1$ is a reasonable approximation, in which C_d is the sum of form drag and viscous drag. Equation 13 assumes vegetation-generated turbulence is present, which requires $Re_d > 120$ (Liu and Nepf, 2016). Equation 7 requires *a priori* knowledge of $k_{t,\nu(\mathrm{nb})}$. To avoid iterative calculations, τ_b in Equation 13 was predicted with the following model from Yang and Nepf (2018),

$$\tau_b = \begin{cases} \frac{4\rho\nu U_0}{d}, & Re_d < \frac{4}{C_f} \\ \rho C_f U_0^2, & Re_d \geq \frac{4}{C_f}. \end{cases} \tag{14}$$

Using the predicted TKE, the deposition probability was estimated using the TKE model (Equation 4). For comparison, deposition probability was also estimated using the τ_b model (Equation 2), with the bed shear stress predicted using Equation 7. This comparison was used to illustrate the influence of root-generated turbulence on the time and length scales that describe deposition.

For a tidal cycle of duration T, we can simplify the transport into a period of a positive velocity U flooding the forest, followed by a negative U draining the forest. On average, water remains in the forest for a residence time $T_R = T/2$. The fraction of sediment entering the forest that is deposited and retained can be estimated by comparing the residence time to the time scale for deposition. Consistent with Equation 1, deposition is modeled as a first-order reaction, $\partial C/\partial t = -\left(\frac{pw_s}{H}\right)C$, which indicates the settling time

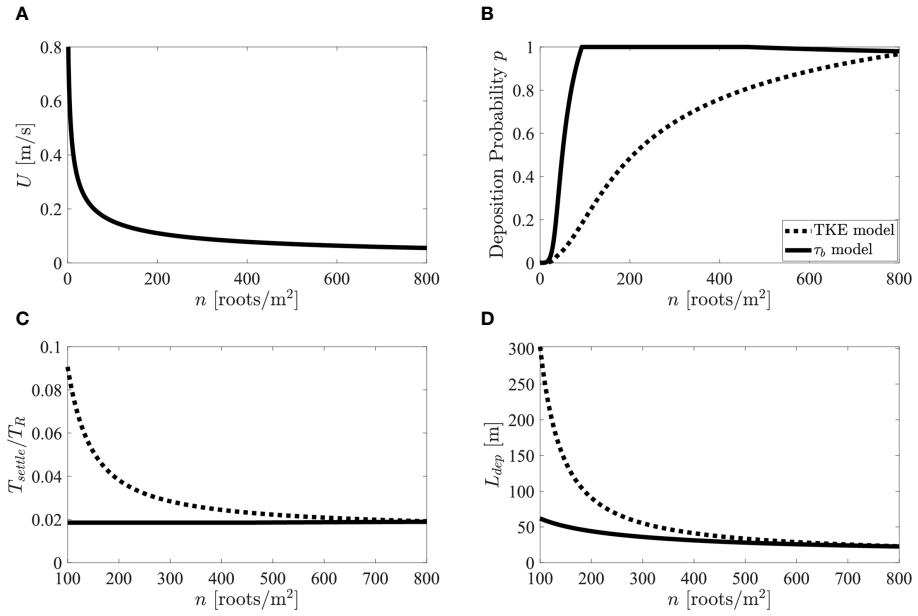

FIGURE 6
(A) Velocity in mangrove root layer versus root density. **(B)** Deposition probability versus root density. **(C)** Ratio of settling time to residence time versus root density. **(D)** Deposition length-scale. τ_b model (solid black line) and TKE model (dashed black line) in Figures 7B–D.

scale,

$$T_{settle} = \frac{H}{pw_s} \tag{15}$$

Further, deposition near the channel or ocean edge reduces the sediment supplied to regions farther from the edge, which results in net deposition that decays away from the edge over an e-folding length-scale (e.g., Equation 2 in Furukawa and Wolanski, 1996),

$$L_{dep} = T_{settle}U \ . \tag{16}$$

Equations 2, 4, 7, 12, 13, 14, 15, and 16 were used to estimate U, p, T_{settle}/T_R and L_{dep} as a function of root density (Figure 6). Physical parameters were chosen based on representative field conditions: tidal cycle of $T =$ 12 hours, water depth $H = 20$ cm, for which pneumatophores should be emergent, root diameter $d =$ 0.8 cm, and root density $n = 0$ to 800 roots /m^2, which corresponds to $\phi \approx 0$ to 0.04. To achieve velocities within typical ranges observed in mangrove forests (0 to 0.2 m/s, Furukawa and Wolanski, 1996; Norris et al., 2021), the water surface slope was set to $S =$ 0.001 (Mullarney et al., 2017b). The settling velocity was set to $w_s = 0.05$ cm/s, which is within the typical range of settling velocities measured for flocs with $d_s = O(10)$ µm (Gibbs, 1985). The bed friction coefficient was set to $C_f =$ 0.002. Note that this analysis ignores spatial and temporal variability in tidal velocity, water depth, and sediment characteristics that would be present in natural systems but are beyond the scope of a simplified scale analysis.

As n increased, U decreased (Figure 6A), resulting in a decrease in both TKE (Equation 13) and τ_b (Equation 7), both of which increased p (Figure 6B). Thus, the strong reduction in velocity due to vegetation drag makes regions of vegetation more conducive to deposition compared to bare regions. Including the influence of root-generated turbulence (dashed line, Figure 6B) produced lower values of p over the entire range of root density when compared to the τ_b model (solid line, Figure 6B), which did not reflect the influence of root-generated turbulence. The lower values of p associated with root-generated turbulence kept sediment in suspension longer (i.e., TKE model produced longer T_{settle}, Figure 6C). However, the longer settling time did not influence the ability of the forest to capture the sediment, since $T_{settle}/T_R << 1$ across the range of root density associated with mangrove forests ($n > 100$ roots/m^2, Figure 6C), suggesting that a typical mangrove forest captures the majority of sediment carried in by tidal flux. However, root-generated turbulence did impact the distance into the forest that sediment can be supplied, L_{dep}, with root-turbulence enhancing L_{dep} by up to a factor of five (Figure 6D).

To conclude, root-generated turbulence enhanced resuspension and diminished the rate of net deposition. Specifically, for the same velocity, as root density increased, TKE increased and net deposition decreased. The influence of root-generated turbulence can be described in terms of a deposition probability (p), which was predicted from a modified version of Engelund and Fredsøe's (1976) model written in terms of near-bed TKE. For the range of root densities found in

mangrove forests, the model suggested that root-generated turbulence did not change the amount of sediment captured during a tidal cycle but greatly increased the distance over which the captured sediment was deposited within the forest.

Data availability statement

The original contributions presented in the study are included in the article/Supplementary Material. Further inquiries can be directed to the corresponding author.

Author contributions

AD: Conceptualization, Data curation, Formal Analysis, Investigation, Methodology, Visualization, Writing – original draft, Writing – review & editing. EH: Formal Analysis, Investigation, Writing – review & editing. DR: Conceptualization, Formal Analysis, Supervision, Writing – original draft, Writing – review & editing. HN: Conceptualization, Formal Analysis, Funding acquisition, Methodology, Project administration, Resources, Supervision, Writing – original draft, Writing – review & editing.

Funding

The author(s) declare financial support was received for the research, authorship, and/or publication of this article. This study was supported by Shell International Exploration and Production through the MIT Energy Initiative. AD was supported in part by the National Science Foundation Graduate Research Fellowship under Grant No. 2141064.

Acknowledgments

We would like to thank Stephen Rudolph for his help with designing and constructing the flume inserts that made this research possible.

Conflict of interest

The authors declare that the research was conducted in the absence of any commercial or financial relationships that could be construed as a potential conflict of interest.

Publisher's note

Supplementary material

The Supplementary Material for this article can be found online at: https://www.frontiersin.org/articles/10.3389/fmars.2023.1266241/full#supplementary-material

References

Adame, M. F., and Lovelock, C. E. (2011). Carbon and nutrient exchange of mangrove forests with the coastal ocean. *Hydrobiologia* 663 (1), 23–50. doi: 10.1007/s10750-010-0554-7

Alongi, D. M. (2014). Carbon cycling and storage in mangrove forests. *Annu. Rev. Mar. Sci.* 6 (1), 195–219. doi: 10.1146/annurev-marine-010213-135020

Bagnold, R. A. (1941). *The physics of blown sand and desert dunes* (London, Methuen: Courier Corporation).

Barbier, E. B., Hacker, S. D., Kennedy, C., Koch, E. W., Stier, A. C., and Silliman, B. R. (2011). The value of estuarine and coastal ecosystem services. *Ecol. Monogr.* 81 (2), 169–193. doi: 10.1890/10-1510.1

Conde-Frias, M., Ghisalberti, M., Lowe, R. J., Abdolahpour, M., and Etminan, V. (2023). The near-bed flow structure and bed shear stresses within emergent vegetation. *Water Resour. Res.* 59 (4), e2022WR032499. doi: 10.1029/2022WR032499

de Groot, R., Brander, L., van der Ploeg, S., Costanza, R., Bernard, F., Braat, L., et al. (2012). Global estimates of the value of ecosystems and their services in monetary units. *Ecosystem Serv.* 1 (1), 50–61. doi: 10.1016/j.ecoser.2012.07.005

Diplas, P., Dancey, C. L., Celik, A. O., Valyrakis, M., Greer, K., and Akar, T. (2008). The role of impulse on the initiation of particle movement under turbulent flow conditions. *Science* 322 (5902), 717–720. doi: 10.1126/science.1158954

Engelund, F., and Fredsøe, J. (1976). A sediment transport model for straight alluvial channels. *Hydrology Res.* 7 (5), 293–306. doi: 10.2166/nh.1976.0019

Etminan, V., Ghisalberti, M., and Lowe, R. J. (2018). Predicting bed shear stresses in vegetated channels. *Water Resour. Res.* 54 (11), 9187–9206. doi: 10.1029/2018WR022811

Etminan, V., Lowe, R. J., and Ghisalberti, M. (2017). A new model for predicting the drag exerted by vegetation canopies. *Water Resour. Res.* 53 (4), 3179–3196. doi: 10.1002/2016WR020090

Fagherazzi, S., Bryan, K. R., and Nardin, W. (2017). Buried alive or washed away: the challenging life of mangroves in the Mekong Delta. *Oceanography* 30 (3), 48–59. doi: 10.5670/oceanog.2017.313

Furukawa, K., and Wolanski, E. (1996). Sedimentation in mangrove forests. *Mangroves Salt Marshes* 1 (1), 3–10. doi: 10.1023/A:1025973426404

Furukawa, K., Wolanski, E., and Mueller, H. (1997). Currents and sediment transport in mangrove forests. *Estuarine Coast. Shelf Sci.* 44 (3), 301–310. doi: 10.1006/ecss.1996.0120

Ghisalberti, M., and Nepf, H. (2006). The structure of the shear layer in flows over rigid and flexible canopies. *Environ. Fluid Mechanics* 6 (3), 277–301. doi: 10.1007/s10652-006-0002-4

Gibbs, R. J. (1985). Estuarine flocs: Their size, settling velocity and density. *J. Geophysical Research: Oceans* 90 (C2), 3249–3251. doi: 10.1029/JC090iC02p03249

Goring, D. G., and Nikora, V. I. (2002). Despiking acoustic doppler velocimeter data. *J. Hydraulic Eng.* 128 (1), 117–126. doi: 10.1061/(ASCE)0733-9429(2002)128:1(117

Horstman, E. M., Dohmen-Janssen, C. M., Narra, P. M. F., van den Berg, N. J. F., Siemerink, M., and Hulscher, S. J. M. H. (2014). Wave attenuation in mangroves: A quantitative approach to field observations. *Coast. Eng.* 94, 47–62. doi: 10.1016/j.coastaleng.2014.08.005

Horstman, E. M., Mullarney, J. C., Bryan, K. R., and Sandwell, D. R. (2017). "Deposition gradients across mangrove fringes," in *Coastal Dynamics 2017 Conference*. 911–922. Available at: https://researchcommons.waikato.ac.nz/handle/10289/11160.

Hutchison, J., Spalding, M., and zu Ermgassen, P. (2014). *The role of mangroves in fisheries enhancement* (The Nature Conservancy and Wetlands International).

Jennerjahn, T. C., and Ittekkot, V. (2002). Relevance of mangroves for the production and deposition of organic matter along tropical continental margins. *Naturwissenschaften* 89 (1), 23–30. doi: 10.1007/s00114-001-0283-x

Julien, P. Y. (2010). *Erosion and sedimentation* (Cambridge: Cambridge University Press).

Kauffman, J. B., Adame, M. F., Arifanti, V. B., SChile-Beers, L. M., Bernardino, A. F., Bhomia, R. K., et al. (2020). Total ecosystem carbon stocks of mangroves across broad global environmental and physical gradients. *Ecol. Monogr.* 90 (2), e01405. doi: 10.1002/ecm.1405

Kline,, and McClintock, (1953). The description of uncertainties in a single-sample experiment. *Mechanical Eng.* 75, 3–8.

Liu, D., Diplas, P., Fairbanks, J. D., and Hodges, C. C. (2008). An experimental study of flow through rigid vegetation. *J. Geophysical Research: Earth Surface* 113 (F4). doi: 10.1029/2008JF001042

Liu, C., and Nepf, H. (2016). Sediment deposition within and around a finite patch of model vegetation over a range of channel velocity. *Water Resour. Res.* 52 (1), 600–612. doi: 10.1002/2015WR018249

Liu, C., Shan, Y., and Nepf, H. (2021). Impact of stem size on turbulence and sediment resuspension under unidirectional flow. *Water Resour. Res.* 57 (3), e2020WR028620. doi: 10.1029/2020WR028620

Liu, C., Yan, C., Sun, S., Lei, J., Nepf, H., and Shan, Y. (2022). Velocity, turbulence, and sediment deposition in a channel partially filled with a phragmites australis canopy. *Water Resour. Res.* 58 (8), e2022WR032381. doi: 10.1029/2022WR032381

Mazda, Y., Magi, M., Ikeda, Y., Kurokawa, T., and Asano, T. (2006). Wave reduction in a mangrove forest dominated by Sonneratia sp. *Wetlands Ecol. Manage.* 14 (4), 365–378. doi: 10.1007/s11273-005-5388-0

Mazda, Y., Wolanski, E., King, B., Sase, A., Ohtsuka, D., and Magi, M. (1997). Drag force due to vegetation in mangrove swamps. *Mangroves Salt Marshes* 1 (3), 193–199. doi: 10.1023/A:1009949411068

Mcleod, E., Chmura, G. L., Bouillon, S., Salm, R., Björk, M., Duarte, C. M., et al. (2011). A blueprint for blue carbon: Toward an improved understanding of the role of vegetated coastal habitats in sequestering CO2. *Front. Ecol. Environ.* 9 (10), 552–560. doi: 10.1890/110004

Mullarney, J. C., Henderson, S. M., Norris, B. K., Bryan, K. R., Fricke, A. T., Sandwell, D. R., et al. (2017a). A question of scale: how turbulence around aerial roots shapes the seabed morphology in mangrove forests of the Mekong Delta. *Oceanography* 30 (3), 34–47. doi: 10.5670/oceanog.2017.312

Mullarney, J. C., Henderson, S. M., Reyns, J. A. H., Norris, B. K., and Bryan, K. R. (2017b). Spatially varying drag within a wave-exposed mangrove forest and on the adjacent tidal flat. *Continental Shelf Res.* 147, 102–113. doi: 10.1016/j.csr.2017.06.019

Nellemann, C., Corcoran, E., Duarte, C. M., Valdés, L., De Young, C., Fonseca, L., et al. (2009). *Blue carbon. A rapid response assessment* (GRID-Arendal: United Nations Environment Programme). Available at: www.grida.no.

Nezu, I., and Rodi, W. (1986). Open-channel flow measurements with a laser doppler anemometer. *J. Hydraulic Eng.* 112 (5), 335–355. doi: 10.1061/(ASCE)0733-9429(1986)112:5(335

Nino, Y., and Garcia, M. (1996). Experiments on particle–turbulence interactions in the near–wall region of an open channel flow: Implications for sediment transport. *J. Fluid Mechanics* 326, 285–319. doi: 10.1017/S0022112096008324

Norris, B. K., Mullarney, J. C., Bryan, K. R., and Henderson, S. M. (2017). The effect of pneumatophore density on turbulence: A field study in a Sonneratia-dominated mangrove forest, Vietnam. *Continental Shelf Res.* 147, 114–127. doi: 10.1016/j.csr.2017.06.002

Norris, B. K., Mullarney, J. C., Bryan, K. R., and Henderson, S. M. (2019). Turbulence within natural mangrove pneumatophore canopies. *J. Geophysical Research: Oceans* 124 (4), 2263–2288. doi: 10.1029/2018JC014562

Norris, B. K., Mullarney, J. C., Bryan, K. R., and Henderson, S. M. (2021). Relating millimeter-scale turbulence to meter-scale subtidal erosion and accretion across the fringe of a coastal mangrove forest. *Earth Surface Processes Landforms* 46 (3), 573–592. doi: 10.1002/esp.5047

Poggi, D., Porporato, A., Ridolfi, L., Albertson, J. D., and Katul, G. G. (2004). The effect of vegetation density on canopy sub-layer turbulence. *Boundary-Layer Meteorology* 111 (3), 565–587. doi: 10.1023/B:BOUN.0000016576.05621.73

Smart, G., and Habersack, H. (2007). Pressure fluctuations and gravel entrainment in rivers. *J. Hydraulic Res.* 45 (5), 661–673. doi: 10.1080/00221686.2007.9521802

Soulsby, R. L. (1981). Measurements of the Reynolds stress components close to a marine sand bank. *Mar. Geology* 42 (1), 35–47. doi: 10.1016/0025-3227(81)90157-2

Stokes, G. G. (1851). "On the effect of the internal friction of fluids on the motion of pendulums," in *Transactions of the cambridge philosophical society, part II.* 9, 8–106.

Tanino, Y., and Nepf, H. M. (2008). Lateral dispersion in random cylinder arrays at high Reynolds number. *J. Fluid Mechanics* 600, 339–371. doi: 10.1017/S0022112008000505

Temmink, R. J. M., Lamers, L. P. M., Angelini, C., Bouma, T. J., Fritz, C., van de Koppel, J., et al. (2022). Recovering wetland biogeomorphic feedbacks to restore the world's biotic carbon hotspots. *Science* 376 (6593). doi: 10.1126/science.abn1479

Tinoco, R. O., and Coco, G. (2018). Turbulence as the main driver of resuspension in oscillatory flow through vegetation. *J. Geophysical Research: Earth Surface* 123 (5), 891–904. doi: 10.1002/2017JF004504

Tomlinson, P. B. (2016). *The botany of mangroves* (Cambridge: Cambridge University Press).

Twilley, R. R., Castañeda-Moya, E., Rivera-Monroy, V. H., and Rovai, A. (2017). "Productivity and carbon dynamics in mangrove wetlands," in *Mangrove ecosystems: A global biogeographic perspective*. Eds. V. Rivera-Monroy, S. Lee, E. Kristensen and R. Twilley (Cham: Springer). doi: 10.1007/978-3-319-62206-4_5

Vo-Luong, P., and Massel, S. (2008). Energy dissipation in non-uniform mangrove forests of arbitrary depth. *J. Mar. Syst.* 74 (1), 603–622. doi: 10.1016/j.jmarsys.2008.05.004

Woodroffe, C. D., Rogers, K., McKee, K. L., Lovelock, C. E., Mendelssohn, I. A., and Saintilan, N. (2016). Mangrove sedimentation and response to relative sea-level rise. *Annu. Rev. Mar. Sci.* 8 (1), 243–266. doi: 10.1146/annurev-marine-122414-034025

Xu, Y., Esposito, C. R., Beltrán-Burgos, M., and Nepf, H. M. (2022a). Competing effects of vegetation density on sedimentation in deltaic marshes. *Nat. Commun.* 13 (1), 1. doi: 10.1038/s41467-022-32270-8

Xu, Y., Li, D., and Nepf, H. (2022b). Sediment pickup rate in bare and vegetated channels. *Geophysical Res. Lett.* 49 (21), e2022GL101279. doi: 10.1029/2022GL101279

Yando, E. S., Osland, M. J., Willis, J. M., Day, R. H., Krauss, K. W., and Hester, M. W. (2016). Salt marsh-mangrove ecotones: Using structural gradients to investigate the effects of woody plant encroachment on plant–soil interactions and ecosystem carbon pools. *J. Ecol.* 104 (4), 1020–1031. doi: 10.1111/1365-2745.12571

Yang, J. Q., Chung, H., and Nepf, H. M. (2016). The onset of sediment transport in vegetated channels predicted by turbulent kinetic energy. *Geophysical Res. Lett.* 43 (21), 11,261–11,268. doi: 10.1002/2016GL071092

Yang, J. Q., and Nepf, H. M. (2018). A turbulence-based bed-load transport model for bare and vegetated channels. *Geophysical Res. Lett.* 45 (19), 10,428–10,436. doi: 10.1029/2018GL079319

Zanke, U. (2003). On the influence of turbulence on the initiation of sediment motion. *Int. J. Sediment Res.* 18 (1), 17–31.

Zhang, J., Lei, J., Huai, W., and Nepf, H. (2020). Turbulence and particle deposition under steady flow along a submerged seagrass meadow. *J. Geophysical Research: Oceans* 125 (5), e2019JC015985. doi: 10.1029/2019JC015985

Zhao, T., and Nepf, H. M. (2021). Turbulence dictates bedload transport in vegetated channels without dependence on stem diameter and arrangement. *Geophysical Res. Lett.* 48 (21), e2021GL095316. doi: 10.1029/2021GL095316

Zong, L., and Nepf, H. (2010). Flow and deposition in and around a finite patch of vegetation. *Geomorphology* 116 (3), 363–372. doi: 10.1016/j.geomorph.2009.11.020

frontiers | Frontiers in Marine Science

TYPE Original Research
PUBLISHED 16 October 2023
DOI 10.3389/fmars.2023.1253083

OPEN ACCESS

EDITED BY
Jeff Shimeta,
RMIT University, Australia

REVIEWED BY
S. Laurie Sanderson,
College of William & Mary, United States
Jean Potvin,
Saint Louis University, United States

*CORRESPONDENCE
Leandra Hamann
hamannleandra@gmail.com

RECEIVED 04 July 2023
ACCEPTED 18 September 2023
PUBLISHED 16 October 2023

CITATION
Hamann L, Schreiber K, Hagenmeyer J, Eduardo S, Spanke T and Blanke A (2023) Diversity of filter feeding and variations in cross-flow filtration of five ram-feeding fish species.
Front. Mar. Sci. 10:1253083.
doi: 10.3389/fmars.2023.1253083

Diversity of filter feeding and variations in cross-flow filtration of five ram-feeding fish species

Leandra Hamann [1,2*], Kristina Schreiber [1], Jan Hagenmeyer [1,3], Santiago Eduardo [1,4], Tobias Spanke [5] and Alexander Blanke [1]

[1]Bonn Institute for Organismic Biology, Section Animal Biodiversity, University of Bonn, Bonn, Germany, [2]The Whitney Laboratory for Marine Bioscience, University of Florida, Saint Augustine, FL, United States, [3]Ruhr-University Bochum, Bochum, Germany, [4]Otto-von-Guericke-Universität Magdeburg, Magdeburg, Germany, [5]Centre for Taxonomy and Morphology (ztm), Leibniz Institute for the Analysis of Biodiversity Change, Bonn, Germany

Introduction: Filter-feeding fish separate food particles from the surrounding water by cross-flow filtration in which a suspension flows parallel to a porous filter medium, thereby transporting particles along the surface.

Methods: Here, we investigate cross-flow filtration in five ram-feeding fish species from two groups, Scombridae (*Scomber scombrus* and *Rastrelliger kanagurta*) and Clupeidae (*Clupea harengus*, *Sardina pilchardus*, and *Engraulis encrasicolus*). Using a combination of morphometrics, micro-CT scanning, video analysis, and water tunnel experiments, we give a detailed description of the gill arch system, calculate filtration parameters, observe particle movement, and identify morphological traits that induce cross-flow filtration.

Results: Our findings suggest that these ram-feeding fish species use a combination of cross-flow and dead-end filtration as the underlying filtration principle. Specifically, the particles are transported along the surface of gill rakers and denticles towards the esophagus where they accumulate before being periodically swallowed. We infer three distinct morphotypes characterized by variations in geometry, mesh size, and surface structures, which indicate variations of the general mechanism.

Discussion: The description presented in this study contributes to the development of models for investigating the influence of morphological variation on fluid flow and particle retention in filter-feeding fish and on their ecology and biomimetic application.

KEYWORDS

filter-feeding, cross-flow filtration, morphometrics, gill arch, gill raker, morphotypes, particle separation, water tunnel

1 Introduction

Suspension feeding is an aquatic feeding strategy that separates food particles from water (Jørgensen, 1966) and has evolved multiple times in animals such as sponges, mussels, crustaceans, flamingos, or baleen whales. Through their feeding activity, suspension feeders influence nutrient fluxes, local flow fields, and bio-chemical processes on a local and global level (Hentschel and Shimeta, 2008; Sebens et al., 2017). Filter-feeding fishes are of particular interest to humans. Pilchards, anchovies, and herrings belong to the most commonly fished species for human consumption (Alder et al., 2008). Silver carps and bighead carps were considered for waste water treatment to remove and recycle nutrients and algae and improve water quality (Hernderson, 1983). In addition, bio-inspired filter modules were developed that mimic the filter-feeding mechanism (Hung and Piedrahita, 2014; Schroeder et al., 2019). Filter-feeding fishes also ingest microplastics (Phillips and Bonner, 2015; Ory et al., 2018; Ribeiro et al., 2020). Therefore, their particle separation mechanisms are relevant for ecology, fishery, filtration technologies, and environmental protection.

The particle separation mechanism in filter-feeding fishes was described as cross-flow filtration (CFF), in which water streams parallel to the gill arches (GA) that bear elongated gill rakers (GR) with denticles forming a mesh-like arrangement (Figure 1) (Sanderson et al., 2001). The parallel flow transports the particles along the separation medium towards the esophagus while at the same time cleared water exits through the gill arch system (GAS) and under the opercula (Sanderson et al., 2001). Filter-feeding fishes from 21 families are known, which divide into over 70 ram- and pump-feeding species. Ram feeders use their forward motion to stream water into the mouth, while pump feeders suck water into their mouth through rhythmic contractions of pharyngeal structures (Sanderson and Wassersug, 1993; Storm et al., 2020).

Although the general mechanism of CFF in filter-feeding fishes was identified, the considerably high variability in the filter-feeding morphology may indicate variations of fluid flow and particle retention. For example, GR are long and blade shaped (Gibson, 1988), bushy (Friedland et al., 2006), short with an oval cross-section (Langeland and Nost, 1995), or even fused as in the silver carp (Cohen and Hernandez, 2018b). Pump-feeding cichlids have microbranchiospines that are dermal ossifications on the external faces of the GA whose function is yet unclear (Goodrich et al., 2000). The palatal organ shows morphological modifications in the pump-feeding silver carp compared to other non-filter-feeding Cypriniformes (Cohen and Hernandez, 2018a). Intraspecific variability of CFF morphology was observed in *Sardina pilchardus* with variations in GR number and GR gap size (Garrido and van der Lingen, 2014), which may indicate adaption to local prey characteristics and different feeding environments (Costalago et al., 2015). In the so-called cross-step filtration in the paddlefish, GA and GR form d-type ribs that induce characteristic vortices within the tangential inflow (Sanderson et al., 2016). Specific functions of these different traits within CFF were not assessed so far, and the parameter space is not known.

Therefore, we analyze the morphology of the GAS and identify functional details in five ram-feeding fishes from the groups Scombridae (*Scomber scombrus* and *Rastrelliger kanagurta*) and Clupeidae (*Clupea harengus*, *S. pilchardus*, and *Engraulis encrasicolus*). Endoscopic *in vivo* data from inside the oral cavity of ram-feeding fishes is difficult to obtain (Cheer et al., 2001). Therefore, we used digital microscopy and micro-CT to describe the three-dimensional arrangement of the GAS. Additionally, we conducted a video analysis of the selected filter-feeding species in aquaria and the wild to observe feeding behavior. In order to observe fluid flow and particle movement in the GAS, we examined fish heads with an open-mouth position in a water tunnel. Using a combination of imaging methods and functional analyses allowed us to describe the GAS in detail, calculate filtration parameters, such as mesh size, open area ratio, and fluid exit ratio, and thus identify the parameter space of CFF for these species. The results will help in understanding their particle separation mechanism, the ecological relevance in pelagic nutrient fluxes, and potential biomimetic applications.

2 Materials and methods

2.1 Study organisms

We analyzed seven Atlantic mackerels (*Scomber scombrus*, Linnaeus 1758), seven Indian mackerels (*R. kanagurta*, Cuvier 1816), seven Atlantic herrings (*C. harengus*, Linnaeus 1758), 11 Atlantic pilchards (*S. pilchardus*, Walbaum 1792), and 11 Atlantic anchovies (*E. encrasicolus*, Linnaeus 1758) to account for potential variation in the GAS (Figure 1). All species are ram-feeding filter feeders (Sanderson and Wassersug, 1993; Storm et al., 2020). The fishes were ordered from "FrischeParadies" (Cologne, Germany) and caught fresh from fishing grounds in the North East Atlantic, West Indian Ocean, Mediterranean, and Black Sea 1 day before they were picked up at the shop. The fishes were round, not decapitated or gutted, and cooled on ice during transport. After being visually inspected for damages, they were immediately frozen at −18°C.

2.2 Morphometrics based on digital microscopy

Before dissection, the fishes were thawed in cold water for 1 h. Each specimen was weighed and photographed with their mouth closed and open. The head was cut off and dissection was begun on the left side of the GAS and proceeded from larger to smaller structures, i.e., head, gill arches, gill rakers, and denticles. Larger structures were photographed with a Nikon D850 equipped with an AF-S Micro NIKKOR 60 mm 1:2.8G ED lens. Smaller structures were photographed with a Keyence VHX-700F (Ver 2.3.8.2 with lens VH-Z20R RZx20-x200, System Ver 1.93) at the University of Cologne. Photos were taken by one operator (LH) and analyzed by two operators (LH and JH) using ImageJ. In total, 20 parameters were measured (Figure 2A). To measure parameters 3–10, the mouth was held in an open position with pins and needles so that the jaw was opened with the GAS fully expanded and the GR closing the gap between the GA as previously established

10.3389/fmars.2023.1253083

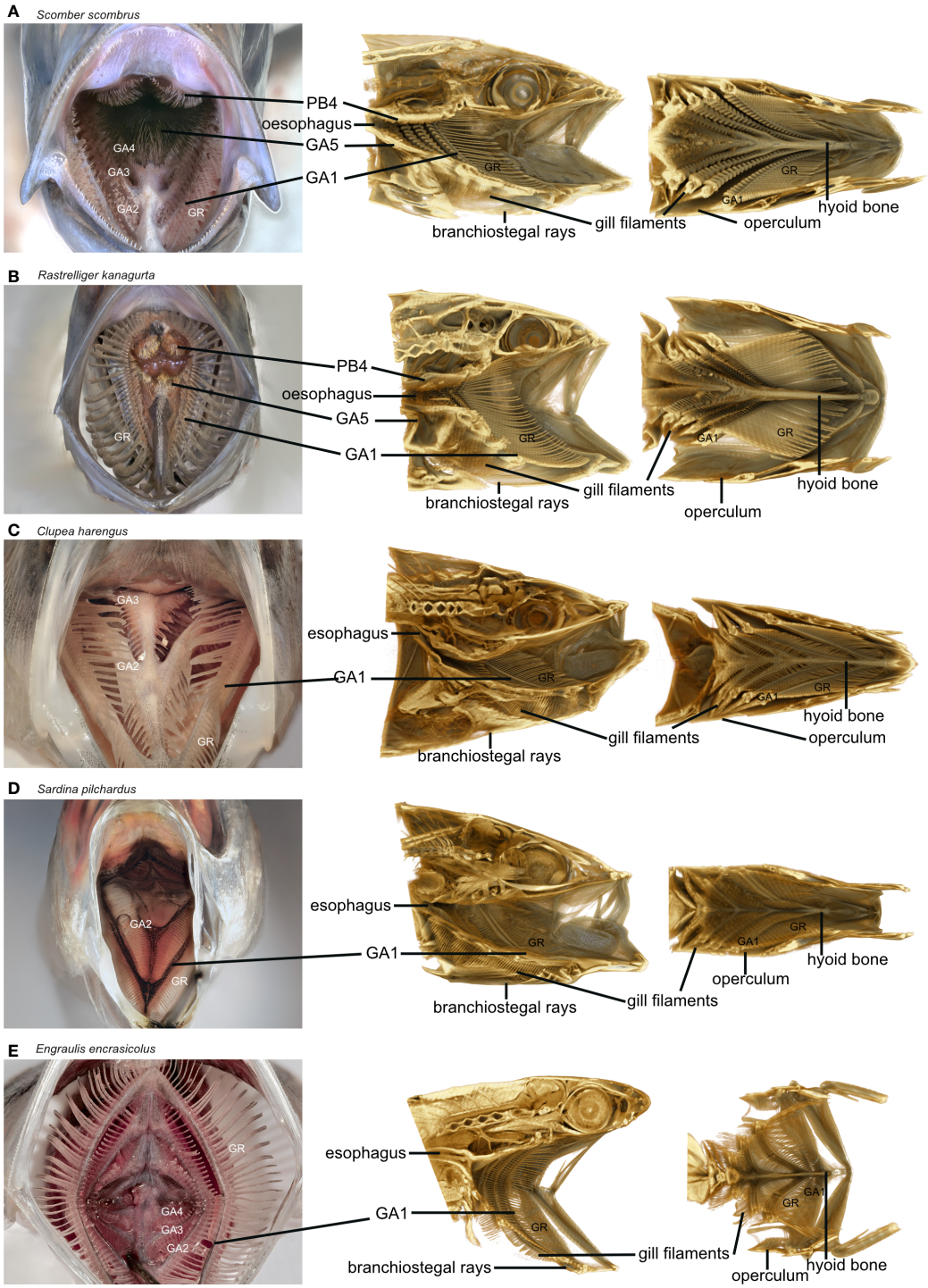

FIGURE 1
Stacked photographs of the frontal view into the buccal cavity (left column) and micro-CT volume renders through the sagittal mid-plane with view of the left side (middle column) and through the frontal plane with view of the ventral GAS of the studied ram-feeding fish: **(A)** Atlantic mackerel (*Scomber scombrus*, Linnaeus 1758, Fishing ground: North east Atlantic—Food and Agricultural Organisation (FAO) 27), **(B)** Indian mackerel (*Rastrelliger kanagurta*, Cuvier 1816, West Indian Ocean—FAO 51), **(C)** Atlantic herring (*Clupea harengus*, Linnaeus 1758, North East Atlantic—FAO 27), **(D)** Atlantic pilchard (*Sardina pilchardus*, Walbaum 1792, Mediterranean and Black Sea—FAO 37), and **(E)** Atlantic anchovy (*Engraulis encrasicolus*, Linnaeus 1758, Mediterranean and Black Sea—FAO 37), with GA, gill arch; GR, gill raker; PB, pharyngobranchial. Mouth opening angles approximately in physiological configuration. Images and scans not to scale.

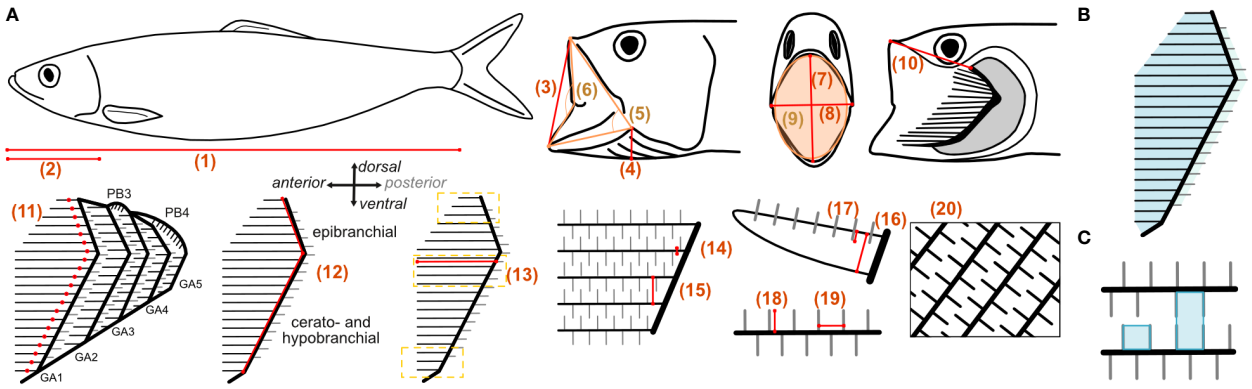

FIGURE 2
(A) Measured parameters in the fishes: 1) standard length (SL) with open and closed mouth; 2) head length; 3) open mouth height (lateral); 4) branchiostegal height; 5) jaw angle (in orange); 6) lip angle (in orange); 7) open mouth height frontal; 8) open mouth width frontal; 9) open mouth area (in orange); 10) upper lip to epibranchial; 11) number of GR; 12) length of GA (sum of epi-, cerato-, and hypobranchial length) and pharyngobranchials (PB, only in Scombridae); 13) length of GR measured for five GR on each branchial: at the ceratobranchial close to epi-cerato joint, at dorsal end of epibranchial, and at the ventral end of the hypobranchial (indicated by yellow lines); 14) width of GR; 15) distance between GR; 16) height of GR; 17) vertical position of denticles on the GR; 18) length of denticles; 19) distance between denticles; 20) open area ratio. Examples of calculated filtration parameters such as **(B)** filtration area for each GA and **(C)** minimum and maximum mesh size.

(Sanderson and Wassersug, 1993; Storm et al., 2020). Needles were inserted through the cranium to hold the head in position, and the mouth was opened by pulling on the hyoid retractor muscle and fixed with needles through the hyoid from outside the head. No needles were inserted inside the buccal cavity to not damage relevant structures. We are aware that measurements on soft and moveable structures are difficult to analyze. However, the open mouth position is an essential feature in ram-feeding fishes. We therefore compared the open mouth position, represented by the jaw angle, to measurements extracted from our video analysis to ensure that the angle represented a natural feeding position. The GAS is described with anatomical terminology along the anterior–posterior axis, the dorso-ventral axis, and the medial–lateral axis (Figure 2, Storm et al., 2020). The GA are described in ascending order from the most anterior GA1 to the most posterior GA5 close to the esophagus. On each GA, the GR protrude either anteriorly or posteriorly (Figure 2A). Posterior GR only occurred in some species and arches. To measure parameters 11–20 on each GA, the GAS was removed from the head. In the smaller species (*S. pilchardus* and *E. encrasicolus)*, the GAS remained intact because the structures were too fragile to be separated, whereas in the larger species, each GA was separated for taking the measurements.

GA length (parameter 12) was determined as the sum of the measured length of epi-, cerato- and hypobranchial, respectively (Figure 2). The length of the epibranchial was measured from the epibranchial–ceratobranchial joint to the last dorsal GR along the anterior facing side of the GA. The length of the ceratobranchial was measured from the epibranchial–ceratobranchial joint to the last ventral GR before the cerato-hypobrachial joint, and the length of the hypobranchial was measured from the cerato-hypobrachial joint to the last ventral GR of the hypobranchial along the anterior facing side of the GA. If the cerato-hypobrachial joint was not visible, the cerato- and hypobranchial were measured together. The length of the pharyngobranchials, if present, was measured separately and not accounted into the GA length. GR length (parameter 13) was measured for five anterior and, if present, posterior facing GR on each epi-, cerato-, and hypobranchial, i.e., at the dorsal and ventral ends of the epibranchial and hypobranchial, respectively, where they are shortest, and close to the epibranchial–ceratobranchial joint at the ceratobranchial where they are longest (Magnuson and Heitz, 1971). GR width, distance, and height were measured at their base close to the GA (parameters 14–16). Vertical position of the denticles was measured laterally from the GR edge facing the buccal cavity to the base of the denticles (parameter 17). Length and distance between denticles (parameter 18 and 19) were measured on GR close to the base. Measurements on structures were taken five times for different GR and 10 times for different denticles. The open area ratio (parameter 20) was determined in a black–white image by measuring the area occupied by GR and denticles compared to the open area where water can flow through (Figure 2A). The fish heads and GAS were rinsed in the direction of the natural flow with tap water to remove blood, food particles, and mucus. If agglomerations of mucus were present, it was removed with tweezers and noted in Table 1 as "yes" for mucus presence.

A maximum of 765 measurements were taken per individual, when all measurements were applicable (see Supplementary Information for raw data). Dissections and measurements on the fresh samples were carried out within 8 h, and all analyzed structures were kept in water at all times to prevent artifacts from drying. After dissection, each GAS was fixed in 5% formaldehyde and dehydrated in increasing ethanol concentration up to 70% ethanol for long-term fixation.

2.3 Micro-CT scanning

One additional individual of each species, was selected for micro-CT scanning to visualize the three-dimensional arrangement of the GAS in an open-mouth position (Figure 1). The head was cut off from the body and pinned upwards in an open-

10.3389/fmars.2023.1253083

TABLE 1 Selection of measured and calculated parameters for the analyzed species divided into: habitus and head, gill arches, gill raker and denticles, filtration parameters, and feeding behavior and fluid dynamics.

Parameter	*Reference to Figure 2 and equations*	*S. scombrus*	*R. kanagurta*	*C. harengus*	*S. pilchardus*	*E. encrasicolus*	*Parameters and abbreviations used in PCA*
N		7	7	7	11	11	
Weight [g]		197.9 ± 22.4	168.0 ± 40.4	193.6 ± 16.6	23.0 ± 3.4	9.3 ± 0.7	Weight [g]
Standard length (SL) [mm]	Parameter 1	269.4 ± 4.0	210.1 ± 12.4	248.2 ± 7.3	118.7 ± 6.4	97.9 ± 2.4	
Head length (relative to SL) [%]*	Parameter 2	24.0 ± 0.9	27.0 ± 0.8	19.8 ± 1.5	24.6 ± 1.3	25.4 ± 0.8	Head length [mm]
Branchiostegal height [mm]	Parameter 4	9.5 ± 4.2	13.0 ± 1.6	10.2 ± 4.9	5.7 ± 2.8	3.4 ± 1.3	
Jaw angle [°]	Parameter 5	43.8 ± 9.9	63.1 ± 5.2	58.5 ± 15.1	52.9 ± 12.5	70.0 ± 8.3	
Lip angle [°]	Parameter 6	97.2 ± 30.4	133.5 ± 10.3	168.0 ± 36.0	163.2 ± 28.2	94.8 ± 11.3	
Mouth opening ratio (height/width)*	Parameter 7, 8	1.2	1.4	1.3	1.8	1.3	MO ratio*
Mouth opening area [mm²]	Parameter 9	333.1 ± 162.9	831.4 ± 169.4	292.0 ± 154.7	77.0 ± 31.9	158.1 ± 24.3	
Distance from upper lip to epibranchial of GA1 (relative to head length) [%]*	Parameter 10	65.0 ± 3.7	63.6 ± 3.5	59.0 ± 4.2	59.4 ± 2.6	39.7 ± 7.3	Lip-Epi [mm]
GR number GA1	Parameter 11	44.6 ± 1.7	53 ± 2.8	67.1 ± 1.2	91 ± 3.6	64.8 ± 2.3	GR number GA1
Ratio of GA5 length to GA1 length*	Parameter 12	0.35 ± 0.03	0.38 ± 0.04	0.21 ± 0.03	0.33 ± 0.03	0.21 ± 0.03	GA 5-1 ratio*
GAS length [mm]	Parameter 13	25.4 ± 1.1	32.5 ± 2.5	21.2 ± 1.3	15.8 ± 0.8	10.6 ± 0.8	GAS length [mm]
GR length GA1 [mm]	Parameter 13	14.5 ± 0.6	18.6 ± 1.6	11.0 ± 0.9	6.7 ± 0.5	4.6 ± 0.2	GR length GA1 [mm]
GR distance GA1 (anterior, cerato) [mm]	Parameter 15	0.765 ± 0.148	0.659 ± 0.083	0.302 ± 0.034	0.187 ± 0.025	0.248 ± 0.055	
GR number GA1	Parameter 11	44.6 ± 1.7	53 ± 2.8	67.1 ± 1.2	91 ± 3.6	64.8 ± 2.3	GR number GA1
GR shape at GA1 (length/width)*	Parameter 13, 14	50.4	106.8	52	114.1	46.3	GR length/ width*
Fineness ratio of GR at GA1 (height/width)*	Parameter 14, 16	4.8	7.2	2.5	6	3.6	GR height/ width*
Position of denticles at cerato GA1 (relative to GR height)*	Parameter 17	0	0	0.17	0.27	0.23	
Denticle width at GA1 (anterior, cerato) [mm]	Parameter 19	0.592 ± 0.155	0.593 ± 0.158	0.098 ± 0.015	0.091 ± 0.013	0.085 ± 0.018	Denticle length GA1
Mucus		Yes	Yes	No	No	No	
Pharyngobranchials		Yes	Yes	No	No	No	
Filtration area [mm²]	Figure 2B, Equation 1	1,952.5 ± 307.2	2,280.8 ± 156.2	1,082.6 ± 136.6	480.2 ± 46.0	367.2 ± 29.0	Filtration area [mm²]
Symmetry of upper and lower GA at GA1*	Equation 2	0.27	0.28	0.32	0.34	0.39	Symmetry*
Open area ratio at cerato GA1*	Parameter 20, Equation 3	0.574	0.566	0.518	0.567	0.714	Open area ratio GA1*

(Continued)

10.3389/fmars.2023.1253083

TABLE 1 Continued

Parameter	*Reference to Figure 2 and equations*	*S. scombrus*	*R. kanagurta*	*C. harengus*	*S. pilchardus*	*E. encrasicolus*	*Parameters and abbreviations used in PCA*
Open area [mm²]	"Open area ratio at cerato GA1" x "Filtration area"	1121.5 ± 176.5	1291.0 ± 88.4	560.5 ± 70.7	272.1 ± 26.1	262.0 ± 20.7	
Relative open area gap 1 [%]*	Equation 4	60.4	63.8	59.1	50.8	61.0	Rel OA GA1 [%]*
Relative open area gap 2 [%]*	Equation 4	13.9	16.9	21.7	21.9	21.2	
Relative open area gap 3 [%]*	Equation 4	15.3	9.5	12.4	14.8	12.0	
Relative open area gap 4 [%]*	Equation 4	10.5	9.7	6.8	12.5	5.8	
Fluid exit ratio*	Equation 5	2.8	1.4	2.5	4.5	1.7	Fluid exit ratio*
Mesh size min [mm²]	Figure 2C, Equation 6	0.113	0.048	0.015	0.007	0.0097	Mesh size min [mm²]
Mesh size max [mm²]	Figure 2C, Equation 7	0.148	0.053	0.048	0.014	0.028	Mesh size max [mm²]
Mesh size ratio*		1.61	1.18	0.91	2.24	1.84	Mesh size ratio*
Location (video credits)		Sea Life Center Oberhausen, Germany (Leandra Hamann)	Red Sea (field), Egypt (Swantje Neumeyer, Bodo Kallwitz)	Aquarium Stralsund, Germany (Leandra Hamann)	Aquarium La Rochelle, France (Leandra Hamann)	Aquarium San Sebastian, Spain (Amalia Martínez de Murguía)	
N		20	5	9	15	24	
Feeding state		Feeding	Feeding	Feeding	Feeding	Feeding	
Swimming speed (SL/s)		1.85	2.24	1.36	3.48	3.58	
SL of dissected species [m]		0.27	0.21	0.25	0.12	0.1	
Swimming speed (m/s)		0.5	0.47	0.34	0.41	0.35	
Re around fish (based on SL)	Equation 8	137,166	101,201.3	85,417.3	50,150.7	34,995.1	
Re at mouth opening (based on equivalent spherical diameter)	Equation 8	8,725	13,037	5,522	3,480	4,222	
Re around denticles at cerato GA1	Equation 8	128	121	14	16	13	
Volume flow rate through open mouth [L/min]	Parameter 9 x "Swimming speed"	8.29	19.57	4.91	1.59	2.76	

The asterisk (*) indicates parameters without units as they are ratios. Swimming speed (SS) and Reynold's numbers (Re) were calculated based on the standard length (SL) of the dissected species. Parameters that were included in the principal component analysis (PCA, Figure 3) are given with their abbreviation in the last column. A spreadsheet with the raw data of all morphometric measurements can be found in the Supplementary Information.

mouth position onto Styrofoam with needles inserted through the cranium and hyoid retractor muscle to pull down the lower jaw. The samples were then fixed in 5% formaldehyde, dehydrated in increasing ethanol concentrations up to 70%, and stained with PTA. Afterwards, the large needles were removed and replaced by small needles to hold the head in place for scanning. The fixation process was sufficient to harden the tissues and keep the head in an open mouth position. Each head was scanned with a Bruker SkyScan 1173 (for scanning parameters, see Supplementary Information S1) at the Leibniz-Institute for the Analysis of Biodiversity Change (LIB). The scans were reconstructed with NRecon (Version 1.7.5.9), and volume renders were created with

Drishti (Version 2.6.4) (Limaye, 2012). Virtual cross-sections of the fish heads were made in the sagittal plane along the hyoid bone and in the frontal plane close to the epi-ceratobranchial joint on GA1 with dorsal view on the ventral side of the GAS (Figure 1).

2.4 Feeding behavior

Public aquaria across Europe were contacted to film the feeding behavior and determine swimming speed before and during feeding. Fishes were filmed for several minutes with the camera (Sony RX 10 Mark IV, 25 fps) and LED light positioned on tripods outside the tanks. The fishes were given their usual food, but it was crushed and decreased in size to increase the chances of filter feeding (Crowder, 1985; Garrido et al., 2007). *Scomber scombrus* were fed with a mixture of small crustaceans, shrimps, and blue mussels, which were crushed by hand to decrease the size. *Clupea harengus* were fed with small crustaceans and pellets, and *S. pilchardus* were fed with pellets crushed in a blender. Due to travel restrictions during the coronavirus disease 2019 (COVID-19) pandemic, a video footage for *E. encrasicolus* was taken by the aquarium curator with a GoPro (30 fps) in a quarantine tank and sent to the authors. From these recordings, only swimming speed was measured because of quality issues. *Rastrelliger kanagurta* is not held in captivity, so field footage was organized from dives in the Red Sea by amateur divers.

The footage was analyzed in ImageJ (Version 2.3.0). Measurements were taken only in frames where the individuals were parallel to the camera with their total length visible. Head length and jaw angle were measured relative to standard length of each individual (parameters 1, 2, 4, and 5 in Figure 2A). Assuming isometric allometry in adult fish of these species, the measurements were multiplied by the mean standard length of each species obtained from the dissected individuals to allow comparison. The swimming speed was determined by using the Manual Particle Tracing Module in ImageJ. Sequences of at least 10 frames were measured by following the eye of the fish and dividing the travelled distance by the standard length. Feeding behavior was determined based on whether the mouth was open or closed. Filter feeding in *S. scombrus* and *R. kanagurta* was followed by quick closing and opening of the mouth, which is likely to be swallowing of the prey items and was described for ram-feeding basking sharks (Hallacher, 1977; Sims, 2000). In accordance with technical filters, we describe this behavior as "cleaning" because particles are removed from the buccal cavity and GAS. Due to the aquaria holding conditions, it is possible that the same individuals of the shoal were measured several times.

2.5 Fluid flow and particle movement in GAS

The same fish heads that were prepared for micro-CT scanning were also used to analyze the particle movement in the buccal cavity under laminar flow conditions in a water tunnel. Therefore, the fish heads were pinned on a streamlined holder in the test section facing the incoming flow (for water tunnel setup and description, see Supplementary Information S2). The flow velocity was set to 6.5 cm/s because this shows the best laminar conditions in this water tunnel. Four dissection steps were proceeded: 1) intact head, 2) removal of the right operculum and replacement with a transparent foil, 3) removal of the left operculum and replacement with a transparent foil, and 4) removal of the right GA1 to be able to look inside the buccal cavity (Supplementary Information Figure S2A). In step 2, the transparent foil was cut from clear sheet protectors for papers and held in position with needles in the anterior part of the mouth to close up with the fish skin. The posterior part was left open and positioned in such a way that it mirrored the remaining left operculum regarding length, dorsal–ventral curvature, and opening distance. Brine shrimp eggs (*Artemia salina*, 1.09 g/cm^3, (Haines and Sanderson, 2017)) were added to the water in the last dissection step to analyze particle velocity and particle movement inside the buccal cavity. A zoom body tube (Navitar 1-60135) combined with a coupler (Navitar 1-6010) and a c-mount (LMScope) to fit the Nikon D850 camera were used to take close-up videos (100 fps) of the brine shrimp eggs without the fish heads in the test section and when the fish heads were added at the entrance of the mouth opening and at the inside of the GR of the left GA1. The videos of brine shrimp eggs were analyzed using ImageJ (Version 2.3.0) and the Manual Tracking plugin. The average egg size was determined under a microscope (Keyence VHX-700F, Ver 2.3.8.2 with lens VH-Z20R RZx20-x200, System Ver 1.93) as 0.242 ± 0.019 mm (N = 30) and was used to set the scale in the videos and approximate the velocity of the moving eggs. The velocity was only measured for particles within the focal plane to ensure that the interaction with the focused structures was tracked. Four different particle movements were distinguished: free (no contact with surfaces), out (particles leaves the GAS through the mesh), roll (contact with a surface and particle keeps moving), or stop (contact with a surface that leads to no further movement). The number of particles for each behavior was divided by the total number of particles for each species to describe the share of particle movement.

In order to observe the influence of the dissection on the flow through the head, black ink was injected at the middle axis of the mouth opening for each dissection step. A camera (Nikon D850, Nikkor AF-S 24-120 mm 1:4 G ED) was mounted outside the tank to film the right side of the fish. Three videos were taken for each dissection step. The ink streamline was checked for laminarity between each video without the fish head. Close-up videos were taken of the GAS at the entrance of the mouth opening, the outside of the GR of the right GA1, and the inside of the GR of the left GA1 during dissection step 3 and 4. The videos were visually analyzed, and the ink streamlines were described by direction, distribution, and diffusion for each dissection step of each species. Single frames were extracted that are exemplary for the recorded videos and show all aspects of observed ink motion (Supplementary Information S3).

2.6 Calculation of filtration parameters

The calculation of the total filtration area (A) of each GA of the left side is based on the sum of the area calculated for the upper (u) and lower (l) GA individually, similar to Magnuson and Heitz,

1971. As we only measured five GR on each epi-, cerato- and hypobranchial, we multiplied the mean GR length and the mean distance between GR with GR number (N_{GR}) for each upper and lower GA, as shown here for the anterior side of GA1:

$$\begin{aligned} A_{GA1} &= A_{u,GA1} + A_{l,GA1} \\ &= \left(\frac{\overline{L_{GR,E}}+\overline{L_{GR,C}}}{2} * \frac{\overline{D_{GR,E}}+\overline{D_{GR,C}}}{2} * N_{u,\,GR}\right) \\ &+ \left(\frac{\overline{L_{GR,C}}+\overline{L_{GR,H}}}{2} * \frac{\overline{D_{GR,C}}+\overline{D_{GR,E}}}{2} * N_{l,\,GR}\right) \end{aligned} \quad \begin{aligned} &with \\ &A_{GA1} = total\ filtration\ area\ of\ GA1 \\ &A_{GA1} = upper\ area\ of\ GA1 \\ &A_{GA1} = lower\ area\ of\ GA1 \\ &L = length\ of\ GR \\ &D = distance\ between\ GR \\ &N = number\ of\ GR \\ &l = lower\ GA \\ &u = upper\ GA \\ &E = epibranchial \\ &C = ceratobranchial \\ &H = hypobranchial \end{aligned} \tag{1}$$

We assume that GR length decreases linearly from the longest GR at the ceratobranchial towards the distal ends of the epibranchial and hypobranchial, respectively (Figure 2B). The same calculation was used to calculate the posterior area if present. The total filtration area is the sum of all calculated areas between the GA and the area between GA and the operculum. The area between GA4 and GA5 was not included because epibranchial and hypobranchial GR on GA5 were partly missing in the clupeid species and absent on GA5 in the scombrid species. The filtration area formed by posterior GR in the clupeid species was also not included because there were only a few GR on the ceratobranchial and the formula was not applicable. The total filtration area was only calculated for individuals for which all measurements were possible. Finally, the area was doubled to include the filtration area of the right side of the fish. The symmetry of the GAS is determined by the ratio of upper area (UA), formed by the GR of the epibranchial, to lower area (LA), formed by the GR of the cerato- and hypobranchial of each GA.

$$Symmetry = \frac{A_{u,\,GA1}}{A_{l,\,GA1}} \quad \begin{aligned} &with \\ &A_{GA1} = lower\ area\ of\ GA1 \\ &l = lower\ GA \\ &u = upper\ GA \end{aligned} \tag{2}$$

The closed area (area that is covered by the GR and denticles) and open area (open space through which the water can flow) were measured in pictures taken at the anterior ceratobranchial of each GA. The open area ratio is calculated as the ratio of open area to the sum of open and closed area:

$$Open\ area\ ratio = \frac{open\ area}{open\ area + closed\ area} \tag{3}$$

Because the open area ratio remained similar from GA1 to GA5 in the clupeiform species, the mean open area ratio at the ceratobranchial of GA1 was used to calculate the open area of each GA based on the calculated total filtration area. It was not possible to measure the open and closed area on GA2 to GA4 in the scombriform species because of the high density of denticles, and we thus calculated the open area ratio in the same way as for the Clupeiformes.

The relative open area of each GA is calculated by the open area of that GA divided by the total area of all GA.

$$Rel\ \ open\ \ area_{GA1}\ [\%] = \frac{open\ area_{GA1}\ [mm^2]}{open\ area\ [mm^2]} \tag{4}$$

The fluid exit ratio (Brooks et al., 2018) is calculated as the ratio of the total open area to the open mouth area:

$$Fluid\ exit\ ratio = \frac{open\ area\ [mm^2]}{open\ mouth\ area\ [mm^2]} \tag{5}$$

Depending on the position of opposing GR and denticles, the mesh size can be calculated as minimum or maximum mesh size (Figure 2C) and also be understood as the minimum size of particles that are retained (Collard et al., 2017). The minimum mesh size (MS_{min}) is formed if denticles between two GR are alternating, so it is calculated as the product of denticle distance and denticle length:

$$MS_{min} = D_{De} * L_{DE} \quad \begin{aligned} &with \\ &MS = meshsize \\ &D = distance \\ &L = length \\ &De = denticle \end{aligned} \tag{6}$$

The maximum mesh size (MS_{max}) is formed if denticles between two GR are directly opposite of each other, so it is calculated as the product of the denticle distance and the gap between the two GR:

$$MS_{max} = D_{De} * G_{DR} \quad \begin{aligned} &with \\ &MS = mesh\ size \\ &D = distance \\ &L = length \\ &De = denticle \\ &GR = gill\ raker \end{aligned} \tag{7}$$

A decrease or increase in mesh size from anterior to posterior GA can be determined by the ratio of the mesh size from GA1 to GA4. The mesh size ratio was based on the mean of the minimum and maximum mesh size.

The Reynolds number describes the local flow regime based on the ratio of inertial to viscous forces. It is an important indicator to identify the type of particle encounter with the filter medium, e.g., hydrosol filtration theory (Rubenstein and Koehl, 1977). It was calculated as:

$$Re = \frac{\rho * L * v}{\mu} \quad \begin{aligned} &with \\ &\rho = density \\ &v = flow\ velocity \\ &L = characteristic\ length \\ &\mu = dynamic\ viscosity \end{aligned} \tag{8}$$

The density ρ is 1.027×10^3 kg m^{-3}, and the dynamic viscosity μ is 0.00141 kg/(m^{-1} s^{-1}) for seawater at 10°C. The flow velocity v was measured as the swimming velocity in the videos during feeding as standard length per second multiplied by the standard length of the dissected species (Table 1). The Reynolds number was calculated around the fish (L = standard length, Table 1), at the mouth opening (L = equivalent spherical diameter of open mouth height and width), and around the denticles (L = denticle width on anterior GR of GA1, Table 1). To account for the reduced flow velocity inside the buccal cavity due to hydrodynamic drag, we calculated a reduction factor based on our measurements in the water tunnel experiments. The reduction factor at the mouth opening was calculated as 83.2% ± 10.7%, which is the mean velocity of brine shrimp eggs at the mouth opening across all species divided by the brine shrimp egg velocity when no fish head was in the water tunnel. The reduction factor at the denticles was calculated as 42.3% ± 11.8%, which is the mean velocity of brine shrimp eggs at GA1 across all species divided by the brine shrimp egg velocity when no fish head was in the water tunnel. For comparison, the Reynolds number was calculated at the mouth opening for the fish heads in the water tunnel with v = 0.065 m/s and the reduction factor of 83.2 ± 10.7%. The volume flowrate through the mouth was calculated as the open mouth area multiplied by the mean swimming velocity and the reduction factor at the mouth opening.

2.7 Statistics

The results were analyzed and visualized using the R programming environment (R Core Team, R Studio Version 3.6.3.) and Scribus (Version 1.5.6.1). Descriptive statistics of untransformed data were calculated for all measured and calculated parameters. Measurements are reported as mean with standard deviations. Ratios were calculated based on means and reported without standard deviation. All boxplots show the median and upper and lower quartiles as whiskers and outliers, respectively. In order to investigate the relationship of morphological traits, we used principal component analysis (PCA) based on 19 parameters, including 10 absolute values and nine relative values (Table 1). Variables were not included if they were binary or partly binary (i.e., number of posterior GR, position of denticles, mucus, teeth, additional structures), angles (i.e., lip angle, jaw angle), or if they were used to calculate filtration parameters and therefore not independent. To limit the number of variables, only data concerning GA1 were included, e.g., for GR number, open area ratio, or mesh sizes. Of the included 817 data points, 98 were missing, which were imputed for the PCA by the mean of each variable for each species, respectively (Dray and Josse, 2015). Afterwards, we performed a regression of each log-transformed variable with the log-transformed standard length to extract the residuals and correct for size. The PCA with the residuals was based on a correlation matrix (scale = TRUE, center = TRUE). A threshold of 75% was chosen to select the principal components (PCs) that explain most of the variance. The loadings of these PCs were extracted and ranked, respectively, based on their absolute values (or modulus) to identify essential contributors. The same dataset was used to calculate a correlation matrix and identify potential functional relation for each parameter combination. Because some of the data were not normal distributed, we used the Spearman rank test to calculate the correlation coefficient. The comparison of the jaw angle in the dissected individuals and the videos and the comparison of the swimming speed before and during feeding were done with a Kruskal–Wallis rank sum test (chi-squared) with a *post-hoc* Dunn test (method "Holm").

3 Results

3.1 Morphometrics and filtration parameters

Scomber scombrus is the largest species analyzed with 269.4 ± 4 mm as standard length, followed by *C. harengus* (248.2 ± 7.3 mm), *R. kanagurta* (210.1 ± 1 2.4 mm), *S. pilchardus* (118.7 ± 6.4 mm), and *E. encrasicolus* (97.9 ± 2.4 mm; Table 1). Standard length ranges an extra ± 2% when the mouth is open. The mouth height-to-width ratio ranges from 1.2 to 1.8, which indicates an oval opening along the ventral–dorsal axis. The jaw angle of the open mouth ranges from 45° in *S. scombrus* to 74° in *E. encrasicolus* (Table 1). The branchiostegal height is largest in *R. kanagurta* and smallest in *E. encrasicolus* ranging between 3.5 mm ± 1.3 mm to 13.0 mm ± 1.6 mm. The angle of the protruded lips is 94.8° ± 11.3° up to 168° ± 36°, closing the mouth opening at the sides. The head makes up approximately 19.8% in *C. harengus* and maximum 27% in *R. kanagurta* of the standard length. The epibranchial of GA1 begins at around two-thirds into the buccal cavity, except in *E. encrasicolus* in which the epibranchial starts already in the first third (Table 1).

GA length decreases from anterior to posterior (Figure 3A). An exception is *S. pilchardus*, in which GA2 is longer than GA1. The GA ratio describing the decrease in length from GA1 to GA5 is largest in *R. kanagurta* with 0.38 and smallest in *C. harengus* and *E. encrasicolus* with 0.21, meaning that GA5 is only 38% and 21% of the length of GA1, respectively (Table 1). The same trend can also be seen in the GR number on each GA (Figure 3B). Here, *S. pilchardus* has more GR on GA2 and GA3 than on the first, while GR distance remains similar. The two mackerel species *S. scombrus* and *R. kanagurta* have anterior and posterior GR, of which the number of posterior GR is only marginally reduced. For example, *R. kanagurta* has, on average, 53 anterior GR and 43 posterior GR with similar GR distance. There are no GR on GA5 in the two mackerel species. *Clupea harengus* and *E. encrasicolus* have posterior GR only on GA4 and GA5. *Sardina pilchardus* has posterior GR only on GA4. One individual has posterior GR on GA2 and GA3, counting 7 and 3 in number (Figure 3B).

The total filtration area is largest in *R. kanagurta* with 2,280.8 ± 156.2 mm^2 and smallest in *E. encrasicolus* with 367.2 ± 29.0 mm^2 (Table 1, Figure 3C). The symmetry of upper to lower GA darea is in all species between 0.28 and 0.4, meaning that the filtration area created by the GR on the epibranchial is smaller than the filtration area on cerato and hypobranchial of each GA (Table 1, Figure 3H). The open area ratio of GA1 ranges between 0.51 and 0.57 in *S. scombrus*, *R. kanagurta*, *C. harengus*, and *S. pilchardus*. In *E.*

10.3389/fmars.2023.1253083

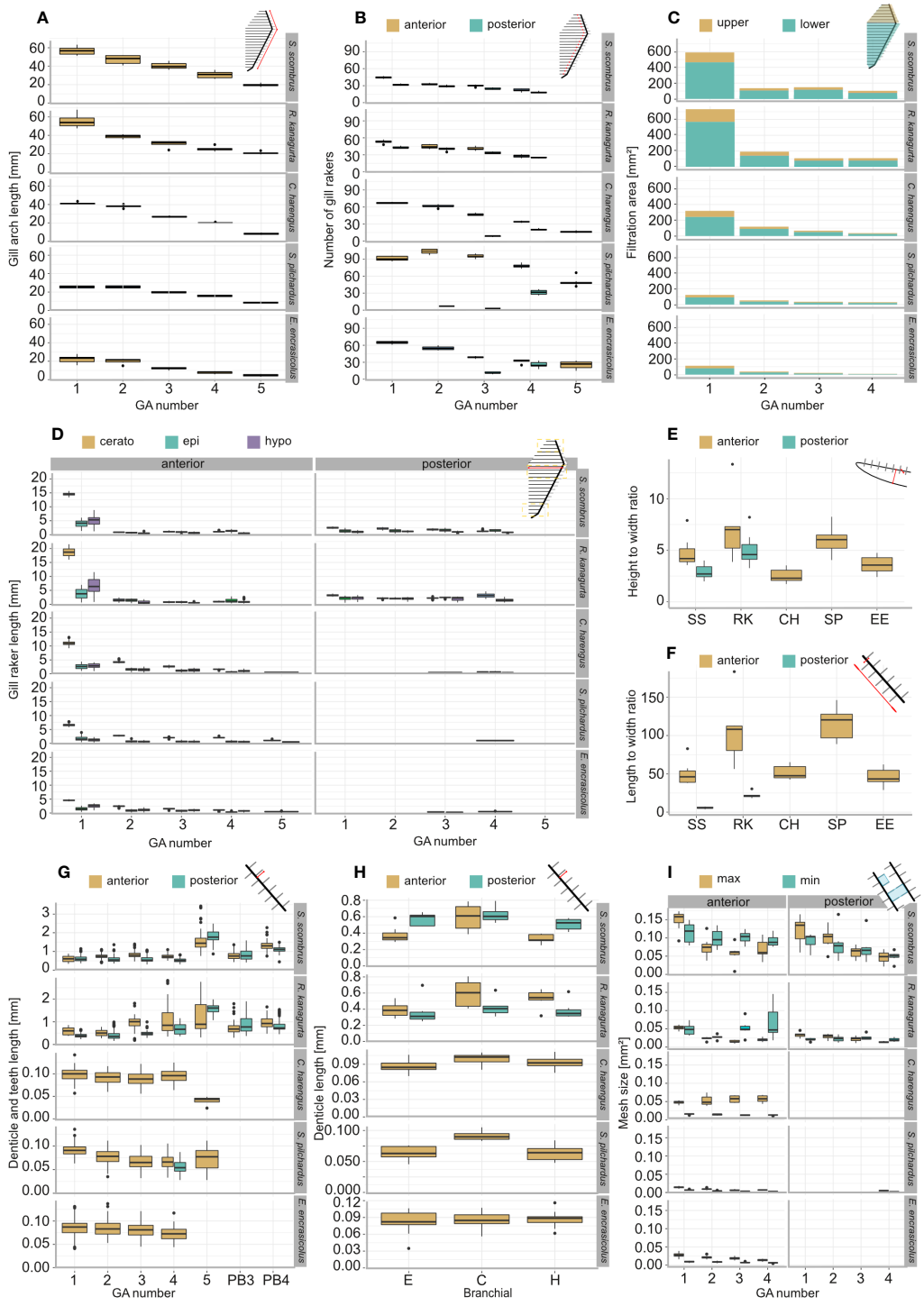

FIGURE 3
Morphometric measurements and filtration parameters of the studied ram-feeding fishes *S. scombrus* (SS), *R. kanagurta* (RK), *C. harengus* (CH), *S. pilchardus* (SP), and *E. encrasicolus* (EE): **(A)** Gill arch (GA) length, **(B)** gill raker (GR) number on the anterior and posterior side of each GA, **(C)** filtration area of upper (epibranchial) and lower (cerato- and hypobranchial) GA, **(D)** GR length on epi-, cerato- and hypobranchial on the anterior and posterior side of each GA, **(E)** height-to-width ratio of GR on GA1, **(F)** length-to-width ratio of the GR on GA1, **(G)** denticle length of the anterior and posterior GR of each GA and on pharyngobranchial 3 and pharyngobranchial 4 in the two scombrid species, **(H)** denticle length of the anterior and posterior GR on each branchial of GA1, and **(I)** minimum and maximum mesh size of the anterior and posterior sides of the first four GA.

encrasicolus, the open area ratio is 0.71 (Table 1). In *S. scombrus* and *R. kanagurta*, the relative open area is highest at the first gap with 60.4% and 63.8% and lowest at the fourth gap formed by the posterior GR of GA3 and anterior GR of GA4 with 10.5% and 9.7%, respectively. In the three clupeid species, the relative open area at the first gap ranges between 50.8% and 61.0%, at the second gap between 21.2% and 21.7%, at the third gap between 12.0% and 14.8%, and at the fourth gap between 5.8% and 12.5% (Table 1). The

fluid exit ratio ranges between 1.4 in *R. kanagurta* and 4.5 in *S. pilchardus*, which means that the open area of the filtration area is larger than the open mouth area (Table 1).

GR are longest on GA1 in all five species (Figure 3D). In Scombriformes, the length of the GR is abruptly shorter in GA2 to GA4, and GA5 has no GR. In Clupeiformes, the length decreases more evenly from GA1 to GA5. Within one GA, GR length is largest on the ceratobranchial and smallest on the distal ends of epi and hypobranchial. The GAS length, determined by the sum of the mean GR length at the ceratobranchial of all GA, is longest in *R. kanagurta* with 32.5 mm ± 2.5 mm and smallest in *E. encrasicolus* with 10.6 mm ± 0.8 mm (Table 1). The mean of the length-to-width ratio of the anterior GR on GA1 varies between 46.3 and 114.1 (Table 1, Figure 3F). The mean length-to-width ratio of the posterior GR in *S. scombrus* and *R. kanagurta* ranges from 10 to 25. The height-to-width ratio of the GR on GA1 ranges between 3.5 and 8 (Figure 3F).

The denticles in *S. scombrus* and *R. kanagurta* sit on top of the anterior, blade-shaped GR on GA1. They are spaced at regular intervals, thin (Figure 4), and measure approximately 0.59 mm ± 0.16 mm in length on GA1 in both species (Table 1). The denticles on the ceratobranchial of the GR on GA1 are longer than on the epi- and hypobranchial (Figure 3H). On the shorter, posterior GR of GA1 and anterior and posterior GR on GR2, GR3, and GR4, the denticles vary strongly in size (Figure 3G) but are irregularly arranged and closer together (Figure 4). Other scombrids were described to bear patches of tiny teeth on most GA (Collette and Gillis, 1992). Based on the outer appearance, it is difficult to tell denticles and teeth originating from GR apart (Figure 4), which might explain the high variance in length. We assume that structures originating from the GA are mainly teeth and less denticles. Because GA5 has no GR, we assume that the measured structures are only teeth. These teeth are generally longer, ranging in length approximately 1.5 mm (Figure 3G), and appear thicker and sturdier. Additionally, part of the five GA in the two species of Scombriformes are four pharyngobranchials, of which the third and fourth are visible within the oral cavity and bear teeth (Figures 1, 5), as described for *R. kanagurta* (Gnanamuttu, 1966). On each side, the pharyngobranchials are located dorsally between the epibranchials of GA3 and GA4 and opposite of GA5 (Figure 5). The more anterior third pharyngobranchial is small and slender with small teeth, and the posterior fourth pharyngobranchial is rectangular and has more pronounced teeth. For other species within the Scombridae, e.g., *Grammatorcynus bicainatus*, the pharyngobranchials were also described as pharyngeal tooth patches (Collette and Gillis, 1992).

The denticles of *C. harengus*, *S. pilchardus*, and *E. encrasicolus* are at regular distances at the sides of the GR blades of GA1 at approximately a relative distance of 0.17, 0.27, and 0.23 of the height measured from the interior face of the GR (Table 1). They are short, vary in shape between the three species (Figure 4), and were described as conical, diabolo shaped, and sickle shaped (Collard et al., 2017). The denticle length remains similar across all GA and is 0.098 mm ± 0.015 mm in *C. harengus*, 0.091 mm ± 0.013 mm in *S. pilchardus*, and 0.085 mm ± 0.018 mm in *E. encrasicolus* (Table 1, Figure 3F). The denticle length is similar across all branchials on GA1 (Figure 3H).

The calculated minimum and maximum mesh sizes are smallest in *S. pilchardus* with 0.007 mm^2 and 0.014 mm^2 and largest in *S. scombrus* with 0.113 mm^2 and 0.148 mm^2. In the clupeid species, the minimum mesh size is smaller than the maximum mesh size on all GA. In the scombrid species, this is only true for the anterior and posterior GR on GA1 and the posterior GR on GR2 (Figure 3I). Otherwise, the minimum mesh size is larger than the maximum

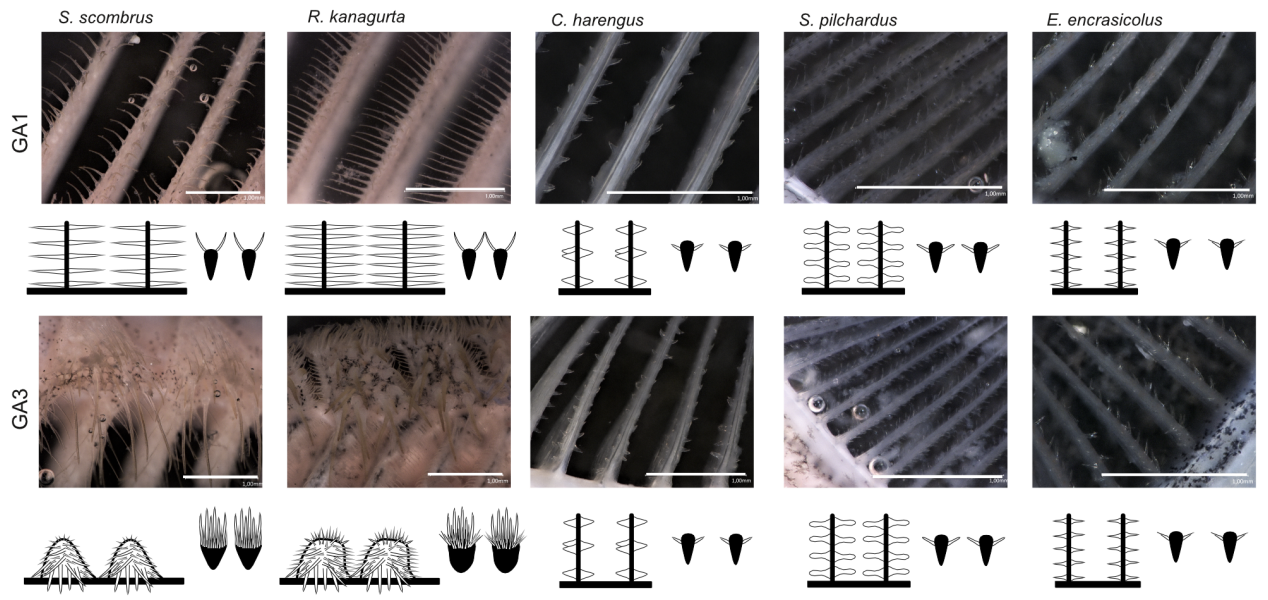

FIGURE 4
Denticle shape of the anterior GR on GA1 and GA3 for each species with view from inside the buccal cavity onto the flow facing side of GR and denticles (left) and cross-section through the GR and denticles (right), respectively. Scale bar 1 mm, drawings not to scale to each other.

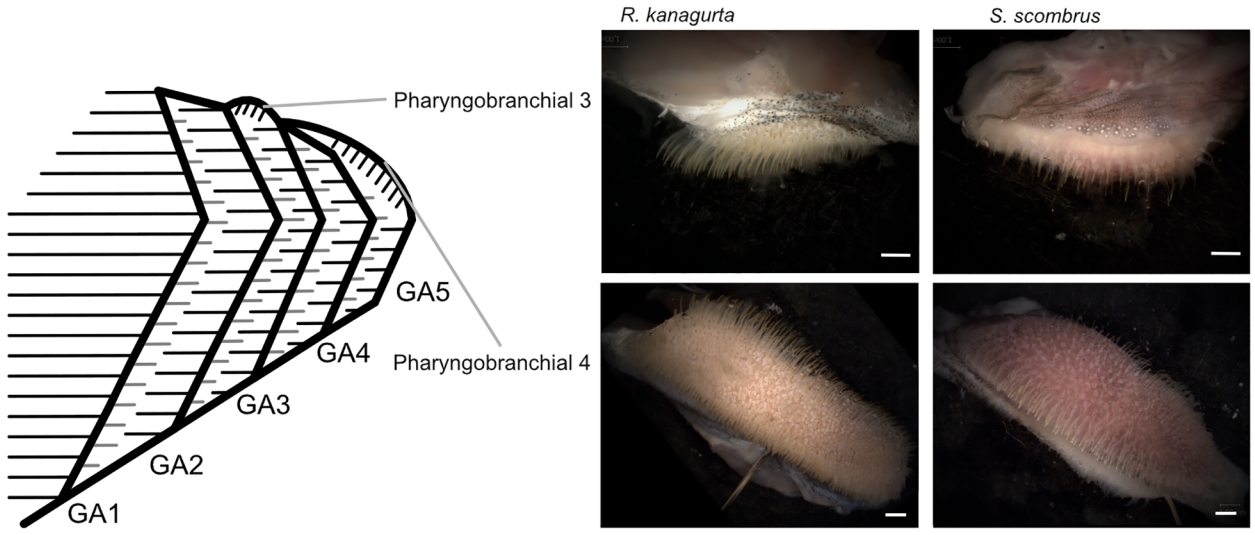

FIGURE 5
Position of pharyngobranchial 3 and pharyngobranchial 4 within the gill arch system and gill arches in *R. kanagurta* and *S. scombrus*. Scale bar, 1 mm.

mesh size. This is because of the different orientations of the denticles on GA2 to GA4 in the scombrid species. The denticles are directed inwards into the buccal cavity allowing much smaller distances between the denticles (see denticles on GA3 in Figure 3), which is one of the two factors in mesh size calculation (Equations 6, 7). The mesh size ratio based on the mean mesh size of GA1 to GA4 shows that the mesh size becomes smaller from anterior to posterior in *S. scombrus*, *R. kanagurta*, *S. pilchardus*, and *E. encrasicolus*. Only in *C. harengus*, the mesh size is smaller on GA1 compared to GA4 (Table 1).

During the dissection of the fish, mucus formation was noticed close to the esophagus in *S. scombrus* and *R. kanagurta*. GA5 and the fourth pharyngobranchial show a high amount of dark pigmented areas between the denticles and in the groove between the pharyngobranchials (Figure 6). These pigments are arranged on structures that we termed "mucus villi" because they remind of intestinal villi.

3.2 Principal component analysis and correlation matrix

The first three PCs explain 80.7% of the variance in the data (Figure 7). Based on the ranking of the loadings (Supplementary Information S4), PC1 (36.8%) relates to overall geometry and size (highest loadings in descending order: GAS length, GR length on GA1, length ratio of GA1 to GA5 (GA1–5 ratio), GR height-to-width ratio, and the filtration area), whereas PC2 (31.3%) relates to the filter medium and the fluid flow (highest loadings: GR number, mesh size max, mesh size min, relative open area of GA1, and MO ratio), and PC3 (12.6%) represents the symmetry (highest loadings:

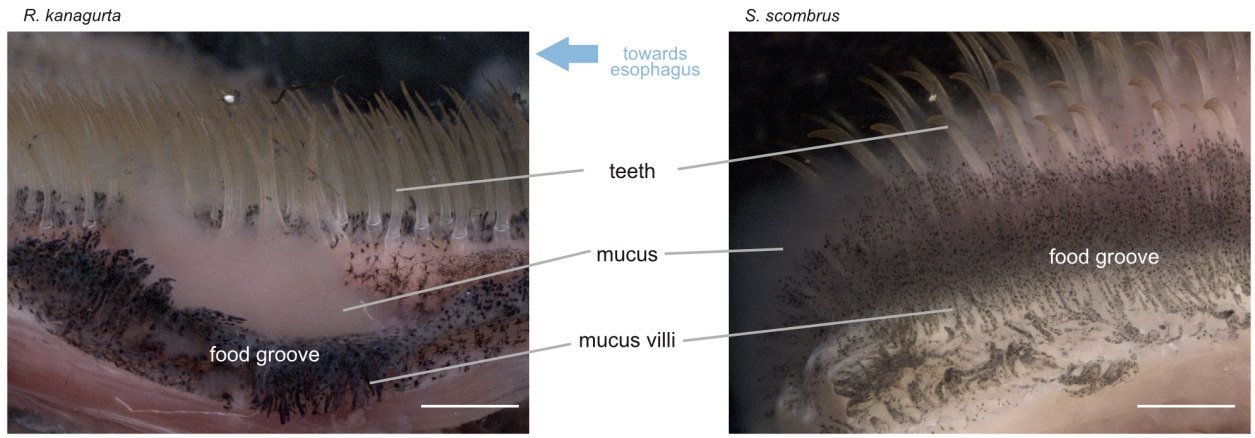

FIGURE 6
View of the food groove and medial side of GA5 in *R. kanagurta* and *S. scombrus*. Water flows from right to left towards the esophagus. Mucus was observed to originate from the mucus villi, which are located between the denticles and in the food groove. Scale bar, 1 mm.

symmetry, mesh size ratio, weight, fluid exit ratio, and mesh size min). In all of the combinations of the PCs, the individuals of one species cluster into distinct groups with little overlap between each other. While groups are evenly distributed in PC1, PC2 results in two groups that consist of *R. kanagurta*, *S. scombrus*, and *E. encrasicolus*, on the one hand, and *C. harengus* and *S. pilchardus*, on the other hand, thus not representing the two taxonomic groups Scombridae and Clupeiformes. PC3 shows a higher spread of the individuals within each group and separates the two scombrids, *R. kanagurta*, and *S. scombrus*, with the clupeid species in between them.

Most variables in the correlation matrix correlate positively with each other (Figure 8). Due to the high number of combinations, only the significant correlations with a correlation coefficient of ρ >0.7 are described (for detailed description and graphs, see Supplementary Information S5). For example, weight correlates positively with GAS length (ρ = 0.7), GAS length positively correlates with GR length of GA1 (ρ = 0.92), and head length correlates positively with denticle length (ρ = 0.83). Given the correction for size, this might indicate an allometric component in the above parameters and, consequently, on the filter-feeding mechanism. The longer the denticles on GA1, the larger the filtration area (ρ = 0.79), and the longer the GAS, the more cone-shaped (higher GA 1–5 ratio) and not cylindrical the GAS (ρ = 0.81). The shape of the mouth opening is more oval shaped in *C. harengus* and *S. pilchardus* and more round in the other three species. The more oval the mouth shape, the higher the number of GR on GA1 (ρ = 0.73). GR number on GA1 negatively correlates with minimum (ρ = −0.74) and maximum mesh size (ρ = −0.80).

3.3 Micro-CT scans

The micro-CT scans of the fish heads show the three-dimensional arrangement of the GAS within the buccal cavity in an open mouth position (Figure 1). In *S. scombrus* (Figure 1A) and *R. kanagurta* (Figure 1B), GA1 is very prominent in the anterior part of the buccal cavity. GA5 and the fourth pharyngobranchial narrow down the buccal cavity towards the esophagus forming a cylindrical geometry of the GAS. However, GR in *R. kanagurta* only touch the operculum with their distal tip, whereas the GR in *S. scombrus* are directed inwards. Even though the jaw angle of the head in this *S. scombrus* specimen is 56.3° and lies within the range of jaw angles during feeding (Figure 9), we assume that the mouth was not fully opened sideways, so the opercula did not open and the GAS could not expand to a natural feeding position. In the lateral view of *C. harengus* (Figure 1C) and *S. pilchardus* (Figure 1D), the buccal cavity has a narrow, cylindrical shape that bends upwards towards the esophagus. In the frontal cross-section with the view on the dorsal side, the buccal cavity is narrow and opens up at the GAS. In *S. pilchardus*, GA1 is in contact with the inner sides of the opercula, which again might indicate that the GAS is not fully expanded. The buccal cavity, the opercula, and the GAS in *E. encrasicolus* (Figure 1E) are shorter in an anterior–posterior direction compared to the other species. From both views, the GAS has a conical, almost rotational symmetric shape.

3.4 Behavior during ram feeding

Jaw angle and swimming velocity were measured in 20 *S. scombrus*, five *R. kanagurta*, nine *C. harengus*, 15 *S. pilchardus*, and 24 *E. encrasicolus* during feeding with an open mouth position (Table 1). The jaw angles of the manually opened mouth in the dissected individuals compared to the filter-feeding individuals in the videos show no significant differences (Figure 9A). The mean swimming velocity ranges between 0.34 m/s in *C. harengus* up to 0.5 m/s in *S. scombrus* (Table 1). In *S. scombrus*, *C. harengus*, and *E. encrasicolus*, the swimming velocity is higher during feeding than during non-feeding (Figure 9B). There is only a significant

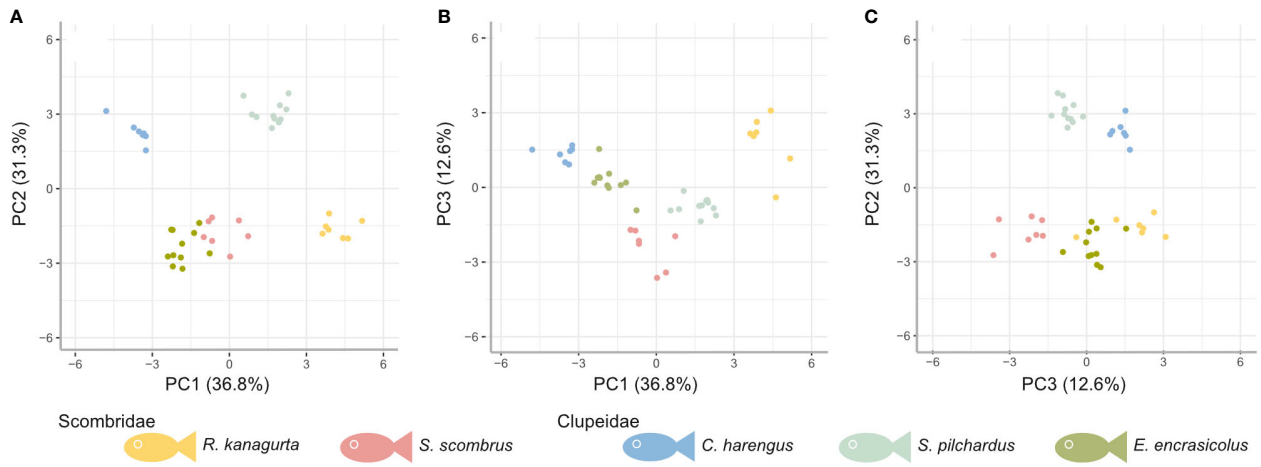

FIGURE 7
PCA based on the residuals to correct for allometry for five ram-feeding species (colors) in the combination of **(A)** principal component (PC) 1 and PC2, **(B)** PC1 and PC3, and **(C)** PC3 and PC2. PC1, PC2, and PC3 account for approximately 78.5% of the variation.

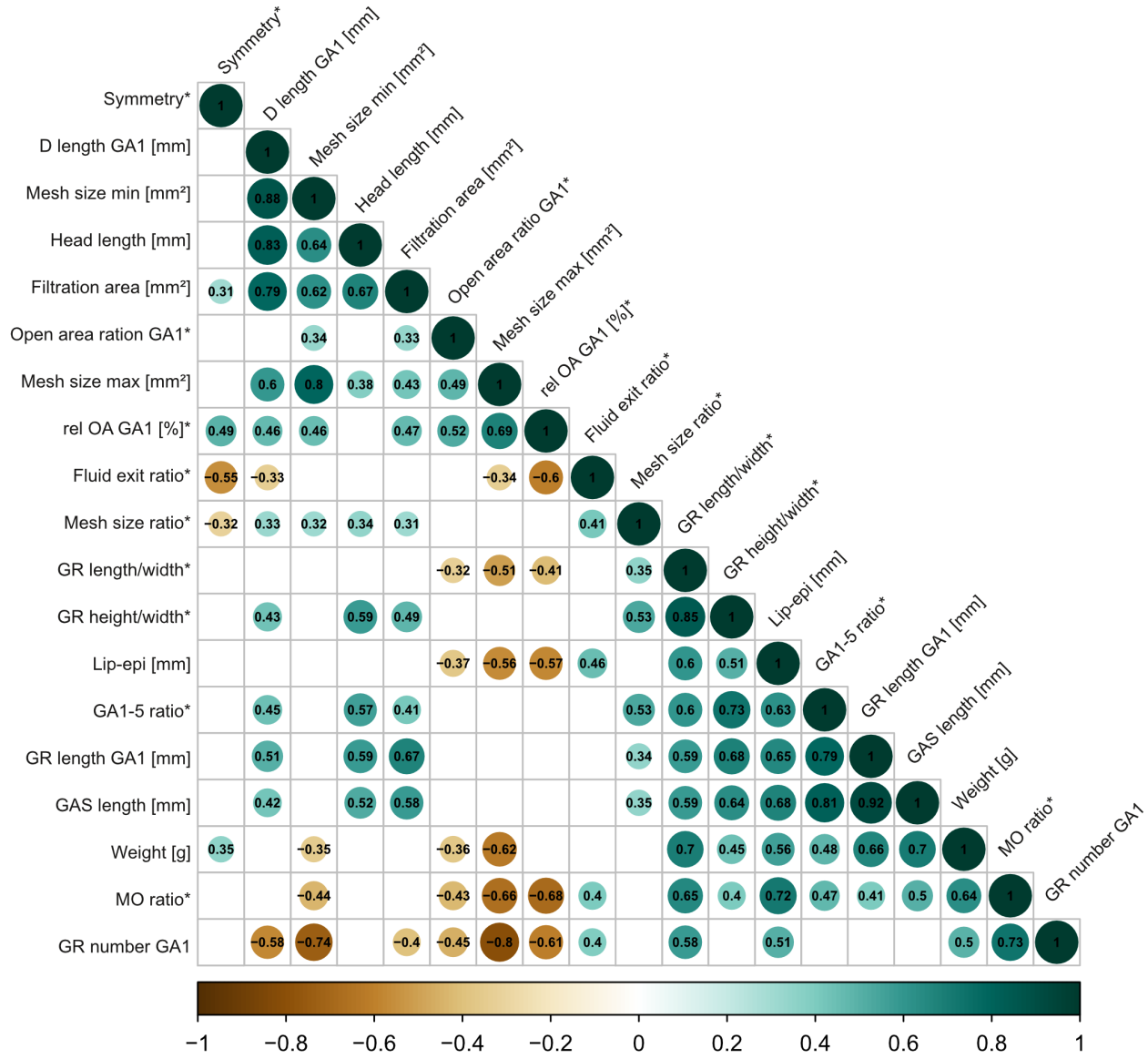

FIGURE 8
Correlation matrix based on Spearman rank tests with 19 size-corrected parameters across the five ram-feeding species to describe the GAS system. Only significant correlations ($p<0.05$) are indicated by color (positive correlations in green, negative correlations in brown) and the respective correlation coefficient. Relative parameters are indicated with an asterisk (*). See Table 1 for description of parameters.

difference in the swimming speed for *S. pilchardus* before and while feeding (Kruskal–Wallis rank sum test (chi-squared), *post-hoc* Dunn test (method "Holm"), $p = 0.0009$).

Based on the SL, the Reynolds number ranges between 35,000 in *E. encrasicolus* and 137,000 in *S. scombrus*. At the mouth opening, the Reynolds number ranges between 3,480 in *S. pilchardus* and 13,037 in *R. kanagurta* and around the denticles, the Reynolds number ranges between 13 in *E. encrasicolus* and 128 in *S. scombrus* (Table 1). With an open mouth position, the volume flowrate ranges between 1.59 L/min in *S. pilchardus* and up to 19.57 L/min in *R. kanagurta* (Table 1).

The feeding behavior was observed in six individuals each of *S. scombrus*, *R. kanagurta*, *C. harengus*, and *S. pilchardus* (Figure 9C). *Clupea harengus* and *S. pilchardus* show frequent mouth opening and closing with an average opening time of 0.17 s and 0.27 s, respectively. The average opening time in *S. scombrus* and *R. kanagurta* is 0.53 s and 3.7 s, respectively. In both species, cleaning was observed after the mouth was held open. Cleaning lasted, on average, 0.25 s in *S. scombrus* and 0.71 s in *R. kanagurta*.

3.5 Particle movement in GAS

With no fish head in the water tunnel, the brine shrimp eggs move at an average velocity of 66.5 ± 0.7 mm/s (N = 49). With a fish head in the water tunnel, the velocity of free-moving brine shrimp eggs decreases the further they move posteriorly within the buccal cavity (Figure 10A). At the open mouth, the velocity ranges between

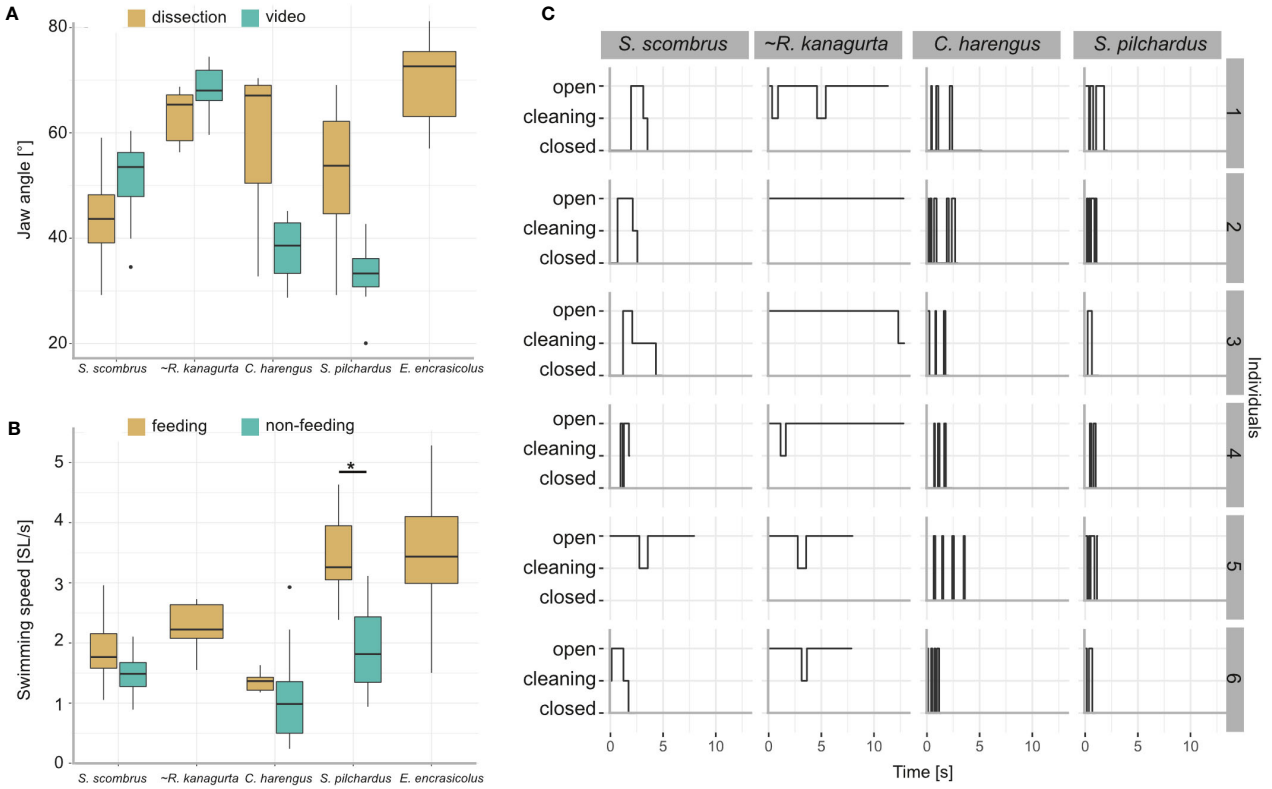

FIGURE 9
Results from the videography of five ram-feeding fishes during feeding. *S. scombrus*, *C. harengus*, *S. pilchardus*, and *E. encrasicolus* were filmed in public aquaria. *R. kanagurta* was filmed in the field, indicated by (~). **(A)** Comparison of the jaw angle in feeding individuals and the manually opened jaws during dissection. Due to video quality, the jaw angle in *E. encrasicolus* was not measured. Kruskal–Wallis rank sum test (chi-squared) with *post-hoc* Dunn test (method "Holm") showed no significant differences of jaw angle measurement type within each species. **(B)** Comparison of the swimming speed before feeding (non-feeding) and during feeding. Data were not available for *R. kanagurta* and *E. encrasicolus*. Kruskal–Wallis rank sum test (chi-squared) with *post-hoc* Dunn test (method "Holm") showed a significant difference in the swimming speed for *S. pilchardus* before and while feeding ($p = 0.0009$, indicated by asterisk). **(C)** Feeding behavior of six individuals described by the mouth position, i.e., closed, cleaning, opened over time.

43.9 mm/s ± 3 mm/s in *R. kanagurta* and 62.7 mm/s ± 4.3 mm/s in *C. harengus*, which equals a velocity decrease of 66% and 94.3%, respectively. At GA1, the velocity decreases to 19.2 mm/s ± 7.2 mm/s (28.9%) in *E. encrasicolus* and 40.4 mm/s ± 12.7 mm/s (60.7%) in *C. harengus*. The particle trajectories at the mouth entrance show a relatively straight line into the mouth in *R. kanagurta* and *C. harengus*, which changes at GA1 to an upwards motion in *R. kanagurta* and a downwards motion in *C. harengus* (Figure 10B). At GA1, between 50% of the particles in *E. encrasicolus* and 83.3% in *C. harengus* move freely in a posterior direction and have no contact with GR or denticles (Figure 10C). Particle rolling along the surface of GR and denticles is observed in 3.3% of the particles in *C. harengus* and 16.7% in *S. pilchardus*. The share of particles that stop on the surface of the mesh at GA1 ranges between 5% in *C. harengus* and 20% in *E. encrasicolus*. Between 8.3% of the particles in *C. harengus* and 32.7% in *R. kanagurta* move through the meshes of GA1 and out of the GAS. No particles are lost in *S. pilchardus*. In the intact fish heads, the ink shows a stable rotational vortex at the mouth entrance in *R. kanagurta* and *E. encrasicolus* that diffuses the ink (Supplementary Information S3, Supplementary Figure S2). The vortex is not present when GA1 is removed, and both opercula are replaced with transparent foil. This indicates that drag posed by the GAS and the head is reduced with opercula and right GA1 removal, and hence, particle velocity might be even slower in intact fish heads. At the set flow velocity of 6.5 cm/s, the Reynolds number at the open mouth ranges between 468 in *S. pilchardus* and 975 in *S. scombrus*, which is 13%–19% of the Reynolds number calculated for the feeding behavior experiments (Table 1). The flow visualized with black ink remains laminar when passing GR and denticles (Supplementary Information 3, Supplementary Figure 2).

4 Discussion

Based on GAS morphology, feeding behavior, and particle movement, we suggest that the filtration mechanism in these ram-feeding fishes in fact combines cross-flow and dead-end filtration (Figure 11). The parallel orientation of the anterior GA and GR towards the incoming flow is a morphological characteristic for cross-flow filtration (CFF) in ram feeders (Cheer et al., 2001; Paig-Tran et al., 2011). Our functional analysis further supports the morphological evidence, as 75% of the brine shrimp eggs move freely or roll along the surface of GA1. Free-moving particles in a

10.3389/fmars.2023.1253083

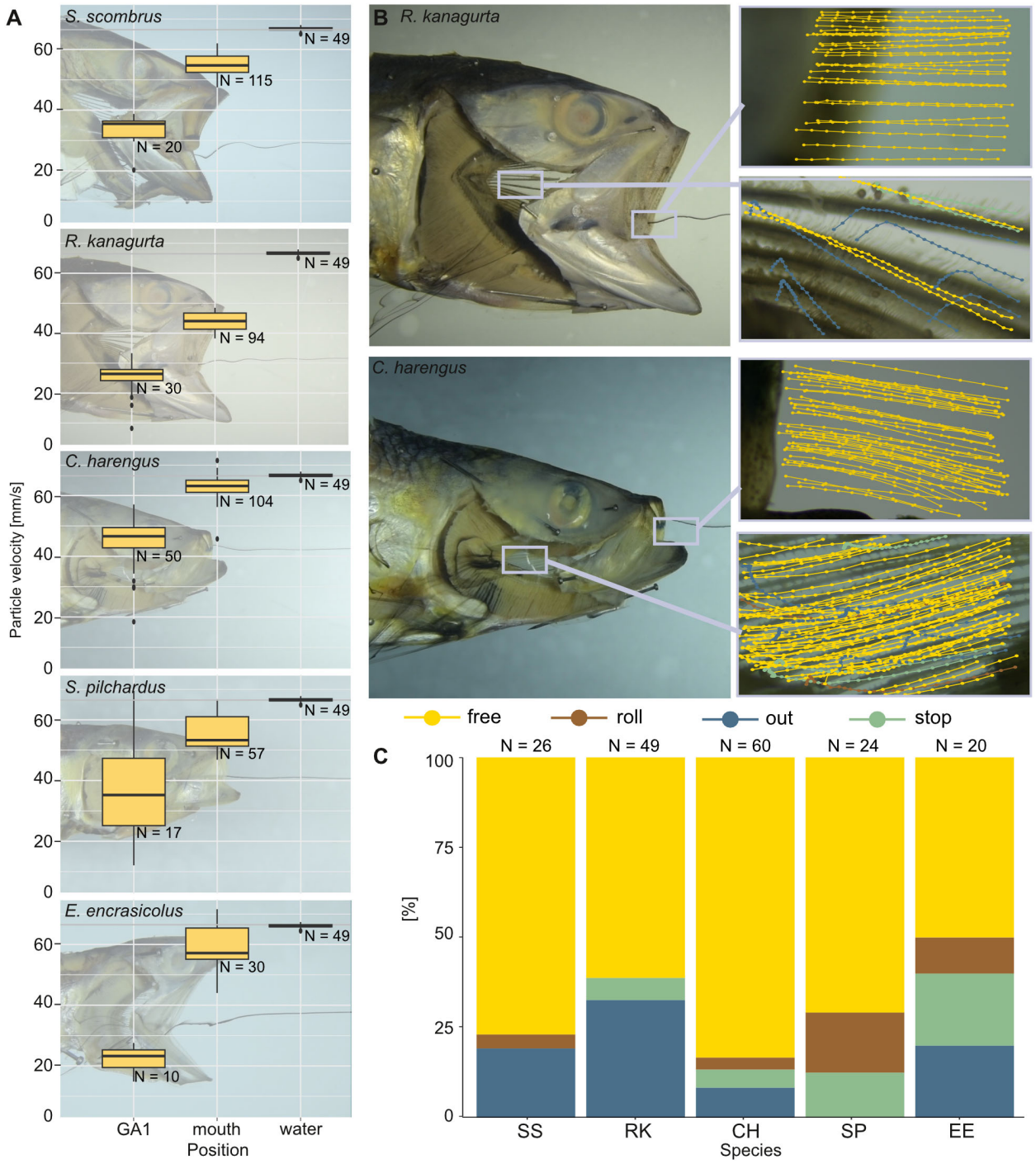

FIGURE 10
Velocity of brine shrimp eggs in ram-feeding fish in an open-mouth position in the water tunnel. The opercula are replaced by transparent foil, and GA1 is removed (dissection step 4). Particle behavior is divided into free (yellow), out (blue), roll (brown), and stop (green). **(A)** Velocity of the free moving brine shrimp eggs (mm/s) in the water without the fish, at the mouth entrance and at the left ceratobranchial of GA1. **(B)** Examples for the sections filmed in *R. kanagurta* and *C. harengus* with tracked particle movement plotted in the image. **(C)** Share [%] of particle movement at GA1 and PB for the five ram-feeding species: *S. scombrus* (SS), R. *kanagurta* (RK), *C. harengus* (CH), *S. pilchardus* (SP), and *E. encrasicolus* (EE).

posterior direction were also identified as typical for CFF in the filter-feeding tilapia *Oreochromis aureus* (Smith and Sanderson, 2007). However, the conically tapered GAS geometry from GA1 to the more posterior GA together with the observed reduction of particle velocity also suggest a transition from cross-flow to dead-end filtration. In technical filtration processes, the angle of the filter medium towards the flow, which we define as the angle of attack α (Figure 11D), is typically 0° in CFF and 90° in dead-end filtration (Sutherland, 2008). Based on our results, we suggest the term "semi-CFF," for which 90° > α > 0°, in order to differentiate this

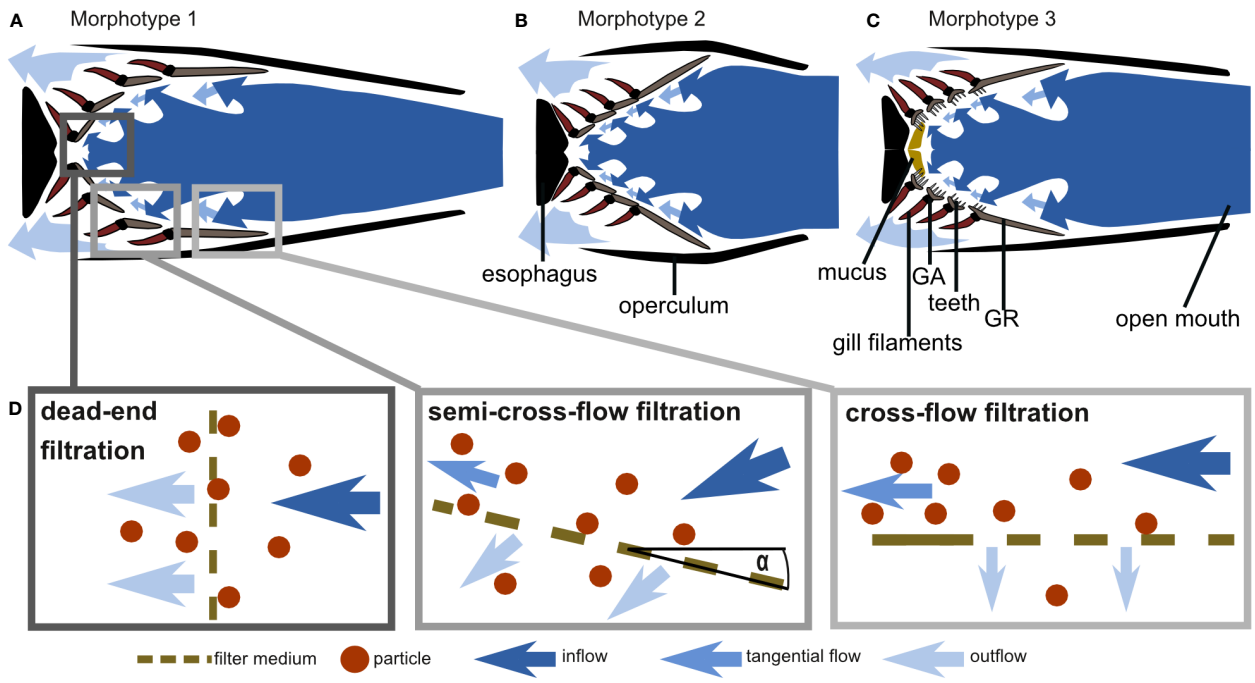

FIGURE 11
Schematic drawings of cross-sections through the frontal plane of the GAS at the height of the epi-ceratobranchial joints (compare right-hand images in Figure 1) and hypothesized water flow through the three morphotypes based on morphometric measurements, micro-CT scans, and flow tank experiments: **(A)** *C. harengus* and *S. pilchardus* represent morphotype 1, **(B)** *E. encrasicolus* represents morphotype 2, and **(C)** *S. scombrus* and *R. kanagurta* represent morphotype 3 (drawings not to scale). **(D)** Schematic drawing of cross-flow, semi-cross-flow, and dead-end filtration and their position in the fish mouth as exemplarily shown for morphotype 1.

suspension feeding system from dead-end and CFF (Figure 11D). We further hypothesize that the share of free and rolling particles will decrease with increasing α, an aspect that deserves further study in other species. In general, our results provide evidence for the hypotheses of previous studies in which a combination of CFF and dead-end filtration was suggested for the ram-feeding American shad (Storm et al., 2020). The combination of CFF and dead-end filtration enables ram-feeding fishes to direct the incoming food particles towards the esophagus where they are accumulated before being periodically swallowed.

In addition, based on our morphometric measurements, we can describe three GAS morphotypes that further indicate variation of the general particle separation mechanism (Figure 11). The three clupeid species represent two morphotypes in which the GA, GR, and denticles form a smooth filtration surface with regular meshes. However, *S. pilchardus* and *C. harengus* differ from *E. encrasicolus* regarding the geometry of the open mouth, the pipe length, and the GAS symmetry. Therefore, *S. pilchardus* and *C. harengus* is represented by morphotype 1 that has an oval-shaped mouth opening and a narrow buccal cavity leading towards the GAS (Figure 11A), whereas *E. encrasicolus* represents morphotype 2 with a wide, round mouth opening, and a short distance to the short, symmetrical, cone-shaped GAS (Figure 11B). The two scombrid species represent morphotype 3 that can be clearly distinguished to the other two morphotypes by the round mouth opening, the presence of two GR types (only GR on GA1 are blade shaped), the densely packed denticles on GA2 to GA4 on the inner facing edge of the GR, long teeth on GA that are oriented into the buccal cavity, two visible pharyngobranchials, and the presence of mucus (Figure 11C). In the following, we describe the morphotypes in detail to identify their function related to filter feeding.

In all five species, the lips protrude forward, and the opercula and branchiostegal rays stretch outwards when the jaw opens for filter feeding. The protruded lips and the open operculum form a pipe-like structure to guide the water towards and through the cone-shaped GAS (Figures 1, 11). This "pipe length" correlates positively with a long, cone-shaped GAS, but negatively with mesh size and open area ratio. We assume that a longer pipe breaks down large turbulences from the ambient flow and allows for smaller mesh sizes with slow flow. Additionally, a large filtration area, a high open area ratio, and a high fluid exit ratio reduce the resistance to flow (Sutherland, 2008; Brooks et al., 2018) and slow down the flow velocity at the mesh, as observed in our experiments and described for filter-feeding manta rays (continuity equation, see Divi et al., 2018). Around the denticles, the ratio between inertial and viscous forces ranges between Re 13 in the smaller species and Re 128 in the larger species, which indicates laminar flow and is in line with results of other studies (Rykaczewski, 2009; Brooks et al., 2018). Because of the cone shape with the closed esophagus at the end and given the distribution of the calculated relative open area, most of the water exists at the anterior opening of the cone (largest circumference). Besides the anterior–posterior geometry, the GAS is asymmetric in its dorso-ventral orientation. The area formed by the upper GA is in all species smaller than the lower area; hence, more

water is exiting laterally from the operculum and ventrally from the branchiostegal rays.

All GR in the clupeid species and the GR on GA1 in the scombrid species are blade shaped with length-to-width and height-to-width ratios (Figures 3E, F) that are similar to other filter-feeding species (Gibson, 1988; Storm et al., 2020). The height-to-width ratio of the GR cross-section is also defined as the fineness ratio in hydrodynamics and describes the geometry of streamlined bodies to minimize drag, which optimally ranges between 2 and 8 (Vogel, 1996; Ahlborn et al., 2009). The fineness ratio of the GR on GA1 in the selected species is between 2.6 and 7.2 and lies within the optimal range for streamlined bodies.

In both, cross-flow and dead-end filtration, the particles are retained on the surface of the filter medium. The tangential flow in CFF transports particles along the filter medium, which is facilitated by a smooth surface. This can be seen in morphotypes 1 and 2 in which the denticles extend laterally from the GR to form small meshes (Rykaczewski, 2009; Collard et al., 2017). Surface structures, such as teeth in the scombrid species, will probably pose an obstacle that induces the particles to stop. As observed with the brine shrimp eggs, the clupeid species with a smooth surface show a higher share of rolling particles with 9.8 ± 6.4% than *S. scombrus* with 3.8% and *R. kanagurta* 0%, which both have teeth. Therefore, the mackerel species might capture food particles between the inwards directed teeth and denticles. This mechanism resembles the technical depth filtration in which particles are retained inside the pores of a filter medium (Sutherland, 2008). It is unclear if the observed differences in denticle shape influence mesh size or have other functions. Mesh size is calculated based on the assumption of evenly distributed, rectangular, stiff meshes (Sutherland, 2008; Collard et al., 2017). However, denticles from neighboring GR do not touch and form closed meshes and might bend in the oncoming flow. Additionally, denticles and teeth are oriented not laterally but medially into the buccal cavity in the scombrid species, which challenges the applied calculation for rectangular meshes. Therefore, GR might be more relevant in mesh formation than denticles, as demonstrated by the positive correlation of GR number and minimum mesh size (Figure 8). Still, it is unclear how mesh size influences particle retention because removing GR and microbranchiospines in Galilee Saint Peter's fish (*Tilapia galilaea*) did not affect particle ingestion rate and selectivity (Drenner et al., 1987). However, this species is a pump-feeding fish, and its GR are not as long as the ones of the ram-feeding fishes in our study. GR length, GR shape, and GR gap might thus be indicators for different filter-feeding mechanisms and morphotypes. All five analyzed species are large shoal, pelagic fishes at an intermediate trophic level with a wide distribution (Bullen, 1912; Garrido and van der Lingen, 2014). As shown for filter- and particulate-feeding anchovies, pilchards (Garrido and van der Lingen, 2014), or Tilapia (Dempster et al., 1995), plasticity in feeding behavior allows dietary opportunism on plankton, as it is a heterogeneous food source. Adaption to different food sizes allows the co-occurring of several species within one habitat, as observed for anchovy and sardine species (Garrido and van der Lingen, 2014). As expected, the dimensions of the GAS are a significant factor in selecting particle size. For example, *C. harengus* and *S. pilchardus* have similar mesh sizes in the size-corrected data. They cluster together in the PCA and correlation matrix (Figures 3, 8; Supplementary Information 3), probably using very similar mechanisms, even though the standard length of *C. harengus* is around twice as long as of *S. pilchardus*.

Cross-flow filtration in technical applications is characterized by a time-dependent, steady-state particle distribution and the prolonged occurrence of clogging (Ripperger and Altmann, 2002; Makabe et al., 2021). Clogging reduces filtration performance. Therefore, cleaning is an important step in any filtration process. In the case of filter-feeding organisms, cross-flow filtration was assumed to reduce clogging (Brooks et al., 2018), avoid clogging (Storm et al., 2020), or that it is prevented by periodic swallowing (Paig-Tran et al., 2011). Therefore, it is crucial to consider the time-dependent behavior in our study to identify cross-flow filtration. During the behavioral studies, we observed frequent cleaning in ram-feeding *R. kanagurta* in the field (Figure 9). This further supports the hypothesis that cross-flow filtration is not the only filtration mechanism present in the observed species. However, our ability to interpret the results obtained in the environment of the aquaria is limited. While we measured 0.5 m/s for *S. scombrus* in the aquarium, it was reported that the swimming speed of *S. scombrus* in the Norwegian Sea ranged between 1.1 and 1.8 m/s measured with sonar (Nøttestad et al., 2016). Most ram-filter-feeding fish species also show opportunistic particulate feeding, which differs regarding swimming speed, mouth opening time, and cleaning frequency (Batty et al., 1986; Pepin et al., 1988; James and Findlay, 1989). Within the current literature, there are no established criteria to identify these feeding types. Filter feeding was either identified when the mouth was opened longer than 0.5 s in *S. scombrus* (Pepin et al., 1988), 1–3 s in *Scomber japonicus* (O'Connell and Zweifel, 1972), or >0.4–3 s in *Engraulis capensis* (James and Findlay, 1989). Additionally, the occurrence of filter feeding depends on particle concentration (O'Connell and Zweifel, 1972; Gibson and Ezzi, 1985) and particle size (Garrido et al., 2007), especially in relation to fish size (Crowder, 1985). For the Gizzard shad, particle selectivity was also based on nutrient content (Heidman et al., 2012). Therefore, we cannot clearly identify filter feeding in the aquaria experiments.

Each of the applied methods to investigate aspects of filter feeding has strengths and limitations. The morphometric analysis of fresh dissected specimens prevented artifacts due to fixation methods. Yet, micro-CT scans were necessary to reveal the three-dimensional arrangement of the GAS. Even though micro-CT scans are non-invasive, they are prone to fixation artifacts, e.g., regarding the opercula position. The usage of preserved fish in the water tunnel experiments shows the same problem. Nevertheless, using preserved fish is advantageous, as they do not lack morphological detail that is difficult to manufacture in artificial models, such as denticles. In this context, the step-wise removal of the opercula and the right GA1 might have influenced the flow through the buccal cavity even though the opercula were replaced by transparent foil. Additionally, the water tunnel experiments were performed only in laminar flow conditions with a constant flow velocity and one individual per species.

At this point, with the limitations of the experimental procedures and the complexity of filter feeding, i.e., the interaction of

environmental conditions, feeding behavior, the variety in filter-feeding morphology, and food particle characteristics (Cheer et al., 2012), it is challenging to predict filtration efficiency. Looking at gut content, *S. scombrus* and *R. kanagurta* feed mainly on copepods, cladocerans, diatoms, peridinians, and larvae of adult decapoda, but also appendicularians, polychaeta larvae, post-larvae bivalves, pteropods, cirripede nauplii, small hydromedusae, and fish eggs and larvae (Bullen, 1912; Bhimachar and George, 1952; Runge et al., 1987), which indicates a retention ability for a diversity of particle types and sizes. One study showed that the gut content of *R. kanagurta* was the same as the ambient plankton, indicating non-selectivity (Rao and Rao, 1957). This is also supported by the fact that ram-feeding fish ingest microplastics: 40%–50% of *C. harengus*, *S. pilchardus*, and *E. encrasicolus* had microplastics in their stomachs in sizes between 0.13 mm to 22.4 mm (Collard et al., 2017).

5 Conclusions

Based on the GAS morphology, we were able to identify three morphotypes in the studied ram-feeding fishes that all use a combination of cross-flow and dead-end filtration as the general particle separation mechanism. Within the conical GAS, the particles are directed through cross-flow filtration in the anterior GAS towards the posterior esophagus where they accumulate through dead-end filtration. The transition of the two, termed semi-CFF and characterized with an angle of attack of the filter medium between 0° and 90°, might also be relevant for other ram-feeding suspension feeders, such as manta rays, whale sharks, or baleen whales. We identified differences in geometry, filter media, symmetry, and surface structures, and described these in three morphotypes. Each morphotype is most likely to influence fluid flow and particles retention. Even though we analyzed only five species, we identified many distinct morphological traits, which leads us to expect a large morphological diversity in filter-feeding fishes.

Data availability statement

The raw data supporting the conclusions of this article will be made available by the authors, without undue reservation.

Ethics statement

Ethical approval was not required for the study involving animals in accordance with the local legislation and institutional requirements because the fishes were obtained dead and frozen from a commercial delicatessen shop.

Author contributions

LH: conceptualization and methodology, experimental investigation of gill arch system morphology and filter-feeding behavior, conduction of experiments in water tunnel, data analysis and visualization, formal analysis, writing: original draft, writing: review and editing; KS: water tunnel assembly, conduction of experiments in water tunnel, writing: review and editing; JH: experimental investigation of GAS morphology, writing: review and editing; SE: experimental investigation of GAS morphology, writing: review and editing; TS: PTA staining and micro-CT scans, writing: review and editing; AB: writing, review and editing, supervision, project administration, funding acquisition and conceptualization. All authors contributed to the article and approved the submitted version.

Funding

LH, KS, JH, SE, and AB were supported by the European Research Council (ERC) under the European Union's Horizon 2020 research and innovation program (grant agreement no. 754290) and the Federal Ministry of Education and Research (BMBF) under the programme "Ideenwettbewerb Biologisierung der Technik" (grant agreement no. 13XP5164A). TS was supported by Leibniz Association grant P91/2016 (SAW-Ricefish).

Acknowledgments

We thank the following aquaria for enabling us to film the fishes in their tanks: SeaLife Center Oberhausen (Germany), Ozeaneum (Stralsund, Germany), Aquarium La Rochelle (France), and Aquarium San Sebastian (Spain). We also thank Swantje Neumeyer and Bodo Kallwitz for sharing their videos of *R. kanagurta* in the Red Sea. We are grateful for the support by Jens Hamann in taking photos and videos, the workgroup around Prof. Dr. Reinhard Predel (University of Cologne) for letting us use his Keyence, and Dr. Hendrik Herzog and Christian Grünewald for designing and assembling the water tunnel.

Conflict of interest

The authors declare that the research was conducted in the absence of any commercial or financial relationships that could be construed as a potential conflict of interest.

Publisher's note

Supplementary material

The Supplementary Material for this article can be found online at: https://www.frontiersin.org/articles/10.3389/fmars.2023.1253083/full#supplementary-material

References

Ahlborn, B. K., Blake, R. W., and Chan, K. H. S. (2009). Optimal fineness ratio for minimum drag in large whales. *Can. J. Zoology* 87, 124–131. doi: 10.1139/Z08-144

Alder, J., Campbell, B., Karpouzi, V., Kaschner, K., and Pauly, D. (2008). Forage fish: from ecosystems to markets. *Annu. Rev. Environ. Resour.* 33, 153–166. doi: 10.1146/annurev.environ.33.020807.143204

Batty, R. S. S., Blaxter, J.H.S.H.S., and Libby, D. A. A. (1986). "Herring (Clupea harengus) filter-feeding in the dark," in *Marine Biology*. (Springer). doi: 10.1007/BF00428631

Bhimachar, B. S., and George, P. C. (1952). Observations on the food and feeding of the Indian mackerel,Rastrelliger canagurta (Cuvier). *Proc. Indian Acad. Sci.* 36, 105–118. doi: 10.1007/BF03050438

Brooks, H., Haines, G. E., Lin, M. C., and Sanderson, S. L. (2018). Physical modeling of vortical cross-step flow in the American paddlefish, Polyodon spathula. *PloS One* 13, e0193874. doi: 10.1371/journal.pone.0193874

Bullen, G. E. (1912). Some notes upon the feeding habits of mackerel and certain clupeoids in the english channel. *J. Mar. Biol. Assoc. United Kingdom* 9, 394–403. doi: 10.1017/S0025315400048335

Cheer, A., Cheung, S., Hung, T.-C., Piedrahita, R. H., and Sanderson, S. L. (2012). Computational fluid dynamics of fish gill rakers during crossflow filtration. *Bull. Math. Biol.* 74, 981–1000. doi: 10.1007/s11538-011-9709-6

Cheer, A. Y., Ogami, Y., and Sanderson, S. L. (2001). Computational fluid dynamics in the oral cavity of ram suspension-feeding fishes. *J. Theor. Biol.* 210, 463–474. doi: 10.1006/jtbi.2001.2325

Cohen, K. E., and Hernandez, L. P. (2018a). The complex trophic anatomy of silver carp, Hypophthalmichthys molitrix, highlighting a novel type of epibranchial organ. *J. Morphology* 279, 1615–1628. doi: 10.1002/jmor.20891

Cohen, K. E., and Hernandez, L. P. (2018b). Making a master filterer: Ontogeny of specialized filtering plates in silver carp (Hypophthalmichthys molitrix). *J. Morphology* 279, 925–935. doi: 10.1002/jmor.20821

Collard, F., Gilbert, B., Eppe, G., Roos, L., Compère, P., Das, K., et al. (2017). Morphology of the filtration apparatus of three planktivorous fishes and relation with ingested anthropogenic particles. *Mar. pollut. Bull.* 116, 182–191. doi: 10.1016/j.marpolbul.2016.12.067

Collette, B. B., and Gillis, G. B. (1992). Morphology, systematics, and biology of the double-lined mackerels (Grammatorcynus, Scombridae). *Fishery Bull.* 90, 13–53. doi: 10.1016/j.marpolbul.2016.12.067

Costalago, D., Garrido, S., and Palomera, I. (2015). Comparison of the feeding apparatus and diet of European sardines Sardina pilchardus of Atlantic and Mediterranean waters: Ecological implications. *J. Fish Biol.* 86, 1348–1362. doi: 10.1111/jfb.12645

Crowder, L. B. (1985). Optimal foraging and feeding mode shifts in fishes. *Environ. Biol. Fishes* 12, 57–62. doi: 10.1007/BF00007710

Dempster, P., Baird, D. J., and Beveridge, M. C. M. (1995). Can fish survive by filter-feeding on microparticles? Energy balance in tilapia grazing on algal suspensions. *J. Fish Biol.* 47, 7–17. doi: 10.1111/j.1095-8649.1995.tb01868.x

Divi, R. V., Strother, J. A., and Paig-Tran, E. W. M. (2018). Manta rays feed using ricochet separation, a novel nonclogging filtration mechanism. *Sci. Adv.* 4, eaat9533. doi: 10.1126/sciadv.aat9533

Dray, S., and Josse, J. (2015). Principal component analysis with missing values: a comparative survey of methods. *Plant Ecol.* 216, 657–667. doi: 10.1007/s11258-014-0406-z

Drenner, R. W., Hambright, K. D., Vinyard, G. L., and Gophen, M. (1987). Particle ingestion by tilapia galilaea is not affected by removal of gill rakers and microbranchiospines. *Trans. Am. Fisheries Soc.* 116, 272–276. doi: 10.1577/1548-8659(1987)116<272:PIBTGI>2.0.CO;2

Friedland, K. D., Ahrenholz, D. W., Smith, J. W., Manning, M., and Ryan, J. (2006). Sieving functional morphology of the gill raker feeding apparatus of atlantic menhaden. *J. Exp. Zoology Part A: Comp. Exp. Biol.* 305, 974–985. doi: 10.1002/jez.a.348

Garrido, S., Marçalo, A., Zwolinski, J., and van der Lingen, C. (2007). Laboratory investigations on the effect of prey size and concentration on the feeding behaviour of Sardina pilchardus. *Mar. Ecol. Prog. Ser.* Boca Raton, FL: CRC Press) 330, 189–199. doi: 10.3354/meps330189

Garrido, S., and van der Lingen, C. D. (2014). "Feeding biology and ecology," in *Biology and Ecology of Sardines and Anchovies*. Ed. K. Ganias (CRC Press), 122–189.

Gibson, R. N. N. (1988). Development, morphometry and particle retention capability of the gill rakers in the herring, Clupea harengus L. *J. Fish Biol.* 32, 949–962. doi: 10.1111/j.1095-8649.1988.tb05438.x

Gibson, R. N., and Ezzi, I. A. (1985). Effect of particle concentration on filter- and particulate-feeding in the herring Clupea harengus. *Mar. Biol.* 88, 109–116. doi: 10.1007/BF00397157

Gnanamuttu, B. Y. J. C. (1966). Osteology of the Indian mackerel, rastrelliger kanagurta (Cuvier). *Indian J. Fisheries* 13, 1–26.

Goodrich, J. S. S., Sanderson, S. L. L., Batjakas, I. E. E., and Kaufman, L. S. S. (2000). Branchial arches of suspension-feeding Oreochromis esculentus: Sieve or sticky filter? *J. Fish Biol.* 56, 858–875. doi: 10.1111/j.1095-8649.2000.tb00877.x

Haines, G. E., and Sanderson, S. L. (2017). Integration of swimming kinematics and ram suspension feeding in a model American paddlefish, Polyodon spathula. *J. Exp. Biol.* 220, 4535–4547. doi: 10.1242/jeb.166835

Hallacher, L. E. (1977). On the feeding behavior of the Basking shark, Cetorhinus maximus. *Environ. Biol. Fishes* 2, 297–298. doi: 10.1007/BF00005996

Heidman, M., Holley, L., Chambers, R., and Sanderson, S. (2012). Selective feeding on nutrient-rich particles by gizzard shad Dorosoma cepedianum does not involve mechanical sorting. *Aquat. Biol.* 17, 129–139. doi: 10.3354/ab00470

Hentschel, B. T., and Shimeta, J. (2008). "Suspension feeders," in *Encyclopedia of Ecology* (Amsterdam: Elsevier Science Ltd), 3437–3442.

Hernderson, S. (1983). *An Evaluation of Filter Feeding Fishes for Removing Excessive Nutrients and Algae from Wastewater* (Washington D.C., USA: United States Environmental Protection Agency).

Hung, T., and Piedrahita, R. H. (2014). Experimental validation of a novel bio-inspired particle separator. *Aquacultural Eng.* 58, 11–19. doi: 10.1016/j.aquaeng.2013.09.005

James, A., and Findlay, K. (1989). Effect of particle size and concentration on feeding behaviour, selectivity and rates of food ingestion by the Cape anchovy Engraulis capensis. *Mar. Ecol. Prog. Ser.* 50, 275–294. doi: 10.3354/meps050275

Jørgensen, C. B. (1966). *Biology of Suspension Feeding* (Oxford: Pergamon Press).

Langeland, A., and Nost, T. (1995). Gill raker structure and selective predation on zooplankton by particulate feeding fish. *J. Fish Biol.* 47, 719–732. doi: 10.1111/j.1095-8649.1995.tb01937.x

Limaye, A. (2012). *Drishti: a volume exploration and presentation tool*. Ed. S. R. Stock, 85060X. doi: 10.1117/12.935640

Magnuson, J. J., and Heitz, J. G. (1971). Gill raker apparatus and food selectivity among mackerels, tunas, and dolphins. *Fishery Bull.* 69, 361–370.

Makabe, R., Akamatsu, K., Tatsumi, R., Koike, O., and Nakao, S.i. (2021). Numerical simulations of lift force and drag force on a particle in cross-flow microfiltration of colloidal suspensions to understand limiting flux. *J. Membrane Sci.* 621, 118998. doi: 10.1016/j.memsci.2020.118998

Nøttestad, L., Diaz, J., Penã, H., Søiland, H., Huse, G., and Fernö, A. (2016). Feeding strategy of mackerel in the Norwegian Sea relative to currents, temperature, and prey. *ICES J. Mar. Sci.* 73, 1127–1137. doi: 10.1093/icesjms/fsv239

O'Connell, C. P., and Zweifel, J. R. (1972). A laboratory study of particulate and filter feeding of the pacific mackerel, Scomber japonicus. *Fishery Bull.* 70, 973–981.

Ory, N., Chagnon, C., Felix, F., Fernández, C., Ferreira, J. L., Gallardo, C., et al. (2018). Low prevalence of microplastic contamination in planktivorous fish species from the southeast Pacific Ocean. *Mar. pollut. Bull.* 127, 211–216. doi: 10.1016/j.marpolbul.2017.12.016

Paig-Tran, E. W. M., Bizzarro, J. J., Strother, J. A., and Summers, A. P. (2011). Bottles as models: Predicting the effects of varying swimming speed and morphology on size selectivity and filtering efficiency in fishes. *J. Exp. Biol.* 214, 1643–1654. doi: 10.1242/jeb.048702

Pepin, P., Koslow, J. A., and Pearre, S. (1988). Laboratory study of foraging by Atlantic mackerel, Scomber scombrus, on natural zooplankton assemblages. *Can. J. Fisheries Aquat. Sci.* 45, 879–887. doi: 10.1139/f88-106

Phillips, M. B., and Bonner, T. H. (2015). Occurrence and amount of microplastic ingested by fishes in watersheds of the Gulf of Mexico. *Mar. pollut. Bull.* 100, 264–269. doi: 10.1016/j.marpolbul.2015.08.041

Rao, K. V. N., and Rao, K. P. (1957). Differences in the food of the young and the adult Indian mackerel, rastrelliger kanagurta (Cuv.). *Nature* 180, 711–712. doi: 10.1038/180711b0

Ribeiro, F., Okoffo, E. D., O'Brien, J. W., Fraissinet-Tachet, S., O'Brien, S., Gallen, M., et al. (2020). Quantitative analysis of selected plastics in high-commercial-value Australian seafood by pyrolysis gas chromatography mass spectrometry. *Environ. Sci. Technol.* 54, 9408–9417. doi: 10.1021/acs.est.0c02337

Ripperger, S., and Altmann, J. (2002). Crossflow microfiltration - State of the art. *Separation Purification Technol.* 26, 19–31. doi: 10.1016/S1383-5866(01)00113-7

Rubenstein, D. I., and Koehl, M. A. R. (1977). The mechanisms of filter feeding: some theoretical considerations. *Am. Nat.* 111, 981–994. doi: 10.1086/283227

Runge, J. A., Pepin, P., and Silvert, W. (1987). Feeding behavior of the Atlantic mackerel Scomber scombrus on the hydromedusa Aglantha digitale. *Mar. Biol.* 94, 329–333. doi: 10.1007/BF00428238

Rykaczewski, R. R. (2009). *Influence of Oceanographic Variability on the Planktonic Prey and Growth of Sardine and Anchovy in the California Current Ecosystem* (San Diego, USA: University of California).

Sanderson, S. L., Cheer, A. Y., Goodrich, J. S., Graziano, J. D., and Callan, W. T. T. (2001). Crossflow filtration in suspension-feeding fishes. *Nature* 412, 439–441. doi: 10.1038/35086574

Sanderson, S. L., Roberts, E., Lineburg, J., and Brooks, H. (2016). Fish mouths as engineering structures for vortical cross-step filtration. *Nat. Commun.* 7, 11092. doi: 10.1038/ncomms11092

Sanderson, S. L. L., and Wassersug, R. J. (1993). "Convergent and alternative designs for vertebrate suspension feeding," in *The skull*. Eds. J. Hanken and B. K. Hall (Chicago and London: University of Chicago Press), 37–112.

Schroeder, A., Marshall, L., Trease, B., Becker, A., and Sanderson, S. L. L. (2019). Development of helical, fish-inspired cross-step filter for collecting harmful algae. *Bioinspiration Biomimetics* 14, 056008. doi: 10.1088/1748-3190/ab2d13

Sebens, K., Sarà, G., and Nishizaki, M. (2017). "Energetics, particle capture, and growth dynamics of benthic suspension feeders," in *Marine Animal Forests: The Ecology of Benthic Biodiversity Hotspots* (New York: Springer), 813–854.

Sims, D. W. (2000). Filter-feeding and cruising swimming speeds of basking sharks compared with optimal models: They filter-feed slower than predicted for their size. *J. Exp. Mar. Biol. Ecol.* 249, 65–76. doi: 10.1016/S0022-0981(00)00183-0

Smith, J. C., and Sanderson, S. L. (2007). Mucus function and crossflow filtration in a fish with gill rakers removed versus intact. *J. Exp. Biol.* 210, 2706–2713. doi: 10.1242/jeb.000703

Storm, T. J., Nolan, K. E., Roberts, E. M., and Sanderson, S. L. (2020). Oropharyngeal morphology related to filtration mechanisms in suspension-feeding American shad (Clupeidae). *J. Exp. Zoology Part A: Ecol. Integr. Physiol.* 333, 493–510. doi: 10.1002/jez.2363

Sutherland, K. (2008). *Filters and Filtration HandbookFifth Edit* (Oxford, UK: Elsevier).

Vogel, S. (1996). *Life in Moving Fluids: The Physical Biology of Flow - Revised and Expanded Second Edition* (Princeton: Princeton University Press).

frontiers | Frontiers in Marine Science

TYPE Original Research
PUBLISHED 04 January 2024
DOI 10.3389/fmars.2023.1327581

OPEN ACCESS

EDITED BY
Stuart Humphries,
University of Lincoln, United Kingdom

REVIEWED BY
Paul Carl Sikkel,
University of Miami, United States
Roy Harpaz,
Harvard University, United States

*CORRESPONDENCE
Hadar Ella
Hadar.ella@mail.huji.ac.il

RECEIVED 25 October 2023
ACCEPTED 11 December 2023
PUBLISHED 04 January 2024

CITATION
Ella H and Genin A (2024) Capture of zooplankton by site-attached fish: striking dynamics under different flow speeds and prey paths.
Front. Mar. Sci. 10:1327581.
doi: 10.3389/fmars.2023.1327581

Capture of zooplankton by site-attached fish: striking dynamics under different flow speeds and prey paths

Hadar Ella[1,2]* and Amatzia Genin[1,2]

[1]Department of Ecology, Evolution & Behavior, The Alexander Silberman Institute of Life Sciences, The Hebrew University of Jerusalem, Jerusalem, Israel, [2]The Interuniversity Institute of Marine Sciences in Eilat, Eilat, Israel

Consumption of pelagic zooplankton plays a vital role in the functioning of benthic communities such as coral reefs and kelp forests. Many fish that consume zooplankton in those habitats are site attached, foraging for drifting prey while maintaining a fixed position close to a shelter such as a branching coral or a perforated rock. Therefore, the flow, in which their planktonic prey drifts, is expected to affect their foraging movements. However, most attributes of those movements are poorly understood- a gap that our study seeks to fulfil. Our experiments were carried out in a laboratory flume with 4 common coral-reef site-attached species. Their movements were recorded in 3D, using two orthogonal video cameras. Different fishes exhibited similar trends despite noticeable differences in their body size, their morphology, the type of shelters they use, and the typical size of the groups in which they reside. In all species, the strike distance decreased with increasing flow speed. Similarly, the distance between the fish and prey at the moment of strike initiation ("Reactive Distance") decreased with increasing flow speed, as well as the angle between that "Reactive Distance" and flow direction. Surprisingly, striking speeds (relative to Earth) remained nearly unchanged under different flows speeds. However, faster strikes occurred when oriented at wider angles relative to the flow. Taken together, the fish appear to determine the speed and angle of their strikes based on a cognitive ability to assess the prey's drifting speed and path in order to reach on time the intercepting point. A rough estimate of the time it takes the fish to decide on the strike's orientation and speed, would suggest a few hundred of milliseconds. Using published data on the fishes' feeding rates, we found that the fish significantly differed in their feeding efficiencies, defined as the percent of prey they captured from those passing through their actual foraging space. That difference may explain inter-specific differences in the habitats the fish use and their group size.

KEYWORDS

coral-reef, planktivores, foraging, movement, Red Sea

Introduction

Coral-reef fishes live in rich communities within complex environmental conditions in which their abundance and distribution is thought to be tightly related to their feeding ecology (Bellwood et al., 2017). Many planktivorous fish in that habitat are site-attached (Kiflawi and Genin, 1997), capturing drifting zooplankton while maintaining quasi-stationary positions next to a shelter. The shelters can be coral heads, large rocks or other complex substrates. In some places, those fish are extremely abundant, titled by Hamner et al. (1988) "a wall of mouths". The concentration of pelagic zooplankton strongly declines in the waters down-current of that "wall". A substantial import of allochthonous nutrients via such predation was proposed as an explanation of the "Paradox of the Reef" (Erez, 1990; Genin et al., 2009; Wyatt et al., 2010; Wyatt et al., 2013; Morais and Bellwood, 2019), referring to the unknown source(s) of nutrients needed to support the exceptionally high productivity of the reef. Coral reefs are typically surrounded by oligotrophic waters with low abundance of zooplankton. The constraint in zooplankton availability requires planktivorous fish to capture individual prey (Confer and Blades, 1975; Werner, 1977; Vinyard, 1980; Kiflawi and Genin, 1997), rather than filter-feed (Nonacs et al., 1994). Prey capture in site-attached fishes consists of three steps: (i) a quasi-stationary wait-and-search interval, where the fish faces the on-coming current, waiting for a drifting prey to reach a sufficiently close range to be visually detected (ii) a strike, characterized by rapid swimming toward the prey, and (iii) capturing the prey using ram-jaw suction (Coughlin and Strickler, 1990; Wainwright et al., 2007; Jacobs and Holzman, 2018; Olsson et al., 2020).

A visual detection of zooplanktonic prey and the use of suction to ingest it, is shared by numerous adult fish and larvae (Turingan et al., 2005; China and Holzman, 2014; Holzman et al., 2015). Unlike adult fish, small larvae frequently miss prey. A low success rate is mostly due to the larvae's minute size relative to their prey, their limited swimming ability, and lack of experience (Krebs and Turingan, 2003; Turingan et al., 2005; China et al., 2017). The effects of the above factors are greatly reduced in the larger, faster, and experienced adults (Coughlin and Strickler, 1990; Olsson et al., 2020). In their work with coral-reef fishes in a flume, Genin et al. (submitted[1]) found 100% success rate in fish striking a non-evasive prey (*Artemia* nauplii). The rates of feeding, however, also depends on external factors such as the concentration of the prey, current speed, and light (Kiflawi and Genin, 1997; Manatunge and Asaeda, 1998; Clarke et al., 2005; Rickel and Genin, 2005; Clarke et al., 2009; Palstra et al., 2015; Khrizman et al., 2018; Ishikawa et al., 2022; Genin et al., submitted).

The mechanisms through which site-attached zooplanktivorous fish strike their prey in the flow are not fully understood and warrant further investigations. For example, Kiflawi and Genin (1997) characterized the effects of flow and prey density on zooplankton capture, but their study used only 2 individuals from one species and a single individual from another. McFarland and Levin (2002) studied the effect of flow on the fish's striking strategies, but focused on juveniles, not adults. Studies by Holzman and colleagues (Holzman et al., 2012; Jacobs and Holzman, 2018; Olsson et al., 2020) focused only on the final step in the fish's strikes, the ram-jaw suction without addressing the other components of the strikes. Clarke et al. (2009) and Finelli et al. (2009) studied 2 species of gobies that differ from the common site-attached fishes since their strikes are intermittent, having to emerge from shelter in order to strike a passing-by prey. Therefore, the gobies' feeding rate is much slower than that of common site-attached fishes (1-3 min^{-1} vs. 0.5-2 s^{-1}, respectively; Kiflawi and Genin, 1997; Clarke et al., 2009; Genin et al., submitted).

Current speed appears to be a key factor in determining the foraging behavior and feeding rates in site-attached fish (Kiflawi and Genin, 1997; O'Brien et al., 2001; Clarke et al., 2009; Khrizman et al., 2018; Ishikawa et al., 2022). As those fish typically have a fusiform or compressed-fusiform shape (Fulton, 2007; Cano-Barbacil et al., 2020; Siqueira et al., 2020), they lack the ability to swim sideward, as puffers and boxfish do (Gordon et al., 1996). To reduce the area projected perpendicular to the flow, thereby reducing pressure drag (Khrizman et al., 2018), the fish narrow down the angle between the side of their body and the direction of the current (Kiflawi and Genin, 1997). Narrower angles under stronger flows may explain the surprising absence of increased feeding rates under higher flow speed, expected to occur under higher prey flux (Kiflawi and Genin, 1997; Videler and Wardle, 1991; Genin et al., submitted). Alternatively, McFarland and Levin (2002) showed that flow speed can change the fish's striking strategy, in which under weak flows (10–14 cm/s) the fish swim directly toward the prey but under stronger currents they tend to fall back with the flows and capture the prey during their drift.

Large variations in body forms and fin functions occur in site-attached fishes. Such variations are expected to affect the fish's striking motions and their ability to capture fast-drifting prey (Hobson and Chess, 1978; Webb, 1984; Clarke et al., 2005). The ratio of body length to height (fineness ratio) is considered to be a key factor determining the fish ability to maneuver and overcome drag forces (Webb and Weihs, 1983; Webb, 1984). However, later studies (Walker and Westneat, 2002; Blake, 2004; Fulton et al., 2005; Lauder et al., 2012; Fulton et al., 2013; Heatwole and Fulton, 2013; Walker et al., 2013; Schakmann and Korsmeyer, 2023) revised that view, emphasizing, in addition, the role of fin shape and motion in determining maneuvrability. For example, paired motions of pelvic and pectoral fins are commonly used to perform the maneuvers required to capture a drifting prey (Fulton et al., 2013; Engel et al., 2021).

The objectives of this study are: (1) to quantitatively characterize the key attributes of striking movements in 4 species of site-attached coral-reef fishes, and (2) to test the alleged relationships between feeding rates and flow-driven changes in the fish's body orientation. Our study also allows an approximation of the fish's cognitive ability in determining its striking attributes.

Methods

Study site

Our field work was carried out in the coral reef in front of the Interuniversity Institute for Marine Sciences (IUI), Gulf of Eilat/

1 Genin, A., Rickel, S., Zarubin, M., and Kiflawi, M. (submitted)Effects of flow speed and prey density on the rate and efficiency of prey capture in 4 species of zooplanktivorous coral-reef fishes. Submitt. to Front. Mar. Sci.

Aqaba, Red Sea. A detailed description of the reef and its environment is found in Yahel et al. (1998); Biton and Gildor (2011), and Shaked and Genin (2022), and references therein. Briefly, this fringing reef is located on a steep slope. A diverse guild of stony corals, consisting of branching and massive corals cover 20-50% of the rocky substrate (Fishelson, 1971; Benayahu and Loya, 1977; Shaked and Genin, 2022). The currents are weak, with a mean speed of 10 cm/s and the waves are small most of the time (Genin et al., 1994; Reidenbach et al., 2006). The Gulf of Eilat/Aqaba is oligotrophic with clear waters; visibility typically extends tens of meters. The fish community in the reef includes >260 species, including piscivores, zooplanktivores, and herbivores (Brokovich, 2001). Within this highly diverse community, zooplanktivorous fishes comprise >40% of the total (Shaked and Genin, 2022).

Fish

Four species of common site-attached, zooplanktivorous fish were studied: the damselfishes *Neopomacentrus miryae* (hereafter Nm; mean ± SD fineness ratio of 2.54 ± 0.143; N = 5), *Chromis viridis* (Cv; 2.32 ± 0.11; N = 8), and *Dascyllus marginatus* (Dm; 1.49 ± 0.07; N = 6), and the serranid *Pseudanthias squamipinnis* (Ps; 2.68 ± 0.072; N = 5). Those species share a similar lifestyle, including the formation of social groups and a long-term fidelity to their shelters (Allen and Randall, 1980; Smith and Heemstra, 1986; Myers, 1989; Lieske and Myers, 1994; Baensch and Riehl, 1997). A detailed description of three species (Nm, Dm, Ps) is given in Genin et al. (submitted). Dm and Cv are usually associated with corals of the genus *Acropora*. Typical group size in Cv is substantially larger than in Dm (tens vs several, respectively; Supplementary Table 1). The four species are diurnal, using vision to detect and capture meso-zooplankton. Their diet is diverse, reflecting the wide taxonomic composition of the planktonic community in the surrounding waters (Smith and Heemstra, 1986; Karpestam et al., 2007; Genin et al., submitted). In captivity, those fish readily feed on live substitute prey, such as nauplii of *Artemia salina* (Genin et al., submitted).

Adult fish were used in all our experiments. Females were used in Ps, while the gender of Cv, Dm and Nm in our experiment remained indeterminate due an undifferentiated morphology of the two sexes.

The fish were collected in the IUI reef at 6-15 m depth. Cv and Dm were collected with small hand nets at their home corals after partially anaesthetizing the fish with clove oil. Ps and Nm were collected using a gill net, into which the fish were carefully scared by divers. The collected fish were rapidly (<15 min) transported to an acclimation tank (50-60 L in volume) in the laboratory. This acclimation period lasted 1-3 weeks. A fish was considered acclimated once it started to readily feed upon prey that was added to the tank by a person standing nearby. Acclimated fish were transferred to the flume a day or more prior to the beginning of trials. During the entire acclimation periods the fish were fed ad libitum with nauplii of brine shrimps. A light/darkness cycle identical to the natural cycle was maintained in the tank and flume.

All fish were returned to the reef, preferably to the exact sites where they had been collected. A total of ≥5 individuals were used per species. The methods used to collect and handle the fish were done under a permit from Israel Nature & Parks Authority and fully complied with the ethical rules of animal treatment at the Hebrew University of Jerusalem.

Prey

Live, 1-day old nauplii of brine shrimps (*Artemia salina*) were used as prey. The nauplii were similar in size (length mean ± SD of 0.60 ± 0.07 mm, n = 50) and transparency to the natural prey the fishes feed on in the reef. Unlike most zooplankters, *Artemia* nauplii are poor swimmers and lack any form of escape behavior (Trager et al., 1994). However, those differences can be considered advantageous for a comparative study seeking to experimentally isolate the effects of prey density and flow from other factors.

Flume

Our experiments were carried out in the recirculating flume (Supplementary Figure 2) that was used by Kiflawi and Genin (1997) and Genin et al. (submitted). The flume contained 330 L of water. The transparent work section was 200x30x30 cm in size. Fish movement in the flume was restricted to a 50 cm long experimental arena in the downstream part of the work section by coarse plastic-coated grid. A shelter (branching coral skeleton or a small pipe) was placed near the flume's down-current end. Sea water in the tank was replenished between trials. The replenishing water was pumped from the nearby reef at 30 m depth. Natural zooplankton was removed from the pumped water using a 65 μm plankton net. The flume was thoroughly cleaned, removing fouling organisms and dirt, at least 3 times a week. Water temperature was maintained at 24° ± 1° C. A single Metal Halide and 4 fluorescent lamps were used to illuminate the work section with intensity of 2700 Lx, similar to that prevailing during mid-day at the fish's natural habitat.

The flow in the flume was generated using a controlled propeller. Effective flow straighteners provided nearly uniform flow profiles across the flume. The uniformity of the flow was verified using 3D tracking of suspended particles (see below) and a 1 MHz acoustic velocity meter (ADV, Nortek, Norway). An examination of the boundary layer made during the construction of the flume by Kiflawi and Genin (1997), revealed a ~1 cm-thick boundary layer over the walls and bottom. The fish rarely foraged within that layer. Similarly, the fish always foraged up-current of their shelter, away from the zone where it affected the water motion. The flow speeds used in our experiments were 5, 10, 15, and 20 cm/s, covering the typical range of currents at the local coral reef.

Two high-resolution, orthogonally-oriented video cameras (UI-3070CP-C-HQ Rev.2, IDS, Obersulm, Germany) were used to record fish strikes in 3D. A down-looking camera with a 16 mm lens (IDS-8M118-C1620) was positioned 50 cm above the flume and a side-looking camera with 25 mm lens (IDS-8M118-C2520) was positioned 75 cm from the flume's wall oriented directly to the

center of the water column. The cameras recorded frames at a rate of 100 fps, synchronized to within one frame (± 3ms). Calibration and quality control of the 3D data were performed with the EasyWand Camera Calibration tool (Theriault et al., 2014), using 1840 frames of a calibration stick that was manually moved across the camera field of view. Calibration records were processed using MATLAB DLTdv8a digitizing tool, indicating a spatial precision of ±2 mm.

Work protocol

A single fish was used in each trial. The fish was not fed during the 12 hrs preceding the trial. A day of trials always started by cleaning the flume water and closing the valve to the freshly-pumped seawater. Suspended particles that sometimes remained in the flume were filtered out using a 20 μm plankton net. The net, having a frame that tightly fit inside the flume's cross section, was inserted inside the flume and the flow speed was raised to 25 cm/s for a few minutes, assuring several filtering cycles of the water. Approximately 10 min before the start, a few (5-8) nauplii were added to the flume, verifying that the fish readily started to capture the prey. Then, 10-12 nauplii were gradually ejected to the flume using a syringe positioned above the propeller, while keeping the fish in its shelter. Thereby, the prey was nearly homogeneously distributed along the flume. The low density of the prey and its homogenous distribution assured that the strikes would be well-separated, so that each strike would start with the fish waiting for a prey to drift into its detection space. Video recording started as soon as the operator left and entered a control room, hidden from the flume with a dark, separation curtain. The recording session lasted a few minutes, after which recording was stopped and another cycle of prey ejection started. At least 30 strikes were recorded for each flow speed for each individual. Each work day consisted of several trials using different, haphazardly-selected flow speeds. Once the trials covering all flow speeds with one fish were completed, it was replaced by another fish (after thoroughly cleaning the flume). The total number of individuals per species were 5 for Ps and Nm, and 6 for Cv and Dm. The corresponding total numbers of recorded strikes for each species were 434, 538, 369, and 496, respectively.

"Strike distance" (Supplementary Figure 3) was measured based on the clearly-observed points of the strike initiation (the steady, direct, and rapid swim toward the prey) and ram-jaw capture. "Strike angle" (β in Supplementary Figure 3) was defined as the angle between the direction of the flow and the strike path. "Reactive Distance" was defined as the distance between the fish and the prey at the instance the strike was initiated. It was computed considering the duration of the strike and a back-calculation of the location at which the passively drifting prey was found when the strike was initiated (i.e., up-current of the capture point). "Detection Angle" (α in Supplementary Figure 3) was the angle between the flow direction and the imaginary line extended between the fish snout and the distal point of the Reactive Distance. For each Detection Angle we also calculated its horizontal component (α_H), referring to a 2D distance on the horizontal plane perpendicular to the flow direction. In order to test the effect of flow speed on Reactive Distance independently of possible effects of Detection Angle, we limited the Detection Angles we used to ≤45°. Based on purely geometric considerations, under equal flow speeds and striking distance, the reactive distance under 45° is 14% shorter than under 0°.

In order to assess the relationships between Detection Angles and the strike attributes, values of α_H were sorted into 3 categories: "narrow" (α_H<10), "mid" (10≤α_H<20), and "wide" (α_H≥20). Both strike and Detection Angles are presented below using absolute values, disregarding their left or right direction with respect to the flow.

Statistical analysis

The effect of flow speed and species on the strike's distance, speed, duration, and angle, and the effect of flow on Reactive Distance and Detection Angle were tested using Repeated Measures ANOVA. The measured parameter was the dependent variable (measured repeatedly for the same individual under all flow speeds) and the species was used for testing the Between Subject Effect. Sphericity and Homogeneity of Variance were verified prior to testing. Tukey *post hoc* assessed the differences between pairs of species in cases where the aforementioned ANOVA indicated significant species effects. To test the Interaction among factors, we used Compare Mean Effects with Bonferroni for confident interval adjustment. Values of the aforementioned strike parameters that were measured through replicated trials (N=28 ± 15) were averaged, yielding a single mean value for each individual for each flow speed, which was then used as the input variable for the Repeated Measures ANOVA.

Due to non-homogeneous variances, the effects of the three α_H categories (wide, mid, and narrow) on strike attributes were tested using Bootstrap with 10,000 samplings and Biased corrected acceleration, with flow speed and species as fixed Factor.

Repeated Measures ANOVA and *post hoc* tests were performed using R Studio (packages "agricolae","emmeans"). Bootstrap tests were performed using SPSS (v. 28).

Results

Flow and strike attributes

Mean 3D strike distances ranged ~1.7 to 5.9 cm, depending on species and flow-speed. The horizontal (perpendicular to the flow) and vertical components ranged ~0.9-4.1 and ~1-2.4 cm, respectively (Figure 1). In all species, the total strike distance and the horizontal and vertical components decreased with increasing flow speeds (Repeated Measures ANOVA, total distance- $F(2)=43$ $P<0.0001$; horizontal component- $F(2)=23.7$ $P<0.0001$; vertical component- $F(2)=30.6$ $P<0.0001$). The extent of that decrease in the total and horizontal components was steeper in Cv and Ps than in the other two species when the flow intensified from 10 to 15 cm/s (Figures 1A, B). The decrease in all distance components when the flow changed from 15 to 20 cm/s was relatively small and similar in

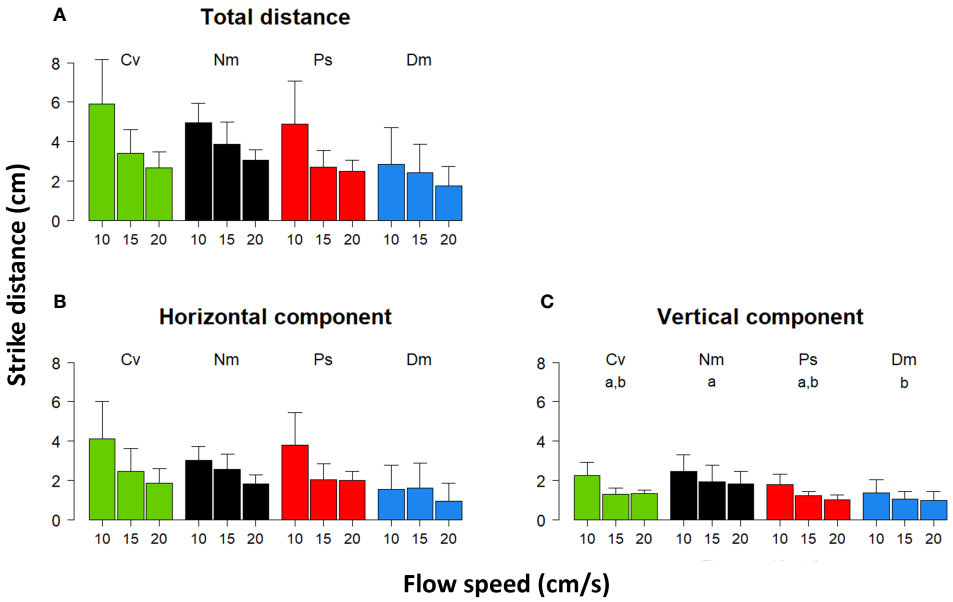

FIGURE 1
Strike distance vs. flow speed. Mean (± SD) of the **(A)** - total strike distance in 3D, **(B)** - the horizontal component of the strike, and **(C)** - the vertical component of the strike under flow speeds of 10, 15, and 20 cm/s. Species are color coded (Cv-green, Nm-black, Ps-red, Dm-blue) and their acronyms indicated above the bars. Small letters above the bars in **(C)** - indicate the results of *post hoc* testing of inter-specific differences, so that pair of species that significantly differed ($P<0.05$) are indicated using different letters.

all species (Figure 1). The former inter-species difference was reflected in the significant interaction between species and flow (total distance-$F(6)=2.7$ $P<0.03$; horizontal component-$F(6)=2.7$ $P<0.03$), although the effect of species alone was insignificant. On the other hand, a significant effect of species was found for the strikes' vertical component ($F(3)=3.8$ $P<0.03$), with a *post hoc* test indicating that Nm (higher vertical component) and Dm (lower vertical component) significantly differed one from another (Tukey, $P<0.03$).

The shorter strike distances under stronger flow corresponded to a significant decrease in the strike duration (Figure 2, Repeated Measures ANOVA, $F(2)=163$ $P<0.0001$). Also here, the effect of species was significant ($F(3)=9$ $P<0.0008$) with a *post hoc* test indicating that the strike duration in Cv was significantly shorter than in all other species (Tukey, $P<0.03$). The interaction between species and flow was significant ($F(6)=5$ $P<0.0008$), reflecting a weaker flow effect on Cv, compared with all other species.

The effects of flow on the strike's distance and duration were balanced so that no significant effect on strike speed (relative to Earth) was found (Figure 3A, Repeated Measures ANOVA, $F(2)=0.9$ $P=0.42$). Conversely, the strike speed relative to the water became significantly faster with increasing flow speed

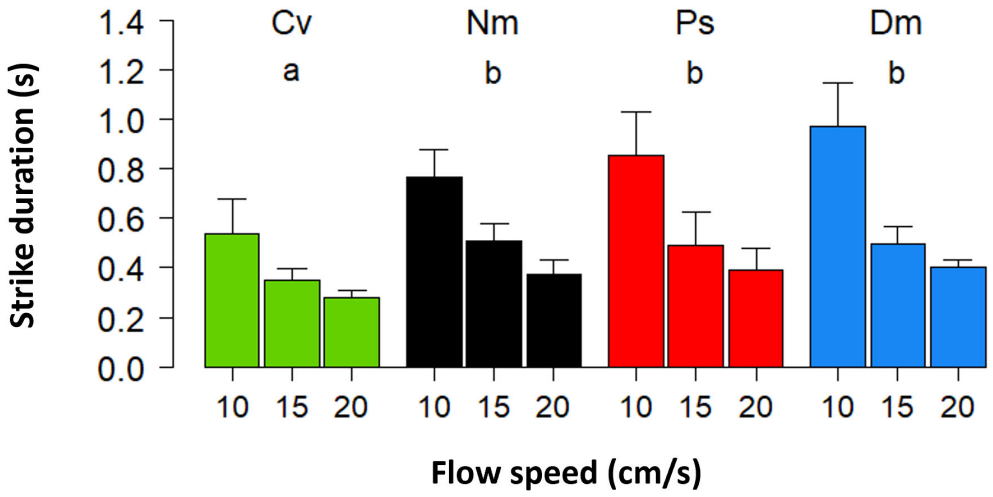

FIGURE 2
Strike duration vs. flow speed. Mean (± SD) duration of strikes. Different species and indications of statistics are coded as in Figure 1.

(Figure 3B, Repeated Measures ANOVA, $F(2)=877.4$ $P<0.0001$). Different species significantly differed in their striking speeds relative to both Earth and water ($F(3)=10.3$ $P<0.0004$; $F(3)=10.7$ $P<0.0003$, respectively), with a *post hoc* test indicating that strikes by Cv were significantly faster relative to the Earth ($P<0.02$) and water ($P<0.003$) than those of Ps and Dm. The strikes of Dm were significantly slower relative to Earth than those of Nm ($P<0.04$). A significant interaction between flow speed and species was found relative to both Earth and water ($F(6)=3.5$ $P<0.01$; $F(6)=5.5$ $P<0.0004$, respectively).

Strike angles in 3D slightly but significantly widened under faster flows (Figure 4B, Repeated Measures ANOVA, $F(2)=7$ $P<0.003$). Despite this widening, the horizontal angles were not significantly affected by flow speed (Figure 4C, Repeated Measures ANOVA, $F(2)=2.9$ $P=0.07$), indicating that the significant effect on the total (3D) angels was mostly due to the corresponding changes of the vertical angles (Figure 4D, Repeated Measures ANOVA, $F(2)=12$ $P<0.0001$). Inter-specific differences of the strike and horizontal angles (Figures 4B, C; $F(3)=4.4$ $P<0.02$; $F(3)=18$ $P<0.0001$, respectively) showed that both the total and horizontal angles were widest in Ps.

Flow and reactive distance

In all species the Reactive Distance, that is, the distance to the prey at the moment the strike started, significantly decreased with increasing flow speed (Figure 5, Repeated Measures ANOVA, $F(2)=28.6$ $P<0.001$) with non-significant interaction of species and flow. A *post hoc* test indicated that the decrease in Reactive Distance was significant only when the flow intensified from 10 cm/s to 15 (or 20) cm/s (Bonferroni, $P<0.001$), with a non-significant difference between 15 and 20 cm/s.

Under stronger flows, Detection Angles significantly narrowed down (Figure 4A, Repeated Measures ANOVA, $F(2)=28$ $P<0.001$) with a significant effect of species ($F(3)=9.7$, $P<0.001$). A *post hoc* test indicated that the Detection Angles of Dm were significantly narrower ($P<0.001$) than those of Cv and Nm.

Body orientation and strike attribute

Most strike attributes appeared to depend on the horizontal Detection Angle (α_H). In all species, the frequency distribution of α_H was strongly skewed to the left (Figure 6), reflecting a preference to strike prey that was drifting nearly head-on toward the fish. Using the categorial sorting of α_H to narrow (N), mid (M), and wide (W) angles, we found that in all species and under all levels of flow speeds, the total strike distance significantly increased with the widening α_H (Figure 7; bootstrap, flow: $F(2)=88.9$, $P<0.001$ angle: $F(2)=231.2$, $P<0.001$ species: $F(3)= 16.1$, $P<0.001$). The strikes were approximately twice as long under a wide α_H than under narrow α_H (Figure 7). Despite a general decrease of strike duration with increasing flow speed (Figure 2), the within-speed effect of α_H on strike duration was significant (bootstrap, flow: $F(2)=332.3$, $P<0.001$ angle: $F(2)=8.5$, $P<0.001$ species: $F(3)=56.3$, *$P<0.001$*). Though, no consistent trend was apparent. That is, under some changes in flow speed the strike duration increased in others it decreased (Figure 8). Nevertheless, in all species, the striking speed relative to both Earth and water significantly increased with widening of α_H (Figures 9, 10, bootstrap, flow: $F(2)=49.2$, $P<0.001$ angle: $F(2)=513.5$, *$P<0.001$* species: $F(3)=119.3$, *$P<0.001$*; flow: $F(2)=2335$, $P<0.0001$ angle: $F(2)=140.3$, *$P<0.001$* species: $F(3)=113.9$, *$P<0.001$*, respectively). Noteworthy is the finding that despite the significant effects of α_H on strike distance, duration, and speed, its effect on Reactive Distance was insignificant (Supplementary Figure 5, bootstrap, flow: $F(2)=34.8$, $P<0.001$ angle: $F(2)=0.6$, $P=0.5$ species: $F(3)=26.2$, $P<0.001$).

Discussion

To forage for drifting zooplankters while keeping a position near a fixed shelter, site-attached fish steadily swim against the current. Our observations show that their mean striking speed relative to the water was always positive and faster than the flow speed (Figure 3B), indicating that in order to capture prey, the fish mostly swam forward into the flow. (Note that rare occurrences of

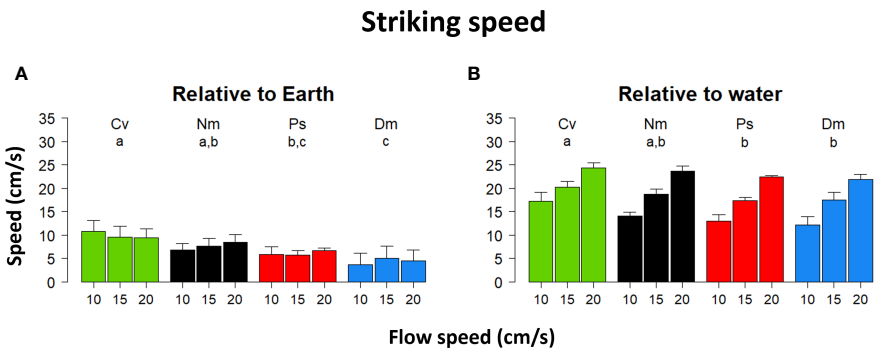

FIGURE 3
Striking speed vs. flow speed. Mean (± SD) striking speed relative to the **(A)** – Earth, **(B)** - the flowing water. Species codes and statistics are as in Figure 1.

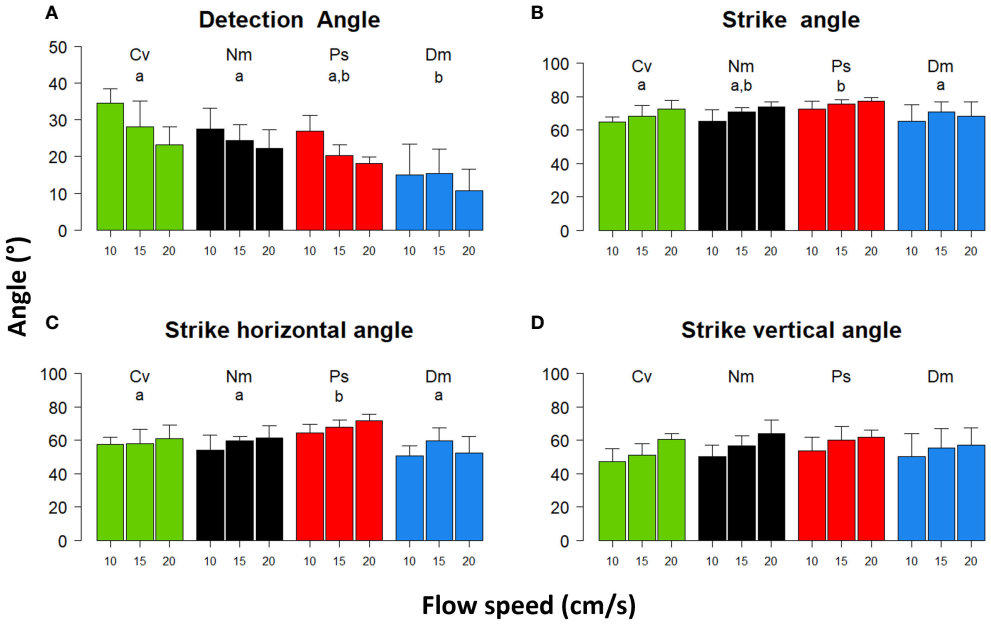

FIGURE 4
Detection and striking angles vs. flow speed. Shown are mean (± SD) angles with respect to the flow direction of **(A)** - Reactive Distance vector, **(B)** - strike angle in 3D, **(C)** - the strike angle along the horizontal plane perpendicular to the flow direction, and **(D)** - the strike angle along the vertical plane perpendicular to the flow direction. Species and statistics are coded as in Figure 1.

down-stream strikes were omitted from our database.) Moreover, with increasing flow speed, the fish striking speed relative to the water became significantly faster (Figure 3B), but not relative to Earth, where it remained nearly unchanged (Figure 3A). Similar findings, namely, an absence of flow effect on striking speed relative to Earth, was reported by Piccolo et al. (2008) for freshwater (stream) fish. However, our results do not agree with their conclusion that in order to strike, the fish use their maximum sustainable speed. Had they done so, the striking speed should have been slower under conditions of stronger head currents, as seen, for example, in competitive bike-riding, where maximum sustainable paddling force is typically used (Atkinson et al., 2003). Instead, the fish modulated their striking speed based on the ambient flow, on the prey's distance, and on the angle at which the prey was located at the moment of strike initiation (Figures 7, 9, 10). We suggest that the striking speed in the fish we studied is determined by, and based on cognitive decisions (see below).

The studied species are fusiform, morphologically adapted to swim forward, rather than sideway as non-fusiform boxfishes and pufferfishes do (Videler and Wardle, 1991; Wardle et al., 1995;

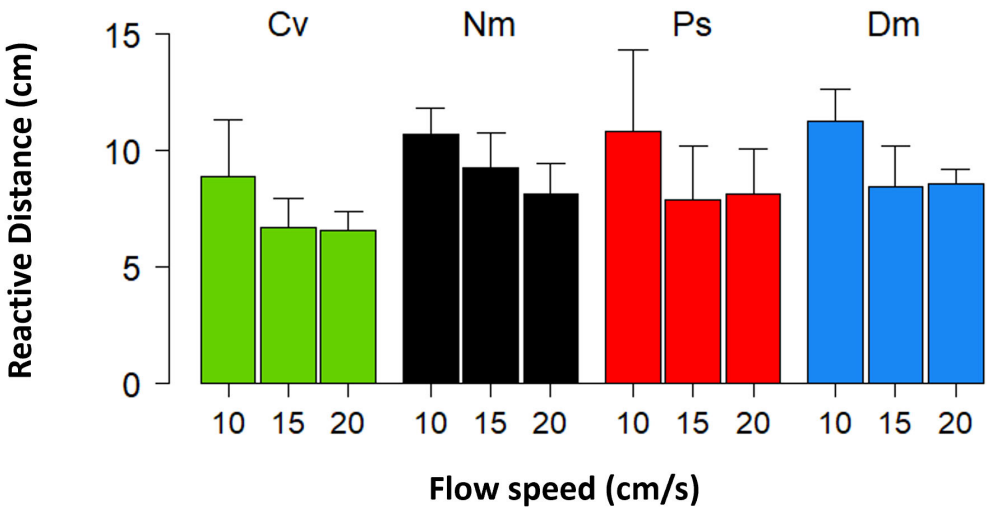

FIGURE 5
Reactive Distance vs. flow speed. Mean (± SD) Reactive Distances for cases in which the prey drifted almost directly (≤45°) toward the fish. Species are coded as in Figure 1.

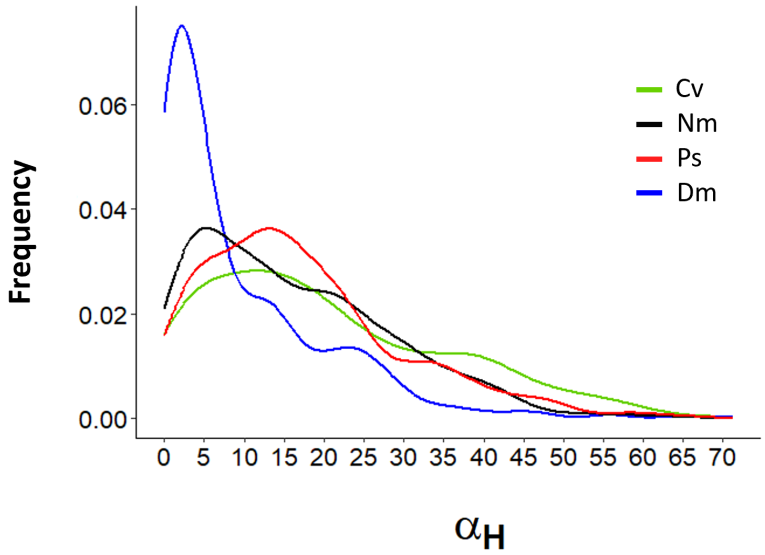

FIGURE 6
Frequency distribution of α_H. Detection Angles (α_H) were measured on the horizontal plane perpendicular to the flow direction. Lines are plotted based on measurements made every 1 cm/s increment. Species are color coded as in Figure 1.

Gordon et al., 1996; Gordon et al., 2000; Siqueira et al., 2020). To lower the pressure-drag that pushes the fish down-current (Khrizman et al., 2018), the fish gradually narrow down their angle to the flow under stronger currents (Schakmann et al., 2020; Schakmann and Korsmeyer, 2023; Figure 7 in Genin et al., submitted). In doing so, the fish reduce the chance of being swept down-current and the ensuing risk of being captured by predators. The orientation to the flow also reduces the energetic cost of maintaining a fixed position near a shelter. Unexpectedly, the narrowing-down of the body orientation while foraging, as observed by Genin et al. (submitted), was observed by us for Detection Angles (Figures 4A, 6; Supplementary Figure 6), not strike angles (Figure 4B). Based on geometry alone, at a given Detection Angle, under stronger flows, the prey would reach closer to the position of strike initiation. Therefore, under stronger flows, the strike's total, vertical, and horizontal angles were expected to

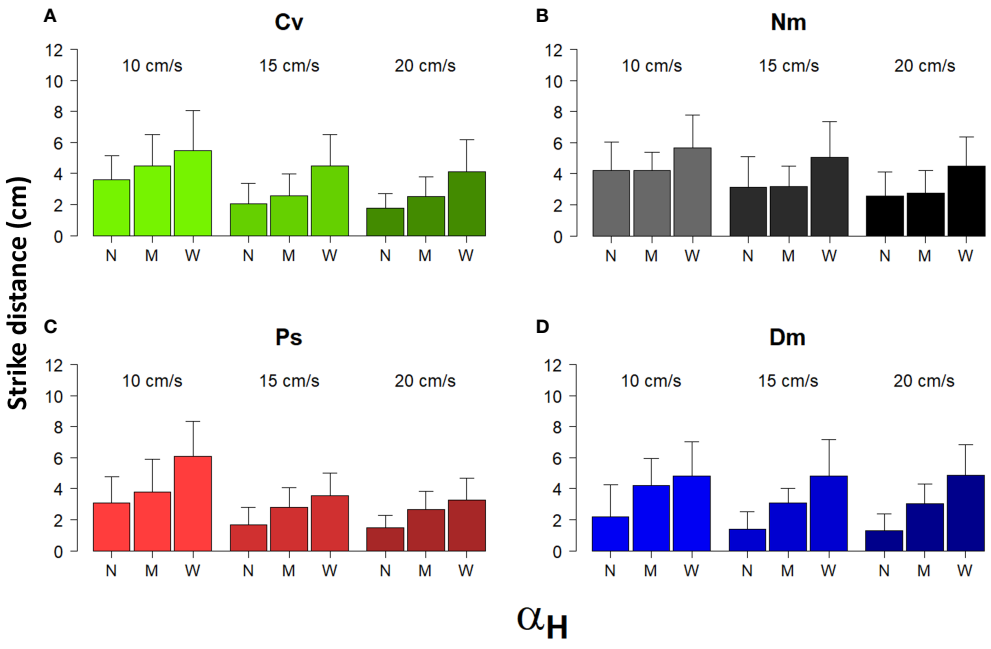

FIGURE 7
Strike distance under different categories of α_H and different flow speed. Shown are the mean (± SD) distances in 3D of strikes performed under different flow speeds (between bar triplicates) in the three different categories of α_H: N-narrow, M-mid, and W-wide (within bar triplicates) for the 4 different species **(A)**-Cv, **(B)**-Nm, **(C)**-Ps, and **(D)**-Dm (color coded as in Figure 1).

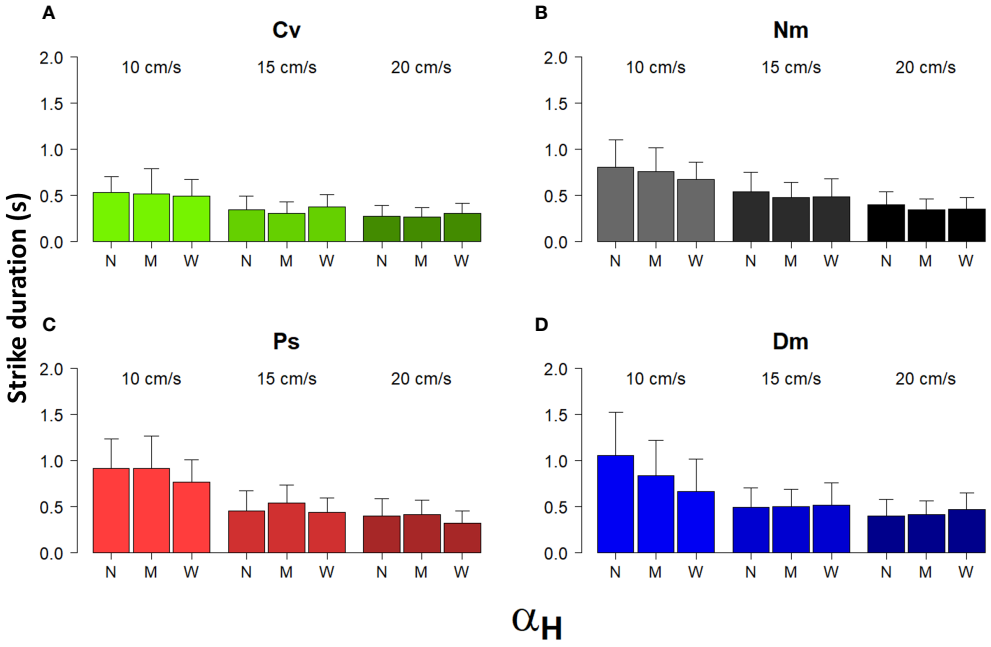

FIGURE 8
Strike duration vs. α_H and flow speed. Shown are the means (± SD) of the duration of strikes performed under different flow speeds (between bar triplicates) in the three different categories of α_H: N-narrow, M-mid, and W-wide (within bar triplicates) for the 4 different species **(A)**-Cv, **(B)**-Nm, **(C)**-Ps, and **(D)**-Dm (color coded as in Figure 1).

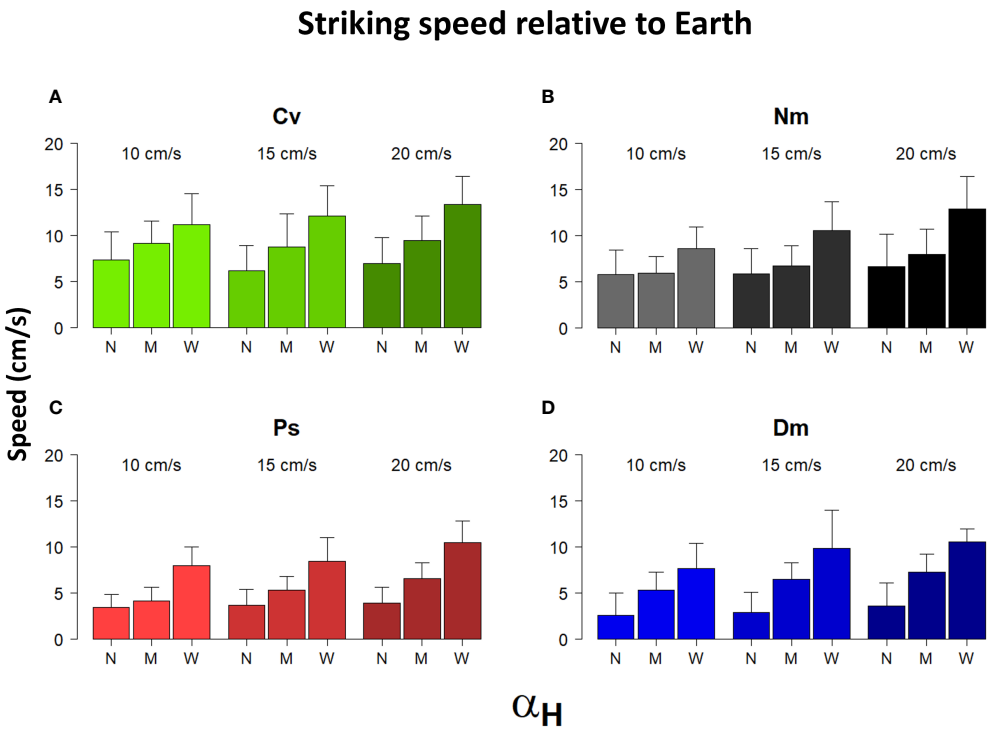

FIGURE 9
Striking speed relative to Earth vs. α_H and flow speed. Shown are the means (± SD) of the speed of strikes in Earth coordinates performed under different flow speeds (between bar triplicates), in the three different categories of α_H: N-narrow, M-mid, and W-wide (within bar triplicates) for the 4 different species **(A)**-Cv, **(B)**-Nm, **(C)**-Ps, and **(D)**-Dm (color coded as in Figure 1).

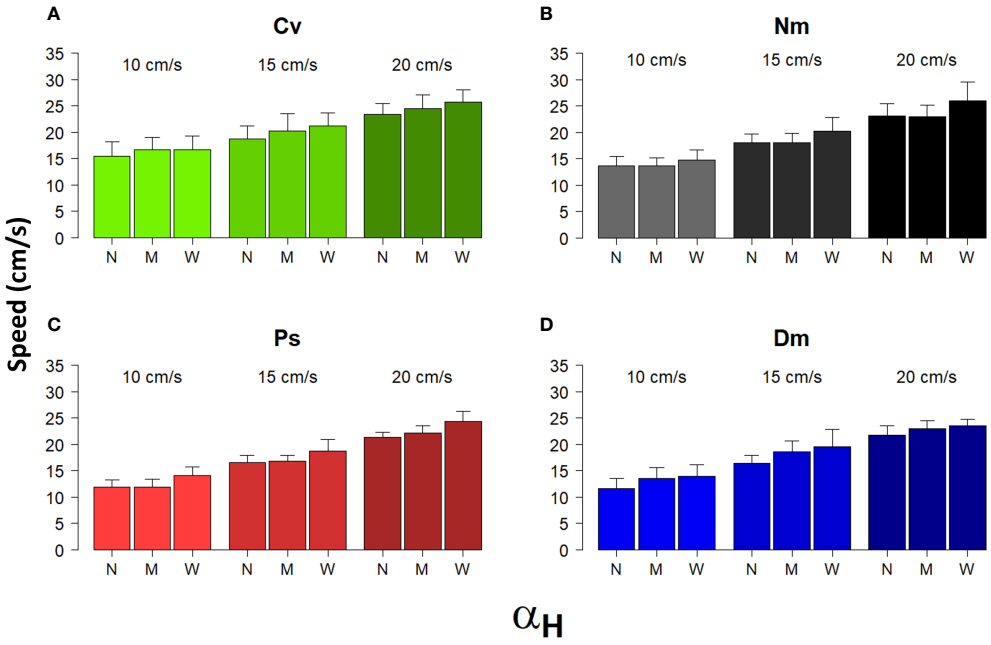

FIGURE 10
Striking speed relative to water vs. α_H and flow speed. Shown are the means (± SD) of the speed of strikes relative to water performed under different flow speeds (between bar triplicates) in the three different categories of α_H: N-narrow, M-mid, and W-wide (within bar triplicates) for the 4 different species **(A)**-Cv, **(B)**-Nm, **(C)**-Ps, and **(D)**-Dm (color coded as in Figure 1).

become wider (Supplementary Figure 3). The fact that the horizontal strike angles remain unchanged (Figure 4C) is likely an outcome of the fish's preference to strike prey that have lower Detection Angles as the flow becomes stronger. Noteworthy is the observation that the strike's vertical angles do follow the expectation that follows the above geometric considerations, becoming larger with increasing flow speed (Figure 4D). This dichotomy between the horizontal and vertical movements may indicate a cognitive ability by the fish to decide which prey to strike and which to give up, based on the prey's location and drifting speed.

Among the four species we studied, the morphology of Dm was the least "hydrodynamic", having the smallest fineness ratio and a non-forked caudal fin (see Method Fish and Supplementary Figure 1). Accordingly, Dm exhibited slower striking speeds relative to Earth, and its Detection Angles were narrower than those of Nm and Cv (Figures 3A, 4A, 6). Furthermore, its striking speed relative to water was slower than that of Cv (Figure 4B). The non-forked caudal fin of Dm, compared with a forked fin in the other species, may limit the swimming speed and require higher energetic cost (Sambilay, 1990; Lauder et al., 2012; Xin and Wu, 2013). Likewise, Cv, the fish with the largest fineness ratio, exhibited faster striking speeds than those of Ps and Dm (relative to both Earth and water; Figure 3, and Method Fish).

Noteworthy is the inter-specific difference in the vertical component of the strikes, which was higher in Nm than in Dm (Figure 1C). Higher vertical vectors, hence larger space in which prey may be captured, could explain the higher feeding rates of Nm (Genin et al., submitted). Moreover, Genin et al. (submitted) hypothesized that despite the occurrence of higher prey fluxes under faster flow (with unchanged prey concentrations), the corresponding feeding rates did not increase because of the gradual narrowing down of the fish's body orientation with respect to the flow direction. That is, as the flow becomes stronger, the "true" prey flux (hereafter "Actual Flux") was not the one passing through a fixed area (e.g., the flume's cross section), but through a gradually shrinking area defined by the narrowing down angle of detection (Figures 11B–D; Table 1). To explain the unchanged feeding rates when the flow becomes stronger, we defined an "Effective Efficiency"- the percent of prey captured off forming the Actual Flux. If the narrowing down of the foraging angle explains the absence of higher feeding rates under stronger flows, we expect the Effective Efficiency to remain constant. In order to test this hypothesis, we used the feeding rates measured by Genin et al. (submitted) for Ps, Dm, and Nm, who measured predation rates in the same flume and under the same experimental setting. Our findings (Figure 11A; Table 1) refute that hypothesis for Nm and Ps, for which the Effective Efficiency decreased or increased, respectively. Dm was the only species in which the Effective Efficiency remained nearly constant in the range of 9-15 cm/s, though it decreased at 21 cm/s.

Noteworthy is the finding that in Ps, the Effective Efficiency increased despite a decrease in Actual Flux (Figure 11C), indicating that in the narrower foraging space Ps was able to catch relatively more prey. In other words, this species is well-adapted to living at

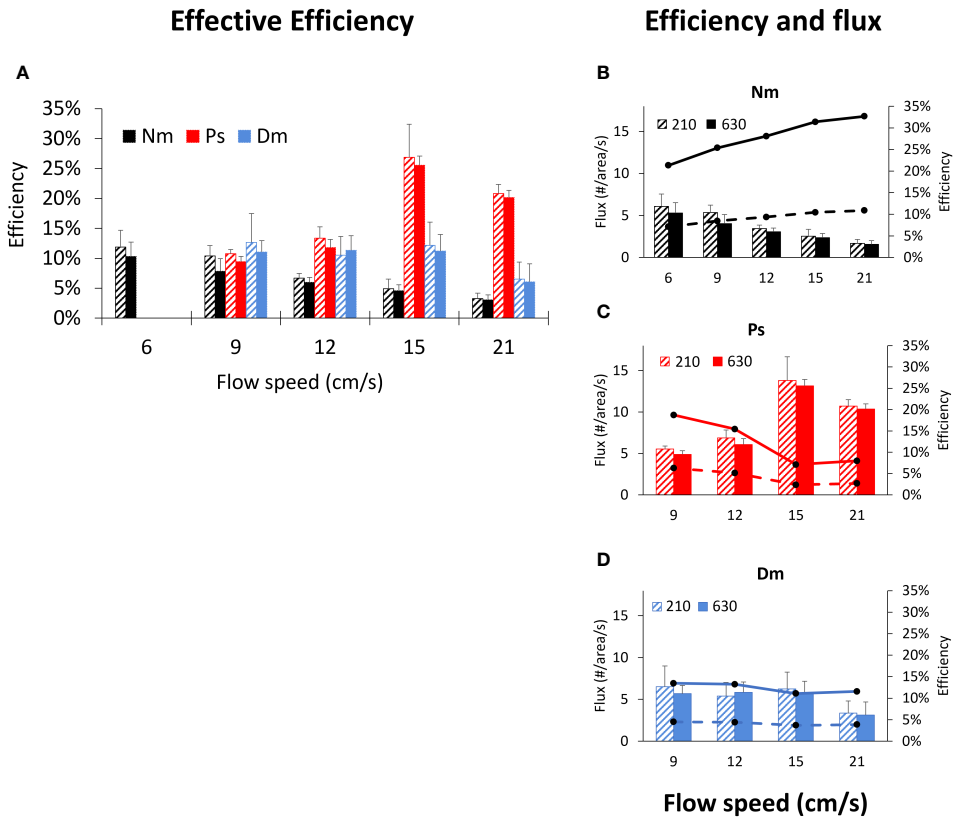

FIGURE 11
Effective Efficiencies vs. flow speed. **(A)** - Mean (± SD) Effective Efficiency under different flow speeds for 3 different species (color coded as in Figure 1) under conditions of prey densities of 210 prey m^{-3} (hatched bars) and 630 prey m^{-3} (full bars). **(B–D)**: as in **(A)** with added lines indicating actual prey fluxes under prey densities of 210 prey m^{-3} (dashed lines) and 630 prey m^{-3} (full lines). Calculations are based on feeding rates reported by Genin et al. (submitted; see text). The foraging area used to calculate "Effective Efficiencies" and "Actual Fluxes" are taken from our measurements. The distal area of the feeding space, through which potentially-captured prey pass, was calculated as an ellipse in which the longer and shorter axes were twice the maximum horizontal and maximum vertical components of the Reactive Distance, respectively. Since those dimensions were calculated for Dm and Ps at 10, 15, and 20 cm/s (and 5 cm/s for Nm), and since feeding rates were measured by Genin et al. (submitted) at 3, 6, 9, 12, 15, and 21 cm/s, the dimensions measured in this study were linearly interpolated or extrapolated to the flow speeds for which feeding rates are available (Figure 2 in Genin et al., submitted): 9, 12, 15, and 21 cm/s (and 6 cm/s for Nm). The corresponding statistics are reported in Table 1, showing that the effect of flow speed, but not of prey density, was significant and the different species significantly differed one from another.

sites exposed to strong currents. Conversely, in Nm, a decreasing Effective Efficiency under stronger flow (Figure 11B), indicated a poor functional response to intensifying flows. Indeed, our extensive survey of exposed coral reefs along the Gulf of Aqaba (unpublished) agree well with those inter-specific differences: Ps, the species that appears well-adapted to strong flows, is extremely abundant at sites exposed to strong currents (up to ~100 cm/s, mean of 40 cm/s; Genin et al., 1994), whereas Nm is totally absent. Both species are common at bays and sheltered sites in the Gulf, where the currents are much weaker (mean of 10 cm/s; Genin and Paldor, 1998).

Among the four species we studied, Dm and Cv use branching corals as shelters, whereas Ps and Nm favor large protruding knolls and complex rocks. Therefore, Dm and Cv usually forage at lower heights above the bottom than the latter ones. However, despite the use of similar shelters by Cv and Dm, the former is found in groups that are ~4 times more crowded than Dm (Supplementary Table 1; Brokovich, 2008). This difference agrees with the occurrence of significantly shorter strike durations, faster striking speeds (relative to Earth and water), and wider Detection Angle in Cv, allowing Cv to maintain higher feeding rates and efficiencies. Indeed, observations reported in Figure 2 of Kiflawi and Genin (1997) for a single Cv and two Dm suggest higher feeding rates in the former species.

Note that the average Effective Efficiencies in the fish we studied ranged 3 to 27%, considerably lower than 100% (Figure 11). Namely, much of the prey passing through the fish's foraging space is not captured. Therefore, the wider Detection Angles and faster striking speed in Cv may allow this species to maintain relatively higher feeding rates despite crowding. Unfortunately, feeding rates by Cv have not yet been quantified.

Under unchanged strike durations, geometric calculations show that for wider Detection Angles, longer strike distances are expected (Supplementary Figure 4). Indeed, in all species, strike distances under wide Detection Angles were approximately twice as long compared with narrow angles (Figure 7). Moreover, significantly higher swimming speeds were exhibited for wider Detection Angles in all species (Figures 9, 10). While the fish have no control on the

TABLE 1 Statistics of the trends presented in Figure 11.

Panel in Figure 11	Tested factor	(df) *F-value*/Std. error for *post hoc*	*P-value*
11A **All species**	Density	(1) 0.067	0.802
	Flow speed	(3) 16.2	<0.001
	species	(2) 62	<0.001
11A species Tukey *post hoc*	Dm-Nm	0.01	0.018
	Dm-Ps	0.01	<0.001
	Ps-Nm	0.01	<0.001
11B **Nm**	Density	(1) 600.4	<0.001
	Flow speed	(4) 58.4	<0.001
Figure 11B flow speed Tukey *post hoc*	6-9 (cm/s)	0.003	0.051
	6-12 (cm/s)	0.004	0.007
	6-15 (cm/s)	0.01	0.047
	6-21 (cm/s)	0.007	0.01
	9-12 (cm/s)	0.006	0.124
	9-15 (cm/s)	0.009	0.128
	9-21 (cm/s)	0.008	0.034
	12-15 (cm/s)	0.008	1
	12-21 (cm/s)	0.005	0.058
	15-21 (cm/s)	0.004	0236
11C **Ps**	Density	(1) 0.58	0.525
	Flow speed	(3) 177.3	<0.001
11C flow speed Tukey *post hoc*	9-12 (cm/s)	0.004	0.276
	9-15 (cm/s)	0.012	0.04
	9-21 (cm/s)	0.005	0.016
	12-15 (cm/s)	0.009	0.029
	12-21 (cm/s)	0.002	0.004
	15-21 (cm/s)	0.007	0.126
11D **Dm**	Density	(1) 1.374	0.326
	Flow speed	(3) 4	0.047
11D flow speed Tukey *post hoc*	9-12 (cm/s)	0.019	1
	9-15 (cm/s)	0.022	1
	9-21 (cm/s)	0.02	1
	12-15 (cm/s)	0.006	1
	12-21 (cm/s)	0.017	0.425
	15-21 (cm/s)	0.016	0.251

Shown are the P values (4th column) and detailed statistics (3rd column) of the factors indicated in the 2nd column, referring to the results shown in the figure's panels indicated in the 1st column.

angle at which the prey approaches them, they are free to decide which angle to use for the strike, and, in turn, choose the swimming speed needed to reach the intercept point on time. The decision on the combination of angle and speed, where the speed depends on the angle, is chosen out of a wide repertoire of possible values (as indicated by high SD in Figures 3, 4B). Hence, the occurrence of those decisions likely indicates a cognitive ability in those fish.

The broad definition of cognition refers to the way animals acquire information through their senses, process that information, and decide to act on it (Shettleworth, 2001; Bshary and Triki, 2022).

Spatial cognition refers to the ability to make such decisions based on environmental information (Poucet, 1993). For example, spatial cognition was demonstrated in goldfish (*Carassius auratus*), referring to their ability to obtain food in a four-arm maze (Rodriguez et al., 1994) and effective navigation in complex settings (Givon et al., 2022). The suggested occurrence of cognitive behavior in the fish we studied refers to the individual ability to visually sense the location of its drifting prey, to process its movement velocities, and, based on that information, to decide which speed and direction to use in its strikes. Under a null hypothesis where the fish have no cognitive behavior, the fish would always strike the approaching prey at the same speed. For example, a use of the maximum speed should increase the chance of reaching the prey before a neighboring fish does. However, Figure 3B shows a dependency of the strike speed on the ambient current: under stronger currents faster strikes are made. Similarly, under the null hypothesis, one would not expect the striking speed to become faster when the angle to the prey is wider (Figure 9). These observations indicate the occurrence of cognitive decisions among foraging zooplanktivorous fish.

A cognitive ability of zooplanktivorous fish was also shown by McFarland and Levin (2002), demonstrating that the three species of site-attached fishes they studied were able to change their striking strategy based on flow speed. While under weak flows, those fish instantaneously struck the prey, when the flow speed exceeded a threshold of 10-14 cm/s, the fish deferred their strikes until the drifting prey got closer to them. An indication that a similar threshold occurred in 3 of the 4 species we studied (Ps, Dm, and Cv) is shown in Figure 5. A relatively long Reactive Distance was found in all species under a weak flow (10 cm/s), becoming shorter and statistically unchanged when the flow speed exceeded that level.

How long does it take the fish to initiate a strike? That decision must be made during the time elapsed between the moment of prey detection to the time the strike is initiated. Alas, we have no information on the moment of detection. Here we suggest an indirect way to determine the upper limit of the decision time (hereafter: Information Processing Time, or IPT). We assume that a strike is initiated immediately after IPT without delay (for other considerations such as energetic costs). During IPT, the planktonic prey continues to drift toward the fish, thereby gradually closing the gap to the fish. Due to that drift, a shortening of Reactive Distance occurs. For example, let's consider a flow speed of 10 cm/s, oriented directly onto the fish, a detection distance of 8 cm, and an IPT of 100 msec. Simple calculations indicate that by the end of IPT, the prey had advanced 1 cm, and is found 7 cm up-current of the fish when the strike starts. Note that this is a maximum bound of the predator-prey gap because delays in initiating the strike beyond IPT should further shorten that gap. Indeed, Figure 5 shows a significant decrease in Reactive Distance with increasing flow speed. For unknown reasons, for all species, the decrease of Reactive Distance was greater for the change from 10 to 15 cm/s than from 15 to 20 cm/s. Perhaps the change to flows stronger than 10 cm/s require longer IPT that is associated with a shift to a different mode of strikes (McFarland and Levin, 2002). Our calculations of the upper bound of IPT, referring to the greatest decline of Reactive Distance between 10 and 15 cm/s (Figure 5), indicate 429 msec. This value is of the same order of magnitude as that reported for cognitive-based decisions in birds (Pomeroy and Heppner, 1977) and mammals (Proctor and Brosnan, 2013). Interestingly, also in humans, that decision time is approximately 400 ms (Thorpe et al., 1996). While zooplanktivorous, site-attached fishes provide an appealing way to calculate IPT, studies are still needed in order to further develop this idea.

Why does it take longer for the fish to initiate a strike when the flow speed is faster (Figure 5)? We propose that a likely explanation is the well-known association between flow speed and turbulence, especially over the rough topography of coral reefs (Lowe et al., 2008; Asher and Shavit, 2019). A stronger turbulence means that the zooplankton's drifting path is more erratic, making it more difficult for the fish to predict the precise location of the intercept point. By deferring the strike initiation until the prey is closer, the fish can improve its ability to correctly predict the intercept point.

Several caveats should be considered. First, the type of prey we used was *Artemia* nauplii. Unlike copepods, the dominant taxon in the fish's natural diet (Noda et al., 1992), those nauplii are poor swimmers and lack an escape response (Trager et al., 1994). However, poor swimming and the absence of escape response are unlikely to have a considerable effect of the strike parameters that we measured. Secondly, in nature, the fish we studied live in social groups, whereas in the flume we always used single fish. Our attempts to concurrently use more than one fish in the flume failed due to extreme aggressive interactions among the fish. A third caveat is that our experiments were carried out in a laboratory flume (Supplementary Figure 2), where conditions are different from nature and the fish movements are constrained by the walls. Hence, our results should be evaluated in a comparative sense, comparing one species or one flow speed to another. Extra caution should be applied if an extrapolation of our results natural conditions is sought.

Overall, our flume study presents for the first time some of the key attributes of prey strikes by site-attached coral-reef fishes. In planning their strikes, including the initiation, orientation, and speed of striking, the fish appear to use their cognitive ability to perceive the location and drifting speed of their prey. Decisions are made within a few hundred of milliseconds. Inter-specific differences of strike attributes may explain the corresponding differences in their feeding rates and their preferred habitats, as well as inter-specific differences in group sizes in two of the studied species.

Data availability statement

The raw data supporting the conclusions of this article will be made available by the authors, without undue reservation.

Ethics statement

The animal study was approved by The Hebrew University of Jerusalem, Ethics Committee for Maintenance and Experimentation on Laboratory Animals, Permit # NS-24540-08. The study

was conducted in accordance with the local legislation and institutional requirements.

Author contributions

HE: Conceptualization, Data curation, Formal Analysis, Investigation, Methodology, Project administration, Software, Visualization, Writing – original draft, Writing – review & editing. AG: Conceptualization, Data curation, Formal Analysis, Investigation, Methodology, Project administration, Software, Visualization, Writing – original draft, Writing – review & editing.

Funding

The author(s) declare financial support was received for the research, authorship, and/or publication of this article. This study was funded by Israel Science Foundation (ISF) grant #1422-19 to AG.

Acknowledgments

We thank Moti Ohevia for his ingenious assistance with the flume and video cameras and Daniela Genin for thoroughly editing our manuscript. Nachumi Sela professionally assisted our diving operations, both above- and under-water. He, Michal Sela, and Aharon Adam kindly and effectively helped with the collection of fish in the reef. We are indebted to Irena Kolesnikov for her help with diverse undertakings at the lab. We thank the IUI staff for our use of the institutional facilities.

Conflict of interest

The authors declare that the research was conducted in the absence of any commercial or financial relationships that could be construed as a potential conflict of interest.

Publisher's note

Supplementary material

The Supplementary Material for this article can be found online at: https://www.frontiersin.org/articles/10.3389/fmars.2023.1327581/full#supplementary-material

References

Allen, G. R., and Randall, J. E. (1980). A review of the damselfishes (Teleostei: Pomacentridae) of the red sea. *Isr. J. Zool* 29, 1-98. doi: 10.1080/00212210.1980.10688486

Asher, S., and Shavit, U. (2019). The effect of water depth and internal geometry on the turbulent flow inside a coral reef. *J. Geophys. Res. Ocean.* 124, 3508–3522. doi: 10.1029/2018JC014331

Atkinson, G., Davison, R., Jeukendrup, A., and Passfield, L. (2003). Science and cycling: Current knowledge and future directions for research. *J. Sports Sci.* 21, 767–787. doi: 10.1080/0264041031000102097

Baensch, H. A., and Riehl, R. (1997). *Aquarien Atlas. 5th ed* (Melle: Mergus Verlag).

Bellwood, D. R., Goatley, C. H. R., and Bellwood, O. (2017). The evolution of fishes and corals on reefs: Form, function and interdependence. *Biol. Rev.* 92, 878–901. doi: 10.1111/brv.12259

Benayahu, Y., and Loya, Y. (1977). Space partitioning by stony corals soft corals and benthic algae on the coral reefs of the northern Gulf of Eilat (Red Sea). *Helgoländer Wissenschaftliche Meeresuntersuchungen* 30, 362–382. doi: 10.1007/BF02207848

Biton, E., and Gildor, H. (2011). The general circulation of the Gulf of Aqaba (Gulf of Eilat) revisited: The interplay between the exchange flow through the Straits of Tiran and surface fluxes. *J. Geophys. Res. Ocean.* 116. doi: 10.1029/2010JC006860

Blake, R. W. (2004). Fish functional design and swimming performance. *J. Fish Biol.* 65, 1193–1222. doi: 10.1111/j.0022-1112.2004.00568.x

Brokovich, E. (2001). The community structure and biodiversity of reef fishes at the northern Gulf of Aqaba (Red Sea) with relation to their habitat. *Fac. Life Sci. Tel Aviv Univ. Isr.* 116.

Brokovich, E. (2008). *Coral reef fish assemblages in the upper twilight zone (< 65 m). Aqaba-Eilat, improbable Gulf Environ* (Jerusalem: Biodivers. Preserv. Magnes Press), 255–266.

Bshary, R., and Triki, Z. (2022). Fish ecology and cognition: insights from studies on wild and wild-caught teleost fishes. *Curr. Opin. Behav. Sci.* 46. doi: 10.1016/j.cobeha.2022.101174

Cano-Barbacil, C., Radinger, J., Argudo, M., Rubio-Gracia, F., Vila-Gispert, A., and García-Berthou, E. (2020). Key factors explaining critical swimming speed in freshwater fish: a review and statistical analysis for Iberian species. *Sci. Rep.* 10, 1–12. doi: 10.1038/s41598-020-75974-x

China, V., and Holzman, R. (2014). Hydrodynamic starvation in first-feeding larval fishes. *Proc. Natl. Acad. Sci. U. S. A.* 111, 8083–8088. doi: 10.1073/pnas.1323205111

China, V., Levy, L., Liberzon, A., Elmaliach, T., and Holzman, R. (2017). Hydrodynamic regime determines the feeding success of larval fish through the modulation of strike kinematics. *Proc. R. Soc B Biol. Sci.* 284. doi: 10.1098/rspb.2017.0235

Clarke, R. D., Buskey, E. J., and Marsden, K. C. (2005). Effects of water motion and prey behavior on zooplankton capture by two coral reef fishes. *Mar. Biol* 146, 1145-1155. doi: 10.1007/s00227-004-1528-y

Clarke, R. D., Finelli, C. M., and Buskey, E. J. (2009). Water flow controls distribution and feeding behavior of two co-occurring coral reef fishes: II. Laboratory experiments. *Coral Reefs* 28, 475-488. doi: 10.1007/s00338-009-0479-7

Confer, J. L., and Blades, P. I. (1975). Omnivorous zooplankton and planktivorous fish. *Limnol. Oceanogr* 20 (4), 571-579. doi: 10.4319/lo.1975.20.4.0571

Coughlin, D. J., and Strickler, J. R. (1990). Zooplankton capture by a coral reef fish: an adaptive response to evasive prey. *Environ. Biol. Fishes* 29, 35-42. doi: 10.1007/BF00000566

Engel, A., Reuben, Y., Kolesnikov, I., Churilov, D., Nathan, R., and Genin, A. (2021). *In situ* three-dimensional video tracking of tagged individuals within site-attached social groups of coral-reef fish. *Limnol. Oceanogr. Methods* 19, 579–588. doi: 10.1002/lom3.10444

Erez, J. (1990). On the importance of food sources in coral-reef ecosystems. *Ecosyst. World* 25, 411–418.

Finelli, C. M., Clarke, R. D., Robinson, H. E., and Buskey, E. J. (2009). Water flow controls distribution and feeding behavior of two co-occurring coral reef fishes: I. Field measurements. *Coral Reefs* 48, 461–473. doi: 10.1007/s00338-009-0481-0

Fishelson, L. (1971). Ecology and distribution of the benthic fauna in the shallow waters of the Red Sea. *Mar. Biol.* 10, 113–133.

Fulton, C. J. (2007). Swimming speed performance in coral reef fishes: Field validations reveal distinct functional groups. *Coral Reefs* 26, 217–228. doi: 10.1007/s00338-007-0195-0

Fulton, C. J., Bellwood, D. R., and Wainwright, P. C. (2005). Wave energy and swimming performance shape coral reef fish assemblages. *Proc. R. Soc B Biol. Sci.* 272, 827–832. doi: 10.1098/rspb.2004.3029

Fulton, C. J., Johansen, J. L., and Steffensen, J. F. (2013). Energetic extremes in aquatic locomotion by coral reef fishes. *PloS One* 8. doi: 10.1371/journal.pone.0054033

Genin, A., Karp, L., and Miroz, A. (1994). Effects of flow on competitive superiority in scleractinian corals. *Limnol. Oceanogr.* 39, 913–924. doi: 10.4319/lo.1994.39.4.0913

Genin, A., Monismith, S. G., Reidenbach, M. A., Yahel, G., and Koseff, J. R. (2009). Intense benthic grazing of phytoplankton in a coral reef. *Limnol. Oceanogr.* 54, 938–951. doi: 10.4319/lo.2009.54.3.0938

Genin, A., and Paldor, N. (1998). Changes in the circulation and current spectrum near the tip of the narrow, seasonally mixed Gulf of Elat. *Isr. J. Earth Sci.* 47, 87–92.

Givon, S., Samina, M., Ben-Shahar, O., and Segev, R. (2022). From fish out of water to new insights on navigation mechanisms in animals. *Behav. Brain Res.* 419, 113711. doi: 10.1016/j.bbr.2021.113711

Gordon, M. S., Hove, J. R., Webb, P. W., and Weihs, D. (2000). Boxfishes as unusually well-controlled autonomous underwater vehicles. *Physiol. Biochem. Zool.* 73, 663–671. doi: 10.1086/318098

Gordon, M. S., Plaut, I., and Kim, D. (1996). How puffers (Teleostei: Tetraodontidae) swim. *J. Fish Biol.* 49, 319–328. doi: 10.1111/J.1095-8649.1996.TB00026.X

Hamner, W. M., Jones, M. S., Carleton, J. H., Hauri, I. R., and Williams, D. M. (1988). Zooplankton, planktivorous fish, and water currents on a windward reef face: Great Barrier Reef, Australia. *Bull. Mar. Sci.* 42, 459–479.

Heatwole, S. J., and Fulton, C. J. (2013). Behavioural flexibility in reef fishes responding to a rapidly changing wave environment. *Mar. Biol.* 160, 677–689. doi: 10.1007/s00227-012-2123-2

Hobson, E., and Chess, J. (1978). Trophic relationships among fishes and plankton in the lagoon at Enewetak Atoll, Marshall Islands. *Fish Bull.* 76, 133–153.

Holzman, R., China, V., Yaniv, S., and Zilka, M. (2015). "Hydrodynamic constraints of suction feeding in low reynolds numbers, and the critical period of larval fishes," in *Integrative and Comparative Biology* (Oxford University Press), 48–61. doi: 10.1093/icb/icv030

Holzman, R., Collar, D. C., Mehta, R. S., and Wainwright, P. C. (2012). An integrative modeling approach to elucidate suction-feeding performance. *J. Exp. Biol.* 215, 1–13. doi: 10.1242/jeb.057851

Ishikawa, K., Wu, H., Mitarai, S., and Genin, A. (2022). Effects of prey density and flow speed on plankton feeding by garden eels: A flume study. *J. Exp. Biol.* 225, 1–10. doi: 10.1242/jeb.243655

Jacobs, C. N., and Holzman, R. (2018). Conserved spatio-temporal patterns of suction-feeding flows across aquatic vertebrates: A comparative flow visualization study. *J. Exp. Biol* 221 (7). doi: 10.1242/jeb.174912

Karpestam, B., Gustafsson, J., Shashar, N., Katzir, G., and Kröger, R. H. H. (2007). Multifocal lenses in coral reef fishes. *J. Exp. Biol.* 210, 2923–2931. doi: 10.1242/jeb.002956

Khrizman, A., Ribak, G., Churilov, D., Kolesnikov, I., and Genin, A. (2018). Life in the flow: Unique adaptations for feeding on drifting zooplankton in garden eels. *J. Exp. Biol* 221 (16). doi: 10.1242/jeb.179523

Kiflawi, M., and Genin, A. (1997). Prey flux manipulation and the feeding rates of reef-dwelling planktivorous fish. *Ecology* 78, 1062–1077. doi: 10.1890/0012-9658(1997)078[1062:PFMATF]2.0.CO;2

Krebs, J. M., and Turingan, R. G. (2003). Intraspecific variation in gape-prey size relationships and feeding 561 success during early ontogeny in red drum, Sciaenops ocellatus.

Lauder, G. V., Flammang, B., and Alben, S. (2012). Passive robotic models of propulsion by the bodies and caudal fins of fish. *Integr. Comp. Biol.* 52, 576–587. doi: 10.1093/icb/ics096

Lieske, E., and Myers, R. F. (1994). Coral reef fishes: caribbean, indian ocean and pacific ocean including 565 the red sea.

Lowe, R. J., Shavit, U., Falter, J. L., Koseff, J. R., and Monismith, S. G. (2008). Modeling flow in coral communities with and without waves: A synthesis of porous media and canopy flow approaches. *Limnol. Oceanogr.* 53, 2668–2680. doi: 10.4319/lo.2008.53.6.2668

Manatunge, J., and Asaeda, T. (1998). Optimal foraging as the criteria of prey selection by two centrarchid fishes. *Hydrobiologia* 391, 223–240.

McFarland, W., and Levin, S. (2002). Modelling the effects of current on prey acquisition in planktivorous fishes. *Mar. Freshw. Behav. Physiol.* 35, 69–85. doi: 10.1080/10236240290025626

Morais, R. A., and Bellwood, D. R. (2019). Pelagic subsidies underpin fish productivity on a degraded coral reef. *Curr. Biol.* 29, 1521–1527. doi: 10.1016/j.cub.2019.03.044

Myers, R. (1989) *Micronesian Reef Fishes: A Practical Guide to the Identification of the Coral Reef Fishes of the Tropical Central and Western Pacific*. Available at: https://api.semanticscholar.org/CorpusID:140187433.

Noda, M., Kawabata, K., Gushima, K., and Kakuda, S. (1992). Importance of zooplankton patches in foraging ecology of the planktivorous reef fish Chromis chrysurus (Pomacentridae) at Kuchinoerabu Island, Japan. *Mar. Ecol. Prog. Ser.* 87, 251–263. doi: 10.3354/meps087251

Nonacs, P., Smith, P. E., Bouskila, A., and Luttbeg, B. (1994). Modeling the behavior of the northern anchovy, Engraulis mordax, as a schooling predator exploiting patchy prey. *Deep. Res. Part II* 41, 147–169. doi: 10.1016/0967-0645(94)90065-5

O'Brien, W. J., Barfield, M., and Sigler, K. (2001). The functional response of drift-feeding Arctic grayling: the effects of prey density, water velocity, and location efficiency. *Can. J. Fish. Aquat. Sci.* 58, 1957–1963. doi: 10.1139/cjfas-58-10-1957

Olsson, K. H., Martin, C. H., and Holzman, R. (2020). Erratum: Hydrodynamic simulations of the performance landscape for suctioneeding fishes reveal multiple peaks for different prey types (Integrative and Comparative Biology DOI: 10.1093/icb/icaa021). *Integr. Comp. Biol* 60 (5), 1251-1267. doi: 10.1093/icb/icaa122

Palstra, A. P., Mes, D., Kusters, K., Roques, J. A. C., Flik, G., Kloet, K., et al. (2015). Forced sustained swimming exercise at optimal speed enhances growth of juvenile yellowtail kingfish (Seriola lalandi). *Front. Physiol.* 6. doi: 10.3389/fphys.2014.00506

Piccolo, J. J., Hughes, N. F., and Bryant, M. D. (2008). Water velocity influences prey detection and capture by drift-feeding juvenile coho salmon (Oncorhynchus kisutch) and steelhead (Oncorhynchus mykiss irideus). *Can. J. Fish. Aquat. Sci.* 65, 266–275. doi: 10.1139/F07-172

Pomeroy, H., and Heppner, F. (1977). Laboratory determination of startle reaction time of the starling (Sturnus vulgaris). *Anim. Behav.* 25, 720–725. doi: 10.1016/0003-3472(77)90121-X

Poucet, B. (1993). Spatial cognitive maps in animals: new hypotheses on their structure and neural mechanisms. *Psychol. Rev.* 100, 163–182. doi: 10.1037/0033-295x.100.2.163

Proctor, D., and Brosnan, S. F. (2013). Visual Processing Speed in Capuchin Monkeys (Cebus apella) and Rhesus Macaques (Macaca mulatta). *Int. J. Comp. Psychol.* 26, 166-175. doi: 10.46867/ijcp.2013.26.02.01

Reidenbach, M. A., Monismith, S. G., Koseff, J. R., Yahel, G., and Genin, A. (2006). Boundary layer turbulence and flow structure over a fringing coral reef. *Limnol. Oceanogr.* 51, 1956–1968. doi: 10.4319/lo.2006.51.5.1956

Rickel, S., and Genin, A. (2005). Twilight transitions in coral reef fish: The input of light-induced changes in foraging behaviour. *Anim. Behav.* 70, 133–144. doi: 10.1016/J.ANBEHAV.2004.10.014

Rodriguez, F., Duran, E., Vargas, J. P., Torres, B., and Salas, C. (1994). Performance of goldfish trained in allocentric and egocentric maze procedures suggests the presence of a cognitive mapping system in fishes. *Anim. Learn. Behav.* 22, 409–420. doi: 10.3758/BF03209160

Sambilay, J. V. (1990). Interrelationships between swimming speed, caudal fin aspect ratio and body length of fishes. *Fishbyte* 8, 16–20. Available at: https://hdl.handle.net/20.500.12348/3181.

Schakmann, M., and Korsmeyer, K. E. (2023). Fish swimming mode and body morphology affect the energetics of swimming in a wave-surge water flow. *J. Exp. Biol.* 226. doi: 10.1242/jeb.244739

Schakmann, M., Steffensen, J. F., Bushnell, P. G., and Korsmeyer, K. E. (2020). Swimming in unsteady water flows: Is turning in a changing flow an energetically expensive endeavor for fish? *J. Exp. Biol.* 223. doi: 10.1242/jeb.212795

Shaked, Y., and Genin, A. (2022). The Israel National Monitoring Program in the Northern Gulf of Aqaba – scientific report. *Isr. Minist. Environ. Prot*. Available at: https://iui-eilat.huji.ac.il/uploaded/NMP/reports/NMP%20Report%202022.pdf.

Shettleworth, S. J. (2001). Animal cognition and animal behaviour. *Anim. Behav.* 61, 277–286. doi: 10.1006/anbe.2000.1606

Siqueira, A. C., Morais, R. A., Bellwood, D. R., and Cowman, P. F. (2020). Trophic innovations fuel reef fish diversification. *Nat. Commun.* 11, 1–11. doi: 10.1038/s41467-020-16498-w

Smith, M., and Heemstra, P. (1986). *Smiths' Sea Fishes.* (Berlin: Springer-Verlag).

Theriault, D. H., Fuller, N. W., Jackson, B. E., Bluhm, E., Evangelista, D., Wu, Z., et al. (2014). A protocol and calibration method for accurate multi-camera field videography. *J. Exp. Biol.* 217, 1843–1848. doi: 10.1242/jeb.100529

Thorpe, S., Fize, D., and Mralot, C. (1996). Speed of processing in the human visual system. *Nature* 381, 520–522. doi: 10.1038/381520a0

Trager, G., Achituv, Y., and Genin, A. (1994). Effects of prey escape ability, flow speed, and predator feeding mode on zooplankton capture by barnacles. *Mar. Biol.* 120, 251–259. doi: 10.1007/BF00349685

Turingan, R. G., Beck, J. L., Krebs, J. M., and Licamele, J. D. (2005). "Development of feeding mechanics in marine fish larvae and the swimming behavior of zooplankton prey: implications for rearing marine fishes," in *Copepods in Aquaculture* (Copepods in Aquaculture, Hoboken, New Jersey: Blackwell Publishing Professional), 119–132. doi: 10.1002/9780470277522.ch10

Videler, J. J., and Wardle, C. S. (1991). Fish swimming stride by stride: speed limits and endurance. *Rev. Fish Biol. Fish.* 1, 23–40. doi: 10.1007/BF00042660

Vinyard, G. L. (1980). Differential Prey Vulnerability and Predator Selectivity: Effects of Evasive Prey on Bluegill (Lepomis macrochirus) and Pumpkinseed (L . gibhosus) Predation. *Can. J. Fish. Aquat. Sci* 37 (12), 2294-2299. doi: 10.1139/f80-276

Wainwright, P., Carroll, A. M., Collar, D. C., Day, S. W., Higham, T. E., and Holzman, R. A. (2007). Suction feeding mechanics, performance, and diversity in fishes. *Integr. Comp. Biol* 47 (1), 96-106. doi: 10.1093/icb/icm032

Walker, J. A., Alfaro, M. E., Noble, M. M., and Fulton, C. J. (2013). Body fineness ratio as a predictor of maximum prolonged-swimming speed in coral reef fishes. *PloS One* 8, 1–13. doi: 10.1371/journal.pone.0075422

Walker, J. A., and Westneat, M. W. (2002). Performance limits of labriform propulsion and correlates with fin shape and motion. *J. Exp. Biol.* 205, 177–187. doi: 10.1242/jeb.205.2.177

Wardle, C. S., Videler, J. J., and Altringham, J. D. (1995). Tuning in to fish swimming waves: body form, swimming mode and muscle function. *J. Exp. Biol.* 198, 1629–1636. doi: 10.1242/jeb.198.8.1629

Webb, P. W. (1984). Form and function in fish swimming. *Sci. Am.* 251 (1), 72–83. doi: 10.1038/scientificamerican0784-72

Webb, P., and Weihs, D. (1983) *Fish biomechanics*. Available at: https://cir.nii.ac.jp/crid/1130000797018149888. (Accessed October 22, 2023).

Werner, E. E. (1977). Species packing and niche complementarity in three sunfishes. *Am. Nat.* 111, 553–578. doi: 10.1086/283184

Wyatt, A. S. J., Lowe, R. J., Humphries, S., and Waite, A. M. (2010). Particulate nutrient fluxes over a fringing coral reef: Relevant scales of phytoplankton Production and mechanisms of supply. *Mar. Ecol. Prog. Ser* 405, 113-130. doi: 10.3354/meps08508

Wyatt, A. S. J., Lowe, R. J., Humphries, S., and Waite, A. M. (2013). Particulate nutrient fluxes over a fringing coral reef: Source-sink dynamics inferred from carbon to nitrogen ratios and stable isotopes. *Limnol. Oceanogr.* 58, 409–427. doi: 10.4319/lo.2013.58.1.0409

Xin, Z. Q., and Wu, C. J. (2013). Shape optimization of the caudal fin of the three-dimensional self-propelled swimming fish. *Sci. China Physics Mech. Astron.* 56, 328–339. doi: 10.1007/s11433-013-4994-8

Yahel, G., Post, A. F., Fabricius, K., Marie, D., Vaulot, D., and Genin, A. (1998). Phytoplankton distribution and grazing near coral reefs. *Limnol. Oceanogr.* 43, 551–563. doi: 10.4319/lo.1998.43.4.0551

frontiers | Frontiers in Marine Science

TYPE Original Research
PUBLISHED 04 March 2024
DOI 10.3389/fmars.2024.1330379

OPEN ACCESS

EDITED BY
Stuart Humphries,
University of Lincoln, United Kingdom

REVIEWED BY
Iain M. Suthers,
University of New South Wales, Australia
Stein Kaartvedt,
University of Oslo, Norway

*CORRESPONDENCE
Alexandra Khrizman
khrizman@stanford.edu

†PRESENT ADDRESS
Alexandra Khrizman,
Department of Earth System Science, Doerr School of Sustainability, Stanford University, Stanford, CA, United States

RECEIVED 30 October 2023
ACCEPTED 29 January 2024
PUBLISHED 04 March 2024

CITATION
Khrizman A, Kolesnikov I, Churilov D and Genin A (2024) Zooplanktivory in garden eels: benefits and shortcomings of being "anchored" compared with other coral-reef fish.
Front. Mar. Sci. 11:1330379.
doi: 10.3389/fmars.2024.1330379

Zooplanktivory in garden eels: benefits and shortcomings of being "anchored" compared with other coral-reef fish

Alexandra Khrizman[1,2*†], Irena Kolesnikov[1], Dmitri Churilov[1] and Amatzia Genin[1,3]

[1]The Interuniversity Institute for Marine Sciences in Eilat, Eilat, Israel, [2]Fredy and Nadine Hermann Institute of Earth Sciences, The Hebrew University of Jerusalem, Jerusalem, Israel, [3]Department of Ecology, Evolution, and Behavior, Alexander Silberman Institute of Life Sciences, The Hebrew University of Jerusalem, Jerusalem, Israel

Garden eels are elongated zooplanktivorous fish that live in colonies on sandy bottoms, often adjacent to coral reefs. Each eel digs its own burrow, from which it partially emerges to forage on drifting zooplankton while being "anchored" with its tail inside the burrow. Feeding rates and foraging movements were examined in the garden eel *Gorgasia sillneri* and compared with corresponding measurements carried out as part of this study and by (Genin et al.)[1] with 3 species of "free", site-attached coral-reef fish. Feeding rates by the garden eels were substantially lower than those of the free fish. In the eels, those rates monotonically increased with increasing current speed up to ~20 cm/s, whereas in the free fish maximum rates were observed under moderate flows. A nearly linear increase in feeding rate as function of prey density was observed in both the garden eels and the free fish. However, the slope of that increase in the eels was over an order of magnitude more gradual than that reported for the free fish. The different functional responses of the two fish groups appear to be related to their morphology and maneuverability capabilities. Being elongated, anchored in a burrow and able to modulate body posture according to the flow speed allow the eels high feeding rates under strong currents. The tradeoff, compared with free fish, include limited maneuverability, slower swimming, and smaller foraging volume, rendering the eels' functional response less efficient to increasing prey density. This cost appears to be compensated by the eels' ability to occupy sandy, shelter-less bottoms, which in some locations are immensely more abundant than coral-covered rocks, where most planktivorous free fish live.

KEYWORDS

foraging, movement, flow, prey density, Red Sea, niche

1 Introduction

A nearly ubiquitous mode of foraging for zooplankton among coral-reef fishes is being site-attached (Hobson, 1991), where the fish feed on drifting plankton while maintaining a position near a shelter (Popper and Fishelson, 1973). Once a prey is detected, typically from a distance of 15-20 cm (Genin et al.)[1], a short (a few cm) strike is initiated, at the end of which the prey is captured. In coral reefs, zooplanktivorous fish form "a wall of mouths" (Hamner et al., 1988), thereby an important pathway of nutrient subsidy to the coral reef ecosystem (Erez, 1990; Morais and Bellwood, 2019).

Garden eels are unique members of the guild of site-attached zooplanktivorous fish as they feed while being "anchored" to the seafloor. Each eel lives in a burrow that it digs in the sand (Smith, 1989). To feed, the eel emerges from the burrow but keeps the distal part of its body inside the burrow, that serves the eels as a shelter, into which it retreats during the night and when threatened. Garden eels are visual zooplanktivores, feeding on copepods, gelatinous zooplankton, arrow worms, and other zooplankton (Fricke, 1970; Smith, 1989; Donham et al., 2017). Prey is captured individually.

Feeding and foraging behavior of "free" (non-anchored) reef-dwelling planktivorous fish have been extensively studied. Their feeding rate is strongly affected by prey density, exhibiting a nearly linear functional response to increasing prey density (Noda et al., 1992; Kiflawi and Genin, 1997; Genin et al.[1]). No such response is observed for an increase in prey flux due to faster flow (Kiflawi and Genin, 1997; Genin et al.[1]). The latter effect is due to a biomechanical limitation on the maximum angle that the fish can orient its body sideways of the oncoming current: the stronger the current the closer the fish is heading directly onto the flow direction (Kiflawi and Genin, 1997). Consequently, the effective volume across which the fish strikes its prey becomes smaller (narrower) as flow speed increases.

The effects of prey density and current speed on feeding rates by garden eels were studied by Khrizman et al. (2018) and Ishikawa et al. (2022). Similar to free fish, the eel's feeding rate monotonically increases with increasing prey densities. However, for the Red Sea Garden eel *Gorgasia sillneri*, unlike free fish, its feeding rates also increase with increasing current speeds. This deviation from the trend observed for free fish was attributed by to the ability of the eels to modulate their body posture to minimize drag forces exerted on them by the flowing water (Khrizman et al., 2018). While foraging in weak currents, the eels stretch their bodies out of the burrows, keeping them relatively straight and reaching to all directions. When the currents are strong, the eels minimize drag forces by a partial retreat into the burrows, curving the body in a posture resembling a question mark, and orient the head onto the currents (Khrizman et al., 2018).

Swimming performance and maneuverability are essential for foraging on drifting prey (Webb, 1984) and depend on morphology and deformation of body and fins (Webb, 1984; Webb, 1994; Webb, 2011; Lauder, 2015). Most planktivorous coral-reef fishes use their pectoral and pelvic fins (Fulton, 2007). Eels, on the other hand, use mostly their body to generate undulatory waves that propagate down the body through the caudal fin (Lauder, 2015). However, the anchored garden eels are unable to use their caudal fin, as free eels do, because that fin is kept inside the burrow as an anchor. While the two aforementioned fish groups reside at similar depths, feed on the same taxa, both are visual predators, and strike individual prey, garden eels and free fish have remarkably distinct morphologies and swimming mechanisms. The objectives of this study were to: (1) measure the feeding rates and the functional response of garden eels with respect to changes in prey density and current speed; (2) compare those functional responses with those reported by (Genin et al.)[1] for free, site-attached fish; and (3) assess the differences of foraging movements and maneuverability between the garden eels and the free fish.

2 Materials and methods

In this study, we compare several attributes of plankton foraging among anchored garden eels and free, site-attached coral-reef fishes. The analyses of those attributed in the garden eels are based on our own work, the methods of which are detailed below. The corresponding information on the free fish is based on an earlier study at our laboratory (Genin et al.)[1], the methods of which are briefly described at the end of this section. Note that our study with the garden eels was carried out *in situ*, whereas the work with the free fish was carried out both in a flume and *in situ*. The ensuing limitations of such a comparison are addressed below.

2.1 *In situ* foraging by garden eels

2.1.1 Study animal

The garden eel *Gorgasia sillneri* (subfamily *Heterocongrinae*, Klausewitz, 1962) is highly abundant throughout the Red Sea (Clark, 1980). It forms large colonies, consisting of hundreds of individuals (Clark, 1980), usually on sandy bottoms near or inside sea-grass meadows at depth of 4-55 m (Fricke, 1970; Clark, 1980). The typical length of males and females is 75-95 cm and 55-75 cm, respectively (Clark, 1980). Their body is nearly circular, 10-16 mm in diameter (Fricke, 1969; Fricke, 1970; Clark, 1980). *Gorgasia* species have a small pectoral fin and a dorsal fin that extends along the entire body (Klausewitz, 1962). Pelvic fins are absent and the caudal fins have evolved as a tool for burrowing (De Schepper et al., 2007). During foraging, the eels remain "anchored" to the bottom by keeping the distal ~25-30% of their body inside the burrow (Fricke, 1970), depending on the ambient current speed (Khrizman et al., 2018).

2.1.2 Study site

The field work was carried out in the oligotrophic northern Gulf of Aqaba, Red Sea (29°36' N, 34°56' E) during November 2015 - March 2017. A detailed description of the local reef and its environmental conditions is found in Reiss and Hottinger (1984);

1 Genin, A., Rickel, S., Zarubin, M., and Kiflawi, M. Effects of flow speed and prey density on the rate and efficiency of prey capture in 4 species of zooplanktivorous coral-reef fishes. *Front. Mar. Sci. (Submitted to)*.

Yahel et al. (2002), and Genin et al. (2009). Data were collected at 6 –9 m depth at two sites: the "Lighthouse", 0.4 km south of the Interuniversity Institute for Marine Sciences (IUI) and "Taba/ Princess", adjacent to the Israel-Egypt border crossing, ~1.4 km to the south. The habitat is exposed to oscillating, long-shore tidal currents (Monismith and Genin, 2004) with a mean speed of ~10 cm/s and a maximum of 50 cm/s (Genin and Paldor, 1998).

2.1.3 Feeding rates

Following Khrizman et al. (2018), feeding rates were measured by visually counting strikes, both *in situ* by divers and by counts obtained from video records. Concurrent estimates of feeding rates, using video (y) and direct counts (x), obtained for different individuals during the same runs, indicated a similarity between the two methods (y=1.16x; R^2 = 0.96; N=11 runs; the paired t-test indicated a non-significant difference between the two methods P>0.05; Supplementary Information Figure S1). The results of the two methods were pooled and the relative average of both methods where applicable was used. Overall, counts were obtained for a total of 10-52 eels per session, during a 1 min long interval per eel (N=702; Table 1).

2.1.4 Prey density measurements

Zooplankton (prey) densities were measured *in situ* using a plankton net (200 µm mesh size; 50 cm mouth diameter) through two methods of operations: tows and stationary. For the first mode, the net was towed by 2 scuba divers for ca. 10 minutes up-current of the eel colony. Volume filtered by the net were measured using a TSK Flowmeter. For the stationary sampling, the net was moored 20 cm above the bottom upstream to the eel colony for a period of 30-60 minutes. Divers verified desired net extension during the sampling interval. Volume filtered were calculated based on the net's mouth diameter, current speed measured during the deployment using a Aquadopp current meter (see below), and

TABLE 1 Details on times, conditions and methods of the *in-situ* feeding experiments with the garden eel *G.sillneri*.

Date and Time	Current speed (cm/s)	Plankton density (prey/m^3)	# Eels	Counting method	Prey density range	
14/10/2014 11:30	9.4	492.7	9	Underwater	Low + Moderate	*
19/10/2014 18:00	3.9	323.7	10	Underwater	Low + Moderate	
22/10/2014 07:50	10.0	1227.0	10	Underwater	Moderate	*
04/11/2014 14:10	7.8	136.4	10	Underwater	Low + Moderate	
12/11/2014 13:15	6.3	69.9	10	Underwater	Low	
10/12/2014 11:20	20.7	1176.7	10	Underwater	Moderate	
21/12/2014 10:55	5.0	168.2	10	Underwater	Low + Moderate	
23/12/2014 10:10	14.2	1080.8	10	Underwater	Moderate	*
31/12/2014 13:25	14.7	1018.2	10	Underwater	Low + Moderate	*
02/08/2016 08:40	17.5	110.2	44	Video	Low	
22/08/2016 09:00	17.5	38.1	21	Video	Low	
23/08/2016 10:20	27.7	27.1	52	Video	Low	
04/07/2017 08:30	9.1	21.8	47	Underwater + Video	Low	*
05/07/2017 07:00	8.5	85.5	52	Underwater + Video	Low	*
06/07/2017 07:50	7.9	29.9	49	Underwater + Video	Low	
11/07/2017 18:00	8.2	25.9	52	Underwater + Video	Low	*
12/07/2017 08:00	6.7	95.2	49	Underwater + Video	Low	
13/07/2017 08:00	3.9	206.8	50	Underwater + Video	Low + Moderate	
18/07/2017 07:55	9.4	54.1	39	Underwater + Video	Low	*
19/07/2017 07:55	18.9	110.6	51	Underwater + Video	Low	
20/07/2017 07:55	11.7	37.9	38	Underwater + Video	Low	*
25/07/2017 08:20	7.1	132.0	28	Underwater + Video	Low	
26/07/2017 08:10	5.3	51.6	16	Underwater	Low	
27/07/2017 07:50	3.8	51.7	25	Underwater + Video	Low	

*Included in comparison with feeding rates of free fish that were quantified in moderate current speed (12 cm/s).

thefiltering efficiency of the net under different current speeds. The net's filtering efficiency was measured by comparing the ambient current speed with that at the mouth of the stationary net using two current meters (ADV, Sontek, Norway).

Despite the fact that both zooplankton and phytoplankton in the oligotrophic waters of the Gulf of Aqaba are small, both the eels and the free fish studied by (Genin et al.)[1] and referred to in this study feed on zooplankters that are retained on 200 µm plankton net (A. Genin unpublished observations).

2.1.5 Current mesurements

Current velocities were measured concurrently with each video record, using a current profiler (2 MHz Aquadopp, Nortek, Norway). The profiler was placed on the bottom looking upward, using 0.4 m bin widths, starting at 0.2 m above bottom. Here we used the average of the two lowermost bins (0.2-1.0 m above seafloor), corresponding to the heights of the eels' heads above bottom. Currents were recorded at 1 Hz and averaged over 2 min intervals.

2.1.6 Foraging movements

The foraging movements of garden eels were assessed from 3D reconstruction of the eels' body shape and its change using *in situ* video records. Video records were acquired using two GoPro cameras positioned on a stand inside the eel colony. Videos were analyzed through DLTdv5 in Matlab (Hedrick, 2008) as described in Khrizman et al. (2018). Details regarding the method are provided in the Supplementary Information. The foraging movements calculated included (1) the volume of water across which the eel's mouth moved (hereafter "foraging volume"), (2) the movement speed of the eel's head (hereafter "swimming speed"), and (3) the orientation (angle) of the eel's upper body with respect to the direction of the oncoming flow (hereafter "angle to the current").

To calculate the foraging volume across which the eel foraged during a 20 min interval, we used the ~700 locations of the head recorded every 1.67 sec during that interval, yielding 3D "foraging polygons" of 6-15 neighboring eels in each interval (Figure 1, Supplementary Information Figure S2). The foraging volumes of a total of 79 eels were obtained during 8 different intervals collected from 6 video sessions (Supplementary Information Table S1). The speed of the head movements was calculated as distance divided by time between consecutive frames (intervals of 1.67 sec). A total of 36,158 speed calculations were made during 11 sessions (Supplementary Information Table S1), covering a wide range of current speeds (3-27 cm/s). To measure the angle of the eel's upper body to the current direction, we digitized several points along the eel's upper body and calculated the angle between the current direction and the direction of the eel's upper section (Supplementary Information Figure S3). This analysis was performed for 3 eels every 10 sec during 3.5 min long sections, 3-9 sections per video session in each of 11 different sessions (Supplementary Information Table S1). The variance of the angles (in radians) was used as a proxy of the eels' maneuverability.

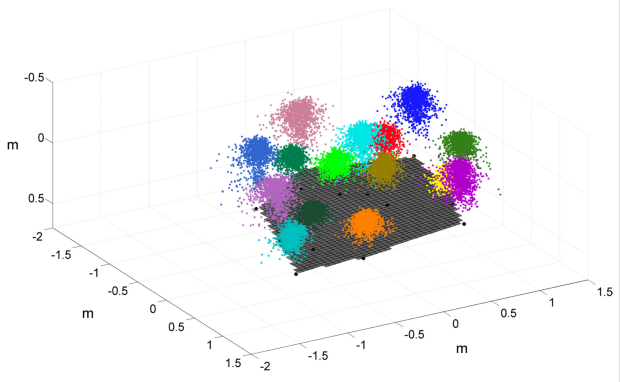

FIGURE 1
Reconstruction of foraging space of 15 garden eels during 40 min on 18/05/2016 at a depth of 7 m, under mean current speed of 7.5 cm/s. Each color indicates an individual eel, and each point indicates the location of its head in 1.67 sec. Black points - the eels' burrows; grey surface - the seafloor.

2.2 Comparison with free fish

To compare the foraging behavior of the anchored eels with that of the free, site-attached planktivorous fish we used the data reported in by (Genin et al.)[1] for the serranid *Pseudanthias squamipinnis* (Peters, 1855), and two pomacentrids - *Dascyllus marginatus* (Rüppell, 1829) and *Neopomacentrus miryae* Dor and Allen, 1977. P. *squamipinnis* is a common species in the Indo-Pacific Ocean, *D. marginatus* is endemic to the Red Sea, Gulf of Aden and Gulf of Oman, and *N. miryae* is endemic to the Red Sea. All three species are common in the Gulf of Aqaba (Brokovich, 2001) and reside in proximity to shelters provided by branching corals and perforated rocks.

2.2.1 Feeding rates

Feeding rates of the free fish were measured in a flume by (Genin et al.)[1], whereas our measurements with the eels were carried out *in situ*. Since the effect of flow speed on feeding rates in the free fish was examined by (Genin et al.)[1] under two prey densities (210 prey/m^3 and 630 prey/m^3), the data obtained for the eels were sorted into two groups covering similar conditions: one with a mean prey density of 113 prey/m^3 (range: 22 – 493) and the other with a mean of 648 prey/m^3 (range: 136 – 1227). Moreover, due to the absence of measurements under a combination of low current speeds and high prey densities, the effect of current speed on feeding rates by the garden eels was evaluated in the range of 8.2 – 17.5 cm/s (average of 11.8 cm/s), corresponding to the measurements of (Genin et al.)[1] under a flow speed of 12 cm/s.

2.2.2 Body orientation

As part of our *in-situ* measurements, we recorded the angle to the flow, defined as the angle between the current direction and the longitudinal axis of the body (line connecting the fish's snout and tail), for the free fish *P. squamipinnis* and *D. marginatus*. For these measurements, we deployed an up-looking video camera on the seafloor under a group of ~15 *D. marginatus* inhabiting the

branching coral *Stylophora pistilla* and under a group of ~50 *P. squamipinnis* inhabiting a large knoll at 8-10 m depth in the coral reef off IUI. Current speed and direction were concurrently recorded using a S4 current meter (InterOcean, San Diego, USA) positioned at the height above bottom corresponding to the center of the fish group. The snout and the base of the tail of each of several, best seen fish were digitized in sequences of 30 frames each obtained during different days, covering flow speeds of 3-28 and 1.6-34 cm/s for *P. squamipinnis* (total N=3023 records) and *D. marginatus* (N =3025), respectively.

2.3 Concurrent tracking of garden eels and free fish

Our comparison of the foraging behavior between the eels and free fish benefitted from a single session (26 Dec. 2016) in which a branching coral (*Pocillopora* spp.) with 3 *D. marginatus* fish was recorded simultaneously with neighboring garden eels (Figure 2). This *in situ* record was used to compare the concurrent swimming speed, foraging volume, and nearest neighbor distances of the two taxa under identical conditions. Foraging volume, defined as the volume of the water across which the fish moved, and its swimming speed, both in 3D, were based on digitizing the precise location of the fish's snout every 50 frames (1.67 sec).

2.4 Statistical analysis

Statistical tests were performed using SYSTAT (V. 13) and Matlab (R2017b). Regression analyses were used to test the effects of prey density and current speed on feeding rates and the effect of current speed on several attributes of the fish's swimming angle in respect to the current direction. Since the latter relationships were nearly logarithmic, the regression analysis was performed on log-transformed data. Difference among the distributions of swimming speed under different conditions of current speeds in garden eels were examined using the Kolmogorov-Smirnov test. Differences in nearest-neighbor distances, foraging volumes and head movement speeds (swimming speeds) between *G. sillneri* and *D. marginatus* were tested using a two-sample t-test assuming unequal variances.

3 Results

3.1 Feeding rates

In *G. sillneri*, feeding rates monotonically increased with increasing prey densities. For moderate current speeds (8-14 cm/s), the slope of that functional response was 0.007 (R^2 = 0.77; Supplementary Information Table S2), reflecting an increase from feeding rates of 15-20 prey/min at low prey densities to feeding rates of 25 prey/min (Figure 3A). Feeding rates of *G. sillneri* monotonically increased with increasing current speeds up to 20 cm/s, maintaining approximately the same feeding rates under stronger currents. The increase in feeding rates with flow speed was observed under both low and moderate densities of prey (Figure 3, Supplementary Information Table S3).

3.2 Foraging movements

The mean orientation angle of the eels' upper body with respect to the current direction (where 0° direction is facing directly onto the current) ranged 6.2° to 67.8°. Both the magnitude of that angle (Figure 4A) and its variance (Figure 4B) significantly decreased with increasing current speed (R^2 = 0.53, P<0.00001 and R^2 = 0.65, P<0.00001, respectively), with the decrease in the variance being ~2 times sharper than that of the magnitude. The decrease in the mean absolute angle and the variance with increasing current speeds were significantly more gradual in the eels than in each of the free fish (UNIANOVA – *G. sillneri* vs. *D. marginatus* P<0.02, P<0.001, and *G. sillneri* vs. *P. squamipinnis* P<0.003, P<0.001 for the mean angle and the variance, respectively). The differences in the slopes of *D. marginatus* and *P. squamipinnis* were significant for the variance (P<0.002) but not for the mean (Figure 4, Supplementary Information Table S4). The difference in the variance, reflecting the animal's maneuverability, was most conspicuous under conditions of weak currents (3-10 cm/s; Figure 4B).

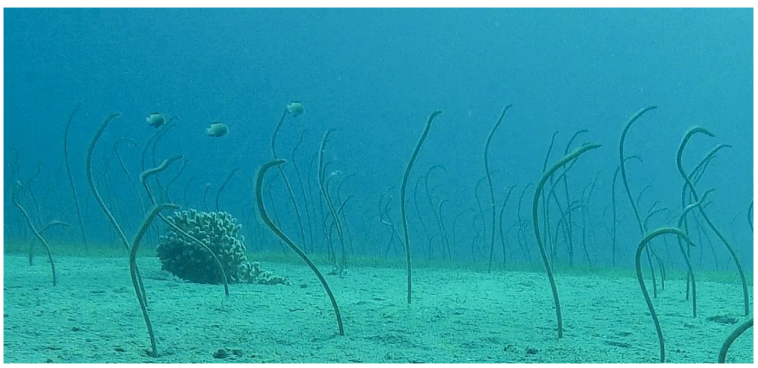

FIGURE 2
A photo taken from the simultaneous video recording of the eels together with 3 *D. marginatus* on 26 Dec. 2016 at a depth of 8 m.

10.3389/fmars.2024.1330379

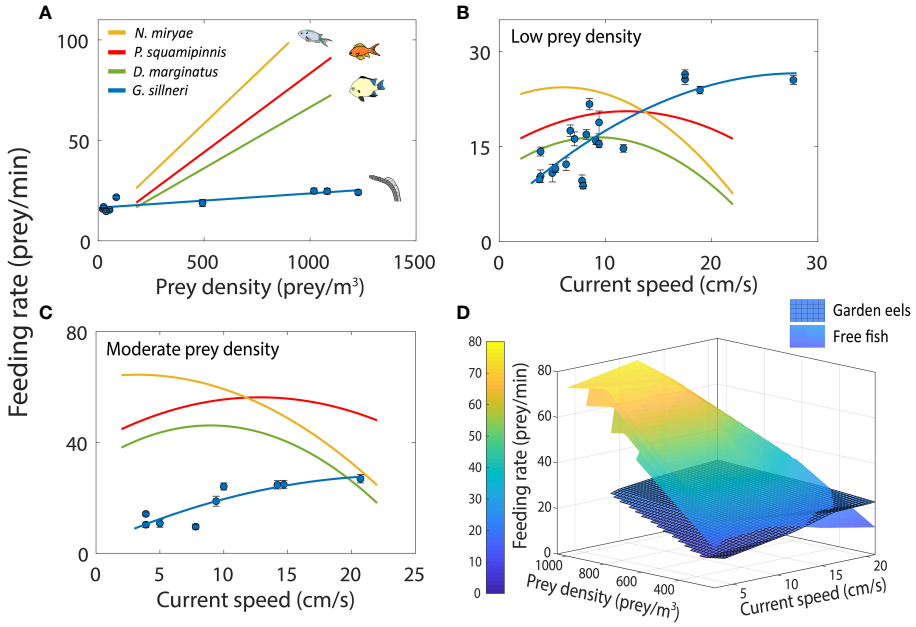

FIGURE 3
Feeding rates of garden eels (*G. sillneri*- blue) and free site-attached planktivorous fish (*P. squamipinnis*- red, *D. marginatus*- green, *and N. miryae*- yellow). **(A)** Feeding rates as a function of prey density for moderate current speed (12 cm/s for free fish and 8.2-14.7 cm/s for garden eels), **(B)** Feeding rates as a function of current speed at low prey density (210 prey/m^3 for free fish and 27.8-492.7 prey/m^3 for garden eels), **(C)** Feeding rates as a function of current speed at moderate prey density (630 prey/m^3 for free fish and 136.4-1227.0 prey/m^3 for garden eels), **(D)** Average feeding rates as a function of both current speed and prey density. For figures **(A–C)**, error bars indicate standard error among individuals. Data for the free fish were obtained from (Genin et al.)[1] (N=4 for *P. squamipinnis*, N=3 for *D. marginatus* and *N. miryae*, and 10<N<52 for *G. sillneri*).

The differences in the body orientation are shown in Supplementary Movie 1. During foraging under weak currents, both garden eels and free fish frequently changed their movement directions, although the frequency of those changes was markedly lower in *G. sillneri*. Under strong flows, *P. squamipinnis* were foraging with their head orientated directly onto flow most of the time. Under these conditions, a strike towards a plankter was often followed with a passive drift down current. For *G. sillneri*, such a down current drift was not observed since the strikes involved motions of the head only (not the entire body) in addition to the eels being "anchored" at the bottom.

The volume of the eels' foraging space monotonically decreased with increasing current speed. Although the best fit was exponential (Figure 5; R^2 = 0.35, N=75, P<0.0001), the large variance and wide range (3-90 L, CV = 0.51) rendered uncertain the mode of that change. The movement speed of the eels' heads also decreased with increasing current speed (Figure 6A, R^2 = 0.51; N=22; P<0.001), exhibiting a left-skewed distribution (slower head movements) under strong currents (Kolmogorov-Smirnov P<0.0001; Figure 6B).

When recorded together with the group of *D. marginatus*, the eels were significantly more separated one from another (Figure 7),

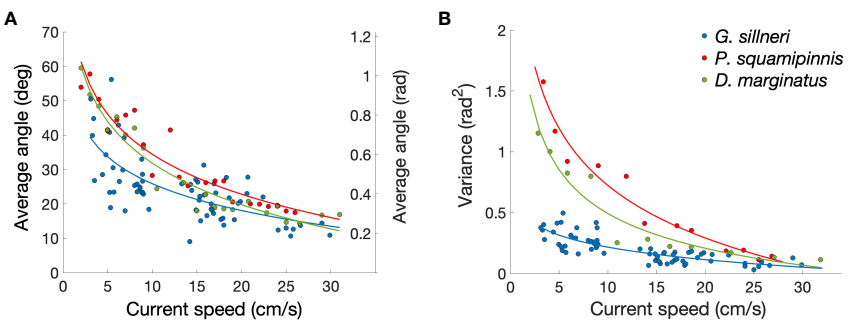

FIGURE 4
Angles between the fish's body and the current direction in garden eels (*G. sillneri*-blue, N=4230, mean of 63 measurements per data point) and two free zooplanktivorous fish – *P. squamipinnis* (red, N=3023, mean of 144 measurements per data point) and *D. marginatus* (green, N=3025, mean of 97 measurements per data point). For the free fish, the axis was defined as the snout-tail line, while for the eels the axis was defined for the upper part of the body, as snout-maximum curvature line. **(A)** The average angle between the body main axis and the current direction. **(B)** The corresponding variance between the swimming angles.

10.3389/fmars.2024.1330379

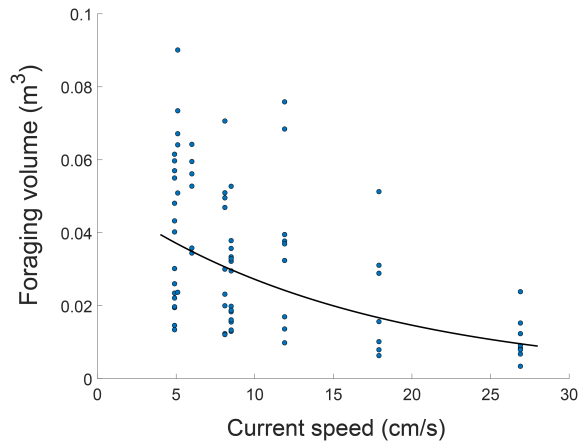

FIGURE 5
Foraging volume of garden eels as function of current speed. The best fit for the data (within confidence interval of 95%): $y=0.0506*e^{-0.062*x}$, R^2 = 0.345, P<0.000001.

with their nearest neighbor distance being on average x3 larger than the free fish (51.9 [± 13.0] and 17.1 [± 1.6] cm, respectively; two sample t-test P<0.0001; Figure 8A). The foraging volume of *D. marginatus* was 2.3 larger (0.032 [± 0.005] vs. 0.01 [± 0.004] m^3; two sample t-test P<0.01; Figure 8B). *D. marginatus* swam 23% faster than the eels (4.9 vs 4.0 cm/s, respectively; two sample t-test P<0.0001; Figure 8C).

4 Discussion

Both garden eels and the free fish are visual predators that capture drifting zooplankters while maintaining their position near a shelter: a burrow in the case of the garden eels and a branching coral or a complex rock in the case of the site-attached, free fish. The diets in both groups are similar, consisting mostly of copepods (Fricke, 1970; Smith, 1989; Donham et al., 2017).

While in the free fish, the effect of prey density on feeding rates was more pronounced than the effect of current speed, the opposite was found with the eels (Figure 3). Across the spectrum of prey densities and current speeds examined in our study and by (Genin et al.)[1], feeding rates by the eels were substantially lower except for the combination of the strongest currents and lowest prey densities (Figure 3D). Note that for the free fish this comparison is based on measurements made in a flume using *Artemia* nauplii as prey (Genin et al.)[1]. Nevertheless, comparable feeding rates (22-40 bites/min) were found for *Chromis dispilus*, living in temperate rocky reefs (Kingsford and MacDiarmid, 1988). Also, a similarity between feeding rates measured *in situ* and in the flume was reported by (Genin et al.)[1], who found that rates measured in the flume were similar to those based on *in situ* counts of bite rates in *P. squamipinnis*. Thus, the result of higher feeding rates of the free fish compared with the eels should hold.

The monotonic increase in feeding rates with increasing prey densities was found for both the free fish and the garden eels. However, the slope of this trend was 8-14 times steeper in the free fish (Figure 3A, Supplementary Information Table S2). For example, a doubling in prey density led to 1.84 – 1.89 times increase (92-94%) in the feeding rates of the free fish, compared with 1.21 times (60%) in the eels (Figure 3A, Supplementary Information Table S2). Similarly, a 3-fold increase in prey density led to nearly triplication of feeding rates in the free fish *Chromis viridis* (Kiflawi and Genin, 1997), compared with 1.4 times increase in the eels (Supplementary Information Table S2).

Why is the functional response to increasing prey density in the eels not as effective as that of the free fish? We suggest that the cause is the eels' relatively poor maneuverability. In quasi-stationary fishes, fast movements and effective maneuverability are needed to rapidly capture zooplankters that drift with the flow, especially under conditions of high prey fluxes. The three species of free fish

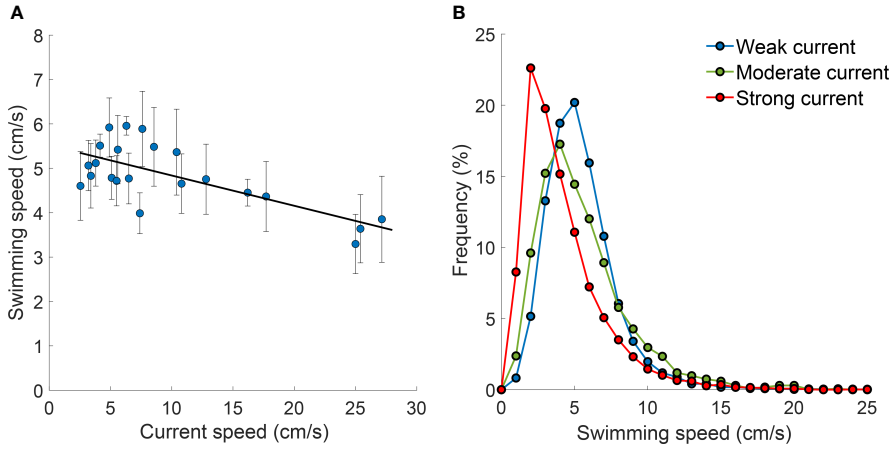

FIGURE 6
Swimming speed of garden eels as a function of current speed **(A)** Average swimming speed, defined as the speed of the eels' head movements, examined in the ~10 min intervals. Error bars indicate sd. The linear fit to the data (within confidence interval of 95%): $y=-0.0682*x+5.52$, R^2 = 0.51, N=22, P<0.001. **(B)** Frequency distribution of the eels' swimming speed under three levels of average current speeds: weak (3.7 cm/s; blue), moderate (13.1 cm/s; green), and strong (26.1 cm/s; red).

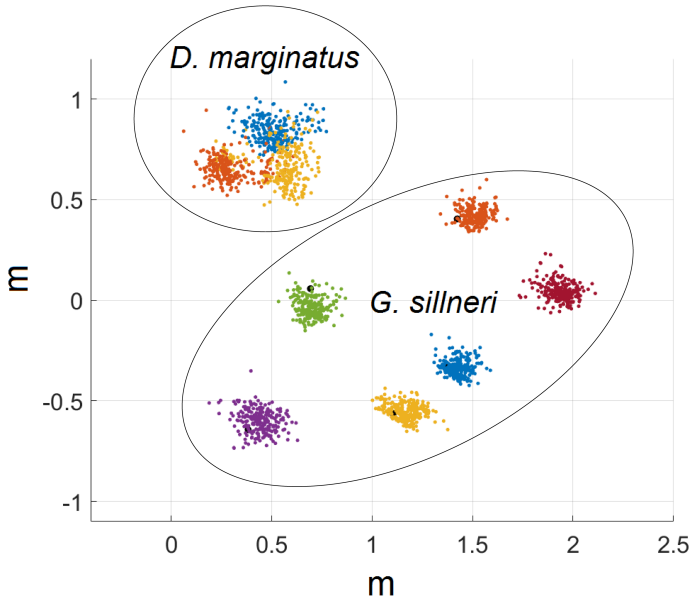

FIGURE 7
Foraging space of six garden eels (*G. sillneri*) and three free fish (*D. marginatus*) recorded simultaneously *in situ* under a current speed of 7.4 cm/s. Data points indicate the locations of the heads as viewed from above every 1.67 s during a time interval of 6.44 min. Each color indicates a different individual.

examined here, as well as *C. viridis* examined by Kiflawi and Genin (1997), are median paired fin swimmers, using mostly their pectoral fins for locomotion (Fulton and Bellwood, 2005; Fulton, 2007). This swimming mode is characterized by high maneuverability (Webb, 1994; Weihs, 2002). Garden eels are body-caudal fin swimmers, as most Anguilliformes are. Fish belonging to this group use body undulations (Blake, 2004; Lauder, 2015), generating a wave along their body to thrust themselves forward (Long et al., 1997). Moreover, unlike free eels, garden eels are incapable of using their posterior body part for movements because it is used as an anchor inside the burrow. Unfortunately, it was impossible to visualize the eels' dorsal and pectoral fins, which may have a role in their foraging motion. Free fish accelerate and maneuver mostly by using fin strokes, overcoming external drag and viscosity forces. Anchored garden eels, on the other hand, move their body mostly by contracting and expanding the muscles along the body, the rapidity of which is limited internally, by the pace of muscle contraction and relaxation. The need to bend the body to reach a prey appears to impede maneuverability. This limitation is best reflected in the substantially lower variance of body angles with respect to the current direction in the eels compared with the free fish, especially under weak current speeds (Figure 4B).

As currents became stronger, garden eels decreased their foraging volume (Figure 5), became more narrowly oriented

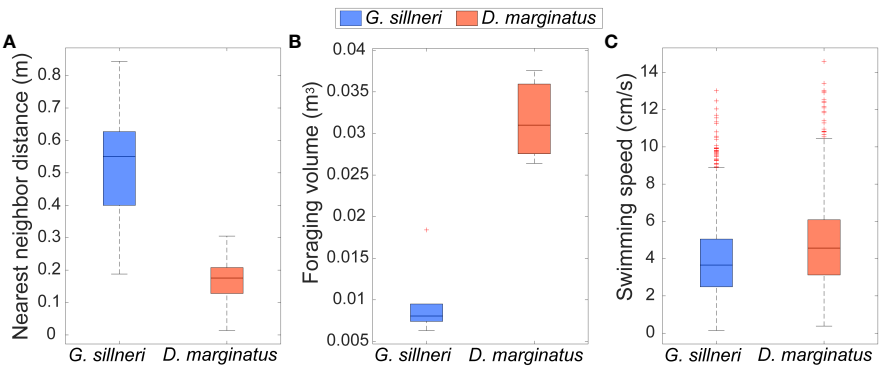

FIGURE 8
Box plot of the median (central mark), 25th and 75th percentiles (bottom and top edges), and range (whiskers) of the **(A)** nearest neighbor distance, **(B)** foraging volume, and **(C)** swimming speed of the six garden eels (blue bars) and three free fish (red) shown in Figure 7. Calculations were based on the locations of the heads recorded every 1.67 s during a time interval of 6.44 min. The difference between the garden eels and the free fish were significant for all the three parameters examined ($p<0.001$ for the nearest neighbor distance and swimming speed and $p<0.01$ for foraging volume; two sample t-test). Red dots indicate outliers.

around the flow direction (Figure 4A), reduced the variance of that orientation (Figure 4B), and slowed down the speed of their head movements (Figure 6). Despite these effects, the eels' functional response to increasing current speeds was surprisingly efficient, exhibiting a monotonous increase in feeding rates up to 20 cm/s (Figure 3). No such increase was observed in the free fish. On the contrary, above some threshold of relatively weak currents (6-12 cm/s), feeding rates by the free fish decreased with increasing current speed (Figure 3). In *C. viridis* (Kiflawi and Genin, 1997), a triplication of current speed (e.g., from 4 to 12 cm/s) did not increase feeding rates. In the eels such a triplication of current speed nearly doubled the feeding rate. The lack of increase in the feeding rates when prey flux increases due to faster currents in the free fish was explained in terms of biomechanical limitations on the fish's orientation to the current (Hamner et al., 1988; Kiflawi and Genin, 1997). That is, as the currents become stronger, the orientation of the fish with respect to the flow gradually narrows down (Figure 4A) because the fish gradually minimizes the projection of its body side to the flow, presumably to avoid being swept down with the flow. In contrast, the garden eels are less likely to be swept down current because they are anchored to the bottom and are capable of modulating their body posture to minimize drag forces (Khrizman et al., 2018; Supplementary Movie S1). Also, as the cross section of an eel's body is nearly circular, the drag force exerted on it by the flow does not vary much when the eel projects its side to the flow (Figure 4). Overall, the anchored and elongated garden eels appear to be better adapted to strong flows than the free fish. The effect of elongated morphology was also examined by Ishikawa et al. (2022) for another garden eel, *Heteroconger hassi*, which has a smaller body than *G. sillneri* (23 vs. 75 cm in length, respectively). *H. hassi* does not modulate its body posture to reduce the drag associated with stronger currents, which, in turn, led to non-increasing feeding rates under stronger flows (Ishikawa et al., 2022).

The opportunity to simultaneously record the eels and *D. marginatus* allowed us to directly compare their foraging movements under identical conditions. Figures 7, 8 showed that the free fish were significantly closer one to another, with their mean nearest-neighbor distance being 3 times smaller than that of *G. sillneri* and their mean foraging volume being 2.3 time larger. In addition, the head movements of the free fish were 23% faster. The relative crowdedness of the free fish was likely due to their association with a single coral that provided shelter for all members of the group. In the eels, on the other hand, each individual can select where to dig its burrow over a large sandy area, thereby balancing between living sufficiently separated one from another to reduce competition for food and yet sufficiently congregated to allow spawning, vigilance and other benefits of group living (Smith, 1989; Donham et al., 2017).

5 Conclusions

The anchored mode of feeding in garden eels, using burrows that they themselves dig, is unique among marine planktivorous fishes (e.g., Hobson and Chess, 1978; Sackley and Kaufman, 1996). This lifestyle enables the eels to occupy spacious, sandy bottoms that are, by and large, uninhabitable by side-attached planktivorous coral reef fishes. The ability of the eels to dig their burrows away from neighbors likely further lowers competition by reduction in intra-specific competition. The eels' elongated morphology- a fundamental requirement for being planktivorous and living in a burrow - appears to limit their foraging maneuverability, with slower head movements and smaller foraging volumes, relative to free fish. On the other hand, the eels are capable of modulating their posture to effectively reduce drag forces imposed by strong currents (Khrizman et al., 2018), allowing their effective functional response to increasing flow speed. Free fish cannot achieve the latter because strong flows impose high drag forces that severely limit side-projection to the flow (Kiflawi and Genin, 1997).

We suggest that the aforementioned demarcation between garden eels and free fish presents a dichotomy between two different strategies related to planktivory among site-attached fishes. While free fish, having superb maneuverability, exhibit an effective functional response to increases in prey density but poor response to increasing flow speed, the anchored eels exhibit the opposite– effective response to increasing flow speed and relatively poor response to increases in prey density.

Data availability statement

The original contributions presented in the study are included in the article/Supplementary Material. Further inquiries can be directed to the corresponding author.

Ethics statement

The animal study was approved by Israel Nature and Parks Authority. The study was conducted in accordance with the local legislation and institutional requirements.

Author contributions

AK: Conceptualization, Data curation, Formal analysis, Investigation, Methodology, Software, Visualization, Writing – original draft, Writing – review & editing. IK: Data curation, Investigation, Writing – review & editing. DC: Data curation, Investigation, Writing – review & editing. AG: Conceptualization, Data curation, Formal analysis, Funding acquisition, Investigation, Methodology, Project administration, Resources, Supervision, Validation, Writing – review & editing.

Funding

The author(s) declare financial support was received for the research, authorship, and/or publication of this article. This research was funded by the Israel Science Foundation (grant 1211-14 to AG).

Acknowledgments

We thank Charlotte Wynn, Shir Bar, Yoav Lindeman and Anael Engel for their great help with the challenging work in the field and laboratory. We are grateful to the IUI staff for the assistance with logistics.

Conflict of interest

The authors declare that the research was conducted in the absence of any commercial or financial relationships that could be construed as a potential conflict of interest.

Publisher's note

All claims expressed in this article are solely those of the authors and do not necessarily represent those of their affiliated organizations, or those of the publisher, the editors and the reviewers. Any product that may be evaluated in this article, or claim that may be made by its manufacturer, is not guaranteed or endorsed by the publisher.

Supplementary material

The Supplementary Material for this article can be found online at: https://www.frontiersin.org/articles/10.3389/fmars.2024.1330379/full#supplementary-material

References

Blake, R. W. (2004). Fish functional design and swimming performance. *J. Fish Biol.* 65 (5), 1193–1222. doi: 10.1111/j.0022-1112.2004.00568.x

Brokovich, E. (2001). The community structure and biodiversity of reef fishes at the Northern Gulf of Aqaba (Red Sea) with relation to their habitat (Israel: Tel Aviv University). M.Sc. thesis (in Hebrew).

Clark, E. (1980). Distribution, mobility, and behavior of the Red Sea garden eel. *Natl. Geographic Res. Rep.* 12, 91–102.

De Schepper, N., De Kegel, B., and Adriaens, D. (2007). Morphological specializations in Heterocongrinae (Anguilliformes: Congridae) related to burrowing and feeding. *J. Morph.* 268 (4), 343–356. doi: 10.1002/jmor.10525

Donham, E., Foster, M. S., Rice, M. R., Cailliet, G. M., Yoklavich, M. M., and Hamilton, S. L. (2017). Natural history observations of Hawaiian Garden Eels, Gorgasia hawaiiensis (Congridae: heterocongrinae), from the island of Hawai'i. *Pacific Sci.* 71 (2), 135–147. doi: 10.2984/71.2.3

Erez, J. (1990). On the importance of food sources in coral-reef ecosystems. *Ecosyst. World* 25, 411–418.

Fricke, H. W. (1969). Biologie et compartementde Gorgasia sillneri (Klausewitz) et Taenioconger hassi (Klausewitz, Eibesfeldt). (Teleosteen). *Comptes Rendus Hebdomadaires Des. Seances Del'Academie Des. Sci.* 269 (17), 1678–1680.

Fricke, H. W. (1970). Ökologische und verhaltensbiologische Beobachtungen an den Röhrenaalen Gorgasia sillneri und Taenioconger hassi (Pisces, Apodes, Heterocongridae). *Z. für Tierpsychologie* 27, 1076–1099. doi: 10.1111/j.1439-0310.1970.tb01918.x

Fulton, C. J. (2007). Swimming speed performance in coral reef fishes: field validations reveal distinct functional groups. *Coral Reefs* 26 (2), 217–228. doi: 10.1007/s00338-007-0195-0

Fulton, C. J., and Bellwood, D. R. (2005). Wave-induced water motion and the functional implications for coral reef fish assemblages. *Limnol. Oceanogr.* 50 (1), 255–264. doi: 10.4319/lo.2005.50.1.0255

Genin, A., Monismith, S. G., Reidenbach, M. A., Yahel, G., and Koseff, J. R. (2009). Intense benthic grazing of phytoplankton in a coral reef. *Limnol. Oceanogr.* 54 (3), 938–951. doi: 10.4319/lo.2009.54.3.0938

Genin, A., and Paldor, N. (1998). Changes in the circulation and current spectrum near the tip of the narrow, seasonally mixed Gulf of Elat. *Israel J. Earth Sci.* 47, 87–92.

Hamner, W. M., Jones, M. S., Carleton, J. H., Hauri, I. R., and Williams, D. M. (1988). Zooplankton, planktivorous fish and water movement on windward reef-face: Great Barrier Reef, Australia. *Bull. Mar. Sci.* 42, 459–479.

Hedrick, T. L. (2008). Software techniques for two-and three-dimensional kinematic measurements of biological and biomimetic systems. *Bioinsp. Biomim.* 3 (3), 034001. doi: 10.1088/1748-3182/3/3/034001

Hobson, E. S. (1991). "Trophic relationships of fishes specialized to feed on zooplankters above coral reefs," in *The ecology of fishes on coral reefs* (San Diego: Academic Press), 69–95.

Hobson, E. S., and Chess, J. R. (1978). Trophic relationships among fishes and plankton in the lagoon at Enewetak Atoll, Marshall Islands. *Fish. Bull.* 76 (1), 133–153.

Ishikawa, K., Wu, H., Mitarai, S., and Genin, A. (2022). Effects of prey density and flow speed on plankton feeding by garden eels: a flume study. *J. Exp. Biol.* 225 (8), jeb243655. doi: 10.1242/jeb.243655

Khrizman, A., Ribak, G., Churilov, D., Kolesnikov, I., and Genin, A. (2018). Life in the flow: unique adaptations for feeding on drifting zooplankton in garden eels. *J. Exp. Biol.* 221 (16). doi: 10.1242/jeb.179523

Kiflawi, M., and Genin, A. (1997). Prey flux manipulation and the feeding rates of reef-dwelling planktivorous fish. *Ecology* 78 (4), 1062–1077. doi: 10.1890/0012-9658(1997)078[1062:PFMATF]2.0.CO;2

Kingsford, M. J., and MacDiarmid, A. B. (1988). Interrelations between planktivorous reef fish and zooplankton in temperate waters. *Mar. Ecol. Prog. Ser. Oldendorf* 48 (2), 103–117. doi: 10.3354/meps048103

Klausewitz, W. (1962). *Gorgasi sillneri*, ein neuer Rohrenaal aus dem Roten Meer. *Senckenbergiana Biologica* 43 (6), 433–435.

Lauder, G. V. (2015). Fish locomotion: recent advances and new directions. *Annu. Rev. Mar. Sci.* 7, 521–545. doi: 10.1146/annurev-marine-010814-015614

Long, J. H. Jr, Shepherd, W., and Root, R. G. (1997). "Maneuverability and reversible propulsion: How eel-like fish swim forward and backward using travelling body waves," in *Proc. Special Session on Bio-Engineering Research Related to Autonomous Underwater Vehicles, 10th Int. Symp. Unmanned Untethered Submersible Technology.* Arlington, VA: Office of Naval Research. 118–134.

Monismith, S. G., and Genin, A. (2004). Tides and sea level in the Gulf of Aqaba (Eilat). *J. Geophys. Res.* 109, C04015. doi: 10.1029/2003JC002069

Morais, R. A., and Bellwood, D. R. (2019). Pelagic subsidies underpin fish productivity on a degraded coral reef. *Curr. Biol.* 29 (9), 1521–1527. doi: 10.1016/j.cub.2019.03.044

Noda, M., Kawabata, K., Gushima, K., and Kakuda, S. (1992). Importance of zooplankton patches in foraging ecology of the planktivorous reef fish Chromis chrysurus (Pomacentridae) at Kuchinoerabu Island, Japan. *Mar. Ecol. Prog. Ser.* 87, 251–263. doi: 10.3354/meps087251

Popper, D., and Fishelson, L. (1973). Ecology and behavior of Anthias squamipinnis (Peters 1855) (Anthiidae, Teleostei) in the coral habitat of Eilat (Red Sea). *J. Exp. Zool.* 184 (3), 409–424. doi: 10.1002/jez.1401840314

Reiss, Z., and Hottinger, L. (1984). "The Gulf of Aqaba," in *Ecological Micropaleontology* (Berlin, Heidelberg: Springer-Verlag).

Sackley, P. G., and Kaufman, L. S. (1996). Effect of predation on foraging height in a planktivorous coral reef fish, *Chromis nitida*. *Copeia* 1996 (3), 726–729. doi: 10.2307/1447539

Smith, D. G. (1989). "Family congridae," in *Fishes of the western North Atlantic. Part 9*, vol. 1 . Ed. E. B. Böhlke (New Haven, CT: Sears Foundation for Marine Research), 460–567.

Webb, P. W. (1984). Body form, locomotion and foraging in aquatic vertebrates. *Am. Zool.* 24 (1), 107–120. doi: 10.1093/icb/24.1.107

Webb, P. W. (1994). "The biology of fish swimming," in *Mechanics Physiology of Animal Swimming*. Eds. L. Maddock, Q. Bone and J. V. Rayner (Cambridge: Cambridge University Press), 45–62.

Webb, P. W. (2011). "Buoyancy, locomotion, and movement in fishes: maneuverability," in *Encyclopedia of fish physiology: from genome to environment*. Ed. A. P. Farrell (London, UK: Academic Press), 575–580.

Weihs, D. (2002). Stability versus maneuverability in aquatic locomotion. *Integr. Comp. Biol.* 42 (1), 127–134. doi: 10.1093/icb/42.1.127

Yahel, R., Yahel, G., and Genin, A. (2002). Daily cycles of suspended sand at coral reefs: a biological control. *Limnol. Oceanogr.* 47 (4), 1071–1083. doi: 10.4319/lo.2002.47.4.1071

frontiers | Frontiers in Marine Science

TYPE Original Research
PUBLISHED 08 March 2024
DOI 10.3389/fmars.2024.1337358

OPEN ACCESS

EDITED BY
Stuart Humphries,
University of Lincoln, United Kingdom

REVIEWED BY
Sriyutha Murthy,
Bhabha Atomic Research Centre, India
Vincent Hickl,
Swiss Federal Laboratories for Materials Science and Technology, Switzerland

*CORRESPONDENCE
Katherine Beaudry
katherine.beaudry@umontreal.ca
Christopher B. Cameron
c.cameron@umontreal.ca

RECEIVED 12 November 2023
ACCEPTED 23 February 2024
PUBLISHED 08 March 2024

CITATION
Beaudry K and Cameron CB (2024) Oil Droplet Capture and Ingestion by Filter-Feeding Sabellid and Serpulid Polychaetes. *Front. Mar. Sci.* 11:1337358. doi: 10.3389/fmars.2024.1337358

Oil Droplet Capture and Ingestion by Filter-Feeding Sabellid and Serpulid Polychaetes

Katherine Beaudry* and Christopher B. Cameron*

Department of Biological Sciences, University of Montreal, Montreal, QC, Canada

Benthic filter-feeders form an essential role in marine food chains as they constitute the bridge between the microscopic primary producers and the consumers. Although filter-feeders mainly feed on solid particles, they also capture and ingest oil droplets. Usually, these microdroplets come from the decomposition of animals or algae or from petroleum oils that enter water via spills and leakages. Here, we used videography, TRITC fluorescence microscopy, and fluid mechanics to study the capture mechanisms of canola, fish, and four petroleum motor oil droplets by the filter feeding sabellid and a serpulid polychaetes. *Schizobranchia insignis*, *Eudistylia vancouveri, Myxicola infundibulum* and *Serpula columbiana* actively feed on waste motor oil droplets in seawater. A further experiment found that *S. insignis* fed on all types of oil droplets, demonstrating no selectivity based on type. The oil droplet capture mechanism of *S. insignis* were direct interception and sieving, like that of solid particles. The size range of droplets ingested was 10 to 300 µm in diameter, but these ranges differed depending on the density and viscosity of the oils. Higher density and viscous oils were captured at smaller droplet sizes. These results are the first to characterize the mechanics of oil droplet capture, transport and ingestion by benthic ciliary filter feeders, and contribute to understanding the behavior of animals in response to oil emulsions, and how oils enter marine food webs.

KEYWORDS

benthic ecology, petroleum pollution, emulsion, density, viscosity, carbon cycle, marine food web

1 Introduction

Invertebrates have evolved a remarkable array of strategies for survival, and one such adaptation is particle capture. This process involves the acquisition of food particles suspended in the surrounding environment, typically in aquatic habitats. Various invertebrates employ specialized structures and behaviors to achieve this feat including bivalves that use gills, crustaceans that employ specialized appendages with setae, and sponges that use specialized choanocyte cells and a unique water flow system. These

adaptations showcase the incredible diversity and ingenuity of invertebrates in their quest for sustenance, underscoring the vital role they play in ecological systems.

Key to understanding the mechanics of particle capture is the theoretical treatment of particle interactions developed by Rubenstein and Koehl (1977). These interactions between a particle in water and a filter include i) direct interception, ii) inertial interactions, iii) gravitational deposition, iv) diffusional deposition, and v) sieving. Extending this theory to oil droplet in water and filter fiber interactions, Mehrabian et al. (2018) introduce the role of different parameters including oil-to-water viscosity ratio, oil-water interfacial tension, oil-water density difference, and the wettability of the fiber on the success of oil droplet capture and detachment. Wettability is the affinity of one fluid (oil) to adhere to and spread on a solid surface in the presence of another immiscible fluid (water). It is governed by the texture and surface chemistry of the solid surface (Mehrabian et al., 2018; Letendre and Cameron, 2022). Experimental tests of this theory include investigating oil droplet capture by *Daphnia* and barnacles at different Reynolds numbers (Letendre and Cameron, 2022), the role of droplet size and viscosity on capture using copepods and barnacles (Letendre et al., 2020), and the role of surfactants in droplet capture and loss by *Daphnia* and copepods (Almeda et al., 2014; Letendre et al., 2023). The rate of oil droplets captured increases with increased droplet concentration by the pelagic doliolid *Dolioletta gehenbauri* (Lee et al., 2012). Doliolids capture particles with ciliated gills, but the capture mechanism of the oil droplets was not documented. Here we investigate oil droplet capture by benthic polychaetes that capture particles using ciliated radioles.

Polychaete worms are one of the most common groups of macro-invertebrates found in benthic environments. They come in many forms and have adapted to fill different niches such as predator, scavenger, surface deposit-feeder and filter-feeders (Fauchald and Jumars, 1979). Some of the most common of these are serpulids and sabellids that use a crown of radioles that capture and transport particles to the mouth (Riisgård and Larsen, 2000). Each radiole is lined by a pair of pinnules. On a pinnule, there are cilia, which are used to retain food particles in the water and carry them towards the frontal side of the radiole were a similarly ciliated groove guides the particles to the mouth (Fauchald and Jumars, 1979; Riisgård and Larsen, 2000). The cilia also create a water current to bring food towards the worm, the current flowing upwards through the crown and in between the pinnules. The animals can separate particles by their size: those that are too large are rejected, the medium-sized particles are used for tube building, and the smaller ones are eaten (Shimeta, 1996; Nash and Keegan, 2003). Filter-feeding polychaetes eat diatoms, dinoflagellates, and other unicellular algae, as well as small invertebrates including larvae (Fauchald and Jumars, 1979). It is unknown if polychaetes capture and ingest oil droplets that arise from the decomposition of animals or algae, or from petroleum oils enter the water from spills and leakages.

Here we determined whether three sabellids and a serpulid polychaetes (*Schizobranchia insignis, Eudistylia vancouveri, Myxicola infundibulum* and *Serpula columbiana*) capture and ingest droplets of waste motor oil. We then investigate oil droplet taste selection by *Schizobranchia insignis* on canola oil, fish oil and four types of motor oil. We then used *S. insignis* to quantify droplet size selectivity, depending on the density and viscosity of the oils. At low Re, density and viscosity are important variable for oil droplet capture by fibers. According to theory, neutrally buoyant and small droplets will be preferentially captured (Mehrabian et al., 2018). If the oil is less dense than water, then gravitational forces will move the oil to the top (creaming), and when the oil is heavier than water, the oil will move downwards (sedimentation). The smaller the emulsion size, the slower it will move, increasing the chance of capture. Similarly, neutrally buoyant droplets will have more opportunity to be captured by filter feeders because they have a longer duration in the environment. The effect of oil-to-water viscosity ratio (which we will henceforth refer to as 'viscosity') is important only in inertial interaction and gravitational deposition. Oil viscosity is generally greater than water viscosity. Therefore, all parameters being equal, a less viscous oil droplet has higher chance of being captured by a filter feeder compared to a higher viscous oil droplet through inertial interaction and gravitation deposition (Mehrabian et al., 2018). This study is significant to understand the physics of oil droplet capture, the behavior of animals in response to oil emulsions, the bioaccumulation and trophic transfer of oils and because it informs oil spill remediation strategies.

2 Materials and methods

2.1 Preparation of emulsions

To study and compare the ingestion of different types of oils, three types of oil emulsions were prepared. The first one, for larger animals, was mixed using either light crude, canola, fish, waste motor oil or motor oil (Table 1), and artificial saltwater or filtered seawater (1µm filtration). The salt water was made with dechlorinated tap water and Instant Ocean Sea salt at a specific gravity of 1.020 to 1.022 to simulate seawater. Seventy-five µL of oil was pipetted into 1 L of water. The second emulsion for smaller animals was prepared the same way, except that 32.5 µL of oil was mixed with 500 ml of water. The third one was exactly like the first

TABLE 1 Information on the types of oil used.

Type of oil	Density ρ (kg/m^3)	Viscosity µ (mPa·s)
Canola oil	950	121
Fish oil	902	40
Waste synthetic motor oil 5W-20	813	107
4-stroke marine engine oil 10W-30	838	156
Semi-synthetic 2-cycle engine oil	831	92
Light petroleum oil (API = 34)	855	98

one but using unfiltered sea water. All solutions were then mixed for 20 min using a magnetic stirrer at 900 RPM.

The density of each oil was calculated by using weight of 10 ml with a Mettler Toledo balance. The viscosity was determined using an Anton Paar Physica MCR 501. Both the density and viscosity were measured at room temperature (23°C).

2.2 Collection and animal care

Four species of polychaete worms from the eastern Pacific Ocean were used for this experiment: *Schizobranchia insignis*, *Eudistylia vancouveri, Myxicola infundibulum* and *Serpula columbiana* (Table 2). These species were chosen because they are common to marinas on the west coast of Canada, where individuals are habituated to boats, waves, and people, they can easily be removed from their tubes, they are commercially available through West Wind SeaLabs, and do well in aquariums. The dock and pilings or intertidal habitat of these species moreover likely exposes them to spilled motor oil droplets.

A survey of oil droplet capture by polychaetes was performed at the Bamfield Marine Sciences Centre, British Columbia, Canada. The animals were collected on the docks, or on the sea floor while diving. They fed on the algae and other particles in the sea water and were supplemented once a week with a plankton and algae blend. In Montreal, Schizobranchia insignis was bought and shipped from WestWind Sealabs, Vancouver Island, B.C., Canada, and kept in a saltwater aquarium. They were fed with the algae growing in the tank and supplemented with spirulina powder.

2.3 Feeding experiments

The four species of polychaete worms (*Schizobranchia insignis*, *Eudistylia vancouveri, Myxicola infundibulum* and *Serpula columbiana*) were exposed to oil-in-water emulsions to determine feeding on waste motor oil droplets. They were starved for 24 hours beforehand in artificial saltwater or filtered seawater to ensure a clear digestive tract and to facilitate oil observations, then put in an oil-in-water emulsion for 24 hours. Oil feeding was determined by observation of oil droplets in the fecal pellets using a light microscope mounted with a Samsung S21 camera.

TABLE 2 Information on the investigated polychaete species.

Species	Family	Sampling site	Habitat
Schizobranchia insignis	Sabellidae	Bamfield Inlet, Barkley Sound and Victoria Harbor, northeast Pacific, Canada.	floating docks, hard bottom
Eudistylia vancouveri	Sabellidae	Bamfield Inlet, Barkley Sound, northeast Pacific, Canada.	floating docks
Serpula columbiana	Serpulidae	Bamfield Inlet, Barkley Sound, northeast Pacific, Canada.	hard bottom
Myxicola infundibulum	Sabellidae	Bamfield Inlet, Barkley Sound, northeast Pacific, Canada.	sediment

Schizobranchia insignis was also used as a model species and tested with all types of oil. The individuals were starved in filtered seawater for 24 hours, then put in an oil-in-water emulsion for 24 hours. After the feeding period, the individuals were dissected and samples from the cilia, gut and fecal pellets were mounted on slides and photographed under fluorescence microscopy using a TRITC filter mounted on an Olympus BX51 equipped with a Teledyne Luminera Infinity 3 camera or a light microscope with a Samsung S21 camera.

Schizobranchia insignis was also tested with unfiltered seawater emulsion. Oil feeding was determined by observation of the fecal pellets using a light microscope.

2.4 Capture experiments

To understand the mechanics of particle capture, a single radiole was removed from the worm and placed in a small petri dish with the oil-in-water emulsion. The only flow was that generated by the cilia. The capture of oil was recorded with a Samsung S21 camera mounted on an SX16 Olympus microscope (Figure 1). Despite separation from the body, the radiole continued to filter food from the water, which facilitated observations. Pictures were taken of the oil droplets that were captured and transported along the radiole, including proximally where they normally would have been transported to the mouth. Different types of oils were used to determine changes in minimum, maximum and average droplet size range depending on the oil density (canola and waste engine oil) and viscosity (marine and semi-synthetic engine oil). To ensure that no difference in the results came from the size of the animals, the same individual was used with both emulsions. The oil droplet sizes captured by *S. insignis* were measured from light and fluorescence microscopy photographs of the oil droplets accumulated on the radioles. We used the program ImageJ and its 'Analyze particles' feature to calculate the area of round shapes on images using a set scale, when possible, and calculated the remainder by hand. The same technique was used to measure the droplets sizes in the emulsions. The minimum, maximum, and average size were determined. Using Rstudio, the normality of all distributions was confirmed or denied with a Shapiro-Wilk test, then the distributions were compared to determine if they were significantly different with multiple Mann–Whitney U tests.

3 Results

3.1 Feeding experiments

In the first experiment, the four species (*Schizobranchia insignis, Eudistylia vancouveri, Myxicola infundibulum* and *Serpula columbiana*) were exposed for 24 hours to an oil-in-water emulsion made with waste motor oil. All individuals fed on the oil droplets, as was seen from the presence of multiple oil drops in their fecal matter after the experiment (Figure 2). As a control, pictures of the normal fecal pellets of each species were taken. This highlights the translucent nature and round shape of the droplets in the pellets.

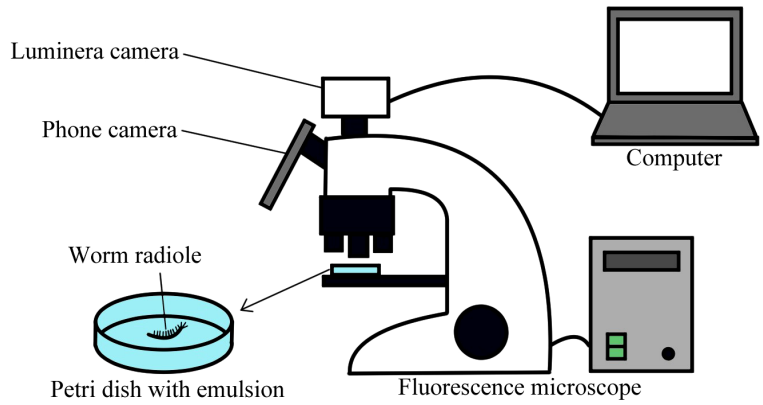

FIGURE 1
Experimental set up for the capture experiment.

This experiment was repeated with multiple individuals to verify the replicability of the results.

The next experiment was performed using light crude oil, to determine the feeding capture mechanism. Crude oil was used because it is autofluorescent under a TRITC filter. After feeding, a dissection of an individual *S. insignis* was done. Oil droplets were present on the pinnules, in the gut, and in the fecal matter (Figure 3). Additional worms were put in filtered seawater and fed canola, fish, and motor oils (Figure 4). In all cases, oil droplets were present in the fecal matter of the worm. The semi-synthetic engine oil and marine engine oil droplets did not appreciably coalesce (Figures 4D, E). The fish oil was cleared from the seawater, and the feces were translucent, but with fewer distinct droplets, suggesting that it coalesced and was absorbed by the gut (Figure 4C). Canola oil was like fish oil in that few droplets were observed in translucent feces (Figures 4A, B). Then, individuals of *S. insignis* were put in unfiltered seawater with waste engine oil droplets. *S. insignis* was seen ingesting the oil droplets, and a high concentration of droplets was found in the feces (Figure 4F).

These experiments were done at a Reynolds number of 0.000154, where the fluid velocity was 0.001 m/s, the characteristic cilia diameter was 0.2 µm, the seawater density was 1024 kg/m^3, and the dynamic viscosity was 1.33 mPa•s. At Re of <1 flow is laminar.

3.2 Capture experiments

The mechanics of oil droplet capture was like that of particle capture (Figure 5; Supplementary Movie 1). The oil droplets in water (Figure 5A) were captured by the cilia and mucus on the pinnule (Figure 5B), transported down the pinnule to the radiole (Figure 5C), and then to the base of the radiole (Figure 5D). Supplementary Movie 2 also shows the transport of multiple droplets along the apical groove of a radiole.

The next two experiments were done to understand the roles of density and viscosity on particle capture. Regarding density, the canola oil and waste motor oil were used as they have different densities and similar viscosities (Table 1). To ensure that the variation between the droplet sizes came from the oil density and not the size of the worm and its radioles, the same worm was used for the canola and the waste motor oil experiments. The waste motor oil emulsion droplet diameter varied from 2.77 to 281.35 µm (mean 40.12 µm) (Figure 6), whereas those captured varied from 27.67 to 225.25 µm (mean 95.88 µm). The mean emulsion droplet diameter for canola oil varied from 11.40 to 315.80 µm (mean 42.62 µm) (Figure 6), whereas those captured varied from 21.15 to 183.17 µm (mean 73.01 µm). To determine the normality of these distributions, Shapiro-Wilk tests were conducted, and all proved to be statistically significant at ($P < 0.05$), rejecting the null-hypothesis of normality. Thus, two Mann–Whitney U tests were performed to determine if the difference between the pre- and post-experimental canola oil and the pre- and post-experimental waste oil size distributions were statistically significant, and a p-value of $P < 2.2e\text{-}16$ was obtained for both in R. This shows that the droplet size distributions of the emulsion and the captured droplets are significantly different, be it canola oil or waste oil. Additionally, the capture size distribution between the canola and waste oil were compared with another Mann–Whitney U test, for which the p-value was of $P = 2.84e\text{-}06$. The sizes of the droplets captured were significatively different when the worm was exposed to two types of oils with different densities but similar viscosities, with the waste oil droplets captured being larger on average, with a higher minimum and maximum size droplets, despite the emulsion canola oil droplet having a larger maximum.

Finally, regarding viscosity, the same method was used as the density experiment, but the experimental oils were the marine engine oil and the semi-synthetic engine oil, because of similar densities and different viscosities (Table 1). The average marine engine oil emulsion droplet diameter varied from 25.50 to 365.36 µm (mean 95.27 µm), whereas those captured varied from 14.29 to 232.88 µm (mean 60.20 µm) (Figure 7). The semi-synthetic engine oil emulsion droplet diameter varied from 16.13 to 385.80 µm (mean 84.60 µm) (Figure 7), and the captured droplets varied from 14.43 to 310.15 µm (mean 93.63 µm). Since all distributions proved to be statistically significant at $P < 0.05$, rejecting the null-hypothesis of normality, two Mann–Whitney U tests were

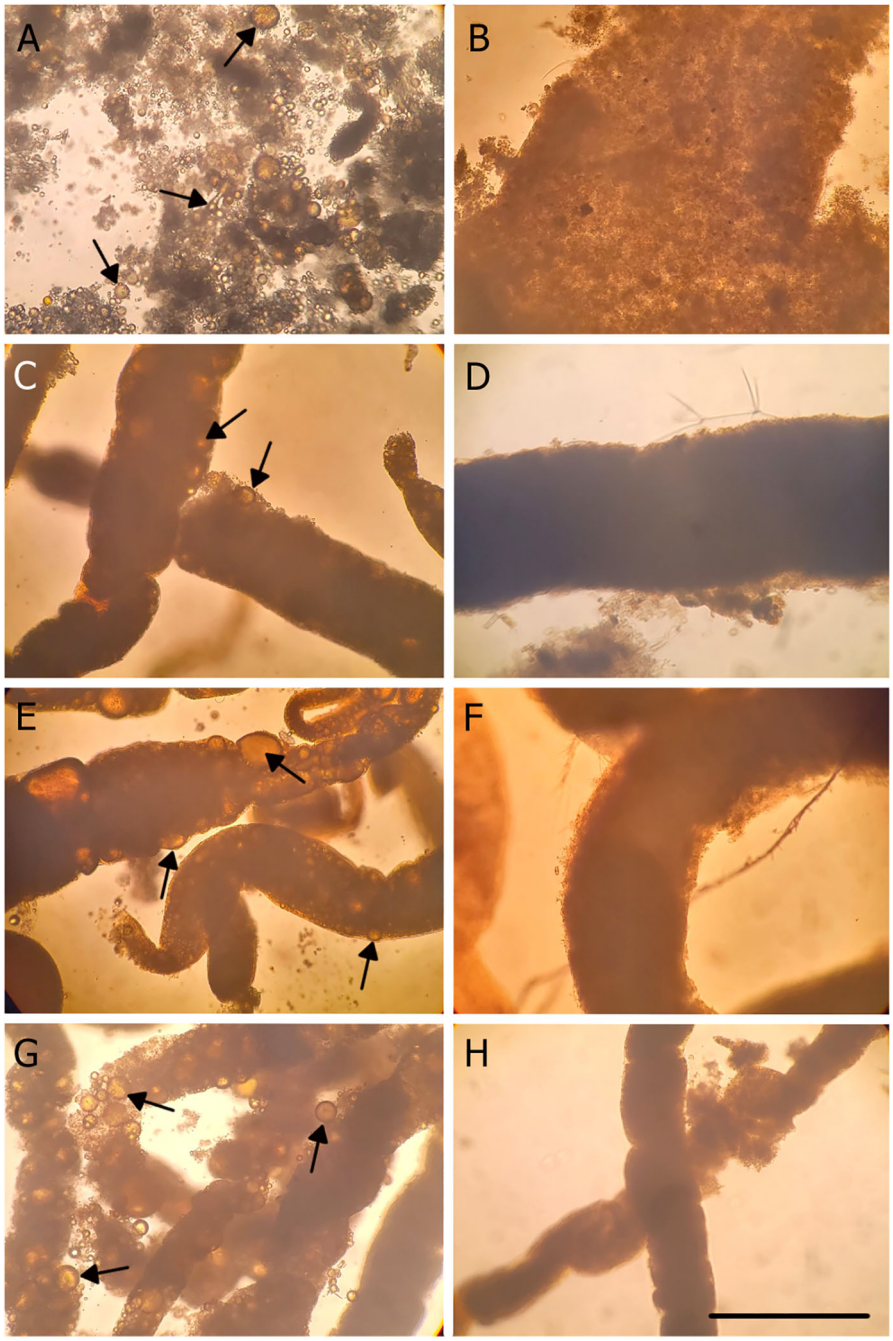

FIGURE 2
Fecal matter of multiple species of filter-feeding polychaete worms following feeding on a waste oil in seawater emulsion. Left column: fecal matter contaminated with oil; right column: control (without oil) fecal matter of the same species. **(A, B)** *Eudistylia vancouveri*. **(C, D)** *Serpula columbiana*. **(E, F)** *Schizobranchia insignis*. **(G, H)** *Myxicola infundibulum*. Arrows point to a sample of oil droplets. Scale bar: 500 µm.

performed to determine if the difference between the two marine oil and the two semi-synthetic oil distributions were statistically significant. Whereas the marine oil distributions were significantly different with a p-value of < 2.2e-16, the semi-synthetic oil distributions were not (p-value = 0.1768). Additionally, the capture size distribution between the marine and semi-synthetic oils were compared with another Mann–Whitney U test, for which the p-value was of P = 4.768e-10, and so the distributions were significantly different. Although the size distributions for the marine and semi-synthetic oil emulsions were similar, it seems that the droplets captured by the worm were, on average, smaller with the more viscous marine engine oil.

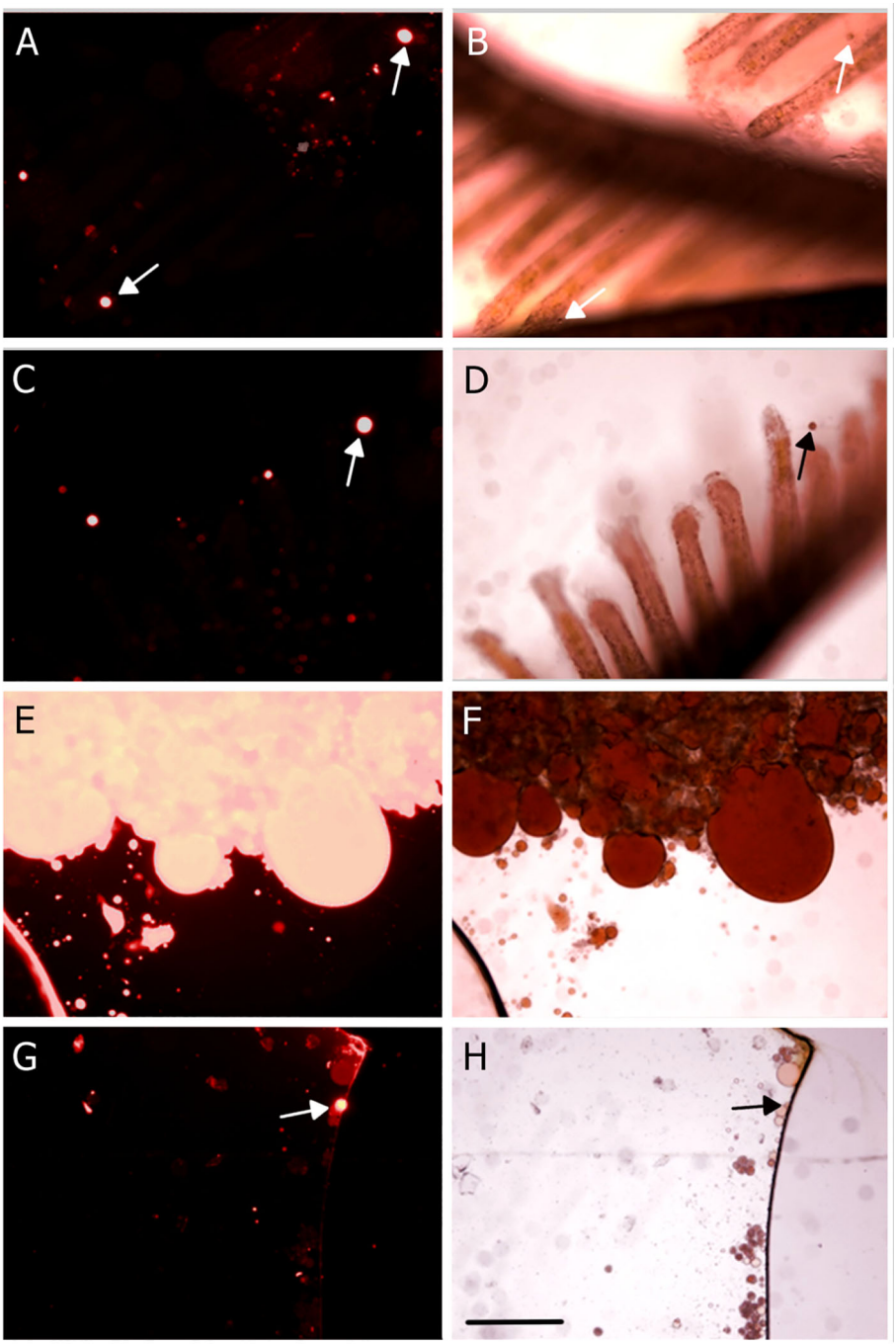

FIGURE 3
Captured and ingested crude oil droplets by *Schizobranchia insignis* following feeding on a waste oil in seawater emulsion and photographed under a TRITC filter (left column) and light (right column). **(A, B)** Radiole with a paired row of pinnules after feeding. **(C, D)** A different radiole of the same individual. **(E, F)** Fecal matter. **(G, H)** Gut contents. Arrows point to a sample of oil droplets. Scale bar: 200 µm.

4 Discussion

Particle capture by polychaetes and other ciliated organisms is a crucial mechanism that plays a significant role in aquatic and marine systems ecology and pollution (Shimeta and Jumars, 1991; Ostroumov, 2005; Dean, 2008; Jang et al., 2018; Knutsen et al., 2020). These organisms have developed specialized mechanisms to capture and feed on suspended particles, such as phytoplankton, detritus, and small organic matter, helping to regulate nutrient cycling and energy transfer within aquatic food webs (Wallace et al, 1977; Humphrey et al., 1987; Gin et al., 2001). Concurrent with organic particles in aquatic systems are oil droplets, but the extent to which they are captured, and the mechanisms of the capture are unknown. Here we found that the sabellid polychaetes *Schizobranchia insignis, Eudistylia vancouveri, Myxicola infundibulum* and the serpulid *Serpula columbiana* readily

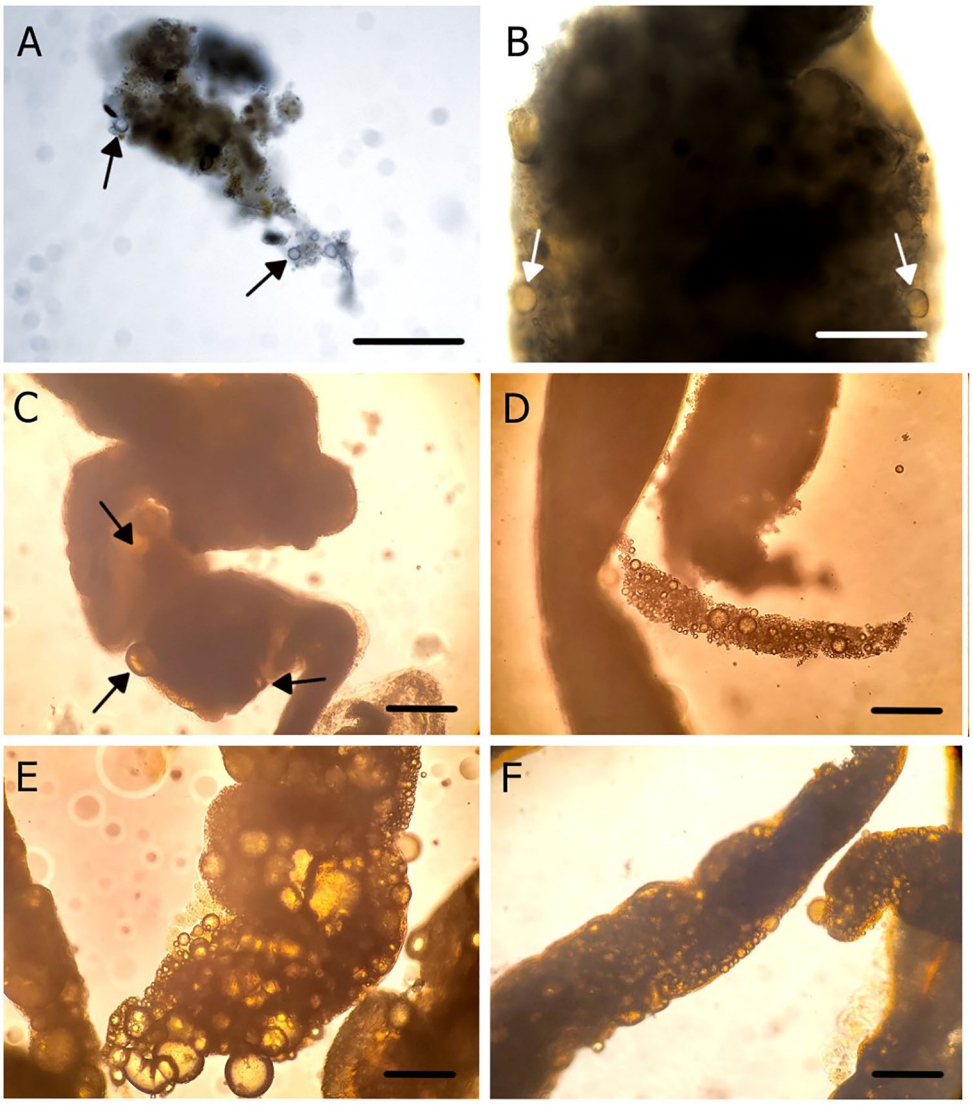

FIGURE 4
Captured and ingested oil droplets in the fecal matter of *Schizobranchia insignis* following feeding on a waste oil in seawater emulsion. **(A, B)** Canola oil. **(C)** Fish oil. **(D)** Marine engine oil. **(E)** Semi-synthetic engine oil. **(F)** Waste oil with unfiltered seawater. Arrows point to a sample of oil droplets. Scale bar: 200 µm.

capture waste motor oil droplets using their ciliated radioles. Closer observations with *S. insignis* found that, like particles, oil droplets were capture by the ciliated pinnules, then transported to the mouth along the apical groove of the radioles (Shimeta and Jumars, 1991; Riisgård and Larsen, 1995; Shimeta and Koehl, 1997). Further feeding trials found that *S. insignis* did not select oil droplets based on oil type. Following feeding trials, canola oil, fish oil and three kinds of motor oil were observed on the radioles, in the gut and fecal castings. Similarly, *S. insignis* fed on an oil emulsion in unfiltered seawater that contained food particles, seemingly not discriminating against oil in its diet. In fact, the fecal pellets mostly contained oil droplets and few if any algae cells. Amongst filter feeders, particle selectivity based on taste is common, such as with some copepods, *Daphnia*, cladocerans, and rotifers (Friedman and Strickler, 1975; Hartman and Hartman, 1977; DeMott and Watson, 1991; Kerfoot and Kirk, 1991), though non-selective particle capture is also common (DeMott, 1986). The capture of waste motor oil droplets in each of the species suggests that they do not differentiate oils based on type. Petroleum oil droplets are not a frequent food source for filter-feeders so they may generally lack adaptations to avoid them.

We did not find support for the hypothesis that small droplets are preferentially captured (Mehrabian et al., 2018). This hypothesis is based on theory that was developed for stiff fibers, whereas sabellid and serpulid worms capture droplets with flexible cilia. *S. insignis* preferentially captured droplets in its natural food particle range, no matter the type of oil used (canola and three different motor oils). Compared to the emulsion distributions, the particles captured with the canola and waste oil were significantly larger, whereas those captured with marine oil were significantly smaller,

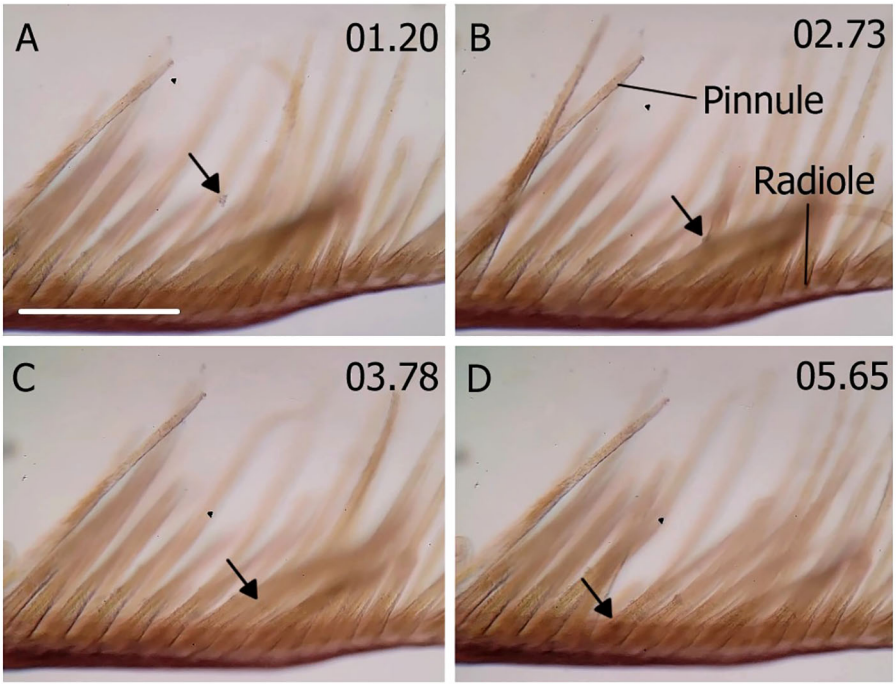

FIGURE 5
Transport of captured oil droplets on a pinnule and radiole of Schizobranchia insignis. The arrows point to a single droplet and follow its path. **(A)** An oil droplet in suspension. **(B)** The droplet captured by the cilia, **(C)** transported down the pinnule to the radiole and **(D)** to the base of the radiole. Time in seconds on top right corner. Scale bar: 200μm. See movie 1 and 2.

and for semi-synthetic oil insignificantly larger. In all cases, the droplets were around the same range of 10 to 300 μm, which corresponds with the normal particle size that sabellids capture. The filter-feeding polychaete *Terebrasabella heterouncinata* feeds in the range of 20 to 100 μm (Chalmers, 2003) and *Serpula columbiana* consumes particles that range at least from 40 to 250 μm (Pernet and Kohn, 1998). The emulsions created some larger droplets (>300 μm), but there were no droplets greater than 310 μm captured. At very small sizes, oil droplets interact with the cilia like particles due to the oil-to-water viscosity ratio and oil-water interfacial tension (Mehrabian et al., 2018). Our experiments were done at Reynolds numbers less than one where even miscible fluids are exceedingly difficult to mix (Vogel, 1994), and droplets are expected to maintain a spherical (un-deformed) shape (Taylor, 1934). Indeed, we found that the oil and seawater were not miscible, and the small oil droplets did not deform when contacted by cilia. Adding to droplet shape stability is an internal flow within the droplet that causes the oil to recirculate, and interfacial effects that resist droplet deformation (Mehrabian et al., 2018). All five of our oils were weakly buoyant, with a density ratio of 0.8 to 0.9 (Espinosa-Gayosso et al, 2015). The higher buoyancy of larger droplets meant that they had less time in the proximity of the animal and thus less time to be captured. Some of the larger droplets that were captured, may have then detached from the feeding appendage due to the positive buoyancy and deformation. For the same reasons, large droplets are difficult to manipulate comparted to small droplets (or particles).

Cilia and pinnule wettability were low for the oils. The oil and the water compete to wet the surface of cilia, and the water showed a higher affinity (i.e., the cilia are hydrophilic) compared to the oil (Mehrabian et al., 2018). We saw no oil droplets form a clam-shell shape along a cilium, further suggesting that the cilia are relatively oil-phobic. The droplets captured remained round, showing low affinity for these biological structures. In this way, the droplets were captured and behaved like solid particles. We can then assume that some droplets, like particles, might have been dislodged and rejected by a pinnule, and others might have been lost due to retention failure. In the latter case, the droplets slip off the pinnule because of an inadequate retention with the cilia or mucus (Shimeta and Koehl, 1997).

We were not able to clearly separate capture due to droplet size from capture due to viscosity or density. To do this, we would need to show that droplets of the same size (no variation) are preferentially captured based on a density or a viscosity closer to that of water. Unlike solid particles, oil droplets cannot be filtered to specific sizes because they coalescence and cream. Despite the inherent challenge with working with oils, we can draw some conclusions about capture based on viscosity and density.

We found that the captured oil droplets sizes varied depending on viscosity and density of oil, and the capture mechanism was sieving, and not inertial impaction or gravitational deposition. Our hypothesis stated that neutrally buoyant droplets would remain in the emulsion for a longer period, increasing the

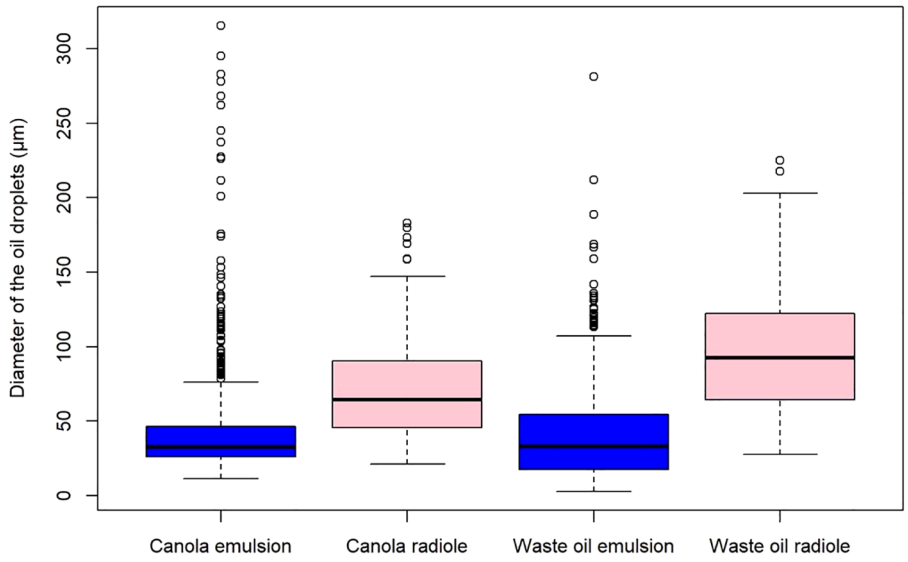

FIGURE 6
Boxplot of the distribution of canola oil (ρ = 950 kg/m^3) and waste motor oil (ρ = 813 kg/m^3) droplets present in the seawater emulsion versus those captured by *Schizobranchia insignis*. Canola emulsion n=812, canola radiole n=113, waste oil emulsion n=693, waste oil radiole n=132.

opportunity for capture. The denser canola oil is closer to the density of water, so the density difference is less, and the oil is less buoyant. As expected, this increased time in the capture field allowed for the capture of smaller droplets. A caveat here is that the denser canola oil droplets were significantly smaller than the lighter waste motor oil. The alternate interpretation, that capture was governed by inertial impaction and/or gravitational deposition is unlikely. In inertial impaction, the density difference between the particle and the fluid gives the particle momentum, thus its trajectory will deviate from the fluid streamlines around the fiber and cause the particle to be captured. Similarly, in gravitational deposition, the density difference between the particle and the fluid causes it to diverge and settle onto the fiber (Mehrabian et al., 2018). When using a

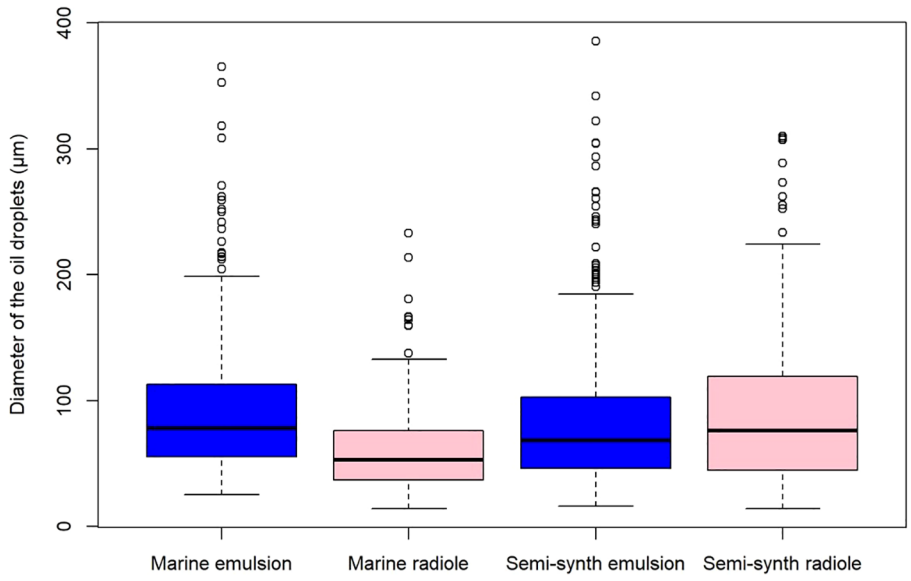

FIGURE 7
Boxplot of the distribution of the diameter of marine (µ = 156 mPa·s) and semi-synthetic (µ = 92 mPa·s) engine oil droplets present in the seawater emulsion versus those captured by *Schizobranchia insignis*. Marine emulsion n=456, marine radiole n=245, semi-synthetic emulsion n=482, semi-synthetic radiole n=253.

lighter oil, the droplets are more likely to deviate from the streamlines due to buoyancy. In this scenario, smaller droplets would be more readily captured. Instead, we found that smaller droplets from more dense (less buoyant) oil were captured. For this reason, the length of time spent in the capture environment appears to be more important to capture than the divergence from streamlines. Sieving is not affected by the density of the droplets (or particles) (Mehrabian et al., 2018).

Viscous forces in the fluid might be expected to play a role in droplet capture. A less viscous oil droplet has a greater chance of capture through inertial interaction and gravitation deposition by a fiber. This may indicate that *S. insignis* would capture smaller droplets when using a less viscous oil, but this is not what we found. We found that smaller droplets of the more viscous marine engine oil were captured compared to the less viscous semi-synthetic oil. This may be due to the non-fiber like properties of cilia and pinnules, or because direct interception and sieving were the main capture mechanisms.

The fluid mechanics of oil droplet capture by filter feeding animals is a nascent field of study. Here we address the role of oil type, droplet size, oil density, oil viscosity and gravitational forces (buoyancy) on the capture, transport, and ingestion of droplets by sabellids and a serpulid polychaete. Some key factors and principals involved in the fluid mechanics of oil droplet capture that we did not test include the interfacial tension between the oil and the seawater that affects the stability of oil droplets. Lower interfacial tension makes it harder to coalesce droplets, potentially leading to smaller, more stable droplets that could affect capture. Our observations were done in calm water and so we did not investigate the role of Reynolds numbers at different flow regimes. In high Reynolds number flows, inertial forces dominate, which can affect oil droplet capture and detachment by fibrous appendages (Letendre and Cameron, 2022). Having said this, animals that use cilia for capture may especially be constricted to low Re numbers (Humphries, 2009). We did not investigate the Weber number that relates inertial forces to surface tension forces. It is important in understanding the breakup of oil droplets, which can influence capture (Mehrabian et al., 2018; Letendre et al., 2020). The addition of surfactants or demulsifying agents can alter the stability of emulsions and promote droplet coalescence (Letendre et al., 2023). There are no references to how these chemical agents may alter droplet capture by ciliated appendages. This new and nascent field of oil droplet capture by filter feeding animals parallels that of the more mature field of plastic particulate capture (Rogers et al., 2020). With respect to petroleum oils, it offers exciting new insights into animal form and function and needs to be accelerated with the same urgency to minimize environmental impacts and maximize biodiversity health.

Data availability statement

The raw data supporting the conclusions of this article will be made available by the authors, without undue reservation.

Author contributions

KB: Conceptualization, Data curation, Formal analysis, Investigation, Methodology, Writing – original draft, Writing – review & editing. CC: Conceptualization, Funding acquisition, Methodology, Project administration, Resources, Supervision, Writing – original draft, Writing – review & editing.

Funding

The author(s) declare financial support was received for the research, authorship, and/or publication of this article. KB is supported by a NSERC graduate student scholarship. This project was funded by NSERC Discovery grant RGPIN-2023-05647 to CC.

Acknowledgments

We are grateful to the director and staff of the Bamfield Marine Sciences Centre for accommodating our research.

Conflict of interest

The authors declare that the research was conducted in the absence of any commercial or financial relationships that could be construed as a potential conflict of interest.

Publisher's note

Supplementary material

The Supplementary Material for this article can be found online at: https://www.frontiersin.org/articles/10.3389/fmars.2024.1337358/full#supplementary-material

SUPPLEMENTARY MOVIE 1
Transport of captured oil droplets on a pinnule and radiole of *Schizobranchia insignis*.

SUPPLEMENTARY MOVIE 2
Transport of captured oil droplets along the apical groove on a radiole of *Schizobranchia insignis*.

References

Almeda, R., Baca, S., Hyatt, C., and Buskey, E. J. (2014). Ingestion and sublethal effects of physically and chemically dispersed crude oil on marine planktonic copepods. *Ecotoxicology* 23, 988–1003. doi: 10.1007/s10646-014-1242-6

Chalmers, R. (2003) *An investigation into the feeding biology and factors influencing the population dynamics of* Terebrasabella heterouncinata *(Polychaeta: Sabellidae), a problematic tube-dwelling polychaete in farmed abalone in South Africa*. Available online at: http://vital.seals.ac.za:8080/vital/access/manager/Repository/vital:5291?site_name=GlobalView.

Dean, H. K. (2008). The use of polychaetes (Annelida) as indicator species of marine pollution: a review. *Rev. Biología Trop.* 56, 11–38.

DeMott, W. R. (1986). The role of taste in food selection by freshwater zooplankton. *Oecologia* 69, 334–340. doi: 10.1007/BF00377053

DeMott, W. R., and Watson, M. D. (1991). Remote detection of algae by copepods: responses to algal size, odors and motility. *J. Plankton Res.* 13, 1203–1222. doi: 10.1093/plankt/13.6.1203

Espinosa-Gayosso, A., Ghisalberti, M., Ivey, G. N., and Jones, N. L. (2015). Density-ratio effects on the capture of suspended particles in aquatic systems. *J. Fluid Mechanics* 783, 191–210. doi: 10.1017/jfm.2015.557

Fauchald, K., and Jumars, P. A. (1979). The diet of worms: A study of polychaete feeding guilds. *Oceanography Mar. Biol. Annu. Rev.* 17, 193–284.

Friedman, M. M., and Strickler, J. R. (1975). Chemoreceptors and feeding in calanoid copepods (Arthropoda: Crustacea). *Proc. Natl. Acad. Sci.* 72, 4185–4188. doi: 10.1073/pnas.72.10.4185

Gin, K. Y. H., Kamrul Huda, Md., Kiat Lim, W., and Tkalich, P. (2001). An oil spill–food chain interaction model for coastal waters. *Mar. pollut. Bull.* 42, 590–597. doi: 10.1016/S0025-326X(00)00205-8

Hartman, H. B., and Hartman, M. S. (1977). The stimulation of filter feeding in the porcelain crab *Petrolisthes cinctipes* Randall by amino acids and sugars. *Comp. Biochem. Physiol. Part A: Physiol.* 56, 19–22. doi: 10.1016/0300-9629(77)90435-2

Humphrey, B., Boehm, P. D., Hamilton, M. C., and Norstrom, R. J. (1987). The fate of chemically dispersed and untreated crude oil in arctic benthic biota. *Arctic* 40, 149–161. doi: 10.14430/arctic1810

Humphries, S. (2009). Filter feeders and plankton increase particle encounter rates through flow regime control. *Proc. Natl. Acad. Sci.* 106, 7882–7887. doi: 10.1073/pnas.0809063106

Jang, M., Shim, W. J., Han, G. M., Song, Y. K., and Hong, S. H. (2018). Formation of microplastics by polychaetes (*Marphysa sanGuinea*) inhabiting expanded polystyrene marine debris. *Mar. pollut. Bull.* 131, 365–369. doi: 10.1016/j.marpolbul.2018.04.017

Kerfoot, W. C., and Kirk, K. L. (1991). Degree of taste discrimination among suspension-feeding cladocerans and copepods: Implications for detritivory and herbivory. *Limnology Oceanography* 36, 1107–1123. doi: 10.4319/lo.1991.36.6.1107

Knutsen, H., Cyvin, J. B., Totland, C., Lilleeng, Ø., Wade, E. J., Castro, V., et al. (2020). Microplastic accumulation by tube-dwelling, suspension feeding polychaetes from the sediment surface: A case study from the Norwegian Continental Shelf. *Mar. Environ. Res.* 161, 105073. doi: 10.1016/j.marenvres.2020.105073

Lee, R. F., Koster, M., and Paffenhofer, G.-A. (2012). Ingestion and defecation of dispersed oil droplets by pelagic tunicates. *J. Plankton Res.* 34, 1058–1063. doi: 10.1093/plankt/fbs065

Letendre, F., and Cameron, C. B. (2022). The capture of crude oil droplets by filter feeders at high and low Reynolds numbers. *J. Exp. Biol.* 225, jeb243819. doi: 10.1242/jeb.243819

Letendre, F., Mehrabian, S., Etienne, S., and Cameron, C. B. (2020). The interactions of oil droplets with filter feeders: A fluid mechanics approach. *Mar. Environ. Res.* 161, 105059. doi: 10.1016/j.marenvres.2020.105059

Letendre, F., Ramos, P. A. S., and Cameron, C. B. (2023). The loss of crude oil droplets by filter feeders and the role of surfactants. *Mar. pollut. Bull.* 193, 115174. doi: 10.1016/j.marpolbul.2023.115174

Mehrabian, S., Letendre, F., and Cameron, C. B. (2018). The mechanisms of filter feeding on oil droplets : Theoretical considerations. *Mar. Environ. Res.* 135, 29–42. doi: 10.1016/j.marenvres.2018.01.006

Nash, R., and Keegan, B. F. (2003). Aspects of the feeding biology of the fanworm *Bispira volutacornis* (Polychaeta: Sabellidae). *J. Mar. Biol. Assoc. United Kingdom* 83, 453–456. doi: 10.1017/S002531540300732Xh

Ostroumov, S. A. (2005). Some aspects of water filtering activity of filter-feeders. *Hydrobiologia* 542, 275–286. doi: 10.1007/s10750-004-1875-1

Pernet, B., and Kohn, A. J. (1998). Size-related obligate and facultative parasitism in the marine gastropod *Trichotropis cancellata*. *Biol. Bull.* 195, 349–356. doi: 10.2307/1543146

Riisgård, H. U., and Larsen, P. (1995). Filter-feeding in marine macro-invertebrates: Pump characteristics, modelling and energy cost. *Biol. Rev. Cambridge Philos. Soc.* 70, 67–106. doi: 10.1111/j.1469-185X.1995.tb01440.x

Riisgård, H. U., and Larsen, P. S. (2000). Comparative ecophysiology of active zoobenthic filter feeding, essence of current knowledge. *J. Sea Res.* 44, 169–193. doi: 10.1016/S1385-1101(00)00054-X

Rogers, K. L., Carreres-Calabuig, J. A., Gorokhova, E., and Posth, N. R. (2020). Micro by-micro interactions: How microorganisms influence the fate of marine microplastics. *Limnology Oceanography Lett.* 5, 18–36. doi: 10.1002/lol2.10136

Rubenstein, D. I., and Koehl, M. (1977). The Mechanisms of filter feeding: Some theoretical considerations. *Am. Nat.* 111, 981–994. doi: 10.1086/283227

Shimeta, J. (1996). Particle-size selection by *Pseudopolydora paucibranchiata* (Polychaeta: Spionidae) in suspension feeding and in deposit feeding: influences of ontogeny and flow speed. *Mar. Biol.* 126, 479–488. doi: 10.1007/BF00354630

Shimeta, J., and Jumars, P. A. (1991). Physical mechanisms and rates of particle capture by suspension feeders. *Oceanogr. Mar. Biol. Annu. Rev.* 29, 191–257.

Shimeta, J., and Koehl, M. A. R. (1997). Mechanisms of particle selection by tentaculate suspension feeders during encounter, retention, and handling. *J. Exp. Mar. Biol. Ecol.* 209, 47–73. doi: 10.1016/S0022-0981(96)02684-6

Taylor, G. I. (1934). The formation of emulsions in definable fields of flow. *Proceedings of the Royal Society of London. Ser. A Containing Papers Math. Phys. Character* 146, 501–523. doi: 10.1098/rspa.1934.0169

Vogel, S. (1994). *Life in Moving Fluids: The Physical Biology of Flow. 2nd edition* (Princeton, USA: Princeton University Press).

Wallace, J., Webster, J., and Woodal, W. (1977). The role of filter feeders in flowing waters. *Hydrobiology* 79, 506–532.

frontiers | Frontiers in Marine Science

TYPE Original Research
PUBLISHED 21 March 2024
DOI 10.3389/fmars.2024.1330477

OPEN ACCESS

EDITED BY
Stuart Humphries,
University of Lincoln, United Kingdom

REVIEWED BY
Jesse Balaban-Feld,
University of Saint Joseph, United States
Geoffrey Mazue,
The University of Sydney, Australia

*CORRESPONDENCE
Amatzia Genin
a.genin@mail.huji.ac.il

RECEIVED 30 October 2023
ACCEPTED 23 February 2024
PUBLISHED 21 March 2024

CITATION
Genin A, Rickel S, Zarubin M and Kiflawi M (2024) Effects of flow speed and prey density on the rate and efficiency of prey capture in zooplanktivorous coral-reef fishes. *Front. Mar. Sci.* 11:1330477. doi: 10.3389/fmars.2024.1330477

Effects of flow speed and prey density on the rate and efficiency of prey capture in zooplanktivorous coral-reef fishes

Amatzia Genin[1,2]*, Svetlana Rickel[1,2], Margarita Zarubin[1,2] and Moshe Kiflawi[1,3]

[1]The Interuniversity Institute for Marine Sciences of Eilat, Eilat, Israel, [2]Department of Ecology, Evolution and Behavior, The Hebrew University of Jerusalem, Jerusalem, Israel, [3]Department of Life-Sciences, Ben Gurion University of the Negev, Beer Sheva, Israel

Holling's classical functional response model describes the mechanistic foundations of the relationships between predation rate and prey density. As such, the model is pertinent to predators that actively search for prey, but not to stationary predators in which additional factors, such as flow speed, determine the rates of prey encounter. The main objective of this study was to measure the rates and corresponding efficiencies of zooplanktivory among different common species of coral-reef fishes under a wide range of prey densities and current speeds. All our experiments were carried out in a flume with different combinations of flow speeds (3-28.5 cm/s) and prey densities (210 - 1050 prey m^{-3}). Nauplii of *Artemia salina* were used as prey. Despite major differences in the taxonomic origin of the studied species, their morphologies, and the types of shelters they use, the foraging performances of the fish, their predation rates, and the way those rates were affected by prey density and flow speed were surprisingly similar. Under a fixed prey density, capture rates did not change much as function of flow speed. Under conditions of equal prey flux, predation rates were always higher under conditions of high density and weaker flow than under lower density and faster flow. A sharp decline in capture efficiency with increasing flow speed was explained by a corresponding narrowing of the fish's body orientation relative to the flow. In other words, with increasing flow speed, the fish gradually became more-narrowly oriented head-on onto the flow, exhibiting a decrease in the frequency of body turns ("maneuverability"). These trends, especially the reduced maneuverability under strong currents, can explain our findings that predation rates did not increase when the flow, hence prey flux, increased. Inter-specific differences in predation rates and efficiencies, however small, agree well with observed differences in the type of habitats the different species occupy.

KEYWORDS

zooplankton, predation, foraging, site-attached, movement, Red Sea

1 Introduction

Much like oases in the desert, coral reefs flourish in oligotrophic seas, where the productivity of the reef commonly exceeds by up to an order of magnitude that of phytoplankton in the surrounding open waters. The enigmatic source(s) of the allochthonous nutrients needed to support this exceptionally high productivity of the reef has long captivated coral-reef researchers (Odum and Odum, 1955; Erez, 1990). One possible source is the consumption of pelagic plankton by benthic animals in the reef. Indeed, Genin et al. (2009) and Wyatt et al. (2010) found that intense consumption of small picoplankton can provide sufficient nutrients to explain this so called "paradox of the reef". However, the relative contribution of zooplankton predation, is yet poorly known, despite suggestions that such predation is a major link of the reef's benthic-pelagic coupling (Morais and Bellwood, 2019; Morais et al., 2021).

Generally, predation is a fundamental ecological link that frequently determines key attributes of individuals, populations, and communities (Begon et al., 2006). While this notion is widely recognized, studies in which rates of predation are directly measured are claimed to be infrequent, especially in aquatic systems (Mihalitsis et al., 2022). However, quite a few examples of studies in which predation rates of zooplankton by marine fishes are found in the literature (e.g., Kingsford and MacDiarmid, 1988; Noda et al., 1992; Kiflawi and Genin, 1997; Holzman and Genin, 2003; Clarke et al., 2009; Finelli et al., 2009; Khrizman et al., 2018; Ishikawa et al., 2022). As indicated above, several studies recently highlighted the importance of fish zooplanktivory in the coral reef ecosystem (Brandl et al., 2019; Morais and Bellwood, 2019; Morais et al., 2021; Siqueira et al., 2021; Mihalitsis et al., 2022). However, none of those studies included direct measurements of predation rates. Instead, the alleged intensity of zooplanktivory in those studies was indirectly deduced from measurements of biomass and growth of different fish that, in turn, were incorporated in a Von Bertalanffy Growth Model. Thus, the contribution of zooplankton predation by fish to the overall productivity of the reef is still debatable (Allgeier and Cline, 2019; Brandl et al., 2019), further highlighting the need for direct measurements of that predation.

Planktivorous fish are ubiquitous members of fish communities in many coral reefs, especially across the western Indo-Pacific (Siqueira et al., 2021) and the Red Sea (Fishelson et al., 1974). In some reefs, such as the outer GBR, those fish form a "wall of mouths" (Hamner et al., 1988), that substantially reduces the zooplankton densities down current. Similar down-current depletions of zooplankton also occur in kelp forests, temperate rocky reefs, and over seamounts (Gaines and Roughgarden, 1987; Kingsford and MacDiarmid, 1988; Genin et al., 1994).

In coral reefs, many fishes belonging to this guild are site-attached (Hobson, 1991; Kiflawi and Genin, 1997), keeping their position near a shelter where they capture zooplankton that drift toward them with the currents (Sale, 1971; Fishelson et al., 1974). A similar mode of predation is found in freshwater streams, where many fish capture drifting prey while temporarily keeping a stationary place (O'Brien et al., 2001). The majority of site-attached fishes in the coral reef form social groups, where the group's fidelity to the same shelter can last several months and beyond (Sale, 1971; Booth, 2016). The shelters used by those site-attached fishes include branching corals, rocky knolls and other complex substrates. The fish maintain their foraging space sufficiently close to the shelter, allowing a fast retreat when threatened (Fishelson et al., 1974; Hobson, 1991). Their foraging space is almost always found up-current of the shelter, with the individual fish commonly facing the oncoming current (Hobson, 1991; Engel et al., 2021). The fish rapidly switch their search direction and position relative to the shelter when the currents change direction (Bray et al., 1981; Hobson, 1991; Engel et al., 2021). While foraging, the fish actively avoid being swept by the currents to a position found down-current of the shelter (Engel et al., 2021; A. Genin unpublished observations).

Site-attached fishes are not filter feeders (e.g., Nonacs et al., 1994); instead, they always strike individual prey. Their capture of a prey consists of three steps: (1) wait & search - slowly swimming near the shelter, waiting for a drifting prey to enter the foraging space; (2) strike - a rapid swim toward a detected prey, bringing their mouth sufficiently close to ingest the prey; (3) ram-jaw suction, an extremely rapid extension of the jaws in order to rapidly suck the prey (Coughlin and Strickler, 1990; Hobson, 1991; Wainwright et al., 2007). The duration of step 1 (wait & search) depends on the flow. Under constant prey densities, the frequency of prey arrival into the fish's foraging space is a function of current speed (e.g., Finelli et al., 2009; Khrizman et al., 2018; Khrizman et al., 2024). However, the fish do not always increase their predation rates under stronger flows (Kiflawi and Genin, 1997; Clarke et al., 2009), allegedly due to flow-dependent biomechanical constraints that limit the ability of the fish to strike the prey at wide angles in respect to the flow direction (Kiflawi and Genin, 1997; O'Brien et al., 2001; Ella and Genin, 2023). In contrast, the fish's functional response to changes in zooplankton density, is expected to monotonically increase with increasing prey densities (Kiflawi and Genin, 1997; Clarke et al., 2009), until a yet-unknown saturation level is reached (Holling, 1959).

The main objective of this study was to evaluate the effects of prey density and flow speed on the rates and efficiencies of plankton capture in 3 common species of site-attached coral-reef fishes under a wide, natural range of those parameters. Specifically, we examine the linearity of the fishes' functional responses to increasing prey density, the occurrence of saturation, and the role of biomechanical limitations in determining the fishes' functional responses to increasing flow speed.

2 Materials and methods

2.1 Study site

The study was carried out at the Interuniversity Institute for Marine Sciences in Eilat (IUI), northern Red Sea, Israel (29°30′ N, 34° 56′E). Fish were collected at the local coral reef, at 6-14 m depth. Detailed descriptions of the reef's benthic communities are found in Fishelson (1971), Benayahu and Loya (1977), and Yahel et al. (1998). Briefly, those fringing reefs are dominated by stony

corals, growing on a steep slope (10-30°). The currents are generally slow (average speed of 10 cm/s; maximum of ~50 cm/s) exhibiting a strong semidiurnal periodicity during the warm months (Genin and Paldor, 1998; Monismith and Genin, 2004). Northerly winds prevail >90% of the time. Due to a short fetch, the sea around our study site in the northern part of the Gulf is calm with waves < 0.5 m in height, except for rare times of strong southerly winds. The region is extremely arid, with average precipitation rate of 22 mm/y. The water is clear with visibility typically extending 10s of meters. Among the ca. 260 species of fish inhabiting the local reefs, the guild of zooplanktivorous fish is numerically the largest, comprising >40% of the total number of fish (Brokovich et al., 2006; Shaked and Genin, 2023).

2.2 Fish

The 3 site-attached species we studied (Figure 1) included 2 common damselfishes: *Dascyllus marginatus* (acronym: *Dm*; Standard length: 52 ± 6.36 mm) and *Neopomacentrus miryae* (*Nm*; 94 ± 10.9 mm) and a common serranid *Pseudanthias squamipinnis* (*Ps*; 103 ± 13.5 mm) (Figure 1). *Dm* is endemic to the Red Sea, Gulf of Aden and Gulf of Oman. *Nm* is endemic to the Red Sea. *Ps* is found throughout the Indian Ocean and West Pacific. *Ps* and *Nm* are the most abundant species in the local coral reefs (Khalaf and Kochzius, 2002; Brokovich et al., 2006; Megdadi et al., 2017). As other species belonging to the guild of diurnal, site-attached, coral-reef planktivores, the fish are generalist visual feeders (Coates, 1980) with diets consisting of meso-zooplankton that are usually larger than 400 μm in length (Noda et al., 1992; Hanson et al., 2016). The fish capture individual zooplankters using ram-jaw suction, as described above (Coughlin and Strickler, 1990; Hobson, 1991).

The species we studied live in social groups, varying in size from several individuals, in *Dm*, to hundreds in *Ps* and *Nm* (Fricke, 1977; Megdadi et al., 2017). Typical group sizes in those species appear to be related to the type of shelters they use, with those living in association with single coral colonies (*Dm*) commonly form smaller groups than those associated with large rocky substrates (*Ps*, *Nm*) (Fricke, 1977; Khalaf et al., 2006).

Adult individuals were used in our experiments. In *Ps*, only females were used because males are morphologically different and considerably larger than females and their proportion in the groups are considerably lower (Shapiro and Lubbock, 1980). No such separation was used with the other species, where males and females are morphologically indistinguishable and the gender could not be determined without scarifying the fish.

An additional damselfish, *Chromis dimidiata* (80-90 mm), was studied as part of a complementary work using the same experimental procedures but different levels of flow speeds and examined parameters. The results of this species are reported in the Supplementary Information.

2.3 The flume

Predation experiments were carried out in a recirculating flume (Figure S1). Briefly, the flume was 330 L in volume, with a glass

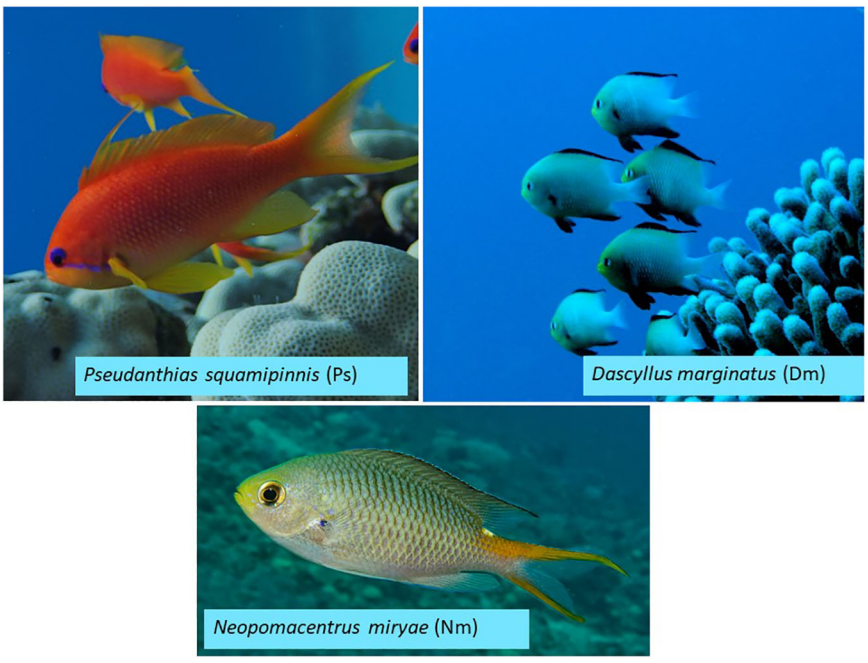

FIGURE 1
Studied species. *Pseudanthias squamipinnis* (acronym *Ps*; mean ± sd standard length 6.2 ± 0.6 cm, N = 5), *Dascyllus marginatus* (*Dm*; 4.3 ± 0.5 cm, N = 6), and *Neomopacentrus miryae* (*Nm*; 6.8 ± 0.8 cm; N = 5). Fish standard lengths were measured by Ella and Genin (2023) using 3D photography.

10.3389/fmars.2024.1330477

walled working section, 200 cm in length and 30 × 30 cm in cross-section. The fish were kept inside the working section using plastic-coated wire mesh (1 cm mesh size) 50 cm up-current and a few cm down-current of the work section. A small skeleton of a branching coral or a short piece of PVC pipe, ~4 cm in diameter (Figure S1) were placed as a shelter near the down-current end of the work section. The type of shelter was species dependent, using the coral skeleton for *Dm*, which in the reef finds shelter inside branching corals, and the pipe for *Ps, Nm*, and *Cd*, which typically find shelter in perforated rocks and knolls.

A propeller driven by a 560 W DC motor (Doer Electric Corporation, Cedarburg, Wisconsin, USA) and regulated by an electric motor speed controller generated water movement within the flume. An acoustic Doppler current meter (ADV, Nortek, Norway) was used to calibrate the flume's controller to generate flows in the range of 3-28.5 cm/s. A 1 cm wide benthic boundary layer was found along the flume's walls, in which the fish were rarely found. Water temperature was maintained at ± 3° C of the ambient sea-surface temperature. Part of the water in the flume was replaced almost daily, by allowing 1 hr-long exchange with freshly-pumped, pre-filtered seawater. During that time, the propeller was set to high speed and a 65 μm net was tightly inserted in the flume to remove sediments and other suspended particles. Additionally, fouling organisms growing on the walls were scrubbed off every 2-3 weeks, thereby maintaining clear walls for the side-looking video camera. The light intensity in the flume was ~180 μmol m^{-2} s^{-1}, provided by fluorescent lights from above. This light intensity was similar to that prevailing at the local reef during midday at ~10 m, a depth at which the studied species were common. A natural light-dark cycle was maintained throughout the period of our experiments.

All trials used a single fish in the flume. Different combinations of flow speed and prey density covered the range of 3 to 28.5 cm/s and 210 to 1050 prey m^{-3}, respectively (Table 1). These values were well within those occurring in the coral reef of Eilat (Genin et al., 1995; Genin and Paldor, 1998; Reidenbach et al., 2006; Khrizman et al., 2018) and other coral reefs (e.g., Noda et al., 1992; Gahan et al., 2023).

2.4 Experimental protocol

Fish were collected by scuba divers at depths of 5-14 m in the coral reef off the Interuniversity Institute for Marine Sciences of Eilat (IUI) using either a gill net for fish that reside over rocky substrates (*Nm*, *Ps*) or by lightly anesthetizing fish using diluted clove-oil for the coral-associated *Dm*. The captured fish were transferred to the laboratory for pre-acclimation in 8 L individual holding tanks containing running seawater. Following this initial acclimation, lasting a few days to several weeks, an acclimated fish was transferred to the flume for 3-7 days prior to the onset of its experiments. To avoid acclimation to a certain flow speed, different speeds were used during the acclimation period. A fish was considered acclimated and ready for trials once it readily exited its shelter and commenced feeding immediately after we added prey to the flume.

TABLE 1 Details of the experiments performed and the number of replicates.

Dependent variable	Factor	Levels	Co-factor	Levels	Species	Individuals per species	Trials or samples per species
Predation rate, predation efficiency	Prey Density	210, 420, 630, 840, 1050* prey m^{-3}	Flow speed	4, 12 cm/s	*Ps, Dm, Nm*	4	192
Predation rate, predation efficiency	Flow speed	3,6,9, 12,15, 21 cm/s	Prey density	210, 630 prey m^{-3}	*Ps, Dm, Nm*	4	192
Body orientation	Flow speed	3,6,9, 12,15, 21 cm/s	–	–	*Ps, Dm, Nm*	7 (*Dm*-3)	999, 1100, 1116 in *Ps, Dm, Nm*, respectively

*Density of 1050 m^{-3} was not examined for Nm.

Throughout that period, the fish were fed with live, 24-36 hrs post-hatching nauplii of *Artemia salina*. At that stage, their mean [± SD] length was 600 [± 70] μm (n = 50), similar to size of the fish's natural prey in the reef. Note, however, that in comparison with copepods, a common taxon in the fish diet (Hobson, 1991; Noda et al., 1992), *Artemia* nauplii are poor swimmers and lack an escape response from approaching fish (Trager et al., 1994). However, in the context of this mechanism-oriented study, the use of a single type of non-evasive prey had many advantages, including the logistic ease of getting high numbers of live prey and a use of identical prey in all our experiments, an approach that minimized confounding effects in experiments designed to resolve the effects of only prey density and flow speed.

Each day started with a preparation of syringes (10 ml) filled with the intended numbers of prey for the trials of that day. Using a syringe with a piece of a thin, flexible, transparent tubing attached to its opening, the nauplii were manually collected from a holding tank under a dissecting microscope. Trials using different, haphazardly ordered combinations of prey densities and flow speeds were performed with the same individual fish no more than 4 times a day, with breaks lasting ≥30 min between consecutive trials. To keep the fish hungry during trials, they were kept unfed for at least 12 hrs prior to the initiation of trials. To prevent feeding during the introduction of the nauplii to the flume, the fish were chased into the shelter by introducing a long plastic rod into the flume. During the prey introduction interval, the flow was temporarily raised and the nauplii were gradually ejected from the syringe to the flume near the propellor, assuring their mixing throughout the flume. Following the setting of the controller to the target flow speed, the plastic rod withdrawn, upon which the (now acclimated) fish immediately commenced feeding. Each trial lasted 30 or 60 s, depending on the target flow speed, keeping the trial duration equal to or shorter than the time it took the water to complete a full revolution. Thereby, predation during the trial did not reduce the density of prey in the water flowing by the fish. Upon the completion of a trial, the plastic rod was re-introduced, chasing the fish back to shelter, and the surviving nauplii were collected by filtering the water through a 65 μm plankton net, mounted on an aluminum frame that tightly fitted the flume's cross section. The filtering stage lasted ~5 min with the flow set at 6 cm/s, thus allowing at least four complete revolutions of the recirculating water through the net. The surviving nauplii were counted using a dissecting microscope. Twenty-eight "control runs" ran under different flow speeds, with no fish in the flume, showed a recapture success of 98 ± 2%.

The difference between the number of nauplii introduced to the flume prior to the trial and those that survived the trial, together with the trail's duration, were used to calculate predation rates (prey s^{-1}). The values of predation rates were then used to calculate capture efficiency, defined as the percent of prey captured from the total approaching the fish, that is, predation rate divided by the flux. Note that the area used to calculate the flux was the cross section of the flume (width X height of water; 30 X 30 cm).

Details on the setting and number of replicates used are reported in Table 1. The study took about a decade to complete (1999-2009). Within that period, the trials with each species were completed through a single series of back-to-back trials, lasting several months. Within a series, different individuals were collected at the reef one after the other, so that no individual would remain in the lab more than 2-3 months. Long breaks between species allowed interim processing and analyses of data prior to proceeding with the next species. Due to logistic reasons, a break lasting several years was taken prior to the initiation of experiments with *Cd*.

The collected fish were returned to the reef, preferably to the exact sites where they had been collected. The methods used to collect and handle the fish were carried out under a permit from Israel Nature & Parks Authority and fully complied with the ethical rules of animal treatment at the Hebrew University of Jerusalem.

2.5 Orientation to the flow

A video camera was used to measure the body orientation of the fish with respect to the direction of the flow as viewed from above. Here, our goal was to examine the narrowing of the orientation of the fish with respect to the direction of the oncoming flow as the flow speed was increased, as reported by Kiflawi and Genin (1997) for a few individual fish. Down-looking video recordings of the fish were obtained in the flume during foraging under different flow speeds. Single video frames were digitized using ImageJ in order to measure the angle between the flume's longitudinal axis (i.e., the flow direction) and the direction of a digitized line connecting the fish's snout and the base of its tail. The measured angles were converted to absolute values, disregarding left and right with respect to the flow direction. Zero angles referred to a head-on orientation to the flow, while 90° corresponded to a situation where the fish projected its full side to the flow. Video records, each lasting 10 min, were made for each individual (N=3), for each flow speed (3, 6, 9, 12, 15, 18, and 21 cm/s) for each of the 3 studied species. Approximately 50 frames were haphazardly selected from each 10 min record, yielding a total of 3042 data points.

The data were processed to provide the 95th percentile of the angles and their variance for each flow speed. The former value was used as a measure of horizontal width of the up-current "aperture" of the fish's foraging space. The variance was considered a proxy of the frequency of left-right turnings (hereafter "maneuverability") of the fish under each flow speed.

2.6 Statistical analysis

The effect of flow speed on predation rates was tested using Mixed-Design Two-Way Repeated Measures ANOVA with 6 levels of flow speed (3, 6, 9, 12, 15, and 21 cm/s), used as Within-Subject Variable. Two levels of prey density, low and medium (210 and 630 prey m^{-3}, respectively) and three species (*Ps*, *Dm*, and *Nm*) were used as Between-Subject Factors, as detailed in Table 1. Bonferroni *post hoc* was used to test for differences between pairs of species. The same test was used to test the effect of prey density, using its 4-5 levels (210, 420, 630, 840, and, except for *Nm*, 1050 prey m^{-3}) as

Within-Subject Variable, with the two levels of flow speed (4 and 12 cm/s) and species being Between-Subject Factors. The dependent variables, predation rates and capture efficiency, were tested separately using the same tests. For efficiency, log-transformed values were used in order comply with the assumptions of homogeneity of variance (Levene's test). Following a finding of an overall significant effect of species in the above ANOVA, a Bonferroni *Post Hoc* test was used to test the differences between pairs of species.

Linear relationships between flow speed and the 95th percentile of the orientation angles and between flow speed and the log-transformed variance of the orientation angles were tested for each flow speed and each species using ANCOVA with flow speed as a covariate and species as a fixed factor and Bonferroni *post hoc* test of differences between species. To test the equality of the intercepts, flow speed was centered on 12 cm/s by subtracting 12 from the original values.

A logarithmic fit of the relationships between flow speed and the variance of the angles in each category of flow speed was tested in two steps: in the first step, performed separately for each species, the fit to a logarithmic regression was tested. After corroborating that fit, the original values were log-transformed and tested using ANCOVA with flow speed as a covariate and species as a fixed factor. Bonferroni *post hoc* was used to test for differences between pairs of species.

Assumptions of sphericity and homogeneity of variance were verified in each test, as needed. All statistical tests were carried out using SPSS (v. 28).

3 Results

The results of all statistical tests are listed in Tables 2, 3.

3.1 Effects of prey density

A nearly linear functional response to increasing density with no apparent saturation was observed in the 3 studied species (Figure 2). Prey density had a significant effect on predation rates (Mixed-Design Two-Way Repeated Measures ANOVA, $F_{1,3} = 596.6$, $p < 0.0001$), with no significant effect of flow speed (two levels) and non-significant interaction between prey density and flow speed. Across all prey densities and two flow speeds included in this analysis, predation rates by *Nm* were 1.4-1.7 times higher than those of *Ps* and *Dm* (Figure 2B), resulting in an overall significant

TABLE 2 Mixed-Design Two-Way Repeated Measures ANOVA testing the effects of prey density (A, B) and of flow speed (C, D) as Within-Subjects factors, on predation rates (A, C) and on predation efficiencies (B, D), with two Between-Subjects Factors: species and flow speed in A, B or species and prey density in C, D.

(A) Effect of prey density on predation rates				
Factor	SS	df	F	*p*-value
Prey	10.34	3	596.6	< 0.001
prey * flow	0.02	3	1.1	NS
prey * species	0.5	6	14.53	< 0.001
Flow	0	1	0	NS
Species	3.28	2	28.96	< 0.001
Error (prey)	0.31	54		
Post Hoc (*Ps, Dm, Nm*)	a,a,b			
(B) Effect of prey density on predation efficiency (log transformed)				
Factor	SS	df	F	*p*-value
Prey	0.032	3	5.55	< 0.003
prey * flow	0.006	3	1.1	NS
prey * species	0.012	6	1.0	NS
Flow	5.11	1	251.4	< 0.0001
Species	0.933	2	0.67	< 0.0001
Error (prey)	0.1	54		
Post Hoc (*Ps, Dm, Nm*)	a,a,b			

(Continued)

10.3389/fmars.2024.1330477

TABLE 2 Continued

(C) Effect of flow speed on predation rates				
Factor	SS	df	F	*p*-value
Flow	1.14	5	38.14	< 0.0001
Flow * prey	0.189	5	6.31	< 0.0001
Flow * species	0.616	10	10.29	< 0.0001
Prey	9.0	1	275.1	< 0.0001
Species	1.0	2	15.23	< 0.0001
Error (flow)	0.48	80		
Post Hoc (*Ps, Dm, Nm*)	a,b,a			
(D) Effect of flow speed on predation efficiency (log transformed)				
Factor	SS	df	F	*p*-value
Flow	77.1	5	444.4	< 0.0001
Flow * prey	0.06	5	0.35	NS
Flow * species	2.68	10	7.72	< 0.0001
Prey	0.18	1	1.25	NS
Species	4.12	2	14.2	< 0.0003
Error (flow)	2.78	80		
Post Hoc (*Ps, Dm, Nm*)	ab,c,a			

The bottom row in each part indicates the results of Bonferroni Post Hoc testing differences among pairs of species. In that row, the 3 letters in the second column respectively indicate the 3 species listed in the first column. Different letters in the second column indicate a species that significantly differed ($p < 0.05$) one from another.

effect of species on predation rates (Mixed-Design Two-Way Repeated Measures ANOVA, $F_{1,2} = 28.96$, $p < 0.0001$) and significant interaction between prey density and species ($p < 0.001$). However, Bonferroni *post hoc* test indicated that only the difference between *Nm* and the other two species was significant ($p < 0.05$), with no significance difference between *Ps* and *Dm* (Table 2).

The linear functional response reported in Figure 2 indicated no saturation up to the maximum prey density examined (1050 prey m^{-3}). The effect of prey density on the efficiency of prey capture (Figure 3) was indiscernible, however statistically significant (Mixed-Design Two-Way Repeated Measures ANOVA, $F_{1,3} = 5.55$, $p < 0.003$). Capture efficiencies were strongly affected by flow speed ($p < 0.0001$; Table 2), being ~2X higher under slow (4 cm/s) than fast (12 cm/s) flows ($p < 0.0001$). The overall effect of species on capture efficiency was significant ($p < 0.003$), however, again, Bonferroni *post hoc* test indicated that the capture efficiency of only *Nm* was higher than *Ps* and *Dm*, with no significant difference between the latter two. The higher capture efficiencies of *Nm* were most conspicuous under weak flows (Figure 3B).

3.2 Effects of flow speed

The effects of flow speed on predation rates (Figure 4) were generally smaller than those of prey density, especially under conditions of low prey density (210 prey m^{-3}). Under the higher density (630 prey m^{-3}), the functional response was weakly unimodal, exhibiting maxima at different, species-specific speeds. Overall, the effect of flow speed on predation rates was significant (Mixed-Design Two-Way Repeated Measures ANOVA, $F_{1,5} = 9$, $p < 0.0001$; Table 2). Under strong flows (≥ 12 cm/s), *Ps* exhibited higher predation rates than those of the other species, whereas under weak flows (≤ 9 cm/s) *Nm* had the highest predation rates (Figure 4B), resulting in an overall significant effect of species ($p < 0.0001$). However, Bonferroni *post hoc* test indicated a significant difference only between *Dm* and the other two species. The interactions between flow speed and prey density and between flow speed and species were highly significant ($p < 0.0001$; Table 2).

A sharp, nearly exponential decrease in the efficiency of prey capture with increasing flow speed was observed in all species (Figure 5), declining from 40-50% at 3 cm/s to approximately 10% at 15-21 cm/s (Mixed-Design Two-Way Repeated Measures ANOVA, $F_{1,5} = 9$, $p < 0.0001$; Table 2). As the effect of flow speed on the rate of predation was small, especially under low prey densities (Figure 4), the observed decline in efficiency was due to the fish's inability to effectively utilize higher fluxes of prey when the density of prey remained constant but the number of prey passing by the fish per unit of time (i.e., prey flux) increased due to the increasing flow speeds. Neither prey density nor the interaction between flow speed and prey density had a significant effect on the capture efficiency, but the effect of the interaction between flow speed and

TABLE 3 Statistical tests of the relationships between flow speed and the fish's orientation angles with respect to the flow direction.

(A) ANCOVA testing the effect of flow speed on the 95% percentile of body orientation				
Factor	SS	df	F	*p*-value
Flow (covariate)	15354	1	380	< 0.0001
Species (fixed)	821	2	10.1	< 0.002
Error	686.8	17		
Post hoc (*Ps, Dm, Nm*)	a,b,b			

(B) Logarithmic regression and the 95% Confidence Interval of the variance in the orientation angles (*y*) under different flow speeds (*f*) using the equation: $y = a + b * \text{Ln}(f)$					
Species	*A*	*b*	R^2	95% CI of *a*	95% CI of *b*
Nm	-678	2072	0.96	-841 to -515	1680-2463
Dm	-419	1358	0.97	-503 to -335	1157-1559
Ps	-644	2107	0.99	-714 to - 573	1937-2277

(C) ANCOVA testing the effect of flow speed on the log-transformed variance of the orientation angles				
Factor	SS	df	F	*p*-value
Flow (covariate)	2.5	1	196.1	< 0.0001
Species (fixed)	0.132	2	5.18	< 0.02
Error	0.217	17		
Post hoc (*Ps, Dm, Nm*)	a,b,b			

(A) Testing the linear regression between flow speed and the 95% percentile of the orientation angles, using species as a fixed factor.
(B) Coefficients and 95% confidence intervals of the logarithmic regression between the variance of the fish's orientation (angle^2) and flow speed.
(C) ANCOVA of the linear regression between the long-transformed angle-variance and flow speed. Flow speed was scaled to the mid-point of the flow speed (12 cm/s) so that this mid-point was used for the intercept instead of zero. The results of Bonferroni post hoc pairwise comparisons between species are indicated in the bottom row of A and C. In that row, the 3 letters in the second column respectively indicate the 3 species listed in the first column. Different letters in the second column indicate a species that significantly differed ($p < 0.05$) one from another.

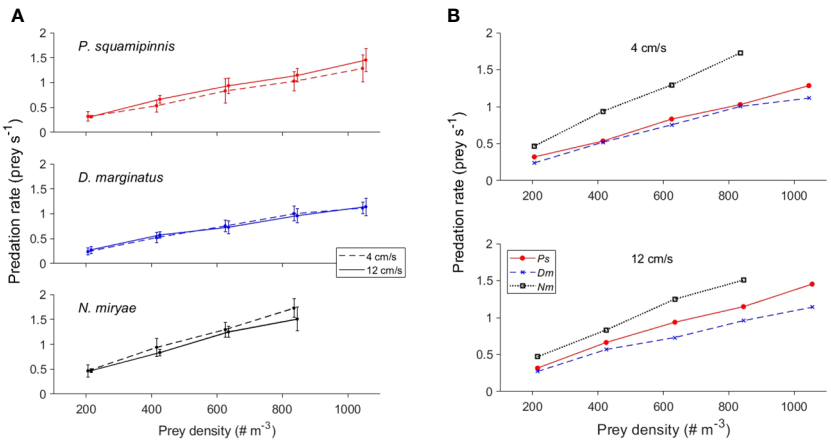

FIGURE 2
Effects of prey density on predation rate. **(A)** Mean (± sd) predation rates as function of prey density in the 3 species under two levels of flow speed (4 and 12 cm/s; dashed and full lines, respectively). **(B)** Combined plots of the means of all species (color coded) under flow speeds of 4 (upper panel) and 12 cm/s (lower panel). To improve visualization, error bars are not plotted in **(B)** For statistics see Table 2.

species was ($p < 0.0001$; Table 2). Despite a general similarity among the 3 studied species (Figure 5), the small inter-specific differences in the capture efficiency between them were statistically significant ($p < 0.0003$). Bonferroni *post hoc* test indicated significant differences ($p < 0.05$) between *Dm* and the two other species but not between *Ps* and *Nm* (Table 2).

Note that efficiency was calculated using the flux of prey across the full cross section of the flume, disregarding the observation that

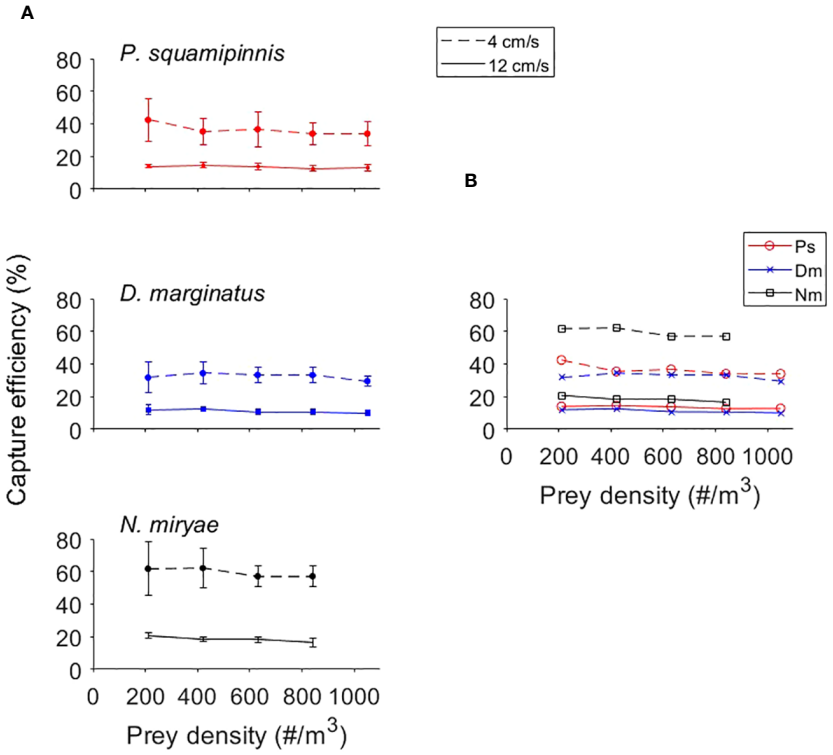

FIGURE 3
Effects of prey density on capture efficiency, defined as the percent of prey captured by the fish from those approaching it during a trial. **(A)**- Mean (± sd) efficiencies in the range of 210-1050 prey/m^3 under flow speeds of 4 cm/s (dashed lines) and 12 cm/s (full lines) in Ps (top panel), Dm (mid panel) and Nm (lower panel). **(B)** - Visualization of inter-specific differences for the 3 species (color coded as in **A**) under flow speeds of 4 cm/s (dashed lines) and 12 cm/s (full lines). Note the higher capture efficiencies of Nm, especially under the weaker flow. For statistics see Table 2.

fish's foraging space narrowed down with increasing flow speed, as presented by Ella and Genin (2023). In that paper, we show that the decrease in capture efficiency with increasing flow speed (Figure 5) does not always occur when the fluxes are calculated using the actual, flow-dependent "apertures" of the foraging space (addressed below in the Discussion).

3.3 Prey flux

Under identical levels of prey flux, the combinations of weak flow (3-6 cm/s) and high density (630 prey m^{-3}) resulted in 2 to 4 times higher predation rates than in combinations of fast flow (10-21 cm/s) and low prey density (210 prey m^{-3}) (Figure 6). This difference is

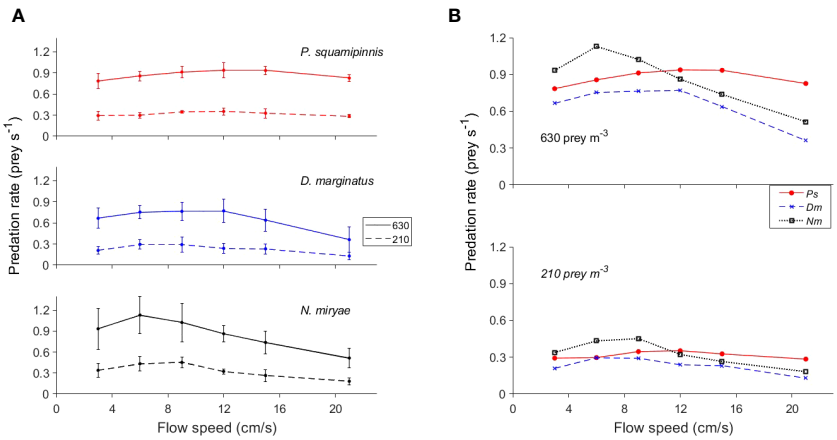

FIGURE 4
Effects of flow speed on predation rate. **(A)** Mean (± sd) predation rates as function of flow speed in the 3 species under 2 levels of prey density (dashed line: 210 prey m^{-3}; full lines: 630 prey m^{-3}). **(B)** Combined plots of the means of all species (color coded) under prey density of 210 prey m^{-3} (upper panel) and 630 prey m^{-3} (lower panel) prey m^{-3}. To improve visualization, error bars are not plotted in **(B)**. For statistics see Table 2.

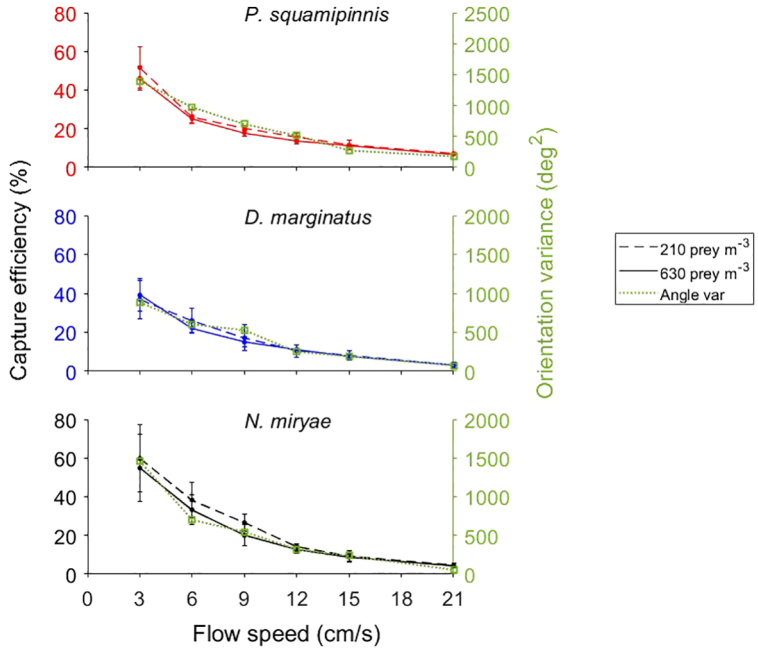

FIGURE 5
Effects of flow speed on the capture efficiency of prey and on the variance of the orientation angle. Left axes (color coded dashed and full lines): average (± sd) capture efficiency as function of flow speed under two levels of prey density: 210 prey m^{-3} (dashed lines) and 630 prey m^{-3} (full lines) for *Ps, Dm,* and *Nm*. Right axes (green dotted lines): the variance of the orientation angles was copied from Figure 7B) to demonstrate the fit between the three plotted lines for each species. The scale of the right axes was set so that the plots of the orientation variance would be positioned close to the respective plots of capture efficiencies. For statistics see Table 2.

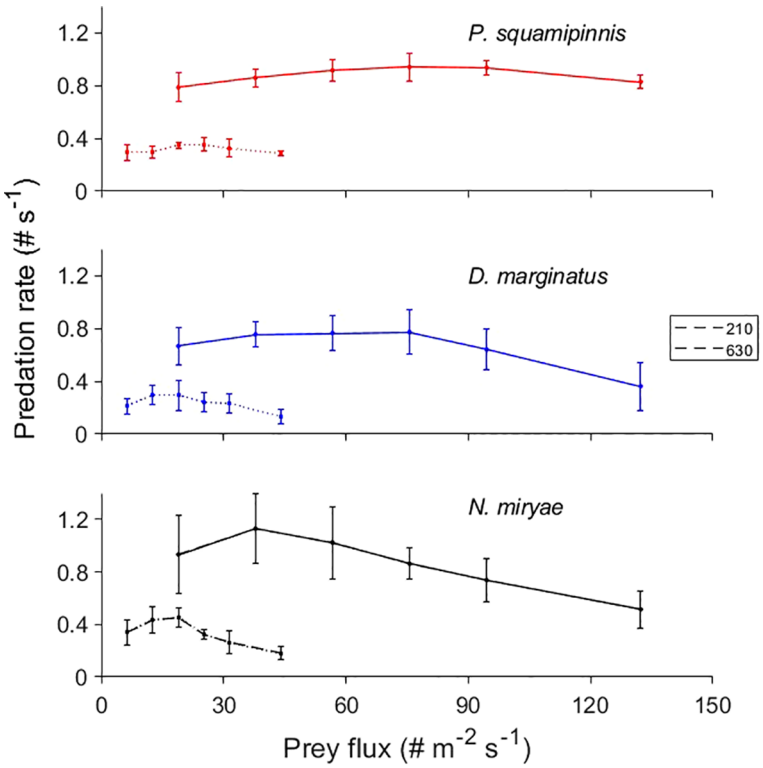

FIGURE 6
Effects of prey flux on predation rate. Mean (± sd) predation rates as function of prey flux in the studied species under prey densities of 210 prey $^{-3}$ (dotted lines) and 630 prey^{-3} (full lines). Each point indicates a different combination of prey density and flow speed.

consistent with the aforementioned findings that predation rates were strongly affected by prey density but not by flow speed (Figures 2, 3).

3.4 Body orientation

The linear decrease in the 95th percentile of the orientation angles with increasing flow speed (Figure 7A) was highly significant ($p < 0.0001$; Table 3). Similarly significant (ANCOVA, $p < 0.0001$) was the decrease in the variance of those angles with increasing flow speed (Figure 7B), with a significant effect of species ($p < 0.02$) and a non-significant interaction between species and flow speed (Table 3). Bonferroni *post hoc* tests indicated that the angles of the 95th percentile and the variance were significantly higher ($p < 0.05$) in *Ps* than in the other two species (Figure 7), while *Dm* and *Nm* were not significantly different one from another (Table 3).

3.5 *C. dimidiata*

In general, the trends of predation rates as function of prey density and flow speed observed for *Chromis dimidiata* (Supplementary Material) were similar to those reported above for *Ps, Nm*, and *Dm*.

4 Discussion

The site-attached coral reef fishes we studied were surprisingly similar in their flow-dependent body orientation (rheotaxis), their predation rates and the way those rates were affected by prey density and flow speed. This similarity prevails despite major differences in their taxonomic origin at the family level, their morphologies, the group sizes they typically form, and the types of shelters they use.

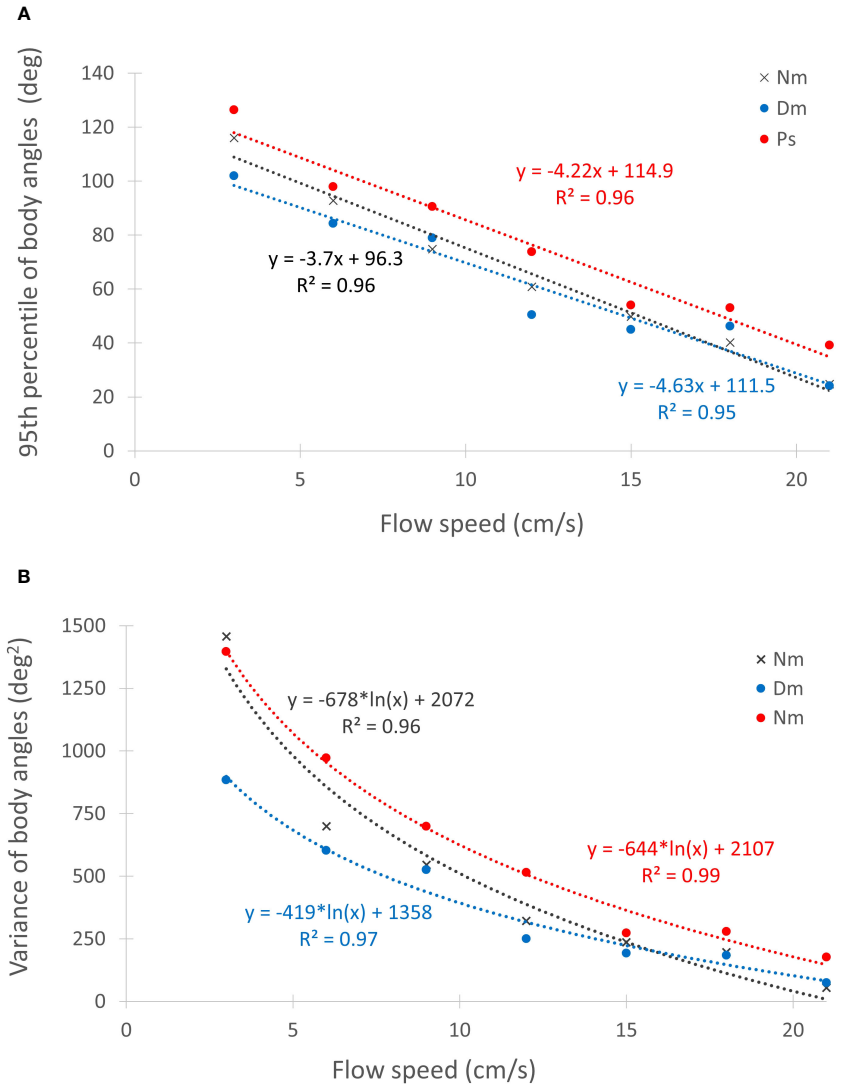

FIGURE 7
Effect of flow speed on body orientation during foraging. **(A)** - The 95th percentiles of the orientation angles under different flow speeds for the 3 different species (color coded). Linear regression equations and R^2 values are indicated next to each line using the same coded colors. Angles exceeding 90° under weak flows indicate down-current orientations. **(B)** - The corresponding variance of the orientation angles and their respective logarithmic regression lines. Regression equations and R^2 values are color-coded as in **(A)**. For statistics see Table 3.

On a much larger scale, McLean et al. (2021) found that similar environments host similar trait compositions in reef fish assemblages across the world despite the species' separation by thousands of kilometers and millions of years of evolution. Thus, environmental conditions have likely shaped global patterns in reef fish traits regardless of geography, species identity, or evolutionary history (Bellwood et al., 2017), as observed among the different species explored in our study. This similarity, together with ample evidence that such planktivorous fishes are generalist feeders (Hobson, 1991; Noda et al., 1992; A. Genin unpublished data), suggest that feeding biology is not the principal contributor to the separation of their niches. Other factors such as waves, biomechanical constraints imposed by rapid currents and waves (Fulton et al., 2005; Finelli et al., 2009), different types of shelters the fishes use, and their own exposure to predation (e.g., Hixon, 1991; Hixon and Beets, 1993; Holbrook and Schmitt, 2002) and parasites (e.g., Mikheeva et al., 2020) may have a greater role in determining the habitats the species occupy. For example, *Dm* is an obligatory resident of live branching corals (Fricke, 1980; Goldshmid et al., 2004), rendering their group sizes limited by the size of the home coral. Therefore, this species cannot form groups of hundreds of individuals, as *Ps* and *Nm* do because they occupy large rocky substrates and knolls. Nevertheless, in both types of habitats the fish use a similar rheotactic behavior and exhibit similar responses to changes in prey density and flow speed.

On the other hand, some of the inter-specific differences observed in this study, however small, can contribute to the understanding of the fishes' adaptations to different types of habitats. For example, differences in predation rates under different flow speeds (Figure 4) indicate that *Nm* is best adapted to conditions of slow currents while *Ps* to fast currents. This conclusion agrees well with our extensive, qualitative survey carried out in exposed and sheltered coral reefs around the Straits of Tiran in the southern Gulf of Aqaba (Genin et al., 1994). While in the exposed reefs (mean current speed of ~40 cm/s), *Ps* flourishes, no *Nm* is found at those sites. Both species are similarly abundant at sheltered habitats (10-15 cm/s) throughout the Gulf.

A saturation of predation rates under conditions of high prey densities is expected under the classical model of functional response (Holling, 1959). However, no saturation was apparent in our experiments (Figure 2). The most likely explanation is that the range of prey densities we used (210-1050 m^{-3}) did not reach a saturation level. Higher densities sometimes occur over coral reefs, both in Eilat (Holzman et al., 2005) and elsewhere (Noda et al., 1992).

The functional response model characterizes the rates of predation as function of prey density (Holling, 1959; Denny, 2014). There, the density of the prey determines the rate at which a predator encounters prey through a coefficient α, relating capture rate (C) to prey density (N). This scenario applies to predators that actively search for prey across some area or space. Different mechanisms are likely for predators in which prey encounter depends on additional parameters, such as flow speed. Examples include a flow-depended feeding by passive suspension feeders such as crinoids (Leonard et al., 1988) and corals (Sebens and Johnson, 1991; Fabricius et al., 1995) and by site-attached fishes (Kiflawi and Genin, 1997; O'Brien et al., 2001; Clarke et al., 2009; Finelli et al., 2009). Therefore, our findings (Figure 4) that flow speed only had a minor effect on predation rates were surprising. The major effect of prey density on the fish's functional response (Figure 2), render those fish similar to active, terrestrial predators for which the classical functional response model had been developed. That flow had such a small effect of the fish's functional response (Figure 4), requires an explanation.

A simple explanation was suggested by Kiflawi and Genin, 1997, based on their observation that the fish's body orientations to the right and left of the oncoming current became more narrowly distributed around the flow direction as flow speed increased (O'Brien et al., 2001). That is, the "aperture" through which the prey drifts into the fish's foraging space shrinks as flow becomes stronger. This conclusion was corroborated by our observations, using the 95th percentile of the fish orientation angles (Figure 7A). When such shrinking occurs, an "*effective*" flux should be considered for each flow speed; that is, the flux through the actual, flow-dependent size of the aperture. This idea was tested in our companion paper (Ella and Genin, 2023), indicating that the above explanation applies for *Dm*, but not for *Ps* and *Nm*. In fact, in *Nm* predation rates decreased when the flow speed exceeded 9 cm/s despite a corresponding increase in the *effective* flux. Obviously, mechanisms other than the shrinkage of the aperture should be considered in order to explain the absence of flow-driven increase in predation rates. An alternative explanation is related to the fish's maneuverability during its foraging movements. If turnings to the left or right of the oncoming current becomes bio-mechanically more limited as flow speed increases, it may restrict the ability of the fish to turn sufficiently fast in order to strike a prey that appears far on its right (or left). Figure 7 showed that wide turns (>70°) with respect to the flow direction rarely occurred when the flow was stronger than 15 cm/s. The close similarity between the logarithmic slopes of the declines in the "maneuverability" and the capture efficiency (Figure 5) supports this explanation. In other words, under the assumption that the variance in the orientation angle can be used as a proxy of foraging maneuverability, the sharp decrease in that maneuverability with increasing flow speeds can explain the absence of increasing predation rates under higher prey fluxes.

An additional explanation refers to the time a fish would need to strike the "next prey". *In situ* observations of prey strikes by *Dm* made by Engel et al. (2021) indicated that under strong currents of 13-17 and >17 cm/s, almost all strikes (95th and 100%, respectively) targeted prey that was found up-current relative to the strikes' initiation points. Therefore, we suggest that a fish would avoid striking a "next" prey, once it drifted past (down-current of) its present location. Occurrence of such "pass-over" cases become more likely under higher flow speeds. Figure 2 of Ella and Genin (2023) shows that under flow speeds of 15 and 20 cm/s, the mean duration of a strike by *Nm*, *Ps*, and *Dm* is ~380 ms, or a maximum of 2.6 prey/s when prey are caught continuously, one after the other. Under prey density of 630 m^{-3} and flow speed of 15 cm/s, the flux of prey across the flume (0.3 X 0.3 m) is ~8.5 s^{-1}, whereas under a slower flow (3 cm/s) and the same prey density the flux is 1.7 s^{-1}. This difference means that under a continuous series of strikes, the fish would be able to capture all the prey drifting by it under the weaker flow (3 cm/s) and higher density (630 m^{-3}) but only ~30% of the flux under the stronger flow.

Likely, each of the three explanations suggested above can contribute to the observation that the functional responses of the fish we studied does not depend on prey flux, only on prey density. In our opinion, based on a visualization of the fish foraging movements (Video S1), the shrinking aperture and the reduced maneuverability contribute the most.

Several caveats should be considered. The first, as mentioned above, is our use of *Artemia* nauplii as prey. Those nauplii are poor swimmers and do not use an escape response, as copepods do (Trager et al., 1994). Copepods are the dominant taxon in the diet in fishes belonging to the guild of the species we studied (Hobson, 1991; Noda et al., 1992; A. Genin unpublished observations). The advantage of using those readily available nauplii was their similarity in size and general morphology to the fish's natural prey and the uniformity of the prey used in different trials. A second caveat is introduced by our use of a single fish at a time. In nature, all those fish live in social groups, never alone. Our attempts to add more fish to the flume failed because they always incited enduring aggressive interactions, inhibiting predation by both subordinate and dominant individuals. A third caveat that should be considered is our use of a flume with walls that could restrict the fish movements. Obviously, the use of a flume was the only way to independently control flow speed and prey density. On the other hand, the use of a flume with a 30 X 30 cm cross section seems to introduce some, however not an extreme restriction on the foraging of fish in which prey strikes are, on average, 2-6 cm long (Ella and Genin, 2023).

Taken together, those 3 caveats render our results pertinent to the mechanisms underlying the effects of flow speed and prey density, rather than the absolute values of predation rates that are found in situ. While we are confident that the nearly linear increase in predation rate with increasing prey density (Figure 2) holds under *in-situ* conditions, the slope of that increase and the predation-rate values may be different.

Our study provides the most extensive quantitative information to-date on predation rates by zooplanktivorous coral-reef fishes and the effects of prey density and flow speed on those rates. The rapid advent of ocean optics, including an *in-situ* visualization of zooplankton (Orenstein et al., 2020; Robinson et al., 2021), together with recent advances in computerized tracking of fish *in situ* (Engel et al., 2021), assure the prospects of extending our flume study to *in-situ* conditions.

Data availability statement

The raw data supporting the conclusions of this article will be made available by the authors, without undue reservation.

Ethics statement

The animal study was approved by (1) Israel Nature & Parks Authority and by (2) The ethical committee of animal treatment at the Hebrew University of Jerusalem. The study was conducted in accordance with the local legislation and institutional requirements.

Author contributions

AG: Conceptualization, Formal analysis, Funding acquisition, Investigation, Methodology, Project administration, Resources, Supervision, Validation, Visualization, Writing – original draft, Writing – review & editing. SR: Conceptualization, Formal analysis, Investigation, Methodology, Writing – original draft. MZ: Data curation, Formal analysis, Investigation, Methodology, Validation, Writing – original draft, Writing – review & editing. MK: Conceptualization, Formal analysis, Investigation, Methodology, Supervision, Writing – review & editing.

Funding

The author(s) declare financial support was received for the research, authorship, and/or publication of this article. Israel Science Foundation (ISF) grants 576/96, 455/99, 1211/14.

Acknowledgments

We thank Moty Ohevia for his extensive assistance with the flume, video recording, and other technical tasks. For discussions and comments, we thank R. Holzman, O. Ben-Tzvi, D. Cohencius, S. Eckstein, B. Farstey, R. Goldshmid, R. Kent, S. Sabah, R. Yahel, G. Yahel, D. Genin, and two reviewers. We are indebted to the staff of the Interuniversity Institute (IUI) for general support and logistics and to the Underwater Observatory Park for their help in collecting the fish at the reef. Finally, we thank the Israel Science Foundation for their continuous support.

Conflict of interest

The authors declare that the research was conducted in the absence of any commercial or financial relationships that could be construed as a potential conflict of interest.

Publisher's note

Supplementary material

The Supplementary Material for this article can be found online at: https://www.frontiersin.org/articles/10.3389/fmars.2024.1330477/full#supplementary-material

References

Allgeier, J. E., and Cline, T. J. (2019). Comment on "Demographic dynamics of the smallest marine vertebrates fuel coral reef ecosystem functioning". *Science* 366. doi: 10.1126/science.aay9321

Begon, M., Townsend, C. R., and Harper, J. L. (2006). *Ecology: From Individuals to Ecosystems* (New York: Wiley).

Bellwood, D. R., Goatley, C. H. R., and Bellwood, O. (2017). The evolution of fishes and corals on reefs: Form, function and interdependence. *Biol. Rev.* 92, 878–901. doi: 10.1111/brv.12259

Benayahu, Y., and Loya, Y. (1977). Space partitioning by stony corals soft corals and benthic algae on the coral reefs of the northern Gulf of Eilat (Red Sea). *Helgol. Wiss. Meer.* 30, 362–382. doi: 10.1007/BF02207848

Booth, D. J. (2016). Ability to home in small site-attached coral reef fishes. *J. Fish Biol.* 89, 1501–1506. doi: 10.1111/jfb.13043

Brandl, S. J., Tornabene, L., Goatley, C. H. R., Casey, J. M., Morais, R. A., Côté, I. M., et al. (2019). Demographic dynamics of the smallest marine vertebrates fuel coral reef ecosystem functioning. *Science* 364, 1189–1192. doi: 10.1126/science.aav3384

Bray, R. N., Miller, A. C., and Geesey, G. G. (1981). The fish connection: A trophic link between planktonic and rocky reef communities? *Science* 214, 204–205. doi: 10.1126/science.214.4517.204

Brokovich, E., Baranes, A., and Goren, M. (2006). Habitat structure determines coral reef fish assemblages at the northern tip of the Red Sea. *Ecol. Indic.* 6, 494–507. doi: 10.1016/j.ecolind.2005.07.002

Clarke, R. D., Finelli, C. M., and Buskey, E. J. (2009). Water flow controls distribution and feeding behavior of two co-occurring coral reef fishes: II. Laboratory experiments. *Cor. Reef.* 28, 475–488. doi: 10.1007/s00338-009-0479-7

Coates, D. (1980). Prey-size intake in humbug damselfish, Dascyllus aruanus (Pisces, Pomacentridae) living within social groups. *J. Anim. Ecol.* 49, 335–340. doi: 10.2307/4292

Coughlin, D. J., and Strickler, J. R. (1990). Zooplankton capture by a coral reef fish: an adaptive response to evasive prey. *Environ. Biol. Fishes.* 29, 35–42. doi: 10.1007/BF00000566

Denny, M. (2014). Buzz holling and the functional response. *Bull. Ecolog. Soc Am.* 95, 200–203. doi: 10.1890/0012-9623-95.3.200

Ella, H., and Genin, A. (2023). Capture of zooplankton by site-attached fish: striking dynamics under different flow speeds and prey paths. *Front. Mar. Sci.* 10. doi: 10.3389/fmars.2023.1327581

Engel, A., Reuben, Y., Kolesnikov, I., Churilov, D., Nathan, R., and Genin, A. (2021). *In situ* three-dimensional video tracking of tagged individuals within site-attached social groups of coral-reef fish. *Limnol. Ocean. Meth.* 19, 579–588. doi: 10.1002/lom3.10444

Erez, J. (1990). "On the importance of food sources in coral reef ecosystems," in *Coral reefs*. Ed. Z. Dubinsky (Elsevier, Amsterdam), 411–418.

Fabricius, K. E., Benayahu, Y., and Genin, A. (1995). Herbivory in asymbiotic soft corals. *Science* 268, 90–92. doi: 10.1126/science.268.5207.90

Finelli, C. M., Clarke, R. D., Robinson, H. E., and Buskey, E. J. (2009). Water flow controls distribution and feeding behavior of two co-occurring coral reef fishes: I. Field measurements. *Cor. Reef.* 28, 461–473. doi: 10.1007/s00338-009-0481-0

Fishelson, L. (1971). Ecology and distribution of the benthic fauna in the shallow waters of the Red Sea. *Mar. Biol.* 10, 113–133. doi: 10.1007/BF00354828

Fishelson, L., Popper, D., and Avidor, A. (1974). Biosociology and ecology of pomacentrid fishes around the Sinai Peninsula (northern Red Sea). *J. Fish Biol.* 6, 119–133. doi: 10.1111/j.1095-8649.1974.tb04532.x

Fricke, H. W. (1977). Community structure, social organization and ecological requirements of coral reef fish (Pomacentridae). *Helgol. Wiss. Meer.* 30, 412–426. doi: 10.1007/BF02207851

Fricke, H. W. (1980). Control of different mating systems in a coral reef fish by one environmental factor. *Anim. Behav.* 28, 561–569. doi: 10.1016/S0003-3472(80)80065-0

Fulton, C. J., Bellwood, D. R., and Wainwright, P. C. (2005). Wave energy and swimming performance shape coral reef fish assemblages. *Proc. R. Soc B* 272, 827–832. doi: 10.1098/rspb.2004.3029

Gahan, J., Bellwood, D. R., Nankervis, L., and Tebbett, S. B. (2023). Spatial and temporal variability in tropical off-reef zooplankton across broad spatial and temporal scales. *Mar. Env. Res.* 191. doi: 10.1016/j.marenvres.2023.106169

Gaines, S. D., and Roughgarden, J. (1987). Fish in offshore kelp forests affect recruitment to intertidal barnacle populations. *Science* 235, 479–478. doi: 10.1126/science.235.4787.479

Genin, A., Gal, G., and Haury, L. (1995). Copepod carcasses in the ocean. II. Near coral reefs. *Mar. Ecol. Prog. Ser.* 123, 65–71. doi: 10.3354/meps123065

Genin, A., Karp, L., and Miroz, A. (1994). Effects of flow on competitive superiority in scleractinian corals. *Limn. Ocean.* 39, 913–924. doi: 10.4319/lo.1994.39.4.0913

Genin, A., Monismith, S. G., Reidenbach, M. A., Yahel, G., and Koseff, J. R. (2009). Intense benthic grazing of phytoplankton in a coral reef. *Limn. Ocean.* 54, 938–951. doi: 10.4319/lo.2009.54.3.0938

Genin, A., and Paldor, N. (1998). Changes in the circulation and current spectrum near the tip of the narrow, seasonally mixed, Gulf of Elat. Isr. *J. Earth Sci.* 47, 87–92.

Goldshmid, R., Holzman, R., Weihs, D., and Genin, A. (2004). Aeration of corals by sleep-swimming fish. *Limn. Ocean.* 49, 1832–1839. doi: 10.4319/lo.2004.49.5.1832

Hamner, W. M., Jones, M. S., Carleton, J. H., Hauri, I. R., and Williams, D.M. (1988). Zooplankton, Planktivorous Fish, and water currents on a Windward Reef Face: great barrier reef, Australia. *Bull. Mar. Sci.* 42, 459–479.

Hanson, K. M., Schnarr, E. L., and Leichter, J. J. (2016). Non-random feeding enhances the contribution of oceanic zooplankton to the diet of the planktivorous coral reef fish *Dascyllus flavicaudus*. *Mar. Biol.* 163, 77. doi: 10.1007/s00227-016-2849-3

Hixon, M. A. (1991). "Predation as a process structuring coral-reef fish communities," in *The ecology of fishes on coral reefs*. Ed. P. Sale (San Diego, USA: Academic Press). doi: 10.1016/C2009-0-02443-X

Hixon, M. A., and Beets, J. P. (1993). Predation, prey refuges, and the structure of coral-reef fish assemblages. *Ecol. Mon.* 63, 77–101. doi: 10.2307/2937124

Hobson, E. S. (1991). "Trophic relationships of fishes specialized to feed on zooplankters above coral reefs," in *The ecology of fishes on coral reefs*. Ed. P. Sale (San Diego, USA: Academic Press). doi: 10.1016/C2009-0-02443-X

Holbrook, S. J., and Schmitt, R. J. (2002). Competition for shelter space causes density-dependent predation mortality in damselfishes. *Ecology* 83, 2855–2868. doi: 10.1890/0012-9658(2002)083[2855:CFSSCD]2.0.CO;2

Holling, C. S. (1959). Some characteristics of simple types of predation and parasitism. *Canad. Entom.* 91, 385–398. doi: 10.4039/Ent91385-7

Holzman, R., and Genin, A. (2003). Zooplanktivory by a nocturnal coral-reef fish: Effects of light, flow, and prey density. *Limnol. Ocean.* 48, 1367–1375. doi: 10.4319/lo.2003.48.4.1367

Holzman, R., Reidenbach, M. A., Monismith, S. G., Koseff, J. R., and Genin, A. (2005). Near-bottom depletion of zooplankton over a coral reef: II. Relationships with zooplankton swimming ability. *Cor. Reef.* 24, 87–94. doi: 10.1007/s00338-004-0450-6

Ishikawa, K., Wu, H., Mitarai, S., and Genin, A. (2022). Effects of prey density and flow speed on plankton feeding by garden eels: A flume study. *J. Exp. Biol.* 225, 1–10. doi: 10.1242/jeb.243655

Khalaf, M. A., Al-Horani, F. A., Al-Rousan, S. A., and Manasrah, R. S. (2006). Community structure of the family Pomacentridae along the Jordanian coast, Gulf of Aqaba, Red Sea. *Zool. Mid. East* 37, 47–62. doi: 10.1080/09397140.2006.10638148

Khalaf, M. A., and Kochzius, M. (2002). Community structure and biogeography of shore fishes in the Gulf of Aqaba, Red Sea. in the Gulf of Aqaba, Red Sea. *Helgol. Wiss. Meer.* 55, 252–284. doi: 10.1007/s10152-001-0090-y

Khrizman, A., Kolesnikov, I., Churilov, D., and Genin, A. (2024). Zooplanktivory in garden eels: benefits and shortcomings of being "anchored" compared with other coral-reef fish. *Front. Mar. Sci.* 10. doi: 10.3389/fmars.2024.1330379

Khrizman, A., Ribak, G., Churilov, D., Kolesnikov, I., and Genin, A. (2018). Life in the flow: Unique adaptations for feeding on drifting zooplankton in garden eels. *J. Exp. Biol.* 221. doi: 10.1242/jeb.179523

Kiflawi, M., and Genin, A. (1997). Prey flux manipulation and the feeding rates of reef-dwelling planktivorous fish. *Ecology* 78, 1062–1077. doi: 10.1890/0012-9658(1997)078[1062:PFMATF]2.0.CO;2

Kingsford, M. J., and MacDiarmid, A. B. (1988). Interrelations between planktivorous reef fish and zooplankton in temperate waters. *Mar. Ecol. Prog. Ser.* 48, 103–117. doi: 10.3354/meps048103

Leonard, A. B., Strickler, J. R., and Holland, N. D. (1988). Effects of current speed on filtration during suspension feeding in *Oligometra serripinna* (Echinodermata: Crinoidea). *Mar. Biol.* 97, 111–125. doi: 10.1007/BF00391251

McLean, M., Stuart-Smith, R. D., Villéger, S., Auber, A., Edgar, G. J., MacNeil, M. A., et al. (2021). Trait similarity in reef fish faunas across the world's oceans. *Proc. Nat. Acad. Sci.* 118, 1–10. doi: 10.1073/pnas.2012318118

Megdadi, J. M., Khalaf, M. A., Al-Horani, F. A., and Manasrah, R. S. (2017). Community structure of coral reef fishes in relation to habitat and depth in the northern Gulf of Aqaba, Red Sea. *Fres. Env. Bull.* 26, 1824–1834.

Mihalitsis, M., Morais, R. A., and Bellwood, D. R. (2022). Small predators dominate fish predation in coral reef communities. *PloS Biol.* 20, e3001898. doi: 10.1371/journal.pbio.3001898

Mikheeva, V. N., Zhokhovb, A. E., and Britaeva, T. A. (2020). Macroparasite burden of obligate and facultative symbionts in symbiotic communities of scleractinian corals. *Biol. Bull. Rev.* 10, 456–463. doi: 10.1134/S2079086420050059

Monismith, S. G., and Genin, A. (2004). Tides and sea level in the Gulf of Aqaba (Eilat). *J. Geo. Res.* 109, C04015. doi: 10.1029/2003JC002069

Morais, R. A., and Bellwood, D. R. (2019). Pelagic subsidies underpin fish productivity on a degraded coral reef. *Curr. Biol.* 29, 1521–1527. doi: 10.1016/j.cub.2019.03.044

Morais, R. A., Siqueira, A. C., Smallhorn-West, P. F., and Bellwood, D. R. (2021). Spatial subsidies drive sweet spots of tropical marine biomass production. *PloS Biol.* 19, e3001435. doi: 10.1371/journal.pbio.3001435

Noda, M., Kawabata, K., Gushima, K., and Kakuda, S. (1992). Importance of zooplankton patches in foraging ecology of the planktivorous reef fish Chromis chrysurus (Pomacentridae) at Kuchinoerabu Island, Japan. *Mar. Ecol. Prog. Ser.* 87, 251–263. doi: 10.3354/meps087251

Nonacs, P., Smith, P. E., Bouskila, A., and Luttbeg, B. (1994). Modeling the behavior of the northern anchovy, Engraulis mordax, as a schooling predator exploiting patchy prey. *Deep-Sea Res.* 41, 147–169. doi: 10.1016/0967-0645(94)90065-5

O'Brien, W. J., Barfield, M., and Sigler, K. (2001). The functional response of drift-feeding Arctic grayling: the effects of prey density, water velocity, and location efficiency. *Can. J. Fish. Aquat. Sci.* 58, 1957–1963. doi: 10.1139/f01-138

Odum, H. T., and Odum, E. P. (1955). Trophic structure and productivity of a windward coral reef community on Eniwetok Atoll. *Ecol. Monog.* 25, 291–320. doi: 10.2307/1943285

Orenstein, E. C., Ratelle, D., Briseño-Avena, C., Carter, M. L., Franks, P. J. S., Jaffe, J. S., et al. (2020). The Scripps Plankton Camera system: A framework and platform for in *situ* microscopy. *Limnol. Ocean. Meth.* 18, 681–695. doi: 10.1002/lom3.10394

Reidenbach, M. A., Monismith, S. G., Koseff, J. R., Yahel, G., and Genin, A. (2006). Boundary layer turbulence and flow structure over a fringing coral reef. *Limnol. Ocean.* 51, 1956–1968. doi: 10.4319/lo.2006.51.5.1956

Robinson, K. L., Sponaugle, S., Luo, J. Y., Gleiber, M. R., and Cowen, R. K. (2021). Big or small, patchy all: Resolution of marine plankton patch structure at micro- to submesoscales for 36 taxa. *Sci. Adv.* 7, (47). doi: 10.1126/sciadv.abk2904

Sale, P. F. (1971). Extremely limited home range in a coral reef fish, *dascyllus aruanus* (Pisces; pomacentridae). *Copeia* 1971, 324–327. doi: 10.2307/1442839

Sebens, K. P., and Johnson, A. S. (1991). Effects of water movement on prey capture and distribution of reef corals. *Hydrobiol* 226, 91–101. doi: 10.1007/BF00006810

Shaked, Y., and Genin, A. (2023). *The Israel National Monitoring Program in the Northern Gulf of Aqaba – scientific report* (Jerusalem, Israel: Israel Ministry of Environmental Protection). Available at: https://iui-eilat.huji.ac.il/uploaded/NMP/reports/NMP%20Report%202022.pdf.

Shapiro, D. Y., and Lubbock, R. (1980). Group sex ratio and sex reversal. *J. Theor. Biol.* 83, 411–426. doi: 10.1016/0022-5193(80)90048-X

Siqueira, A. C., Morais, R. A., Bellwood, D. R., and Cowman, P. F. (2021). Planktivores as trophic drivers of global coral reef fish diversity patterns. *Proc. Nat. Acad. Sci.* 118, e2019404118. doi: 10.1073/pnas.2019404118

Trager, G., Achituv, Y., and Genin, A. (1994). Effects of prey escape ability, flow speed, and predator feeding mode on zooplankton capture by barnacles. *Mar. Biol.* 120, 251–259. doi: 10.1007/BF00349685

Wainwright, P., Carroll, A. M., Collar, D. C., Day, S. W., Higham, T. H., and Holzman, R. A. (2007). Suction feeding mechanics, performance, and diversity in fishes. *Integ. Comp. Biol.* 47, 96–106. doi: 10.1093/icb/icm032

Wyatt, A. S. J., Lowe, R. J., Humphries, S., and Waite, A. M. (2010). Particulate nutrient fluxes over a fringing coral reef: Relevant scales of phytoplankton Production and mechanisms of supply. *Mar. Ecol. Prog. Ser.* 405, 113–130. doi: 10.3354/meps08508

Yahel, G., Post, A. F., Fabricius, K., Marie, D., Vaulot, D., and Genin, A. (1998). Phytoplankton distribution and grazing near coral reefs. *Limnol. Ocean.* 43, 551–563. doi: 10.4319/lo.1998.43.4.0551

frontiers | Frontiers in Marine Science

TYPE Review
PUBLISHED 02 April 2024
DOI 10.3389/fmars.2024.1331164

OPEN ACCESS

EDITED BY
Marco Ghisalberti,
University of Western Australia, Australia

REVIEWED BY
Jeff Shimeta,
RMIT University, Australia
Karly Cohen,
University of Florida, United States

*CORRESPONDENCE
S. Laurie Sanderson
slsand@wm.edu

RECEIVED 31 October 2023
ACCEPTED 15 March 2024
PUBLISHED 02 April 2024

CITATION
Sanderson SL (2024) Particle separation mechanisms in suspension-feeding fishes: key questions and future directions.
Front. Mar. Sci. 11:1331164.
doi: 10.3389/fmars.2024.1331164

Particle separation mechanisms in suspension-feeding fishes: key questions and future directions

S. Laurie Sanderson*

Department of Biology, William & Mary, Williamsburg, VA, United States

Key unresolved questions about particle separation mechanisms in suspension-feeding fishes are identified and discussed, focusing on areas with the potential for substantial future discovery. The published hypotheses that are explored have broad applicability to biological filtration and bioinspired improvements in commercial and industrial crossflow microfiltration processes and microfluidics. As the first synthesis of the primary literature on the particle separation mechanisms of marine, estuarine, and freshwater suspension-feeding fishes, the goals are to enable comparisons with invertebrate suspension-feeding processes, stimulate future theoretical and empirical studies, and further the development of biomimetic physical and computational fluid dynamics models. Of the eight particle separation mechanisms in suspension-feeding fishes, six have been proposed within the past twenty years (inertial lift and shear-induced migration, reduction of effective gap size by vortices, cross-step filtration, vortical flow along outer faces of gill raker plates, ricochet filtration, and lateral displacement). The pace of discovery is anticipated to continue accelerating. Multidisciplinary collaboration and integration among biologists and engineers (including chemical, mechanical, biomedical, and filtration engineering) will result in new perspectives to identify patterns and potential unifying mechanisms across the breadth of suspension-feeding fish taxa, morphology, and function.

KEYWORDS

suspension feeding, filter feeding, particle separation, gill rakers, crossflow filtration, microfiltration, inertial microfluidics, lateral displacement arrays

1 Introduction

Suspension-feeding (SF) fishes are of substantial ecological and economic importance. Because they feed on small suspended particles such as phytoplankton, zooplankton, and detritus but serve as prey for larger predatory fish, birds, and mammals, SF fishes are key components of marine and freshwater food webs. Approximately 25% of the annual global fish harvest is composed of SF fishes (FAO, 2021). SF fish species have been subjects of recent concern regarding microplastics in the food chain (e.g., Savoca et al., 2020; Misic et al., 2022).

Biomanipulation to improve the quality of inland waters has involved the introduction or the removal of SF fishes (review in Lürling and Mucci, 2020). In addition, biomimetic and bioinspired solutions for separation technology and water filtration are topics of intense current interest (Goel et al., 2021; Bianciardi and Cascini, 2022; Hamann and Blanke, 2022; Zhang et al., 2022b). Recent discoveries of particle separation mechanisms in SF fishes have stimulated the development of biomimetic models with potential applications in microfluidics and commercial and industrial filtration for foods and beverages, wastewater, irrigation, oil spill remediation, and biotechnology products (e.g., Dou et al., 2017; Schroeder et al., 2019; Clark and San-Miguel, 2021; Adelmann et al., 2022; Masselter et al., 2023; Xu et al., 2023).

The application of industrial aerosol filtration theory to biological hydrosol filtration (Rubenstein and Koehl, 1977) and the development of particle encounter rate models in aquatic ecosystems (Shimeta and Jumars, 1991; Espinosa-Gayosso et al., 2021) provide a valuable framework for mechanistic studies of suspension feeding. As established by Shimeta and Jumars (1991), particle encounter (i.e, "initial contact of the particle and the feeding structure, regardless of retention") is distinct conceptually from particle capture. Inertial impaction and/or direct interception have been identified as particle encounter mechanisms in SF fishes (e.g., Sanderson et al., 1996b; Paig-Tran et al., 2011; Divi et al., 2018; Witkop et al., 2023). Rather than reviewing these particle encounter mechanisms that result in the initial contact between the particle and the filter element, this article focuses on a comprehensive analysis of particle separation mechanisms that could result in the concentration of particles within the oral cavity, including sieving, mucus entrapment, inertial lift and shear-induced migration, reduction of effective gap size by vortices, cross-step filtration, vortical flow along outer faces of gill raker plates, ricochet filtration, and lateral displacement. The functional morphology, biomechanics, and fluid dynamic processes that cause particles to interact with the filter elements in SF fishes will be examined, and key questions and research priorities will be identified and discussed.

1.1 Scope and diversity of SF fishes

Suspension feeding can be defined as the separation of small suspended particles from volumes of water, involving both microphagy and planktivory (Jørgensen, 1966; Sanderson and Wassersug, 1993). Fish suspension feeding refers here to feeding on suspended prey ranging from single-celled bacteria and microalgae (~ 5 μm diameter) to planktonic crustaceans (~ 5 mm length) that are too small to be sensed and consumed individually (Lazarro, 1987; Sanderson and Wassersug, 1993; Gerking, 1994). Because size is relative, a whale shark with a total length of 6 m can consume multiple small fishes during SF, along with planktonic crustaceans and fish eggs (Motta et al., 2010).

Detritivorous fish species, including microphagous benthic feeders that filter edible particles from sediment suspended inside the oral cavity during a process referred to as winnowing (e.g., Weller et al., 2017; Brodnicke et al., 2022), could also be studied from the perspective of particle separation mechanisms. In contrast, fish particulate feeding involves targeting and consuming larger planktonic prey individually. However, many SF fish species are facultative suspension feeders that also use particulate feeding to consume larger prey individually, and criteria for distinguishing between suspension feeding and particulate feeding have not been established among species (Hamann et al., 2023).

SF fishes include familiar species such as goldfish and carp (Cyprinidae), menhaden (Clupeidae), paddlefish (Polyodontidae), manta and devil rays (Mobulidae), the whale shark (Rhincodontidae) and basking shark (Cetorhinidae), a number of mackerel species (Scombridae), and many tilapia (Cichlidae), herring (Clupeidae), and anchovy (Engraulidae) (Figure 1). There are as many as 21 families of SF fishes in 12 orders (Cheer et al., 2012). Sanderson and Wassersug (1993) provided a comprehensive summary on the pump and ram SF fish species from the primary literature. That list of approximately 50 species has not been updated, and there are now more than 100 additional SF fish species reported in the literature.

1.2 Anatomical framework

The filter of SF fishes consists of a network of filter elements enclosed inside the mouth, typically termed the branchial arches, gill rakers, and associated protrusions (Figure 2). The morphology of the filter elements can change substantially during ontogeny (e.g., Cohen and Hernandez, 2018). The term oral cavity will be used to refer to the entire buccal cavity and pharyngeal cavity of fishes, also called the buccopharyngeal, oropharyngeal, or orobranchial cavity. The oral cavity of most extant osteichthyan fishes and elasmobranchs has five pairs of branchial arches (BAs), also referred to as gill arches or pharyngeal arches (Nelson, 1967a; Wegner, 2015). While there is substantial variability among orders and families, in general each of the anterior five BAs has a row of bony or cartilaginous protuberances called gill rakers (GRs) on the anterolateral side of each BA. In addition, many fish species also have a row of GRs on the posteromedial side of each BA. The keratinized GRs of basking sharks (*Cetorhinus maximus*) lack epithelial tissue (Paig-Tran and Summers, 2014).

The GRs frequently have protrusions on their surfaces which can be rounded or spiny and which may be unnamed or may be termed "denticles", "branchiospinules", or "teeth" depending on the taxon and the author (e.g., "Filter Element" in Table 1 and "Dimension Measured" in Table 2). Because the genetic, developmental, and evolutionary origins of these protrusions on the gill rakers have not been studied, potential relationships between these protrusions and odontodes, oral teeth, and dermal denticles are not known (Paig-Tran and Summers, 2014; Mori and Nakamura, 2022; Cooper et al., 2023). In general, the BAs, GRs, and associated protrusions have an epithelial tissue layer with multiple cell types that can include mucus-secreting cells and taste buds (Sanderson and Wassersug, 1993).

There is no evidence that fish swallow a notable volume of water at the esophagus during SF (Provini et al., 2022). Flow that enters the mouth during SF passes between the GRs and their associated

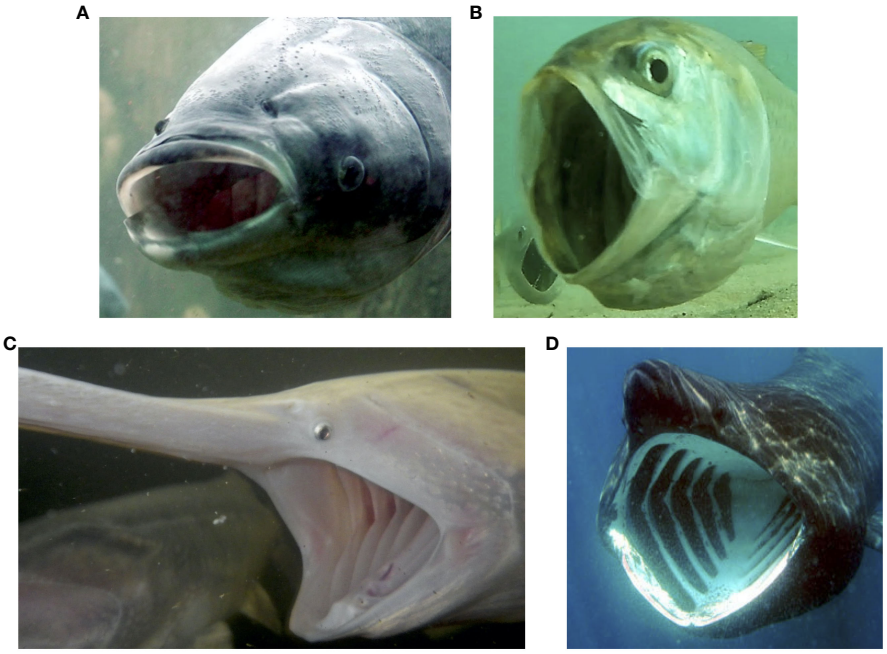

FIGURE 1
Examples of SF fish species belonging to four orders, shown during SF. **(A)** Pump SF bighead carp, *Hypophthalmichthys nobilis*, Cyprinidae, Cypriniformes. © Solomon David, used with permission, not covered by the CC BY license. **(B)** Ram SF Atlantic menhaden, *Brevoortia tyrannus*, Clupeidae, Clupeiformes. © myfishingcapecod.com, used with permission, not covered by the CC BY license. **(C)** Ram SF American paddlefish, *Polyodon spathula*, Polyodontidae, Acipenseriformes. Rob Helm, USFWS https://www.flickr.com/photos/usfwsmtnprairie/9546645557/ CC BY 2.0 https://creativecommons.org/licenses/by/2.0/ **(D)** Ram SF basking shark, *Cetorhinus maximus*, Cetorhinidae, Lamniformes. jidanchaomian https://www.flickr.com/photos/10565417@N03/6246022639, CC BY-SA 2.0 https://creativecommons.org/licenses/by-sa/2.0/.

protrusions to exit from the oral cavity into the opercular cavities (also called the branchial cavities in osteichthyan fishes) or parabranchial cavities (in elasmobranchs). In the opercular cavities, the gill filaments where gas exchange occurs are attached to the aboral (i.e., external) surfaces of the BAs. After traveling across the gill filaments, the water exits from the opercular cavities on the ventral and/or lateral sides of the head by passing beneath the bony operculum. Thus, in all SF fishes, water exits from the oral

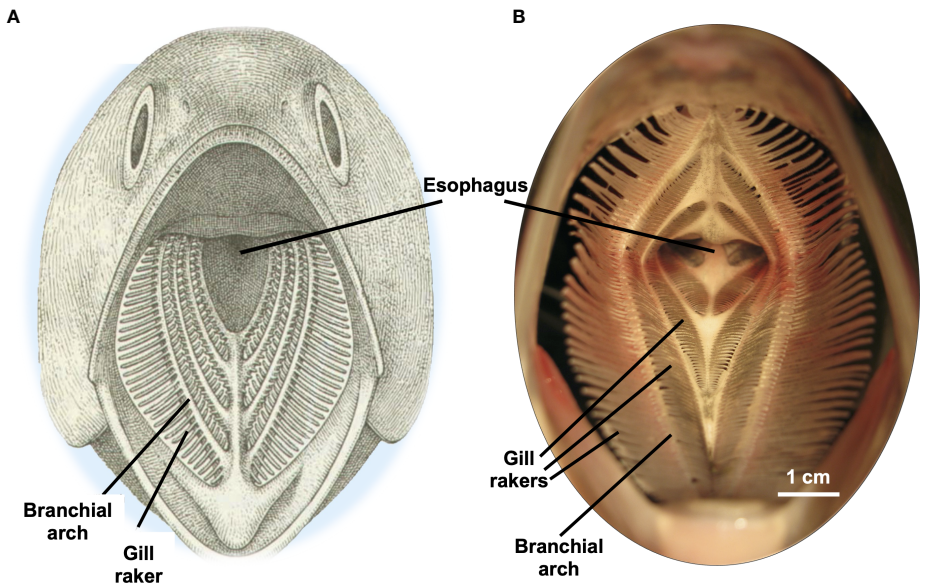

FIGURE 2
Examples of SF fish oral cavities shown in frontal view, illustrating branchial arches with gill rakers extending laterally from each branchial arch. **(A)** Generalized SF fish. Modified from Sanderson and Wassersug (1990), with permission. **(B)** American shad, *Alosa sapidissima*, Clupeidae. Modified from Witkop et al. (2023), CC BY 4.0.

TABLE 1 Compilation of reported Reynolds numbers (Re) that have been calculated at the level of the proposed filter elements in suspension-feeding (SF) fishes.

Family	Species	Common Name	Pump or Ram	Body Size	Filter Element	Filter Element Size	Flow Speed	Re	Reference
Cichlidae	*Oreochromis esculentus*	Ngege (Singida) tilapia	Pump	26 cm SL	Gill raker	250 - 1500 µm width	35 - 70 cm s^{-1}	150 - 600	Sanderson et al., 2001
Clupeidae	*Alosa sapidissima*	American shad	Ram	38 - 41 cm SL	Gill raker	1000 µm height	45 cm s^{-1}	500	Storm et al., 2020
Clupeidae	*Brevoortia tyrannus*	Atlantic menhaden	Ram	15 cm FL	Branchio-spinule	10 µm width	23 - 38 cm s^{-1}	2 - 3	Friedland, 1985
Clupeidae	*Clupea harengus*	Atlantic herring	Ram	25 cm SL	Denticle	98 µm width	34 cm s^{-1}, RF	14	Hamann et al., 2023
Clupeidae	*Dorosoma cepedianum*	Gizzard shad	Pump	29 cm SL	Gill raker	250 - 1500 µm width	35 - 70 cm s^{-1}	150 - 600	Sanderson et al., 2001
Clupeidae	*Sardina pilchardus*	Atlantic pilchard	Ram	12 cm SL	Denticle	91 µm width	41 cm s^{-1}, RF	16	Hamann et al., 2023
Clupeidae	*Sardinops sagax*	Pacific sardine	Ram	7.4 - 16.5 cm SL	Gill raker	23 - 38 µm width	7 - 24 cm s^{-1}	2 - 9	Rykaczewski, 2009
Cyprinidae	*Carassius auratus*	Goldfish	Pump	17 cm SL	Gill raker	250 - 1500 µm width	35 - 70 cm s^{-1}	150 - 600	Sanderson et al., 2001
Engraulidae	*Engraulis encrasicolus*	Atlantic anchovy	Ram	10 cm SL	Denticle	85 µm width	35 cm s^{-1}, RF	13	Hamann et al., 2023
Engraulidae	*Engraulis mordax*	Northern anchovy	Ram	7.3 - 15.0 cm SL	Gill raker	110 - 130 µm width	7 - 20 cm s^{-1}	9 - 25	Rykaczewski, 2009
Mobulidae	7 *Mobula* species	Manta and devil rays	Ram	~ 340 - 500 cm disc length	Filter lobe pore	0.36 - 3.34 mm^2 average pore area		10-350	Paig-Tran et al., 2013
Mobulidae	*Manta birostris*	Manta ray	Ram		Distance between lobes	1.7 mm	55 cm s^{-1}	1075	Divi et al., 2018
Mobulidae	*Mobula tarapacana*	Manta ray	Ram		Distance between lobes	3.63 mm	30 cm s^{-1}	1115	Divi et al., 2018
Rhinco-dontidae	*Rhincodon typus*	Whale shark	Pump and Ram	~ 600 cm TL	Reticulated mesh pore	1200 µm width		300	Motta et al., 2010
Scombridae	*Rastrelliger kanagurta*	Indian mackerel	Ram	21 cm SL	Denticle	593 µm width	47 cm s^{-1}, RF	121	Hamann et al., 2023
Scombridae	*Scomber scombrus*	Atlantic mackerel	Ram	27 cm SL	Denticle	592 µm width	50 cm s^{-1}, RF	128	Hamann et al., 2023

The column for filter element size lists the measurement of the dimension that was used for the Re calculation; flow speed is the speed used for the calculation at the level of the filter element. FL, fork length; RF, not including reduction factor of 42.3% used in Re calculation to account for hydrodynamic drag inside oral cavity; SL, standard length; TL, total length.

cavity via gaps between the GRs and associated protrusions, although the extent to which there are larger gaps between the tips of GRs on adjacent BAs or between the tips of GRs on the first BA and the internal walls of the oral cavity during SF is not known. For consistency among diverse SF animals and industrial filtration, the gaps will be referred to here as pores, with the important caveat that the gaps between the filter elements of SF fishes tend to have the three-dimensional shape of elongated slots with a height as well as a width and length (Sanderson et al., 2016; Storm et al., 2020). Multi-species analyses of the 2D and 3D shapes for pores between the filter elements of SF fishes have not been conducted (but see Hamann et al., 2023, for 2D mesh shapes and sizes).

The ecological and morphological diversity of SF fishes extends to the level of the smallest filter elements: the GRs and associated protrusions (Figure 3). Comprehensive ultrastructural comparisons of the locations and morphology of GRs and their protrusions in multiple taxa are rare for SF or non-SF fishes (but see extensive morphological and functional analyses of Hamann et al., 2023, and compilation of published studies in Storm et al., 2020). The degree of detail needed for physical and computational models necessitates the use of scanning electron microscopy, histology, confocal microscopy, and/or micro-CT scanning, ideally including quantitative data on size and shape changes resulting from preservation and preparation or from limitations in resolving soft tissues (e.g., in micro-CT). Such data are lacking for almost all SF fish species (but see Paig-Tran et al., 2013; Paig-Tran and Summers, 2014; Cohen and Hernandez, 2018).

TABLE 2 Pore sizes reported between filter elements in SF fishes.

Family	Species	Common Name	Pump or Ram	Body Size	Dimension Measured	Pore Size	Reference
Cichlidae	*Oreochromis niloticus*	Nile tilapia	Pump	14 - 23 cm	Mean distance between GRs on BAs 1-4	340 - 500 µm	Ibrahim et al., 2015
Clupeidae	*Alosa sapidissima*	American shad	Ram	38 - 41 cm SL	Mean distance between denticles for each of five BAs	200 - 340 µm	Storm et al., 2020
Clupeidae	*Brevoortia tyrannus*	Atlantic menhaden	Ram	3.4 - 32.6 cm FL	Mean distance between branchiospinules on BAs 1-4	12 - 37 µm	Friedland et al., 2006
Clupeidae	*Clupea harengus*	Atlantic herring	Ram	29 cm TL	Mean minimum distance between denticles on BA 1	323 µm	Collard et al., 2017
Clupeidae	*Clupea harengus*	Atlantic herring	Ram	2.5 - 30 cm TL	Mean distance between GRs on BA 1	90 - 470 µm	Gibson, 1988
Clupeidae	*Dorosoma cepedianum*	Gizzard shad	Pump	5 - 25 cm SL	Cumulative frequency distributions of distances between GRs on BAs 1-5	~ 30 - 110 µm	Mummert and Drenner, 1986
Clupeidae	*Sardina pilchardus*	Sardine	Ram	21 cm TL	Mean minimum distance between denticles on BA 1	214 µm	Collard et al., 2017
Clupeidae	*Sardinops sagax*	Pacific sardine	Ram	8 - 16 cm SL	Distance between GRs on BA 1	190 - 280 µm	Rykaczewski, 2009
Cyprinidae	*Abramis brama*	Common bream	Pump	25 - 33 cm SL	Distance between GR ridges on BAs 1-5	~ 1000 µm	Hoogenboezem et al., 1991
Engraulidae	*Engraulis encrasicolus*	European anchovy	Ram	15 cm TL	Mean minimum distance between denticles on BA 1	216 µm	Collard et al., 2017
Engraulidae	*Engraulis mordax*	Northern anchovy	Ram	8 - 14 cm SL	Distance between GRs on BA 1	270 - 470 µm	Rykaczewski, 2009
Mobulidae	7 *Mobula* species	Manta and devil rays	Ram	~ 340 - 500 cm DL	Filter lobe pores on BA 3	0.36 - 3.34 mm^2 average pore area	Paig-Tran et al., 2013
Mobulidae	*Manta birostris*	Manta ray	Ram		Filter lobe pores	340 µm	Divi et al., 2018
Mobulidae	*Mobula tarapacana*	Manta ray	Ram		Filter lobe pores	1100 µm	Divi et al., 2018
Poly-odontidae	*Polyodon spathula*	American paddlefish	Ram	27 - 85.5 cm EFL	Mean distance between GRs in middle of BA 1	~ 40 - 65 µm	Rosen and Hales, 1981
Rhinco-dontidae	*Rhincodon typus*	Whale shark	Pump/Ram	593 - 622 cm TL	Mean reticulated mesh size, all filtering pads	900 - 1400 µm	Motta et al., 2010

Although the gaps between the filter elements are referred to here as two-dimensional pores, such gaps in SF fishes tend to have the three-dimensional shape of slots with a height as well as a width and length. Filter element height has been reported rarely. BA, branchial arch; DL, disc length; EFL, eye-to-fork length; FL, fork length; GR, gill raker; SL, standard length; TL, total length.

1.3 Filter media and particle separation

There is an important functional distinction between (1) SF animals in which all fluid passes through the filter medium due to the enclosure of the filter either within the mouth (e.g., fish, baleen whales) or within another body cavity (e.g., ascidians, bivalves) versus (2) the many SF invertebrate taxa in which water is not constrained to pass through the filter medium, i.e., the water can travel around the margins of the filter (e.g., cnidarians, crinoids, bryozoans) (Sanderson and Wassersug, 1993; Hamann and Blanke, 2022).

In many SF invertebrate taxa that have an unenclosed filter, particle capture requires contact (i.e., encounter) with a filter element such as a sticky mucus-covered tentacle or appendage on which the particle is then retained (Rubenstein and Koehl, 1977; Shimeta and Jumars, 1991). In contrast, because the filter medium of fish is enclosed inside the mouth, particles may remain suspended while traveling to the posterior of the mouth with minimal or no contact on the filter (Sanderson et al., 2001; Cheer et al., 2012). Alternatively in SF fishes, particles may contact the filter repeatedly by rolling or bouncing posteriorly (Divi et al., 2018; Witkop et al., 2023). Thus, unlike the case in many SF invertebrates, particle separation in SF fishes may occur without particle contact and/or without particle capture on the filter elements.

Throughout the biological and industrial filtration literature, there are inconsistencies in the definitions and uses of the terms filtration versus particle separation. Here, the more inclusive term particle separation will be used to refer broadly to solid-liquid separation processes that result in the retention and concentration of particles but do not necessarily involve particle capture on a

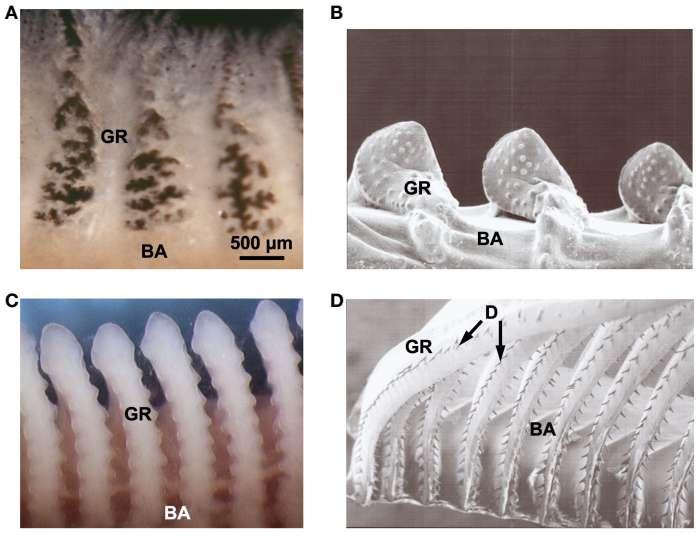

FIGURE 3
Examples of gill rakers in SF fish species belonging to three orders, shown in frontal view. **(A)** Pump SF Sacramento blackfish, *Orthodon microlepidotus*, Cyprinidae, Cypriniformes (fresh specimen). **(B)** Pump SF Singida tilapia (ngege), *Oreochromis esculentus*, Cichlidae, Cichliformes (scanning electron microscopy, SEM). **(C)** Pump SF goldfish, *Carassius auratus*, Cyprinidae, Cypriniformes (fresh specimen). **(D)** Ram SF American shad, *Alosa sapidissima*, Clupeidae, Clupeiformes (SEM). 500 µm scale bar refers to all images. BA, branchial arch; D, denticles; GR, gill raker.

porous filter. While industrial and biomedical particle separation mechanisms can involve the passage of water through a porous filter medium often referred to as a membrane (e.g., Chew et al., 2020), particle separation can alternatively involve the passage of water through microfluidic devices and other non-porous pipes or channels that have solid walls instead of a filter medium (e.g., Tang et al., 2022; Lee et al., 2023). As discussed in later sections for SF fishes, most but not all proposed particle separation mechanisms involve the simultaneous passage of water through the filter medium, with the branchial arches, gill rakers, and associated protrusions serving as the filter.

2 Pump versus ram suspension feeding and pulsatile or oscillatory flow

Sanderson and Wassersug (1993) identified four categories of vertebrate suspension feeders based on the methods used to transport water into the mouth. Here, SF fishes will be referred to as either pump suspension feeders ("intermittent suction feeders") or ram suspension feeders ("continuous ram feeders"), depending on the method of generating water flow through the oral and opercular cavities (Sanderson and Wassersug, 1993).

The functional morphology and hydrodynamics of pump SF appear similar to suction feeding in fish, but pump SF consists of a series of repetitive pumps. Pump suspension feeders either remain stationary or swim forward slowly while pumping. In contrast, ram (also referred to as "tow-net", Lazarro, 1987) suspension feeders swim forward with an open mouth to engulf water continuously as the filtrate exits from beneath the flared opercular bones. At intervals ranging from seconds to minutes, pump SF and ram SF are interrupted by prey processing movements that are thought to transport, aggregate, and/or enable swallowing of prey (e.g., Sanderson et al., 1991; Sanderson et al., 1996b; Hamann et al., 2023).

Experiments using high-speed endoscopic videos, thermistor flow probes, pressure transducers, and high-speed X-ray particle tracking have established that flow through fish oral cavities during SF is pulsatile and/or oscillatory (e.g., Sanderson et al., 1991, Sanderson et al., 1994; Callan and Sanderson, 2003; Haines and Sanderson, 2017; Provini et al., 2022). Pulsatile flow involves repetitive cycles of increasing and subsequently decreasing flow speed, whereas oscillatory flow is defined by periodic reversals in flow direction. In pump SF species, these dynamic flows are caused by changes in oral cavity volume as the BAs abduct and adduct in three dimensions, resulting in flow reversals (i.e., from posterior to anterior) that contribute to particle and mucus suspension and transport (Sanderson et al., 1996b; Smith and Sanderson, 2008; Provini et al., 2022). As ram SF species swim forward with an open mouth, locomotor kinematics, particularly yaw and heave, cause pulsatile fluctuations in intra-oral flow speeds and pressures that reduce clogging (Haines and Sanderson, 2017). CFD simulations of fish SF that incorporate the underlying kinematics are problematic and few physical models have explored dynamic flow (Haines and Sanderson, 2017; Schroeder et al., 2019). This is a promising area for further research, as pulsatile and oscillatory flow have been shown to delay clogging in microfluidics and crossflow membrane microfiltration (e.g., Wang et al., 2021; Dincau et al., 2022).

3 Fundamental differences between SF in fishes versus invertebrates

While there is a rich history of research on filtration mechanisms in SF invertebrates (reviews in Jørgensen, 1966; Riisgård and Larsen, 2010; Hamann and Blanke, 2022), relatively

few studies on the biomechanics and fluid dynamics of vertebrate SF have been conducted, with most published after Sanderson and Wassersug (1993). Relevant data and models for SF fishes are rare, particularly with respect to the 3D spatially and temporally variable size, shape, and fluid dynamics of the oral cavity (e.g., Divi et al., 2018; Paskin et al., 2022; Van Wassenbergh and Sanderson, 2023; Witkop et al., 2023).

Despite limitations in our knowledge, the novel particle separation mechanisms proposed recently for SF fishes (Sanderson et al., 2001; Cheer et al., 2012; Sanderson et al., 2016; Cohen et al., 2018; Divi et al., 2018; Witkop et al., 2023) appear to be fundamentally distinct from those described for invertebrates. Due to the morphological and ecological diversity of SF fishes and SF invertebrates, broad generalizations are difficult. However, based on SF fish research published during the past twenty years, a suite of differences between the structures and fluid dynamics of SF fishes versus most SF invertebrates is identified below in this section. Together, these differences indicate that the particle separation mechanisms of SF fishes can be anticipated to extend beyond the hydrodynamic principles applied for particle separation in SF invertebrates.

3.1 Fishes are active suspension feeders

Unlike many subphyla or phyla of SF invertebrates (Hentschel and Shimeta, 2019), all SF fishes are active rather than passive suspension feeders, i.e., actively generate a flow of water into and through their oral cavity. In addition, the filter elements of SF fishes are completely enclosed within a roughly conical oral cavity (Cheer et al., 2001; Sanderson et al., 2016; Brooks et al., 2018; Witkop et al., 2023), which serves as the equivalent of the channel or pipe in industrial filtration and microfluidics. Active SF using an enclosed filter medium results in the potential ability to (a) control and adjust pore sizes as well as flow speed and direction along and between the filter elements (e.g., Sanderson et al., 1991; Provini et al., 2022), (b) control the pressure differential across the filter (e.g., Haines and Sanderson, 2017; Divi et al., 2018), and (c) employ particle separation mechanisms that require flow in pipes and channels for optimal operation (e.g., Sanderson et al., 2001; Cheer et al., 2012; Sanderson et al., 2016; Divi et al., 2018; Witkop et al., 2023), as discussed further below.

3.2 Large filter element sizes and flow speeds in fishes

Advantages of active SF using an enclosed filter medium are detailed above in section 3.1. In addition, the sizes of the filter elements between which water passes, and the flow speeds at the filter, tend to be larger in SF fishes than in SF invertebrates. Consequently, Reynolds numbers calculated at the level of the proposed filter elements in SF fishes range from ~ 2 – 1115 across two orders of magnitude in body size (~10 cm – 6 m, Table 1).

3.3 Large pore sizes in fishes

The available data on SF fishes are not sufficient for statistical comparisons of pore sizes between filter elements in SF fishes versus SF invertebrates relative to particle sizes in the diet and body size of the suspension feeder. However, while some SF fish species have small pore sizes (e.g., as small as 12 μm in juvenile menhaden, Friedland et al., 2006), the pore sizes can be relatively large in SF fishes (frequently 100 – 500 μm, Table 2).

4 Distinct hydrodynamic configurations: dead-end versus crossflow

In SF fishes, two distinct hydrodynamic configurations for the orientation of the filter with respect to the approaching flow have been proposed: dead-end and crossflow. The hydrodynamic configuration that is used is of fundamental importance because the orientation of the filter determines the types of particle separation mechanisms that are feasible. Historically, these configurations have been referred to in the primary literature as “dead-end filtration” and “crossflow filtration”.

4.1 Dead-end configuration

Dead-end has been the conventional configuration hypothesized for SF fishes (Gerking, 1994; Ross, 2013). In dead-end filtration (Figure 4A), the fluid to be filtered travels approximately perpendicular (approximately orthogonal or “normal”, i.e., ~ 90 degrees) to the filter medium, such that there are two streams of fluid: (1) the mainstream flow (i.e., the freestream flow or feed flow of unfiltered fluid) that approaches the GRs and (2) the filtrate (i.e., permeate) that has passed between the GRs. Filtrate is forced between the GRs by higher pressures inside the oral cavity relative to the opercular cavities. In the dead-end configuration, particles are trapped on the GRs when the particles are too large to pass through the gaps (pores) (Rubenstein and Koehl, 1977; LaBarbera, 1984; Shimeta and Jumars, 1991). Therefore, hypotheses for particle separation mechanisms using dead-end filtration in SF fishes are limited to sieving of particles that are equal to or larger than the pore size and/or mucus entrapment of particles with sizes that can be less than the pore size.

4.2 Crossflow configuration

Dead-end filtration was the sole hydrodynamic configuration considered for porous filters in SF vertebrates until crossflow filtration was discovered in SF fishes (Figure 4B). When a miniature fiberoptic endoscope was inserted through a dermal bone into the oral cavities of unrestrained fish as they pump suspension fed freely (goldfish, *Carassius auratus*, Cyprinidae; ngege or Singida tilapia, *Oreochromis esculentus*, Cichlidae;

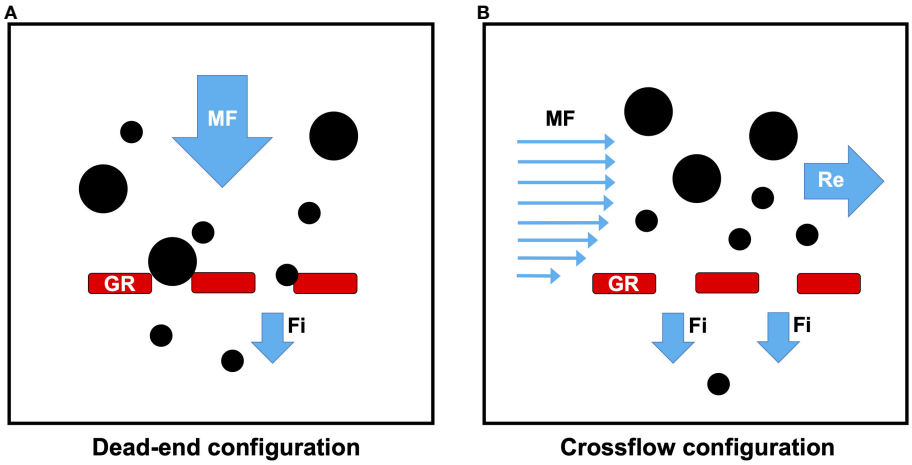

FIGURE 4
The two hydrodynamic configurations in SF fishes: dead-end versus crossflow. Gill rakers (red) are shown in cross-section. **(A)** In the dead-end configuration, the fluid to be filtered (mainstream flow) approaches the GRs at an angle of approximately 90 degrees while the filtrate passes through the gaps between the GRs (i.e., through the GR pores). Particles (black) that are larger than the GR pores are captured by direct sieving on the GR surfaces. In the dead-end configuration, particles that are smaller than the GR pores are captured only if particle flocculation or clumping occurs on the GR surface or inside the GR pores, or if mucus entrapment occurs on an adhesive GR surface. **(B)** In the crossflow configuration, the flow approaching the GRs travels tangentially or approximately parallel to the GRs before exiting as filtrate. However, particles are carried posteriorly in crossflow along the GRs of SF fishes, resulting in the formation of a retentate or concentrate of particles (Brainerd, 2001; Sanderson et al., 2001). Due to the tangential flow across the GRs in the crossflow configuration, particles can be retained inside the oral cavity using particle separation mechanisms other than or in addition to sieving and mucus entrapment, including inertial lift and shear-induced migration, reduction of effective gap size by vortices, vortical flow along outer faces of gill raker plates, cross-step filtration, ricochet filtration, and lateral displacement. Fi, filtrate; GR, gill rakers; MF, mainstream flow; Re, retentate.

gizzard shad, *Dorosoma cepedianum*, Clupeidae), dead-end filtration did not occur on GR surfaces and particles were not trapped in mucus (Sanderson et al., 2001). Instead, particles (40 μm – 1 mm diameter) were transported in flow moving along the channel between the roof and the floor of the oral cavity, traveling approximately parallel to the GRs. Particles that contacted the GRs infrequently did not accumulate on GR surfaces and were instead carried posteriorly in the oral cavity toward the esophagus. Sanderson et al. (2001) identified this unexpected hydrodynamic configuration as crossflow filtration. The crossflow configuration has also been proposed for balaenopterid (Goldbogen et al., 2007; Potvin et al., 2009) and balaenid whales (Werth and Potvin, 2016).

Since the 1980s, crossflow has been the preferred configuration for the industrial microfiltration of beverages and foods (e.g., fruit juices, beer, dairy products), although the dead-end configuration continues to be used as an option for dilute feeds (e.g., drinking water treatment) (Chew et al., 2020). More recently, the crossflow configuration reported in SF fishes has inspired crossflow systems for oil-water separation (Dou et al., 2017; Li et al., 2018) that have then stimulated extensive further research on similar uses of the crossflow configuration with superwetting membranes. Prior to the bioinspired crossflow configuration, membranes for oil-water separation had been used in a gravity-driven dead-end configuration that led to rapid fouling of the membranes by oil (Su et al., 2021).

Crossflow filtration is also known as tangential filtration because the flow approaching the GRs travels tangentially or approximately parallel to the GRs, i.e., along and over the GRs inside the oral cavity. Hamann et al. (2023) proposed the term "semi-cross-flow filtration" to differentiate crossflow configurations in which the tangential flow is between 0 and 90 degrees. During crossflow filtration, higher pressure inside the oral cavity of SF fishes (relative to the pressure of the fluid that is located immediately external of the GRs) causes filtrate to exit between the GRs. However, particles can be carried posteriorly in crossflow along the GRs of SF fishes, resulting in the formation of a retentate or concentrate of particles suspended in a limited volume of water near the terminus of the oral cavity (Brainerd, 2001; Sanderson et al., 2001). Due to the tangential flow across the GRs during crossflow filtration, particles can be retained inside the oral cavity using particle separation mechanisms other than or in addition to sieving and mucus entrapment.

4.3 Major advantages of the crossflow configuration

In SF fishes, there are three major advantages of the crossflow configuration compared to the dead-end configuration. The net outcome of these advantages is that the crossflow configuration could result in the retention of particles that are smaller than the distances between filter elements, while transporting particles toward the esophagus without accumulation of particles on the filter surfaces and therefore with reduced clogging.

4.3.1 Transport concentrated particles, reducing clogging

Dead-end filters are designed to retain particles by clogging, but this clogging causes the filter to cease functioning and therefore requires a separate process for the removal of particles from the filter. In SF fishes using the crossflow configuration, as the filtrate

exits through the pores between GRs, the tangential shear force of the crossflow along the filter surfaces minimizes the accumulation of particles on the filter. The crossflow transports concentrated particles downstream, thereby reducing clogging (Sanderson et al., 2001). During *in vivo* endoscopic observations of crossflow filtration in pump SF fishes, the crossflow that travels across the GR surfaces (as fast as ~ 55 cm s^{-1}, Sanderson et al., 1991) has been observed to transport suspended particles, or particles aggregated in mucus strands, posteriorly toward the esophagus (Sanderson et al., 1991; Sanderson et al., 1996b, Sanderson et al., 2001).

4.3.2 Retain particles smaller than pore sizes

Particles that are smaller than the pore sizes between filter elements cannot be retained using a non-adhesive filter in the dead-end configuration, unless such smaller particles flocculate (i.e., clump) or are retained in pores that are already partially clogged as suggested by Friedland et al. (1984). In the crossflow configuration, a number of particle separation mechanisms have been proposed that could retain particles smaller than the pore sizes (e.g., Sanderson et al., 2001; Cheer et al., 2012; Sanderson et al., 2016; Divi et al., 2018; Witkop et al., 2023). Therefore, pore sizes could evolve to target the retention of small particles with minimal clogging in the crossflow configuration.

4.3.3 Generate vortical flow

As the approaching flow passes tangentially along the filter elements inside the oral cavity during crossflow filtration, vortical flow is generated inside the gaps between BAs and/or between GRs (Cheer et al., 2012; Sanderson et al., 2016). Dead-end filtration has not been proposed to result in vortical flow that could play a role in the filtration process. In contrast, the vortical flow that results from crossflow is an important component of all recently hypothesized particle separation mechanisms in fish (Cheer et al., 2012; Sanderson et al., 2016; Cohen et al., 2018; Divi et al., 2018; Witkop et al., 2023).

5 Proposed particle separation mechanisms in SF fishes

Suspension-feeding processes are extremely difficult to observe or quantify inside the oral cavity of live fish. Therefore, SF mechanisms have often been inferred from gut contents, X-ray or endoscopic videos of particle retention in live fish, physical modeling, and computational fluid dynamics (CFD) simulations. Although multiple hypotheses have been proposed for particle separation mechanisms at the level of the GRs and associated protrusions, limited published evidence supports each mechanism in specific species (Table 3) and no clear consensus has emerged on broader patterns or unifying principles based on morphology, function, or taxonomy. Synthesis of the data available thus far indicates that particle separation mechanisms can differ between SF fish species belonging to the same family or genus (e.g., Goodrich et al., 2000), and may differ even within species depending on the type or size of particle being retained (e.g., Sanderson et al., 1996b; Callan and Sanderson, 2003). Here, each of the proposed particle separation mechanisms is discussed with a focus on unresolved questions and current challenges.

5.1 Sieving

Shimeta and Jumars (1991) noted that sieving is best considered as a particle retention mechanism, not a particle encounter mechanism. During sieving, also referred to as mechanical sieving or direct sieving in suspension feeders (Riisgård and Larsen, 2010; Conley et al., 2018a), particles are retained on the filter elements when the particle size is larger than the pore size (Rubenstein and Koehl, 1977; LaBarbera, 1984; Shimeta and Jumars, 1991).

In theory, if all gaps between GRs have the same minimum dimension, sieving in SF fishes could be identified by a distinct threshold in the minimum size of the retained particles, i.e., the retained particles would include 100% of the particles larger than the gap size but none smaller. In practice, the sizes of the gaps between GRs of SF fishes can vary within and among BAs as well as vary when the mouth is opened and closed during a pumping cycle or during ram SF (e.g., Mummert and Drenner, 1986; Gibson, 1988). In addition, the entrapment of small particles in mucus on the GRs during sieving could result in the capture of particles that are smaller than the gap size.

Historically, mechanical sieving in the dead-end configuration has been the conventional view of fish SF (LaBarbera, 1984; Gerking, 1994; Ross, 2013, Figures 5A, B). From primary literature (1984-1994), Sanderson et al. (1996b) summarized six proposed locations for sieving between different filter elements (e.g., between lateral and medial GRs on adjacent BAs, between adjacent GRs on a single BA, between denticles, etc.). Based on congruence between pore sizes and the particle sizes in gut contents, sieving has been proposed recently as the primary or sole particle separation mechanism in several SF fish species belonging to the families Clupeidae and Engraulidae (e.g., Friedland et al., 2006; Rykaczewski, 2009; Idris et al., 2016; Collard et al., 2017). For example, Mummert and Drenner (1986) quantified the sizes and numbers of microspheres (10 – 80 μm diameter) and zooplankton in water samples taken while gizzard shad fed in laboratory experiments. They reported that the particle-size-dependent removal of microspheres and zooplankton in water samples was consistent with their model of filtering efficiency based on the cumulative frequency of inter-raker distances measured in preserved gizzard shad.

However, the retention of prey that are smaller than the pore sizes has been reported for certain prey types and fish size classes in some of the species for which sieving has been proposed, leading the authors to suggest that other particle separation mechanisms may be operating in addition to or instead of sieving (Friedland et al., 2006; Rykaczewski, 2009). Mechanical sieving has not been observed endoscopically in the three tilapia species, two cyprinid species, and one clupeid species that have been studied during pump SF (Sanderson et al., 1991; Sanderson et al., 1996b; Goodrich et al., 2000; Sanderson et al., 2001; Callan and Sanderson, 2003; Smith and Sanderson, 2008). Particle retention has not been studied endoscopically *in vivo* for ram SF species.

TABLE 3 Particle separation mechanisms proposed in the primary literature for specific SF fish species.

Family	Species	Common Name	Pump or Ram	Proposed Particle Separation Mechanism	Reference
CICHLIDAE	*Oreochromis aureus*	Blue tilapia	Pump	Inertial lift/Shear-induced migration	Smith and Sanderson, 2007, 2013
	Oreochromis esculentus	Ngege (Singida) tilapia	Pump	Inertial lift/Shear-induced migration	Sanderson et al., 2001; Smith and Sanderson, 2013
	Oreochromis niloticus	Nile tilapia	Pump	Mucus entrapment	Northcott and Beveridge, 1988; Sanderson et al., 1996b
CLUPEIDAE	*Alosa sapidissima*	American shad	Ram	Cross-step filtration (with dead-end filtration near esophagus)	Storm et al., 2020
				Lateral displacement	Witkop et al., 2023
	Brevoortia tyrannus	Atlantic menhaden	Ram	Sieving	Friedland, 1985; Friedland et al., 2006
	Clupea harengus	Atlantic herring	Ram	Sieving	Gibson, 1988; Collard et al., 2017
				Crossflow filtration (with dead-end filtration near esophagus)	Hamann et al., 2023
	Dorosoma cepedianum	Gizzard shad	Pump	Sieving	Drenner et al., 1984; Mummert and Drenner, 1986
				Inertial lift/Shear-induced migration	Sanderson et al., 2001
	Sardina pilchardus	Sardine	Ram	Sieving	Collard et al., 2017
				Crossflow filtration (with dead-end filtration near esophagus)	Hamann et al., 2023
	Sardinops sagax	Pacific sardine; southern African sardine	Ram	Sieving	Rykaczewski, 2009; Idris et al., 2016
CYPRINIDAE	*Abramis brama*	Common bream	Pump	Sieving	van den Berg et al., 1993; van den Berg et al., 1994b
	Blicca bjoerkna	White bream	Pump	Sieving	van den Berg et al., 1993; van den Berg et al., 1994b
	Carassius auratus	Goldfish	Pump	Inertial lift/Shear-induced migration	Sanderson et al., 2001
	Cyprinus carpio	Carp	Pump	Sieving	van den Berg et al., 1994b
				Crossflow filtration	Callan and Sanderson, 2003
	Hypophthalmichthys molitrix	Silver carp	Pump	Vortical flow along outer faces of gill raker plates	Cohen and Hernandez, 2018
	Hypophthalmichthys nobilis	Bighead carp	Pump	Crossflow filtration	Cohen and Hernandez, 2018
	Orthodon microlepidotus	Sacramento blackfish	Pump	Mucus entrapment	Sanderson et al., 1991
	Rutilus rutilus	Roach	Pump	Sieving	van den Berg et al., 1993; van den Berg et al., 1994b
ENGRAULIDAE	*Engraulis anchoita*	Argentine anchovy	Ram	Sieving	Ciechomski, 1967
	Engraulis encrasicolus	European anchovy	Ram	Sieving	Collard et al., 2017
				Crossflow filtration (with dead-end filtration near esophagus)	Hamann et al., 2023
	Engraulis mordax	Northern anchovy	Ram	Sieving	Rykaczewski, 2009
MUGILIDAE	> 10 mugilid genera	Mullet	Pump	Sieving	Harrison and Howes, 1991
MOBULIDAE	~ 9 *Mobula* species	Manta and devil rays	Ram	Sieving	Paig-Tran et al., 2013
	Manta birostris	Manta ray	Ram	Ricochet filtration	Divi et al., 2018
	Mobula tarapacana	Manta ray	Ram	Ricochet filtration	Divi et al., 2018

(Continued)

TABLE 3 Continued

Family	Species	Common Name	Pump or Ram	Proposed Particle Separation Mechanism	Reference
RHINCO-DONTIDAE	*Rhincodon typus*	Whale shark	Pump/Ram	Crossflow filtration	Motta et al., 2010
SCOMBRIDAE	*Rastrelliger kanagurta*	Indian mackerel	Ram	Crossflow filtration (with dead-end filtration near esophagus)	Hamann et al., 2023
	Scomber scombrus	Atlantic mackerel	Ram	Crossflow filtration (with dead-end filtration near esophagus)	Hamann et al., 2023

Two rows are provided for species in which two separation mechanisms have been proposed. Crossflow filtration is listed for species that were reported to use the crossflow configuration but for which a more specific particle separation mechanism was not reported.

5.2 Mucus entrapment and particle transport

During hydrosol filtration, a number of fluid mechanical processes (e.g., direct interception and inertial impaction) can cause particles to encounter a filter surface that has adhesive properties (Rubenstein and Koehl, 1977; Shimeta and Jumars, 1991). Particles can then be retained by adhesion to the mucus-covered surface of the filter. Note that the particle encounter mechanisms (e.g., direct interception, inertial impaction) occur independently of the particle capture mechanism (e.g., the sticky filter surface) (Shimeta and Jumars, 1991). This section focuses on particle separation that results from adhesion of particles to mucus-covered filter surfaces, including the roles of mucus in particle aggregation and transport.

Mucus is a viscoelastic heterogeneous hydrogel with adhesive properties, consisting primarily of glycosylated proteins termed

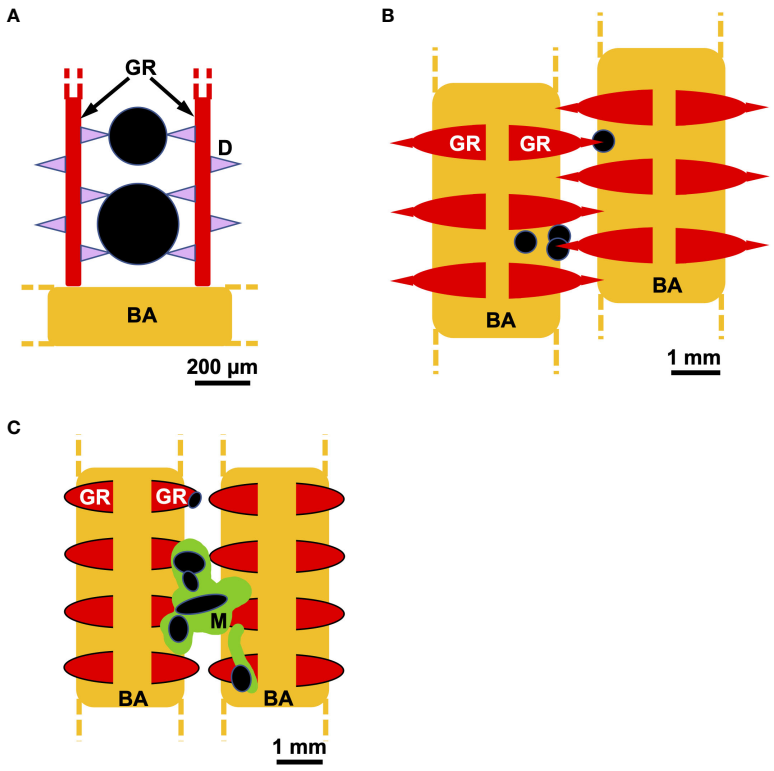

FIGURE 5
Schematic examples of direct sieving versus mucus entrapment, shown in frontal view. **(A)** Denticles (pink), gill rakers (red), and branchial arches (gold) have been proposed to connect to form a sieve that captures particles (black) in ram SF species such as herring (Clupeidae) and anchovy (Engraulidae) (e.g., Gibson, 1988; Collard et al., 2017). **(B)** Gill rakers, including protrusions that may be movable, have been proposed to form a branchial sieve that can capture particles in the channels between the gill rakers in pump SF species such as common bream and carp (Cyprinidae) (e.g., Hoogenboezem et al., 1991; van den Berg et al., 1994a, van den Berg et al., 1994b). **(C)** In pump SF Nile tilapia (Cichlidae), strands or aggregates of mucus (green) on the gill rakers and branchial arches have been observed in endoscopic videotapes to capture particles that were otherwise small enough to pass between the filter elements. Subsequently, particle-laden mucus was observed to be transported posteriorly in crossflow toward the esophagus (Sanderson et al., 1996b). Dashed lines indicate that structures repeat. BA, branchial arch; D, denticle; GR, gill raker; M, mucus.

mucins (Cerullo et al., 2020; Bayer, 2022). Mucins and mucin-like proteins are found in taxa throughout the Metazoa (Lang et al., 2016), and the use of mucus for SF is widespread among invertebrates (Hamann and Blanke, 2022). Multiple types of mucin proteins are ubiquitous in vertebrate taxa and are essential for many respiratory, digestive, reproductive, and immunological functions (Shephard, 1994; Lang et al., 2016; Bansil and Turner, 2018).

Mucus-secreting cells (e.g., goblet cells) are typically found in fish oral epithelia, on or near the GRs as well as on the gill filaments. Based on the locations of mucus-secreting cells identified in the oral cavity, the use of mucus for particle separation and/or transport has been proposed in multiple taxa of SF fishes (e.g., Atlantic menhaden, *Brevoortia tyrannus*, Clupeidae, Friedland, 1985; three species of rays, *Mobula*, Mobulidae, Paig-Tran and Summers, 2014; silver carp and bighead carp, *Hypophthalmichthys molitrix* and *Hypophthalmichthys nobilis*, Cyprinidae, Cohen and Hernandez, 2018; American shad, *Alosa sapidissima*, Clupeidae, Storm et al., 2020; earlier studies summarized in Sanderson et al., 1996b). In endoscopic videotapes, omnivorous pump SF Nile tilapia (*Oreochromis niloticus*, Cichlidae) were observed to retain particles (40 μm – 1 mm diameter) in mucus strands or aggregates on the GR surfaces (Sanderson et al., 1996b, Figure 5C). However, despite belonging to the same genus and specializing on phytoplankton and colonial blue-green algae, the ngege tilapia *O. esculentus* was not observed endoscopically to have mucus strands or aggregates on or near the GRs during pump SF, and particles were not retained on any oral surfaces (Goodrich et al., 2000).

The physical properties of mucus, such as viscosity and electrostatic charge, can vary with the type of cell that secretes the mucus and therefore can vary with location inside the oral cavity (Friedland, 1985; Sibbing and Uribe, 1985; Northcott and Beveridge, 1988). While mucus properties are of substantial biomedical interest, there are few studies on the biochemistry and biomechanics of mucus in fish oral cavities. Bulusu et al. (2020) have provided the first macro-rheological study of oral mucus for a fish species, including shear thinning. Such data for SF fishes are important because shear thinning of mucus within a boundary layer or a vortical flow has the potential to enable particle transport processes that could be essential components of particle separation mechanisms.

Available data are not sufficient to assess whether there are interspecific or intraspecific patterns in mucus occurrence and mucus-secreting cell locations and abundance based on food particle type, pump versus ram SF, fish body size, or particle separation mechanism. A useful first step for further study could be to identify specific SF fish species that lack mucus-secreting cells on filter element surfaces. For example, Friedland (1985) noted that mucus cells are absent on Atlantic menhaden branchiospinules, small protrusions on the GRs. Therefore, he concluded that menhaden use mechanical sieving to retain particles on the branchiospinules. Another productive future approach could be to incorporate synthetic hydrogels and other mucus analogues (e.g., Authimoolam and Dziubla, 2016; Bej and Haag, 2022) into computational models as done with drag-reducing agents and microgrooves (Zhang et al., 2022a), or into physical models as suggested by Witkop et al. (2023).

As is the case for sieving, mucus entrapment of particles is potentially problematic because the trapped particles must be transported posteriorly toward the esophagus for swallowing. However, mucus can serve as both a particle aggregation and particle transport medium. The hydrodynamics of particle transport in the oral cavity of SF and non-SF fishes are one of the least understood aspects of fish feeding (Sanderson and Wassersug, 1993; Cheer et al., 2001; Day et al., 2015; Provini et al., 2022). Limited data are available on particle transport processes in SF fishes. When SF Nile tilapia interrupted a series of pumps periodically to perform a prey-handling process termed a post-pump flow reversal, particle-laden mucus was observed endoscopically to lift slightly from the GRs and travel briefly in an anterior direction in association with hyoid and branchial arch abduction during closed premaxillary protrusion (Sanderson et al., 1996b). The subsequent resumption of pump SF transported the mucus posteriorly toward the esophagus. Hoogenboezem and van den Boogaart (1993) described boluses of mucus containing large numbers of zooplankters (up to 900 in a single bolus) inside the oral cavities of freshly caught common bream (*Abramis brama*, Cyprinidae). van den Berg et al. (1994a) suggested that the zooplankters were trapped in the bream's branchial sieve initially (Figure 5B) but were then coated by mucus and aggregated during flow reversals termed back-washing.

Another process by which mucus may serve to aggregate and transport particles involves the epibranchial organs. Epibranchial organs are bilaterally paired muscular sac-like structures in the posterior oral cavity near the esophagus that aggregate small prey in at least five SF and detritivorous otomorphan fish families (e.g., many clupeid and engraulid species and two cyprinid species, Cohen et al., 2022). Epibranchial organs have abundant mucus-secreting cells and chemosensory cells and appear to receive minute prey that have been transported along the rows of GRs that extend into the organs. Subsequently, the epibranchial organs are thought to expel boli of food-laden mucus into the posterior pharynx for swallowing (Hansen et al., 2014; Cohen et al., 2020). Detailed studies on morphology, development, and evolution have only recently been conducted for a subset of the more than seven types of epibranchial organs that have been described (Cohen et al., 2022). Given that particle aggregation and transport are integral components of fish SF, the roles of mucus and the epibranchial organs in these processes deserve further study.

Holley et al. (2015) developed an experimental protocol and equations for calculating mucus content in the epibranchial organs and the foregut of pump SF gizzard shad. They reported that mucus constituted an average of 12% of the epibranchial organ content and 10% of the foregut content by dry mass, indicating the importance of mucus for pump SF in gizzard shad. However, mucus entrapment of particles (40 μm – 1 mm diameter) was not observed endoscopically on the GRs of gizzard shad, and particles rarely contacted the filter elements during SF (Sanderson et al., 2001). Thus, the available data suggest that mucus may be used for particle transport in gizzard shad rather than as a particle separation mechanism.

5.3 Inertial lift and shear-induced migration

In industrial filtration using the dead-end configuration, sieving separates particles by retaining them on the filter medium. In contrast, in inertial microfluidics and industrial membrane microfiltration using the crossflow configuration, inertial lift and shear-induced migration aid in particle separation by causing particle migration across streamlines and away from the porous or non-porous walls of the channel or pipe, thereby reducing particle contact with the walls. Inertial lift and shear-induced migration cause larger particles to migrate farther than smaller particles from the walls of an inertial microfluidics channel or from a microfiltration membrane with small pore sizes (Belfort et al., 1994; Di Carlo et al., 2007). Therefore, in inertial microfluidics devices, particles can be separated by size within the main channel at equilibrium positions that are specific distances from the walls (Di Carlo, 2009; Di Carlo et al., 2009). Such size-segregated particles can then be collected from the main channel using outlets in specific locations.

Inertial lift has been observed in experiments with particles as large as ~ 1 mm in diameter (Martel and Toner, 2014), and shear-induced migration has been quantified for particles with diameters up to 30 μm (Schroën et al., 2017). The crossflow configuration takes advantage of inertial lift forces and shear-induced migration for the separation of particles smaller than approximately 10 – 20 μm diameter, including microalgae, bacteria, and blood cells (Di Carlo et al., 2007; Bouhid de Aguiar and Schroën, 2020; Xiang and Ni, 2022). In SF fishes that use the crossflow configuration, Sanderson et al. (2001) proposed that, rather than being a mechanical threshold for retention, particle size could be a hydrodynamic threshold that affects the magnitude of the lift and shear acting on particles at the interface between the crossflow and the filtrate flow.

Inertial lift (Figure 6) has also been referred to as inertial migration, inertial focusing, hydrodynamic lift, or the tubular pinch effect, but should not be confused with inertial impaction. Inertial lift is primarily the net result of two opposing forces known as the wall-induced lift ("wall effect") versus the shear-gradient induced lift (or shear-induced lift). Due to asymmetries in the flow profile around a particle near a wall and the net result of the wall-induced lift (directing the particle toward the channel center and away from the walls) versus the shear-gradient induced lift (directing the particle toward the walls and away from the channel center), inertial lift leads to differential particle migration across streamlines on the basis of particle size, generally at Re 1 – 100 (van Dinther et al., 2013b; Martel and Toner, 2014; Kumar and Das, 2022).

Shear-induced migration (Figure 7), most commonly modeled in membrane microfiltration, is also referred to as shear-induced diffusion or hydrodynamic diffusion, but should not be confused with hydrodynamic shear, tangential shear, or shear-gradient induced lift. Shear-induced migration causes particles to deviate from streamlines and move away from walls due to particle-particle interactions (Drijer and Schroën, 2018). These particle-particle interactions are affected by gradients in particle concentration, shear, and viscosity (Schroën et al., 2017; Di Vaira et al., 2022), particularly at high particle concentrations (van Dinther et al., 2013a; Dijkshoorn et al., 2017).

Although inertial lift and shear-induced migration are central to the fields of inertial microfluidics and crossflow membrane microfiltration, studies have not been conducted on the potential

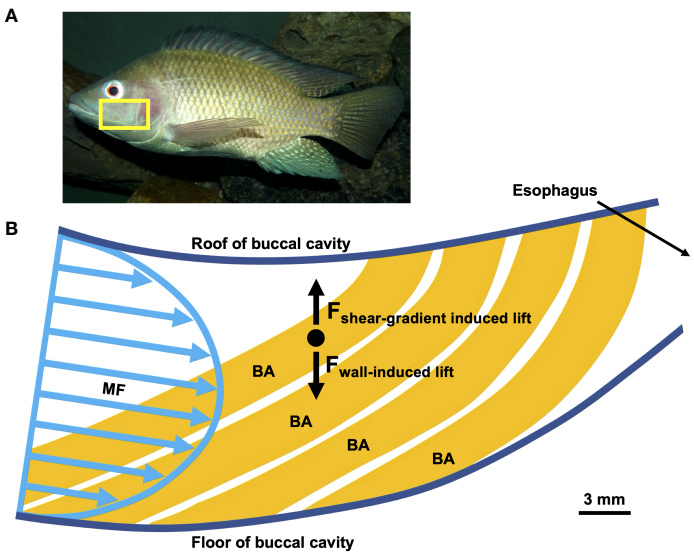

FIGURE 6
Schematic example of proposed inertial lift during crossflow in a generalized pump SF fish that is not using mucus entrapment (e.g., Sanderson et al., 2001; Smith and Sanderson, 2007, 2013). **(A)** The yellow box indicates the region of the oral cavity illustrated in **(B)**. Modified from © Bjørn Christian Tørrissen Bjørn Christian, CC BY-SA 3.0 https://creativecommons.org/licenses/by-sa/3.0/deed.en **(B)** Sagittal section through oral cavity, branchial arches in gold, spherical particle in black. During inertial lift in a pipe or channel, the wall-induced lift force acts opposite to the shear-gradient induced lift force. The net result is that particles migrate across streamlines to equilibrium positions in the pipe or channel (e.g., Di Carlo et al., 2009; Martel and Toner, 2014). These principles have been proposed to apply to SF fishes, including pump SF tilapia (Cichlidae) (e.g., Sanderson et al., 2001; Smith and Sanderson, 2007, 2013). Sagittal section in **(B)** modified from Sanderson et al. (2001), with permission. F, force; BA, branchial arch; MF, mainstream flow.

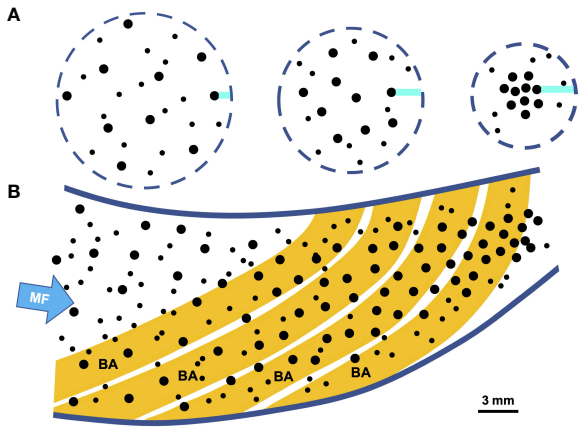

FIGURE 7
Schematic example of proposed shear-induced migration during crossflow in a generalized pump SF fish that is not using mucus entrapment (e.g., Sanderson et al., 2001). During shear-induced migration, particles deviate from streamlines and migrate away from walls due to particle-particle interactions, particularly at higher particle concentrations (e.g., van Dinther et al., 2013a; Drijer and Schroën, 2018). Larger particles migrate faster than smaller particles, resulting in separation of particles by size as smaller particles are lost through the pores in a porous tube or channel. **(A)** Frontal views (head-on) illustrating a suspension of small and large particles (black circles) in three cross-sections of a SF fish oral cavity shown sequentially from anterior (left) to posterior (right). Larger particles are proposed to migrate away from oral cavity surfaces more rapidly than smaller particles (indicated by the horizontal blue bars denoting increasing distance between larger particles and oral cavity surfaces as the oral cavity tapers posteriorly), while smaller particles are lost through the pores. **(B)** Sagittal section through oral cavity (branchial arches in gold), showing proposed concentration of predominantly larger particles away from walls as flow travels posteriorly. Cross-sections shown in **(A)** correspond approximately to locations from anterior to posterior along sagittal section in **(B)**. Panel **(B)** modified from Sanderson et al. (2001), with permission. BA, branchial arch; MF, mainstream flow.

importance of these hydrodynamic processes during crossflow at the scale of the pore sizes, Reynolds numbers, and channel diameters in SF fishes. For pump SF fishes, approximations have indicated that inertial lift would be at least an order of magnitude too low to account for the lack of particle contact with the GRs (Sanderson et al., 2001). However, those approximations were based on estimations of the channel Re, wall shear rate, and trans-raker pressure for the entire oral cavity of generalized suction-feeding fish, and did not account for GR shape or protrusions, oral cavity shape, or spatial/temporal variability during SF.

Clark and San-Miguel (2021) designed microfluidic devices (channel width 200 µm, channel height 60 µm) that scaled down the filter lobes and the target particle sizes used in research on ram SF manta rays (*Mobula birostris*, *M. tarapacana*; Divi et al., 2018) by approximately six times. Operating at Re ~ 1000 and a pore size of ~ 50 µm, these devices separated and concentrated particles (15 µm and 25 µm diameter) at a wide range of initial particle concentrations. The highest filtration efficiencies of 99% were achieved at inlet flow rates of 20 mL min^{-1}. Clark and San-Miguel (2021) referred to this as microfluidic "lobe filtration" and suggested that inertial lift forces play a key role. They demonstrated that the shapes of the scaled-down lobes caused complex velocity profiles in the device's main channel, and that calculations of the inertial lift forces resulting from the velocity profiles could predict the filtration efficiencies for particles of different sizes as the flow rate through the device was varied.

Since inertial lift and shear-induced migration require crossflow in an enclosed channel or pipe, and such prerequisites are found in relatively few invertebrate taxa (Hamann and Blanke, 2022), these processes have not yet been investigated in invertebrate SF. However, these processes may be relevant in some invertebrates, such as members of the subphylum Tunicata (e.g. appendicularians, thaliaceans, or ascidians, Morris and Deibel, 1993; Conley et al., 2018a, Conley et al., 2018b).

5.4 Reduction of effective gap size by vortices

Using CFD simulations of the complex posterior oral cavity in a generalized SF fish during crossflow filtration, Cheer et al. (2006, 2012) discovered and quantified a vortex located in each gap between the elliptical GRs (Figure 8). Subsequently, these were identified as trapped vortices that are generated because the GRs form a series of backward-facing steps in crossflow (Sanderson et al., 2016; also referred to as captive vortices, Divi et al., 2018). While these vortices appear similar to the trapped vortices used as flow control in aerodynamics and hydrodynamics (e.g., Lysenko et al., 2023), the proposed functions of the vortices for particle separation in SF fishes are unique because the trapped vortices are located in the slots (i.e., elongated gaps) between GRs rather than being located inside grooves with a solid floor (Sanderson et al., 2016).

Cheer et al. (2006, 2012) reported that the recirculating flow in the vortices partially blocked the flow of water between the GRs by preventing flow from exiting directly downstream of each GR. Therefore, each vortex served as a barrier that reduced the effective gap size by approximately 50% and led to particle retention in the mainstream flow. In CFD simulations, the vortices limited the exit of particles (82.5 – 160 µm diameter) through the gaps (250 µm) between the GRs, even though the particles were smaller than the gaps. The Reynolds numbers were 37.5 – 225, calculated using the major axis of the elliptical GRs and the mainstream flow speeds ranging from 10 – 60 cm s^{-1}. The specific flow patterns between the GRs varied depending on the speed and angle of the crossflow (60 – 75 degrees from the normal direction, i.e., the perpendicular, through the gap). Based on data from the simulations, Cheer et al. (2012) suggested that particle size and, to a lesser extent, particle density affected the inertial force and therefore affected the drag on particles as the particles deviated from the streamlines of water exiting between the GRs. The result was that particles were retained in the mainstream flow that continued toward the posterior of the oral cavity (Cheer et al., 2012).

Hung et al. (2012) and Hung and Piedrahita (2014) designed and tested a particle separator stated to be inspired by the computational models of Cheer et al. (2001, 2006, 2012). However, the structures of Hung et al. (2012) and Hung and Piedrahita (2014) differed substantially from SF fishes in shape,

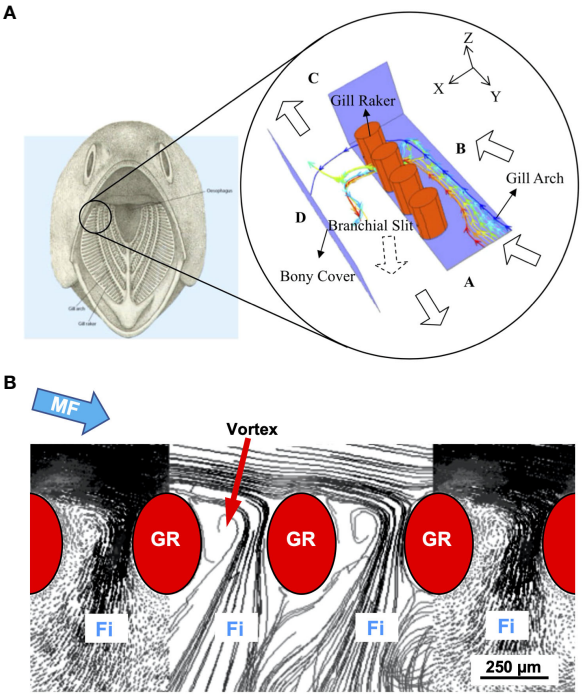

FIGURE 8
In CFD simulations of generalized SF fish, a vortex that formed in each gap between the elliptical gill rakers reduced the effective gap size by approximately 50% and led to particle retention in the mainstream flow (Cheer et al., 2006, 2012). **(A)** Geometric structure of the simulated oral cavity, showing placement of elliptical gill rakers (red). **(B)** Series of GRs with velocity vectors and path lines for flow along and between the GRs, including vortex that was generated posterior of each GR in crossflow at a mainstream flow speed of 60 cm s^{-1}, Re = 225. Adapted from Cheer et al. (2012), with permission from Springer Nature Customer Service Center (SNCSC). Fi, filtrate; GR, gill raker; MF, mainstream flow.

location, and function. For example, the particle separator (a) required that the investigator inject an annulus of particle-free water to encircle the entering flow as a "shield" to reduce the loss of particles through slits along the sides of the device, and (b) relied on particle accumulation and collection using suction through a tube connected to a hole in the bottom of the device approximately halfway between the device's anterior and posterior (Hung et al., 2012; Hung and Piedrahita, 2014). The highest particle removal efficiency achieved in experiments using a physical model of this separator was approximately 43% (particle diameter 500 µm, density 1050 kg m^{-3}; Hung and Piedrahita, 2014).

5.5 Cross-step filtration

Obstacles as diverse as rocks in a river, automobiles, and buildings form backward-facing steps that generate downstream vortices (Chen et al., 2018; Montazer et al., 2018). In CFD simulations and flow tank experiments with physical models using the crossflow configuration, the BAs and GRs acted as backward-facing steps that generated a vortical recirculation zone when flow separation (not to be confused with particle separation) occurred at the downstream edge of each step (Figure 9) (Sanderson et al., 2016; Van Wassenbergh and Sanderson, 2023; Witkop et al., 2023; Xu et al., 2023). As flow travels over each step, a trapped vortex forms directly downstream near the step due to the sudden expansion of cross-sectional area in the channel there (Chen et al., 2018).

A series of backward-facing steps forms a rib-and-groove arrangement, with the BAs and/or GRs in SF fishes serving as rib-shaped structures and the grooves between them serving as the slots through which filtrate exits past the trapped vortex in each slot (Figure 9, Sanderson et al., 2016; Storm et al., 2020). Therefore, BAs and GRs differ from backward-facing steps that are found commonly in heat exchangers, petroleum pipe-flow transport systems, and other industrial applications (Salman et al., 2020; Hong et al., 2021) because the floor of the slots between the steps (i.e., the floor of the groove between the ribs in industrial applications) is not solid in fish. A major distinction between slots versus most pores or meshes is that a slot is a three-dimensional structure with height as well as width and an elongated length. The slot aspect ratio (slot width divided by rib height, Figure 9D) is a key design metric affecting the fluid dynamics, including the vortical flow, in cross-step systems (e.g., Stel et al., 2012; Sanderson et al., 2016; Schroeder et al., 2019; Xu et al., 2023).

Based on flow tank experiments using American paddlefish specimens (*Polyodon spathula*) that had been preserved in ram SF position and 3D-printed physical models of paddlefish oral cavities, Sanderson et al. (2016) proposed vortical cross-step filtration as a novel particle separation mechanism (Figure 9A). By broadening the CFD simulations of Sanderson et al. (2001) and Cheer et al. (2006, 2012) to three dimensions in a flow tank, Sanderson et al. (2016) demonstrated how trapped vortices could suspend, concentrate, and transport particles in the slots between the BAs of paddlefish and basking sharks (Figure 9B). In these two species, the GRs have evolved convergently to form the porous floors of the deep slots between the BAs. In the flow tank experiments, a mesh was used to simulate the GRs on the floors of the deep slots between BAs. As filtrate exited through the mesh between the BAs in the preserved paddlefish and the physical models, the flow that had separated at the downstream edge of each BA wrapped around the trapped vortex inside each slot. This separated flow, known as a shear layer, caused a high shear rate along the surface of the mesh (Van Wassenbergh and Sanderson, 2023) and thereby transported particles (~ 250 µm diameter) to the margins of the slots (Sanderson et al., 2016). Transport of concentrated particles to the esophagus was hypothesized to occur via the ceratobranchial-epibranchial junctions, but was not modeled. The Reynolds number was ~ 600, calculated using the mainstream flow speed (10 cm s^{-1}) and the height of the backward-facing step.

Vortical cross-step filtration reduces clogging by causing a high shear rate along the filter surfaces downstream of each backward-facing step (Sanderson et al., 2016; Xu et al., 2023). Vortical cross-step filtration has been hypothesized to operate in SF clupeids (e.g., herring, menhaden, shad) and engraulids (anchovies), with the denticles on the GRs proposed to serve as the porous filter surfaces inside the slots between the backward-facing steps formed by the GRs (Sanderson et al., 2016; Storm et al., 2020).

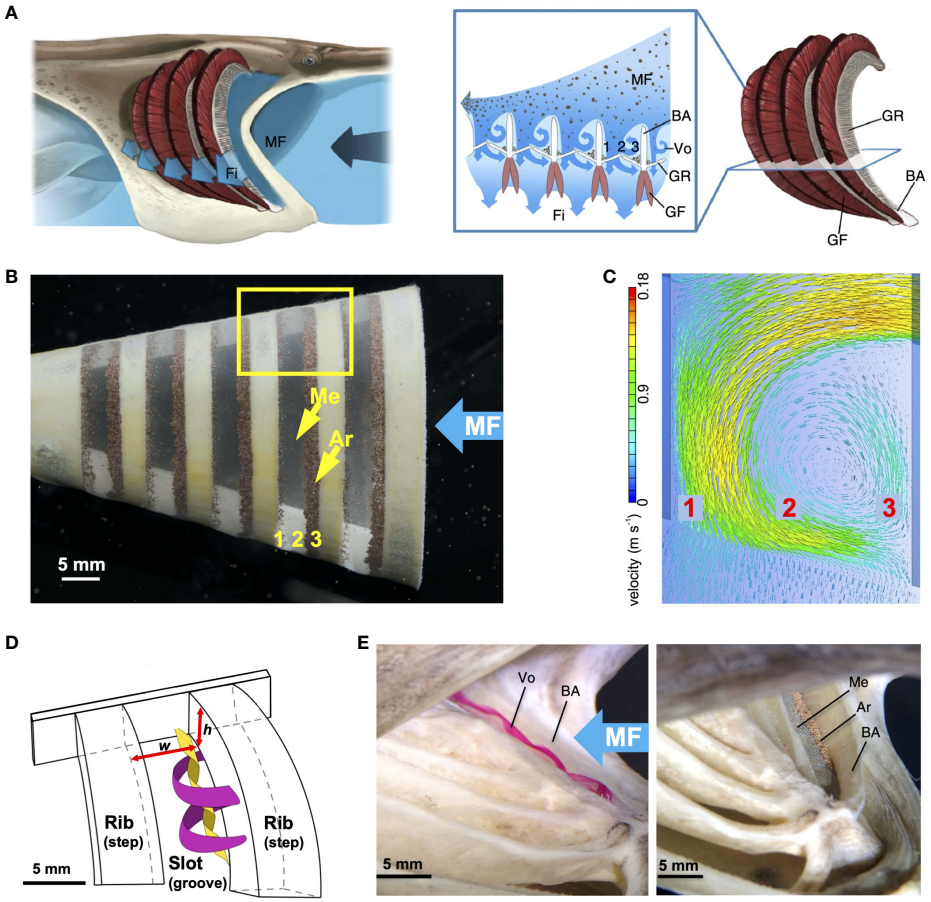

FIGURE 9
Vortical cross-step filtration has been proposed to generate trapped vortices that could suspend, concentrate, and transport particles in the slots between the branchial arches and gill rakers of SF fishes (Sanderson et al., 2016; Storm et al., 2020; Van Wassenbergh and Sanderson, 2023). **(A)** Illustration of cross-step filtration proposed in paddlefish, with BAs acting as backward-facing steps to generate vortical recirculation that concentrates particles in zones 1 and 3 along the slot margins. **(B)** 3D-printed model in flow tank experiments with 140-µm mesh simulating the paddlefish GRs by covering the exterior of the slots between BAs (Re ~ 600). Particles (*Artemia* cysts, ~ 250 µm diameter) were concentrated in zones 1 and 3 of the slots, while vortical flow reduced clogging in zone 2. **(C)** CFD simulation of vortical flow in slots of model used for flow tank experiments. **(D)** Enlargement of yellow rectangle from **(B)**, showing a series of backward-facing steps with a slot between each pair of steps, forming a rib-and-groove arrangement with slot width *w* and rib height *h*. Representative locations of outer (magenta) and inner (yellow) path lines of the vortical flow were obtained from flow tank experiments. **(E)** Vortical flow and particle concentration in paddlefish preserved in SF position in a flow tank, with mesh simulating the GRs which do not abduct in dead specimens. **(A)** © Virginia Greene/virginiagreeneillustration.com, used with permission, not covered by the CC-BY license. **(B, E)** adapted from Sanderson et al. (2016), CC BY 4.0. **(C)** adapted from Van Wassenbergh and Sanderson (2023), CC BY 4.0. **(D)** adapted from Brooks et al. (2018), CC BY 4.0. Ar, *Artemia* cysts; BA, branchial arch; Fi, filtrate; GF, gill filament; GR, gill raker; *h*, rib height; Me, mesh; MF, mainstream flow; Vo, vortex; *w*, slot width.

Schroeder et al. (2019), Masselter et al. (2023), and Xu et al. (2023) have applied vortical cross-step filtration to construct filters with reduced clogging for harmful algae collection, washing machines, and drip-irrigation systems, respectively. In their physical models, vortices generated in the slots between ribs served to reduce clogging by transporting particles to the margins of the slots. They did not quantify particle removal efficiency because the objective of the cross-step designs was to reduce clogging. From their CFD simulations, Xu et al. (2023) determined that approximately 10 - 18% of the particles retained by the mesh in the slots were trapped in the region scoured by the shear layer downstream from each step, demonstrating that the shear layer was effective in reducing clogging. However, with continued use, the cross-step filters of Schroeder et al. (2019) clogged eventually unless active anti-clogging strategies were introduced (i.e., perturbation of the physical model by tapping or by rotation of the model). The physical models of Schroeder et al. (2019) differed from SF fishes by using helical slots that reduced clogging by enabling the transport of particles to the open posterior end of the model, following resuspension of the particles by tapping or by rotation of the model.

5.6 Vortical flow along outer faces of gill raker plates in silver carp

Cohen et al. (2018) used 3D particle image velocimetry in flow tank experiments to quantify flow past 3D-printed physical models based on micro-CT scans of the GRs in silver carp and bighead carp. In silver carp, the highly modified GRs form specialized filtering plates

(Figure 10A) (Cohen and Hernandez, 2018). Physical models of the silver carp GR plates (Figure 10B) induced a strong organized vortical flow on the outer faces of the plates (Figure 10C) at Re ~ 18,000 (calculated using a flow tank speed of 15 cm s^{-1} and the downstream length of the filtering plates that had been scaled to match the Re for a silver carp body length of 80 cm and a flow speed of 0.75 body lengths s^{-1}). Cohen et al. (2018) hypothesized that the vortices increased the number of interactions between the particles and pores inside the channels on the outer faces of the silver carp filtering plates, leading to particle transport through the pores and subsequent accumulation at the inner faces of the plates. Because the physical models of the less modified GRs in the bighead carp induced only limited disorganized vortices, they suggested that bighead carp use a haphazard crossflow filtration which could be related to decreased filtration efficiency on small particles relative to silver carp (Cohen et al., 2018).

5.7 Ricochet filtration

Manta rays and devil rays (*Mobula*, Mobulidae) have a specialized SF apparatus with highly modified GRs consisting of arrays of lobes attached to the chevron-shaped BAs (Figure 11A). The lobes are arranged in two sets of filter plates, one oriented anteriorly and the other oriented posteriorly (Paig-Tran et al., 2013). Based on two-dimensional CFD simulations and 3D-printed models of the lobe arrays that were tested in a customized flume, Divi et al. (2018) reported that ricochet filtration is a novel particle separation mechanism in manta rays that does not resemble previously described filtration systems. Their computational and physical models used morphological measurements of the lobe arrays in *M. birostris* as well as micro-CT scans of *M. tarapacana*. For *M. birostris*, the Re was 1075, calculated using the freestream velocity estimated for the buccal cavity of a freely swimming manta ray (55 cm s^{-1}) and the distance between lobes.

Based on the orientation of the filter plates within the oral cavity, Divi et al. (2018) suggested that water impinges on the lobes in both the forward direction ("wing-like" posterior filters) and the reversed direction ("spoiler-like" anterior filters) (Figures 11B, C). As water traveled across the wing-like or spoiler-like lobes in the models, flow separation occurred behind the leading edge of each lobe and a captive vortex was generated directly downstream inside the pore between two consecutive lobes (Figure 11D).

In the CFD simulations, fluid streamlines immediately above the lobes entered the pores and were swept around the captive

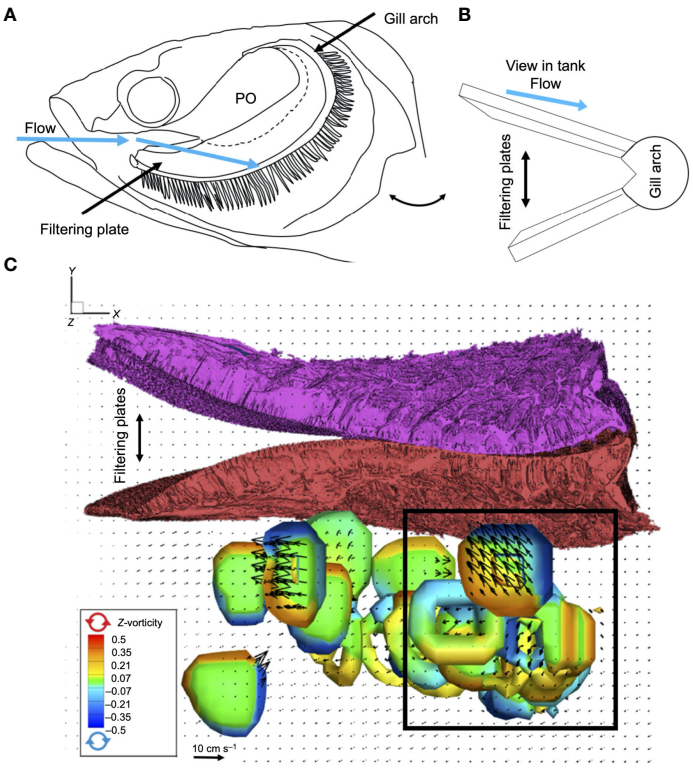

FIGURE 10
Vortical flow quantified along the outer faces of 3D-printed physical models of silver carp (Cyprinidae) filtering plates using 3D particle image velocimetry in a recirculating flow tank (Cohen et al., 2018). **(A)** Orientation of filtering plates in crossflow inside the oral cavity. **(B)** Orientation of physical model during flow tank experiments, with flow moving across the model in an anterior to posterior direction from the dorsal edge of the filtering plates to the ventral base of the gill arch. **(C)** Particle volumetric data from the flow tank speed (0.75 body lengths s^{-1}) that developed and maintained strong, organized vortical flow (bottom) across the outer faces of the filtering plates (top). Black box denotes region where vortices changed direction such that vortical flow was in the direction of the epibranchial organ, traveling through channels along the outer faces of the filtering plates. Adapted with permission of The Company of Biologists Ltd from Cohen et al. (2018), permission conveyed through Copyright Clearance Center, Inc. PO, palatal organ.

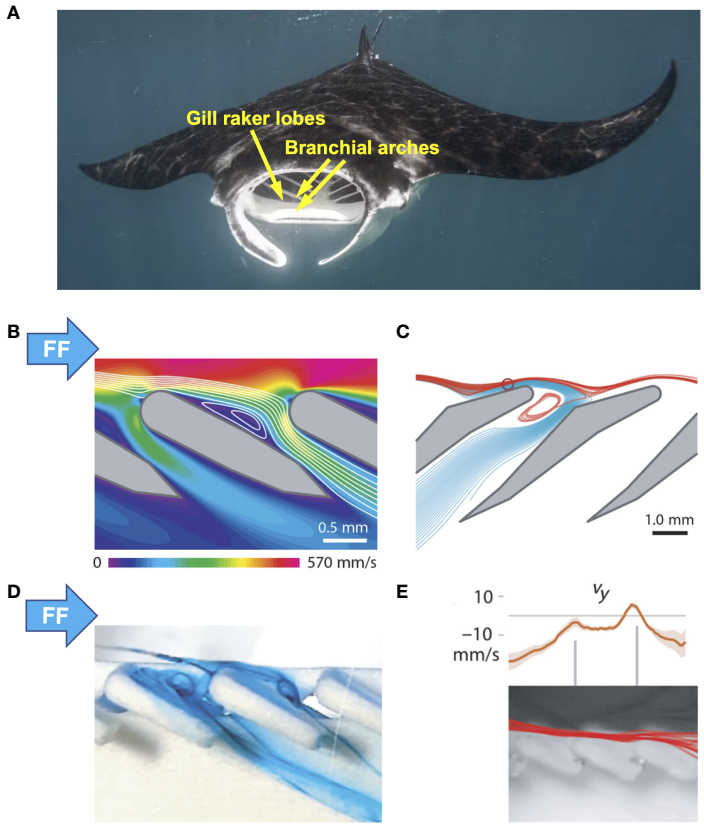

FIGURE 11
Ricochet filtration has been proposed by Divi et al. (2018) as a unique nonclogging particle separation mechanism operating in the highly modified gill raker lobes of ram SF manta rays (Mobulidae). **(A)** Unlike in bony fishes, water in the buccal cavity of mobulids must make an abrupt 90° turn to reach the rows of GR lobes that extend dorso- and ventro-laterally between the branchial arches. *Mobula alfredi*, © Edy Setyawan, modified and used with permission, not covered by the CC-BY license. **(B)** CFD simulation of flow speed and streamlines along and between *Mobula birostris* GR lobes in the wing-like orientation (Re = 990). Water forms a thin boundary layer on the upstream surface of each lobe and passes around a large, captive vortex in the pore between consecutive lobes before exiting as filtrate. **(C)** CFD simulation of fluid streamlines (blue) and particle trajectories (350 µm diameter; neutrally buoyant; center of mass, red) as they pass over *Mobula tarapacana* lobes in the spoiler-like orientation (Re = 1115). Particles (e.g., dark red outline) encounter the tips of the lobes by direct interception. Consequently, solid-liquid separation occurs as contact forces cause particles to recoil elastically from the lobe surface and ricochet back into the faster freestream flow, deviating from the fluid streamlines that pass through the filter pore. **(D)** Dye injection in flow tank experiments with physical models at 4x scale to visualize fluid pathlines around *M. birostris* lobes in the wing-like orientation (Re = 745), for comparison with **(B)**. **(E)** Trajectories (red) of *Artemia* cysts passing over physical models of *M. birostris* lobes in the wing-like orientation at 1x scale (Re = 309) in flow tank experiments. Increases in the vertical velocity of particles corresponded to the location of the leading edge of each lobe. **(B–E)** adapted from Divi et al. (2018), © the Authors, some rights reserved; exclusive licensee AAAS. **(B–E)** distributed under a CC BY-NC 4.0 license http://creativecommons.org/licenses/by-nc/4.0/. **(B–E)** reprinted with permission from AAAS. FF, freestream flow.

vortex prior to exiting as filtrate from the pores (Figures 11A, B) (Divi et al., 2018). However, particles (~ 200 – 800 µm diameter) deviated from these streamlines and did not enter the pores (Figure 11E). Instead, particles encountered the leading edge of the lobes by direct interception. The CFD simulations indicated that contact forces caused particles to recoil elastically from the lobe surfaces (i.e., "ricochet" away from the pores), thereby concentrating the particles in the water above the lobes. Divi et al. (2018) concluded that ricochet filtration in mobulid rays is a unique nonclogging filtration mechanism that operates at high flow rates and effectively filters particles with densities ranging from 950 to 1100 kg m^{-3}. Unlike the physical principles of deterministic lateral displacement (see critical separation radius and stagnation streamline discussed in section 5.8 below), ricochet separation involves contact forces that cause particles to recoil elastically (i.e., ricochet) from uniquely structured lobe surfaces.

Adelmann et al. (2022) applied ricochet filtration to design either flat filters or cylindrical filters that could be employed in hoses and pipe systems as precipitators for sand. Their cylindrical design differed from the relatively flat filter plates of manta rays. The highest precipitator efficiency of > 95% was achieved in experiments using the cylindrical "spoiler-like" arrangement (sand diameter ~ 240 µm; Adelmann et al., 2022).

5.8 Lateral displacement

Deterministic lateral displacement arrays, termed "bump arrays", of staggered obstacles (e.g., microposts) were discovered by Huang et al. (2004) and are used today in microfluidics and mesofluidics for the size separation of particles at gap Re ranging from 10^{-3} to 10^{3} and particle sizes from submicron to millimeters

(Hochstetter et al., 2020; Burns et al., 2021). In deterministic lateral displacement devices and similar sieve-based lateral displacement arrays in crossflow (Dijkshoorn et al., 2018), the physical principle that results in particle separation is that particles with a radius larger than the critical separation radius are repeatedly displaced laterally across streamlines (i.e., are "bumped") upon direct interception with the obstacles, whereas smaller particles follow streamlines (Salafi et al., 2019; Pease et al., 2022). The critical separation radius is determined by the specific geometry and operating parameters of each lateral displacement array, and is identified with reference to the stagnation streamline that terminates on each obstacle (Hochstetter et al., 2020).

Witkop et al. (2023) conducted flume experiments with conical physical models that had 3D-printed arrays of generalized GRs (gap Re 260 – 350, calculated using the flume speed of 19.3 cm s^{-1} and the slot width of 1.35 or 1.8 mm, scaled to match the swimming speed and GR dimensions from SEMs of the ram SF American shad, *Alosa sapidissima*, Clupeidae) (Figures 12A, B). To approximate the value of the critical separation radius at each GR (i.e., obstacle) using CFD simulations and the principles of deterministic lateral displacement, the streamline that terminated at the stagnation point on each GR was traced back to the location where that streamline passed over the GR immediately upstream in the array (Figure 12C). The shortest distance between that "dividing streamline" (i.e.,

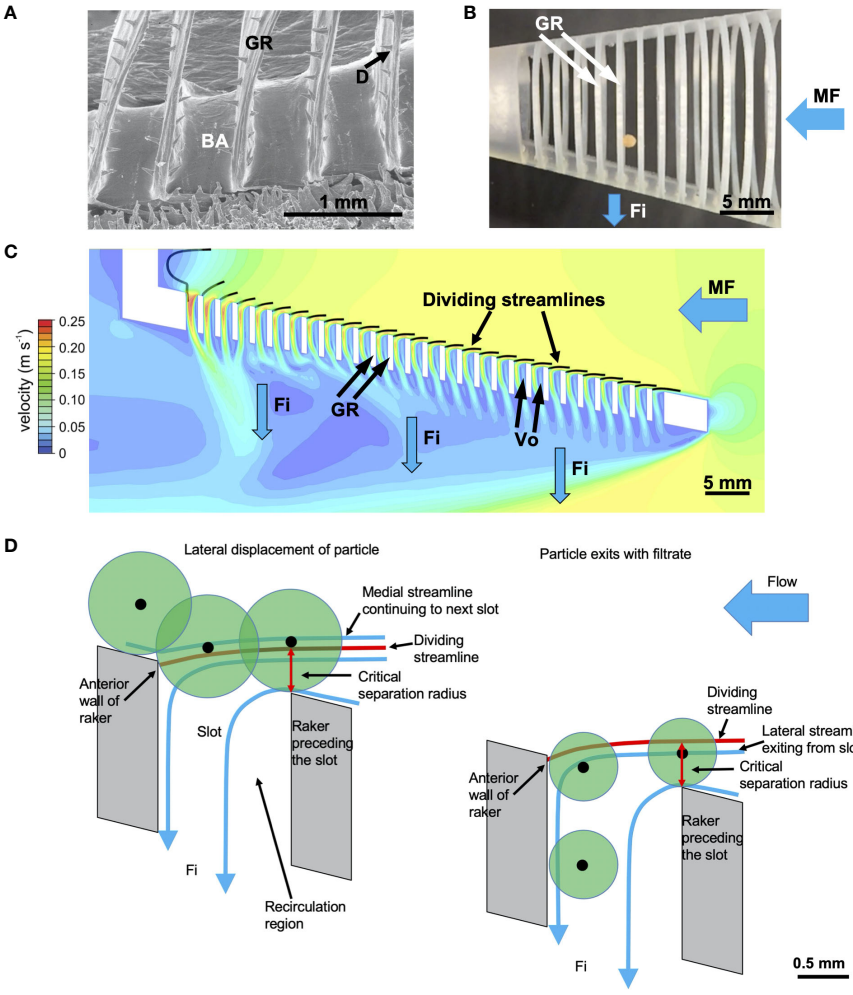

FIGURE 12
The gill rakers of SF fishes have been proposed by Witkop et al. (2023) to function using the principles of lateral displacement arrays for the size separation of particles in microfluidics and mesofluidics. **(A)** SEMs of GRs on the BAs of ram SF American shad (Clupeidae) were the basis for the design of generalized models. **(B)** 3D-printed conical models were used in flume experiments to quantify particle exit from each slot between adjacent GRs (gap Re 260 – 350). **(C)** CFD simulations of flow patterns in the conical physical models were used to quantify the location of each dividing streamline (i.e., stagnation streamline). **(D)** Schematic illustration of particle separation that was recorded in the flume experiments using the physical models. Statistical analyses supported the hypothesis that the shortest distance between the dividing streamline and the surface of the preceding GR predicts the maximum radius of a particle that will exit from the physical model by passing through that slot in the flume experiments. This theoretical maximum radius is analogous to the critical separation radius in microfluidic and mesofluidic devices that use deterministic lateral displacement and sieve-based lateral displacement for the size separation of particles. **(A–D)** adapted from Witkop et al. (2023), CC BY 4.0. BA, branchial arch; D, denticle; Fi, filtrate; GR, gill raker; MF, mainstream flow; Vo, vortex.

stagnation streamline) and the surface of the preceding GR was identified as the maximum radius of a particle that would exit through the gaps between GRs (Van Wassenbergh and Sanderson, 2023; Witkop et al., 2023, Figure 12D).

In the immediate vicinity of the GRs, particles that were smaller than the gap between GRs but had a radius larger than the critical separation radius skipped over the trapped vortex that was generated downstream from each GR and then approached the surface of the subsequent GR (Figure 12D, left). Because the center of these particles was located medial to the dividing streamline (i.e., closer to the interior of the model), these particles deviated from streamlines as they were displaced toward the interior of the model and then continued to travel toward the posterior of the model. This lateral displacement of particles with a radius larger than the critical separation radius is called "deterministic" because the specific locations of the dividing streamlines constrain the center of these particles to be displaced closer to the interior of the model.

Particles that had a radius smaller than the critical separation radius exited with the filtrate through the gaps between GRs (Figure 12D, right). The hypothesis predicting the exit of particles based on mass flow rates, the critical separation radius as determined by the location of the dividing streamlines, and particle size was supported by the results of the flume experiments, indicating that the physical principles of lateral displacement arrays can be applied to the design of biomimetic models based on the gill rakers of SF fishes (Witkop et al., 2023).

This functional analogy between lateral displacement arrays and the arrangement of SF fish filter elements provides new perspectives and metrics for exploring particle separation in SF fishes and lateral displacement arrays (Witkop et al., 2023). Further research is needed to determine whether lateral displacement systems in SF fishes are dependent on the contact forces modeled in ricochet filtration by Divi et al. (2018), and whether ricochet filtration in manta rays and devil rays is dependent on the critical separation radius identified in lateral displacement systems with reference to the stagnation streamline (e.g., Hochstetter et al., 2020).

5.9 Multiple or hybrid mechanisms within species

Experiments are needed to determine whether species use multiple or hybrid particle separation mechanisms during suspension feeding. Very limited data are available to address whether SF fishes exhibit intra-individual variation in particle separation mechanisms depending on fish ontogenetic stage and on prey size, density, etc. (e.g., Sanderson et al., 1996b; Callan and Sanderson, 2003), and no experiments have tested for inter-individual variation within species. Because four of the eight particle separation mechanisms discussed here for SF fishes have been proposed within the past ten years only, the potential for hybrid mechanisms that combine morphological and functional aspects of more than one mechanism has not been explored. The possibility of multiple or hybrid particle separation mechanisms within SF fish species has important ecological and evolutionary implications, particularly if the composition of prey species is in flux due to environmental changes, and warrants study.

6 Retention of particles smaller than the pore sizes

Researchers have been particularly interested in the retention of particles that are smaller than the pore sizes between the filter elements in SF fishes. Such retention may characterize the occurrence of novel particle separation mechanisms that do not involve the accumulation of particles on the filter elements and that could therefore reduce clogging. The rationale is that, if a non-adhesive filter can evolve or can be designed by a filtration engineer to separate particles that are smaller than the pore size, then such a filter should retain the targeted particles (i.e., the desired particles of interest) with minimal clogging.

However, primary literature articles that have been cited previously as supporting the retention of particles smaller than the pore sizes in SF fishes have often been studies of species that were particulate feeding on individual prey rather than SF, species for which pore measurements were made on the first BA only, and/or species in which the prey sizes that were retained were larger than the pore sizes (e.g., Seghers, 1975; Wright et al., 1983; Langeland and Nøst, 1995). In one of the clearest examples of the retention of particles smaller than the pore sizes, Friedland et al. (2006) noted that transitional juvenile Atlantic menhaden showed significant particle retention at a threshold just below 10 μm (Friedland et al., 1984), despite minimum pore sizes of approximately 16 μm between the branchiospinules. Friedland et al. (2006) commented that potential explanations for this discrepancy include a reduction in the effective pore size when particles are crowded on the branchial sieve (Friedland et al., 1984), and/or the retention of particles due to other mechanisms such as those involving crossflow filtration.

As discussed earlier, entrapment in mucus on filter element surfaces in Nile tilapia has been observed endoscopically to result in the capture of particles that can be much smaller than the pores between the filter elements (Sanderson et al., 1996b). Even when SF fishes such as menhaden retain particles that are smaller than the pores, mucus entrapment can be rejected as a particle separation mechanism if mucus cells are not located on the filter elements, as has been documented for Atlantic menhaden branchiospinules (Friedland, 1985) and basking shark GRs (Paig-Tran and Summers, 2014; Surapaneni et al., 2022). Mucus has also been rejected as a particle separation mechanism when endoscopic observations have indicated that mucus does not trap particles during feeding in specific species (e.g., ngege tilapia, Goodrich et al., 2000). However, in all these cases, mucus secreted by cells on other oral surfaces could still be involved in particle aggregation and transport toward the esophagus, as hypothesized for basking sharks (Matthews and Parker, 1950; Sanderson et al., 2016).

The most puzzling example of the retention of particles smaller than the pore sizes was reported by Drenner et al. (1987) for the Galilee Saint Peter's fish or mango tilapia (*Sarotherodon galilaeus*,

Cichlidae) following surgical removal of the GRs and microbranchiospines. Comparable results were reported subsequently by Smith and Sanderson (2007, 2008, 2013) for two related SF cichlid species. Microbranchiospines are denticulate projections (~ 150 μm length) arranged in a row on the BAs of most SF and non-SF species in the family Cichlidae, for which the function is uncertain (Beveridge et al., 1988). Fish that had only partially regenerated the GRs and microbranchiospines on the healed BAs nonetheless retained large numbers of microspheres (20 – 70 μm in diameter) while feeding on zooplankton. The surgical procedure did not affect particle ingestion rates or size selectivity of microspheres (Drenner et al., 1987).

In experiments with two species that are closely related to *S. galilaeus* (*Oreochromis aureus*, blue tilapia, and *O. esculentus*, ngege tilapia, Cichlidae), Smith and Sanderson (2007, 2008, 2013) modified the experimental protocol of Drenner et al. (1987). The procedures were refined by ensuring that the healed BAs were smooth without regeneration of GRs and microbranchiospines, by confirming with a fiberoptic endoscope that mucus was not visible and that particles were not retained on the BAs during crossflow filtration, and by measuring and counting microspheres in all fecal strings to quantify particle retention. Surgical removal of all GRs and microbranchiospines in these two tilapia species affected particle size selectivity in *O. esculentus* but did not significantly affect the total number of particles (11 – 200 μm diameter) retained by either species. Both species continued to selectively ingest particles > 50 μm. Interestingly, after the surgery, *O. esculentus* retained significantly more microspheres 51 – 70 μm in diameter and significantly fewer microspheres 91 – 130 μm in diameter compared to retention with intact oral structures (Smith and Sanderson, 2013). The continued size selectivity and the decreased retention of larger particles following removal of the filter elements suggests that particle separation mechanisms such as inertial lift, shear-induced migration, or lateral displacement may have occurred at the level of the BAs themselves.

7 3D movement of gill rakers and associated protrusions

Despite the critical importance of the pore sizes between filter elements, there have been very few studies on the extent and control of the three-dimensional movement of GRs and associated protrusions during SF. Although BA and GR abduction during mouth opening can be observed readily *in vivo* in multiple taxa of SF fishes, the functional morphological mechanisms that control the erection, rotation, and spreading of GRs on the BAs in SF and non-SF fishes have been investigated rarely (e.g., Matthews and Parker, 1950; Kirchhoff, 1958). Consequently, data are not available to describe and explain the apparent ability of the GRs on the BAs of many SF and non-SF fishes to move during BA abduction as the mouth is opened. Such GR movements can be observed readily in many taxa by manually manipulating freshly dead specimens to cause abduction of the BAs. Further study is a high priority, because the specific 3D orientations of the GRs relative to the approaching flow while the mouth is opened and closed and the BAs are abducted and adducted, as well as concomitant changes in the sizes and shapes of the gaps between GRs, are key for further progress in modeling fish SF.

Paddlefish and basking sharks have evolved convergent morphology consisting of long, thin GRs attached to the anterolateral and posteromedial margins of deep slots formed by the BAs (Sanderson et al., 2016). During ram SF *in vivo*, the GRs of both species can be observed to abduct and extend across much of each slot between adjacent BAs. However, unlike the case in many other SF fish species, the GRs in freshly dead paddlefish specimens lie relatively flat against the BAs rather than erecting passively when the BAs are abducted by manual manipulation. This suggests that GR abduction in paddlefish may be caused actively (e.g., by muscle contraction) or passively (e.g., by water pressure).

Imms (1904) and Matthews and Parker (1950) described muscle fibers as well as elastic fibers attached to the basal part of each GR, connecting the base of the GR to the BA in paddlefish and the basking shark, respectively. Both suggested that contraction of these muscle fibers could pull the GRs away from the sides of the BAs during SF, whereas the elastic fibers could return the GRs to lie flat on the BAs. However, unlike Imms (1904), Matthews and Parker (1950, p. 565) suggested that elastic fibers in a band of connective tissue connecting the bases of the basking shark GRs could serve to maintain GR position "against the pressure of the gill current", and could subsequently return the GRs to their resting position flat on the BA surfaces when the mouth had closed and the pressure had ceased. In what appears to be the only report for bony fishes, Kirchhoff's (1958) extensive study on the functional morphology of the herring (*Clupea harengus*, Clupeidae) included a detailed description of a hypothesized mechanism for GR movement in three dimensions during SF. In contrast to the proposed mechanisms for paddlefish and basking sharks, Kirchhoff (1958) suggested that stretching of an elastic band connecting the GRs along the BA was responsible for GR abduction and rotation during mouth opening and BA abduction.

In a comprehensive assessment of teleost striated muscles, Winterbottom (1974) described minute muscles called interbranchiales abductores connecting the respiratory gill filaments to the lateral faces of the BAs. He noted that these muscle fibers may become "intimately associated" with the GRs, especially in species with well-developed GRs, and he illustrated the interbranchiales abductores attaching to the filaments and to the bases of the GRs in a planktivorous deep-sea fish (Winterbottom, 1974, p. 261). Springer and Johnson (2004) referred to "gill filament muscles" that they considered to be essentially the same as the interbranchiales abductores, and noted that these fine muscles could be obscured by or fused with adductor muscles on the BAs that attach the epibranchial to the ceratobranchial. They recommended additional study of these adductors and gill filament muscles. The extent to which any of these muscles are thought to cause gill filament and GR movement is not clear.

Using histological sections of the BAs of SF common bream (*Abramis brama*, Cyprinidae), Hoogenboezem et al. (1991) identified a complex of minute muscles connecting the bases of the lateral GRs to the BA. Using X-ray cinematography, they observed that zooplankton prey to which a 1-mm iron sphere had

been glued were retained between adjacent BAs. They proposed a reducible-channel model of branchial sieve adjustment in which muscles could retain particles by moving the tips of lateral GRs into the channels between the medial GRs. Subsequently, van den Berg et al. (1994b) revised the names and functions of the muscles in this complex and expanded the application of the reducible-channel model to carp (*Cyprinus carpio*, Cyprinidae). Vandewalle et al. (2000) addressed the discrepancies between these earlier reports and summarized the most recently proposed names, locations, and functions of these muscles. However, the functional morphology of these muscles and their ability to control GR movement do not appear to have been explored subsequently in the primary literature on SF or non-SF species (e.g., Hoogenboezem, 2000; Sibbing and Nagelkerke, 2001; Presti et al., 2020). Endoscopic videotapes of SF *Cyprinus carpio* did not record GR movements that were independent of BA movements (Callan and Sanderson, 2003).

Similarly, the potential for active or passive movement of denticles and other protrusions on the GRs is virtually unstudied. For example, in specimens of Pacific sardine (*Sardinops sagax*, Clupeidae) and northern anchovy (*Engraulis mordax*, Engraulidae) that had been frozen and subsequently thawed, Rykaczewski (2009) noted under a light microscope that the denticles on the GRs deflected passively at their bases in response to water pressure, abducting to extend toward the adjacent GR. Thus, there is an urgent need for research on active or passive movements of GRs and associated protrusions during SF in multiple taxa.

Fortunately, the functional, morphological, and biomechanical mechanisms that are responsible for BA abduction and the 3D expansion of fish oral cavity volume during feeding have been well studied using innovative approaches (e.g., Camp et al., 2015; Kenaley and Lauder, 2016; Olsen et al., 2020). In addition, techniques and equipment for the 3D reconstruction, visualization, and manipulation of complex and dynamic biological structures are advancing rapidly (Irschick et al., 2022). Such research provides a wealth of knowledge on which future progress in our understanding of 3D movements of the BAs and oral cavity during SF can build. For example, a new shape space-based approach for estimating complex 3D shapes from single monocular 2D images is being developed to create 3D skeletal representations of the basking shark head (Paskin et al., 2022). The ultimate goal of that work is to enable a 3D reconstruction of the head skeleton, including identification of the skeletal joint locations, from a 2D image of a basking shark oral cavity during SF (Paskin et al., 2022). This is valuable because 2D images of ram SF oral cavities can be obtained relatively easily *in vivo*.

8 Unidentified SF fish taxa, diets, and particle separation mechanisms

8.1 Unidentified SF fish taxa

At present, whether a fish species has been identified as a suspension feeder is based primarily on whether the species has been observed to exhibit either pump or ram SF behavior, and/or whether minute particles such as phytoplankton are abundant in the gut. For these reasons, at least three genera of SF fishes in a non-SF family were reported to have been overlooked previously (*Seriola*, *Pseudocaranx*, *Oligoplites*, Carangidae, Sanderson et al., 1996a; Sazima, 1998), and other species, genera, and even families of SF fishes may remain yet unrecognized. Such oversights are of concern because the GRs of non-SF fish species are generally assumed to serve simply as barriers that block the exit of large particles between the BAs and thereby protect the gill filaments. The intraoral morphology and fluid dynamics of non-SF species have not been evaluated from the perspectives of the types and sizes of particles that might be retained during SF processes. Therefore, species that have been assumed to be solely particulate feeders might obtain ecologically important dietary components from the non-selective retention of suspended particles, particularly species that are also ram ventilators (e.g., scombrids such as tuna, Magnuson and Heitz, 1971; Estrada et al., 2005).

8.2 Particle retention by non-SF fish species

Sanderson et al. (1998) quantified the retention of suspended polystyrene microspheres (31 – 90 μm diameter) and brine shrimp cysts (210 – 300 μm diameter) by two non-SF cyprinid species (insectivorous Sacramento squawfish, *Ptychocheilus grandis*; omnivorous benthic-feeding California roach, *Hesperoleucus symmetricus*) in the presence of finely crushed Tetramin flakes or dead adult brine shrimp. Although SF behavior was not observed during the experiments and electron microscopy of these species did not show unique intraoral morphology, the large number of brine shrimp cysts quantified in the fish feces after 10 minutes of exposure to the particles was equivalent to the amount in a volume of aquarium water that was 1 - 15 times the fish body volume. In addition, small numbers of microspheres were excreted in the fecal strings. The brine shrimp cysts were large enough to have been trapped between GRs, while both the brine shrimp cysts and microspheres could have been retained on mucus-covered oral surfaces. Sanderson et al. (1998) concluded that non-SF fish species may routinely retain small suspended particles during particulate feeding on larger prey or during ventilation, and noted that there could be ecological and ecotoxicological implications (as evidenced recently for microplastics, e.g., De Sales-Ribeiro et al., 2020).

8.3 Retention of detritus in SF fishes

The potential retention of detritus is another case in which dietary components of SF and non-SF fishes might not be recognized fully. Detritus refers broadly to aggregates of organic material consisting of dead plankton, decaying vascular plant material, fecal pellets, microbes, etc. In marine environments, similar aggregates have also been termed “marine snow” (Turner, 2015). Detritus appears in the gut of Atlantic menhaden as unidentifiable amorphous material (Lewis and Peters, 1994)

which has relatively low nutritive value compared to zooplankton and phytoplankton but can comprise a significant fraction of the juvenile menhaden diet (Annis et al., 2011). Juveniles of two pump SF mullet species ingested marine snow in laboratory experiments (*Mugil curema*, *M. cephalus*, Mugilidae, Larson and Shanks, 1996). Research is needed to determine whether other SF species as well as non-SF species also ingest suspended detritus and marine snow, as this could impact ecosystem energy budgets and nutrient cycles.

8.4 Oil-water separation mechanisms in fishes

Oil-water separation mechanisms, which could be either solid-liquid or liquid-liquid separations depending on temperature, warrant study in SF fishes. A number of SF fish species can protrude the dorsal portion of their oral jaws above the surface of the water, and either swim the open mouth forward around the surface layers (ram SF) or suck the surface layers into the oral cavity (pump SF). Ram SF fishes have been reported to swim forward with their open jaws in this position (e.g., whale shark, *Rhincodon typus*, Motta et al., 2010; manta ray, *Mobula birostris*, Paig-Tran et al., 2013), whereas pump SF fishes can remain stationary or swim forward slowly while pumping the surface layers into their oral cavity (e.g., goldfish, Edwards et al., 2017). Bighead carp have been reported to use both ram and pump SF to engulf surface layers of water (Kolar et al., 2007).

In laboratory experiments, untrained goldfish used pump SF behavior to feed voluntarily on liquid canola oil in a layer on the surface of the water in the aquarium (Edwards et al., 2017). Nine of 15 individuals swallowed oil that was quantifiable in the gut using fatty acid methyl ester (FAME) preparations for gas chromatography-mass spectrometry (GC-MS) analysis. Whereas control fish that were in aquaria without access to the oil on the water surface had no detectable oil in their guts, fish with access to the surface swallowed 0.01% - 14% of the 2.0 ml of oil present in the aquaria during the 20-minute experiments. SF goldfish in manmade outdoor ponds also exhibited pump SF behavior at the pond surface in response to vegetable oils that had been added to the surface (Edwards et al., 2017). In laboratory experiments, zooplankton and barnacles use their appendages to capture edible as well as crude oil droplets up to ~ 10 μm diameter (Letendre et al., 2020; Letendre and Cameron, 2022). Mechanisms by which SF fishes might retain surface films, suspended droplets, or floating globules of hydrophobic organics have not been investigated, although crossflow membrane filtration and hydrocyclones are major technologies for separating oils from wastewater (e.g., Nunes et al., 2021; Su et al., 2021; Yang et al., 2022).

Natural slicks at the air-sea interface can cover up to ~ 80% of the surface during calm weather conditions in coastal marine areas. Recent data indicate that natural slicks often have high organic matter content, composed primarily of biosurfactants produced by bacteria and by micro- and macroalgae (review by Voskuhl and Rahlff, 2022). In the sea-surface microlayer, these polymeric materials orient according to their hydrophobic constituents (e.g., glycolipids, lipopeptides, and fatty acids) versus hydrophilic constituents (Ron and Rosenberg, 2001).

Thus far, the potential abilities of SF fishes and continuous skim-feeding balaenid whales to separate and ingest the hydrophobic organics in natural slicks and/or ingest zooplankton associated with surface slicks are unknown. However, Couturier et al. (2013a, 2013b) noted that signature fatty acid analyses of tissue from whale sharks and the reef manta ray *Mobula alfredi* raised questions about the origin of their primary food source, suggesting the importance of both pelagic and demersal zooplankton. Recently, the fatty acid profiles of whale shark tissues and feces were identified as being most similar to those of the floating macroalgae *Sargassum*, leading Meekan et al. (2022) to suggest that whale sharks are omnivores that consume *Sargassum* fronds and associated epibionts. To date, the potential roles that naturally occurring surface films and droplets of hydrophobic organics (such as might be produced by the degradation of *Sargassum*) might have in the diet of SF fishes, and the particle separation mechanisms that could be used, remain virtually unstudied (Edwards et al., 2017).

9 Conclusions and challenges

This comprehensive synthesis has assessed our knowledge of particle separation mechanisms in SF fishes, related recent developments to industrial, commercial, and biomedical separation processes and applications, identified critical gaps in our understanding and approaches, and offered perspectives on future research priorities. Recent research has led to transformational discoveries in the fluid dynamics and biomechanics of filter element function in SF fishes. Particle separation mechanisms in SF fishes are not limited to dead-end filtration through porous filter media or mucus entrapment on an adhesive filter. Of the eight particle separation mechanisms for SF fishes presented here, six have been proposed since 2001.

Although substantial progress has been made over the past three decades in understanding the ecological, morphological, and functional complexity of fish SF, important unresolved questions vastly outnumber answers. A major goal continues to be the identification of patterns and unifying principles for particle separation across the breadth of SF fish taxa, morphology, ecology, and function (e.g., patterns of evolutionary convergence or divergence related to facultative versus obligate SF, pump versus ram; Reynolds numbers; dietary particle size, shape, density, and concentration). Challenges in this endeavor will be the diversity of SF fishes and the likely operation of multiple or hybrid particle separation mechanisms within species. As discussed here, unidentified SF fish taxa, diets, and particle separation mechanisms await discovery, including the potential separation of hydrophobic films and droplets by SF fishes.

During the past twenty years, transformational research in filtration engineering has also opened entirely new directions for particle manipulation and separation, such as inertial microfluidics (Di Carlo et al., 2007; Di Carlo, 2009) and deterministic lateral displacement (Huang et al., 2004). Substantial future synergies will be achieved by combining the techniques, approaches, and insights of diverse biologists, biomechanics and fluid dynamics researchers, and engineers (including chemical, mechanical, biomedical, and filtration engineering). As biomimetics and bioinspired design continue to

expand, additional innovative solutions will be developed for particle separation with industrial and commercial applications. Nonlinear dynamics are a promising focus of research for microfluidics at moderate Re ($1 < Re < \sim 100$, Stoecklein and Di Carlo, 2019; Xia et al., 2021; Battat et al., 2022), and biological systems are inherently nonlinear. For example, nonlinearities arising from secondary flows (e.g., curved channels, oscillatory flow; Zhao et al., 2020) and the active and passive movement of oral cavity structures (BAs, GRs, and associated protrusions) during fish SF have the potential for nonintuitive effects on particle separation.

The novel particle separation mechanisms proposed recently in SF fishes are distinct from mechanisms described in SF invertebrates. This could be related to fundamental differences between SF fishes and most SF invertebrates, including (1) the oral cavity of SF fishes forms an enclosed porous channel or pipe, (2) all SF fishes are active suspension feeders with control over pore size, pressure, and flow velocity, and (3) the filter elements, pore sizes, and flow speeds can be larger in SF fishes, resulting in higher Re. All recently proposed particle separation mechanisms in SF fishes (inertial lift and shear-induced migration, reduction of effective gap size by vortices, cross-step filtration, vortical flow along outer faces of gill raker plates, ricochet filtration, lateral displacement) require crossflow in a channel or pipe, usually involving the generation of vortical flow. Studies of convergence/divergence in form and function of SF fishes and other SF vertebrates (e.g., tadpoles, flamingos and anatine ducks, balaenid and balaenopterid whales; Sanderson and Wassersug, 1993), as well as invertebrate taxa in which the filter elements operate in enclosed body cavities or tubes (e.g., Cephalochordata, Tunicata, Bivalvia, Brachiopoda; Hamann and Blanke, 2022) are also promising future directions.

Author contributions

SS: Conceptualization, Visualization, Writing – original draft, Writing – review & editing, Formal Analysis.

Funding

The author(s) declare that financial support was received for the research, authorship, and/or publication of this article. Supported by a research leave from William & Mary to SS, and by an international travel grant from the Reves Center for International Studies at William & Mary.

Acknowledgments

With gratitude and admiration for my graduate and post-doctoral mentors: Karel Liem, Richard Wassersug, Angela Cheer, and Joseph J. Cech, Jr., and appreciation for my collaborators. Special thanks to Mason Dean and Venkata A. Surapaneni for their expertise in initiating and organizing the Filters in Biology + Biomimetics conference, Berlin, May 2023.

Conflict of interest

SS is the inventor on US Patent No. 9,480,951; William & Mary, assignee. "Mass transfer device and system generating vortices for particle suspension, concentration, and transport", issued November 1, 2016.

Publisher's note

References

Adelmann, B., Schwiddessen, T., Götzendorfer, B., and Hellmann, R. (2022). Evaluation of SLS 3D-printed filter structures based on bionic manta structures. *Materials* 15, 8454. doi: 10.3390/ma15238454

Annis, E. R., Houde, E. D., Harding, L. W. Jr., Mallonee, M. E., and Wilberg, M. J. (2011). Calibration of a bioenergetics model linking primary production to Atlantic menhaden *Brevoortia tyrannus* growth in Chesapeake Bay. *Mar. Ecol. Prog. Ser.* 437, 253–267. doi: 10.3354/meps09254

Authimoolam, S. P., and Dziubla, T. D. (2016). Biopolymeric mucin and synthetic polymer analogs: Their structure, function, and role in biomedical applications. *Polymers* 8, 71. doi: 10.3390/polym8030071

Bansil, R., and Turner, B. S. (2018). The biology of mucus: Composition, synthesis and organization. *Adv. Drug Deliv. Rev.* 124, 3–15. doi: 10.1016/j.addr.2017.09.023

Battat, S., Weitz, D. A., and Whitesides, G. M. (2022). Nonlinear phenomena in microfluidics. *Chem. Rev.* 122, 6921–6937. doi: 10.1021/acs.chemrev.1c00985

Bayer, I. S. (2022). Recent advances in mucoadhesive interface materials, mucoadhesion characterization, and Technologies. *Adv. Mater. Interfaces* 9, 2200211. doi: 10.1002/admi.202200211

Bej, R., and Haag, R. (2022). Mucus-inspired dynamic hydrogels: Synthesis and future perspectives. *J. Am. Chem. Soc* 144, 20137–20152. doi: 10.1021/jacs.1c13547

Belfort, G., Davis, R. H., and Zydney, A. L. (1994). The behavior of suspensions and macromolecular solutions in crossflow microfiltration. *J. Membr. Sci.* 96, 1–58. doi: 10.1016/0376-7388(94)00119-7

Beveridge, M. C. M., Briggs, M. R. P., Northcott, M. E., and Ross, L. G. (1988). The occurrence, structure, and development of microbranchiospines among the tilapias (Cichlidae: Tilapiini). *Can. J. Zool.* 66, 2564–2572. doi: 10.1139/z88-377

Bianciardi, A., and Cascini, G. (2022). A bio-inspired approach for boosting innovation in the separation technology sector. *Proc. IMechE Part C: J. Mech. Eng. Sci.* 236, 4533–4550. doi: 10.1177/09544062211052128

Bouhid de Aguiar, I., and Schroën, K. (2020). Microfluidics used as a tool to understand and optimize membrane filtration processes. *Membranes* 10, 316. doi: 10.3390/membranes10110316

Brainerd, E. L. (2001). Caught in the crossflow. *Nature* 412, 387–388. doi: 10.1038/35086666

Brodnicke, O. B., Hansen, C. E., Huie, J. M., Brandl, S. J., and Worsaae, K. (2022). Functional impact and trophic morphology of small, sand-sifting fishes on coral reefs. *Funct. Ecol.* 36, 1936–1948. doi: 10.1111/1365-2435.14087

Brooks, H., Haines, G. E., Lin, M. C., and Sanderson, S. L. (2018). Physical modeling of vortical cross-step flow in the American paddlefish, *Polyodon spathula*. *PloS One* 13, e0193874. doi: 10.1371/journal.pone.0193874

Bulusu, K. V., Racan, S., and Plesniak, M. W. (2020). Macro-rheology characterization of gill raker mucus in the silver carp, *Hypophthalmichthys molitrix*. *J. Vis. Exp.* 161, e61379. doi: 10.3791/61379

Burns, C. A., Veldman, T. G., Serkowski, J., Daniel, R. C., Yu, X. Y., Minette, M. J., et al. (2021). Mesofluidic separation versus dead-end filtration. *Sep. Purif. Technol.* 254, 117256. doi: 10.1016/j.seppur.2020.117256

Callan, W. T., and Sanderson, S. L. (2003). Feeding mechanisms in carp: Crossflow filtration, palatal protrusions and flow reversals. *J. Exp. Biol.* 206, 883–892. doi: 10.1242/jeb.00195

Camp, A. L., Roberts, T. J., and Brainerd, E. L. (2015). Swimming muscles power suction feeding in largemouth bass. *Proc. Natl. Acad. Sci. U.S.A.* 112, 8690–8695. doi: 10.1073/pnas.1508055112

Cerullo, A. R., Lai, T. Y., Allam, B., Baer, A., Barnes, W. J. P., Barrientos, Z., et al. (2020). Comparative animal mucomics: Inspiration for functional materials from ubiquitous and understudied biopolymers. *ACS Biomater. Sci. Eng.* 6, 5377–5398. doi: 10.1021/acsbiomaterials.0c00713

Cheer, A., Cheung, S., Hung, T.-C., Piedrahita, R. H., and Sanderson, S. L. (2012). Computational fluid dynamics of fish gill rakers during crossflow filtration. *Bull. Math. Biol.* 74, 981–1000. doi: 10.1007/s11538-011-9709-6

Cheer, A. Y., Cheung, S., and Sanderson, S. L. (2006). "Computational fluid dynamics of crossflow filtration in suspension-feeding fishes," in *Computational Fluid Dynamics 2004*. Eds. C. Groth and D. W. Zingg (Springer, Berlin), 301–306. doi: 10.1007/3-540-31801-1_4

Cheer, A. Y., Ogami, Y., and Sanderson, S. L. (2001). Computational fluid dynamics in the oral cavity of ram suspension-feeding fishes. *J. Theor. Biol.* 210, 463–474. doi: 10.1006/jtbi.2001.2325

Chen, L., Asai, K., Nonomura, T., Xi, G., and Liu, T. (2018). A review of backward-facing step (BFS) flow mechanisms, heat transfer, and control. *Therm. Sci. Eng. Prog.* 6, 194–216. doi: 10.1016/j.tsep.2018.04.004

Chew, J. W., Kilduff, J., and Belfort, G. (2020). The behavior of suspensions and macromolecular solutions in crossflow microfiltration: An update. *J. Membr. Sci.* 601, 117865. doi: 10.1016/j.memsci.2020.117865

Ciechomski, J. (1967). Investigations of food and feeding habits of larvae and juveniles of the Argentine anchovy *Engraulis anchoita*. *Calif. Coop. Ocean. Fish. Investig. Rep.* 11, 72–81.

Clark, A. S., and San-Miguel, A. (2021). A bioinspired, passive microfluidic lobe filtration system. *Lab. Chip* 21, 3762. doi: 10.1039/D1LC00449B

Cohen, K. E., Ackles, A. L., and Hernandez, L. P. (2022). The role of heterotopy and heterochrony during morphological diversification of otocephalan epibranchial organs. *Evol. Dev.* 24, 79–91. doi: 10.1111/ede.12401

Cohen, K. E., George, A. E., Chapman, D. C., Chick, J. H., and Hernandez, L. P. (2020). Developmental ecomorphology of the epibranchial organ of the silver carp, *Hypophthalmichthys molitrix*. *J. Fish Biol.* 97, 527–536. doi: 10.1111/jfb.14409

Cohen, K. E., and Hernandez, L. P. (2018). Making a master filterer: Ontogeny of specialized filtering plates in silver carp (*Hypophthalmichthys molitrix*). *J. Morphol.* 2018, 1–11. doi: 10.1002/jmor.20821

Cohen, K. E., Hernandez, L. P., Crawford, C. H., and Flammang, B. E. (2018). Channeling vorticity: Modeling the filter-feeding mechanism in silver carp using μCT and 3D PIV. *J. Exp. Biol.* 221, jeb183350. doi: 10.1242/jeb.183350

Collard, F., Gilbert, B., Eppe, G., Roos, L., Compère, P., Das, K., et al. (2017). Morphology of the filtration apparatus of three planktivorous fishes and relation with ingested anthropogenic particles. *Mar. pollut. Bull.* 116, 182–191. doi: 10.1016/j.marpolbul.2016.12.067

Conley, K. R., Ben-Tal, A., Jacobi, Y., Yahel, G., and Sutherland, K. R. (2018a). Not-so-simple sieving by ascidians: re-examining particle capture at the mesh and organismal scales. *Mar. Biol.* 165, 45. doi: 10.1007/s00227-018-3300-8

Conley, K. R., Lombard, F., and Sutherland, K. R. (2018b). Mammoth grazers on the ocean's minuteness: A review of selective feeding using mucous meshes. *Proc. R. Soc B* 285, 20180056. doi: 10.1098/rspb.2018.0056

Cooper, R. L., Nicklin, E. F., Rasch, L. J., and Fraser, D. J. (2023). Teeth outside the mouth: The evolution and development of shark denticles. *Evol. Dev.* 25, 54–72. doi: 10.1111/ede.12427

Couturier, L. I. E., Rohner, C. A., Richardson, A. J., Marshall, A. D., Jaine, F. R. A., Bennett, M. B., et al. (2013a). Stable isotope and signature fatty acid analyses suggest reef manta rays feed on demersal zooplankton. *PloS One* 8, e77152. doi: 10.1371/journal.pone.0077152

Couturier, L. I. E., Rohner, C. A., Richardson, A. J., Pierce, S. J., Marshall, A. D., Jaine, F. R. A., et al. (2013b). Unusually high levels of n-6 polyunsaturated fatty acids in whale sharks and reef manta rays. *Lipids* 48, 1029–1034. doi: 10.1007/s11745-013-3829-8

Day, S. W., Higham, T. E., Holzman, R., and Van Wassenbergh, S. (2015). Morphology, kinematics, and dynamics: The mechanics of suction feeding in fishes. *Integr. Comp. Biol.* 55, 21–35. doi: 10.1093/icb/icv032

De Sales-Ribeiro, C., Brito-Casillas, Y., Fernandez, A., and Caballero, M. J. (2020). An end to the controversy over the microscopic detection and effects of pristine microplastics in fish organs. *Sci. Rep.* 10, 12434. doi: 10.1038/s41598-020-69062-3

Di Carlo, D. (2009). Inertial microfluidics. *Lab. Chip* 9, 3038–3046. doi: 10.1039/b912547g

Di Carlo, D., Edd, J. F., Humphry, K. J., Stone, H. A., and Toner, M. (2009). Particle segregation and dynamics in confined flows. *Phys. Rev. Lett.* 102, 94503. doi: 10.1103/PhysRevLett.102.094503

Di Carlo, D., Irimia, D., Tompkins, R. G., and Toner, M. (2007). Continuous inertial focusing, ordering, and separation of particles in microchannels. *Proc. Natl. Acad. Sci. U.S.A.* 104, 18892–18897. doi: 10.1073/pnas.0704958104

Dijkshoorn, J. P., de Valença, J. C., Wagterveld, R. M., Boom, R. M., and Schutyser, M. A. (2018). Visualizing the hydrodynamics in sieve-based lateral displacement systems. *Sci. Rep.* 8, 12861. doi: 10.1038/s41598-018-31104-2

Dijkshoorn, J. P., Schutyser, M. A. I., Wagterveld, R. M., Schroën, C. G. P. H., and Boom, R. M. (2017). A comparison of microfiltration and inertia-based microfluidics for large scale suspension separation. *Sep. Purif. Technol.* 173, 86–92. doi: 10.1016/j.seppur.2016.09.018

Dincau, B., Tang, C., Dressaire, E., and Sauret, A. (2022). Clog mitigation in a microfluidic array *via* pulsatile flows. *Soft Matter* 18, 1767–1778. doi: 10.1039/D2SM00013J

Di Vaira, N. J., Laniewski-Wollk, L., Johnson, R. L. Jr., Aminossadati, S. M., and Leonardi, C. R. (2022). Influence of particle polydispersity on bulk migration and size segregation in channel flows. *J. Fluid Mech.* 939, A30. doi: 10.1017/jfm.2022.166

Divi, R. V., Strother, J. A., and Paig-Tran, E. W. M. (2018). Manta rays feed using ricochet separation, a novel nonclogging filtration mechanism. *Sci. Adv.* 4, eaat9533. doi: 10.1126/sciadv.aat9533

Dou, Y., Tian, D., Sun, Z., Liu, Q., Zhang, N., Kim, J. H., et al. (2017). Fish gill inspired crossflow for efficient and continuous collection of spilled oil. *ACS Nano* 11, 2477–2485. doi: 10.1021/acsnano.6b07918

Drenner, R. W., Hambright, K. D., Vinyard, G. L., and Gophen, M. (1987). Particle ingestion by *Tilapia galilaea* is not affected by removal of gill rakers and microbranchiospines. *Trans. Am. Fish. Soc* 116, 272–276. doi: 10.1577/1548-8659(1987)116<272:PIBTGI>2.0.CO;2

Drenner, R. W., Mummert, J. R., deNoyelles, F. Jr., and Kettle, D. (1984). Selective particle ingestion by a filter-feeding fish and its impact on phytoplankton community structure. *Limnol. Oceanogr.* 29, 941–948. doi: 10.4319/lo.1984.29.5.0941

Drijer, I., and Schroën, K. (2018). Modelling shear induced diffusion based particle segregation: A basis for novel separation technology. *Appl. Sci.* 8, 108. doi: 10.3390/app8061008

Edwards, K. M., Rice, G. W., and Sanderson, S. L. (2017). Separating oil from water: Suspension-feeding goldfish ingest liquid vegetable oil. *Can. J. Fish. Aquat. Sci.* 74, 524–532. doi: 10.1139/cjfas-2016-0197

Espinosa-Gayosso, A., Ghisalberti, M., Shimeta, J., and Ivey, G. N. (2021). On predicting particle capture rates in aquatic ecosystems. *PloS One* 16, e0261400. doi: 10.1371/journal.pone.0261400

Estrada, J. A., Lutcavage, M., and Thorrold, S. R. (2005). Diet and trophic position of Atlantic bluefin tuna (*Thunnus thynnus*) inferred from stable carbon and nitrogen isotope analysis. *Mar. Biol.* 147, 37–45. doi: 10.1007/s00227-004-1541-1

FAO (2021). *FAO yearbook. Fishery and Aquaculture Statistics 2019* (Rome: Food and Agriculture Organization of the United Nations).

Friedland, K. D. (1985). Functional morphology of the branchial basket structures associated with feeding in the Atlantic menhaden, *Brevoortia tyrannus* (Pisces: Clupeidae). *Copeia* 1985, 1018–1027. doi: 10.2307/1445257

Friedland, K. D., Ahrenholz, D. W., Smith, J. W., Manning, M., and Ryan, J. (2006). Sieving functional morphology of the gill raker feeding apparatus of Atlantic menhaden. *J. Exp. Zool. A Comp. Exp. Biol.* 305, 974–985. doi: 10.1002/(ISSN)1552-499X

Friedland, K. D., Haas, L. W., and Merriner, J. V. (1984). Filtering rates of the juvenile Atlantic menhaden *Brevoortia tyrannus* (Pisces: Clupeidae), with consideration of the effects of detritus and swimming speed. *Mar. Biol.* 84, 109–117. doi: 10.1007/BF00392994

Gerking, S. D. (1994). *Feeding Ecology of Fish* (San Diego: Academic Press).

Gibson, R. N. (1988). Development, morphometry and particle retention capability of the gill rakers in the herring, *Clupea harengus* L. *J. Fish Biol.* 32, 949–962. doi: 10.1111/j.1095-8649.1988.tb05438.x

Goel, G., Hélix-Nielsen, C., Upadhyaya, H. M., and Goel, S. (2021). A bibliometric study on biomimetic and bioinspired membranes for water filtration. *NPJ Clean Water* 4, 41. doi: 10.1038/s41545-021-00131-4

Goldbogen, J. A., Pyenson, N. D., and Shadwick, R. E. (2007). Big gulps require high drag for fin whale lunge feeding. *Mar. Ecol. Prog. Ser.* 349, 289–301. doi: 10.3354/meps07066

Goodrich, J. S., Sanderson, S. L., Batjakas, I. E., and Kaufman, L. S. (2000). Branchial arches of suspension-feeding *Oreochromis esculentus*: Sieve or sticky filter? *J. Fish Biol.* 56, 858–875. doi: 10.1006/jfbi.1999.1205

Haines, G. E., and Sanderson, S. L. (2017). Integration of swimming kinematics and ram suspension feeding in a model American paddlefish, *Polyodon spathula*. *J. Exp. Biol.* 220, 4535–4547. doi: 10.1242/jeb.166835

Hamann, L., and Blanke, A. (2022). Suspension feeders: Diversity, principles of particle separation and biomimetic potential. *J. R. Soc Interface* 19, 20210741. doi: 10.1098/rsif.2021.0741

Hamann, L., Schreiber, K., Hagenmeyer, J., Eduardo, S., Spanke, T., and Blanke, A. (2023). Diversity of filter feeding and variations in cross-flow filtration of five ram-feeding fish species. *Front. Mar. Sci.* 10. doi: 10.3389/fmars.2023.1253083

Hansen, A., Ghosal, R., Caprio, J., Claus, A. W., and Sorensen, P, W. (2014). Anatomical and physiological studies of bigheaded carps demonstrate that the epibranchial organ functions as a pharyngeal taste organ. *J. Exp. Biol.* 217, 3945–3954. doi: 10.1242/jeb.107870

Harrison, I. J., and Howes, G. J. (1991). The pharyngobranchial organ of mugilid fishes: Its structure, variability, ontogeny, possible function, and taxonomic utility. *Bull. Br. Museum Natural History Zoology* 57, 111–132.

Hentschel, B. T., and Shimeta, J. (2019). "Suspension feeders," in *Encyclopedia of Ecology, 2nd edition*, vol. 3 . Eds. S. E. Jørgensen and B. D. Fath (Academic Press, Oxford), 624–629. doi: 10.1016/B978-0-12-409548-9.11133-9

Hochstetter, A., Vernekar, R., Austin, R. H., Becker, H., Beech, J. P., Fedosov, D. A., et al. (2020). Deterministic lateral displacement: Challenges and perspectives. *ACS Nano* 14, 10784–10795. doi: 10.1021/acsnano.0c05186

Holley, L. L., Heidman, M. K., Chambers, R. M., and Sanderson, S. L. (2015). Mucous contribution to gut nutrient content in American gizzard shad *Dorosoma cepedianum*. *J. Fish Biol.* 86, 1457–1470. doi: 10.1111/jfb.12656

Hong, K.-B., Kim, D.-W., Kwark, J., Nam, J.-S., and Ryou, H.-S. (2021). Numerical study on the effect of the pipe groove height and pitch on the flow characteristics of corrugated pipe. *Energies* 14, 2614. doi: 10.3390/en14092614

Hoogenboezem, W. (2000). On the feeding biology of bream (*Abramis brama*). *Neth. J. Zool.* 50, 225–232. doi: 10.1163/156854200505964

Hoogenboezem, W., and van den Boogaart, J. G. M. (1993). Importance of mucus in filter-feeding of bream (*Abramis brama*). *Can. J. Fish. Aquat. Sci.* 50, 472–479. doi: 10.1139/f93-055

Hoogenboezem, W., van den Boogaart, J. G. M., Sibbing, F. A., Lammens, E. H. R. R., Terlouw, A., and Osse, J. W. M. (1991). A new model of particle retention and branchial sieve adjustment in filter-feeding bream (*Abramis brama*, Cyprinidae). *Can. J. Fish. Aquat. Sci.* 48, 7–18. doi: 10.1139/f91-002

Huang, L. R., Cox, E. C., Austin, R. H., and Sturm, J. C. (2004). Continuous particle separation through deterministic lateral displacement. *Science* 304, 5673. doi: 10.1126/science.1094567

Hung, T. C., and Piedrahita, R. H. (2014). Experimental validation of a novel bio-inspired particle separator. *Aquac. Eng.* 58, 11–19. doi: 10.1016/j.aquaeng.2013.09.005

Hung, T. C., Piedrahita, R. H., and Cheer, A. (2012). Bio-inspired particle separator design based on the food retention mechanism by suspension-feeding fish. *Bioinspir. Biomim.* 7, 46003. doi: 10.1088/1748-3182/7/4/046003

Ibrahim, A. N. A. F., Castilho Noll, M. S. M., and Valenti, W. C. (2015). Zooplankton capturing by Nile tilapia, *Oreochromis niloticus* (Teleostei: Cichlidae) throughout post-larval development. *Zoologia* 32, 469–475. doi: 10.1590/s1984-46702015000600006

Idris, I., Moloney, C. L., and van der Lingen, C. D. (2016). Spatial variability in branchial basket meristics and morphology of southern African sardine *Sardinops sagax*. *Afr. J. Mar. Sci.* 38, 351–362. doi: 10.2989/1814232X.2016.1204942

Imms, A. D. (1904). Notes on the gill-rakers of the spoonbill sturgeon, *Polyodon spathula*. *Proc. Zool. Soc Lond.* 2, 22–35. doi: 10.1111/j.1469-7998.1904.tb08311.x

Irschick, D. J., Christiansen, F., Hammerschlag, N., Martin, J., Madsen, P. T., Wyneken, J., et al. (2022). 3D visualization processes for recreating and studying organismal form. *iScience* 25, 104867. doi: 10.1016/j.isci.2022.104867

Jørgensen, C. B. (1966). *Biology of Suspension Feeding* (New York: Pergamon).

Kenaley, C. P., and Lauder, G. V. (2016). A biorobotic model of the suction-feeding system in largemouth bass: The roles of motor program speed and hyoid kinematics. *J. Exp. Biol.* 219, 2048–2059. doi: 10.1242/jeb.132514

Kirchhoff, H. (1958). Funktionell-anatomische untersuchung des visceralapparates von *Clupea harengus* L. *Zoologisches Jahrbücher Abteilung für Anatomie und Ontogenie der Tiere* 76, 461–540.

Kolar, C. S., Chapman, D. C., Courtenay, W. R.Jr., Housel, C. M., Williams, J. D., and Jennings, D. P. (2007). *Bigheaded carps: A biological synopsis and environmental risk assessment* (Bethesda, Maryland: American Fisheries Society, Special Publication 33).

Kumar, G. P., and Das, A. K. (2022). Hybrid microfluidic design for separation of neutrally-buoyant and non-buoyant particles. *Chem. Eng. Process.: Process Intensif.* 180, 108721. doi: 10.1016/j.cep.2021.108721

LaBarbera, M. (1984). Feeding currents and particle capture mechanisms in suspension feeding animals. *Amer. Zool.* 24, 71–84. doi: 10.1093/icb/24.1.71

Lang, T., Klasson, S., Larsson, E., Johansson, M. E. V., Hansson, G. C., and Samuelsson, T. (2016) Searching the evolutionary origin of epithelial mucus protein components — Mucins and FCGBP. *Mol. Biol. Evol.* 33, 1921–1936. doi: 10.1093/molbev/msw066

Langeland, A., and Nøst, T. (1995). Gill raker structure and selective predation on zooplankton by particulate feeding fish. *J. Fish Biol.* 47, 719–732. doi: 10.1111/j.1095-8649.1995.tb01937.x

Larson, E. T., and Shanks, A. L. (1996). Consumption of marine snow by two species of juvenile mullet and its contribution to their growth. *Mar. Ecol. Prog. Ser.* 130, 19–28. doi: 10.3354/meps130019

Lazarro, X. (1987). A review of planktivorous fishes: Their evolution, feeding behaviours, selectivities, and impact. *Hydrobiologia* 146, 97–167. doi: 10.1007/BF00008764

Lee, S., Kim, H., and Yang, S. (2023). Microfluidic label-free hydrodynamic separation of blood cells: Recent developments and future perspectives. *Adv. Mater. Technol.* 8, 2201425. doi: 10.1002/admt.202201425

Letendre, F., and Cameron, C. B. (2022). The capture of crude oil droplets by filter feeders at high and low Reynolds numbers. *J. Exp. Biol.* 225, jeb243819. doi: 10.1242/jeb.243819

Letendre, F., Mehrabian, S., Etienne, S., and Cameron, C. B. (2020). The interactions of oil droplets with filter feeders: A fluid mechanics approach. *Mar. Environ. Res.* 161, 105059. doi: 10.1016/j.marenvres.2020.105059

Lewis, V. P., and Peters, D. S. (1994). Diet of juvenile and adult Atlantic menhaden in estuarine and coastal habitats. *Trans. Am. Fish. Soc* 123, 803–810. doi: 10.1577/1548-8659(1994)123<0803:DOJAAA>2.3.CO;2

Li, Z., Tan, C. M., Tio, W., Ang, J., and Sun, D. D. (2018). Manta ray gill inspired radially distributed nanofibrous membrane for efficient and continuous oil-water separation. *Environ. Sci.:Nano* 5, 1466. doi: 10.1039/C8EN00258D

Lürling, M., and Mucci, M. (2020). Mitigating eutrophication nuisance: in-lake measures are becoming inevitable in eutrophic waters in the Netherlands. *Hydrobiologia* 847, 4447–4467. doi: 10.1007/s10750-020-04297-9

Lysenko, D. A., Donskov, M., and Ertesvåg, I. S. (2023). Large-eddy simulations of the flow past a bluff-body with active flow control based on trapped vortex cells at Re = 50000. *Ocean Eng.* 280, 114496. doi: 10.1016/j.oceaneng.2023.114496

Magnuson, J. J., and Heitz, J. G. (1971). Gill raker apparatus and food selectivity among mackerels, tunas, and dolphins. *Fish. Bull.* 69, 361–370.

Martel, J. M., and Toner, M. (2014). Inertial focusing in microfluidics. *Annu. Rev. Biomed. Eng.* 16, 371–396. doi: 10.1146/annurev-bioeng-121813-120704

Masselter, T., Schaumann, U., Kampowski, T., Ulrich, K., Thielen, M., Bold, G., et al. (2023). Improvement of a microfiber filter for domestic washing machines. *Bioinspir. Biomim.* 18, 016017. doi: 10.1088/1748-3190/acaba2

Matthews, L. H., and Parker, H. W. (1950). Notes on the anatomy and biology of the basking shark (*Cetorhinus maximus* [Gunner]). *Proc. Zool. Soc Lond.* 120, 535–576. doi: 10.1111/j.1096-3642.1950.tb00663.x

Meekan, M. G., Virtue, P., Marcus, L., Clements, K. D., Nichols, P. D., and Revill, A. T. (2022). The world's largest omnivore is a fish. *Ecology* 103, e3818. doi: 10.1002/ecy.3818

Misic, C., Capone, A., and Petrillo, M. (2022). Meteorological and climatic variability influences anthropogenic microparticle content in the stomach of the European anchovy *Engraulis encrasicolus*. *Hydrobiologia* 849, 589–602. doi: 10.1007/s10750-021-04727-2

Montazer, E., Yarmand, H., Salami, E., Muhamad, M. R., Kazi, S. N., and Badarudin, A. (2018). A brief review study of flow phenomena over a backward-facing step and its optimization. *Renew. Sust. Energ. Rev.* 82, 994–1005. doi: 10.1016/j.rser.2017.09.104

Mori, S., and Nakamura, T. (2022). Redeployment of odontode gene regulatory network underlies dermal denticle formation and evolution in suckermouth armored catfish. *Sci. Rep.* 12, 6172. doi: 10.1038/s41598-022-10222-y

Morris, C. C., and Deibel, D. (1993). Flow rate and particle concentration within the house of the pelagic tunicate *Oikopleura vanhoeffeni*. *Mar. Biol.* 115, 445–452. doi: 10.1007/BF00349843

Motta, P. J., Maslanka, M., Hueter, R. E., Davis, R. L., de la Parra, R., Mulvany, S. L., et al. (2010). Feeding anatomy, filter-feeding rate, and diet of whale sharks *Rhincodon typus* during surface ram filter feeding off the Yucatan Peninsula, Mexico. *Zoology* 113, 199–212. doi: 10.1016/j.zool.2009.12.001

Mummert, J. R., and Drenner, R. W. (1986). Effect of fish size on the filtering efficiency and selective particle ingestion of a filter-feeding clupeid. *Trans. Am. Fish. Soc* 115, 522–528. doi: 10.1577/1548-8659(1986)115<522:EOFSOT>2.0.CO;2

Nelson, G. T. (1967a). Gill arches of teleostean fishes of the family Clupeidae. *Copeia* 1967, 389–399. doi: 10.2307/1442129

Northcott, M. E., and Beveridge, M. C. M. (1988). The development and structure of pharyngeal apparatus associated with filter feeding in tilapias (*Oreochromis niloticus*). *J. Zool. Lond.* 215, 133–149. doi: 10.1111/j.1469-7998.1988.tb04889.x

Nunes, S. A., Magalhães, H. L. F., Gomez, R. S., Vilela, A. F., Figueiredo, M. J., Santos, R. S., et al. (2021). Oily water separation process using hydrocyclone of porous membrane wall: A numerical investigation. *Membranes* 11, 79. doi: 10.3390/membranes11020079

Olsen, A. M., Hernandez, L. P., and Brainerd, E. L. (2020). Multiple degrees of freedom in the fish skull and their relation to hydraulic transport in channel catfish. *Integr. Org. Biol.* 2, obaa031. doi: 10.1093/iob/obaa031

Paig-Tran, E. W. M., Bizzarro, J. J., Strother, J. A., and Summers, A. P. (2011). Bottles as models: Predicting the effects of varying swimming speed and morphology on size selectivity and filtering efficiency in fishes. *J. Exp. Biol.* 214, 1643–1654. doi: 10.1242/jeb.048702

Paig-Tran, E. W. M., Kleinteich, T., and Summers, A. P. (2013). The filter pads and filtration mechanisms of the devil rays: Variation at macro and microscopic scales. *J. Morphol.* 274, 1026–1043. doi: 10.1002/jmor.20160

Paig-Tran, E. W. M., and Summers, A. P. (2014). Comparison of the structure and composition of the branchial filters in suspension feeding elasmobranchs. *Anat. Rec.* 297, 701–715. doi: 10.1002/ar.22850

Paskin, M., Baum, D., Dean, M. N., and von Tycowicz, C. (2022). "A Kendall shape space approach to 3D shape estimation from 2D landmarks," in Proceedings of the

European Conference on Computer Vision 2022: 17th European Conference, *Tel Aviv, ISRAEL, October 23-27*. Eds. S. Avidan, G. Brostow, M. Cissé, G. M. Farinella and T. Hassner (Springer-Verlag, Berlin). doi: 10.1007/978-3-031-20086-1_21

Pease, L. F., Philips, N. R., Serkowski, J., Veldman, T. G., Minette, M. J., and Burns, C. A. (2022). Industrial scale mesofluidic particle separation. *Chem. Eng. Proc.: Proc. Intensif.* 173, 108795. doi: 10.1016/j.cep.2022.108795

Potvin, J., Goldbogen, J. A., and Shadwick, R. E. (2009). Passive versus active engulfment: Verdict from trajectory simulations of lunge-feeding fin whales *Balaenoptera physalus*. *J. R. Soc Interface* 6, 1005–1025. doi: 10.1098/rsif.2008.0492

Presti, P., Johnson, G. D., and Datovo, A. (2020). Facial and gill musculature of polynemid fishes, with notes on their possible relationships with sciaenids (Percomorphacea: Perciformes). *J. Morphol.* 281, 662–675. doi: 10.1002/jmor.21134

Provini, P., Brunet, A., Filippo, A., and Van Wassenbergh, S. (2022). *In vivo* intraoral waterflow quantification. *eLife* 11, e73621. doi: 10.7554/eLife.73621

Riisgård, H. U., and Larsen, P. S. (2010). Particle capture mechanisms in suspension-feeding invertebrates. *Mar. Ecol. Prog. Ser.* 418, 255–293. doi: 10.3354/meps08755

Ron, E. Z., and Rosenberg, E. (2001). Natural roles of biosurfactants. *Environ. Microbiol.* 3, 229–236. doi: 10.1046/j.1462-2920.2001.00190.x

Rosen, R. A., and Hales, D. C. (1981). Feeding of paddlefish, Polyodon spathula. *Copeia* 1981, 441–455. doi: 10.2307/1444235

Ross, S. T. (2013). *Ecology of North American Freshwater Fishes* (Berkeley: University of California Press).

Rubenstein, D. I., and Koehl, M. A. R. (1977). The mechanisms of filter feeding: Some theoretical considerations. *Am. Nat.* 111, 981–994. doi: 10.1086/283227

Rykaczewski, R. R. (2009). "Influence of oceanographic variability on the planktonic prey and growth of sardine and anchovy in the California Current Ecosystem," in *Scripps Institution of Oceanography Technical Report* (Scripps Institution of Oceanography, UC San Diego). Available at: http://escholarship.org/uc/item/307453xf.

Salafi, T., Zhang, Y., and Zhang, Y. (2019). A review on deterministic lateral displacement for particle separation and detection. *Nano-Micro Lett.* 11, 77. doi: 10.1007/s40820-019-0308-7

Salman, S., Abu Talib, A. R., Saadon, S., and Hameed Sultan, M. T. (2020). Hybrid nanofluid flow and heat transfer over backward and forward steps: A review. *Powder Technol.* 363, 448–472. doi: 10.1016/j.powtec.2019.12.038

Sanderson, S. L., Cech, J. J.Jr., and Cheer, A. Y. (1994). Paddlefish buccal flow velocity during ram suspension feeding and ram ventilation. *J. Exp. Biol.* 186, 145–156. doi: 10.1242/jeb.186.1.145

Sanderson, S. L., Cech, J. J. Jr., and Patterson, M. R. (1991). Fluid dynamics in suspension-feeding blackfish. *Science* 251, 1346–1348. doi: 10.1126/science.251.4999.1346

Sanderson, S. L., Cheer, A. Y., Goodrich, J. S., Graziano, J. D., and Callan, W. T. (2001). Crossflow filtration in suspension-feeding fishes. *Nature* 412, 439–441. doi: 10.1038/35086574

Sanderson, S. L., Chesnutt, C. R., and Lobel, P. S. (1996a). Evidence for ram suspension feeding by the piscivore, *Seriola dumerili* (Carangidae). *Env. Biol. Fish.* 46, 365–373. doi: 10.1007/BF00005014

Sanderson, S. L., Mort, M. E., and Cech, J. J. Jr. (1998). Particle retention by non-suspension-feeding cyprinid fishes. *Can. J. Fish. Aquat. Sci.* 55, 861–868. doi: 10.1139/f97-292

Sanderson, S. L., Roberts, E., Lineburg, J., and Brooks, H. (2016). Fish mouths as engineering structures for vortical cross-step filtration. *Nat. Commun.* 7, 11092. doi: 10.1038/ncomms11092

Sanderson, S. L., Stebar, M. C., Ackermann, K. L., Jones, S. H., Batjakas, I. E., and Kaufman, L. (1996b). Mucus entrapment of particles by a suspension-feeding tilapia (Pisces: Cichlidae). *J. Exp. Biol.* 199, 1743–1756. doi: 10.1242/jeb.199.8.1743

Sanderson, S. L., and Wassersug, R. (1990). Suspension-feeding vertebrates. *Sci. Am.* 262, 96–102. doi: 10.1038/scientificamerican0390-96

Sanderson, S. L., and Wassersug, R. (1993). "Convergent and alternative designs for vertebrate suspension feeding," in *The Skull, Volume 3: Functional and Evolutionary Mechanisms*. Eds. J. Hanken and B. K. Hall (The University of Chicago Press, Chicago), 37–112.

Savoca, M. S., McInturf, A. G., and Hazen, E. L. (2020). Plastic ingestion by marine fish is widespread and increasing. *Glob. Change Biol.* 27, 2188–2189. doi: 10.1111/gcb.15533

Sazima, I. (1998). Field evidence for suspension feeding in *Pseudocaranx dentex*, with comments on ram filtering in other jacks (Carangidae). *Env. Biol. Fish.* 53, 225–229. doi: 10.1023/A:1007492803796

Schroeder, A., Marshall, L., Trease, B., Becker, A., and Sanderson, S. L. (2019). Development of helical, fish-inspired cross-step filter for collecting harmful algae. *Bioinspir. Biomim.* 14, 056008. doi: 10.1088/1748-3190/ab2d13

Schroën, K., van Dinther, A., and Stockmann, R. (2017). Particle migration in laminar shear fields: A new basis for large scale separation technology? *Sep. Purif. Technol.* 174, 372–388. doi: 10.1016/j.seppur.2016.10.057

Seghers, B. H. (1975). Role of gill rakers in size-selective predation by lake whitefish, *Coregonus clupeaformis* (Mitchill). *Verh. Internat. Verein. Limnol.* 19, 2401–2405. doi: 10.1080/03680770.1974.11896323

Shephard, K. L. (1994). Functions for fish mucus. *Rev. Fish Biol. Fish.* 4, 401–429. doi: 10.1007/BF00042888

Shimeta, J., and Jumars, P. A. (1991). Physical mechanisms and rates of particle capture by suspension-feeders. *Oceanogr. Mar. Biol. Annu. Rev.* 29, 191–257.

Sibbing, F. A., and Nagelkerke, L. A. J. (2001). Resource partitioning by Lake Tana barbs predicted from fish morphometrics and prey characteristics. *Rev. Fish Biol. Fish.* 10, 393–437. doi: 10.1023/A:1012270422092

Sibbing, F. A., and Uribe, R. (1985). Regional specializations in the oro-pharyngeal wall and food processing in the carp (*Cyprinus carpio* L.). *Neth. J. Zool.* 35, 377–422. doi: 10.1163/002829685X00280

Smith, J. C., and Sanderson, S. L. (2007). Mucus function and crossflow filtration in a fish with gill rakers removed versus intact. *J. Exp. Biol.* 210, 2706–2713. doi: 10.1242/jeb.000703

Smith, J. C., and Sanderson, S. L. (2008). Intra-oral flow patterns and speeds in a suspension-feeding fish with gill rakers removed versus intact. *Biol. Bull.* 215, 309–318. doi: 10.2307/25470714

Smith, J. C., and Sanderson, S. L. (2013). Particle retention in suspension-feeding fish after removal of filtration structures. *Zoology* 116, 348–355. doi: 10.1016/j.zool.2013.08.008

Springer, V. G., and Johnson, G. D. (2004). Study of the dorsal gill-arch musculature of teleostome fishes, with special reference to the Actinopterygii. *Bull. Biol. Soc Wash.* 11, 1–260. doi: 10.5962/bhl.title.49077

Stel, H., Franco, A. T., Junqueira, S. L. M., Erthal, R. H., Mendes, R., Gonçalves, M. A. L., et al. (2012). Turbulent flow in d-type corrugated pipes: flow pattern and friction factor. *J. Fluids Eng.* 134, 121202. doi: 10.1115/1.4007899

Stoecklein, D., and Di Carlo, D. (2019). Nonlinear microfluidics. *Anal. Chem.* 91, 296–314. doi: 10.1021/acs.analchem.8b05042

Storm, T. J., Nolan, K. E., Roberts, E. M., and Sanderson, S. L. (2020). Oropharyngeal morphology related to filtration mechanisms in suspension-feeding American shad (Clupeidae). *J. Exp. Zool. A Ecol. Integr. Physiol.* 333, 493–510. doi: 10.1002/jez.2363

Su, R., Li, S., Wu, W., Song, C., Liu, G., and Yu, Y. (2021). Recent progress in electrospun nanofibrous membranes for oil/water separation. *Sep. Purif. Technol.* 256, 117790. doi: 10.1016/j.seppur.2020.117790

Surapaneni, V. A., Schindler, M., Ziege, R., de Faria, L. C., Wölfer, J., Bidan, C. M., et al. (2022). Groovy and gnarly: Surface wrinkles as a multifunctional motif for terrestrial and marine environments. *Integr. Comp. Biol.* 62, 749–761. doi: 10.1093/icb/icac079

Tang, H., Niu, J., Jin, H., Lin, S., and Cui, D. (2022). Geometric structure design of passive label-free microfluidic systems for biological micro-object separation. *Microsyst. Nanoeng.* 8, 62. doi: 10.1038/s41378-022-00386-y

Turner, J. T. (2015). Zooplankton fecal pellets, marine snow, phytodetritus and the ocean's biological pump. *Prog. Oceanogr.* 130, 205–248. doi: 10.1016/j.pocean.2014.08.005

van den Berg, C., van den Boogaart, J. G. M., Sibbing, F. A., and Osse, J. W. M. (1993). Zooplankton feeding in common bream (*Abramis brama*), white bream (*Blicca bjoerkna*) and roach (*Rutilus rutilus*): Experiments, models and energy intake. *Neth. J. Zool.* 44, 15–42. doi: 10.1163/156854294X00024

van den Berg, C., van den Boogaart, J. G. M., Sibbing, F. A., and Osse, J. W. M. (1994a). Implications of gill arch movements for filter-feeding: An X-ray cinematographical study of filter-feeding white bream (*Blicca bjoerkna*) and common bream (*Abramis brama*). *J. Exp. Biol.* 191, 257–282. doi: 10.1242/jeb.191.1.257

van den Berg, C., van Snik, G. J. M., van den Boogaart, J. G. M., and Sibbing, F. A. (1994b). Comparative microanatomy of the branchial sieve in three sympatric cyprinid species, related to filter-feeding. *J. Morphol.* 219, 73–87. doi: 10.1002/jmor.1052190109

Vandewalle, P., Parmentier, É., and Chardon, M. (2000). The branchial basket in teleost feeding. *Cybium* 24, 319–342.

van Dinther, A. M. C., Schroën, C. G. P. H., and Boom, R. M. (2013a). Particle migration leads to deposition-free fractionation. *J. Membr. Sci.* 440, 58–66. doi: 10.1016/j.memsci.2013.03.050

van Dinther, A. M. C., Schroën, C. G. P. H., Imhof, A., Vollebregt, H. M., and Boom, R. M. (2013b). Flow-induced particle migration in microchannels for improved microfiltration processes. *Microfluid. Nanofluid.* 15, 451–465. doi: 10.1007/s10404-013-1158-0

Van Wassenbergh, S., and Sanderson, S. L. (2023). Hydrodynamic analysis of bioinspired vortical cross-step filtration by computational modelling. *R. Soc Open Sci.* 10, 230315. doi: 10.1098/rsos.230315

Voskuhl, L., and Rahlff, J. (2022). Natural and oil surface slicks as microbial habitats in marine systems: A review. *Front. Mar. Sci.* 9. doi: 10.3389/fmars.2022.1020843

Wang, J. M., Jin, Q. Q., Zhang, Y. Y., Fang, H. C., and Xia, H. M. (2021). Reducing the membrane fouling in cross-flow filtration using a facile fluidic oscillator. *Sep. Purif. Technol.* 272, 118854. doi: 10.1016/j.seppur.2021.118854

Wegner, N. C. (2015). "Elasmobranch gill structure," in *Physiology of Elasmobranch Fishes: Structure and Interaction with Environment, Fish Physiology*, vol. 34A . Eds. R. E. Shadwick, A. P. Farrell and C. J. Brauner (London: Elsevier Science and Technology), 101–151. doi: 10.1016/B978-0-12-801289-5.00003-1

Weller, H. I., McMahan, C. D., and Westneat, M. W. (2017). Dirt-sifting devilfish: winnowing in the geophagine cichlid *Satanoperca daemon* and evolutionary implications. *Zoomorphology* 136, 45–59. doi: 10.1007/s00435-016-0335-6

Werth, A. J., and Potvin, J. (2016). Baleen hydrodynamics and morphology of cross-flow filtration in balaenid whale suspension feeding. *PloS One* 11, e0150106. doi: 10.1371/journal.pone.0150106

Winterbottom, R. (1974). A descriptive synonymy of the striated muscles of the Teleostei. *Proc. Acad. Nat. Sci. Philadelphia* 125, 225–317.

Witkop, E. M., Van Wassenbergh, S., Heideman, P. D., and Sanderson, S. L. (2023). Biomimetic models of fish gill rakers as lateral displacement arrays for particle separation. *Bioinspir. Biomim.* 18, 056009. doi: 10.1088/1748-3190/acea0e

Wright, D. I., O'Brien, W. J., and Luecke, C. (1983). A new estimate of zooplankton retention by gill rakers and its ecological significance. *Trans. Am. Fish. Soc* 112, 638–646. doi: 10.1577/1548-8659(1983)112<638:ANEOZR>2.0.CO;2

Xia, H. M., Wu, J. W., Zheng, J. J., Zhang, J., and Wang, Z. P. (2021). Nonlinear microfluidics: device physics, functions, and applications. *Lab. Chip* 21, 1241–1268. doi: 10.1039/D0LC01120G

Xiang, N., and Ni, Z. (2022). Inertial microfluidics: Current status, challenges, and future opportunities. *Lab. Chip* 22, 4792. doi: 10.1039/D2LC00722C

Xu, Z., Mao, X., Gu, Y., Chen, X., Kuang, W., Wang, R., et al. (2023). Analysis of hydrodynamic filtration performance in a cross-step filter for drip irrigation based on the CFD-DEM coupling method. *Biosyst. Eng.* 232, 114–128. doi: 10.1016/j.biosystemseng.2023.07.004

Yang, M., Hou, L., Wang, L., Liu, S., and Xu, J. (2022). Effect of oil properties on spilled oil recovery using a mechanism coupling surface vortices and cyclone separation. *Ocean Eng.* 263, 112383. doi: 10.1016/j.oceaneng.2022.112383

Zhang, K., Ma, C., Zhang, J., Zhang, B., and Zhao, B. (2022a). Drag reduction characteristics of bionic structure composed of grooves and mucous membrane acting on turbulent boundary layer. *J. Appl. Fluid Mech.* 15, 283–292. doi: 10.47176/jafm.15.01.32901

Zhang, X., Ma, J., Zheng, J., Dai, R., Wang, X., and Wang, Z. (2022b). Recent advances in nature-inspired antifouling membranes for water purification. *Chem. Eng. J.* 432, 134425. doi: 10.1016/j.cej.2021.134425

Zhao, Q., Yuan, D., Zhang, J., and Li, W. (2020). A review of secondary flow in inertial microfluidics. *Micromachines* 11, 461. doi: 10.3390/mi11050461

frontiers | Frontiers in Marine Science

TYPE Review
PUBLISHED 12 April 2024
DOI 10.3389/fmars.2024.1347497

OPEN ACCESS

EDITED BY
Marco Ghisalberti,
University of Western Australia, Australia

REVIEWED BY
Michelangelo Bisconti,
University of Turin, Italy
Leandra Hamann,
University of Florida, United States

*CORRESPONDENCE
Alexander J. Werth
awerth@hsc.edu

RECEIVED 30 November 2023
ACCEPTED 26 March 2024
PUBLISHED 12 April 2024

CITATION
Werth AJ and Potvin J (2024) Dynamic filtration in baleen whales: recent discoveries and emerging trends.
Front. Mar. Sci. 11:1347497.
doi: 10.3389/fmars.2024.1347497

Dynamic filtration in baleen whales: recent discoveries and emerging trends

Alexander J. Werth [1]* and Jean Potvin [2]

[1]Department of Biology, Hampden-Sydney College, Hampden-Sydney, VA, United States,
[2]Department of Physics and WATER Institute, Saint Louis University, St. Louis, MO, United States

Recent findings have greatly improved our understanding of mysticete oral filtration, and have upended the traditional view of baleen filtration as a simple process. Flow tank experiments, telemetric tag deployment on whales, and other lab and field methods continue to yield new data and ideas. These suggest that several mechanisms arose from ecological, morphological, and biomechanical adaptations facilitating the evolution of extreme body size in Mysticeti. Multiple lines of evidence strongly support a characterization of baleen filtration as a conceptually dynamic process, varying according to diverse intraoral locations and times of the filtration process, and to other prevailing conditions. We review and highlight these lines of evidence as follows. First, baleen appears to work as a complex metafilter comprising multiple components with differing properties. These include major and minor plates and eroded fringes (AKA bristles or hairs), as well as whole baleen racks. Second, it is clear that different whale species rely on varied ecological filtration modes ranging from slow skimming to high-speed lunging, with other possibilities in between. Third, baleen filtration appears to be a highly dynamic and flow-dependent process, with baleen porosity not only varying across sites within a single rack, but also by flow direction, speed, and volume. Fourth, findings indicate that baleen (particularly of balaenid whales and possibly other species) generally functions not as a simple throughput sieve, but instead likely uses cross-flow or other tangential filtration, as in many biological systems. Fifth, evidence reveals that the time course of baleen filtration, including rate of filter filling and clearing, appears to be more complex than formerly envisioned. Flow direction, and possibly plate and fringe orientation, appears to change during different stages of ram filtration and water expulsion. Sixth, baleen's flexibility and related biomechanical properties varies by location within the whole filter (=rack), leading to varying filtration conditions and outcomes. Seventh, the means of clearing/cleaning the baleen filter, whether by hydraulic, hydrodynamic, or mechanical methods, appears to vary by species and feeding type, notably intermittent lunging versus continuous skimming. Together, these and other findings of the past two decades have greatly elucidated processes of baleen filtration, and heightened the need for further research. Many aspects of baleen filtration may pertain to other biological filters; designers can apply several aspects to artificial filtration, both to better understand natural systems and to design and manufacture more effective

synthetic filters. Understanding common versus unique features of varied filtration phenomena, both biological and artificial, will continue to aid scientific and technical understanding, enable fruitful interdisciplinary partnerships, and yield new filter designs.

KEYWORDS

filter, flow, baleen, keratin, mysticete, biomechanics

1 Introduction

Until recently, accounts of filter feeding in baleen whales (Cetacea: Mysticeti) have been based almost solely on speculative inference from classical anatomy and ecology. These accounts were constructed mainly from limited and brief ship-board observations of whale foraging, and from beachside necropsy dissections of stranded whales, often in poor physical condition. Thanks to the dedicated efforts of many researchers investigating and speculating over centuries, scientists were able to piece together broad outlines of whale feeding, such as the fundamental distinction between steady-state skimming versus brief lunge gulping in various mysticete taxa (Slijper, 1962; Nemoto, 1970; Berta et al., 2015). However, until recently, overall accounts of whale feeding, even in leading publications such as the peer-reviewed and edited *Encyclopedia of Marine Mammals* (EMM), offered only vague description of the processes of baleen filtration. For example, here are four entries from the second (2008) EMM edition:

"Periodically the mouth is closed and plankton are removed from the baleen by the tongue, and ingested." (EMM entry on "Feeding Morphology"; Marshall, 2008)

"Baleen whales … force water containing food out through baleen plates, and then transfer trapped food back to the gullet. The tongue is presumed to be involved." (EMM entry on "Baleen Whales (Mysticetes)"; Bannister, 2008)

"Water is expelled by the pouch and tongue through the still exposed baleen plates. Once the water is expelled, the prey is swallowed." (EMM entry on "Blue Whales"; Sears and Perrin, 2008)

"The tongue and the elastic properties of the ventral walls of the throat act in concert to force water out through the baleen." (EMM entry on "Filter Feeding"; Croll et al., 2008)

Citation of these four sources is by no means intended to criticize EMM authors or editors for vague descriptions, but rather to point out that until a mere two decades ago, these were the best explanations the world's top scientists could offer. In short, our knowledge of whale filtration remained limited, even among experts in the field. This was true not only with the EMM, but also other monographs written by acknowledged experts (e.g., Slijper, 1962; Gaskin, 1982, and the Handbook of Marine Mammal series, whose final volume was published by Ridgway and Harrison, 1999), whereas recent works (e.g., Goldbogen et al., 2017b; Pyenson, 2018; Marshall and Pyenson, 2019) present a far more realistic view of whale feeding.

Fortunately, the past two decades have witnessed an explosive rise in the application of new techniques and technologies, many long used in other fields of science, ushering in a new era for our understanding of mysticete feeding, and particularly of baleen filtration, both in specific details and general outline. Examples of these new techniques and studies notably include but are not limited to hypothesis-based laboratory experiments (e.g., Lambertsen, 1983; Werth, 2013), tag data (Goldbogen et al., 2017a), photogrammetry (e.g., Lambertsen et al., 1989), aerial drones (Werth et al., 2019b), engineering methods (Lambertsen et al., 2005), computational fluid dynamics (Zhu et al., 2020a, Zhu et al., 2020b), morphometrics (Werth et al., 2018a), histology (e.g., Werth et al., 2018b), mathematical modeling (Potvin et al., 2009; Potvin and Werth, 2017), and physical modeling (Werth, 2004).

Nonetheless, for all the insights provided by application of novel approaches, there remain many as-yet unanswered questions. Therefore, the aim here is not to provide an exhaustively comprehensive review of recent projects/publications, methods, and findings, but instead to take stock and reflect on major themes and threads arising from these approaches. A roadmap is hereby offered, surveying the current state of the field, including major advances in current understanding as well as suggestions to guide future researchers in addressing current mysteries concerning baleen filtration.

This review reflects the dawning realization that baleen filtration is considerably more complex than previously presumed by generations of researchers (even the authors, formerly). Moreover, baleen filtration is at heart a dynamic and variable process rather than a static or uniform one. Consider that for a large rorqual such as a 25 m blue whale, a typical lunge feeding event involves engulfment of >80-120 m^3 of water, which is then filtered through a ~4 m^2 filter in roughly 30 seconds, with peak pressures potentially reaching >800–1000 kPa, the equivalent of 10^6 N/m^2 (Werth, 2013). Further, this filter must retain structural integrity and remain functional for the whale's entire lifespan (presumably 100 years or more; George et al., 2021). It must filter incredibly capacious volumes of water and hold massive volumes of water-borne schooling prey, at astonishing pressures, without

TABLE 1 Primary distinctions between ecology and morphology of mysticete feeding types.

Feeding Type	Balaenid	Rorqual (Balaenopterid)	Gray (Eschrichtiid)
Species	4	~9, not including subspecies	1
Adult body length	16 m	8-30 m	14 m
Body form	Stout/stocky	Slim/sleek	Intermediate
Feeding type	Skimming (surface or depth)	Varied; typically lunges	Typically benthic suction, but varied
Filtration	Continuous/ steady state	Intermittent (processes single mouthful)	Intermittent (processes single mouthful)
Driving force	Ram swimming	Ram lunges	Suction (intraoral expansion via tongue depression)
Typical prey	Copepods, krill (1-10 mm)	Krill, schooling fish (1-20 cm)	Benthic amphipods (5 mm-5cm)
Swim speed	~3.5 km/hr (1 m/s)	5-14 km/hr (1.5-4 m/s)*	5-8 km/hr (1.5-2 m/s)**
Filtration speed	~3.5 km/hr (1 m/s)	3.5-7 km/hr (1-2 m/s)	3.5 km/hr (1 m/s)
Baleen form	Very long (to 4 m) flexible plates, very fine, dense fringes	Triangular plates (0.5-1 m long), intermediate fringes	Short (0.25 m), stiff plates, coarse fringes
Baleen plate #	Mean 300 (240-390)	Mean 275 (230-400)	Mean 160 (130-180)
Avg baleen length	300 cm	70 cm	25 cm
Avg fringe density	52/cm	21/cm	7/cm
2D filtration area of internal mat	3-7 m^2	0.4-4.5 m^2	1.3 m^2
3D filtration area including plates	15-240 m^2	18-70 m^2	25-35 m^2
Rostrum	Sharply arched	Flat, broad	Mildly arched
Tongue	Large, firm, muscular	Floppy, sac-like, invaginates into ventral cavity	Large, firm, muscular
Other notable morphological adaptations	Gap between paired baleen racks, high semicircular muscular lips, scoop-like lower jaw, gutter-like channel between lip and baleen, curved mandibles, no throat grooves	Wide gape, expansible accordion-like throat pleats (ventral grooves) with musculature to contract; strongly keeled palate, low lips	2-7 gular (throat) grooves for oropharyngeal expansion
Notable behaviors	Often do U-turn like lawn mower to go back through prey patch; group echelon feeding (probably parallel rather than cooperative)	Very rapid engulfment of aggregated prey; body rotations (including side-swimming) during engulfment; bubble netting; also occasional flipper and tail smacking of prey	Usually rotates body to side to suck up plume of benthic zooplankton (e.g., amphipods, mysids, etc.) in mud

[*Rorqual swim speed much higher (up to 25-30 km/hr) during lunges); **gray whale speed <1 m/s during feeding]

Note that there is substantial variation, such as rorqual sei whales, *Balaenoptera borealis*, that occasionally skim feed like balaenids (Kawamura, 1974; Brodie and Vikingsson, 2009; Horwood, 2017; Segre et al., 2021). Feeding of pygmy right whales, typically classified as the sole species in Neobalaenidae, is unknown but most likely similar to that of balaenids (Sekiguchi et al., 1992; Fordyce and Marx, 2013; Marx and Fordyce, 2016; Kemper, 2017; Werth et al., 2018a).

breaking, clogging, or otherwise failing. Truly, this is a leading contender for the world's most dynamic biomechanical event (Goldbogen, 2010).

As researchers gradually fill in details of this former "black box" phenomenon (as evidenced by the nebulous ambiguity of the above-cited EMM entries), two clear conclusions emerge. First, baleen filtration is a far more complex process than previously presumed. Secondly and relatedly, baleen filtration is generally a highly dynamic process with varying inputs and outputs. As summarized in Table 1, mysticete foraging ecology is itself varied, with three variants—skimming and lunge or suction gulping—corresponding to the three main families of extant baleen whales (Balaenidae, Balaenopteridae, and Eschrichtiidae, respectively; Slijper, 1962; Pivorunas, 1979; Werth, 2000; Goldbogen et al., 2017b; Savoca et al., 2021). Nonetheless, mysticete filtration processes are both varying and variable (Werth et al., 2018a; Werth, 2019). Specifically, each baleen filter appears to display varying properties (e.g., porosity) from one filter region or element to another, and these properties also appear to be variable over time as determined by such input parameters as flow speed, direction, and volume. In brief, it is difficult to precisely characterize baleen filtration without specifying detailed operating conditions or attaching qualifying caveats (Werth, 2013).

In the sections that follow, major findings of the past two decades of research on baleen filtration are summarized. We acknowledge that certain variabilities and complexities outlined here are simpler and currently better known than other items, but all alike contribute to the complete picture of baleen filtration, undoubtedly along with

numerous other factors whose contributions have yet to be learned or appreciated.

2 Baleen as metafilter with structural complexity & variability

Biological filtration operates on numerous levels and with many functions, including retention of *desired* filtered material for nutritive gain or elimination of *undesired* filtered material as excreted waste (Werth, 2019). Baleen does not perform both functions; it solely collects and retains desired material (food) while separating it from seawater. Because of this broad range of function, many biological filters exist, ranging from tissues and organs (e.g., kidneys, livers, and sinusoidal capillaries) to entire ecosystems (e.g., wetlands). In the middle of this continuum lie dedicated filter-feeding structures or whole specialized organs. These may exist *outside* the body, as in the filter-feeding appendages of copepods, barnacles, and other crustaceans, or they may lie *within* the body, as in the gill rakers of bony fishes and cartilaginous sharks and rays (Cheer et al., 2012; Paig-Tran et al., 2013; Paig-Tran and Summers, 2014; Wegner, 2015; Divi et al., 2018). Such filter-feeding configurations may be modified from preexisting structures, as in fish gill rakers, the spined tongues of filter-feeding waterfowl, or the complexly cusped dentition of filter-feeding seals, especially crabeater seals, *Lobodon carcinophagus*, and leopard seals, *Hydrurga leptonyx* (Werth, 2000; Marshall and Goldbogen, 2015; Hocking et al., 2017b; Marshall and Pyenson, 2019; Hamann and Blanke, 2022). Alternatively, filters may be novel arrangements that evolved *de novo*, as is the case for baleen (Werth, 2017). This keratinous filtering material, suspended from the palate of all extant species of crown mysticetes, is a neomorphism that evolved roughly 25 million years ago from early, toothed members of stem Mysticeti (Fordyce and Barnes, 1994; Thewissen, 1998; Thewissen and Bajpai, 2001; Thewissen et al., 2009; Uhen, 2010; Marx and Fordyce, 2015; Pyenson and Vermeij, 2016; Marx et al., 2016a, Marx et al., 2016b; Pyenson, 2017; Slater et al., 2017). Although fossilized baleen exists (Esperante et al., 2008; Bisconti, 2012; Gioncada et al., 2016; Collareta et al., 2017; Marx et al., 2017; Bosio et al., 2021), abundant fossil skulls and teeth of early mysticetes reveal that dentition gradually declined in tooth size and number as it was replaced by this new and highly adaptive key innovation (Fordyce, 1980; Fitzgerald, 2010; Berta et al., 2016; Marx et al., 2016a; Geisler et al., 2017; Lambert et al., 2017; Peredo et al., 2017; Hocking et al., 2017a; Fordyce and Marx, 2018; Ekdale and Deméré, 2021; Gatesy et al., 2022). Although baleen functions roughly analogously to filtering dentition, it is not homologous to teeth, the keratinous palatal ridges of some mammals, or any other tissue (Gatesy and O'Leary, 2001; Deméré et al., 2008; Fudge et al., 2009; Gatesy et al., 2013; Thewissen et al., 2017). Like other oral filters, baleen both collects and separates prey items from water, in this case by bulk filtration of schooling prey, whether zooplankton (ranging from <1-10 cm) or fish (generally ~10-20 cm in body length).

Baleen can variously yet simultaneously be considered as a tissue, as a structural material, and (collectively) as a filtering unit

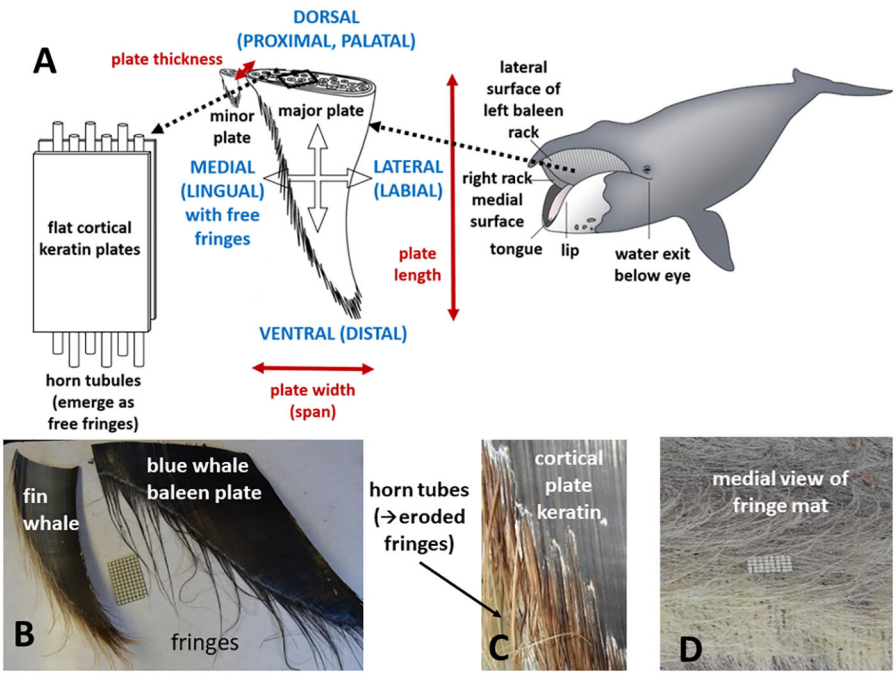

FIGURE 1
Baleen is a complex oral metafilter comprising different alpha-keratinous elements arranged sandwich-style with flat, fingernail-like plates enclosing hollow hair-like horn tubules **(A)**. Each element has its own filter function along with unique structural and biomechanical properties. Paired racks of baleen tissue **(A)** each consist of ~300 triangular major plates **(B)** that erode along their interior (medial, lingual) surfaces **(C)** to reveal the horn tubes as fringes (bristles; **D**). An entire rack, major/minor plate, or fringe can separately or collectively serve as a filter element.

roughly equivalent to an organ (Werth, 2017). The entire filter consists of paired "racks" of baleen hanging from each side of the upper jaw, with each rack comprising approximately 300 individual plates of baleen tissue, each of which is roughly triangular in shape (Figure 1). Because each rack is therefore a layered, comb-like structure, each individual baleen plate is also sometimes called a lamina (Young, 2012; Loch et al., 2020). The precise number of plates varies by species (ranging from ~160-360 plates per rack), and to a lesser degree by a whale's overall body size, which in turn depends on age and sex (Werth et al., 2018a). However, virtually all adult mysticetes have about 300 baleen plates suspended from each side of the rostrum. Baleen plate size varies by species, although plates are generally about 3 mm thick (anteroposteriorly), ~10-20 cm wide (mediolaterally) for most of their length, and 20-40 cm wide at their dorsal-most origin where they emerge from and are anchored within palatal gingiva. In most whales, baleen plates are ~50 cm long (dorsoventrally), but plates range from ~35-75 cm in length for most species, with the major exception of bowhead (*Balaena mysticetus*) and right whales (*Eubalaena* spp.), both of Family Balaenidae, whose plates can, in exceptionally large specimens, exceed 4 m in length (Werth, 2000). Plate dimensions vary by position along the rack, with the longest plates found near the center of a rack (Werth et al., 2018a, Werth et al., 2020). In addition to major (main) plates, most whales have smaller minor plates running medially along each rack. A major plate can have one or multiple adjacent minor plates, all of which resemble fragments broken from the medial edge of a major plate (Williamson, 1973; Pivorunas, 1976). As their name suggests, minor plates are considerably smaller in size than major plates (Figure 1). Relative to their reduced size, minor plates likely also play a greatly reduced functional role in filtration, although this has not been adequately addressed.

Baleen is an ever-growing substance, like many keratinous tissues such as mammalian hair, nails, and claws, but unlike teeth and most other vertebrate filtering materials (Marshall et al., 1991; Wang et al., 2016). In an elegantly simple turnover that balances baleen tissue generation and loss, new filtering material arises to replace eroded material that becomes frayed and shed during filtration (Werth et al., 2020, Werth et al., 2021). This ever-changing nature of filter growth and loss aptly relates baleen's dynamic structure with its dynamic function. Although baleen growth rates vary somewhat by species and age, in most whales the plates grow about 12-18 cm per year (Sumich, 2001; Werth et al., 2021). Bowhead and right whales, which have much longer plates and thus substantially larger baleen filters, are again the exception; balaenid plates typically grow 20-27 cm per year in adults and can exceed 30 cm per year in juveniles (Werth et al., 2020). In most mysticete species, baleen plates grow disproportionately faster in the first 2-3 years of life. This has been explained as young whales needing to prioritize post-weaning growth of their oral filter to obtain calories needed to sustain growth of other body parts, such that skeletal growth is often delayed or downplayed until the filter attains its full adult proportions (Lubetkin et al., 2008; Fortune et al., 2012; George et al., 2016).

As embryos, mysticetes normally bear multiple transient tooth germs or anlagen that do not persist but are absorbed during development (Slijper, 1962; Peredo et al., 2017), so that they serve as temporary vestiges or atavisms. As these germs fade, they are replaced by arcs of tissue, running along both sides of the rostrum, that generate the alpha-keratin components comprising baleen (Fudge et al., 2009; Szewciw et al., 2010; Thewissen et al., 2017). Basically, the two primary paired components are almost exactly like human hair and fingernails. These elements are arrayed as a sandwich (Figure 1), with two flat outer layers of nail-like sheets (Forslind, 1970) surrounding a core of long, hollow "horn tubules" that dangle down ventrally from the palate (Werth, 2000). The interior of every plate consists of an array of one to two dozen variably-sized tubules within a matrix of intertubular keratin (Werth, 2017). This intertubular keratin matrix binds all components together and acts as an important if much lesser third ingredient for the "sandwich" (Werth et al., 2018b). In this way, baleen's construction is reminiscent of a fiberglass composite material, with alternating flat sheets and long, narrow fibers (Greenberg and Fudge, 2012). Together, these components provide baleen with unparalleled flexibility and rigidity, combining to create a highly pliant and bendable yet stiff and resilient material (McKittrick et al., 2012) that absorbs intensely high forces and pressures yet bounces back to its original form, all the while resisting crack propagation (Werth, 2013; Werth et al., 2018b).

Nonetheless, baleen's composite construction not only enables but indeed facilitates its erosion into a tattered curtain of exposed horn tubules that are revealed, like the frayed border of a worn fabric, as hair-like fringes dangling at the exposed, eroded edges of each baleen plate (Werth, 2017). These fringes, also called baleen bristles, not only resemble hairs but in fact are created and grow in virtually the same way as human scalp and body hairs (Fraser et al., 1972, Fraser et al., 1976; Hearle, 2000; Feughelman, 2002), as tubes of alpha-keratin that emerge from a follicle where dermal and epidermal generative cells interact (Thewissen et al., 2017). Because these hair-like fringes run solely dorsoventrally, from a plate's gingival origin to its ventral-most vertex, transverse (mediolateral) cracking of any baleen plate is prohibited even as longitudinal cracking is facilitated. Not only does this make baleen a strong, resilient material, but even more importantly it creates a more elaborate, less coarse filter that consists not only of the flattened baleen plates (major and minor) but also the much smaller, finer, more flexible fringes (Pfeiffer, 1992; Young, 2012; Jensen et al., 2017; Loch et al., 2020; Vandenberg et al., 2023).

Several routine filtering stresses combine to facilitate baleen's erosion into fringes (Werth et al., 2016b). These include prey accumulation, seawater flow, and mechanical abrasion from adjacent impinging oral tissues, particularly the tongue and lips (Werth, 2001). Not only do these forces produce the filter's final structure, but they also contribute to the erosive loss of distal-most fringes, which often appear in whale stomach contents and feces (Werth et al., 2020). Erosive loss is balanced by an equivalent proximal growth of new plate and tubular material (Ruud, 1940), such that the ever-growing baleen filter maintains a near-constant size and shape despite constant turnover from continued wear and tear of feeding (Werth et al., 2021).

Mysticetes are, like many animals, opportunistic and resourceful foragers whose diets are frequently broad (Slijper, 1962; Gaskin, 1982). However, in mysticete taxa whose diet

habitually includes very small prey items (such as rice grain-sized copepods), the eroded fringes are measurably longer, finer (i.e., with smaller diameter), and denser (i.e., more eroded fringes per cm of plate) than the coarser fringes of species that typically feed on schooling fish or large zooplankton such as finger-sized krill (Werth, 2000, Werth, 2001). Whale species with fine filters include the balaenid (bowhead and right) whales and the sei whale, *Balaenoptera borealis*, of the Family Balaenopteridae (Kawamura, 1974, Kawamura, 1980; Brodie and Vikingsson, 2009; Horwood, 2017; Werth et al., 2018a; Segre et al., 2021).

Recent analyses have determined that baleen's flexibility is tempered by the inclusion of mineral salts, particularly calcium, which act to stiffen the filtering plates (Pautard, 1963; Szewciw et al., 2010). Mineral content varies by species and diet, ensuring that baleen of whales that habitually feed on tiny prey is more flexible, creating an overall less porous filter (Werth et al., 2018a). Other studies on baleen's physicochemical properties have demonstrated that baleen is generally hydrophilic (enabling penetration of water, which in turn facilitates flexibility and prevents breakage; Werth et al., 2016a) and largely oleophobic (resisting penetration of oil, which is advantageous for species that live near natural submarine petroleum seeps or man-made oil drilling platforms; Werth et al., 2019a). Baleen has, however, been found to be susceptible to ocean acidification caused by carbon emissions (Werth and Whaley, 2019). Baleen's filtering function is also highly dependent on its remarkably pliant and rubbery zwischensubstanz, the tough, gum-like gingival tissue from which baleen emerges and which surrounds and embeds all plates in the palate. The zwischensubstanz resists shear forces and crack or tear propagation, enabling the filter to withstand powerful flows as it separates food from water (Pinto and Shadwick, 2013; Werth et al., 2019c).

Because baleen grows continually at a generally predictable rate (Werth et al., 2021), and because it, like mammalian hair and nails, therefore encompasses a "snapshot" of a few years of a whale's life, baleen has proven useful in physiological research (Werth et al., 2020). This is even more valuable considering how well baleen (again, like other keratinous tissues) retains both endogenous and exogenous substances within a whale's body, most notably hormones, isotopes, and seawater contaminants (Caraveo-Patiño et al., 2007; Pomerleau et al., 2018). Therefore, baleen has become highly advantageous for biologists whose studies focus not on filtration but instead on endocrinological, isotopic, and toxicological or pollutant research.

So what, then, constitutes the actual baleen filter? The plates alone? Fringes? Racks? All of the above? Although this might appear at first glance to be a simple question, it is one of the lingering mysteries of the comprehensive baleen filtration system, and the subject of ongoing research. Clearly, there is much room for judgment, as the composition of the complete baleen filter depends on one's perspective. When considering an entire baleen rack and its constituent major/minor plates and eroded fringes, baleen acts both structurally and functionally as a complex metafilter comprising multiple components with differing morphological and biomechanical properties (Pivorunas, 1976; McKittrick et al., 2012; Loch et al., 2020). By "metafilter" we mean that each component serves as its own kind of filter, but they work together as a hierchically complex, integrative system. Together, the larger plates and smaller eroded fringes produce a dual-phase (i.e., plate plus fringe) filter, with fringes capturing smaller particles than the larger particles trapped by plates, and with a combined surface area much larger than would be contributed by the flat plates alone (Werth et al., 2018a). This surface area includes the smooth planar surfaces of baleen plates, the tattered region of eroded baleen fringes along each individual plate, and the combined dimensions of each exposed hair-like fringe. Calculations of overall filter area range from roughly 2-4 m^2 in most whales to >6 m^2 in large balaenids (Table 1), if considering only the surface area of the medial mat of eroded fringe hairs (Kawamura, 1974; Werth et al., 2018a). If the planar surfaces of all plates and dimensions of individual fringes are also included, the total surface area ranges from ~30 m^2 in smaller whales to >150 m^2 in large balaenids (Werth et al., 2018a).

At this point, it is best to conclude that far from being a simple system, baleen filtration instead acts on micro- to macroscopic scales as a variable metafilter, with each component—fringe, plate, and whole rack—contributing its own function to the entire baleen filtration system (Pivorunas, 1976; Sekiguchi et al., 1992; Vandenberg et al., 2023). Depending on the size of filtered items (1 mm copepods to 20 cm fish) and parameters of filtration (e.g., flow speed), different component elements are involved.

3 Varied filtration modes from diverse mysticete feeding ecology

In addition to the dynamic intricacy arising from the baleen metafilter's physical structure itself, a second level of complexity arises from differential employment of baleen filters during feeding, which varies widely by taxa (Werth, 2000; Young, 2012). As outlined in Table 1, hinted at in the preceding section, and dealt with in detail in this section, different mysticete families use their filters for different types of bulk prey collection and separation from seawater (Figure 2). In essence, the three main living families employ wholly different foraging strategies (Table 1).

The most fundamental division of mysticete feeders involves continuous versus intermittent filtration (Tomilin, 1954; Nemoto, 1959; Slijper, 1962; Nemoto, 1970; Gaskin, 1982; Sanderson and Wassersug, 1990, Sanderson and Wassersug, 1993; Werth, 2000). Continuous filtration operates over extended bouts of time (typically several minutes of deployment) as a steady-state process (Werth, 2004), the way plankton tow nets are used, except that whales push rather than pull the filter via forward locomotion from steady fluking. In contrast, intermittent feeders engulf and process a single mouthful of prey-laden water at a time (Goldbogen et al., 2017b).

Balaenid (bowhead and right) whales are typically ram skimmers that use continuous bulk filtration to filter small planktonic prey wherever prey accumulate: at the surface or all levels of the water column, including near the bottom (Mayo and Marx, 1990). As the mouth opens to expose the baleen filter, an incurrent flow of prey-laden water enters the mouth between paired racks (Figure 2). Only balaenids have a true subrostral gap between

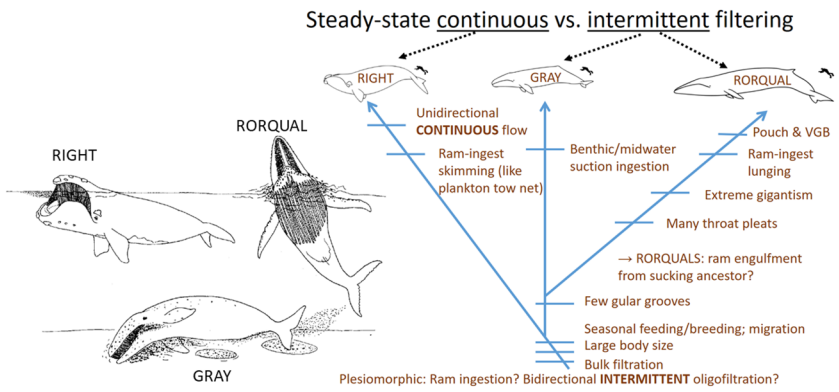

FIGURE 2
Baleen is used for steady-state continuous filtration in bowhead and right whales, or intermittent filtration (processing a single discrete mouthful of prey-laden water) in gray whales and groove-throated rorquals. Cross-sections through mouth at top left indicate that oral morphology parallels these feeding types. There is much speculation but no consensus as to which type of foraging filtration arose in the earliest baleen whales and is ancestral to other types. There is also debate about when gigantism arose in mysticetes; some sources (e.g., Bisconti et al., 2021, Bisconti et al., 2023) argue that at least in right whales (Balaenidae), smaller body size is plesiomorphic.

left and right racks (Werth, 2004). Balaenids also have high, semicircular lips extending above the lower jaw, with a port-like opening just behind the lips and under the eyes for steady excurrent flow (Werth and Potvin, 2016). The resulting scoop-like head can comprise a third of the length of a balaenid's plump body. After flowing through the center of the mouth, water flows laterally through each rack, then through a gutter-like fold, the orolabial sulcus, between the lip and lateral rack surface (Lambertsen et al., 1989; Potvin and Werth, 2017). In addition to laterally supporting and constraining the baleen racks, the lips may be especially important in generating and modifying flow regimes (Werth et al., 2018a; Werth et al., 2019b); their positioning should be the focus of further flow experiments and field observations. The balaenid tongue may preferentially direct flow toward either rack (Werth, 2007; Werth and Crompton, 2023); it also, without moving, sets up a flow regime that channels flow toward each rack (Potvin and Werth, 2017; Werth and Sformo, 2020). Balaenids typically swim at about 0.7-1.0 m/s when filtering prey (van der Hoop et al., 2019; Werth and Sformo, 2020). They close the mouth, apparently to swallow a slurry of accumulated prey, at regular intervals. Data from tags temporarily affixed to whales reveal that balaenids usually feed during dives of approximately 15 min (Werth and Potvin, 2016; Werth and Sformo, 2020). In bowheads, the mouth closes for about 10 s every 2-3 min (Simon et al., 2009), whereas in right whales feeding on concentrated prey, the mouth closes for ~3 s every 50 s (van der Hoop et al., 2019); these behaviors vary in duration with prey density. Fluking data from tags indicate that gape opening to expose baleen for filtration engenders a notable rise in drag (Nowacek et al., 2001; Potvin and Werth, 2017). Drag has been calculated to increase to five times the baseline level in foraging North Atlantic right whales (Nousek-McGregor, 2010; van der Hoop et al., 2019) and sixfold in bowhead whales (Simon et al., 2009). These forces are estimated at 10-100 kN, or 0.1-1 kN per metric ton of body mass (Potvin et al., 2020). As a consequence of this increased drag, swim speed during filtration immediately drops (even with notably increased fluking rates) by 25% in right whales and 40% in bowheads (van der Hoop et al., 2019; Werth and Sformo, 2020). Little is known of feeding in the smallest mysticete species, poorly understood pygmy right whales, *Caperea marginata*, but it is presumed, based on aspects of the baleen filter and related oral morphology, that this species also collects and filters tiny zooplankton via skimming (Kemper, 2017; Werth et al., 2018a).

Foraging in the rorqual or "groove throated" whales, so named for their prominent pattern of ventral throat pleats (Shadwick et al., 2013), occurs in an entirely different manner generally described as "lunge feeding" (Figure 2). These diverse whales of the Family Balaenopteridae, which includes the largest baleen whales (blue and fin; *Balaenoptera musculus* and *physalus*) and much smaller minke whales (*B. acutorostrata* and *bonaerensis*), as well as the familiar humpback whale (*Megaptera novaeangliae*), use intermittent instead of continuous filtration. A single mouthful of prey are engulfed, usually in an energetic, acrobatic lunge or gulp at the surface or at depth. Water is then expelled by contraction of muscles underlying the ventral groove blubber or VGB (Orton and Brodie, 1987; Goldbogen et al., 2010; Shadwick et al., 2013; Werth and Ito, 2017; Kahane-Rapport and Goldbogen, 2018; Pyenson, 2018) and prey are swallowed. Although rorquals normally display sleek bodies adapted for rapid locomotion (both for long migrations and predatory lunges), when they engulf a capacious mouthful of prey-laden water, they briefly assume a bloated "tadpole" shape, as the accordion-like throat pleats expand over the entire ventral region, spreading posteriorly to the umbilicus (Werth et al., 2019b). Adult rorquals have a floppy, flaccid tongue (Werth and Crompton, 2023), which invaginates into a hollow interior space, the *cavum ventrale*, to accommodate the massive temporary influx of water, which may involve over 100 m^3 (100,000 L; Werth, 2013).

Apart from stealthy "trap feeding," in which a stationary whale at the surface holds its jaws open and waits as prey accumulate inside the mouth (McMillan et al., 2019), rorquals generally lunge via rapid forward locomotion. Thus both the entry of water/prey and subsequent expulsion of water are rapid, forceful events (Simon et al., 2012), unlike in balaenid skim feeding (Simon et al., 2009;

Werth and Potvin, 2016). However, both balaenid skim and rorqual lunge feeding depend on locomotion-based ram ingestion (apart from rare cases of passive trap feeding). Sei whales, *B. borealis*, display a morphotype somewhat intermediate between balaenids and other balaenopterids (Werth et al., 2018a), and are known to switch facultatively between lunge feeding and balaenid-style skim feeding depending on targeted prey (Segre et al., 2021).

Scalable parameters of rorqual lunge feeding vary somewhat by species and size yet display remarkable ecological/behavioral and morphological/physiological consistency in traits ranging from gape angle and duration to timing of water filtration and expulsion (Goldbogen et al., 2006, Goldbogen et al., 2007, Goldbogen et al., 2011; Goldbogen et al., 2012a, Goldbogen et al., 2012b; Potvin et al., 2009, Potvin et al., 2012; Goldbogen et al., 2015; Cade et al., 2016; Kahane-Rapport et al., 2020; Potvin et al., 2020, Potvin et al., 2021). Generally, all engulfed water is expelled from the expanded oral and throat pouch within about 20 s (Goldbogen et al., 2017b). Unlike balaenids, balaenopterids have only a small lower lip rising above the mandibles, but this may help to hold the baleen filter and keep it from bulging outward as strong forces and pressures accrue during the brief yet powerful burst of water expulsion (Werth, 2013). Again, the extent to which the lips play a direct or indirect role in filtration remains unknown, and should be the focus of future study.

A third kind of mysticete foraging, and second kind of intermittent baleen feeding (Table 1), occurs in gray whales, *Eschrichtius robustus*. These typically employ intraorally-generated suction, created by rapid tongue depression and retraction, to ingest benthic invertebrates, although gray whales, like other mysticetes, display ecological and behavioral versatility to exploit multiple food resources (Kasuya and Rice, 1970; Rice and Wolman, 1971; Ray and Schevill, 1974; Nerini, 1984; Sumich, 2001; Woodward and Winn, 2006; Young et al., 2015; Webber et al., 2024).

Although this general three-way pattern of mysticete feeding is widely understood (Pivorunas, 1979; Berta et al., 2015, Berta et al., 2016), much speculation surrounds the origins of baleen from early toothed ancestors and the presumed original type of mysticete feeding (Fitzgerald, 2010; Boessenecker and Fordyce, 2015; Tsai and Fordyce, 2015; Marx et al., 2016a; Geisler et al., 2017; Gol'din and Startsev, 2017; Lambert et al., 2017; Peredo et al., 2017; Hocking et al., 2017b; Fordyce and Marx, 2018; Ekdale and Deméré, 2021; Gatesy et al., 2022). Notably, whether the earliest baleen use involved intermittent or continuous filtration remains unknown, despite much conjecture. Several studies have concluded that early baleen use involved suction rather than ram ingestion. The phylogenetic placement of gray whales close to (indeed, within) balaenopterids is now well established (Gatesy et al., 2013), but how their feeding style arose is uncertain. It is possible that the first filtering mysticetes fed similarly to modern gray whales; alternatively, gray whale suction feeding may have arisen as a specialization from lunging ancestry. It is also possible that the earliest baleen filtration involved something akin to the continuous skimming of modern balaenids. A growing record of diverse yet somewhat contradictory fossils raises more questions than answers (Mchedlidze, 1984; Thewissen, 1998; Kimura and Ozawa, 2002; Bisconti and Varola, 2006; Thewissen et al., 2009; El Adli et al., 2014; Berta et al., 2015; Collareta et al., 2015; Berta et al., 2016; Marx et al., 2016b; Werth and Marshall, 2023).

For the purposes of this review paper, the most important point to be made here is that baleen appears to have been a spectacularly successful key innovation, leading, roughly 28 million years ago (Bisconti et al., 2023), to an adaptive radiation of diverse stem and crown Mysticeti (Thewissen, 1998; Marx et al., 2016b), with each lineage evolving its own baleen filter arrangement with plates and fringes of varying number, size, shape, and material properties (Nemoto, 1970; Werth et al., 2018a; Marshall and Pyenson, 2019). Extinct and extant baleen whales have used, and continue to use, their keratinous oral filters in remarkably varied ways. Consequently, baleen filtration systems of different mysticete taxa are subjected to radically differing design requirements ranging from brief bursts of rapid, high volume flow to sustained periods of low-speed flow exposure engendering very high drag forces (Fitzgerald, 2010; Marx et al., 2016a, Marx et al., 2017; Potvin et al., 2020). The bottom-line conclusion is that there is no unified pattern of baleen filtration because there is no single strategy of mysticete filtration. Instead, there are three main strategies (Figure 2; Table 1), with further elaborations for taxa such as sei and pygmy right whales (Sekiguchi et al., 1992; Brodie and Vikingsson, 2009; Werth et al., 2018a). Baleen has evolved to fit a wide variety of dynamically variable situations both within and between different species and lineages.

4 Flow-dependent porosity determined by varying parameters

In addition to baleen's structural and functional diversity arising from the structural complexity of the filter and ecological array of its usage, a third layer of variability (Figure 3) has been made apparent by controlled laboratory experiments (e.g., Werth, 2013; Werth and Potvin, 2016; Potvin and Werth, 2017, Potvin and Werth, 2024) confirming that parameters of baleen filtration vary according to operating conditions. Most notably, these involve flow direction (angle of attack), speed, and volume. Further, because of the baleen's structural complexity (Werth, 2017), these parameters vary by location within the filter (Figure 4), namely: at different sites 1) within a rack (anteroposteriorly and mediolaterally), 2) along an individual plate (dorsoventrally, from palatal origin to the triangular vertex corresponding to the oldest exposed part of a plate), and 3) along a fringe, from where a fringe connects to a plate along its distance to the free tip. The upshot of these variables is that baleen's porosity (Matyka et al., 2008; Vogel, 2013; Potvin and Werth, 2024) is flow-dependent and also region-dependent (Figure 4; Werth, 2013; Potvin and Werth, 2024). Unlike a simple kitchen colander or other strainer, baleen does not demonstrate fixed porosity (Werth, 2019).

This conclusion is at once both obvious (upon reflection) but at the same time unexpected given traditional views of baleen's function as a sieve (Sanderson and Wassersug, 1990, Sanderson and Wassersug, 1993). Further, until recently the structural intricacy of the baleen filter has been greatly underestimated

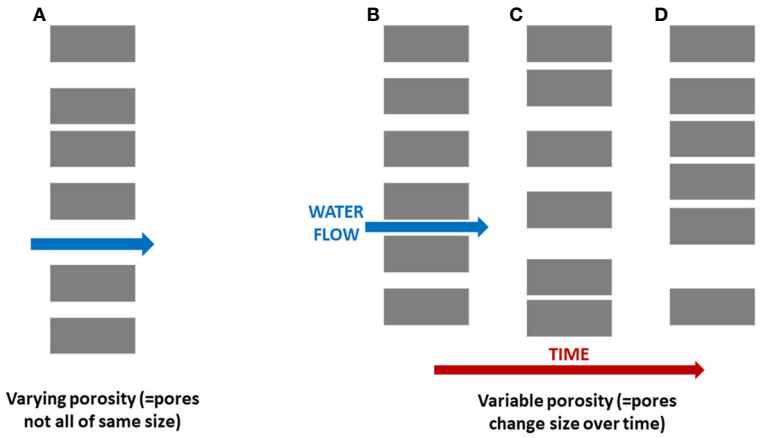

FIGURE 3
Research has revealed that unlike a simple sieve, baleen operates as a highly dynamic filter whose porosity is both spatially varied **(A)** and temporally variable **(B–D)** as well as varied by species. Gray rectangles indicate sections through plates or fringes of baleen, with white gaps representing porous spaces in between.

(Young et al., 2015; Jensen et al., 2017; Vandenberg et al., 2023), as has the array of foraging conditions in which baleen filters are used (Goldbogen et al., 2017b; Goldbogen and Madsen, 2018; Goldbogen et al., 2023). In addition to strong speculative inference from such morphometric and ecological analyses, two additional sources of robust data have revealed much detail about baleen filtration. The first involves field data from biologging tags (archival and telemetric) temporarily affixed via suction cups to the bodies of living whales. These continue to yield great insight into how whales filter prey during feeding (Goldbogen et al., 2017a). Tag data have shown for example that whales control body position (roll, pitch, yaw), open and close the mouth for specific durations, swim at certain speeds, and feed at various depths during filtration, all of which have implications for how the baleen filter operates (Goldbogen et al., 2013; Goldbogen et al., 2017b, Goldbogen et al., 2023).

The second source of data involves less striking but equally valuable laboratory experiments using baleen tissue in circulating flow tanks (also called flumes; Mayo et al., 2001; Werth and Potvin, 2016; Potvin and Werth, 2024). Because of the large size of actual baleen plates, researchers generally cut small sections from plates and assemble them to create "mini-racks," although huge flow tanks

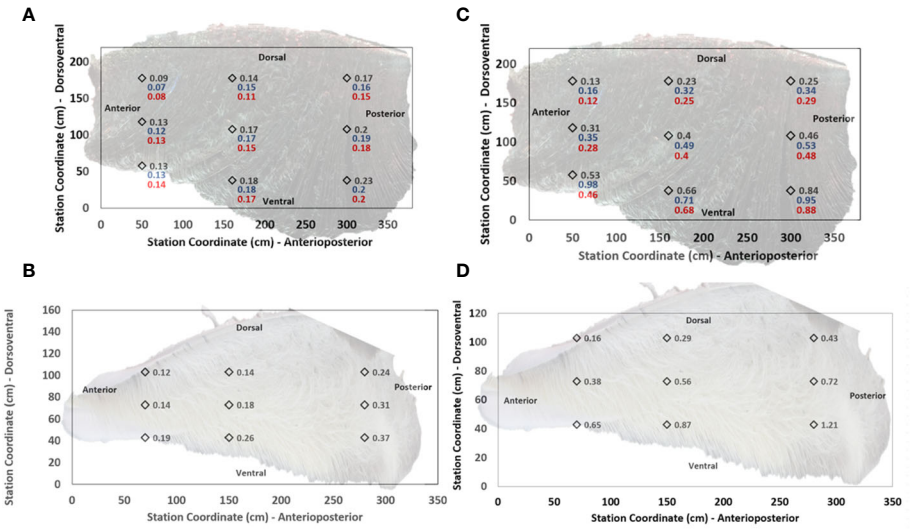

FIGURE 4
Porosity varies by locations on the interior (medial) fringed mat of baleen racks, as indicated on samples collected from bowhead **(A)** and fin **(B)** whale specimens in a flume (Potvin and Werth, 2024). Diamonds indicate approximate locations on a rack, with background photographs rescaled to guide the eye. Labels correspond to porosities measured at flume speeds of 0.75m/s (black print), 0.50m/s (blue) and 0.25m/s (red). Typical uncertainties fall within the SD of ± 0.04 (bowhead) and ± 0.09 (fin) calculated in the observables' average over all anatomical stations. Right panels show through-mat flow speeds (cm/s) versus position on bowhead **(C)** and fin **(D)** whale racks (with symbol conventions as in panels **(A, B)**), calculated at a benchmark pressure gradient set equal to the product of water density, acceleration of gravity and local mat thickness (Potvin and Werth, 2024).

created for naval architecture studies (i.e., to test fluid dynamics of vessel hulls) have also been used (Werth et al., 2018b). The baleen can then be observed as it responds to moving water, either as water circulates past stationary baleen (Werth, 2013) or as baleen is towed or otherwise propelled through water (Werth et al., 2018b). In this way, changes in baleen form and "posture," such as bending and spacing between plates and fringes, can be observed, recorded, and analyzed. Additionally, dyes or other materials can be added to water to better visualize hydrodynamics of baleen-water interactions. Small particles such as plastic beads, or even genuine prey items (e.g., copepods or other zooplankton; Fields and Yen, 1997; Werth, 2012) can be introduced to flow to record actual filtration events via cameras placed directly underwater in the flowstream or by outside viewing ports, ideally with ruled grids or other scales to indicate and quantify flow regimes (Werth, 2013). One way to measure such interactions is by analyzing rates at which baleen plates and fringes capture plastic or prey particles in the water stream; another is to determine the extent to which baleen porosity changes as plates and fringes move within the flow (Figure 5). [Note that "capture" in this sense means that particles are caught by the baleen filter (Shimeta and Jumars, 1991; Potvin and Werth, 2024). Capture could also include ingested particles flow directly into the oropharynx with little or no contact with the filter.] The distance between the free tips of eroded fringes or of another location along fringes (e.g., 1 cm or 10 cm from where it attaches to a plate), defined as *interfringe distance* (IFD), has provided valuable data about porosity and other filter parameters as variables such as flow speed are experimentally manipulated (Werth, 2013, Werth, 2019).

Such experiments have yielded useful information regarding baleen filtration (Figure 5). They have revealed for example that the direction of water flow, determined by the angle of attack at which plates are oriented relative to incurrent flow, considerably alters baleen's filtration ability (as revealed by particle and pigment movement and capture). As with other basic aspects of baleen filtration, this is both surprising and unsurprising. On the one hand, it is entirely obvious that flow direction has a marked effect on filtration (Werth, 2013). On the other hand, this is somewhat unexpected given that people historically viewed baleen filtration as a relatively simple, invariant process (Jorgensen, 1966; Croll et al., 2008). Instead, recent research has shown (as outlined in the next two sections of this paper) that flow direction varies throughout baleen filtration by whale species, as well as by location within the rack and throughout the overall time course of an individual bout of filtration.

In addition to variation in filtration according to the flow angle of attack (Figure 5C), flow speed also leads to differences in baleen's filtering abilities as indicated by mat porosity (Figure 4), particle capture rate (Figure 5A), and IFD, which is a major determinant of porosity (Figure 5B; Werth, 2013; Potvin and Werth, 2024). As flow speed and volume flow rate increase, fringes are generally pushed farther apart, leading to higher IFD (Figure 5B). As noted above, flow speed and volume vary by location and timing within a single filtration event, especially in rorqual lunge feeding but also in

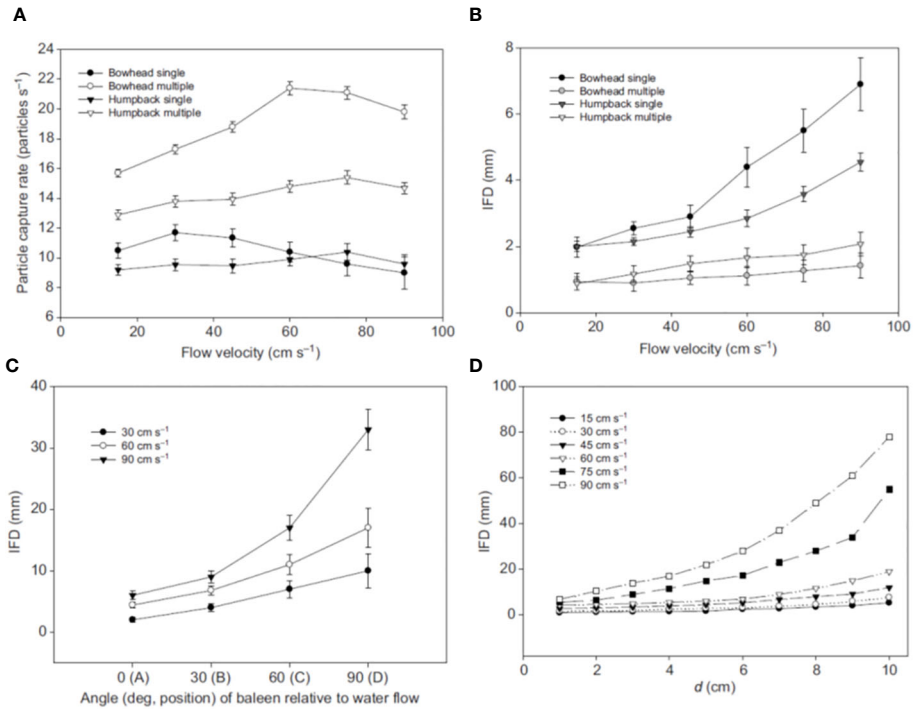

FIGURE 5
Laboratory flume experiments (from Werth, 2013) with baleen samples show that many factors, including flow parameters (speed, direction, volume flow rate) and baleen's orientation (angle of attack) and the distance (d) of fringes from plates, all result in different functional outcomes as measured by such parameters as particle capture or inter-fringe distance (IFD). Panel **(A)** shows particle capture versus flow velocity; **(B)** shows IFD versus flow velocity; **(C)** shows IFD versus angle of attack; **(D)** shows IFD versus distance of fringe from plate.

balaenid skimming and gray whale benthic suction feeding (Werth, 2019). Experiments have revealed the crucial importance of how free baleen fringes interact between adjacent plates (Werth, 2013; Werth et al., 2018b). If a single plate is tested in a flume, it appears that higher flows, particularly above 60 cm/s, lead to diminished particle capture and higher IFD, meaning the filter is more porous (Werth, 2013). However, when multiple plates are tested together in a "mini-rack" formation (Figure 5), it can be seen that baleen fringes swirling in the flow actually overlap and intermingle to form a denser, less porous mat (Potvin and Werth, 2017, Potvin and Werth, 2024). Apart from the overall lesson that basic experimental design is a key consideration for experimental simulations, the more pertinent conclusion is that IFD is a variable parameter that depends on interaction between multiple plates. Each free, eroded horn tube fringe erupts from a single keratinous plate, but fringes from multiple plates work together to create the structurally and functionally important fringe mat (Werth, 2013; Potvin and Werth, 2017; Werth et al., 2018a; Potvin and Werth, 2024). As described earlier, the total baleen filter is a metafilter that is greater than the sum of its individual constituent components. Once again, mysticete filtration is not nearly as simple as traditionally presumed. Specifically, porosity and other measures of filtration depend not only on baleen's physical arrangement and dimensions (e.g., length and density of fringes and plates), but also on flow parameters, notably the speed and direction of water flow.

5 Tangential filtration instead of simple throughput sieving (in balaenids and possibly other mysticetes)

Further analysis and ongoing experimentation have revealed that one of the most fundamental ways in which baleen filtration is more complex than commonly regarded involves the basic type of filtration. Traditional accounts depict baleen as a sieve (Slijper, 1962; Werth, 2001). This is true not only of children's literature, but also of specialized academic works, nearly all of which describe baleen filtration as merely separating prey by size with a passive strainer (Rubenstein and Koehl, 1977). Such passive sieving is presumed to work by *throughput* (AKA *dead-end*) *filtration*, in which prey-laden water flows directly into the filter at a more or less perpendicular angle, thereby collecting and retaining any items larger than the gaps (pores) of the filter, which in this case consist of gaps between baleen plates and/or between fringes (Pivorunas, 1976; LaBarbera, 1984).

Although such a throughput sieve arrangement could work effectively, for several reasons it would not work efficiently for mysticete oral filtration (Werth, 2019). To understand why, it is helpful to consider why throughput filtering is rarely used in commercial filtration scenarios, such as processing to remove particulate matter from beer, wine, juice, or other beverages (Starbard, 2009; Tamime, 2013; Jain and De, 2019). Although such industrial processing seeks to eliminate the solid retentate trapped by the filter (a process called clarification; Sutherland, 2005) and retain/recover just the fluid flowing through it—the opposite of the whale strategy to retain and ingest the filtered solids and expel the watery medium—the overall principles are the same (Blatt et al., 1970). If throughput, perpendicular filtration were used in beverage processing, the filter could readily clog, impeding flow and slowing fluid throughput (and filtration output). Further, the filter might more readily break or otherwise fail and require repairs or replacement, not to mention the fact that repeatedly clearing solid retentate from the filter would be a costly and inefficient chore. Completely replacing the filter, as with coffee machines, is not feasible for whales and seldom a viable option for organismal filters, especially in vertebrates (although filter replacement occurs in larvaceans, caddisfly larvae, some worms and snails, and suspension feeders that continuously produce an internal mucus net to trap prey, including enteropneusts, ascidians, lancelets, and some tadpoles; Hamann and Blanke, 2022).

Tangential filtration, in which the flow strikes the filter at a low angle, reduces or even precludes these problems of solid accumulation, filter clogging, and filter cleaning (Baker et al., 1985; Murkes and Carlsson, 1988; Lu and Ju, 1989; Lu et al., 1993; Belfort et al., 1994; Song and Elimelech, 1995; Vogel, 1996; Zeman and Zydney, 1996; Vogel and Todaro, 1997; Bott et al., 2000; Brainerd, 2001; Sibanda et al., 2001; Ripperger and Altmann, 2002; Espinosa-Gayosso et al., 2012; Makabe et al., 2021). In perhaps its most ideal tangential form, flow runs longitudinally along the filter rather than directly into and through it. In this scenario, called *cross-flow filtration*, the solid retentate is not allowed to accumulate along the filter; rather, solids are propelled past the filter or, depending on the flow regime (Mei, 1992; Humphries, 2009; Peng and Dabiri, 2009), at the most distal part of the filter, where they can be more easily dealt with. In cross-flow filtration, the filter rarely if ever clogs (and if clogging occurs it is delayed substantially; Ripperger and Altmann, 2002; Makabe et al., 2021), and the filter is subjected to less potential damage from high pressures or other physical forces, meaning the filter likely lasts longer (Brainerd, 2001). Thus apart from less filter wear or damage, separation of solid and fluid is more efficient with cross-flow than throughput filtration in terms of delayed or absent clogging, and thus more fluid processed per unit time (Potvin and Werth, 2017). For whale feeding, all these benefits would apply (Potvin and Werth, 2017), with the further benefit that the solid retentate—that is, the collected prey items, which recall are the desired outcome of whale filtration, unlike filtration of commercial beverages or other products—accumulate at or near the excurrent flow output (Werth and Potvin). In the case of the whale mouth, this is right at the entrance of the oropharyngeal opening, where prey are swallowed. Accumulation of a bulk slurry of small prey items that have been efficiently separated from undesirable seawater is an optimal form of filtration (Zhu et al., 2020a, Zhu et al., 2020b, Zhu et al., 2021, Zhu et al., 2023). Cross-flow filtration feeding has been well documented in bony fish (Langeland and Nost, 1995; Goodrich et al., 2000; Brainerd, 2001; Cheer et al., 2001; Sanderson et al., 2001; Smith and Sanderson, 2008; Paig-Tran et al., 2011; Cheer et al.,

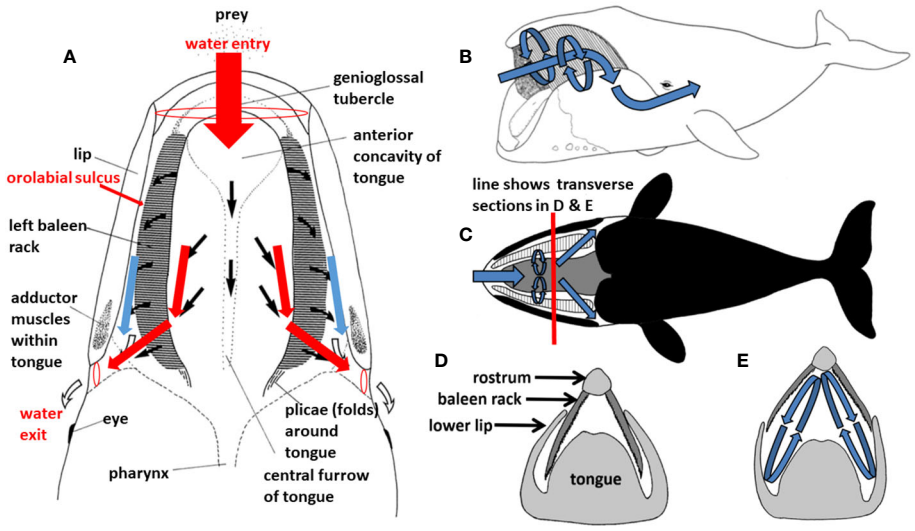

FIGURE 6
During filter feeding in a balaenid whale (**(A)**, showing dorsal view of mouth in cutaway frontal section), prey-laden water flows continuously in branched Y-shaped pipe-like fashion, generating Bernoulli and Venturi effects. This in turn presumably creates helical vortices **(B–E)**, such that water runs tangentially in cross-flow along rather than perpendicularly through baleen.

2012; Sanderson et al., 2016; Witkop et al., 2023), sharks (Sims, 2008; Motta et al., 2010; Wegner, 2015), and rays (Paig-Tran et al., 2013; Paig-Tran and Summers, 2014; Divi et al., 2018).

Such cross-flow filtration would be ideal for continuously feeding balaenid whales, which take in a steady incurrent stream of pre-laden water for a minute or several minutes (depending on prey type and density) before closing the mouth and swallowing accumulated prey; filtration in other (non-balaenid) whales will be covered later in this section. The anatomy of bowhead and right whales is well suited to longitudinal cross flow, with the subrostral gap between baleen racks serving as an input orifice, and paired, "jetport"-like excurrent openings posterior to the large semicircular lips and just below the eyes (Werth, 2004). In this pipe-like flow system, water enters, then divides into a Y-shape to flow along and eventually through either the left or right baleen rack (Figure 6). Water flows through the anterior region of the filtering baleen rack, and then flows along a constrained channel, the gutter-like orolabial sulcus, lateral to the rack but medial to the lip (Figure 6A). As water exits the oral cavity over the entire filter surface, longitudinal flow slows posteriorly (i.e., as it approaches the oropharynx). This makes the accumulated bolus easier to swallow; not only is it devoid of water but it is also moving slowly (Werth and Potvin, 2016).

The very large (up to 1m high and wide and 4+m long), firm muscular tongue of all balaenid species also channels flow, dividing it and directing it into either baleen rack (Werth, 2000; Werth and Crompton, 2023). Lambertsen et al. (1989) speculated that this intraoral morphology might create a Bernoulli effect, as flow speed increases due to narrowing of the pipe-like path, and that this might further generate a Venturi effect to pull water from the center of the mouth, along the tongue, through baleen. These hydrodynamic effects could also slightly diminish pressures where water enters at the anterior of the mouth, perhaps not sufficiently to generate truly notable subambient suction pressures, but at least enough to obviate an anterior compressive bow wave that might physically disperse small prey and/or warn them of an approaching whale. Flow experiments (Werth, 2004, Werth, 2013; Werth and Sformo, 2020) using pressure transducers and videorecording of particles and prey (Werth, 2012) have confirmed that these limited yet real pressure effects in laboratory settings (Figure 7), and tantalizing photographs and video recordings of whales foraging at sea (Werth and Potvin, 2016; Werth and Sformo, 2020; Werth and Crompton, 2023) have likewise supported conclusions of Bernoulli and Venturi effects.

In addition to the likely longitudinal (anteroposterior) aspect of balaenid cross-flow filtration, there are additional presumed dorsoventral elements of a balaenid cross-flow regime that would involve generation of helical vortices within the mouth (Figure 6). Such vortices, again created by steady-state flow through balaenid oral geometry, would remain stable for the duration of continuous skimming. There is strong experimental laboratory flume support for dorsoventral cross-flow and vortical flow generation (Werth, 2004, Werth, 2013; Werth and Potvin, 2016). Set up by anteroposterior (AP) flow along the tongue (APT) and lip (APL), this would create sustained helical cross-flow running along each baleen rack from front to back and top to bottom (Figure 8). Although conjectural, we speculate that the minor baleen plates might assist in generating such helical flow. They are well suited to tripping flow and creating a zone of low pressure along the palate, close to the rack's medial edge. This effect could impart an upward component to the flow, facilitating vortex creation.

Again, this flow regime would most effectively separate prey from water without clogging but with prey accumulation directly on the root of the tongue, where it could be readily swallowed by lingual retraction (Potvin and Werth, 2017). Indirect evidence for

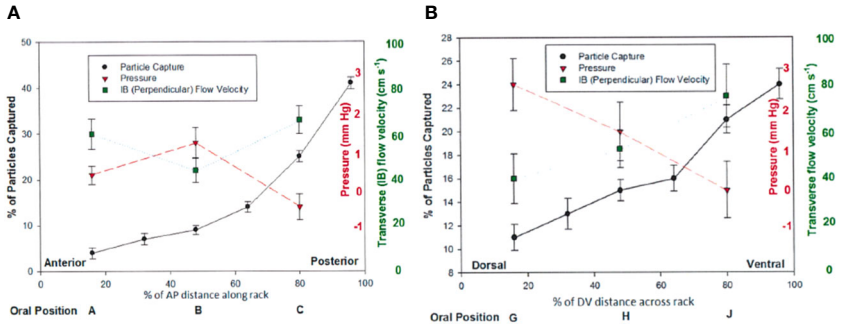

FIGURE 7
Results from flume experiments (Werth and Potvin, 2016) show differential particle capture, pressure, and perpendicular flow speed effects along both the anteroposterior (**A**) and dorsoventral (**B**) dimensions of a full baleen rack, with greater transverse flow and particle accumulation at the posterior end of a full baleen rack, supporting the hypothesis of cross-flow rather than throughput filtration.

this arrangement comes from necropsies on stranded whales or those that die rapidly from ship strikes or other trauma. Despite balaenid feeding on tiny crustacean arthropods (mainly copepods, mysids, amphipods, and euphausiids) with numerous thin, branched exoskeletal appendages that might readily snag in the fine, hair-like fringes of the balaenid filter mat, dead whales are never found with prey items lodged within the baleen filter (Werth and Potvin, 2016).

Although this cross-flow filtration concept has been best considered in balaenid (bowhead and right) whales, it could conceivably apply to all mysticetes (Potvin and Werth, 2017), including intermittently feeding rorqual and gray whales, although likely to a lesser extent. We must note that most recent accounts of baleen filtration (e.g., Hamann and Blanke, 2022; Vandenberg et al., 2023) rely on the notion of throughput filtration in rorquals. However, ongoing flow experiments suggest that at least some flow during rorqual feeding, particularly during latter stages of filtration and water expulsion, involves varying flow pathways that might indicate some cross-flow rather than throughput filtration, and we expect this to be addressed in future publications. Intraoral helical vortices like those envisioned within the balaenid mouth (Figure 6) could likewise form within the mouth of all whales during filtration. This is especially true considering the growing realization that multiple distinct phases of flow are apparent within a single mysticete feeding event, as outlined in the following section.

6 Discrete filtration phases within a single rorqual feeding event

As explained in the first section of this review, traditional accounts of mysticete feeding are greatly simplified and mainly focus on the tongue's role in expelling water from the oral cavity. However, application of modern technologies, notably photography from aerial drones and underwater cameras (Werth et al., 2019b), including cameras and other instruments on digital biologging tags), have revealed that baleen filtration is not so simple as customarily presumed. This is particularly true for rorquals, where an enormous mouthful of water is rapidly (within 10-40 seconds, depending on the species) filtered following a lunge engulfment (Goldbogen, 2010; Goldbogen et al., 2017b; Shadwick et al., 2019). During this rapid process, the flow volume rate and speed of water expulsion are expected to decrease—though precisely how they decrease (for example, linearly or logarithmically) is unknown. Further, there is increasing evidence (Werth et al., 2019b) that the direction of water flow changes as rorqual filtration proceeds.

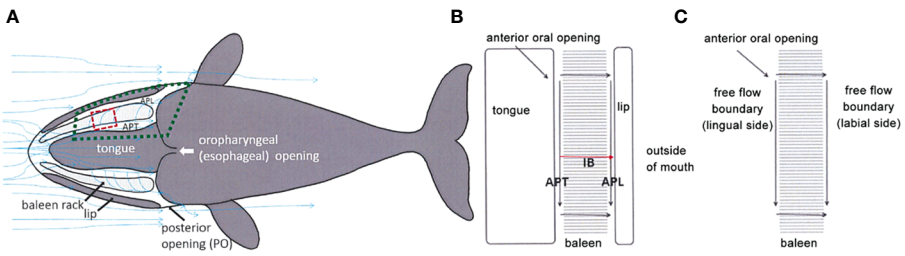

FIGURE 8
Experiments (Werth and Potvin, 2016; Potvin and Werth, 2017) simulating continuous flow through the balaenid mouth **(A)** confirm that solid structures on either side of the baleen rack **(B)** create paired anteroposterior (AP) flow channels along the medial tongue (APT) and lateral semicircular lip (APL) to promote cross-filter flow **(C)**.

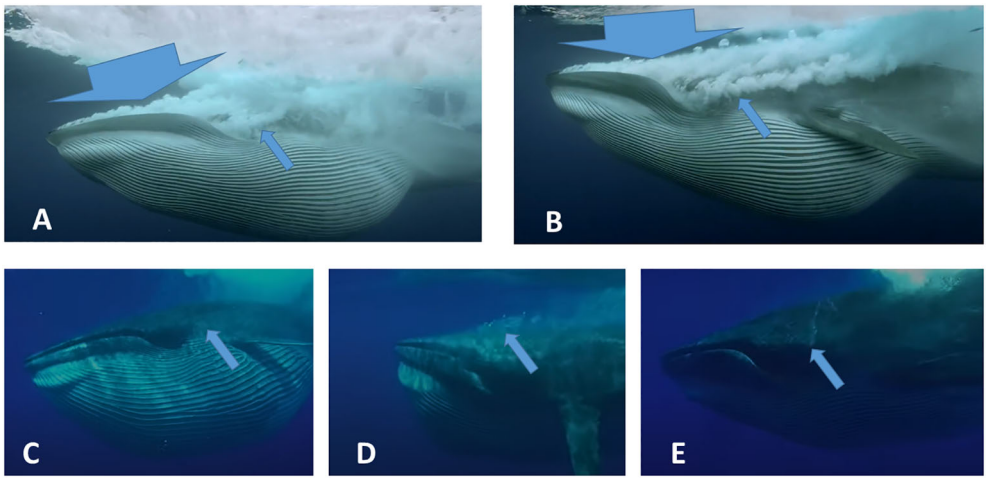

FIGURE 9
Sequential stages of filtration in a Bryde's whale, *Balaenoptera edeni*, reflected here by the uneven, asymmetrical closure of the grooved ventral oral pouch and differential excurrent flow along the jaw margins and angle of the mouth below the eye, indicate different phases of the filtration process, presumably with varied flow directions, speeds, and prey accumulation. Large arrows in **(A, B)** indicate large-scale water expulsion along the entire margin of the jaw; smaller arrows indicate path of water from angle of mouth, which alone exist in later stages **(C–E)** after most water has been expelled. Freeze-frame images from Bob Morgan and BBC *The Hunt* video, courtesy Hugh Pearson.

Specifically, images of asymmetrical VGB contraction and oral pouch compression (Shadwick et al., 2013), along with flow of water and bubble streams indicating the direction and degree of water exiting the mouth (e.g., Figure 8), indicate that flow through baleen occurs in discrete yet characteristic steps or stages. This likely occurs for more effective filtration leading to better capture, collection, and accumulation of prey to be swallowed (Werth and Ito, 2017). In the presumed first phase, initial gape closure appears to cause water expulsion along the full margins of the jaws. This seems to be followed by purging of a distinct stream of water just below the eye at the angle of the mouth—the same place where water steadily exits the posterior of the mouth during continuous filtration in balaenids (Werth, 2004). An apparent third and final stage involves a larger burst of purged water, again from the posterior-most angle of the mouth (Figure 9); this seemingly coincides with hyolingual movements that may correspond to swallowing of accumulated prey (Werth, 2009; Werth and Ito, 2017).

The recognition of apparent discrete phases of mysticete filtration is a new finding that is the subject of ongoing data collection and analysis. In any case, the obvious variation between water flows at different times of whale feeding means not only that filtration is more complicated than conventionally presumed, but also that it seems to involve precisely stereotyped events that can be documented and studied, and which seem to correlate with different flows.

Hydrodynamically, what this apparent division of rorqual filtration into discrete stages means is that water likely flows in varied directions, with apparently different flow speeds and volume flow rates, as outlined in the previous two sections. There is a strong likelihood that this is related to setting up tangential flow for better, more efficient filtration. However, this is far from uncertain. Just as the previous section on tangential filtration plainly applies to balaenids but may also apply to rorquals, so too this section on discrete filtration stages applies to rorquals but may also apply to other (gray and balaenid) whales, even if less markedly.

7 Baleen's biomechanical properties vary by location and conditions

Another largely unappreciated aspect of the baleen filter's biomechanical complexity is related to material properties (primarily stiffness) of the metafilter's combined components. Much more must be learned about how baleen's diverse keratinous elements (i.e., cortical plate, tubular, and intertubular matrix keratin) grow, mature, and interact together (Werth et al., 2020), and how they are altered by inorganic material content such as calcification (Szewciw et al., 2010). The extent to which these factors directly affect plate stiffness or flexibility is gradually being recognized (Werth et al., 2016a, Werth et al., 2018b; Werth and Whaley, 2019) but remains largely unstudied.

Baleen has long been known to be strong and resilient yet pliant (Werth et al., 2018b). It is capable of withstanding strong compressive, tensile, and shear forces (Werth, 2013, Werth, 2019). Calcification stiffens baleen into the hardest alpha keratin tissue (Pautard, 1963; Szewciw et al., 2010); it is much more pliable when hydrated (Werth et al., 2016a). As a tough yet flexible tissue that does not degrade, baleen has long been used by indigenous cultures for artwork, baskets, implements, armor, and weapons (Moffat et al., 2008; Dubner, 2023). During the era of industrial whaling baleen became a highly valuable commodity, peaking in 1853 with over 5.6 million pounds, mostly from right whales, sold in U.S. ports for almost $2,000,000 (Stevenson, 1907). Fringes were made into brushes; plates were used for corset stays, skirt hoops, umbrella ribs, buggy whips, and numerous other items (Lee, 1998).

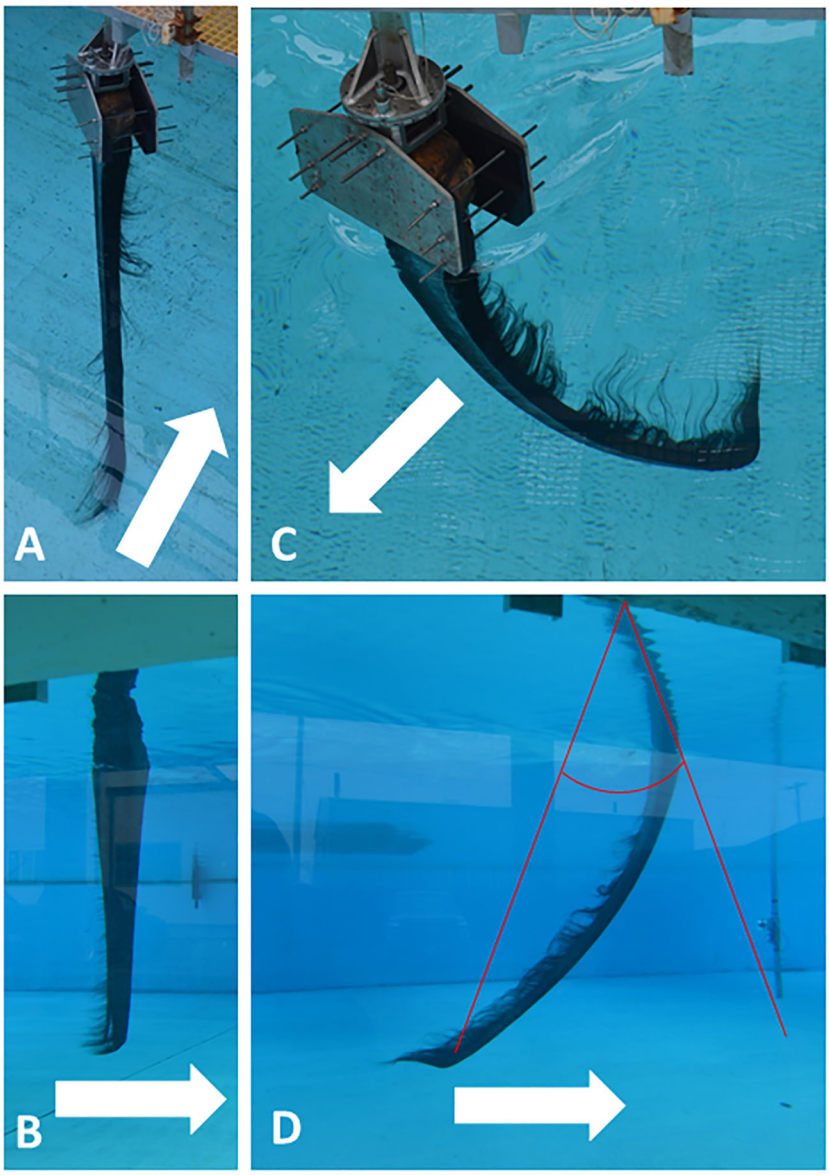

FIGURE 10
Tow tank experiments with "mini-racks" (30 adjacent full baleen plates of a bowhead whale, *Balaena mysticetus*) towed in arrow direction at 0.4 m/s (seen from surface in **A** and from underwater viewing window in **B**) and 1.2 m/s (seen from surface in **C**, underwater in **D**). Images show that baleen plates generally bend differentially along their full length due to dorsal attachment and free ventral vertex, plus varied histology/geometry by length. D also shows how plate tip bending angle was measured from photographs via divergence from the original straight axis.

Prior to the invention of plastic polymers, baleen served as the plastic of its day, such that whaling ports were among the world's most commercially productive locales. Together with whale oil, baleen made whaling the first true American industry (Dubner, 2023).

Baleen's commodity value derived in large part from its exceptional flexibility; its biological value for filtering also arises from this flexibility (Stevenson, 1907). Baleen plates bend along their entire length (Figure 10) in response to the forces acting upon them during filtration (Werth et al., 2018b), which enables baleen to withstand strong forces without cracking, providing great longevity. Three-point bending tests of dried and hydrated baleen specimens using an Instron E1000 ElectroPuls or Mark-10 ES30 universal testing machine enabled calculation of uniaxial flexural stress, strain, and modulus in samples of baleen plates and fringes from different whale species and different locations within a rack and plate (Figure 11). This also enabled creation of a loading (force-deformation) curve (Figure 12), with determination of elastic stiffness and yield and failure points (McKittrick et al., 2012; Werth et al., 2018b). Such experiments showed that baleen can withstand forces >1 kN without breaking (Werth et al., 2018b), and once again at levels that vary along a rack (Figure 11).

These experiments (Werth, 2013; Werth et al., 2016a; Werth et al., 2018b) also demonstrated the importance of studying baleen under natural conditions—namely, when baleen is fully saturated with water, rather than dried out, the way it is typically stored and

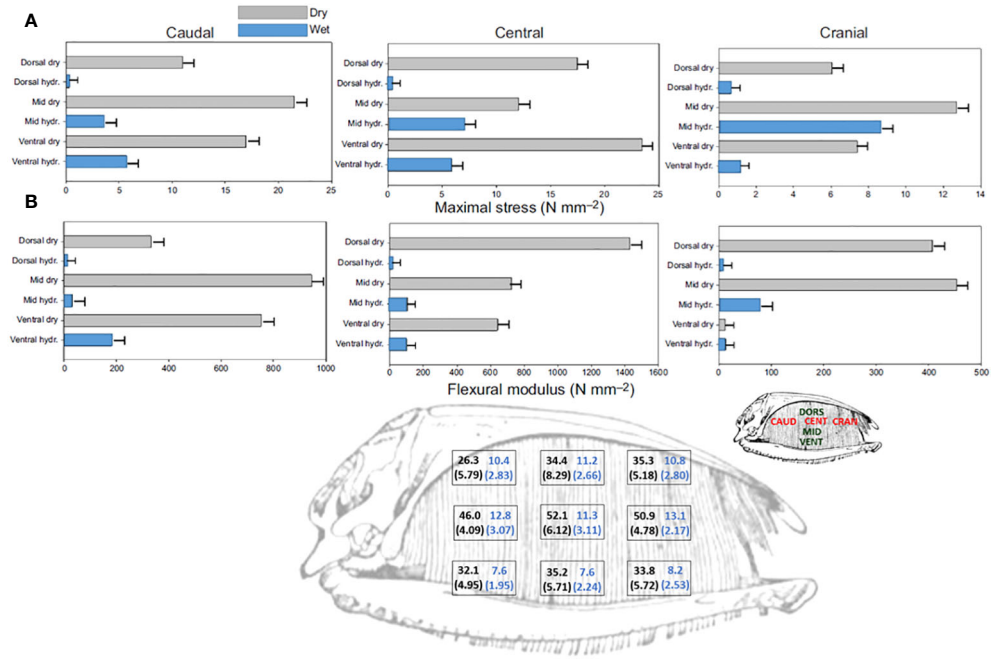

FIGURE 11
Maximal stress **(A)** and flexural stiffness **(B)** along baleen plates, from material strength testing of air-dried (gray bars) vs. hydrated (blue bars) right whale (*Eubalaena glacialis*) samples, showing data from nine locations along anteroposterior and dorsoventral axes (Werth et al., 2018b). Bottom illustration of full right whale baleen rack shows manual bending results, with mean and SD in parentheses, showing force in N from 20 experimental trials to produce 45-degree axial bending in air-dried and hydrated (black and blue numbers, respectively) right whale plates, indicating differences by location in a rack (Werth et al., 2016a; Werth et al., 2018b).

displayed in museum collections and exhibits (Werth et al., 2019c). Baleen in water—the way it perpetually is *in vivo*—itself absorbs and holds much water: 32.35% by weight (Werth et al., 2016a). Mechanical materials testing confirmed that dried baleen is stiff but readily shatters, whereas hydrated baleen (like other hydrated keratins; Kitchener and Vincent, 1987; Feughelman, 1997; Taylor et al., 2004) is much less stiff and bends with little applied force, yet rarely breaks (Werth et al., 2016a; Werth et al., 2018b). This is similar to the difference between dried and fully hydrated pasta noodles, and, further, demonstrates the obvious importance of studying biological materials under natural conditions. Contact angle and wettability tests (Werth et al., 2016a; Werth et al., 2019a) also confirmed that hydrated baleen is highly hydrophilic and oleophobic (i.e., oil-shedding), which is important given that small schooling fish and zooplankton have bodies filled with oil droplets to store energy and maintain neutral buoyancy (St. Aubin et al., 1984; Michaud and Taggart, 2007).

Baleen plates of bowhead and right whales are so long (potentially 4+ m long in large adults) that they must bend to be stowed when the mouth is closed (Werth et al., 2018b). This raises the question of how and where plates bend: uniformly along their length (Figure 10), or are they more "hinged" where they emerge

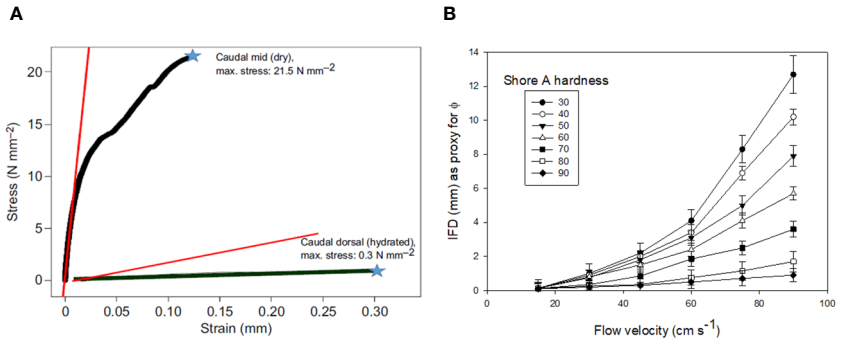

FIGURE 12
Mechanical testing results **(A)** showing maximal stress recorded from three-point bending tests of right whale baleen, showing noodle-like flexibility of wet baleen and brittle fracturing of dried baleen, which failed at 12 mm displacement (strain). **(B)** shows how porosity, as indicated by interfringe distance (IFD), varies by flow speed and Shore hardness, an industrial measure of rubber material softness (measured here in variably hydrated baleen plates) Data from Werth, 2013 and Werth et al., 2016a; Werth et al., 2018b, Werth et al., 2020.

from the dorsal gingiva? Plates were materially tested for differential stiffness, using three-point bending tests, along two axes with a full baleen rack: anteroposterior and dorsoventral. Results indicate that plates are more stiff in the central portion (Figure 12), midway between the newest baleen that emerges from the palate and oldest baleen at the ventral apex of the plate. The baleen at the "top" of each plate is newest and least worn (hence thickest and widest, with fewer free fringes), and it is also stably fixed to the palate; the oldest baleen at the ventral vertex is most eroded (thin and narrow, with many free fringes) and it is furthest from its fixed attachment point. These factors—anatomical, geometric, life history/developmental, etc.—all play crucial roles in the structure and function of the keratinous oral filter. Mechanical testing of baleen from rorquals (blue, fin, humpback, and minke whales; Werth et al., 2018b) indicates similar material properties to balaenid baleen, but markedly less flexibility and fewer dorsoventral differences along the shorter rorqual plates. Baleen fringes from all species are highly flexible and elastically ductile along their length; they bend easily but resume their original form. Thus fringes are not easily broken, but readily they separate from each other to form the fibrous mat portion of the metafilter, to yield rack location-dependent porosities and hydrodynamic performance (Figure 4; Werth et al., 2018a; Potvin and Werth, 2024).

Histological examination reveals that the internal hollow horn tubules which eventually emerge as eroded fringes provide another key way in which baleen plates differ along their axes (Figure 13). In both bowhead and fin whales, tubule density is significantly greater on the medial (lingual) side of plates relative to the lateral (labial) side, as revealed by comparative histological study (Werth et al., 2018b). This abundance of medial fringes likely helps to stiffen and resist fracture on the side of the filter that sees the most "action" from intense water flow, prey accumulation, and possible

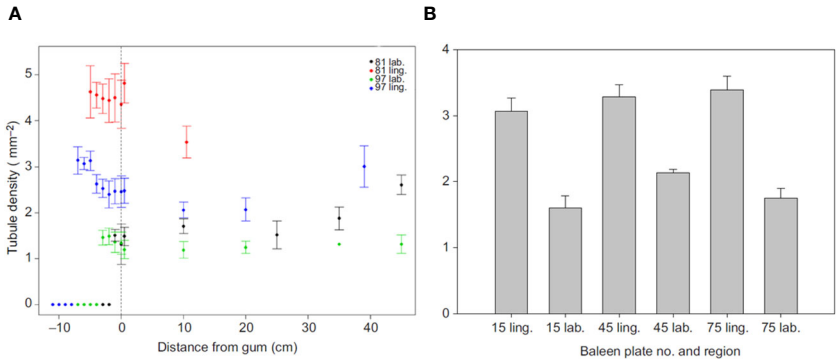

FIGURE 13
Comparative density of hollow horn tubules (mean+SD) in two fin whale baleen plates **(A)** and three bowhead whale plates **(B)** shows greater tubule density in the medial (inner or lingual) plate region relative to the lateral (outer, labial) region in both species. Images revised from Werth et al., 2018b.

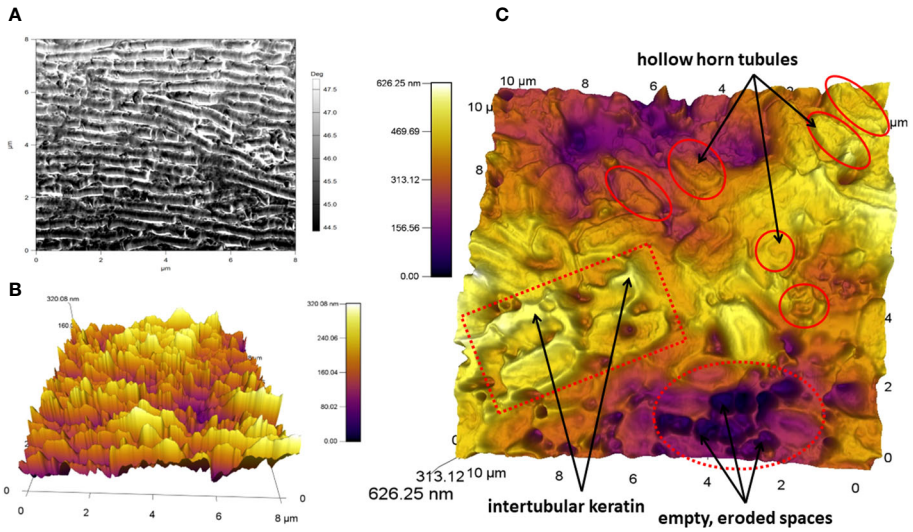

FIGURE 14
Atomic force microscopy (AFM) image of a bowhead baleen sample reveal relative smoothness of plate surface with underlying periodicity of growth lines **(A)**, and topographic 3D rendering of baleen's ultrastructural material complexity **(B, C)** related to diverse keratinous components plus spaces where plates erode and tubules separate. Images revised from Werth et al., 2020.

interaction with the tongue (discussed in the next section). Moreover, the profusion of medial tubules also leads directly to the high density of abundant eroded fringes on the medial or incurrent "business" side of the filter. Modern imaging techniques such as scanning and atomic force microscopy (Figure 14) are helping to resolve the microscopic ultrastructure of the three-dimensional complexity tissue underlying the baleen metafilter (Werth et al., 2018a, Werth et al., 2018b). Our view of the ways in which baleen's ultrastructure influence and determine its porosity, stiffness, and other functional properties is slowly resolving, with much more work to be done.

8 Variable means to clear or clean retentate from baleen filter

A strong benefit of using cross-flow or other tangential filtration during mysticete feeding would be better clearing of the filter, with lesser accumulation of solids directly upon the baleen rack and instead greater accumulation mostly posterior to it. Bulk deposition of prey toward or at the rear of the mouth (by the tongue root) would not only aid swallowing, but also minimize or preclude filter clogging. If water flows mainly along rather than straight through the fringe mat and inter-plate gaps, prey items cannot easily become stuck within the baleen metafilter. As mentioned earlier, the slowed flow through and along the filter's posterior section, along with the accumulated bolus or slurry of prey (with reduced water content) would also facilitate swallowing of prey without swallowing of unnecessary water.

But even if individual or bulk prey were to become enmeshed within the filter, how could they be removed? If baleen were to become clogged, how might it be unclogged? Werth (2001) envisioned three distinct scenarios whereby prey trapped in the baleen filter could be removed. The simplest and most obvious solution involves direct mechanical scraping or shaking of the filter by the tongue (Figure 15). Although this might work, there are several potential problems. First, this overestimates the mobility and muscularity of the tongue body in adult rorquals, which, in order to invaginate and line the ventral cavity of the throat pouch during lunge engulfment (Lambertsen, 1983), resembles a floppy, flaccid waterbed more than a firm tongue akin to that of most mammals (Werth and Crompton, 2023). Second, even if the tongue were not too loose to dislodge ensnared items, prey might be pushed even deeper into the filter mat, compounding the problem. Third, this mechanical abrasion might cause baleen to erode faster than it can be replaced by new growth (Werth et al., 2020). Using the tongue to shake the filtering baleen plates and fringes might work better than directly scraping them, and there is some evidence of a "baleen rattle" of adjacent plates clacking together, although this is generally heard during surface skimming in balaenids when gape is open (Watkins and Schevill, 1976), not when gape closes for presumed filter clearing and swallowing (Werth, 2001).

A second scenario to remove prey trapped in the baleen filter would be to rapidly shake or nod the head, with loosened items

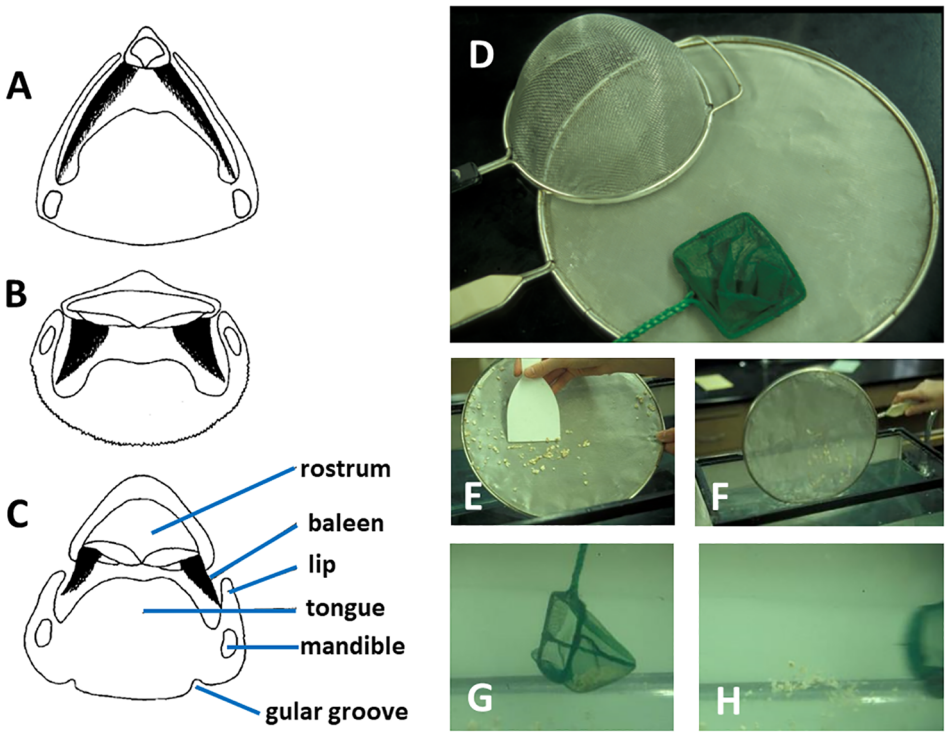

FIGURE 15
Transverse sections of whale heads/mouths (**(A)** balaenid, **(B)** rorqual, **(C)** gray whale) as depicted in Figure 2 show potential physical interactions of dark triangular baleen and other oral structures, which may relate to cleaning/clearing of prey from baleen. This is analogous to three options to clean a clogged filter or dipnet **(D)** by mechanical scraping **(E)**, physical shaking **(F)**, or backwash flushing of the filter **(G, H)**.

falling to the tongue assisted by gravity and inertia (Figure 9). Some field observations, especially of right whales, appear to support claims of head shaking or "nodding" behavior (Gaskin, 1982; Werth, 2001). Although this might provide sufficient force to dislodge items from a clogged filter, it would be difficult to achieve, as head motion would necessitate major expense of metabolic energy. It would also disrupt forward locomotion, which seems not to be impeded during mysticete filtration (beyond typical drag forces) as evidenced by aerial drone recordings (Werth et al., 2019b) and by accelerometers and other instruments from attached tags (Goldbogen et al., 2017a).

A third scenario whereby mysticetes might clear their filter of trapped items would use hydraulic or hydrodynamic rather than brute mechanical forces. Rapid depression and retraction of the tongue, as used to generate intraoral suction for prey ingestion in gray whales (Ray and Schevill, 1974), could create a rapid "backwash" flow to flush and dislodge trapped prey (Figure 15). This could be readily achieved with relatively low metabolic cost and without impeding locomotion or damaging baleen. However, many prey items, both fish and zooplankton, and negatively rheotropic—swimming away from the direction of current flow—so they might burrow deeper into the baleen filter if a backwash current were insufficiently strong to pull them out of the filter (Werth, 2001). Another hydraulic solution could involve the intraoral vortical flows described earlier, which could help to clean baleen fringe mats or indeed to keep them clear from clogging in the first place. To the extent that any tangential flow is involved, it would of course minimize the need to free trapped prey.

All three of these (and other as yet undescribed) possibilities could apply, and they are not mutually exclusive. The best solution might be some combination, or varied mechanisms might be used by different whales in different situations. The main conclusions are that oral filter clogging remains a real even if remote possibility, and that this provides yet another aspect of baleen feeding's multifaceted complexity. Future investigations of this topic should focus on laboratory experiments demonstrating potential baleen clogging and clearing, morphological and prey data from baleen racks studied during necropsy examination, and field observations of whale behavior (e.g., head nodding, shaking, or backwash flow) potentially relating to cleaning of the baleen filter.

9 Conclusions and future plans

Over the past two decades, novel approaches and techniques such as biologging (Goldbogen et al., 2017a) and UAV videography (Werth et al., 2019b) have greatly expanded the number of structural and functional studies on baleen, and have similarly expanded our scientific understanding of baleen's role in filter feeding. Chief among these, as described in the preceding sections, are the recognition of cross-flow filtration, porosity that varies by flow parameters, differing roles for baleen plates and fringes, and biomechanical properties that vary by location within the overall baleen metafilter. We now understand that mysticete filtration does not depend solely on simple sieving. That is the good news. Unfortunately, new questions appear with every answer these new studies reveal, such as how whales locate food over different scales of distance, and how they control and know precisely when to open and close the mouth. Other aspects of whale filtration demanding further study include intraoral pressure gradients and fluid geometry (i.e., how water flow changes direction) as the mouth fills and empties during feeding.

In trading our conventional view of baleen as a static sieve with our newfound appreciation of baleen as a highly complex and dynamically variable filter, we are gaining a more realistic understanding of how whales feed, but at the expense of short, simple conceptual explanations. The more we understand the morphology and fluid dynamics of baleen filtration, the better we can protect whales from crucial environmental risks such as ingestion of plastic debris (Werth et al., 2024) or entanglement of baleen in fishing gear (van der Hoop et al., 2015; Lysiak et al., 2018). For example, determining precisely how water flows into and out of whale mouths could potentially mitigate harm from entangling ropes that bend or otherwise damage baleen plates, disrupting filtration. This could also help to foster strategies for developing fishing lines that detach in ways suited to mysticetes' oral anatomy and flow regimes. Improved knowledge of mysticete filtration could also lower risks posed by whales' ingestion of oil or plastic debris

Future research efforts exploring whale filtration should benefit from advances in UAV "drone" and biologging (i.e., archival and telemetric tag) technology, and in computational fluid dynamics and modeling. Flume experiments should continue to study details of water flow vectors, speeds, timing, and so on. The possibility of recording data from inside a whale mouth, with swallowed, anchored, or "walking" tags, has been a tantalizing dream of scientists. Data from all such investigations would be valuable in addressing gaps in current knowledge, particularly regarding flow parameters, and in connecting the physics of flow with the ecology of living whales, which are remarkably difficult to study due to obvious logistical, legal, and ethical considerations.Biomimetics—the application of biologically inspired designs to build better structures and materials for human use (Trakumas et al., 2001; Cohen et al., 2014)—can apply many useful findings from recent and ongoing baleen research. Specifically, baleen's composite keratinous material, the geometry of the mysticete oral metafilter and its fluid dynamics, the precise mechanisms of particle flow and collection, the pathways of water entry and effluence, the forces and pressure gradients that baleen encounters during filtration, and methods of clearing the filter are all key points that could be exploited via biomimetics. Bioinspired structures and systems based on improved knowledge of baleen function could have many conceivable applications that would prove valuable for a range of technical and industrial design concerns, such as how to improve filter flow and efficiency while limiting breakage and clogging, and how to deal with real-world environmental issues such as clearing waters of microplastics and other waste (Hung et al., 2012; Zhong et al., 2012; Bach et al., 2015; Divi et al., 2018; Schroeder et al., 2019; Witkop et al., 2023).

The other real benefit of our deeper, more genuine understanding of baleen filtration comes from potentially broader application to multiple filtration scenarios, both in biology and in

applied industrial settings. Together, all the findings of the past two decades highlighted in each of the sections above have not only greatly elucidated processes of baleen function but also heightened the need for further research. Many aspects of baleen filtration probably pertain to other biological filters, and can better enable engineers and industrial designers to create artificial filters that are more efficient and longer-lasting.

This is a two-way street, however. One can experiment on or otherwise use knowledge of man-made filters with varying stiffness or other material properties (Mironov et al., 2003; Yeong et al., 2004) to better understand exactly how baleen works *in vivo* in actual whale mouths, something that is still not fully understood. The many prominent hurdles that limit research on whales (legal, logistical, and fiscal) are impediments to carrying out many basic experiments beyond observing structures in dead whales. Fortunately, testing of 3-D printed models of whale baleen (Mironov et al., 2003; Jensen et al., 2017), especially those with exaggerated, unrealistic stiffness or other material properties, can show us how nature does and does not work, better revealing why baleen looks and acts the way it does (Werth, 2019). This reversal of conventional biomimetics—in which, rather than nature inspiring novel technologies, the new technological applications and findings instead further inform our understanding of nature—holds great promise. In this way we can better understand natural systems, allowing us to design and manufacture more effective synthetic filters. Perhaps most importantly and fruitfully, research must continue to study the numerous important ways in which baleen offers a highly dynamic and variable filtering paradigm. Understanding common versus unique features of varied filtration phenomena, both biological and artificial, will continue to aid scientific and technical understanding, enable fruitful interdisciplinary partnerships, and yield new filter designs.

Author contributions

AW: Conceptualization, Supervision, Writing – original draft, Writing – review & editing. JP: Conceptualization, Supervision, Writing – review & editing.

Funding

The author(s) declare that no financial support was received for the research, authorship, and/or publication of this article.

Acknowledgments

The authors acknowledge dozens of research colleagues (including those not specifically listed here), most of whom have been collaborative investigators and all of whom have provided valuable ideas and feedback. Especially helpful collaborators and colleagues include Jeremy Goldbogen, Bob Shadwick, Nick Pyenson, Haruka Ito, Michael Moore, Brian Kot, Peter Madsen, Peter van de Graaf, Margo Lillie, Shirel Kahane-Rapport, Dave Cade, Matt Savoca, Wayne Vogl, Ewan Fordyce, Jan Straley, Tom Ford, Joy Reidenberg, and Ann Pabst. The authors also thank the editor and reviewers for helpful comments and suggestions.

Conflict of interest

The authors declare that the research was conducted in the absence of any commercial or financial relationships that could be construed as a potential conflict of interest.

Publisher's note

References

Bach, D., Schmich, F., Masselter, T., and Speck, T. (2015). A review of selected pumping systems in nature and engineering—potential biomimetic concepts for improving displacement pumps and pulsation damping. *Bioinspiration Biomimetics* 10, 051001. doi: 10.1088/1748-3190/10/5/051001

Baker, R. J., Fane, A. G., Fell, C. J. D., and Yoo, B. H. (1985). Factors affecting flux in crossflow filtration. *Desalination* 53, 81–93. doi: 10.1016/0011-9164(85)85053-0

Bannister, J. L. (2008). *Baleen whales, in Encyclopedia of Marine Mammals 3e*. Eds. B. Würsig, J. G. M. Thewissen and K. Kovacs (New York: Elsevier), pp 80–pp 89.

Belfort, D., Davis, R. H., and Zydney, A. L. (1994). The behavior of suspensions and macromolecular solutions in crossflow microfiltration. *J. Membrane Sci.* 96, 1–58. doi: 10.1016/0376-7388(94)00119-7

Berta, A., Lanzetti, A., Ekdale, E. G., and Deméré, T. A. (2016). From teeth to baleen and raptorial to bulk filter feeding in mysticete cetaceans: the role of paleontological, genetic, and geochemical data in feeding evolution and ecology. *Integr. Comp. Biol.* 56, 1271–1284. doi: 10.1093/icb/icw128

Berta, A., Sumich, J. L., and Kovacs, K. (2015). *Marine Mammals: Evolutionary Biology 3e* (San Diego: Elsevier).

Bisconti, M. (2012). Comparative osteology and phylogenetic relationships of *Miocaperea pulchra*, the first fossil pygmy right whale genus and species (Cetacea, Mysticeti, Neobalaenidae). *Zoological J. Linn. Soc.* 166, 876–911. doi: 10.1111/zoj.2012.166.issue-4

Bisconti, M., Pellegrino, L., and Carnevale, G. (2021). Evolution of gigantism in right and bowhead whales (Cetacea: Mysticeti: Balaenidae). *Biol. J. Linn. Soc.* 134, 498–524. doi: 10.1093/biolinnean/blab086

Bisconti, M., Pellegrino, L., and Carnevale, G. (2023). The chronology of mysticete diversification (Mammalia, Cetacea, Mysticeti): body size, morphological evolution and global change. *Earth Sci. Rev.* 239, e104373. doi: 10.1016/j.earscirev.2023.104373

Bisconti, M., and Varola, A. (2006). The oldest eschrichtiid mysticete and a new morphological diagnosis of Eschrichtiidae (gray whales). *Rev. Italiana di Paleontologia e Stratigraphia* 112, 447–457. doi: 10.13130/2039-4942/6352

Blatt, W., Dravid, A., Michael, A. S., and Nelson, L. (1970). *Solute polarization and cake formation in membrane ultrafiltration: causes, consequences and control techniques, in Membrane Science and Technology*. Ed. J. E. Flinn (New York: Plenum), pp 47–pp 91.

Boessenecker, R. W., and Fordyce, R. E. (2015). Anatomy, feeding ecology, and ontogeny of a transitional baleen whale: a new genus and species of Eomysticetidae (Mammalia: Cetacea) from the Oligocene of New Zealand. *PeerJ* 3, 1129. doi: 10.7717/peerj.1129

Bosio, G., Collareta, A., DiCelma, C., Lambert, O., Marx, F. G., de Muizon, C., et al. (2021). Taphonomy of marine vertebrates of the Pisco Formation (Miocene, Peru): insights into the origin of an outstanding fossil-lagerstätte. *PLoS One* 16, e0254395. doi: 10.1371/journal.pone.0254395

Bott, R., Langeloh, T. H., and Ehrfeld, E. (2000). Dynamic cross flow filtration. *Chem. Eng. J.* 80, 245–249. doi: 10.1016/S1383-5866(00)00097-6

Brainerd, E. L. (2001). Caught in the crossflow. *Nature* 412, 387–388. doi: 10.1038/35086666

Brodie, P., and Vikingsson, G. (2009). On the feeding mechanisms of the sei whale (*Balaenoptera borealis*). *J. Northwest Atlantic Fisheries Sci.* 42, 49–54. doi: 10.2960/J.v42.m646

Cade, D. E., Friedlaender, A. S., Calambokidis, J., and Goldbogen, J. A. (2016). Kinematic diversity in rorqual whale feeding mechanisms. *Curr. Biol.* 26, 2617–2624. doi: 10.1016/j.cub.2016.07.037

Caraveo-Patiño, J., Hobson, K. A., and Soto, L. A. (2007). Feeding ecology of gray whales inferred from stable-carbon and nitrogen isotopic analysis of baleen plates. *Hydrobiology* 586, 17–25. doi: 10.1007/s10750-006-0477-5

Cheer, A., Cheung, S., Hung, T.-C., Piedrahita, R. H., and Sanderson, S. L. (2012). Computational fluid dynamics of fish gill rakers during crossflow filtration. *Bull. Math. Biol.* 74, 981–1000. doi: 10.1007/s11538-011-9709-6

Cheer, A. Y., Ogami, Y., and Sanderson, S. L. (2001). Computational fluid dynamics in the oral cavity of ram suspension-feeding fishes. *J. Theor. Biol.* 210, 463–474. doi: 10.1006/jtbi.2001.2325

Cohen, Y. H., Reich, Y., and Greenberg, S. (2014). Biomimetics: Structure–function patterns approach. *J. Mechanical Design* 136, 111108–111101. doi: 10.1115/1.4028169

Collareta, A., Gioncada, A., Gariboldi, K., Bonnacorsi, A., Marx, F. G., Lambert, O., et al. (2017). *Fossil baleen under the microscope: seeking the key for fine-scale preservation of soft tissues, in Geosciences: a tool in a changing world [abstract book]* (Pisa, Italy: Società Italiana di Mineralogia e Petrografia), p 255.

Collareta, A., Landini, W., Lambert, O., Post, K., Tinelli, C., DiCelma, C., et al. (2015). Piscivory in a Miocene Cetotheriidae of Peru: first record of fossilized stomach content for an extinct baleen-bearing whale. *Sci. Nat.* 102, e00114–015-1319. doi: 10.1007/s00114-015-1319-y

Croll, D. A., Tershy, B. R., and Newton, K. M. (2008). *Filter feeding, in Encyclopedia of Marine Mammals 3e*. Eds. B. Würsig, J. G. M. Thewissen and K. Kovacs (New York: Elsevier), pp 429–pp 433.

Deméré, T. A., McGowen, M. R., Berta, A., and Gatesy, J. (2008). Morphological and molecular evidence for a stepwise evolutionary transition from teeth to baleen in mysticete whales. *Systematic Biol.* 57, 15–37. doi: 10.1080/10635150701884632

Divi, R. V., Strother, J. A., and Paig-Tran, E. W. M. (2018). Manta rays feed using ricochet separation, a novel nonclogging filtration mechanism. *Sci. Adv.* 4, e9533. doi: 10.1126/sciadv.aat9533

Dubner, S. (2023) *The first great American industry* (Freakonomics). Available online at: https://freakonomics.com/podcast/the-first-great-american-industry/ (Accessed 12 July 2023).

Ekdale, E. G., and Deméré, T. A. (2021). Neurovascular evidence for a co-occurrence of teeth and baleen in an Oligocene mysticete and the transition to filter-feeding in baleen whales. *Zoological J. Linn. Soc.* 194, 395–415. doi: 10.1093/zoolinnean/zlab017

El Adli, J. J., Deméré, T. A., and Boessenecker, R. W. (2014). *Herpetocetus morrowi* (Cetacea: Mysticeti), a new diminutive baleen whales from the Upper Pliocene (Piacenzian) of California, USA, with observations on the evolution and relationships of the Cetotheriidae. *Zoological J. Linn. Soc.* 170, 400–466. doi: 10.1111/zoj.2014.170.issue-2

Esperante, R., Brand, L., Nick, K. E., Poma, O., and Urbina, M. (2008). Exceptional occurrence of fossil baleen in shallow marine sediments of the Neogene Pisco Formation, Southern Peru. *Palaeogeography Palaeoclimatology Palaeoecol.* 257, 344–360. doi: 10.1016/j.palaeo.2007.11.001

Espinosa-Gayosso, A., Ghisalberti, M., Ivey, G. N., and Jones, N. L. (2012). Particle capture and low-Reynolds-number flow around a circular cylinder. *J. Fluid Mechanics* 710, 362–378. doi: 10.1017/jfm.2012.367

Feughelman, M. (1997). *The relation between the mechanical properties of wool and hair fibres and the keratin-water system*, in *Mechanical Properties and Structure of Alpha-Keratin Fibres*. Ed. M. Feughelman (Sydney: Univ. of New South Wales Press), pp16–pp27.

Feughelman, M. (2002). Natural protein fibers. *J. Appl. Polymer Sci.* 83, 489–507. doi: 10.1002/app.2255

Fields, D. M., and Yen, J. (1997). The escape behavior of marine copepods in response to a quantifiable fluid mechanical disturbance. *J. Plankton Res.* 19, 1289–1304. doi: 10.1093/plankt/19.9.1289

Fitzgerald, E. M. G. (2010). The morphology and systematics of *Mammalodon colliveri*, a toothed mysticete from the Oligocene of Australia. *Zoological J. Linn. Soc.* 158, 367–476. doi: 10.1111/j.1096-3642.2009.00572.x

Fordyce, R. E. (1980). Whale evolution and Oligocene southern ocean environments. *Palaeogeography Palaeoclimatology Palaeoecol.* 31, 319–336. doi: 10.1016/0031-0182(80)90024-3

Fordyce, R. E., and Barnes, L. G. (1994). The evolutionary history of whales and dolphins. *Annu. Rev. Earth Planetary Sci.* 22, 419–455. doi: 10.1146/annurev.ea.22.050194.002223

Fordyce, R. E., and Marx, F. G. (2013). The pygmy right whale *Caperea marginata*: the last of the cetotheres. *Proc. R. Soc. B: Biol. Sci.* 280, 2645. doi: 10.1098/rspb.2012.2645

Fordyce, R. E., and Marx, F. G. (2018). Gigantism precedes filter feeding in baleen whale evolution. *Curr. Biol.* 28, 1–7. doi: 10.1016/j.cub.2018.04.027

Forslind, B. (1970). Biophysical studies of normal nail. *Acta Dermatol. Venereology* 50, 161–168. doi: 10.2340/0001555550161168

Fortune, S. M. E., Trites, A. W., Perryman, W. L., Moore, M. J., Pettis, H. M., and Lynn, M. S. (2012). Growth and rapid early development of North Atlantic right whales (*Eubalaena glacialis*). *J. Mammalogy* 93, 1342–1354. doi: 10.1644/11-MAMM-A-297.1

Fraser, R. D., MacRae, T. P., and Rogers, G. E. (1972). *Keratins: Their Composition, Structure, and Biosynthesis* (Springfield IL: Charles C. Thomas).

Fraser, R. D. B., MacRae, T. P., and Suzuki, E. (1976). Structure of keratin microfibril. *J. Mol. Biol.* 108, 435–452. doi: 10.1016/S0022-2836(76)80129-5

Fudge, D. S., Szewciw, L. J., and Schwalb, A. N. (2009). Morphology and development of blue whale baleen: An annotated translation of Tycho Tullberg's classic 1883 paper. *Aquat. Mammals* 35, 226–252. doi: 10.1578/AM.35.2.2009.226

Gaskin, D. E. (1982). *The Ecology of Whales and Dolphins* (New York: Heinemann).

Gatesy, J., Ekdale, E. G., Deméré, T. A., LAnzetti, A., Randall, J., Beta, A., et al. (2022). Anatomical, ontogenetic, and genomic homologies guide reconstructions of the teeth-to-baleen transition in mysticete whales. *J. Mamm. Evol.* 29, 891–930. doi: 10.1007/s10914-022-09614-8

Gatesy, J., Geisler, J. H., Chang, J., Buell, C., Berta, A., Meredith, R. W., et al. (2013). A phylogenetic blueprint for a modern whale. *Mol. Phylogenet. Evol.* 66, 479–506. doi: 10.1016/j.ympev.2012.10.012

Gatesy, J., and O'Leary, M. A. (2001). Deciphering whale origins with molecules and fossils. *Trends Ecol. Evol.* 16, 562–571. doi: 10.1016/S0169-5347(01)02236-4

Geisler, J. H., Boessenecker, R. W., Brown, M., and Beatty, B. L. (2017). The origin of filter feeding in whales. *Curr. Biol.* 2017, 2036–2042. doi: 10.1016/j.cub.2017.06.003

George, J. C., Lubetkin, S. C., Zeh, J. E., Thewissen, J. G. M., Wetzel, D., and Givens, G. H. (2021). *Age estimation, in The Bowhead Whale,* Balaena mysticetus*: Biology and Human Interactions*. Eds. J. C. George and J. G. M. Thewissen (San Diego: Academic Press), pp 309–pp 322.

George, J. C., Stimmelmayr, R., Suydam, R., Usip, S., Givens, G., Sformo, T., et al. (2016). Severe bone loss as part of the life history strategy of bowhead whales. *PLoS One* 11, e0156753. doi: 10.1371/journal.pone.0156753

Gioncada, A., Collareta, A., Gariboldi, K., Lambert, O., DiCelma, C., Bonaccorsi, E., et al. (2016). Inside baleen: exceptional microstructure preservation in a late Miocene whale skeleton from Peru. *Geology* 44, 839–842. doi: 10.1130/G38216.1

Goldbogen, J. A. (2010). The ultimate mouthful: lunge-feeding in rorqual whales. *Am. Scientist* 98, 124–131. doi: 10.1511/2010.83.124

Goldbogen, J. A., Cade, D. E., Boersma, A. T., Calambokidis, J., Kahane-Rapport, S. R., Segre, P. S., et al. (2017a). Using digital tags with integrated video and inertial sensors to study moving morphology and associated function in large aquatic vertebrates. *Anatomical Rec.* 300, 1935–1941. doi: 10.1002/ar.23650

Goldbogen, J. A., Cade, D., Calambokidis, J. A., Friedlaender, A. S., Potvin, J., Segre, P. S., et al. (2017b). How baleen whales feed: the biomechanics of engulfment and filtration. *Annu. Rev. Mar. Sci.* 9, 367–386. doi: 10.1146/annurev-marine-122414-033905

Goldbogen, J. A., Calambokidis, J., Croll, D., McKenna, M. F., Potvin, J., Pyenson, N. D., et al. (2012a). Scaling of lunge feeding performance in rorqual whales: mass-specific energy expenditure increases with body size and progressively limits diving capacity. *Funct. Ecol.* 26, 216–226. doi: 10.1111/j.1365-2435.2011.01905.x

Goldbogen, J. A., Calambokidis, J., Friedlaender, A. S., Francis, J., DeRuiter, S. L., Stimpert, A. K., et al. (2012b). Underwater acrobatics by the world's largest predator: 360 degrees rolling manoeuvres by lunge-feeding blue whales. *Biol. Lett.* 9, 0986. doi: 10.1098/rsbl.2012.0986

Goldbogen, J. A., Calambokidis, J., Oleson, E., Potvin, J., Pyenson, N. D., Schorr, G., et al. (2011). Mechanics, hydrodynamics and energetics of blue whale lunge feeding: efficiency dependence on krill density. *J. Exp. Biol.* 214, 131–146. doi: 10.1242/jeb.048157

Goldbogen, J. A., Calambokidis, J., Shadwick, R. E., Oleson, E., McDonald, M. A., and Hildebrand, J. A. (2006). Kinematics of foraging dives and lunge-feeding in fin whales. *J. Exp. Biol.* 209, 1231–1244. doi: 10.1242/jeb.02135

Goldbogen, J. A., Friedlaender, A. S., Calambokidis, J., McKenna, M. F., Simon, M., and Nowacek, D. P. (2013). Integrative approaches to the study of baleen whale diving behavior, feeding performance, and foraging ecology. *Bioscience* 63, 90–100. doi: 10.1525/bio.2013.63.2.5

Goldbogen, J. A., Hazen, E. L., Friedlaender, A. S., Calambokidis, J., DeRuiters, S. L., Stimpert, A. K., et al. (2015). Prey density and distribution drive the three-dimensional foraging strategies of the largest filter feeder. *Funct. Ecol.* 29, 951–961. doi: 10.1111/1365-2435.12395

Goldbogen, J. A., and Madsen, P. T. (2018). The evolution of foraging capacity and gigantism in cetaceans. *J. Exp. Biol.* 221. doi: 10.1242/jeb.166033

Goldbogen, J. A., Potvin, J., and Shadwick, R. E. (2010). Skull and buccal cavity allometry increase mass-specific engulfment capacity in fin whales. *Proc. R. Soc. B: Biol. Sci.* 277, 861–868. doi: 10.1098/rspb.2009.1680

Goldbogen, J. A., Pyenson, N. D., and Madsen, P. T. (2023). How whales dive, feast, and fast: the ecophysiological limits of foraging in the evolution of Cetacea. *Annu. Rev. Ecology Evolution Systematics* 54, 307–325. doi: 10.1146/annurev-ecolsys-102220-025458

Goldbogen, J. A., Pyenson, N. D., and Shadwick, R. E. (2007). Big gulps require high drag for fin whale lunge feeding. *Mar. Ecol. Prog. Ser.* 349, 289–301. doi: 10.3354/meps07066

Gol'din, P., and Startsev, D. (2017). A systematic review of cetothere baleen whales (Cetacea, Cetotheriidae) from the Late Miocene of Crimea and Caucasus, with a new genus. *Papers Palaeontology* 3, 49–68. doi: 10.1002/spp2.1066

Goodrich, J. S., Sanderson, S. L., Batjakas, I. E., and Kaufman, L. S. (2000). Branchial arches of suspension-feeding *Oreochromis esculentus*: sieve or sticky filter? *J. Fish Biol.* 56, 858–875. doi: 10.1111/j.1095-8649.2000.tb00877.x

Greenberg, D. A., and Fudge, D. S. (2012). Regulation of hard alpha-keratin mechanics via control of intermediate filament hydration: matrix squeeze revisited. *Proc. R. Soc. B* 280, e2158. doi: 10.1098/rspb.2012.2158

Hamann, L., and Blanke, A. (2022). Suspension feeders: diversity, principles of particle separation and biomimetic potential. *J. R. Soc. Interface* 19, e0741. doi: 10.1098/rsif.2021.0741

Hearle, J. W. S. (2000). A critical review of the structural mechanics of wool and hair fibres. *Int. J. Biol. Macromolecules* 27, 123–138. doi: 10.1016/S0141-8130(00)00116-1

Hocking, D. P., Marx, F. G., Fitzgerald, E. M. G., and Evans, A. R. (2017a). Ancient whales did not filter feed with their teeth. *Biol. Lett.* 13, 20170348. doi: 10.1098/rsbl.2017.0348

Hocking, D. P., Marx, F. G., Park, T., Fitzgerald, E. M. G., and Evans, A. R. (2017b). A behavioural framework for the evolution of feeding in predatory aquatic mammals. *Proc. R. Soc. B* 284, e2016750. doi: 10.1098/rspb.2016.2750

Horwood, J. (2017). *Sei whale, in Encyclopedia of Marine Mammals 3e, ed*. Eds. B. Würsig, J. G. M. Thewissen and K. Kovacs (San Diego: Academic Press), 845–847.

Humphries, S. (2009). Filter feeders and plankton increase particle encounter rates through flow regime control. *Proc. Natl. Acad. Sci.* 106, 7882–7887. doi: 10.1073/pnas.0809063106

Hung, T.-C., Piedrahita, R. H., and Cheer, A. (2012). Bio-inspired particle separator design based on the food retention mechanism by suspension-feeding fish. *Bioinspiration Biomimetics* 7, 046003. doi: 10.1088/1748-3182/7/4/046003

Jain, A., and De, S. (2019). *Processing of beverages by membranes, in Processing and Sustainability of Beverages*. Eds. A. M. Grumezescu and A. M. Hoban (Cambridge UK: Woodhead Publishing), pp 517–pp 560.

Jensen, M. M., Saladrigas, A. H., and Goldbogen, J. A. (2017). Comparative three-dimensional morphology of baleen: cross-sectional profiles and volume measurements using CT images. *Anatomical Rec.* 300, 1942–1952. doi: 10.1002/ar.23648

Jorgensen, C. B. (1966). *Biology of Suspension Feeding* (Oxford: Pergamon Press).

Kahane-Rapport, S. R., and Goldbogen, J. A. (2018). Allometric scaling of morphology and engulfment capacity in rorqual whales. *J. Morphology* 279, 1256–1268. doi: 10.1002/jmor.20846

Kahane-Rapport, S. R., Savoca, M. S., Cade, D. E., Segre, P. S., Bierlich, K. C., Calambokidis, J., et al. (2020). Lunge filter feeding biomechanics constrain rorqual foraging ecology across scale. *J. Exp. Biol.* 223, jeb224196. doi: 10.1242/jeb.224196

Kasuya, T., and Rice, D. W. (1970). Notes on baleen plates and on arrangement of parasitic barnacles of gray whale. *Sci. Rep. Whales Res. Institute* 22, 39–43.

Kawamura, A. (1974). Food and feeding ecology in the southern sei whale. *Sci. Rep. Whales Res. Institute* 26, 25–144.

Kawamura, A. (1980). A review of food of balaenopterid whales. *Sci. Rep. Whales Res. Institute* 32, 155–198.

Kemper, C. M. (2017). "Pygmy right whale," in *Encyclopedia of Marine Mammals 3e, ed*. Eds. B. Würsig, J. G. M. Thewissen and K. Kovacs (Academic Press, San Diego), 790–792.

Kimura, T., and Ozawa, T. (2002). A new cetothere (Ceatacea: Mysticeti) from the early Miocene of Japan. *J. Vertebrate Paleontology* 22, 684–702. doi: 10.1671/0272-4634(2002)022[0684:ANCCMF]2.0.CO;2

Kitchener, A., and Vincent, J. F. V. (1987). Composite theory and the effect of water on the stiffness of horn keratin. *J. Material Sci.* 22, 1385–1389. doi: 10.1007/BF01233138

LaBarbera, M. (1984). Feeding currents and particle capture mechanisms in suspension feeding animals. *Am. Zoologist* 24, 71–84. doi: 10.1093/icb/24.1.71

Lambert, O., Martínez-Cáceres, M., Bianucci, G., DiCelma, C., Salas-Gismondi, R., Steurbaut, E., et al. (2017). Earliest mysticete from the Late Eocene of Peru sheds new light on the origin of baleen whales. *Curr. Biol.* 27, 1535–1541. doi: 10.1016/j.cub.2017.04.026

Lambertsen, R. H. (1983). Internal mechanism of rorqual feeding. *J. Mammalogy* 64, 76–88. doi: 10.2307/1380752

Lambertsen, R. H., Hintz, R. J., Lancaster, W. C., Hirons, A., Kreiton, K. J., and Moor, C. (1989). *Characterization of the functional morphology of the mouth of the bowhead whale,* Balaena mysticetus, *with special emphasis on the feeding and filtration mechanisms. Report to the Department of Wildlife Management* (Barrow, Alaska: North Slope Borough).

Lambertsen, R. H., Rasmussen, K. J., Lancaster, W. C., and Hintz, R. J. (2005). Functional morphology of the mouth of the bowhead whale and its implications for conservation. *J. Mammalogy* 86, 342–352. doi: 10.1644/BER-123.1

Langeland, A., and Nost, T. (1995). Gill raker structure and selective predation on zooplankton by particulate feeding fish. *J. Fish Biol.* 47, 719–732. doi: 10.1111/j.1095-8649.1995.tb01937.x

Lee, M. (1998). *Baleen basketry of the North Alaskan Eskimo* (Seattle: Univ. of Washington Press).

Loch, C., Viegas, S. V., Waddell, J. N., Kemper, C., Cook, R. B., and Werth, A. J. (2020). Structure and properties of baleen in the Southern Right (*Eubalaena australis*) and Pygmy Right whales (*Caperea marginata*). *J. Mechanical Behav. Biomed. Materials* 110, e103939. doi: 10.1016/j.jmbbm.2020.103939

Lu, W. M., Hwang, K. J., and Ju, S. C. (1993). Studies on the mechanism of cross-flow filtration. *Chem. Eng. Sci.* 48, 863–872. doi: 10.1016/0009-2509(93)80325-K

Lu, W. M., and Ju, S. C. (1989). Selective particle deposition in crossflow filtration. *Separation Sci. Technol.* 24, 517–540. doi: 10.1080/01496398908049789

Lubetkin, S. C., Zeh, J. E., Rosa, C., and George, J. C. (2008). Age estimation for young bowhead whales (*Balaena mysticetus*) using annual baleen growth increments. *Can. J. Zoology* 86, 525–538. doi: 10.1139/Z08-028

Lysiak, N. S. J., Trumble, S. J., Knowlton, A. R., and Moore, M. J. (2018). Fishing gear entanglement on a North Atlantic right whale (*Eubalaena glacialis*) using stable isotopes, steroid and thyroid hormones in baleen. *Front. Mar. Sci.* 5, e168. doi: 10.3389/fmars.2018.00168

Makabe, R., Akamatsu, K., Tatsumi, R., Koike, O., and Nakao, S. (2021). Numerical simulations of lift force and drag force on a particle in cross-flow microfiltration of colloidal suspensions to understand limiting flux. *J. Membrane Sci.* 621, 118998. doi: 10.1016/j.memsci.2020.118998

Marshall, C. D. (2008). *Feeding morphology, in Encyclopedia of Marine Mammals 2e*. Eds. B. Würsig, J. G. M. Thewissen and K. Kovacs (New York: Elsevier), pp 406–pp 414.

Marshall, C. D., and Goldbogen, J. A. (2015). *Marine mammal feeding mechanisms, in Marine mammal physiology: requisites for ocean living*. Eds. M. A. Castellini and J. A. Mellish (Boca Raton FL: CRC), pp 95–pp117.

Marshall, R. C., Orwin, D. F. G., and Gillespie, J. M. (1991). Structure and biochemistry of mammalian hard keratin. *Electron Microscopy Rev.* 4, 47–83. doi: 10.1016/0892-0354(91)90016-6

Marshall, C. D., and Pyenson, N. D. (2019). *Feeding in aquatic mammals: an evolutionary and functional approach, in Feeding in vertebrates: anatomy, biomechanics, evolution*. Eds. V. Bels and I. Q. Whishaw (New York: Springer), pp 743–pp 785.

Marx, F. G., Collareta, A., Gioncada, A., Post, K., Lambert, O., Bonaccorsi, E., et al. (2017). How whales used to filter: exceptionally preserved baleen in a Miocene cetotheriid. *J. Anat.* 231, 212–220. doi: 10.1111/joa.12622

Marx, F. G., and Fordyce, R. E. (2015). Baleen boom and bust: a synthesis of mysticete phylogeny, diversity and disparity. *R. Soc. Open Sci.* 2, 1–14. doi: 10.1098/rsos.140434

Marx, F. G., and Fordyce, R. E. (2016). A link no longer missing: new evidence for the cetotheriid affinities of *Caperea*. *PLoS One* 11, 0164059. doi: 10.1371/journal.pone.0164059

Marx, F. G., Hocking, D. P., Park, T., Ziegler, T., Evans, A. R., and Fitzgerald, E. M. G. (2016a). Suction feeding preceded filtering in baleen whale evolution. *Memoirs Museum Victoria* 75, 71–82. doi: 10.24199/j.mmv.2016.75.04

Marx, F., Lambert, O., and Uhen, M. D. (2016b). *Cetacean Paleobiology* (London: Wiley-Blackwell). doi: 10.1002/9781118561546

Matyka, M., Khalili, A., and Kozal, Z. (2008). Tortuosity–porosity relation in the porous media flow. *Phys. Rev. E* 78, e026306. doi: 10.1103/PhysRevE.78.026306

Mayo, C. A., Letcher, B. H., and Scott, S. (2001). Zooplankton filtering efficiency of the baleen of a North Atlantic right whale, *Eubalaena glacialis*. *J. Cetacean Resource Manage.* 2, 225–229. doi: 10.47536/jcrm.vi.286

Mayo, C. A., and Marx, M. K. (1990). Surface foraging behaviour of the North Atlantic right whale, *Eubalaena glacialis*, and associated zooplankton characteristics. *Can. J. Zoology* 68, 2214–2220. doi: 10.1139/z90-308

Mchedlidze, G. A. (1984). *General Features of the Paleobiological Evolution of Cetacea* (New Delhi: Oxonian).

McKittrick, J., Chen, P. Y., Bodde, S. G., Yan, W., Novitskaya, E. E., and Meyers, M. A. (2012). The structure, functions, and mechanical properties of keratin. *J. Mineral Metals Material Soc.* 64, 449–468. doi: 10.1007/s11837-012-0302-8

McMillan, C. J., Towers, J. R., and Hildering, J. (2019). The innovation and diffusion of "trap-feeding," a novel humpback whale foraging strategy. *Mar. Mammal Sci.* 35, 779–796. doi: 10.1111/mms.12557

Mei, R. (1992). An approximate expression for the shear lift on a spherical particle at finite Reynolds number. *Int. J. Multiphase Flow* 18, 145–147. doi: 10.1016/0301-9322(92)90012-6

Michaud, J., and Taggart, C. T. (2007). Lipid and gross energy content of North Atlantic right whale food, *Calanus finmarchicus*, in the Bay of Fundy. *Endangered Species Res.* 2007, 77–94. doi: 10.3354/esr003077

Mironov, V., Boland, T., Trusk, G., Forgacs, G., and Markwald, R. R. (2003). Organ printing: computer-aided jet-based 3D tissue engineering. *Trends Biotechnol.* 21, 157–161. doi: 10.1016/S0167-7799(03)00033-7

Moffat, R., Spriggs, J., and O'Connor, S. (2008). The use of baleen for arms, armour, and heraldic crests in medieval Britain. *Antiquities J.* 88, 207–215. doi: 10.1017/S0003581500001402

Motta, P. J., Maslanka, M., Hueter, R. E., Davis, R. L., de la Parra, R., Mulvany, S. L., et al. (2010). *Feeding anatomy, filter-feeding rate, and diet of whale sharks* Rhincodon typus *during surface ram filter feeding off the Yucatan Peninsula, Mexico*. *Zoology* 113, 199–212. doi: 10.1016/j.zool.2009.12.001

Murkes, J., and Carlsson, C. G. (1988). *Crossflow Filtration: Theory and Practice* (New York: Wiley).

Nemoto, T. (1959). Food of baleen whales with reference to whale movements. *Sci. Rep. Whales Res. Institute* 14, 149–241.

Nemoto, T. (1970). *Feeding pattern of baleen whales in the ocean, in Marine Food Chains*. Ed. J. H. Steele (Edinburgh: Oliver & Boyd), pp 241–pp 252.

Nerini, M. (1984). *A review of gray whale feeding ecology, in The Gray Whale* Eschrichtius robustus. Eds. M. L. Jones, S. L. Swartz and S. Leatherwood (San Diego: Academic), pp 423–pp 450.

Nousek-McGregor, A. E. (2010). "The cost of locomotion in North Atlantic right whales Eubabalena glacialis," (Durham NC USA: Duke University).

Nowacek, D. P., Johnson, M., Tyack, P., Shorter, K. A., McLellan, W. A., and Pabst, D. A. (2001). Buoyant balaenids: the ups and downs of buoyancy in right whales. *Proc. R. Soc. London* 268, 1811–1816. doi: 10.1098/rspb.2001.1730

Orton, L. S., and Brodie, P. F. (1987). Engulfing mechanisms of fin whales. *Can. J. Zoology* 65, 2898–2907. doi: 10.1139/z87-440

Paig-Tran, E. W. M., Bizzarro, J. J., Strother, J. A., and Summers, A. P. (2011). Bottles as models: predicting the effects of varying swimming speed and morphology on size selectivity and filtering efficiency in fishes. *J. Exp. Biol.* 214, 1643–1654. doi: 10.1242/jeb.048702

Paig-Tran, E. W. M., Kleinteich, T., and Summers, A. P. (2013). The filter pads and filtration mechanisms of the devil rays: variation at macro and microscopic scales. *J. Morphology* 274, 1026–1043. doi: 10.1002/jmor.20160

Paig-Tran, E. W. M., and Summers, A. P. (2014). Comparison of the structure and composition of the branchial filters in suspension feeding elasmobranchs. *Anatomical Rec.* 297, 701–715. doi: 10.1002/ar.22850

Pautard, F. G. E. (1963). Mineralization of keratin and its comparison with the enamel matrix. *Nature* 199, 531–535. doi: 10.1038/199531a0

Peng, J., and Dabiri, J. O. (2009). Transport of inertial particles by Lagrangian coherent structures: Application to predator–prey interaction in jellyfish feeding. *J. Fluid Mechanics* 623, 75–84. doi: 10.1017/S0022112008005089

Peredo, C. M., Pyenson, N. D., and Boersma, A. T. (2017). Decoupling tooth loss from the evolution of baleen in whales. *Front. Mar. Sci.* 4, 1–11. doi: 10.3389/fmars.2017.00067

Pfeiffer, C. (1992). Cellular structure of terminal baleen in various mysticete species. *Aquat. Mammals* 18, 67–73.

Pinto, S. J. D., and Shadwick, R. E. (2013). Material and structural properties of fin whale (*Balaenoptera physalus*) zwischensubstanz. *J. Morphology* 274, 947–955. doi: 10.1002/jmor.20154

Pivorunas, A. (1976). A mathematical consideration of the function of baleen plates and their fringes. *Sci. Rep. Whales Res. Institute* 28, 37–55.

Pivorunas, A. (1979). The feeding mechanisms of baleen whales. *Am. Scientist* 67, 432–440. Available at: https://www.jstor.org/stable/27849332.

Pomerleau, C., Matthews, C. J. D., Gobeil, C., Stern, G. A., Ferguson, S. H., and Macdonald, R. W. (2018). Mercury and stable isotope cycles in baleen plates are consistent with year-round feeding in two bowhead whale (Balaena mysticetus) populations. *Polar Biol.* 41, 1–13. doi: 10.1007/s00300-018-2329-y

Potvin, J., Cade, D. E., Werth, A. J., Shadwick, R. E., and Goldbogen, J. A. (2020). A perfectly inelastic collision: bulk prey engulfment by baleen whales and dynamical implications for the world's largest cetaceans. *Am. J. Phys.* 2020, e1771. doi: 10.1119/10.0001771

Potvin, J., Cade, D. E., Werth, A. J., Shadwick, R. E., and Goldbogen, J. A. (2021). Rorqual lunge-feeding energetics near and away from the kinematic threshold of optimal efficiency. *Integr. Comp. Biol.* 3, obab005. doi: 10.1093/iob/obab005

Potvin, J., Goldbogen, J. A., and Shadwick, R. E. (2009). Passive versus active engulfment: verdict from trajectory simulations of lunge-feeding fin whales *Balaenoptera physalus*. *J. R. Soc. Interface* 6, 1005–1025. doi: 10.1098/rsif.2008.0492

Potvin, J., Goldbogen, J. A., and Shadwick, R. E. (2012). Metabolic expenditures of lunge feeding rorquals across scale: implications for the evolution of filter feeding and the limits to maximum body size. *PLoS One* 7, 44854. doi: 10.1371/journal.pone.0044854

Potvin, J., and Werth, A. J. (2017). Oral cavity hydrodynamics and drag production in balaenid whale suspension feeding. *PLoS One* 12, 5220. doi: 10.1371/journal.pone.0175220

Potvin, J., and Werth, A. J. (2024). Suffused: baleen fringe mat porosity and hydrodynamics in balaenid and balaenopterid whales. *Biol. J. Linn. Soc.* in press. doi: 10.1093/biolinnean/blae030

Pyenson, N. D. (2017). The ecological rise of whales chronicled by the fossil record. *Curr. Biol.* 27, 558–564. doi: 10.1016/j.cub.2017.05.001

Pyenson, N. D. (2018). *Spying on Whales: the Past, Present, and Future of Earth's Most Awesome Creatures* (New York: Penguin Random House).

Pyenson, N. D., and Vermeij, G. J. (2016). The rise of ocean giants: maximum body size in Cenozoic marine mammals as an indicator for productivity in the Pacific and Atlantic Oceans. *Biol. Lett.* 12, 20160186. doi: 10.1098/rsbl.2016.0186

Ray, G. C., and Schevill, W. E. (1974). Feeding of a captive gray whale, *Eschrichtius robustus*. *Mar. Fisheries Rev.* 36, 31–38.

Rice, D. W., and Wolman, A. A. (1971). The life history and ecology of the gray whale (*Eschrichtius robustus*). *Am. Soc. Mammalogy* 3, 1–142. doi: 10.5962/bhl.title.39537

Ridgway, S. H., and Harrison, R. (1999). *Handbook of Marine Mammals, Volume 6: Second Book of dolphins and porpoises* (San Diego: Academic).

Ripperger, S., and Altmann, J. (2002). Crossflow microfiltration—state of the art. *Separation Purification Technol.* 26, 19–31. doi: 10.1016/S1383-5866(01)00113-7

Rubenstein, D. I., and Koehl, M. A. R. (1977). The mechanisms of filter feeding: some theoretical considerations. *Am. Nat.* 111, 981–994. doi: 10.1086/283227

Ruud, J. T. (1940). The surface structure of the baleen plates and a possible clue to age in whales. *Hvalradets Skrifter* 23, 1–24.

Sanderson, S. L., Cheer, A. Y., Goodrich, J. S., Graziano, J. D., and Callan, W. T. (2001). Crossflow filtration in suspension-feeding fishes. *Nature* 412, 439–441. doi: 10.1038/35086574

Sanderson, S. L., Roberts, E., Lineburg, J., and Brooks, H. (2016). Fish mouths as engineering structures for vortical cross-step filtration. *Nat. Commun.* 7, e11092. doi: 10.1038/ncomms11092

Sanderson, S. L., and Wassersug, R. L. (1990). Suspension feeding vertebrates. *Sci. Am.* 262, 96–101. doi: 10.1038/scientificamerican0390-96

Sanderson, S. L., and Wassersug, R. (1993). *Convergent and alternative designs for vertebrate suspension feeding, in The Skull Volume 3: Functional and Evolutionary Mechanisms*. Eds. J. Hanken and B. K. Hall (Chicago: University of Chicago Press), pp 37–pp112.

Savoca, M. S., Czapanskiy, M. F., Kahane-Rapport, S. R., Gough, W. T., Fahlbusch, J. A., Bierlich, K. C., et al. (2021). Baleen whale prey consumption based on high-resolution foraging measurements. *Nature* 599, 85–90. doi: 10.1038/s41586-021-03991-5

Schroeder, A., Marshall, L., Trease, B., Becker, A., and Sanderson, S. L. (2019). Development of helical, fish-inspired cross-step filter for collecting harmful algae. *Bioinspiration Biomimetics* 14, 056008. doi: 10.1088/1748-3190/ab2d13

Sears, R., and Perrin, W. F. (2008). "Blue whales," in *Encyclopedia of marine mammals 2e*. Eds. B. Würsig, J. G. M. Thewissen and K. Kovacs (Elsevier, New York), pp 120–pp 124.

Segre, P. S., Weir, C. R., Stanworth, A., Cartwright, S., Friedlaender, A. S., and Goldbogen, J. A. (2021). Biomechanically distinct filter-feeding behaviors distinguish sei whales as a functional intermediate and ecologically flexible species. *J. Exp. Biol.* 224, e238873. doi: 10.1242/jeb.238873

Sekiguchi, K., Best, P. B., and Kaczmaruk, B. Z. (1992). New information on the feeding habits and baleen morphology of the pygmy right whale *Caperea marginata*. *Mar. Mammal Sci.* 8, 288–293. doi: 10.1111/j.1748-7692.1992.tb00411.x

Shadwick, R. E., Goldbogen, J. A., Potvin, J., Pyenson, N. D., and Vogl, A. W. (2013). Novel muscle and connective tissue design enables high extensibility and controls engulfment volume in lunge-feeding rorqual whales. *J. Exp. Biol.* 216, 2691–2701. doi: 10.1242/jeb.081752

Shadwick, R. E., Potvin, J., and Goldbogen, J. A. (2019). Lunge feeding in rorqual whales. *Physiology* 34, 409–418. doi: 10.1152/physiol.00010.2019

Shimeta, J., and Jumars, P. A. (1991). Physical mechanisms and rates of particle capture by suspension-feeders. *Oceanography Mar. Biol. Annu. Rev.* 29, 191–257.

Sibanda, V., Greenwood, R. W., and Seville, J. P. K. (2001). Particle separation from gases using cross-flow filtration. *Powder Technol.* 118, 193–202. doi: 10.1016/S0032-5910(01)00311-4

Simon, M., Johnson, M., and Madsen, P. T. (2012). Keeping momentum with a mouthful of water: behavior and kinematics of humpback whale lunge feeding. *J. Exp. Biol.* 215, 3786–3798. doi: 10.1242/jeb.071092

Simon, M., Johnson, M., Tyack, P., and Madsen, P. T. (2009). Behaviour and kinematics of ram filtration in bowhead whales (*Balaena mysticetus*). *Proc. R. Soc. B* 276, 3819–3828. doi: 10.1098/rspb.2009.1135

Sims, D. W. (2008). *Sieving a living: a review of the biology, ecology and conservation status of the plankton-feeding basking shark* Cetorhinus maximus. *Adv. Mar. Biol.* 54, 171–220. doi: 10.1016/S0065-2881(08)00003-5

Slater, G. J., Goldbogen, J. A., and Pyenson, N. D. (2017). Independent evolution of baleen whale gigantism linked to Plio-Pleistocene ocean dynamics. *Proc. R. Soc. B* 284, 20170546. doi: 10.1098/rspb.2017.0546

Slijper, E. J. (1962). *Whales* (New York: Basic Books).

Smith, J. C., and Sanderson, S. L. (2008). Intra-oral flow patterns and speeds in a suspension-feeding fish with gill rakers removed versus intact. *Biol. Bull.* 215, 309–318. doi: 10.2307/25470714

Song, L., and Elimelech, M. (1995). Theory of concentration polarization in cross-flow filtration. *J. Chem. Soc. Faraday Trans.* 91, 3389–3398. doi: 10.1039/ft9959103389

Starbard, N. (2009). *Beverage Microfiltration* (Hoboken NJ: Wiley/Blackwell).

St. Aubin, D. J., Stinson, R. H., and Geraci, J. R. (1984). Aspects of the structure and composition of baleen, and some effects of exposure to petroleum hydrocarbons. *Can. J. Zoology* 62, 193–198. doi: 10.1139/z84-032

Stevenson, C. H. (1907). Whalebone: its production and utilization. *Bureau Fisheries Documents* 626, 1–12. Available at: http://hdl.loc.gov/loc.gdc/scd0001.00028900855.

Sumich, J. L. (2001). Growth of baleen in a rehabilitating gray whale calf. *Aquat. Mammals* 27, 234–238.

Sutherland, K. (2005). The A-Z of filtration. *Filtration separation* 42, 40. doi: 10.1016/S0015-1882(05)70731-X

Szewciw, L. J., de Kerkhove, D. G., Grime, G. W., and Fudge, D. S. (2010). Calcification provides mechanical reinforcement to whale baleen alpha keratin. *Proc. R. Soc. B.* 277 (1694), 2597–2605. doi: 10.1098/rspb.2010.0399

Tamime, A. Y. (2013). "Membrane PRocessing: Dairy and Beverage Applications," (Hoboken NJ: Wiley/Blackwell).

Taylor, A. M., Bonser, R. H. C., and Farrent, J. W. (2004). The influence of hydration on the tensile and compressive properties of avian keratinous tissues. *J. Materials Sci.* 39, 939–942. doi: 10.1023/B:JMSC.0000012925.92504.08

Thewissen, J. G. M. (1998). *The emergence of Whales: Evolutionary Patterns in the Origins of Cetacea* (New York: Plenum). doi: 10.1007/978-1-4899-0159-0

Thewissen, J. G. M., and Bajpai, S. (2001). Whale origins as a poster child for macroevolution. *BioScience* 51, 1037–1049. doi: 10.1641/0006-3568(2001)051[1037:WOAAPC]2.0.CO;2

Thewissen, J. G. M., Cooper, L. N., George, J. C., and Bajpai, S. (2009). From land to water: the origin of whales, dolphins, and porpoises. *Evolution: Educ. Outreach* 2, 272–288. doi: 10.1007/s12052-009-0135-2

Thewissen, J. G. M., Hieronymus, T. L., George, J. C., Suydam, R., Stimmelmayr, R., and McBurney, D. (2017). Evolutionary aspects of the development of teeth and baleen in the bowhead whale. *J. Anat.* 230, 549–566. doi: 10.1111/joa.12579

Tomilin, A. G. (1954). Adaptive types of the order cetacea. *Zoologicheskii Zhurnal* 33, 677–691.

Trakumas, S., Willeke, K., Reponen, T., Grinshpun, S. A., and Friedman, W. (2001). Comparison of filter bag, cyclonic, and wet dust collection methods in vacuum cleaners. *Am. Ind. Hygiene Assoc. J.* 62, 573–583. doi: 10.1080/15298660108984656

Tsai, C.-H., and Fordyce, R. E. (2015). The earliest gulp-feeding mysticete from the Oligocene of New Zealand. *J. Mamm. Evol.* 22, 535–560. doi: 10.1007/s10914-015-9290-0

Uhen, M. D. (2010). The origin(s) of whales. *Annu. Rev. Earth Planetary Sci.* 38, 189–219. doi: 10.1146/annurev-earth-040809-152453

Vandenberg, M. L., Cohen, K. E., Rubin, R. D., Goldbogen, J. A., Summer, A. P., Paig-Tran, E. W. M., et al. (2023). Formation of a fringe: a look inside baleen morphology using a multimodal visual approach. *J. Morphology* 284, e21574. doi: 10.1002/jmor.21574

van der Hoop, J. M., Corkeron, P., Kenney, J., Landry, S., Morin, D., Smith, J., et al. (2015). Drag from fishing gear entangling North Atlantic right whales. *Mar. Mammal Sci.* 32, 619–642. doi: 10.1111/mms.12292

van der Hoop, J. M., Nousek-McGregor, A. E., Nowacek, D. P., Parks, S. E., Tyack, P., and Madsen, P. T. (2019). Foraging rates of ram-filtering North Atlantic right whales. *Funct. Ecol.* 33, 1290–1306. doi: 10.1111/1365-2435.13357

Vogel, S. (1996). *Life in moving fluids 2e*. (Princeton: Princeton University Press).

Vogel, S. (2013). *Comparative biomechanics: life's physical world 2e*. (Princeton: Princeton University Press).

Vogel, H. C., and Todaro, C. M. (1997). *Cross flow filtration, in fermentation and biochemical engineering handbook*, ed. RR Bhave, pp 271–322, New York: Elsevier (Noyes).

Wang, B., Yan, W., McKittrick, J., and Meyers, M. A. (2016). Keratin: structure, mechanical properties, occurrence in biological organisms, and efforts at bioinspiration. *Prog. Materials Sci.* 76, 229–318. doi: 10.1016/j.pmatsci.2015.06.001

Watkins, W. A., and Schevill, W. E. (1976). Right whale feeding and baleen rattle. *J. Mammalogy* 57, 58–66. doi: 10.2307/1379512

Webber, M. A., Keener, W., Markowitz, T. M., Chamberlin, D., Allen, D., Lane, R. S., et al. (2024). Fish feeding and rapid foraging behavior switching by gray whales (*Eschrichtius robustus*) in California. *Aquat. Mammals* 50, 132–151. doi: 10.1578/AM.50.2.2024.132

Wegner, N. C. (2015). *Elasmobranch gill structure* Vol. 34 (San Diego, CA, USA: Fish Physiology), 101–151.

Werth, A. J. (2000). *Marine mammals, in Feeding: form, function and evolution in tetrapod vertebrates*. Ed. K. Schwenk (New York: Academic), pp 475–pp 514.

Werth, A. J. (2001). How do mysticetes remove prey trapped in baleen? *Bull. Museum Comp. Zoology* 156, 189–203.

Werth, A. J. (2004). Models of hydrodynamic flow in the bowhead whale filter feeding apparatus. *J. Exp. Biol.* 207, 3569–3580. doi: 10.1242/jeb.01202

Werth, A. J. (2007). Adaptations of the cetacean hyolingual apparatus for aquatic feeding and thermoregulation. *Anatomical Rec.* 290, 546–568. doi: 10.1002/ar.20538

Werth, A. J. (2012). Hydrodynamic and sensory factors governing response of copepods to simulated predation by baleen whales. *Int. J. Ecol.* 2012, 208913. doi: 10.1155/2012/208913

Werth, A. J. (2013). Flow-dependent porosity of baleen from the bowhead whale (*Balaena mysticetus*). *J. Exp. Biol.* 216, 1152–1159. doi: 10.1242/jeb.078931

Werth, A. J. (2017). *Baleen, in Encyclopedia of Marine Mammals 3e*. Eds. B. Würsig, J. G. M. Thewissen and K. Kovacs (San Diego: Elsevier), pp 60–pp 61.

Werth, A. J. (2019). "Variable porosity of throughput and tangential filtration in biological and 3D printed systems," in *Advances in Engineering Research*, vol. 29 . Ed. V. Petrova (Nova Science Publishers, Hauppauge, NY), pp 37–pp 93. Porosity—Properties and Measurement.

Werth, A. J., Blakeney, S. M., and Cothren, A. I. (2019a). Oil adsorption does not structurally or functionally alter whale baleen. *R. Soc. Open Sci.* 6, 182194. doi: 10.1098/rsos.182194

Werth, A. J., and Crompton, A. W. (2023). Cetacean tongue mobility and function: a comparative review. *J. Anat.* 243, 343–373. doi: 10.1111/joa.13876

Werth, A. J., Harriss, R. W., Rosario, M. V., George, J. C., and Sformo, T. L. (2016a). Hydration affects the physical and mechanical properties of baleen tissue. *R. Soc. Open Sci.* 3, 160591. doi: 10.1098/rsos.160591

Werth, A. J., and Ito, H. (2017). Sling, scoop, squirter: anatomical features facilitating prey transport, concentration, and swallowing in rorqual whales (Mammalia: Mysticeti). *Anatomical Rec.* 300, 2070–2086. doi: 10.1002/ar.23606

Werth, A. J., Kahane-Rapport, S. R., Potvin, J., Goldbogen, J. A., and Savoca, M. S. (2024). Baleen–plastic interactions reveal high risk to all filter-feeding whales from clogging, ingestion, and entanglement. *Oceans* 5, 48–70. doi: 10.3390/oceans5010004

Werth, A. J., Kosma, M. A., Chenoweth, E. M., and Straley, J. M. (2019b). New views of humpback whale flow dynamics and morphology during prey engulfment. *Mar. Mammal Sci.* 35, 1556–1578. doi: 10.1111/mms.12614

Werth, A. J., and Marshall, C. D. (2023). "Convergent evolution of secondarily aquatic feeding in mammals," in *Convergent Evolution*. Eds. V. Bels and P. Legreneur (Springer, Cham, Switzerland), pp 183–pp 220.

Werth, A. J., and Potvin, J. (2016). Baleen hydrodynamics and morphology of cross-flow filtration in balaenid whale suspension feeding. *PLoS One* 11, e0150106. doi: 10.1371/journal.pone.0150106

Werth, A. J., Potvin, J., Shadwick, R. E., Jensen, M. M., Cade, D. E., and Goldbogen, J. A. (2018a). Filtration area scaling and evolution in mysticetes: trophic niche partitioning and the curious cases of the sei and pygmy right whales. *Biol. J. Linn. Soc.* 125, 264–279. doi: 10.1093/biolinnean/bly121

Werth, A. J., Rita Espada, D., Rosario, M. V., Moore, M. J., and Sformo, T. L. (2018b). How do baleen whales stow their filter: a comparative biological analysis. *J. Exp. Biol.* 221, 189233. doi: 10.1242/jeb.189233

Werth, A. J., and Sformo, T. L. (2020). "Anatomy and function of feeding," in *The Bowhead Whale,* Balaena mysticetus*: Biology and Human Interactions*. Eds. J. C. George and J. G. M. Thewissen (Academic, San Diego), pp 213–pp 223.

Werth, A. J., Sformo, T. L., Lysiak, N. S., Rita Espada, D., and George, J. C. (2020). Baleen turnover and gut transit in mysticete whales and its environmental implications. *Polar Biol.* 43, 707–723. doi: 10.1007/s00300-020-02673-8

Werth, A. J., Sformo, T. L., Lysiak, N. S., Rita Espada, D., and George, J. C. (2021). Differential baleen growth and its consequences. *Polar Biol.* 44, 1227–1228. doi: 10.1007/s00300-021-02878-5

Werth, A. J., Straley, J., and Shadwick, R. (2016b). Baleen wear reveals intraoral water flow patterns of mysticete filter feeding. *J. Morphology* 277, 453–471. doi: 10.1002/jmor.20510

Werth, A. J., van de Graaf, P., and DesJardins, R. (2019c). Preparation of full baleen racks for long-term exhibition and research. *Aquat. Mammals* 45, 500–506. doi: 10.1578/AM.45.5.2019.500

Werth, A. J., and Whaley, H. R. (2019). Ocean acidification's potential effects on keratin protein in cetacean baleen and other integumentary tissue. *Ann. Ecol. Environ. Sci.* 3, 21–28.

Williamson, G. R. (1973). Counting and measuring baleen and ventral grooves of whales. *Scientific Reports of the Whales Research Institute* 24, 279–292.

Witkop, E. M., Van Wassenbergy, S., Heideman, P. D., and Sanderson, S. L. (2023). Biomimetic models of fish gill rakers as lateral displacement arrays for particle separation. *Bioinspiration Biomimetics* 18, 056009. doi: 10.1088/1748-3190/acea0e

Woodward, B. L., and Winn, J. P. (2006). Apparent lateralized behavior in gray whales feeding off the central British Columbia coast. *Mar. Mammal Sci.* 22, 64–73. doi: 10.1111/j.1748-7692.2006.00006.x

Yeong, W.-Y., Chua, C.-K., Leong, K.-F., and Chandrasekaran, M. (2004). Rapid prototyping in tissue engineering: challenges and potentials. *Trends Biotechnol.* 22, 643–652. doi: 10.1016/j.tibtech.2004.10.004

Young, S. (2012). The comparative anatomy of baleen: evolutionary and ecological implications. San Diego State University, San Diego.

Young, S., Deméré, T. E., Ekdale, E. G., Berta, A., and Zellmer, N. (2015). Morphometrics and structure of complete baleen racks in gray whales (*Eschrichtius robustus*) from the Eastern North Pacific Ocean. *Anatomical Rec.* 298, 703–719. doi: 10.1002/ar.23108

Zeman, L. J., and Zydney, A. L. (1996). *Microfiltration and Ultrafiltration: Principles and Applications* (New York: Dekker).

Zhong, P. S., Chung, T.-S., Jeyaseelan, K., and Armugan, A. (2012). Aquaporin-embedded biomimetic membranes for nanofiltration. *J. Membrane Sci.* 407–408, 27–33. doi: 10.1016/j.memsci.2012.03.033

Zhu, Y., Hu, D., Guo, Y., Ding, H., and Yang, G. (2023). Bio-inspired filter design based on vortex control mechanism of parallel groove structure. *J. Bionic Eng.* 20, 338–348. doi: 10.1007/s42235-022-00247-4

Zhu, Y., Hu, D., Li, C., Zhuang, C., and Yang, G. (2021). CFD-DEM simulation of the hydrodynamic filtration performance in balaenid whale feeding. *Sci. Total Environ.* 787, 147696. doi: 10.1016/j.scitotenv.2021.147696

Zhu, Y., Hu, D., and Yang, G. (2020a). Theoretical analysis of the hydrodynamic filtering system in the balaenid whales suspension feeding. *Bioinspiration Biomimetics* 16, e26006. doi: 10.1088/1748-3190/abc493

Zhu, Y., Yang, G., Zhuang, C., Li, C., and Hu, D. (2020b). Oral cavity flow distribution and pressure drop in balaenid whales feeding: a theoretical analysis. *Bioinspiration Biomimetics* 15, e036004. doi: 10.1088/1748-3190/ab6fb8

frontiers | Frontiers in Mechanical Engineering

TYPE Original Research
PUBLISHED 02 August 2024
DOI 10.3389/fmech.2024.1411361

OPEN ACCESS

EDITED BY
Marco Ghisalberti,
University of Western Australia, Australia

REVIEWED BY
Shi Tao,
Dongguan University of Technology, China
Frederick Gosselin,
Polytechnique Montréal, Canada

*CORRESPONDENCE
Josef D. Ackerman,
ackerman@uoguelph.ca

RECEIVED 13 April 2024
ACCEPTED 01 July 2024
PUBLISHED 02 August 2024

CITATION
Sewak K, Hassan M and Ackerman JD (2024), Fluid-structure interaction of flexible collectors affects particle capture efficiency at ecologically relevant collector Reynolds numbers.
Front. Mech. Eng 10:1411361.
doi: 10.3389/fmech.2024.1411361

Fluid-structure interaction of flexible collectors affects particle capture efficiency at ecologically relevant collector Reynolds numbers

Kyle Sewak[1], Marwan Hassan[2] and Josef D. Ackerman[1]*

[1]Physical Ecology Laboratory, Department of Integrative Biology, University of Guelph, Guelph, ON, Canada, [2]School of Engineering, University of Guelph, Guelph, ON, Canada

Introduction: The capture of suspended particles, which is an important process in many aquatic and terrestrial ecosystems, has been modeled using stationary rigid collectors and, more recently those that move in response to flow-induced vibrations. These models do not, however, account for collector flexibility, despite the fact that many biological collectors, especially aquatic collectors, exhibit flexibility.

Methods: This study examined the effect of collector flexibility (indicated by the Young's Modulus, E; range = 10^{-3}–10^{2} GPa) on particle capture efficiency (η; flux of captured particles: flux of particles) at different collector Reynolds numbers (Re_c where the collector diameter [d_c] is the length scale; range = 30–508) in a recirculating flow chamber.

Results: Patterns in η were generally similar for flexible and rigid collectors until moderate Re_c (~374) when higher η were observed on the most flexible collectors. This threshold corresponded to periods of vortex induced motions in which the oscillation frequency of the collector transverse to the flow direction was >4 Hz and the maximum amplitude of the oscillation relative to d_c was >60% in the transverse and >100% in the longitudinal direction.

Discussion: Given the range in E examined in this study, it is likely that particle capture on flexible natural collectors has been underestimated using the standard model of a rigid stationary or oscillating collector. The role of collector flexibility should be considered in models and studies of particle capture in natural systems.

KEYWORDS

particle capture efficiency, elasticity, collector, collector Reynolds number, flexibility, Cauchy number

1 Introduction

The capture of suspended particles is an important process in many aquatic and terrestrial ecosystem processes including suspension feeding, sexual reproduction and the fate and transport of contaminants (reviews in Niklas, 1985; Shimeta and Jumars, 1991; Ackerman, 2000; Ackerman, 2006; Armitage et al., 2008). For example, aquatic plants capture suspended particles and in doing so retain nutrients in bottom sediments, which affects their production and that of aquatic ecosystems (e.g., Jordan et al., 1986; Leonard

et al., 1995). Essentially, the physical process of particle capture includes the encounter, capture and retention of particles suspended within a fluid medium (Vogel, 1994). Five principal mechanisms of particle capture have been characterized (Rubenstein and Koehl, 1977; Spielman, 1977): (1) direct interception in which a particle flowing within a streamline comes into direct contact (i.e., within a particles radius) of the collector and is intercepted; (2) inertial impaction in which denser particles deviate from fluid streamlines moving around the collector, because of their inertia, and thus impact on the collector; (3) diffusional deposition in which Brownian-like motion causes particles of small diameters ($<10^{-6}$ m) to deviate from streamlines and be intercepted by the collector; (4) gravitational deposition in which particles with excess density settle onto the collector; and (5) electrostatic attraction in which particle and the collector are of opposite electrical charge inducing an attraction that leads to capture by the collector. Typically, larger diameter particles are captured via direct interception and inertial impaction whereas smaller diameter particles are captured through diffusional deposition and electrostatic attraction (Rubenstein and Koehl, 1977).

Axisymmetric cylindrical collectors have been used in particle capture experiments and modeling (Rubenstein and Koehl, 1977; Shimeta and Jumars, 1991; Spielman, 1977; Palmer et al., 2004; Haugen and Kragset, 2010; Gosselin, 2019; Espinosa-Gayosso et al., 2021). The cylindrical shape is analogous to many biological collectors including the siphons and cilia of suspension feeding organisms as well as the stems of aquatic plants (macrophytes; e.g., Shimeta and Jumars, 1991). This shape is also amenable to fluid dynamic characterization using the collector Reynolds number (Re_c) given by

$$Re_c = \frac{d_c U}{\nu} \tag{1}$$

where d_c is the diameter of the collector, U is the velocity and ν is the kinematic viscosity. Re_c provides an indication of the ratio of inertial to viscous forces acting on the scale of the collector in addition to the pattern in the flow field in the immediate vicinity of the collector (e.g., Sumer and Fredsøe, 2006). Considerable literature on the mechanics of particle capture by single cylinders exists for creeping flow (i.e., $Re_c \ll 1$) and for potential flow (i.e., $Re_c >$ 1,000) (e.g., Rubenstein and Koehl, 1977; Spielman, 1977; Shimeta and Jumars, 1991), however, analytical solutions do not exist for $1 < Re_c < 1{,}000$, which are of interest to ecological systems (Palmer et al., 2004; Espinosa-Gayosso et al., 2013; Espinosa-Gayosso et al., 2021; Boudina et al., 2021). Characteristics of the particle capture process are also provided by the particle Stokes number (Stk) given by

$$Stk = 1/9\, Re_c R^2 s \tag{2}$$

where R is the relative particle diameter (ratio of particle diameter to cylinder diameter; i.e., d_p/d_c) and s is the specific gravity (ratio of particle density to the density of the fluid; i.e., ρ_p/ρ_f). Stk describes the ratio of the particle stopping distance to that of the collector radius. When $Stk < 1$ particles are integrated into the streamlines (Raju and Meiburg, 1995), whereas when $Stk > 1$ particles are likely to deviate from the flow, although the magnitude of s may modulate this relationship (Espinosa-Gayosso et al., 2015). Particle capture efficiency (η) is used to determine the effectiveness of the particle capture process and to compare among studies. η is based on the number of particles captured per unit area and time divided by the particle flux that would move through an equivalent rectangular cross-sectional area of the collector in the absence of the collector.

The effects of collector motion on η have been examined using physical modeling and an examination of wind pollination in timothy grass (McCombe and Ackerman, 2018) and numerical modeling of soft coral feeding (Boudina et al., 2021). These studies were motivated by the fact that vortex induced oscillations occur in nature as a result of the shear forces between the fluid and the organisms (de Langre, 2008; de Langre, 2019; Gosselin, 2019) in which vibrations are caused when vortices are shed alternatively downstream, inducing a pressure gradient along the surface of the fluid causing motion of the collector in the transverse direction (e.g., Vandiver and Jong, 1987; Bourguet et al., 2011). McCombe and Ackerman (2018) demonstrated that the effects of oscillatory motion on the η of a rigid collector was substantial (>400 predicted by stationary collectors), varied spatially on the collector, and also varied with Re_c. The effect was greatest for collectors moving transversely to the flow direction at large magnitude, which encountered more particles with higher relative momentum with respect to the moving collector. Those results confirmed earlier computational fluid dynamic models (Espinosa- Gayosso et al., 2012; Espinosa- Gayosso et al., 2013; Krick and Ackerman, 2015), as well as the influence of the direction of the motion on η. During transverse oscillations, the momentum of low Stk particles relative to the approaching moving collector is sufficient for the particle to penetrate the boundary layer and be captured by the collector. The effect of collectors moving longitudinally to the flow on η is lower because the increase in relative momentum in the approaching phase of the collector oscillation is lost in the retreating phase of the collector motion (Krick and Ackerman, 2015). Nonetheless, a sixth mechanism of particle capture, entitled collector chasing, was identified for moving collectors in which particle capture occurs when a moving particle is intercepted by a collector in its retreating phase (Krick and Ackerman, 2015).

The influence of flexibility of the motion of the collector and the concomitant effects on η remain unknown empirically despite the large range in mechanical properties of biological materials (Table 1). The purpose of this study is, therefore, to examine the effects of flexibility of the collector on particle capture efficiency, η. We do so by measuring η empirically on polymers of different flexibility indicated by their Young's moduli in a recirculating flow chamber under differing Re_c and comparing them to a stationary rigid collector (standard model).

2 Materials and methods

Experiments were conducted in a 14.5-L recirculating flow chamber (test section: 170 cm long × 17 cm wide × 4.5 cm water depth; see vanden Byllaardt and Ackerman, 2014) equipped with three flow straighteners (collimators) placed in the 13-cm long expansion section of the inlet to rectify the flow and one 10 cm upstream of the channel outlet to prevent circulation (Figure 1). The chamber was operated at an average velocity (U) of 2 cm s^{-1}, 10 cm s^{-1}, 20 cm s^{-1}, 25 cm s^{-1} and 34 cm s^{-1}, which provided turbulent

TABLE 1 Comparison of Young's modulus (*E*) of biological collectors and physical materials.

Young's modulus (*E*; GPa)	Material (physical and biological within range, and associated *E*)	References
180–200	Stainless Steel (180–200 GPa)	Engineering Toolbox (2003)
130–180	Silicon (130–185 GPa)	Engineering Toolbox (2003)
100–130	Titanium Alloy (105–120 GPa)	Engineering Toolbox (2003)
5–100	Glass (50–90 GPa) Jewel box clam shell–*Chama* (82 GPa) Snail shell–*Conus* (68 GPa) Coral skeleton–*Acropora palmata* (21.5 GPa) Wood (birch)–*Betula lutea* (14.5 GPa) Soft coral skeleton–*Ellisella barbadensis* (9 GPa)	Engineering Toolbox (2003) Wainwright et al. (1982) Wainwright et al. (1982) Chamberlain (1978) Niklas (1992) Jeyasuria and Lewis (1987)
2–5	Polymethylmethacrylate (PMMA; 2.4–3.4 GPa) Wood (willow)–*Salix nigra* (5.0 GPa) Lobster claw–*Homarus* (4.2 GPa) Soft coral skeleton–*Plexaura kuna* (4.1 GPa)	Engineering Toolbox (2003) Niklas (1992) Wainwright et al. (1982) Boller et al. (2002)
1.5–2	Polypropylene (1.5–2 GPa) Soft coral skeleton–*Pterogorgia citrina* (1.5 GPa)	Ellis and Smith (2000) Jeyasuria and Lewis (1987)
0.01–1.5	Polyethylene (high density; HDPE; 1 GPa) Polyethylene (low density; LDPE; (0.45 GPa) Polytetrafluoroethylene (PTFE; 0.4 GPa) Black coral axis–*Cirripathes* (0.3 GPa) Aquatic plant stem–*Myriophyllum alteniflorum* (0.019 GPa) Potato tuber–*Solanum tuberosum* (0.01 GPa) BUNA rubber (0.01 GPa)	Engineering Toolbox (2003) Ellis and Smith (2000) Engineering Toolbox (2003) Wainwright et al. (1982) Miler et al. (2012) Ackerman and Nishizaki (1999) Ellis and Smith (2000)
0.002–0.01	NBR rubber (0.002–0.006 GPa) Silicon Rubber (0.001–0.05 GPa)	Ellis and Smith (2000) Ellis and Smith (2000)
0.001–0.002	VITON = Viton fluoroelastimer (0.001 GPa) Elastin–ligament (0.001 GPa)	Ellis and Smith (2000) Vogel (1988)

conditions based on flow chamber Reynolds number (Re_{dh}) using the hydraulic diameter as the length scale (Table 2). Velocity profiles were taken in the area where the collector was placed (i.e., at x = 143 cm downstream from the last collimator near the inlet) using a 3D side-looking Acoustic Doppler Velocimeter (ADV; Nortek Vectrino+; sampling frequency = 20 Hz, maximum velocity range = 50 cm s^{-1}) to generate velocity profiles at heights of 2.5, 3.5 and 4.0 cm above the bottom, which includes the observation region of the collector used to assess particle capture efficiency. The velocity measurements were generally consistent with theoretical predictions of the 1/7 power law for turbulent flat-plate flow especially at the higher velocities (Supplementary Figure S1). The assessment also indicated that the boundary layer thickness (δ) was greater than the height of the observation region in all cases, and $\delta > l_c$ (length of the collector) for the three lowest velocities (Figure 1 and Supplementary Figure S1). In other words, the observation region of the collectors was contained within the turbulent boundary layer flow of the chamber.

Five materials were used to obtain a range of flexibility in the collectors (d_c = 1.5 mm diameter and l_c = 3.75 cm long) indicated by the Young's Modulus (E) that spanned the range found in nature (i.e., 10^{-3} and 10^{2} GPa; Table 1). These included: (1) rigid Stainless Steel encased in a 3M™ black heat-shrink tubing (final d_c = 1.5 mm) used as a stationary collector or no-movement control (Young's modulus, nominal E = 200 GPa and density, $\rho = 7.85 \times 10^3$ kg m^{-3}; TW Metals, Hamilton, ON); High Density Polyethylene (HDPE; E = 1.0 GPa and $\rho = 0.97 \times 10^3$ kg m^{-3}; eplastics, San Diego, CA); Low Density Polyethylene (LDPE; E = 0.45 GPa and $\rho = 0.94 \times 10^3$ kg m^{-3}; eplastics, San Diego, CA); BUNA rubber (BUNA; $E = 10^{-2}$ GPa and $\rho = 1.35 \times 10^3$ kg m^{-3}; BRP Manufacturing, Lima, OH); and Viton fluoroelastimer (VITON; $E = 10^{-3}$ GPa and $\rho = 1.80 \times 10^3$ kg m^{-3}; BRP Manufacturing, Lima, OH). The natural frequency for mode 1 of these collectors in water was 710.3 Hz for stainless steel, 95.2 Hz for HDPE, 67.9 Hz for LDPE, 9.7 Hz for BUNA and 2.8 Hz for VITON based on the closed form solution

$$f_n = \frac{3.52}{2\pi}\sqrt{\frac{EI}{ql_c^4}} \tag{3}$$

where I is the area moment of inertia, q is the total mass per unit length, which includes both the mass of the collector ($m_c = \rho_c \pi \frac{d_c^2}{4}$, where ρ_c is the density of the collector) and the water added mass ($m_a = \rho_f \pi \frac{d_c^2}{4}$, where ρ_f is the density of the fluid) (Tongue, 2002). A non-dimensional bending stiffness (k') was also determined using the dynamic pressure for each flow chamber velocity given by

$$k' = \frac{EI}{\frac{1}{2}\rho U^2 l_c^3} \tag{4}$$

where ρ is the density (Shukla et al., 2013). Silver-coated, hollow glass spheres (CONDUCT-O-FIL; Potters Industries Inc., Carlstandt, NJ, USA) were used as particles based on their small size (mean diameter ~13 μm) and density (1.6 g cm^{-3}) and reflective properties that facilitated counting. The experimental parameters given by the

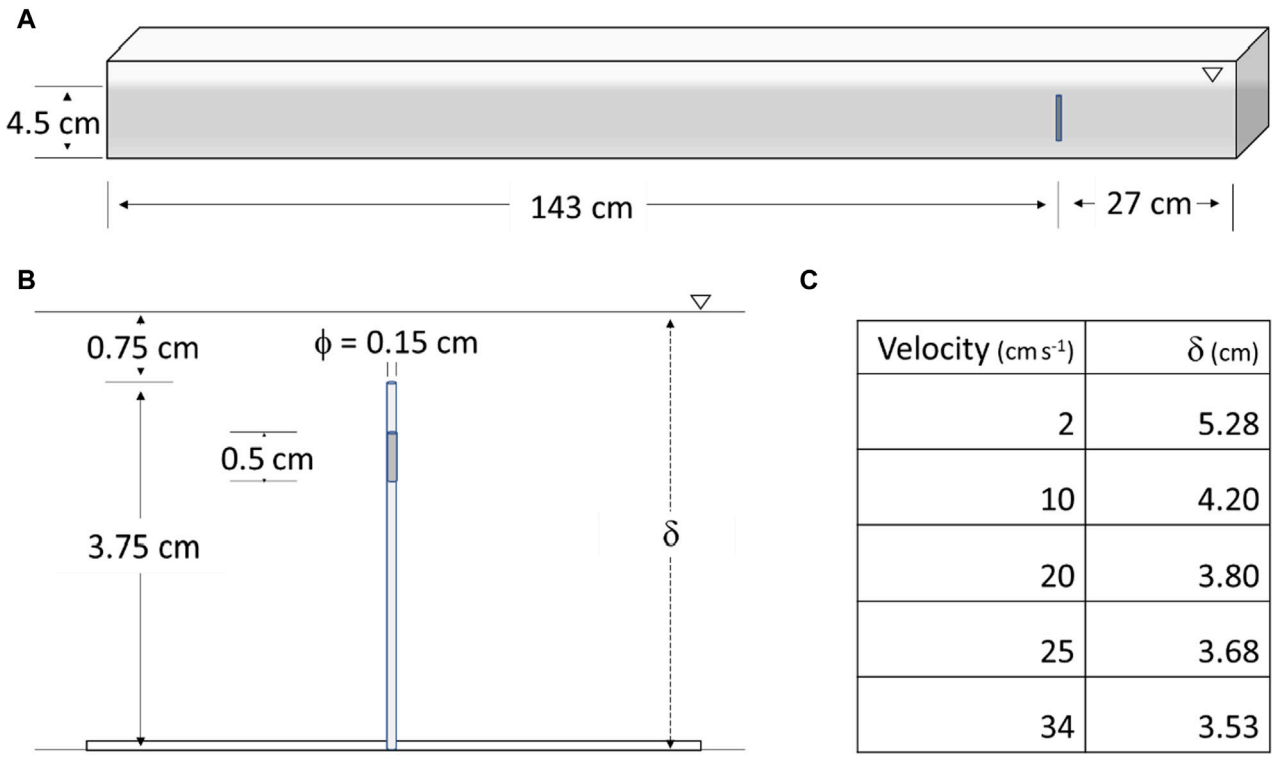

Velocity (cm s^{-1})	δ (cm)
2	5.28
10	4.20
20	3.80
25	3.68
34	3.53

FIGURE 1
Schematic diagram of the experimental system: **(A)** side view of the open channel flow chamber with the collector located at x = 143 cm downstream of the last collimator (flow is from left; chamber is 17 cm wide); **(B)** enlarged image of the collector (length l_c = 3.75 cm) with the observation region identified in dark grey (the collector was held on a plexiglass base tacked adhered onto the bottom of the chamber); **(C)** the relationship between the flow chamber velocity and the thickness of the boundary layer (δ) at x = 143 cm.

TABLE 2 Hydrodynamic conditions in the flow chamber, expected around the collector, and for the particles indicated by the chamber Reynolds number (length scale = hydraulic diameter, d_h; d_h = 0.12 m) and flow regime, the collector Reynolds number (length scale = collector diameter) and flow regimes downstream including the vortex shedding frequency indicated by the predicted Strouhal number, and the particle Stokes number.

Flow chamber			Collector			Particle
Velocity (m s^{-1})	Reynolds number (Re_{dh})	Flow regime	Reynolds number (Re_c)	Flow regime downstream	Strouhal number (St)	Stokes number (Stk)
0.02	2,344	Turbulent	30	Attached pair of vortices	0.035	4.01×10^{-4}
0.10	11,722	Turbulent	149	Vortices shed in laminar street	0.194	2.00×10^{-3}
0.20	23,445	Turbulent	299	Transition to turbulent	0.211	4.01×10^{-3}
0.25	29,306	Turbulent	374	Turbulent	0.213	5.01×10^{-3}
0.34	39,856	Turbulent	508	Turbulent	0.215	6.81×10^{-3}

relative particle diameter, R (ratio of particle diameter to cylinder diameter; $d_p/d_c = 8.67 \times 10^{-3}$) and the specific gravity, s (ratio of particle density to the density of the fluid, ρ_f; $\rho_p/\rho_f = 1.6$), were held constant. Conversely, Stk varied from 4.01×10^{-4} to 6.81×10^{-3} as a function of Re_c based on the flow chamber velocities (Table 2). This range of Re_c represents flow regimes ranging from attached vortices to fully turbulent conditions characterized by flow instabilities, random fluid motion and the presence of a turbulent wake downstream of the collector; this is reflected in the predicted Strouhal number ($St = fd_c/U$, where f is the vortex shedding frequency) for a circular cylinder (data digitized from figure 5.2 in White, 2011; also see Sumer and Fredsøe, 2006; Table 2). They also span the range of ecologically relevant Re_c, which are intermediate between creeping and potential flow (Palmer et al., 2004; Krick and Ackerman, 2015).

Observations of collector motion were made using an iPhone 6 camera (8 megapixels, Apple Inc.) placed on the plexiglass plate supported by the side walls of the flow chamber directly above the collector (240 frames per second). Data from the video recordings, displayed on a computer monitor (30 cm × 45 cm), were digitized manually to characterize collector

motion at each Re_c. Specifically, these included: (1) the maximum amplitude in the transverse direction relative to d_c (%); (2) the maximum deflection in the longitudinal direction relative to d_c (%); and (3) the oscillation frequency (f) in the transverse direction (Hz) to determine the observed Strouhal number for the moving collector. Additional 60 s video recordings were made through the side wall of the flow chamber to determine the longitudinal motion of the collector from an orthogonal perspective.

Degassed tap water was carefully added to the recirculating flow chamber before the collector, which was coated with <0.1 mm of silicon grease to retain particles, was placed in the flow chamber at the test location, i.e., at x = 143 cm downstream. A ~ 15 mL solution of distilled water and 0.5 g of CONDUCT-O-FIL particles was carefully poured into the outlet of the test chamber and time, t = 0 was dictated when the particles reached the collector. Once the experiment concluded (t = 300 s) the model was enclosed in a water-tight plexiglass casing to facilitate removal and photography of its front, back and side portions of the observation region (Figure 1) using a digital camera (Nikon 1 J1; Nikon, Tokyo, Japan) attached to a stereomicroscope (Nikon SMZ-2T). The flow chamber was thoroughly cleaned after each trial to ensure that no residual particles remained in system. A randomized design was used to choose materials and Re_c; 5 replicates were obtained.

Images were uploaded into Adobe Photoshop Creative Cloud version 14.0 and overlaid with a transparent counting grid. The number of particles was counted manually, and particles that fell on the dividing lines of the grid were counted in the segment to the right. The particle counts (N) were normalized by the area of the grid (A_c) given by

$$A_c = \frac{1}{2} H d_c \pi \tag{5}$$

where H is the height of the grid cell; A_c was used to determine the particle count per unit area (N_c)

$$N_c = \frac{N}{A_c} \tag{6}$$

The settlement of particles through the 300 s trial was measured directly by determining the particle concentration (via a hemocytometer) in ~5 mL water samples taken from a depth of ~1.5 cm at the test location (x = 143 cm downstream) at t = 0, 60, 120, 180, 240 and 300 s for each Re_c. Particle settling rates were determined from the slope of the particle concentration vs. time curves at each Re_c, which were linear (R^2 = 0.91 ± 0.02 [mean ± SE]), ranged between 3 – 4 × 10^8 particles m^{-3} s^{-1} and did not differ among Re_c (Analysis of Variance [ANOVA] of particle concentration at t = 300: $F_{4,\ 10}$ = 0.55, p = 0.740). Consequently, the measured value of the particle concentration at t = 150 s (C = (1.26 ± 0.08) × 10^{11} particles m^{-3}; n = 5) was used to determine the particle flux.

Control experiments were conducted to determine whether particle capture varied among collectors, which was necessary because it was not possible to obtain a single material with the range of nominal flexibility used in this research. Experiments were conducted using a 7-cm collector length to facilitate the restriction of its movement using a bulldog clip (1.5 cm wide). The clip was clamped at the top of the collector (above the water surface) and tension was applied (upward) to prevent oscillations from occurring. The data were obtained in the same manner as described above.

2.1 Statistical analysis

Three separate fixed effect Analysis of Covariance (ANCOVA) models were used to examine the effect of collector flexibility (independent variable) on relative amplitude in the transverse direction, the relative deflection in the longitudinal direction, and the oscillation frequency in the transverse direction, respectively (response variable), and using Re_c as a covariate. The particle capture data were analyzed using a mixed model ANCOVA to determine the effect of collector flexibility (independent variable) on particle capture efficiency (response variable) using Re_c as a covariate. The response variable (particle capture efficiency) was $\log_{10}$ (x^2) transformed to meet the assumptions of normality and homogeneity of variance. ANOVA was used to analyze the effect of collector material on particle capture efficiency separately for the control experiments conducted at Re_c = 149 and Re_c = 508. Tukey's Honest Significant Difference test was used to examine pairwise differences when significant factors were found. All statistical tests were completed using a probability of error rate, α = 0.05 in SAS (version 9.4).

3 Results

3.1 Collector motion

The flexible collectors moved in response to the flow and this motion generally increased with increasing collector Reynolds number (Re_c), in contrast to the stationary collector (Stainless steel), which did not exhibit motion (Figures 2, 3). Motion in the longitudinal plane was characterized as a deflection in which the collectors bent downstream under steady state conditions (constant velocity and pressure) and curvature was noted in the most flexible collectors at the higher Re_c (Supplementary Figure S2). Motion in the transverse plane was oscillatory in nature and could be characterized by the amplitude and frequency of the motion.

The total deflection of the collector in the longitudinal direction ranged from 0% to >135% relative to the collector diameter (d_c) as measured above the collector (Figure 2 and Supplementary Figure S2). The magnitude of the deflection was more pronounced as the flexibility (i.e., lower E) of the collector increased and at higher Re_c; i.e., VITON > BUNA > LKPE > HDPE for $Re_c \geq 149$, and VITON deflected by 135.3% ± 0.6% at Re_c = 508 (Figure 2A). The pattern in the magnitude of the deflection measured from the side of the collectors was consistent with this description (compare hollow vs. solid symbols in Figure 2A) as was the angle of the deflection with respect to the vertical (Figure 2B). Statistically significant differences were detected among collectors for flexibility (ANCOVA $F_{4,\ 19}$ = 5.19, p = 0.005) and the collector Reynolds number (covariate; $F_{1,\ 19}$ = 14.94, p = 0.001). In this case, significant pairwise differences were detected between VITON and HDPE (p = 0.008) and between VITON and the stationary collector (p = 0.007).

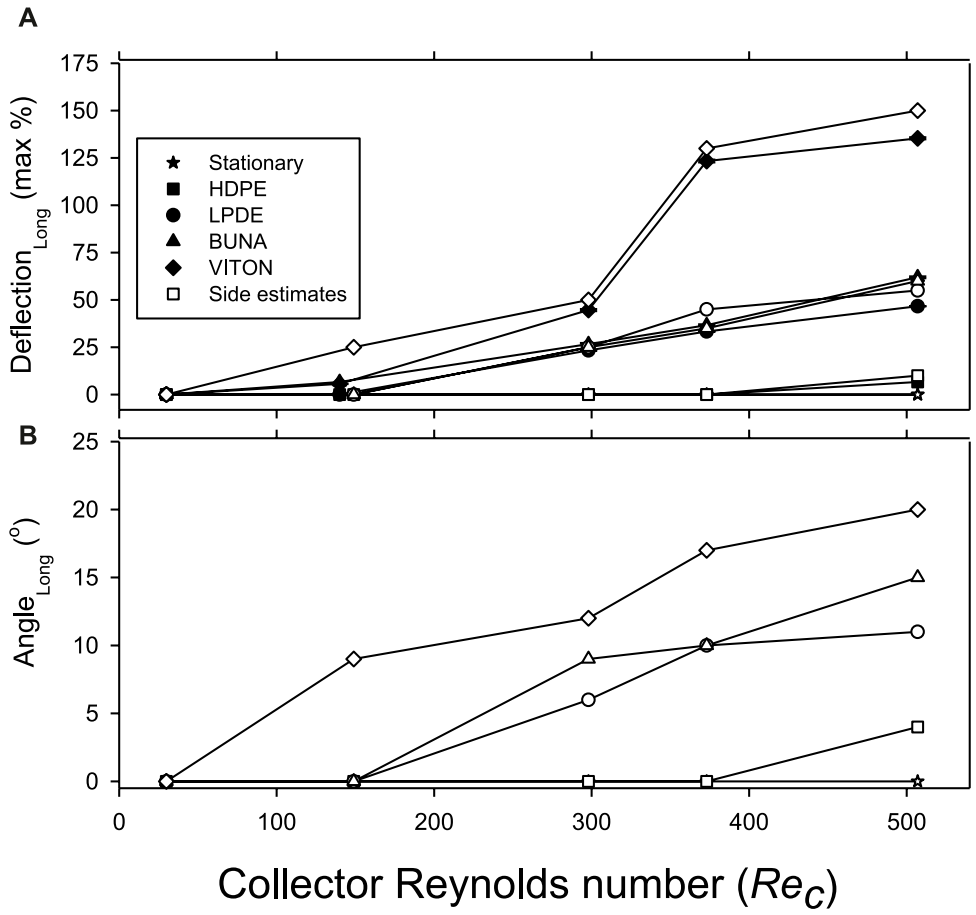

FIGURE 2
Characteristics of the longitudinal motion of elastic collectors vs. collector Reynolds numbers (Re_c): **(A)** Maximum deflection in the longitudinal direction relative to d_c measured from above the collector (solid symbols; mean ± SE, n = 5) and from the side (hollow symbols); and **(B)** Maximum angle of deflection from the vertical measured from the side. Legend: Stationary collector = stainless steel rod encased in heat-shrink tubing (E = 200 GPa; ρ = 7.85 × 10^3 kg m^{-3}); HDPE = High Density Polyethylene (E = 1.0 GPa; ρ = 0.97 × 10^3 kg m^{-3}); LDPE = Low Density Polyethylene (E = 0.45 GPa; ρ = 0.94 × 10^3 kg m^{-3}); BUNA = BUNA rubber (E = 10^{-2} GPa; ρ = 1.35 × 10^3 kg m^{-3}); and VITON = Viton fluoroelastimer (E = 10^{-3} GPa; ρ = 1.80 × 10^3 kg m^{-3}).

The amplitude of the collector deflection in the transverse direction ranged from 0% to >70% relative to d_c (Figure 3A). In general, the magnitude of the amplitude of the collectors increased with flexibility (i.e., lower E) and as Re_c increased (i.e., VITON > BUNA > LDPE > HDPE for $Re_c \geq 299$). Statistically significant differences were detected among collectors ($F_{4,\ 19} = 7.15$, $p = 0.001$) and the covariate was also significant ($F_{1,\ 19} = 40.04$, P = <0.001). Significant pairwise differences were detected between each of the flexible collectors and the stationary collector ($p < 0.027$). The frequency of oscillation of the flexible collectors expressed as Strouhal number (St) followed a similar pattern to what is reported above in terms of magnitude of the response and relationship with increasing Re_c, however the ranking changed with BUNA > VITON > LDPE > HDPE for $Re_c > 299$ (Figure 3B) perhaps due to the greater deflection in VITON. Statistically significant differences were detected among collectors ($F_{4,\ 19} = 9.11$, $p = 0.003$) and the covariate (Re_c) was significant ($F_{1,\ 19} = 32.05$, $p = 0.001$). Significant pairwise differences were detected in the response between VITON, BUNA and LDPE and the stationary collector ($p < 0.009$) and between BUNA and HDPE ($p = 0.035$).

3.2 Collector capture efficiency

The particle capture efficiency (η) declined by an order of magnitude across the range of Re_c examined for all types of collectors (i.e., 0.3%–0.6% at Re_c = 30 vs. 0.03%–0.06% at Re_c = 508; Figure 4A). Whereas the pattern was similar among collectors, HDPE and LDPE had consistently lower η compared to the more flexible collectors (BUNA and VITON) and the stationary collector. Only at the highest Re_c did η of BUNA appear to exceed that of the stationary collector. Statistically significant differences among collectors were detected ($F_{4,\ 119} = 2.46$, $p = 0.049$), and Re_c was a significant covariate ($F_{1,\ 119} = 168$, $p = 0.001$). In this case, significant pairwise differences ($p < 0.001$) were detected between collectors in the higher η group (BUNA, VITON, and stationary collector) and collectors in the lower η group (HDPE and LDPE). Distinction among the collector types was evident when η was plotted vs. the non-dimensional stiffness (k') (Figure 4B). In this case, the curves for each collector type were somewhat parallel with clear separation and ranking matching the Young's modulus of the collector. Two important distinctions were, however, evident: (1) there was overlap among collector curves at given k' values (e.g., HPDE, LDPE and

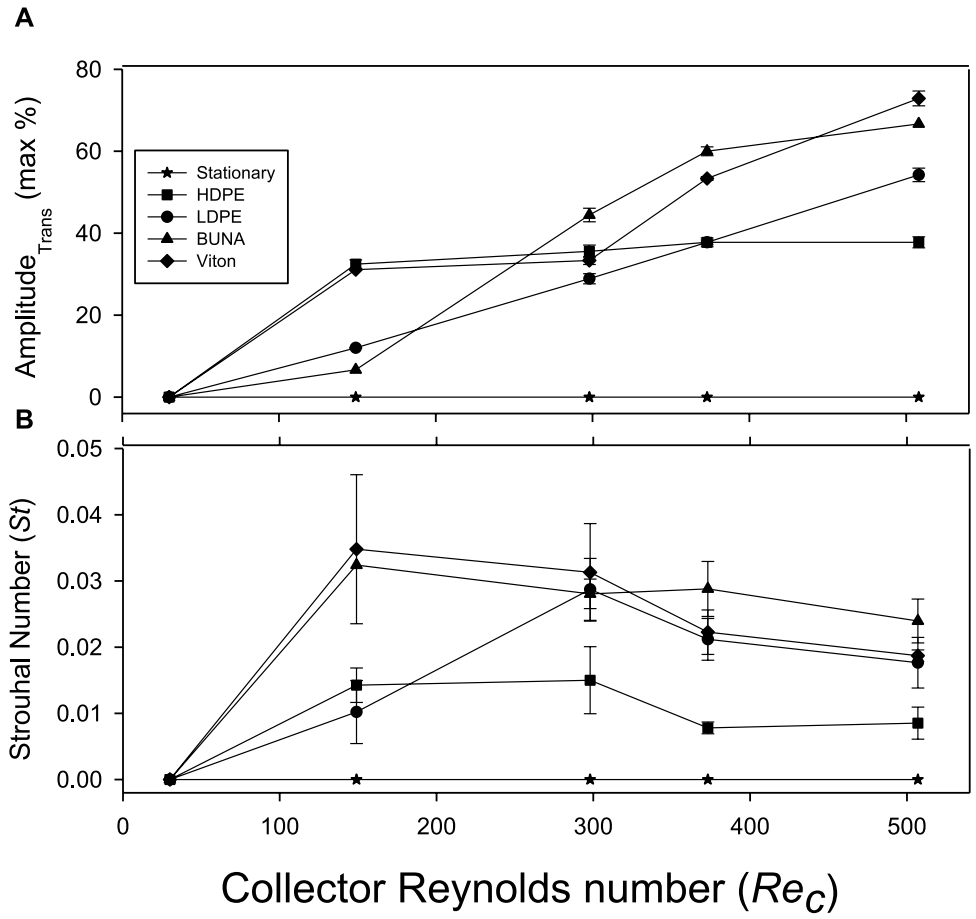

FIGURE 3
Characteristics of the transverse motion of elastic collectors vs. collector Reynolds numbers (Re_c): **(A)** Maximum amplitude in the transverse direction relative to collector diameter (d_c); and **(B)** observed Strouhal number of the collector oscillation frequency in the transverse direction (mean ± SE, n = 5).

BUNA at $k' \sim 10^{-1}$); and (2) collector efficiency (η) for BUNA and VITON were greater than those for the stationary collector when $Re_c > 299$–the left-most point in each curve.

The spatial pattern of capture (Eqs 5, 6) can provide insight into the mechanism of particle capture. Particles were captured circumferentially around collectors at the lowest $Re_c = 30$ with moderately higher capture at 90° and 270°, i.e., 90° from the stagnation point (=0°), for both the stationary collector and VITON, the most flexible collector (Figure 5). The average particle captured increased by ~50% at the highest $Re_c = 508$ for both collectors (47% ± 7% and 52% ± 8% for stationary collector and VITON, respectively) but the pattern differed. The increase in particle capture on the stationary collector was larger restricted to the upstream and to a lesser extent on the downstream sides, whereas particle capture on VITON also increased at 90° on either side of the stagnation point (i.e., 90° and 270°; Figure 5). Similarity on these patterns were observed on the other collectors depending somewhat on their flexibility (data not provided).

No-movement control experiments, in which collectors were held rigid within the flow chamber, were used to determine if the differences among the two groups of collectors identified above were due to material properties of the collectors that may have affected particle capture or particle identification in images. Particle capture efficiency was not uniform among the collectors at $Re_c = 149$ even though they were stationary in orientation (Figure 6). Rather η were higher and more similar on VITON, BUNA and the stationary collector than on the two polyethylene collectors (Figure 6A). Significant differences in η were found among collectors (ANOVA $F_{2,\ 12} = 7.92$, $p = 0.006$) and pairwise differences were found between the stationary collector and the HDPE and LDPE collectors ($p = 0.023$ and $p = 0.008$, respectively). Similar results in which η was lower on HDPE and LDPE were obtained at $Re_c = 508$, but in this case the comparison involved the two polyethylene and stationary collector (Figure 6B). Statistically significant differences in η were detected among collectors ($F_{2,\ 11} = 0.0166$, $p < 0.001$) and pairwise differences were found between the stationary collector and HDPE and LDPE ($p = 0.001$, $p = 0.003$, respectively). On average the HDPE collector captured particles 13.9% ± 0.8% less efficiently relative to the stationary collector and the LDPE collector captured particles 17.4% ± 0.5% less efficiently. These correction factors were used when calculating the relative capture efficiencies between flexible and stationary collectors.

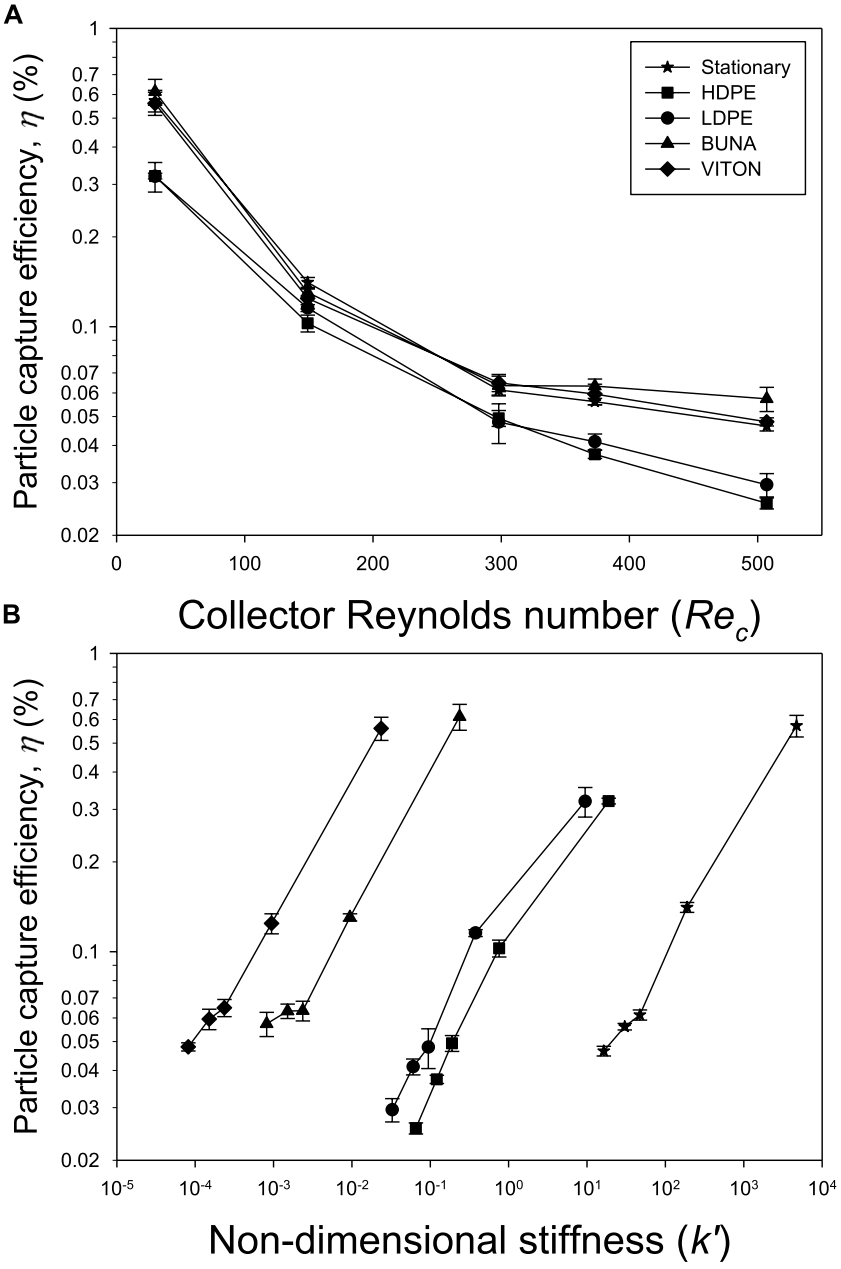

FIGURE 4
Particle capture efficiency (%) of stationary and flexible collectors measured in a flow chamber *versus* **(A)** collector Reynolds number (Re_c) and **(B)** non-dimensional stiffness (k') (mean ± SE; n = 5).

4 Discussion

The results of this study demonstrate that the flexibility of a collector (indicated by the Young's modulus, E) affects the capture efficiency (η) of suspended particles from a fluid medium at ecologically relevant Reynolds numbers (Eq. 1), i.e., 30 < Re_c < 500. Specifically, η appears to be related to the dimensionless stiffness (k'; Eq. 4), which is somewhat comparable to the reciprocal of the Cauchy number (Ca, ratio of inertial forces: compressible [elastic] forces; de Langre, 2008). Capture efficiency declined from Re_c = 30 to 299 but remained somewhat higher for the stiffer collector (Figure 4B), which was more perpendicular to the flow (Figure 2A; longitudinal deflection α $1/k'$). At higher Re_c (i.e., >299), however, the flexible collectors had η that were up to 23% higher (BUNA at Re_c > 508) than the rigid stationary collector because flexible collectors experienced larger transverse amplitudes (Figure 3A; transverse amplitude α $1/k'$) that resulted in additional particles captured on the sides perpendicular to the flow (Figure 5). These higher Re_c corresponded to periods when the most flexible collectors had large transverse oscillation frequencies (>4 Hz), and a large relative amplitude (>60% in the transverse direction and >100% in the longitudinal). It is relevant to note that 4 Hz

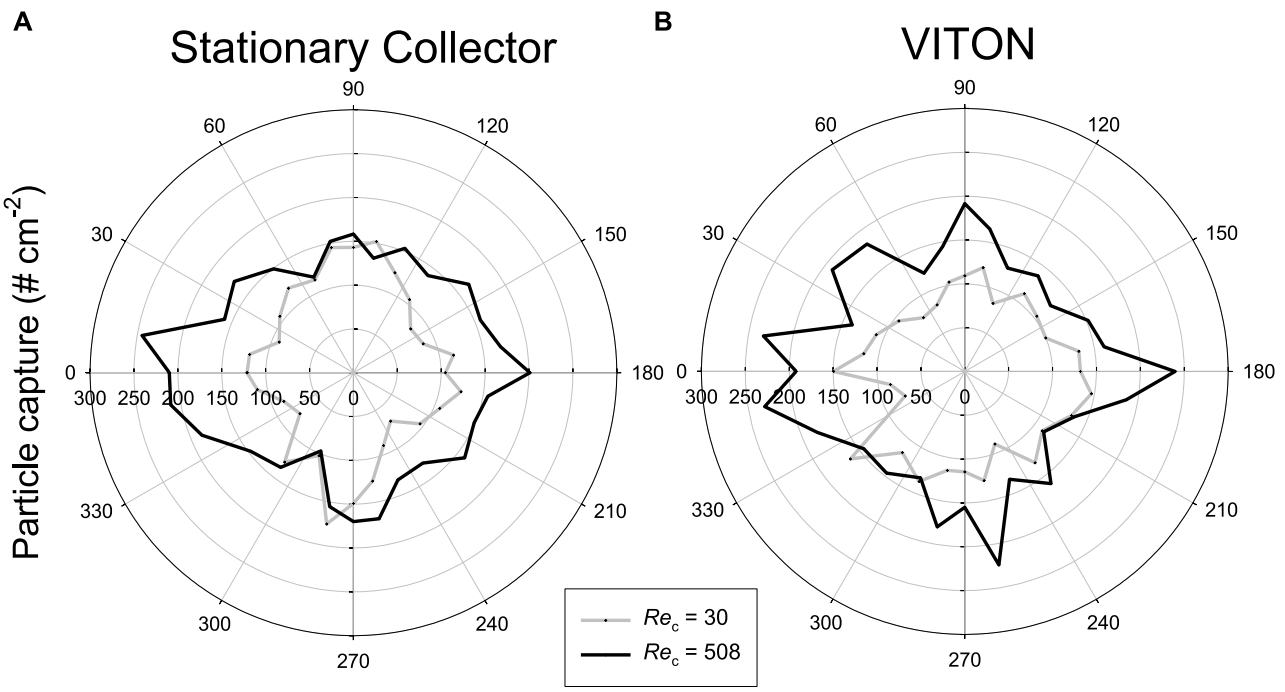

FIGURE 5
Spatial pattern of the distribution of particle capture on the circumference of collectors at the lowest and highest Re_c for **(A)** stationary and **(B)** VITON–the most flexible collector. Flow is from the left and 0° is the stagnation point with the angle increasing to the right.

exceeds the natural frequency (f_n; Eq. 3) of the most flexible collector in water. Given these observations, it is likely that the capture efficiency of flexible collectors has been underestimated at ecologically relevant Re_c using the standard model of a rigid stationary collector.

The material properties of the collector also affect η as was determined in the control experiments. It is likely that part of this difference was due to the difficulty of visualizing bright particles on the polyethylene surfaces, which were white in color relative to the darker grey/black and brown colors of the BUNA, VITON, and stationary collectors, respectively. It is relevant to note that the η measured on the stationary collector were similar to those reported elsewhere (Figure 7). Overall, η of the rigid collector in this study ranged from 0.57% to 0.046% across the Re_c and these values fall within the range reported in other empirical and computational studies (Figure 7). In general, η increases with the relative particle diameter, R, at these Re_c (Palmer et al., 2004). The correspondence between our values for rigid stationary collectors (R = 0.087) and consistent observations using R values similar to ours are indicated by grey colored symbols in Figure 7. Our observations appear to be reasonable within this range, although the value for Re_c = 30 is at the higher end of the range than has been reported elsewhere.

To the best of our knowledge, this is the first empirical examination of the effects of flexible moving collectors on particle capture (Figure 8). Capture efficiency declined rapidly with Re_c in the laminar regime, but the rate of decline decreased for rigid and flexible collectors that experienced motion at higher and turbulent Re_c relative to stationary rigid collectors. Specifically, the movement of the collector through higher frequency oscillations lead to increased η in the case of mechanical actuation of rigid collectors (McCombe and Ackerman, 2018) or in terms of both static drag reconfiguration and flow-induced vibration of flexible collectors examined empirically in the present study and modeled previously for a soft coral (Boudina et al., 2021). An estimate of the static drag contribution to deflection was made through the calculation of the drag force on the collector from the quadratic drag equation and using this is determine the deflection of a uniformly loaded cantilever beam. This technique could only be applied to the LDPE collector because it was the only linearly-elastic material with a response. In this case, the maximum observed deflection (% d_c) increased from 23%, 33% and 47% at 20, 25 and 34 cm/s, respectively vs. 6%, 9% and 15% increases for the calculated static drag. In other words, an average of 28% ± 2% of the deflection observed on LDPE between 20 and 34 cm/s was estimated to be due to static drag reconfiguration. These empirical studies build on the insight obtained through direct numerical simulations (DNS; Espinosa-Gayossa, 2012; Espinosa-Gayossa, 2013; Espinosa-Gayossa, 2015) and computational fluid dynamic models (CFD; Krick and Ackerman, 2015), respectively. Those models investigated the effects of vortex induced vibrations on particle capture efficiency, however they did not include Young's modulus of the collector (i.e., flexibility) as an experimental parameter. The present study demonstrates that flexibility affects the motion of a collector at each Re_c, which is especially important as the flow region downstream of the collector becomes turbulent (Re_c > 299) when vortex induced vibrations are more likely to occur.

The difference in η across E may also be understood through the particle Stokes number (Stk; Eq. 2). When Stk was low (i.e., 10^{-4}) the

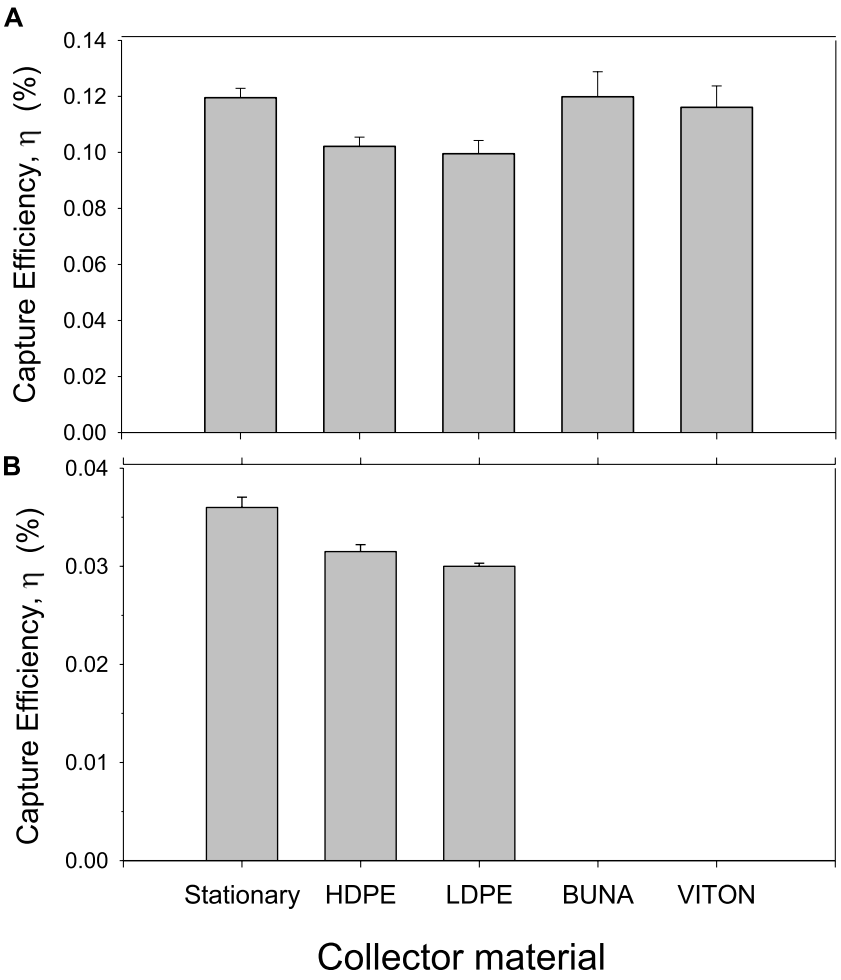

FIGURE 6
Comparison of the effects of the material of rigidly held collectors on particle capture efficiency (mean ± SE): **(A)** All material examined at Re_c = 149 (n = 5); and **(B)** subset of materials that differed from stationary examined at Re_c = 508 (n = 3).

particles did not have enough momentum to penetrate the collector boundary layer to be captured. At intermediate Re_c (Re_c = 149 and 299) the *Stk* increased to 10^{-3} and the relative difference in η between the most flexible and less flexible collector decreased. This was likely due to increased relative momentum of the particles with respect to the collector and subsequent penetration of the collector boundary layer caused by collector motion. Flow-induced collector motion leading to oscillations in the transverse direction adds additional momentum to the system making capture more likely at higher Re_c. When the system becomes turbulent (Re_c = 374 and Re_c = 508), the oscillation frequency of the BUNA collector exceeded 5 Hz and most particles were captured on the upstream surface of the collector. In the case of the VITON, the oscillation frequency was ~4 Hz and the relative amplitude exceeded >60% in the transverse direction and >100% in the longitudinal, leading to more particle capture on the side surfaces of the collector. These results are consistent with those of McCombe and Ackerman (2018) who found that transversely oscillating collectors capture more particles on the downstream and sides of the collector. These results are also supported by the CFD model by Krick and Ackerman (2015), who identified the 'collector chasing' capture mechanism in which a moving collector overtakes a particle. This mechanism is likely responsible for capture on the sides and downstream portion of the collector in this study. Moreover, particles caught in vortices leeward of the collector have high residence times and, therefore, have a higher probability of being captured (i.e., on the downstream side; Shimeta and Jumars, 1991). Higher turbulence (high Re_c) and Stokes number (i.e., $Stk > 10^{-1}$) may lead to higher η through increased encounter rates, but increased relative momentum of such particles would not be relevant because they already have sufficient inertia to penetrate collector boundary layers (Krick and Ackerman, 2015).

There are limitations of this study that may affect the interpretation of the results. Most notable among these is the short length of the collectors used because of the size limitations of the flow chamber. Specifically, the chamber was designed to provide suitable conditions for benthic mass transport studies (e.g., low volume, flow conditioning and entrance length for boundary layer development and fully developed flow, large width to depth ratio to minimize secondary flows [i.e., >3.5], and minimal flow obstruction of channel by the subject of interest; Nowell and Jumars, 1987; Ackerman, 1999).

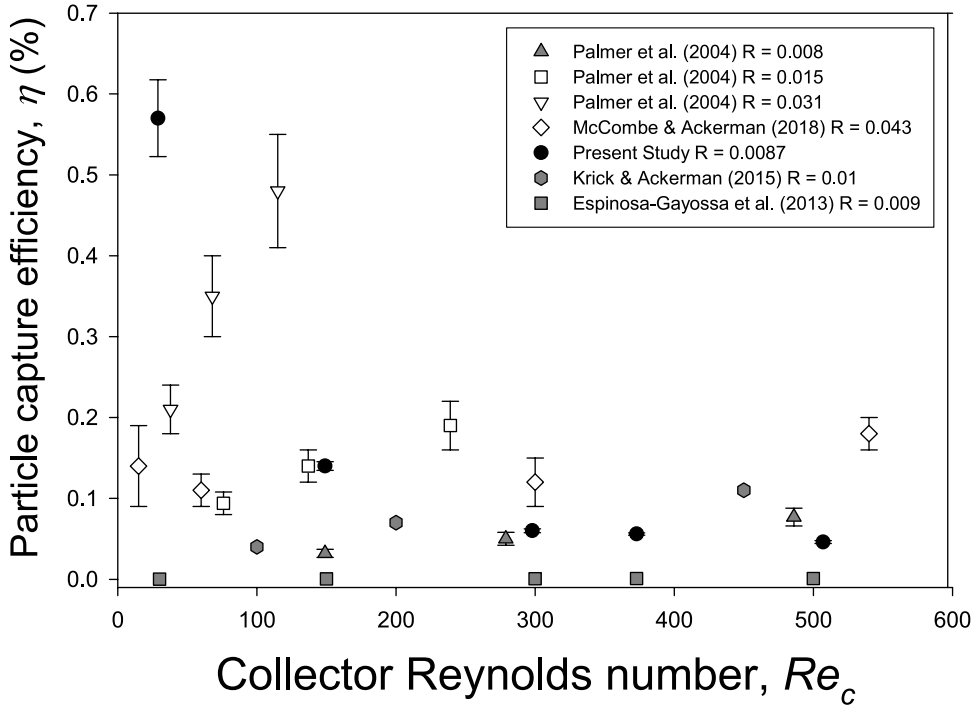

FIGURE 7
Comparison of particle capture efficiency (η) measured on rigid collectors at different collector Reynolds numbers (Re_c) in empirical (Palmer et al., 2004; McCombe and Ackerman, 2018) and computational studies (Espinosa-Gayosso et al., 2013; Krick and Ackerman, 2015). Capture efficiency, η, generally increases with the relative particle diameter, R, which is indicated in the legend. Observations using R similar to the present study are indicated by grey colored symbols.

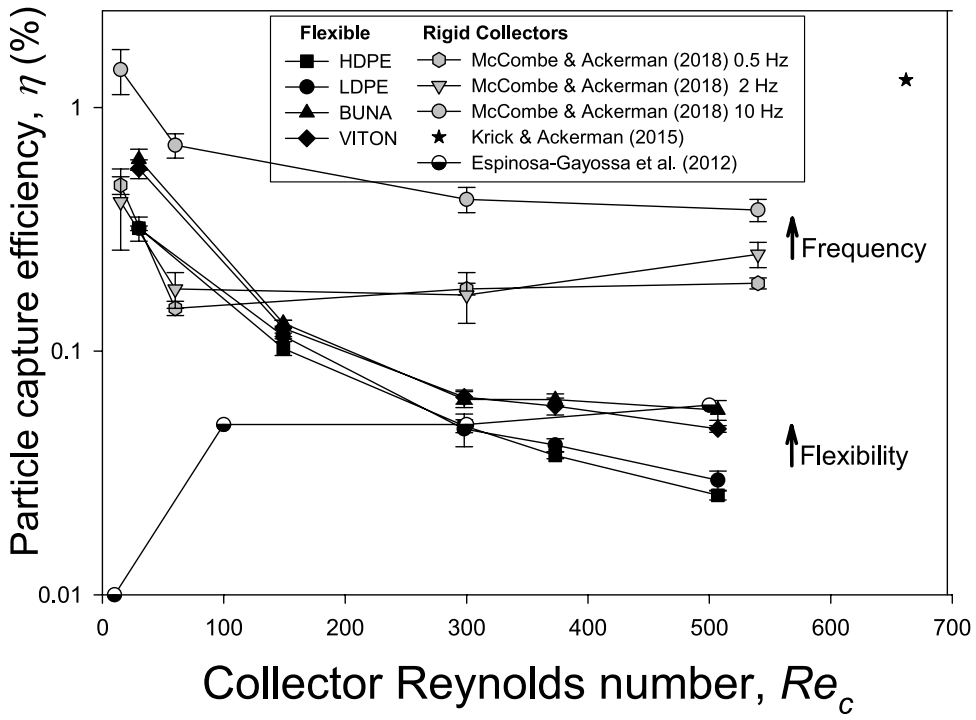

FIGURE 8
Comparison of particle capture efficiency (η) measured on moving collectors at different collector Reynolds numbers (Re_c) including flexible ones examined in this study and rigid ones measured (McCombe and Ackerman, 2018) or modeled previously (Espinosa-Gayosso et al., 2012; Krick and Ackerman, 2015). Note that increasing the movement of the collector through higher frequency oscillations leads to increased η in the case of mechanical actuation of rigid collectors or in terms of flow induced vibration of flexible collectors.

Consequently, a collector length of 3.75 cm (l_c = 0.0375 m) was used. This limited the f_n of the collectors to relatively large values, which decline non-linearly with increases in l_c (i.e., l_c^{-2}); the f_n of longer collectors would occur at higher frequency and thus have relatively more motion under these hydrodynamic conditions. In addition, l_c likely limited the movement of the collector to more rigid-like oscillations and deflections without any large flow induced bends or curvature observed in longer collectors in nature (de Langre, 2008). The effect of such large flow induced morphological changes in flexible collectors on particle capture efficiency, η, is unknown, but would likely be relevant to η because they represent large-scale motions, which have been shown to increase η. Certainly, there is considerable opportunity for future studies involving particle capture.

5 Conclusion

The results of this study indicate that the flexibility of a collector affects its ability to capture suspended particles once the flow regime around the collector leads to larger-scale hydromechanical responses. Specifically, enhanced particle capture efficiency, η, occurs once turbulent flow leads to a collector oscillation frequency transverse to the flow direction >4 Hz along with a relative amplitude >60% of the collector diameter in the transverse and >100% in the longitudinal direction. A variety of mechanisms are responsible for particle capture in nature including direct interception, inertial impaction as well as capture on lateral surfaces and collector chasing due to flow induced vibrations. These results should provide a better understanding of how freely moving flexible collectors capture particles due to vortex induced vibrations at ecologically relevant collector Reynolds numbers. Ultimately it should be possible to better understand the complexity of biological collectors and hence particle capture processes in aquatic and terrestrial environments.

Data availability statement

The original contributions presented in the study are included in the article/Supplementary Material, further inquiries can be directed to the corresponding authors.

Author contributions

KS: Data curation, Formal Analysis, Investigation, Methodology, Visualization, Writing–original draft, Writing–review and editing. MH: Methodology, Validation, Writing–review and editing. JDA: Conceptualization, Formal Analysis, Funding acquisition, Methodology, Project administration, Resources, Supervision, Validation, Writing–original draft, Writing–review and editing.

Funding

The author(s) declare financial support was received for the research, authorship, and/or publication of this article. Funding for this project was provided by NSERC Discovery Grant to JDA.

Acknowledgments

The authors acknowledge the support of Shaylah Tuttle-Raycraft, Chris Farrow, Katherine Tran, Natalie Perrin, and Dori McCombe from the Ackerman Lab.

Conflict of interest

The authors declare that the research was conducted in the absence of any commercial or financial relationships that could be construed as a potential conflict of interest.

Publisher's note

Supplementary material

The Supplementary Material for this article can be found online at: https://www.frontiersin.org/articles/10.3389/fmech.2024.1411361/full#supplementary-material

SUPPLEMENTARY FIGURE S1
Characteristics of the hydrodynamic conditions in the flow chamber at the location at which the collector was placed. Flow profiles are based on the 1/7th power law solution for a turbulent flat plate boundary layer. Symbols represent measured values obtained at heights of 2.5, 3.5 and 4 cm above the bottom at 5, 10 and 25 cm s^{-1} (data were not obtained at the other chamber velocities).

SUPPLEMENTARY FIGURE S2
Drawing of the maximum longitudinal deflection of collectors at different collector Reynolds numbers as viewed from the side of the flow chamber (flow is from left to right). The neutral position of the collector is indicated by dashed lines. Collectors are 0.15 cm in diameter (d_c = 1.5 mm).

References

Ackerman, J. D. (1999). Effect of velocity on the filter feeding of dreissenid mussels (*Dreissena polymorpha* and *Dreissena bugensis*): implications for trophic dynamics. *Can. J. Fish. Aquatic Sci.* 56, 1551–1561. doi:10.1139/f99-079

Ackerman, J. D. (2000). Abiotic pollen and pollination: ecological, functional, and evolutionary perspectives. *Plant Syst. Evol.* 222, 167–185. doi:10.1007/978-3-7091-6306-1_9

Ackerman, J. D. (2006). "Sexual reproduction of seagrasses: pollination in the marine context," in *Seagrasses: biology, ecology and conservation*. Editors A. W. D. Larkum, J. J. Orth, and C. M. Duarte (Dordrecht: Springer), 89–109.

Ackerman, J. D., and Nishizaki, M. T. (1999). How stiff is a French fry? – Teaching biomechanics to biology students. *J. Biol. Educ.* 34, 36–40. doi:10.1080/00219266.1999.9655681

Armitage, J. M., Franco, A., Gomez, S., and Cousins, I. T. (2008). Modeling the potential influence of particle deposition on the accumulation of organic contaminants by submerged aquatic vegetation. *Environ. Sci. Technol.* 42, 4052–4059. doi:10.1021/es702439u

Boller, M. L., Swain, T. D., and Lasker, H. R. (2002). Skeletal morphology and material properties of a fragmenting gorgonian coral. *Mar. Ecol. Prog. Ser.* 228, 131–141. doi:10.3354/meps228131

Boudina, M., Gosselin, F. P., and Étienne, S. (2021). Vortex-induced vibrations: a soft coral feeding strategy? *J. Fluid Mech.* 916, A50. doi:10.1017/jfm.2021.252

Bourguet, R., Karniadakis, S., and Triantafyllou, M. S. (2011). Vortex induced vibrations of a long flexible cylinder in shear flow. *J. Fluid Mech.* 667, 342–382. doi:10.1017/jfm.2011.90

Chamberlain, J. A., Jr. (1978). Mechanical properties of coral skeleton: compressive strength and its adaptive significance. *Paleobiology* 4, 419–435. doi:10.1017/s0094837300006163

de Langre, E. (2008). Effects of wind on plants. *Annu. Rev. Fluid Mech.* 40, 141–168. doi:10.1146/annurev.fluid.40.111406.102135

de Langre, E. (2019). Plant vibrations at all scales: a review. *J. Exp. Bot.* 70, 3521–3531. doi:10.1093/jxb/erz209

Ellis, B., and Smith, R. (2000). *Polymer database- A property database: web version*. Boca Raton, FL: Chapman and Hall/CRC Press. Available at: https://poly.chemnetbase.com/intro/index.jsp#prop (Accessed October 31, 2015).

Engineering ToolBox. (2003). Young's modulus - tensile and yield strength for common materials. Available at: https://www.engineeringtoolbox.com/young-modulus-d_417.html (Accessed August 09, 2018).

Espinosa-Gayosso, A., Ghisalberti, M., Ivey, G. N., and Jones, N. L. (2012). Particle capture and low-Reynolds-number flow around a circular cylinder. *J. Fluid Mech.* 710, 362–378. doi:10.1017/jfm.2012.367

Espinosa-Gayosso, A., Ghisalberti, M., Ivey, G. N., and Jones, N. L. (2013). Particle capture by a circular cylinder in the vortex-shedding regime. *J. Fluid Mech.* 733, 171–188. doi:10.1017/jfm.2013.407

Espinosa-Gayosso, A., Ghisalberti, M., Ivey, G. N., and Jones, N. L. (2015). Density-ratio effects on the capture of suspended particles in aquatic systems. *J. Fluid Mech.* 783, 191–210. doi:10.1017/jfm.2015.557

Espinosa-Gayosso, A., Ghisalberti, M., Shimeta, J., and Ivey, G. N. (2021). On predicting particle capture rates in aquatic ecosystems. *PLOS ONE* 16, e0261400. doi:10.1371/journal.pone.0261400

Gosselin, F. P. (2019). Mechanics of a plant in fluid flow. *J. Exp. Bot.* 70, 3533–3548. doi:10.1093/jxb/erz288

Haugen, N. E. L., and Kragset, S. (2010). Particle impaction on a cylinder in a cross flow as function of Stokes and Reynolds numbers. *J. Fluid Mech.* 661, 239–261. doi:10.1017/s0022112010002946

Jeyasuria, P., and Lewis, J. C. (1987). Mechanical properties of the axial skeleton in gorgonians. *Coral Reefs* 5, 213–219. doi:10.1007/bf00300967

Jordan, T., Pierce, J., and Correll, D. (1986). Flux of particulate matter in the tidal marshes and subtidal shallows of the rhode river estuary. *Estuaries* 9, 310–319. doi:10.2307/1351410

Krick, J., and Ackerman, J. D. (2015). Adding ecology to particle capture models: numerical simulations of capture on a moving cylinder in crossflow. *J. Theor. Biol.* 368, 13–26. doi:10.1016/j.jtbi.2014.12.003

Leonard, L. A., Hine, A. C., and Luther, M. E. (1995). Surficial sediment transport and deposition processes in a *Juncus-roemerianus* marsh, west-central Florida. *J. Coast. Res.* 11, 322–336.

McCombe, D., and Ackerman, J. D. (2018). Collector motion affects particle capture in physical models and in wind pollination. *Am. Nat.* 192, 81–93. doi:10.1086/697551

Miler, O., Albayrak, I., Nikora, V., and O'Hare, M. (2012). Biomechanical properties of aquatic plants and their effects on plant–flow interactions in streams and rivers. *Aquat. Sci.* 74, 31–44. doi:10.1007/s00027-011-0188-5

Niklas, K. J. (1985). The aerodynamics of wind pollination. *Botanical Rev.* 51 (3), 328–386. doi:10.1007/bf02861079

Niklas, K. J. (1992). *Plant biomechanics*. Chicago, IL: University of Chicago Press.

Nowell, A. R. M., and Jumars, P. A. (1987). Flumes: theoretical and experimental considerations for simulation of benthic environments. *Oceanogr. Mar. Biol. Annu. Rev.* 25, 91–112.

Palmer, M. R., Nepf, H. M., Pettersson, T. J., and Ackerman, J. D. (2004). Observations of particle capture on a cylindrical collector: implications for particle accumulation and removal in aquatic systems. *Limnol. Oceanogr.* 49, 76–85. doi:10.4319/lo.2004.49.1.0076

Raju, N., and Meiburg, E. (1995). The accumulation and dispersion of heavy particles in forced two-dimensional mixing layers. Part 2: the effect of gravity. *Phys. Fluids* 7, 1241–1264. doi:10.1063/1.868581

Rubenstein, D. I., and Koehl, M. A. R. (1977). The mechanisms of filter feeding: some theoretical considerations. *Am. Nat.* 111 (981), 981–994. doi:10.1086/283227

Shimeta, J., and Jumars, P. A. (1991). Physical mechanisms and rates of particle capture by suspension-feeders. Oceanography and Marine Biology. *Annu. Rev.* 29, 191–257.

Shukla, S., Govardhan, R. N., and Arakeri, J. H. (2013). Dynamics of a flexible splitter plate in the wake of a circular cylinder. *J. Fluids Struct.* 41, 127–134. doi:10.1016/j.jfluidstructs.2013.03.002

Spielman, L. A. (1977). Particle capture from low speed laminar flows. *Annu. Rev. Fluid Mech.* 9, 297–319. doi:10.1146/annurev.fl.09.010177.001501

Sumer, B. M., and Fredsøe, J. (2006). *Hydrodynamics around cylindrical structures*. Revised Edn. Singapore: World Scientific.

Tongue, B. H. (2002). *Principles of vibrations*. 2nd Edn. New York, NY: Oxford University Press.

Vanden Byllaardt, J., and Ackerman, J. D. (2014). Hydrodynamic habitat influences suspension feeding by unionid mussels in freshwater ecosystems. *Freshw. Biol.* 59, 1187–1196. doi:10.1111/fwb.12339

Vandiver, K. J., and Jong, Y. J. (1987). The relationship between in-line and cross-flow vortex-induced vibration of cylinders. *J. Fluids Struct.* 1, 381–399. doi:10.1016/s0889-9746(87)90279-9

Vogel, S. (1988). *Life's devices*. Princeton, NJ: Princeton University Press.

Vogel, S. (1994). *Life in moving fluids*. 2 revised Edn. Princeton, NJ: Princeton University Press.

Wainwright, S. A., Biggs, W. D., Currey, J. D., and Gosline, J. M. (1982). *Mechanical design in organisms*. Princeton: Princeton University Press.

White, F. M. (2011). *Fluid mechanics*. 17th Edn. New York, NY: McGraw Hill.

Frontiers in Marine Science

Explores ocean-based solutions for emerging global challenges

The third most-cited marine and freshwater biology journal, advancing our understanding of marine systems and addressing global challenges including overfishing, pollution, and climate change.

Discover the latest Research Topics

See more →

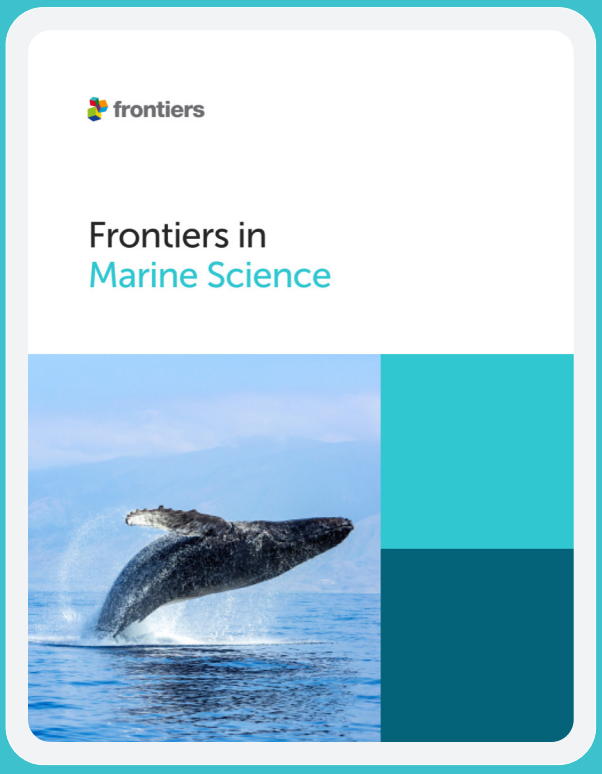

Frontiers

Avenue du Tribunal-Fédéral 34
1005 Lausanne, Switzerland
frontiersin.org

Contact us

+41 (0)21 510 17 00
frontiersin.org/about/contact